Regular Article

HE-LHC: The High-Energy Large Hadron Collider

Future Circular Collider Conceptual Design Report Volume 4

A. Abada[33], M. Abbrescia[118,258], S.S. AbdusSalam[219], I. Abdyukhanov[17], J. Abelleira Fernandez[143], A. Abramov[205], M. Aburaia[285], A.O. Acar[239], P.R. Adzic[288], P. Agrawal[80], J.A. Aguilar-Saavedra[47], J.J. Aguilera-Verdugo[107], M. Aiba[192], I. Aichinger[65], G. Aielli[135,273], A. Akay[239], A. Akhundov[46], H. Aksakal[146], J.L. Albacete[47], S. Albergo[121,261], A. Alekou[313], M. Aleksa[65], R. Aleksan[40], R.M. Alemany Fernandez[65], Y. Alexahin[71], R.G. Alía[65], S. Alioli[127], N. Alipour Tehrani[65], B.C. Allanach[299], P.P. Allport[291], M. Altınlı[63,113], W. Altmannshofer[298], G. Ambrosio[71], D. Amorim[65], O. Amstutz[162], L. Anderlini[124,263], A. Andreazza[128,267], M. Andreini[65], A. Andriatis[168], C. Andris[166], A. Andronic[346], M. Angelucci[116], F. Antinori[130,268], S.A. Antipov[65], M. Antonelli[116], M. Antonello[128,265], P. Antonioli[119], S. Antusch[287], F. Anulli[134,272], L. Apolinário[159], G. Apollinari[71], A. Apollonio[65], D. Appelö[302], R.B. Appleby[303,313], A. Apyan[71], A. Apyan[1], A. Arbey[337], A. Arbuzov[18], G. Arduini[65], V. Arı[10], S. Arias[67,311], N. Armesto[109], R. Arnaldi[137,275], S.A. Arsenyev[65], M. Arzeo[65], S. Asai[237], E. Aslanides[32], R.W. Aßmann[50], D. Astapovych[229], M. Atanasov[65], S. Atieh[65], D. Attié[40], B. Auchmann[65], A. Audurier[120,260], S. Aull[65], S. Aumon[65], S. Aune[40], F. Avino[65], G. Avrillaud[84], G. Aydın[174], A. Azatov[138,215], G. Azuelos[242], P. Azzi[130,268], O. Azzolini[117], P. Azzurri[133,216], N. Bacchetta[130,268], E. Bacchiocchi[267], H. Bachacou[40], Y.W. Baek[75], V. Baglin[65], Y. Bai[333], S. Baird[65], M.J. Baker[335], M.J. Baldwin[168], A.H. Ball[65], A. Ballarino[65], S. Banerjee[55], D.P. Barber[50,318], D. Barducci[138,215], P. Barjhoux[3], D. Barna[173], G.G. Barnaföldi[173], M.J. Barnes[65], A. Barr[191], J. Barranco García[57], J. Barreiro Guimarães da Costa[98], W. Bartmann[65], V. Baryshevsky[96], E. Barzi[71], S.A. Bass[54], A. Bastianin[267], B. Baudouy[40], F. Bauer[40], M. Bauer[55], T. Baumgartner[233], I. Bautista-Guzmán[16], C. Bayındır[20,83], F. Beaudette[33], F. Bedeschi[133,216], M. Béguin[65], I. Bellafont[7], L. Bellagamba[119,259], N. Bellegarde[65], E. Belli[134,209,272], E. Bellingeri[44], F. Bellini[65], G. Bellomo[128,267], S. Belomestnykh[71], G. Bencivenni[116], M. Benedikt[65], G. Bernardi[33], J. Bernardi[233], C. Bernet[33,337], J.M. Bernhardt[3], C. Bernini[44], C. Berriaud[40], A. Bertarelli[65], S. Bertolucci[119,259], M.I. Besana[192], M. Besançon[40], O. Beznosov[318], P. Bhat[71], C. Bhat[71], M.E. Biagini[116], J.-L. Biarrotte[33], A. Bibet Chevalier[28], E.R. Bielert[306], M. Biglietti[136,274], G.M. Bilei[132,271], B. Bilki[307], C. Biscari[7], F. Bishara[50,191], O.R. Blanco-García[116], F.R. Blánquez[65], F. Blekman[342], A. Blondel[305], J. Blümlein[50], T. Boccali[133,216], R. Boels[85], S.A. Bogacz[238], A. Bogomyagkov[24], O. Boine-Frankenheim[229], M.J. Boland[323], S. Bologna[292], O. Bolukbasi[113], M. Bomben[33], S. Bondarenko[18], M. Bonvini[134,272], E. Boos[222], B. Bordini[65], F. Bordry[65], G. Borghello[65,276], L. Borgonovi[119,259], S. Borowka[65], D. Bortoletto[191], D. Boscherini[119,259], M. Boscolo[116], S. Boselli[131,270], R.R. Bosley[291], F. Bossu[33], C. Botta[65], L. Bottura[65], R. Boughezal[12], D. Boutin[40], G. Bovone[44], I. Božović Jelisavčić[341], A. Bozbey[239], C. Bozzi[123,262], D. Bozzini[65], V. Braccini[44], S. Braibant-Giacomelli[119,259], J. Bramante[194,201],

P. Braun-Munzinger[78], J.A. Briffa[312], D. Britzger[170], S.J. Brodsky[226],
J.J. Brooke[292], R. Bruce[65], P. Brückman De Renstrom[100], E. Bruna[137,275],
O. Brüning[65], O. Brunner[65], K. Brunner[173], P. Bruzzone[57], X. Buffat[65],
E. Bulyak[182], F. Burkart[65], H. Burkhardt[65], J.-P. Burnet[65], F. Butin[65],
D. Buttazzo[133,216], A. Butterworth[65], M. Caccia[128,265], Y. Cai[226],
B. Caiffi[125,264], V. Cairo[226], O. Cakir[10], R. Calaga[65], S. Calatroni[65],
G. Calderini[33], G. Calderola[117], A. Caliskan[79], D. Calvet[31,282],
M. Calviani[65], J.M. Camalich[103], P. Camarri[135,273], M. Campanelli[284],
T. Camporesi[65], A.C. Canbay[10], A. Canepa[71], E. Cantergiani[84],
D. Cantore-Cavalli[128,267], M. Capeans[65], R. Cardarelli[135,273], U. Cardella[162],
A. Cardini[120], C.M. Carloni Calame[131,270], F. Carra[65], S. Carra[128,267],
A. Carvalho[159], S. Casalbuoni[147], J. Casas[7], M. Cascella[284], P. Castelnovo[267],
G. Castorina[134,272], G. Catalano[267], V. Cavasinni[133,216], E. Cazzato[287],
E. Cennini[65], A. Cerri[329], F. Cerutti[65], J. Cervantes[65], I. Chaikovska[33],
J. Chakrabortty[88], M. Chala[55], M. Chamizo-Llatas[21], H. Chanal[31], D. Chanal[28],
S. Chance[33], A. Chancé[40], P. Charitos[65], J. Charles[5], T.K. Charles[316],
S. Chattopadhyay[187], R. Chehab[154], S.V. Chekanov[12], N. Chen[175],
A. Chernoded[222], V. Chetvertkova[78], L. Chevalier[40], G. Chiarelli[133,216],
G. Chiarello[134,209,272], M. Chiesa[145], P. Chiggiato[65], J.T. Childers[12],
A. Chmielińska[57,65], A. Cholakian[80,168], P. Chomaz[40], M. Chorowski[348],
W. Chou[98], M. Chrzaszcz[100], E. Chyhyrynets[117], G. Cibinetto[123,262], A.K. Ciftci[141],
R. Ciftci[59], R. Cimino[116], M. Ciuchini[136,274], P.J. Clark[303], Y. Coadou[4,26,32],
M. Cobal[138,276], A. Coccaro[125], J. Cogan[32,33], E. Cogneras[30], F. Collamati[134,272],
C. Colldelram[7], P. Collier[65], J. Collot[33,283], R. Contino[216], F. Conventi[129],
C.T.A. Cook[65], L. Cooley[11,178], G. Corcella[116,117], A.S. Cornell[330], G.H. Corral[36],
H. Correia-Rodrigues[65], F. Costanza[33], P. Costa Pinto[65], F. Couderc[40],
J. Coupard[65], N. Craig[297], I. Crespo Garrido[336], A. Crivellin[192], J.F. Croteau[84],
M. Crouch[65], E. Cruz Alaniz[143], B. Curé[65], J. Curti[168], D. Curtin[331], M. Czech[65],
C. Dachauer[162], R.T. D'Agnolo[226], M. Daibo[74], A. Dainese[130,268], B. Dalena[40],
A. Daljevec[65], W. Dallapiazza[86], L. D'Aloia Schwartzentruber[27], M. Dam[185],
G. D'Ambrosio[129], S.P. Das[250], S. DasBakshi[88], W. da Silva[33], G.G. da Silveira[252],
V. D'Auria[57], S. D'Auria[267], A. David[65], T. Davidek[69], A. Deandrea[33,337],
J. de Blas[130,268], C.J. Debono[312], S. De Curtis[124,263], N. De Filippis[118,258],
D. de Florian[110], S. Deghaye[65], S.J. de Jong[95,176], C. Del Bo[267], V. Del Duca[137,275],
D. Delikaris[65], F. Deliot[40], A. Dell'Acqua[65], L. Delle Rose[124,263], M. Delmastro[153],
E. De Lucia[116], M. Demarteau[12], D. Denegri[40], L. Deniau[65], D. Denisov[71],
H. Denizli[2], A. Denner[334], D. d'Enterria[65], G. de Rijk[65], A. De Roeck[65], F. Derue[33],
O. Deschamps[33], S. Descotes-Genon[33], P.S.B. Dev[343], J.B. de Vivie de Régie[33],
R.K. Dewanjee[179], A. Di Ciaccio[135,273], A. Di Cicco[116], B.M. Dillon[102],
B. Di Micco[136,274], P. Di Nezza[116], S. Di Vita[128,267], A. Doblhammer[233],
A. Dominjon[153], M. D'Onofrio[310], F. Dordei[65], A. Drago[116], P. Draper[306],
Z. Drasal[69], M. Drewes[148], L. Duarte[249], I. Dubovyk[85], P. Duda[348], A. Dudarev[65],
L. Dudko[222], D. Duellmann[65], M. Dünser[65], T. du Pree[176], M. Durante[40],
H. Duran Yildiz[10], S. Dutta[225], F. Duval[65], J.M. Duval[41,283], Y. Dydyshka[56],
B. Dziewit[326], S. Eisenhardt[303], M. Eisterer[233], T. Ekelof[338], D. El Khechen[65],
S.A. Ellis[226], J. Ellis[150], J.A. Ellison[318], K. Elsener[65], M. Elsing[65], Y. Enari[237],
C. Englert[211], H. Eriksson[165], K.J. Eskola[308], L.S. Esposito[65], O. Etisken[10],
E. Etzion[234], P. Fabbricatore[125,264], A. Falkowski[33], A. Falou[154], J. Faltova[69],
J. Fan[22], L. Fanò[132,271], A. Farilla[136,274], R. Farinelli[123,262], S. Farinon[125,264],
D.A. Faroughy[102], S.D. Fartoukh[65], A. Faus-Golfe[33], W.J. Fawcett[299],
G. Felici[116], L. Felsberger[164], C. Ferdeghini[43], A.M. Fernandez Navarro[35],
A. Fernández-Téllez[16], J. Ferradas Troitino[65,305], G. Ferrara[128,267], R. Ferrari[131,270],
L. Ferreira[65], P. Ferreira da Silva[65], G. Ferrera[127,267], F. Ferro[125,264],

M. Fiascaris[65], S. Fiorendi[127], C. Fiorio[267], O. Fischer[147,287], E. Fischer[78],
W. Flieger[326], M. Florio[267], D. Fonnesu[65], E. Fontanesi[119,259], N. Foppiani[80],
K. Foraz[65], D. Forkel-Wirth[65], S. Forte[267], M. Fouaidy[90], D. Fournier[33],
T. Fowler[65], J. Fox[227], P. Francavilla[133,216], R. Franceschini[136,274], S. Franchino[278],
E. Franco[134,272], A. Freitas[197], B. Fuks[157], K. Furukawa[82], S.V. Furuseth[57],
E. Gabrielli[138,276], A. Gaddi[65], M. Galanti[321], E. Gallo[50], S. Ganjour[40],
J. Gao[192], J. Gao[98], V. Garcia Diaz[117], M. García Pérez[65], L. García Tabarés[35],
C. Garion[65], M.V. Garzelli[277,281], I. Garzia[123,262], S.M. Gascon-Shotkin[33,337],
G. Gaudio[131,270], P. Gay[31,33], S.-F. Ge[237,293], T. Gehrmann[335], M.H. Genest[33,283],
R. Gerard[65], F. Gerigk[65], H. Gerwig[65], P. Giacomelli[119,259], S. Giagu[134,272],
E. Gianfelice-Wendt[71], F. Gianotti[65], F. Giffoni[29,267], S.S. Gilardoni[65],
M. Gil Costa[35], M. Giovannetti[116], M. Giovannozzi[65], P. Giubellino[78,137],
G.F. Giudice[65], A. Giunta[255], L.K. Gladilin[222], S. Glukhov[24], J. Gluza[326],
G. Gobbi[65], B. Goddard[65], F. Goertz[169], T. Golling[305], V.P. Goncalves[253],
R. Gonçalo[159], L.A. Gonzalez Gomez[116], S. Gorgi Zadeh[322], G. Gorine[57],
E. Gorini[126,257], S.A. Gourlay[161], L. Gouskos[297], F. Grancagnolo[126,266],
A. Grassellino[71], A. Grau[147], E. Graverini[335], H.M. Gray[161], Ma. Greco[136,274],
Mi. Greco[136,274], J.-L. Grenard[65], O. Grimm[60], C. Grojean[50], V.A. Gromov[144],
J.F. Grosse-Oetringhaus[65], A. Grudiev[65], K. Grzanka[326], J. Gu[142],
D. Guadagnoli[153], V. Guidi[123,262], S. Guiducci[116], G. Guillermo Canton[36],
Y.O. Günaydin[146], R. Gupta[21], R.S. Gupta[55], J. Gutierrez[89], J. Gutleber[65],
C. Guyot[40], V. Guzey[195], C. Gwenlan[191], C. Haberstroh[231], B. Hacışahinoğlu[113],
B. Haerer[65], K. Hahn[188], T. Hahn[345], A. Hammad[287], C. Han[237], M. Hance[298],
A. Hannah[212], P.C. Harris[168], C. Hati[31,282], S. Haug[290], J. Hauptman[111],
V. Haurylavets[96], H.-J. He[220], A. Hegglin[218,221], B. Hegner[21], K. Heinemann[318],
S. Heinemeyer[106], C. Helsens[65], A. Henriques[65], A. Henriques[65], P. Hernandez[105],
R.J. Hernández-Pinto[246], J. Hernandez-Sanchez[16], T. Herzig[99], I. Hiekkanen[165],
W. Hillert[277], T. Hoehn[232], M. Hofer[233], W. Höfle[65], F. Holdener[221], S. Holleis[233],
B. Holzer[65], D.K. Hong[200], C.G. Honorato[16], S.C. Hopkins[65], J. Hrdinka[65],
F. Hug[142], B. Humann[233], H. Humer[13], T. Hurth[142], A. Hutton[238], G. Iacobucci[305],
N. Ibarrola[65], L. Iconomidou-Fayard[33], K. Ilyina-Brunner[65], J. Incandela[297],
A. Infantino[65], V. Ippolito[134,272], M. Ishino[237], R. Islam[87], H. Ita[8], A. Ivanovs[204],
S. Iwamoto[268], A. Iyer[129], S. Izquierdo Bermudez[65], S. Jadach[100], D.O. Jamin[101],
P. Janot[65], P. Jarry[40], A. Jeff[37,65], P. Jenny[166], E. Jensen[65], M. Jensen[67],
X. Jiang[280], J.M. Jiménez[65], M.A. Jones[65], O.R. Jones[65], J.M. Jowett[65], S. Jung[217],
W. Kaabi[33], M. Kado[65,134,272], K. Kahle[65], L. Kalinovskaya[56], J. Kalinowski[332],
J.F. Kamenik[102], K. Kannike[179], S.O. Kara[10,186], H. Karadeniz[76], V. Karaventzas[65],
I. Karpov[65], S. Kartal[113], A. Karyukhin[94], V. Kashikhin[71], J. Katharina Behr[50],
U. Kaya[10,239], J. Keintzel[233], P.A. Keinz[340], K. Keppel[117], R. Kersevan[65],
K. Kershaw[65], H. Khanpour[210,325], S. Khatibi[49,210], M. Khatiri Yanehsari[210],
V.V. Khoze[55], J. Kieseler[65], A. Kilic[245], A. Kilpinen[165], Y.-K. Kim[300],
D.W. Kim[75], U. Klein[310], M. Klein[310], F. Kling[295], N. Klinkenberg[65,68],
S. Klöppel[231], M. Klute[168], V.I. Klyukhin[222], M. Knecht[32,33], B. Kniehl[85],
F. Kocak[245], C. Koeberl[184], A.M. Kolano[65], A. Kollegger[285], K. Kołodziej[326],
A.A. Kolomiets[144], J. Komppula[65], I. Koop[24], P. Koppenburg[176], M. Koratzinos[168],
M. Kordiaczyńska[326], M. Korjik[96], O. Kortner[345], P. Kostka[310], W. Kotlarski[231],
C. Kotnig[65], T. Köttig[65], A.V. Kotwal[54], A.D. Kovalenko[144], S. Kowalski[326],
J. Kozaczuk[306], G.A. Kozlov[144], S.S. Kozub[144], A.M. Krainer[65], T. Kramer[65],
M. Krämer[203], M. Krammer[65], A.A. Krasnov[24], F. Krauss[55], K. Kravalis[204],
L. Kretzschmar[340], R.M. Kriske[168], H. Kritscher[184], P. Krkotic[7], H. Kroha[170],
M. Kucharczyk[100], S. Kuday[112], A. Kuendig[162], G. Kuhlmann[72], A. Kulesza[346],
M. Kumar[57], M. Kumar[330], A. Kusina[100], S. Kuttimalai[226], M. Kuze[240],
T. Kwon[217], F. Lackner[65], M. Lackner[285], E. La Francesca[116,272], M. Laine[290],

G. Lamanna[153], S. La Mendola[65], E. Lançon[21], G. Landsberg[22], P. Langacker[91],
C. Lange[65], A. Langner[65], A.J. Lankford[295], J.P. Lansberg[33], T. Lari[127],
P.J. Laycock[310], P. Lebrun[66], A. Lechner[65], K. Lee[217], S. Lee[25,152], R. Lee[24],
T. Lefevre[65], P. Le Guen[65], T. Lehtinen[202], S.B. Leith[280], P. Lenzi[124,263],
E. Leogrande[65], C. Leonidopoulos[299], I. Leon-Monzon[246], G. Lerner[65],
O. Leroy[32,33], T. Lesiak[100], P. Lévai[173], A. Leveratto[44], E. Levichev[24], G. Li[98],
S. Li[220], R. Li[351], D. Liberati[42], M. Liepe[45], D.A. Lissauer[21], Z. Liu[314],
A. Lobko[96], E. Locci[40], E. Logothetis Agaliotis[65,183], M.P. Lombardo[124,263],
A.J. Long[317], C. Lorin[40], R. Losito[65], A. Louzguiti[65], I. Low[12], D. Lucchesi[130,268],
M.T. Lucchini[198], A. Luciani[62], M. Lueckhof[277], A.J.G. Lunt[65], M. Luzum[251],
D.A. Lyubimtsev[144], M. Maggiora[137,275], N. Magnin[65], M.A. Mahmoud[70],
F. Mahmoudi[33,337], J. Maitre[28], V. Makarenko[96], A. Malagoli[44], J. Malclés[40],
L. Malgeri[65], P.J. Mallon[40], F. Maltoni[148], S. Malvezzi[127], O.B. Malyshev[212],
G. Mancinelli[32,33], P. Mandrik[94], P. Manfrinetti[44,264], M. Mangano[65], P. Manil[40],
M. Mannelli[65], G. Marchiori[33,155], F. Marhauser[238], V. Mariani[132,271],
V. Marinozzi[128,267], S. Mariotto[128,267], P. Marquard[51], C. Marquet[33],
T. Marriott-Dodington[65], R. Martin[65], O. Martin[171], J. Martin Camalich[103,248],
T. Martinez[35], H. Martinez Bruzual[131,270], M.I. Martínez-Hernández[16],
D.E. Martins[254], S. Marzani[125,264], D. Marzocca[138], L. Marzola[179],
S. Masciocchi[78,278], I. Masina[123,262], A. Massimiliano[128], A. Massironi[65],
T. Masubuchi[237], V.A. Matveev[144], M.A. Mazzoni[134], M. McCullough[65],
P.A. McIntosh[212], P. Meade[228], L. Medina[247], A. Meier[162], J. Meignan[65],
B. Mele[134,272], J.G. Mendes Saraiva[159], F. Menez[28], M. Mentink[65], E. Meoni[122,256],
P. Meridiani[128,267], M. Merk[176], P. Mermod[305], V. Mertens[65], L. Mether[57],
E. Métral[65], M. Migliorati[134,272], A. Milanese[65], C. Milardi[116], G. Milhano[159],
B.L. Militsyn[212], F. Millet[41,283], I. Minashvili[140,144], J.V. Minervini[168],
L.S. Miralles[65], D. Mirarchi[65], S. Mishima[82], D.P. Missiaen[65], G. Mitselmakher[304],
T. Mitshuhashi[82], J. Mnich[50], M. Mohammadi Najafabadi[210], R.N. Mohapatra[314],
N. Mokhov[71], J.G. Molson[65], R. Monge[7], C. Montag[21], G. Montagna[131,270],
S. Monteil[31,33], G. Montenero[192], E. Montesinos[65], F. Moortgat[65], N. Morange[154],
G. Morello[116], M. Moreno Llácer[65], M. Moretti[123,262], S. Moretti[213], A.K. Morley[65],
A. Moros[233], I. Morozov[24], V. Morretta[267], M. Morrone[65], A. Mostacci[134,272],
S. Muanza[32,33], N. Muchnoi[24], M. Mühlegger[162], M. Mulder[176], M. Mulders[65],
B. Müller[21,54], F. Müller[99], A.-S. Müller[147], J. Munilla[35], M.J. Murray[309],
Y. Muttoni[65], S. Myers[65], M. Mylona[65], J. Nachtman[307], T. Nakamoto[82],
M. Nardecchia[65], G. Nardini[327], P. Nason[127], Z. Nergiz[239], A.V. Nesterenko[144],
J.A. Netto[318] A. Nettsträter[72], C. Neubüser[65], J. Neundorf[50], F. Niccoli[65],
O. Nicrosini[131,270], Y. Nie[65], U. Niedermayer[229], J. Niedziela[65], A. Niemi[65],
S.A. Nikitin[24], A. Nisati[134,272], J.M. No[106], M. Nonis[65], Y. Nosochkov[226],
M. Novák[173], A. Novokhatski[226], J.M. O'Callaghan[279], C. Ochando[158],
S. Ogur[20], K. Ohmi[82], K. Oide[65], V.A. Okorokov[181], Y. Okumura[237],
C. Oleari[127], F.I. Olness[224], Y. Onel[307], M. Ortino[233], J. Osborne[65],
P. Osland[289], T. Otto[65], K.Y. Oyulmaz[2], A. Ozansoy[10], V. Özcan[20],
K. Özdemir[196], C.E. Pagliarone[53,113,115], H.F. Pais da Silva[65], E. Palmieri[117],
L. Palumbo[134,272], A. Pampaloni[125,264], R.-Q. Pan[350], M. Panareo[126,266],
O. Panella[132,271], G. Panico[263], G. Panizzo[138,276], A.A. Pankov[77], V. Pantsyrny[17],
C.G. Papadopoulos[177], A. Papaefstathiou[176], Y. Papaphilippou[65], M.A. Parker[299],
V. Parma[65], M. Pasquali[65], S.K. Patra[88], R. Patterson[45], H. Paukkunen[308],
F. Pauss[60], S. Peggs[21], J.-P. Penttinen[202], G. Peón[65], E.E. Perepelkin[144],
E. Perez[65], J.C. Perez[65], G. Perez[344], F. Pérez[7], E. Perez Codina[65],
J. Perez Morales[35], M. Perfilov[222], H. Pernegger[65], M. Peruzzi[65], C. Pes[40],
K. Peters[50], S. Petracca[114], F. Petriello[188], L. Pezzotti[131,270], S. Pfeiffer[233],
F. Piccinini[131,270], T. Pieloni[57], M. Pierini[65], H. Pikhartova[205], G. Pikurs[204],

E. Pilicer[245], P. Piminov[24], C. Pira[117], R. Pittau[47], W. Płaczek[167],
M. Plagge[65,190], T. Plehn[278], M.-A. Pleier[21], M. Płoskoń[161], M. Podeur[328],
H. Podlech[92], T. Podzorny[65], L. Poggioli[33], A. Poiron[58], G. Polesello[131,270],
M. Poli Lener[116], A. Polini[119,259], J. Polinski[348], S.M. Polozov[181], L. Ponce[65],
M. Pont[7], L. Pontecorvo[134,272], T. Portaluri[60], K. Potamianos[50], C. Prasse[72],
M. Prausa[8], A. Preinerstorfer[13], E. Premat[27], T. Price[291], M. Primavera[126],
F. Prino[137,275], M. Prioli[128], J. Proudfoot[12], A. Provino[44], T. Pugnat[40],
N. Pukhaeva[144], S. Puławski[326], D. Pulikowski[65,347], G. Punzi[133,216], M. Putti[264],
A. Pyarelal[286], H. Quack[231], M. Quispe[7], A. Racioppi[179], H. Rafique[313],
V. Raginel[78], M. Raidal[179], N.S. Ramírez-Uribe[104], M.J. Ramsey-Musolf[315],
R. Rata[65], P. Ratoff[38], F. Ravotti[65], P. Rebello Teles[34], M. Reboud[153],
S. Redaelli[65], E. Renner[233], A.E. Rentería-Olivo[105], M. Rescigno[134,272],
J. Reuter[50], A. Ribon[65], A.M. Ricci[125,264], W. Riegler[65], S. Riemann[51],
B. Riemann[230], T. Riemann[326], J.M. Rifflet[40], R.A. Rimmer[238], R. Rinaldesi[65],
L. Rinolfi[65], O. Rios Rubiras[65], T. Risselada[65], A. Rivetti[137,275], L. Rivkin[192],
T. Rizzo[226], T. Robens[206], F. Robert[27], A.J. Robson[305], E. Rochepault[40],
C. Roda[133,216], G. Rodrigo[107], M. Rodríguez-Cahuantzi[16], C. Rogan[309], M. Roig[3],
S. Rojas-Torres[246], J. Rojo[176], G. Rolandi[133,216], G. Rolando[65,192], P. Roloff[65],
A. Romanenko[71], A. Romanov[89], F. Roncarolo[65], A. Rosado Sanchez[16],
G. Rosaz[65], L. Rossi[65,267], A. Rossi[132,271], R. Rossmanith[50,147], B. Rousset[41,283],
C. Royon[309], X. Ruan[330], I. Ruehl[65], V. Ruhlmann-Kleider[40], R. Ruiz[55],
L. Rumyantsev[56,223], R. Ruprecht[147], A.I. Ryazanov[180], A. Saba[44], R. Sadykov[56],
D. Saez de Jauregui[147], M. Sahin[339], B. Sailer[23], M. Saito[237], F. Sala[50],
G.P. Salam[191], J. Salfeld-Nebgen[198], C.A. Salgado[109], S. Salini[267], J.M. Sallese[57],
T. Salmi[202], A. Salzburger[65], O.A. Sampayo[108], S. Sanfilippo[192], J. Santiago[47],
E. Santopinto[125], R. Santoro[128,265], A. Sanz Ull[61], X. Sarasola[192], I.H. Sarpün[6],
M. Sauvain[160], S. Savelyeva[231], R. Sawada[237], G.F.R. Sborlini[46,110], A. Schaffer[33],
M. Schaumann[65], M. Schenk[65], C. Scheuerlein[65], I. Schienbein[156], K. Schlenga[23],
H. Schmickler[65], R. Schmidt[65,229], D. Schoerling[65], A. Schoning[207], T. Schörner-
Sadenius[50], M. Schott[199], D. Schulte[65], P. Schwaller[142], C. Schwanenberger[50],
P. Schwemling[40], N. Schwerg[65], L. Scibile[65], A. Sciuto[121,261], E. Scomparin[137,275],
C. Sebastiani[134,272], B. Seeber[214,305], M. Segreti[40], P. Selva[162], M. Selvaggi[65],
C. Senatore[305], A. Senol[2], L. Serin[33], M. Serluca[153], N. Serra[335], A. Seryi[143],
L. Sestini[130,268], A. Sfyrla[305], M. Shaposhnikov[57], E. Shaposhnikova[65],
B.Y. Sharkov[144], D. Shatilov[24], J. Shelton[306], V. Shiltsev[71], I.P. Shipsey[191],
G.D. Shirkov[144], A. Shivaji[131,270], D. Shwartz[24], T. Sian[212,303,313], S. Sidorov[192],
A. Siemko[65], L. Silvestrini[134,272], N. Simand[28], F. Simon[170], B.K. Singh[14],
A. Siódmok[100], Y. Sirois[33], E. Sirtori[29], R. Sirvinskaite[163,212], B. Sitar[39],
T. Sjöstrand[311], P. Skands[172], E. Skordis[65,310], K. Skovpen[342], M. Skrzypek[100],
E. Slade[191], P. Slavich[157], R. Slovak[69], V. Smaluk[21], V. Smirnov[222],
W. Snoeys[65], L. Soffi[45], P. Sollander[65], O. Solovyanov[94], H.K. Soltveit[278],
H. Song[286], P. Sopicki[100], M. Sorbi[128,267], L. Spallino[116], M. Spannowsky[55],
B. Spataro[134,272], P. Sphicas[65], H. Spiesberger[199], P. Spiller[78], M. Spira[192],
T. Srivastava[88], J. Stachel[278], A. Stakia[65], J.L. Stanyard[65], E. Starchenko[180],
A.Y. Starikov[144], A.M. Staśto[236], M. Statera[128,267], R. Steerenberg[65],
J. Steggemann[65], A. Stenvall[202], F. Stivanello[117], D. Stöckinger[231], L.S. Stoel[65],
M. Stöger-Pollach[233], B. Strauss[48,97], M. Stuart[65], G. Stupakov[226], S. Su[286],
A. Sublet[65], K. Sugita[78], L. Sulak[19], M.K. Sullivan[226], S. Sultansoy[239],
T. Sumida[151], K. Suzuki[82], G. Sylva[44], M.J. Syphers[187], A. Sznajder[252],
M. Taborelli[65], N.A. Tahir[78], M. Takeuchi[237], E. Tal Hod[234], C. Tambasco[57],
J. Tanaka[237], K. Tang[168], I. Tapan[245], S. Taroni[319], G.F. Tartarelli[128,267],
G. Tassielli[126,266], L. Tavian[65], T.M. Taylor[65], G.N. Taylor[316], A.M. Teixeira[31,33],
G. Tejeda-Muñoz[16], V.I. Telnov[24,189], R. Tenchini[133,216], H.H.J. ten Kate[65],

K. Terashi[237], A. Tesi[124,263], M. Testa[116], C. Tetrel[28], D. Teytelman[52], J. Thaler[168], A. Thamm[65], S. Thomas[208], M.T. Tiirakari[65], V. Tikhomirov[96], D. Tikhonov[81], H. Timko[65], V. Tisserand[31,33], L.M. Tkachenko[144], J. Tkaczuk[41,283], J.P. Tock[65], B. Todd[65], E. Todesco[65], R. Tomás Garcia[65], D. Tommasini[65], G. Tonelli[133,216], F. Toral[35], T. Torims[204], R. Torre[65], Z. Townsend[65], R. Trant[65], D. Treille[65], L. Trentadue[127,269], A. Tricoli[21], A. Tricomi[121,261], W. Trischuk[331], I.S. Tropin[71], B. Tuchming[40], A.A. Tudora[65], B. Turbiarz[100], I. Turk Cakir[76], M. Turri[267], T. Tydecks[65], J. Usovitsch[241], J. Uythoven[65], R. Vaglio[44], A. Valassi[65], F. Valchkova[65], M.A. Valdivia Garcia[247], P. Valente[128,267], R.U. Valente[272], A.-M. Valente-Feliciano[238], G. Valentino[312], L. Vale Silva[329], J.M. Valet[28], R. Valizadeh[212], J.W.F. Valle[107], S. Vallecorsa[75], G. Vallone[161], M. van Leeuwen[176], U.H. van Rienen[322], L. van Riesen-Haupt[143], M. Varasteh[65], L. Vecchi[57], P. Vedrine[40], G. Velev[71], R. Veness[65], A. Ventura[126,257], W. Venturini Delsolaro[65], M. Verducci[136,274], C.B. Verhaaren[294], C. Vernieri[71], A.P. Verweij[65], O. Verwilligen[118,258], O. Viazlo[65], A. Vicini[128,267], G. Viehhauser[191], N. Vignaroli[130,268], M. Vignolo[44], A. Vitrano[40], I. Vivarelli[329], S. Vlachos[183], M. Vogel[280], D.M. Vogt[328], V. Völkl[93], P. Volkov[222], G. Volpini[128,267], J. von Ahnen[50], G. Vorotnikov[222], G.G. Voutsinas[65], V. Vysotsky[9], U. Wagner[65], R. Wallny[60], L.-T. Wang[300], R. Wang[12], K. Wang[349], B.F.L. Ward[15,345], T.P. Watson[139], N.K. Watson[291], Z. Wąs[100], C. Weiland[197], S. Weinzierl[199], C.P. Welsch[310], J. Wenninger[65], M. Widorski[65], U.A. Wiedemann[65], H.-U. Wienands[12], G. Wilkinson[191], P.H. Williams[212], A. Winter[291], A. Wohlfahrt[72], T. Wojtoń[100], D. Wollmann[65], J. Womersley[67], D. Woog[65], X. Wu[305], A. Wulzer[130,268], M.K. Yanehsari[210], G. Yang[149], H.J. Yang[220,244], W.-M. Yao[161], E. Yazgan[98], V. Yermolchik[96], A. Yilmaz[113], A. Yilmaz[76], H.-D. Yoo[217], S.A. Yost[235], T. You[299], C. Young[226], T.-T. Yu[320], F. Yu[142], A. Zaborowska[65], S.G. Zadeh[322], M. Zahnd[58], M. Zanetti[130,268], L. Zanotto[117], L. Zawiejski[100], P. Zeiler[64], M. Zerlauth[65], S.M. Zernov[73], G. Zevi Dell Porta[296], Z. Zhang[33], Y. Zhang[343], C. Zhang[193], H. Zhang[98], Z. Zhao[324], Y.-M. Zhong[19], J. Zhou[131,270], D. Zhou[82], P. Zhuang[243], G. Zick[3], F. Zimmermann[65,a], J. Zinn-Justin[40], L. Zivkovic[288], A.V. Zlobin[71], M. Zobov[116], J. Zupan[301], J. Zurita[147], and the FCC Collaboration[352]

[1] A.I. Alikhanyan National Science Laboratory (YerPhi), Yerevan, Armenia
[2] Abant Izzet Baysal University (AIBU), Bolu, Turkey
[3] Air Liquide Advanced Technologies (ALAT), Sassenage, France
[4] Aix-Marseille Université (AMU), Marseille, France
[5] Aix-Marseille Univ., Université de Toulon, CNRS, CPT (AMU/UTLN/CNRS/CPT), Marseille, France
[6] Akdeniz University (UAKDENIZ), Antalya, Turkey
[7] ALBA Synchrotron – Consorcio para la Construcción, Equipamiento y Explotación del Laboratorio de Luz Sincrotrón, Cerdanyola del Vallès (CELLS-ALBA), Cerdanyola del Vallès, Spain
[8] Albert-Ludwigs-Universität Freiburg (UFreiburg), Freiburg, Germany
[9] All-Russian Scientific Research and Development Cable Institute (VNIIKP), Moscow, Russia
[10] Ankara University (Ankara U), Tandogan, Ankara, Turkey
[11] Applied Superconductivity Center (ASC), Tallahassee, FL, USA
[12] Argonne National Laboratory (ANL), Argonne, IL, USA
[13] Austrian Institute of Technology (AIT), Vienna, Austria
[14] Banaras Hindu University (BHU), Varanasi, India
[15] Baylor University (Baylor), Waco, TX, USA
[16] Benemérita Universidad Autónoma de Puebla (BUAP), Puebla, Mexico
[17] Bochvar Institute of Inorganic Materials (VNIINM), Mosocw, Russia

[18] Bogoliubov Laboratory of Theoretical Physics (BLTP JINR), Dubna, Russia
[19] Boston University (BU), Boston, MA, USA
[20] Boğaziçi University (BOUN), Istanbul, Turkey
[21] Brookhaven National Laboratory (BNL), Upton, NY, USA
[22] Brown University (Brown), Providence, RI, USA
[23] BRUKER EST (Bruker), Hanau, Germany
[24] Budker Institute of Nuclear Physics (BINP), Novosibirsk, Russia
[25] Center for High Energy Physics (CHEP), Daegu, Republic of Korea
[26] Centre de Physique des Particules de Marseille (CPPM), Marseille, France
[27] Centre d'Etudes des Tunnels (CETU), Bron, France
[28] Centre d'études et d'expertise sur les risques, l'environnement, la mobilité et l'aménagement (CEREMA), Lyon, France
[29] Centre for Industrial Studies (CSIL), Milan, Italy
[30] Centre National de la Recherche Scientifique (CNRS), Aubière, France
[31] Centre National de la Recherche Scientifique (CNRS/IN2P3), Clermont-Ferrand, France
[32] Centre National de la Recherche Scientifique (CNRS), Marseille, France
[33] Centre National de la Recherche Scientifique (CNRS), Paris, France
[34] Centro Brasileiro de Pesquisas Físicas (CBPF), Rio de Janeiro, Brazil
[35] Centro de Investigaciones Energéticas, Medioambientales y Tecnológicas (CIEMAT), Madrid, Spain
[36] Centro de Investigacion y de Estudios Avanzados (CINVESTAV), Merdia, Mexico
[37] Cockcroft Institute (CI Daresbury), Daresbury, UK
[38] Cockcroft Institute (CI Lancaster), Lancaster, UK
[39] Comenius University (CU), Bratislava, Slovakia
[40] Commissariat à l'énergie atomique et aux énergies alternatives – Institut de Recherche sur les lois Fondamentales de l'Univers Saclay (CEA/DSM/Irfu Saclay), Gif-sur-Yvette, France
[41] Commissariat à l'énergie atomique et aux énergies alternatives – Institut Nanosciences et Cryogénie (CEA), Grenoble, France
[42] Consiglio Nazionale delle Ricerche (CNR), Milan, Italy
[43] Consiglio Nazionale delle Ricerche – Superconducting and other Innovative materials and devices institute (CNR-SPIN), Genoa, Italy
[44] Consiglio Nazionale delle Ricerche – Superconducting and other Innovative materials and devices institute (CNR-SPIN), Naples, Italy
[45] Cornell University (Cornell), Ithaca, NY, USA
[46] Departamento de Física Teórica, Universidad de València (UV), València, Spain
[47] Departamento de Física Teórica y del Cosmos and CAFPE, Universidad de Granada (UGR), Granada, Spain
[48] Department of Energy (DoE), Washington, DC, USA
[49] Department of Physics, University of Tehran (UT), Tehran, Iran
[50] Deutsches Elektronen Synchrotron (DESY), Hamburg, Germany
[51] Deutsches Elektronen Synchrotron (DESY ZEU), Zeuthen, Germany
[52] Dimtel, Inc. (Dimtel), San Jose, CA, USA
[53] Dipartimento di Ingegneria Civile e Meccanica, Università degli Studi di Cassino e del Lazio Meridionale (DICEM), Cassino, Italy
[54] Duke University (DU), Durham, NC, USA
[55] Durham University, Institute for Particle Physics Phenomenology (IPPP), Durham, UK
[56] Dzhelepov Laboratory of Nuclear Problems (DLNP JINR), Dubna, Russia
[57] Ecole polytechnique fédérale de Lausanne (EPFL), Lausanne, Switzerland
[58] Ecotec Environnement SA (Ecotec), Geneva, Switzerland
[59] Ege University (EgeU), Izmir, Turkey
[60] Eidgenössische Technische Hochschule Zürich (ETHZ), Zürich, Switzerland
[61] Eindhoven University of Technology (TU/e), Eindhoven, Netherlands
[62] Elle Marmi SARL (EM), Carrara, Italy
[63] Eskişehir Technical University (ESTU), Istanbul, Turkey

[64] Esslingen University of Applied Sciences (HS Esslingen), Göppingen, Germany
[65] European Organization for Nuclear Research (CERN), Geneva, Switzerland
[66] European Scientific Institute (ESI), Archamps, France
[67] European Spallation Source (ESS), Lund, Sweden
[68] Fachhochschule Südwestfalen (FH-SWF), Gelsenkirchen, Germany
[69] Faculty of Mathematics and Physics, Charles University Prague (CU), Prague, Czech Republic
[70] Fayoum University (FU), El-Fayoum, Egypt
[71] Fermi National Accelerator Laboratory (FNAL), Batavia, IL, USA
[72] Fraunhofer-Institut für Materialfluss und Logistik (FIML), Dortmund, Germany
[73] Fuel Company of Rosatom TVEL (TVEL), Moscow, Russia
[74] Fujikura Ltd. (Fujikura), Sakura City, Japan
[75] Gangneung-Wonju National University (GWNU), Gangneung-Wonju, Republic of Korea
[76] Giresun University (Giresun), Giresun, Turkey
[77] Gomel State Technical University (GSTU), Gomel, Belarus
[78] GSI Helmholtz Zentrum für Schwerionenforschung (GSI), Darmstadt, Germany
[79] Gümüşhane University (Gumushane), Gümüşhane, Turkey
[80] Harvard University (Harvard), Cambridge, MA, USA
[81] Helmholtz-Zentrum Berlin (HZB), Berlin, Germany
[82] High Energy Accelerator Research Organization (KEK), Tsukuba, Japan
[83] Işık University (Isikun), Istanbul, Turkey
[84] I-Cube Research (I-Cube), Toulouse, France
[85] II. Institut für Theoretische Physik, Universität Hamburg (UNITH), Hamburg, Germany
[86] ILF Consulting Engineers (ILF), Zürich, Switzerland
[87] Indian Institute of Technology Guwahati (IITG), Guwahati, India
[88] Indian Institute of Technology Kanpur (IITK), Uttar Pradesh, India
[89] Institut de Ciència de Materials de Barcelona (ICMAB-CSIC), Barcelona, Spain
[90] Institut de Physique Nucléaire d'Orsay (CNRS/IN2P3/IPNO), Orsay, France
[91] Institute for Advanced Study (IAS), Princeton, NJ, USA
[92] Institute for Applied Physics, Goethe University (IAP), Frankfurt, Germany
[93] Institute for Astro and Particle Physics, University of Innsbruck (UIBK), Innsbruck, Austria
[94] Institute for High Energy Physics of NRC "Kurchatov Institute" (IHEP), Protvino, Russia
[95] Institute for Mathematics, Astrophysics and Particle Physics, Radboud University (IMAPP), Nijmegen, Netherlands
[96] Institute for Nuclear Problems of Belarusian State University (INP BSU), Minsk, Belarus
[97] Institute of Electrical and Electronic Engineers (IEEE), Piscataway, NJ, USA
[98] Institute of High Energy Physics, Chinese Academy of Science, Beijing (IHEP CAS), Beijing, P.R. China
[99] Institute of Machine Components, University of Stuttgart (IMA), Stuttgart, Germany
[100] Institute of Nuclear Physics Polish Academy of Sciences (IFJ PAN), Krakow, Poland
[101] Institute of Physics, Academia Sinica (AS), Taipei, Taiwan
[102] Institut Jožef Stefan (IJS), Ljubljana, Slovenia
[103] Instituto de Astrofísica de Canarias (IAC), La Laguna, Spain
[104] Instituto de Física Corpuscular (CSIC-UV), Paterna, Spain
[105] Instituto de Física Corpuscular (CSIC-UV), València, Spain
[106] Instituto de Física Teórica, Universidad Autonoma de Madrid (IFT-UAM), Madrid, Spain
[107] Instituto de Física, Universitat de València (CSIC), València, Spain
[108] Instituto de Investigaciones Físicas de Mar del Plata (IFIMAR), Mar del Plata, Argentina
[109] Instituto Galego de Física de Altas Enxerxías, Universidade de Santiago de Compostela (IGFAE), Santiago de Compostela, Spain
[110] International Center for Advanced Studies, Universidad Nacional de San Martin (ICAS-UNSAM), San Martin, Argentina
[111] Iowa State University (ISU), Ames, IA, USA

[112] Istanbul Aydin University (IAU), Istanbul, Turkey
[113] Istanbul University (IÜ), Istanbul, Turkey
[114] Istituto Nazionale di Fisica Nucleare, Gruppo Collegato di Salerno – Sezione di Napoli (INFN SA), Salerno, Italy
[115] Istituto Nazionale di Fisica Nucleare, Laboratori Nazionali del Gran Sasso (INFN LNGS), Assergi (L'Aquila), Italy
[116] Istituto Nazionale di Fisica Nucleare, Laboratori Nazionali di Frascati (INFN LNF), Frascati, Italy
[117] Istituto Nazionale di Fisica Nucleare, Laboratori Nazionali di Legnaro (INFN LNLN), Legnaro, Italy
[118] Istituto Nazionale di Fisica Nucleare Sezione di Bari (INFN BA), Bari, Italy
[119] Istituto Nazionale di Fisica Nucleare, Sezione di Bologna (INFN BO), Bologna, Italy
[120] Istituto Nazionale di Fisica Nucleare, Sezione di Cagliari (INFN CA), Cagliari, Italy
[121] Istituto Nazionale di Fisica Nucleare, Sezione di Catania (INFN CT), Catania, Italy
[122] Istituto Nazionale di Fisica Nucleare, Sezione di Cosenza (INFN CS), Cosenza, Italy
[123] Istituto Nazionale di Fisica Nucleare, Sezione di Ferrara (INFN FE), Ferrara, Italy
[124] Istituto Nazionale di Fisica Nucleare, Sezione di Firenze (INFN FI), Florence, Italy
[125] Istituto Nazionale di Fisica Nucleare, Sezione di Genova (INFN GE), Genoa, Italy
[126] Istituto Nazionale di Fisica Nucleare, Sezione di Lecce (INFN LE), Lecce, Italy
[127] Istituto Nazionale di Fisica Nucleare, Sezione di Milano Bicocca (INFN MIB), Milan, Italy
[128] Istituto Nazionale di Fisica Nucleare, Sezione di Milano (INFN MI), Milan, Italy
[129] Istituto Nazionale di Fisica Nucleare, Sezione di Napoli (INFN NA), Naples, Italy
[130] Istituto Nazionale di Fisica Nucleare, Sezione di Padova (INFN PD), Padua, Italy
[131] Istituto Nazionale di Fisica Nucleare, Sezione di Pavia (INFN PV), Pavia, Italy
[132] Istituto Nazionale di Fisica Nucleare, Sezione di Perugia (INFN PG), Perugia, Italy
[133] Istituto Nazionale di Fisica Nucleare, Sezione di Pisa, Università di Pisa (INFN PI), Pisa, Italy
[134] Istituto Nazionale di Fisica Nucleare, Sezione di Roma 1 (INFN Roma 1), Rome, Italy
[135] Istituto Nazionale di Fisica Nucleare, Sezione di Roma Tor Vergata (INFN Roma 2), Rome, Italy
[136] Istituto Nazionale di Fisica Nucleare, Sezione di Roma Tre (INFN Roma 3), Rome, Italy
[137] Istituto Nazionale di Fisica Nucleare, Sezione di Torino (INFN TO), Turin, Italy
[138] Istituto Nazionale di Fisica Nucleare, Sezione di Trieste (INFN TS), Trieste, Italy
[139] ITER (ITER), Cadarache, France
[140] Ivane Javakhishvili T'bilisi State University (TSU), T'bilisi, Georgie
[141] Izmir University of Economics (IUE), Izmir, Turkey
[142] Johannes-Gutenberg-Universität (JGU), Mainz, Germany
[143] John Adams Institute for Accelerator Science, The Chancellor, Masters and Scholars of the University of Oxford (JAI), Oxford, UK
[144] Joint Institute for Nuclear Research (JINR), Dubna, Russia
[145] Julius-Maximilians-Universität Würzburg (UWUERZBURG), Würzburg, Germany
[146] Kahramanmaras Sutcu Imam University (KSU), Kahramanmaras, Turkey
[147] Karlsruher Institut für Technologie (KIT), Karlsruhe, Germany
[148] Katholieke Universiteit Leuven Research & Development (LRD), Louvain, Belgium
[149] Key Laboratory of Theoretical Physics, Chinese Academy of Science (SKLTP ITP CAS), Beijing, P.R. China
[150] King's College London (KCL), London, UK
[151] Kyoto University (Kyodai), Kyoto, Japan
[152] Kyungpook National University (KNU), Sankyuk-dong, Republic of Korea
[153] Laboratoire d'Annecy-Le-Vieux de Physique des Particules (CNRS/IN2P3/LAPP), Annecy, France
[154] Laboratoire de l'Accélérateur Linéaire, Université de Paris Sud (CNRS/IN2P3/UPSUD/ LAL), Orsay, France
[155] Laboratoire de Physique Nucléaire et de Hautes Energies (LPNHE), Paris, France

[156] Laboratoire de Physique Subatomique et de Cosmologie Grenoble (LPSC), Grenoble, France
[157] Laboratoire de Physique Théorique et Hautes Energies (CNRS/Sorbonne/LPTHE), Paris, France
[158] Laboratoire Leprince-Ringuet, Ecole Polytechnique (LLR), Palaiseau, France
[159] Laboratório de Instrumentação e Física Experimental de Partículas (LIP), Lisbon, Portugal
[160] Latitude Durable (LD), Geneva, Switzerland
[161] Lawrence Berkeley National Laboratory (LBNL), Berkeley, CA, USA
[162] Linde Kryotechnik AG (Linde), Pfungen, Switzerland
[163] Loughborough University (LBoro), Loughborough, UK
[164] Ludwig Maximilians University of Munich (LMU), Munich, Germany
[165] Luvata Pori Oy (Luvata), Pori, Finland
[166] MAN Energy Solutions Schweiz AG (MAN ES), Zürich, Switzerland
[167] Marian Smoluchowski Institute of Physics, Jagiellonian University (UJ), Kraków, Poland
[168] Massachusetts Institute of Technology (MIT), Cambridge, MA, USA
[169] Max-Planck-Institut für Kernphysik (MPIK), Heidelberg, Germany
[170] Max-Planck-Institut für Physik (MPP), Munich, Germany
[171] Ministère de l'Europe et des Affaires étrangères (MEAE), Paris, France
[172] Monash University (Monash), Melbourne, Australia
[173] MTA Wigner Research Centre for Physics (Wigner), Budapest, Hungary
[174] Mustafa Kemal Üniversitesi (MKU), Hatay, Turkey
[175] Nankai University (NKU), Tianjin, P.R. China
[176] Nationaal instituut voor subatomaire fysica (NIKHEF), Amsterdam, Netherlands
[177] National Centre for Scientific Research Demokritos (NCSRD), Athens, Greece
[178] National High Magnetic Field Laboratory, Florida State University (MagLab), Tallahassee, FL, USA
[179] National Institute of Chemical Physics and Biophysics (NICPB), Tallin, Estonia
[180] National Research Center Kurchatov Institute (NRCKI), Moscow, Russia
[181] National Research Nuclear University MEPhI (MEPhI), Moscow, Russia
[182] National Science Centre Kharkov Institute of Physics and Technology (KIPT), Kharkov, Ukraine
[183] National Technical University of Athens (NTUA), Athens, Greece
[184] Naturhistorisches Museum Wien (NHM), Vienna, Austria
[185] Niels Bohr Institute, Copenhagen University (NBI), Copenhagen, Denmark
[186] Nigde Ömer Halisdemir University (OHU), Nigde, Turkey
[187] Northern Illinois University (NIU), DeKalb, IL, USA
[188] Northwestern University (NU), Evanston, IL, USA
[189] Novosibirsk State University (NSU), Novosibirsk, Russia
[190] Otto-von-Guericke-Universityät Magdeburg (OVGU), Magdeburg, Germany
[191] Oxford University (UOXF), Oxford, UK
[192] Paul Scherrer Institute (PSI), Villigen, Switzerland
[193] Peking University (PU), Beijing, P.R. China
[194] Perimeter Institute for Theoretical Physics (PI), Watterloo, Canada
[195] Petersburg Nuclear Physics Institute, NRC "Kurchatov Institute" (PNPI), Gatchina, Russia
[196] Piri Reis University (PRU), Istanbul, Turkey
[197] Pittsburgh Particle physics, Astrophysics & Cosmology Center and Department of Physics & Astronomy, University of Pittsburgh (PITT PACC), Pittsburgh, PA, USA
[198] Princeton University (PU), Princeton, NJ, USA
[199] PRISMA Cluster of Excellence, Inst. für Physik, Johannes-Gutenberg-Universität (PRISMA), Mainz, Germany
[200] Pusan National University (PNU), Busan, Republic of Korea
[201] Queen's University (Queens U), Kingston, Canada
[202] Tampere University (TAU), Tampere, Finland

[203] Rheinisch-Westfälische Technische Hochschule Aachen (RWTH), Aachen, Germany

[204] Riga Technical University (RTU), Riga, Latvia

[205] Royal Holloway University (RHUL), London, UK

[206] Ruder Boskovic Institute (RBI), Zagreb, Croatia

[207] Ruprecht Karls Universität Heidelberg (RKU), Heidelberg, Germany

[208] Rutgers, The State University of New Jersey (RU), Piscataway, NJ, USA

[209] Sapienza Università di Roma (UNIROMA1), Rome, Italy

[210] School of Particles and Accelerators, Institute for Research in Fundamental Sciences (IPM), Tehran, Iran

[211] School of Physics and Astronomy, University of Glasgow (SUPA), Glasgow, UK

[212] Science and Technology Facilities Council, Daresbury Laboratory (STFC DL), Warrington, UK

[213] Science and Technology Facilities Council, Rutherford Appleton Laboratory (STFC RAL), Didcot, UK

[214] scMetrology SARL (scMetrology), Geneva, Switzerland

[215] Scuola Int. Superiore di Studi Avanzati di Trieste (SISSA), Trieste, Italy

[216] Scuola Normale Superiore (SNS), Pisa, Italy

[217] Seoul National University (SNU), Seoul, Republic of Korea

[218] Sevaplan und Wurm Schweiz AG (WURM), Winterthur, Switzerland

[219] Shahid Beheshti University (SBUT), Tehran, Iran

[220] Shanghai Jiao Tong University (SJTU), Shanghai, P.R. China

[221] Shirokuma GmbH (Shirokuma), Wetzikon, Switzerland

[222] Skobeltsyn Institute of Nuclear Physics, Lomonosov Moscow State University (SINP MSU), Moscow, Russia

[223] Southern Federal University (SFU), Rostov, Russia

[224] Southern Methodist University (SMU), Dallas, TX, USA

[225] Sri Guru Tegh Bahadur Khalsa College, University of Delhi (SGTB Khalsa College), New Delhi, India

[226] Stanford National Accelerator Center (SLAC), Menlo Park, CA, USA

[227] Stanford University (SU), Stanford, CA, USA

[228] Stony Brook University (SBU), Stony Brook, NY, USA

[229] Technische Universität Darmstadt (TU Darmstadt), Darmstadt, Germany

[230] Technische Universität Dortmund (TU Dortmund), Dortmund, Germany

[231] Technische Universität Dresden (TU Dresden), Dresden, Germany

[232] Technische Universität Graz (TU Graz), Graz, Austria

[233] Technische Universität Wien (TU Wien), Vienna, Austria

[234] Tel Aviv University (TAU), Tel Aviv, Israel

[235] The Citadel, The Military College of South Carolina (Citadel), Charleston, SC, USA

[236] The Pennsylvania State University (PSU), University Park, PA, USA

[237] The University of Tokyo (Todai), Tokyo, Japan

[238] Thomas Jefferson National Accelerator Facility (JLab), Newport News, VA, USA

[239] TOBB University of Economics and Technology (TOBB ETU), Ankara, Turkey

[240] Tokyo Institute of Technology (Tokyo Tech), Tokyo, Japan

[241] Trinity College Dublin (TCD), Dublin, Ireland

[242] Tri-University Meson Facility (TRIUMF), Vancouver, Canada

[243] Tsinghua University (THU), Beijing, P.R. China

[244] Tsung-Dao Lee Institute (TDLI), Shanghai, P.R. China

[245] Uludag University (ULUÜ), Bursa, Turkey

[246] Universidad Autónoma de Sinaloa (UAS), Culiacán, Mexico

[247] Universidad de Guanajuato (UGTO), Guanajuato, Mexico

[248] Universidad de La Laguna (ULL), La Laguna, Spain

[249] Universidad de la República (Udelar), Montevideo, Uruguay

[250] Universidad de los Andes (Uniandes), Bogotá, Colombia

[251] Universidade de São Paulo (USP), São Paulo, Brazil

[252] Universidade do Estado do Rio de Janeiro (UERJ), Rio de Janeiro, Brazil

[253] Universidade Federal de Pelotas (UFPel), Pelotas, Brazil
[254] Universidade Federal de Rio de Janeiro (UFRJ), Rio de Janeiro, Brazil
[255] Università degli Studi Roma Tre – Centro Ricerche Economiche e Sociali Manlio Rossi-Doria (EDIRC), Rome, Italy
[256] Università della Calabria (UNICAL), Arcavacata, Italy
[257] Università del Salento (UNISALENTO), Lecce, Italy
[258] Università di Bari (UNIBA), Bari, Italy
[259] Università di Bologna (UNIBO), Bologna, Italy
[260] Università di Cagliari (UNICA), Cagliari, Italy
[261] Università di Catania (UNICT), Catania, Italy
[262] Università di Ferrara (UNIFE), Ferrara, Italy
[263] Università di Firenze (UNIFI), Florence, Italy
[264] Università di Genova (UNIGE), Genoa, Italy
[265] Università di Insubria (UNINSUBRIA), Milan, Italy
[266] Università di Lecce (UNILE), Lecce, Italy
[267] Università di Milano (UNIMI), Milan, Italy
[268] Università di Padova (UNIPD), Padua, Italy
[269] Università di Parma (UNIPR), Parma, Italy
[270] Università di Pavia (UNIPV), Pavia, Italy
[271] Università di Perugia (UNIPG), Perugia, Italy
[272] Università di Roma Sapienza (UNIROMA1), Rome, Italy
[273] Università di Roma Tor Vergata (UNIROMA2), Rome, Italy
[274] Università di Roma Tre (UNIROMA3), Rome, Italy
[275] Università di Torino (UNITO), Turin, Italy
[276] Università di Udine (UNIUD), Udine, Italy
[277] Universität Hamburg (UHH), Hamburg, Germany
[278] Universität Heidelberg (HEI), Heidelberg, Germany
[279] Universitat Politecnica de Catalunya (UPC), Barcelona, Spain
[280] Universität Siegen (U Siegen), Siegen, Germany
[281] Universität Tübingen (TU), Tübingen, Germany
[282] Université Clermont Auvergne (UCA), Aubière, France
[283] Université Grenoble Alpes (UGA), Grenoble, France
[284] University College London (UCL), London, UK
[285] University of Applied Sciences Technikum Wien (UAS TW), Vienna, Austria
[286] University of Arizona (UA), Tucson, AZ, USA
[287] University of Basel (UNIBAS), Basel, Switzerland
[288] University of Belgrade (UB), Belgrade, Serbia
[289] University of Bergen (UiB), Bergen, Norway
[290] University of Bern (UNIBE), Bern, Switzerland
[291] University of Birmingham (UBIRM), Birmingham, UK
[292] University of Bristol (UOB), Bristol, UK
[293] University of California Berkeley (UCB), Berkeley, CA, USA
[294] University of California, Davis (UCD), Davis, CA, USA
[295] University of California, Irvine (UCI), Irvine, CA, USA
[296] University of California, San Diego (UCSD), San Diego, CA, USA
[297] University of California Santa Barbara (UCSB), Santa Barbara, CA, USA
[298] University of California Santa Cruz (UCSC), Santa Cruz, CA, USA
[299] University of Cambridge (CAM), Cambridge, UK
[300] University of Chicago (UCHI), Chicago, IL, USA
[301] University of Cincinnati (UC), Cincinnati, OH, USA
[302] University of Colorado Boulder (UCB), Boulder, Co, USA
[303] University of Edinburgh (ED), Edinburgh, UK
[304] University of Florida (UF), Gainesville, FL, USA
[305] University of Geneva (UniGE), Geneva, Switzerland
[306] University of Illinois at Urbana Champaign (UIUC), Urbana Champaign, IL, USA

[307] University of Iowa (UIowa), Iowa City, IA, USA
[308] University of Jyväskylä (JYU), Jyväskylä, Finland
[309] University of Kansas (KU), Lawrence, KS, USA
[310] University of Liverpool (ULIV), Liverpool, UK
[311] University of Lund (ULU), Lund, Sweden
[312] University of Malta (UM), Msida, Malta
[313] University of Manchester (UMAN), Manchester, UK
[314] University of Maryland (UMD), College Park, MD, USA
[315] University of Massachusetts-Amherst (UMass), Amherst, MA, USA
[316] University of Melbourne (UniMelb), Melbourne, Australia
[317] University of Michigan (UMich), Ann Arbor, MI, USA
[318] University of New Mexico (NMU), Albuquerque, NM, USA
[319] University of Notre Dame du Lac (ND), South Bend, IA, USA
[320] University of Oregon (UO), OR Eugene, USA
[321] University of Rochester (Rochester), Rochester, NY, USA
[322] University of Rostock (U Rostock), Rostock, Germany
[323] University of Saskatchewan (USASK), Saskatoon, Canada
[324] University of Science and Technology of P.R. China (USTC), Hefei, P.R. China
[325] University of Science and Technology of Mazandaran (USTM), Behshahr, Iran
[326] University of Silesia (USKAT), Katowice, Poland
[327] University of Stavanger (UiS), Stavanger, Norway
[328] University of Stuttgart (USTUTT), Stuttgart, Germany
[329] University of Sussex (US), Brighton, UK
[330] University of the Witwatersrand (WITS), Johannesburg, South Africa
[331] University of Toronto (UToronto), Toronto, Canada
[332] University of Warsaw (UW), Warszawa, Poland
[333] University of Wisconsin-Madison (WISC), Madison, WI, USA
[334] University of Würzburg (U Würzburg), Würzburg, Germany
[335] University of Zürich (UZH), Zürich, Switzerland
[336] University Rey Juan Carlos (URJC), Madrid, Spain
[337] Univ. Lyon 1, CNRS/IN2P3, Institut de Physique Nucléaire de Lyon (CNRS/IN2P3/ IPNL), Lyon, France
[338] Uppsala University (UU), Uppsala, Sweden
[339] Usak University (Usak), Usak, Turkey
[340] Vienna University of Economics and Business (WU), Vienna, Austria
[341] Vinca Institute of Nuclear Sciences (Vinca), Belgrade, Serbia
[342] Vrije Universiteit Brussel (VUB), Brussels, Belgium
[343] Washington University (WUSTL), St. Louis, MO, USA
[344] Weizmann Institute (Weizmann), Rehovot, Israel
[345] Werner-Heisenberg-Institut, Max-Planck-Institut für Physik (MPP), Munich, Germany
[346] Westfälische Wilhelms-Universität Münster (WWU), Münster, Germany
[347] West Pomeranian University of Technology (ZUT), Szczecin, Poland
[348] Wroclaw University of Science and Technology (PWR), Wroclaw, Poland
[349] Wuhan University of Technology (WHUT), Wuhan, P.R. China
[350] Zhejiang Institute of Modern Physics, Department of Physic (ZIMP), Hangzhou, P.R. China
[351] Zhejiang University (ZJU), Hangzhou, P.R. China
[352] fcc.secretariat@cern.ch

Abstract. In response to the 2013 Update of the European Strategy for Particle Physics (EPPSU), the Future Circular Collider (FCC) study was launched as a world-wide international collaboration hosted by CERN. The FCC study covered an energy-frontier hadron collider (FCC-hh), a highest-luminosity high-energy lepton collider (FCC-ee), the corresponding 100 km tunnel infrastructure, as well as the physics opportunities of these two colliders, and a high-energy LHC, based on FCC-hh technology. This document constitutes the fourth volume of the FCC Conceptual Design Report, devoted to the High-Energy Large Hadron Collider HE-LHC. It summarizes the HE-LHC physics discovery opportunities, presents the HE-LHC accelerator design, performance reach, and operation plan, discusses the underlying technologies, the civil engineering and technical infrastructure, and also sketches a possible implementation. Combining ingredients from the Large Hadron Collider (LHC), the high-luminosity LHC upgrade and adding novel technologies and approaches, the HE-LHC design aims at a hadron collider with about twice the centre-of-mass collision energy that the LHC can reach. Its performance aims at exploring physics beyond the Standard Model, significantly extending the LHC's direct and indirect sensitivity to new physics and discoveries.

[a] e-mail: frank.zimmermann@cern.ch

Preface

The 2013 Update of the European Strategy for Particle Physics (ESPPU) [1] stated, inter alia, that "...*Europe needs to be in a position to propose an ambitious post-LHC accelerator project at CERN by the time of the next Strategy update*" and that "*CERN should undertake design studies for accelerator projects in a global context, with emphasis on proton–proton and electron-positron high-energy frontier machines. These design studies should be coupled to a vigorous accelerator R&D programme, including high-field magnets and high-gradient accelerating structures, in collaboration with national institutes, laboratories and universities worldwide*".

In response to this recommendation, the Future Circular Collider (FCC) study was launched [2] as a world-wide international collaboration under the auspices of the European Committee for Future Accelerators (ECFA). The FCC study was mandated to deliver a Conceptual Design Report (CDR) in time for the following update of the European Strategy for Particle Physics.

European studies of post-LHC circular energy-frontier accelerators at CERN had actually started a few years earlier, in 2010–2013, for both hadron [3–5] and lepton colliders [6–8], at the time called HE-LHC/VHE-LHC and LEP3/DLEP/TLEP, respectively. In response to the 2013 ESPPU, in early 2014 these efforts were combined and expanded into the FCC study.

The international FCC collaboration has developed the design of a high-energy hadron collider (HE-LHC) in the existing LHC tunnel. It would provide proton–proton collisions at a centre-of-mass energy twice that of the LHC, leading to an increased discovery potential for new physics and more precise measurements of the Higgs boson. It could also offer a heavy-ion programme and a lepton-hadron interaction point, thus providing broad perspectives for research at the energy frontier.

Five years of intense work and a steadily growing international collaboration have resulted in the present Conceptual Design Report, consisting of four volumes covering the physics opportunities, technical challenges, cost and schedule of several different circular colliders, some of which could be part of an integrated programme extending until the end of the 21st century.

Geneva, December 2018

Rolf Heuer
CERN Director-General 2009–2015

Fabiola Gianotti
CERN Director-General since 2016

Contents

Executive summary

Overview

Particle physics has arrived at an important moment in its history. The discovery of the Higgs boson, with a mass of 125 GeV, completes the matrix of particles and interactions that has constituted the "Standard Model" for several decades.

This model is a consistent and predictive theory, which has so far proven successful at describing all phenomena accessible to collider experiments. However, several experimental facts require the extension of the Standard Model and explanations are needed for observations such as the abundance of matter over antimatter, the striking evidence for dark matter and the non-zero neutrino masses. Theoretical issues such as the hierarchy problem and, more in general, the dynamic origin of the Higgs mechanism, likewise point to the existence of physics beyond the Standard Model.

This report contains the description of a novel research infrastructure based on a high-energy hadron collider, which extends the current energy frontier by almost a factor 2 (27 TeV collision energy) and delivers an integrated luminosity of at least a factor of 3 larger than the HL-LHC. In connection with four experimental detectors, this infrastructure will deepen our understanding of the origin of the electroweak symmetry breaking, allow a first measurement of the Higgs self-coupling, double the HL-LHC discovery reach and allow for in-depth studies of new physics signals arising from future LHC measurements. This collider would directly produce particles at significant rates at scales up to 12 TeV. The project reuses the existing LHC underground infrastructure and large parts of the injector chain at CERN. This particle collider would succeed the HL-LHC directly and serve the world-wide physics community for about 20 years beyond the middle of the 21st century.

The European Strategy for Particle Physics (ESPP) update 2013 stated "*To stay at the forefront of particle physics, Europe needs to be in a position to propose an ambitious post-LHC accelerator project at CERN by the time of the next Strategy update*". The FCC study has implemented the ESPP recommendation by developing a vision for an "*accelerator project in a global context*". This document describes the detailed design and preparation of a construction project for a post-LHC circular high-energy hadron collider "*in collaboration with national institutes, laboratories and universities worldwide*", and enhanced by a strong participation of industrial partners. A coordinated preparatory effort can now be based on a core of an ever-growing consortium of already more than 135 institutes world-wide.

Accelerator

The HE-LHC would provide pp collisions at about twice the collision energy of the LHC, using the existing LHC tunnel infrastructure, without any increase of the tunnel cross section. Reaching a target beam energy of 13.5 TeV relies on the FCC-hh magnet technology. The accelerator will be built with FCC-class 16 T dipole magnets. Compared to the straight FCC-hh magnets, the HE-LHC magnets will be curved. Achieving a centre-of-mass energy close to 27 TeV with 16 T magnets requires a dipole filling factor similar to that of the LHC.

Parameters

The baseline design parameters are summarised in Table 1, which also presents a comparison with the corresponding values for LHC, HL-LHC and FCC-hh [9]. It is assumed that HE-LHC will accommodate two high-luminosity interaction-points (IPs) 1 and 5, at the locations of the present ATLAS and CMS experiments. IPs 2 and 8 could host secondary experiments combined with injection, as for the present LHC, or the available space could be exploited to serve other needs, e.g. for an extended high-energy injection section or for collimation.

Table 1. Key parameters of HE-LHC compared with FCC-hh, HL-LHC and LHC, for operation with proton beams.

Parameter	Unit	FCC-hh		HE-LHC	(HL-)LHC
Centre-of-mass energy	TeV	100		27	14
Injection energy	TeV	3.3		1.3 (0.9, 0.45)	0.45
Peak arc dipole field	T	16		16	8.33
Circumference	km	97.8		26.7	26.7
Straight-section length	m	1400		528	528
Beam current	A	0.5		1.12	(1.12) 0.58
Bunch population	10^{11}	1.0		2.2	(2.2) 1.15
Number of bunches/beam	–	10400		2808	(2760) 2808
RF voltage	MV	32		16	(16) 16
RMS bunch length	mm	~ 80		90	(90) 75.5
Longitudinal emittance ($4\pi\sigma_z\sigma_E$)	eVs	~ 8		4.2	2.5
Bunch spacing	ns	25		25	25
Norm. transv. rms emittance	μm	2.2		2.5	(2.5) 3.75
IP beta function $\beta^*_{x,y}$	m	1.1	0.3	0.45	(0.15) 0.55
Initial rms IP beam size $\sigma^*_{x,y}$	μm	6.7	3.5	9.0	(7.1 min) 16.7
Half crossing angle	μrad	37	100	165	(250) 142.5
Peak luminosity per IP	$10^{34}\,\mathrm{cm}^{-2}\,\mathrm{s}^{-1}$	5	30	16	(5, levelled) 1
Peak no. of events/crossing	–	170	1000	460	(135) 27
RMS luminous region	mm	53	49	57	(68) 45
Stored energy/beam	GJ	8.4		1.4	(0.7) 0.36
SR power/beam	kW	2400		100	(7.3) 3.6
Transv. emittance damping time	h	1.1		3.6	25.8
No. of high-luminosity IPs	–	2	2	2	(2) 2
Initial proton burn-off time	h	17	3.4	2.5	(15) 40
Allocated physics time/year	days	160	160	160	160 (160)
Average turnaround time	h	5	4	5	4 (5)
Optimum run time	h	11.6	3.7	5.3	(18–13) $\sim$10
Accelerator availability	–	70%	70%	75%	(80%) 71%
Nominal luminosity per day	fb^{-1}	2.0	8.0	4.5	(1.9) 0.4
Luminosity per year (160 days)	fb^{-1}	$\geq$250	$\geq$1000	500	(350) 55

Notes. All values, except for the injection energy itself, refer to the collision energy.

Optics

A large number of possible arc optics for the HE-LHC were surveyed. The two best performing optics were developed further. One of these is LHC-like with 23 cells per arc, and $90°$ phase advance per cell. The other optics features fewer (18), longer cells, which results in a higher dipole filling factor and, hence, energy reach. With reference to the number of optical cells per arc and to their betatron phase advance per cell, these two optics are called 23×90 and 18×90, respectively; see Figure 1. For a dipole field of 16 T, the 18×90 optics yields a collision energy above 27 TeV, the 23×90 optics close to 26 TeV.

In the experiment insertions the higher energy beams of the HE-LHC must be focused and separated within the limited length of the existing straight sections of the LEP/LHC tunnel. Figure 2 compares the layout of the HE-LHC final focus with those of the present LHC and the HL-LHC upgrade. The triplet for the HE-LHC is noticeably longer than either of the other two.

Specific optics were also developed for the other long straight sections, including those accommodating collimation, radiofrequency systems, injection, and extraction.
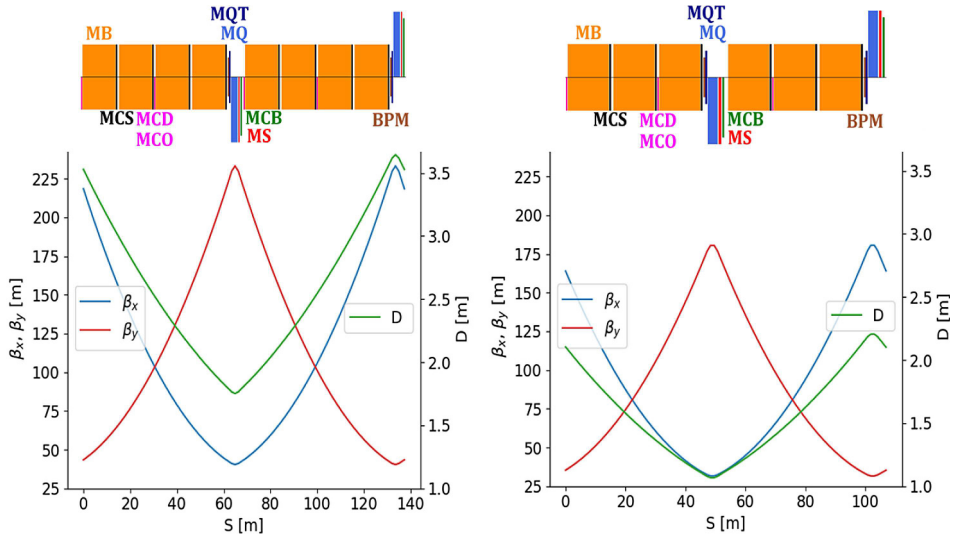
Fig. 1. Optics and magnet layout for the regular arc cell of the 18×90 optics with 18 cells per arc (left) and for the 23×90 optics with 23 cells per arc and longer cells (right).

Performance

The HE-LHC luminosity evolution during a physics fill is determined by the combined effects of proton burn-off and significant radiation damping. An integrated luminosity exceeding $10 \, ab^{-1}$ is within reach over about 20 years of pp operation.

In addition to delivering pp physics at the energy frontier, the HE-LHC could operate as the world's highest-energy heavy-ion and ion-proton collider; and by adding a 60 GeV electron beam from a multi-pass energy-recovery linac, the HE-LHC could also provide high-energy lepton-proton and lepton-ion collisions ("HE-LHeC").

Injection

After the LHC Injector Upgrade (LIU) [10], scheduled to be completed in 2020, an extremely bright proton beam will be available for injection into the HE-LHC. Injection into the HE-LHC could be accomplished from a new fast ramping superconducting (SC) synchrotron in the SPS tunnel (scSPS). SC magnets with double-layer coils would allow an injection energy of 1.3 TeV, which provides an adequate dynamic and physical aperture at injection and has been chosen as a solid baseline. Alternative injector scenarios include injection at 900 GeV from a single-layer coil SC synchrotron in the SPS tunnel, or injection from the existing warm SPS at 450 GeV.

Technologies

In the HE-LHC, both the synchrotron radiation power and, in particular, the photon flux, are much higher than in the LHC. The FCC-hh beamscreen design offers an adequate solution for the challenging cryogenic beam-vacuum system of HE-LHC.

The 16 T dipole magnets for the HE-LHC rely on Nb_3Sn. Experience has been gained in the use of this technology in both the USA and Europe, not only on R&D magnets but, more recently, thanks to the HL-LHC project, also on accelerator
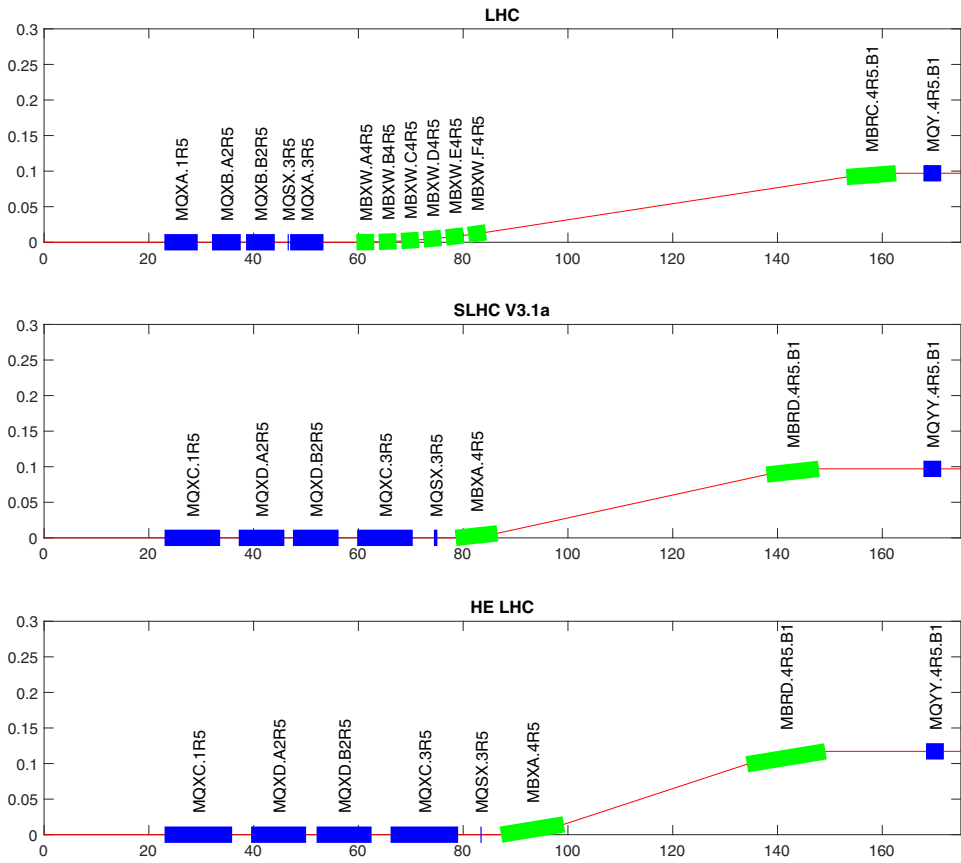
Fig. 2. Geometric layout of the HE-LHC final focus system (bottom) compared with the present LHC (top) and the HL-LHC final focus (centre).

magnets. High-performing Nb_3Sn conductors have already been produced by new collaborating partner institutes and companies, achieving a J_c performance of the order of the specification for HL-LHC. Work performed on grain refinement and artificial pinning centres (APC) [11] has shown promising results, nearly doubling the J_c at 12 T, 4.2 K on small samples.

The nonlinear field component of the Nb_3Sn dipole magnets, due to persistent currents in the superconducting cable, limits the dynamic aperture at injection. To obtain an acceptable field quality for the HE-LHC Nb_3Sn magnets, the effective fila-ment size of the SC wire is chosen as 20 μm, which is smaller than the 50 μm filament diameter of the HL-LHC conductor. A further improvement of the field quality at injection is expected from the addition of APCs, with a realistic target value for the pinning efficiency taken to be 50%. Figure 3 shows the sextupole field error as a func-tion of the dipole field strength without any artificial pinning centres, with an ideal pinning efficiency of 100%, and with the baseline 50% flux pinning efficiency. Table 2 illustrates the simulated off-momentum dynamic aperture (DA) due to the multi-pole errors, including correctors for the systematic sextupole, octupole and decapole components (b_3, b_4 and b_5) in each arc. Requiring a dynamic aperture of at least 12σ, as for the LHC design, means that at present, the only robust solution is the 23×90 optics with an injection energy of 900 GeV or above. The 18×90 optics with an injection energy of 1.3 TeV appears marginally acceptable.
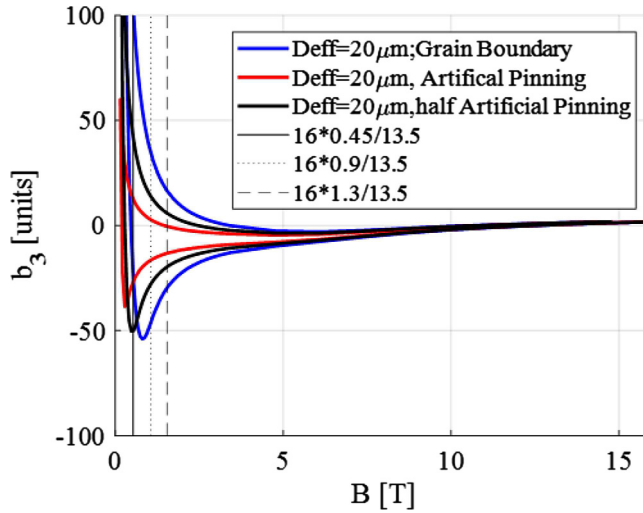
Fig. 3. Sextupolar field error b_3 of the 16 T dipole magnets, in units of 10^{-4} at a reference radius of 16.7 mm, as a function of field strength, for an effective Nb_3Sn filament size of $20\,\mu m$, without flux pinning (blue), with 100% artificial pinning (red), and with a realistic 50% pinning efficiency (black). Three different injection energies are indicated.

Table 2. Simulated minimum dynamic aperture due to all nonlinear multipole errors, up to 20-poles, as obtained by tracking over 10^5 turns.

Optics	Parameter	450 GeV	900 GeV	1.3 TeV
23×90	DA with 50% flux pinning	5.4σ	12.3σ	15.9σ
18×90	DA with 50% flux pinning	2.7σ	7.4σ	11.2σ

Notes. The systematic parts of the b_3, b_4 and b_5 errors were corrected.

The integration into the existing LHC tunnel, along with the larger size of the HE-LHC cryogenic distribution line, limits the maximum outer diameter of the HE-LHC arc cryomagnets to 1.2 m, as is illustrated in Figure 4.

The HE-LHC cryogenics infrastructure provides the conditions to operate the superconducting Nb_3Sn magnets. The magnet windings will be immersed in a pressurised bath of superfluid helium at a maximum temperature of 1.9 K, which allows a sufficient temperature margin for heat transfer across the electrical insulation during stored beam operation. The cryogenic system must cope with load variations and the large dynamic range induced by operation of the collider and be able to fill and cool down the cold mass of the machine (60×10^6 kg) in less than 20 days, while avoiding thermal gradients higher than 50 K in the cryomagnet structure. It must also cope with resistive transitions of the superconducting magnets and recover sufficiently fast from such situations that the operational availability of the HE-LHC is not seriously affected. An effort is made to reuse as much of the existing LHC and HL-LHC infrastructure as possible. Like at present, the cooling power will be produced by 8 refrigeration plants at 5 technical sites and will be distributed to the adjacent sectors over distances of up to 3.3 km. To reduce the size of the cryogenic distribution system and to integrate it within the existing LHC tunnel, active cryogenics must be installed at both sides of the HE-LHC sectors.

Each of the 5 sites comprises an electrical substation, a warm compressor station, cryogen storage (helium and liquid nitrogen), cooling towers and cold-boxes.
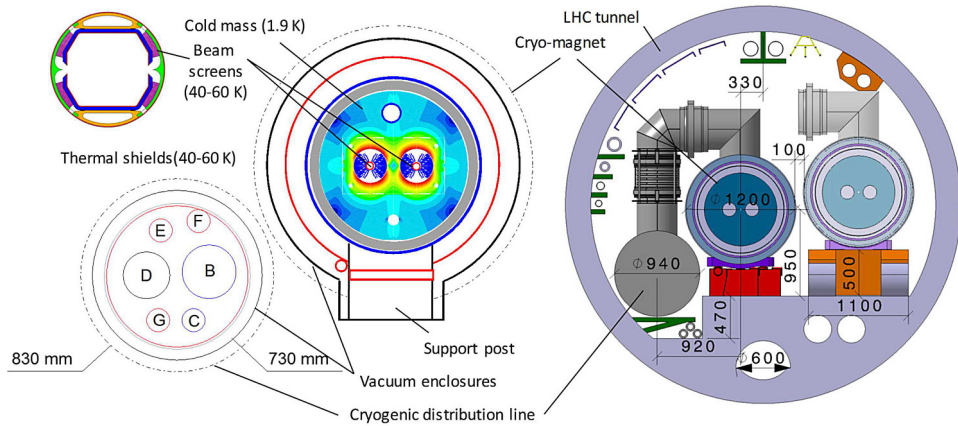
Fig. 4. Cross section of the LHC tunnel and main HE-LHC cryogenic components.

The lower cold-boxes, interconnecting lines and interconnection boxes are located underground. A refrigeration plant comprises one helium refrigerator including two 1.8 K refrigeration units and one turbo-Brayton refrigerator for the efficient production of cooling capacity above 40 K. The two 1.8 K refrigeration units are located at either side of the HE-LHC sectors and pump on a half-sector length, thus reducing the pumping line diameter required. At each site, an interconnection box couples the refrigeration equipment to the cryogenic distribution line and where possible, they also provide redundancy between the refrigeration plants. To limit the environmental impact as well as the pressure build-up during helium discharge in case of a sector quench helium storage is provided at all 8 surface sites. The HL-LHC cryogenic plants will be reused to cool the high-luminosity insertions.

Civil engineering

The existing civil engineering structures will be reused as much as possible to accommodate the equipment required for HE-LHC. Some new structures will be needed to accommodate new components for cryogenics, electricity and ventilation systems.

New caverns are required for cryogenic equipment at points 3 and 7, and new alcoves for electrical equipment to supply the cryogenic installations. Depending on the power consumption and the reliability required from the existing electrical network, additional upgrades might be needed at other locations. Additional space in the underground caverns has been allocated for cooling equipment.

A new shaft is mandatory at LHC point 3.3, since the existing shaft PZ33 is only used for personnel access and its diameter would not allow lowering of the 7 m long cryogenics cylinders. A more detailed analysis remains to be performed for point 2 to confirm that existing caverns can be used to accommodate the new equipment. If the space is not sufficient, a new cavern has to be constructed. Either the existing PM25 and PMI2 shafts can be used to transport the new equipment into the tunnel at point 2, or a new shaft needs to be created. Where new access shafts are needed, head of shaft buildings will be added.

New noise insulated buildings to accommodate cryogenic and electrical equipment are necessary at points 3 and 7. New turbo-Brayton refrigerators need to be installed in existing or new buildings at points 1.8, 2, 4, 6 and 8. A refurbishment of the existing tunnel ventilation and additional ventilation systems are necessary to provide supply and extraction units for each sector. Hence, new surface buildings are

required for ventilation equipment at each point. The existing SDI2/SMI2 building has to be replaced to accommodate a higher-capacity crane for lowering the new accelerator magnets. New access roads will be required at locations where new shafts and buildings are planned.

The vault height of the junction chamber UJ22 will have to be increased by ~1 m, to allow the HE-LHC magnets to be lifted from the TI 2 transfer line into the LHC tunnel once the HE-LHC machine is installed. Parts of TI 2 may need to be locally enlarged by ~30 cm to allow certain magnet groups of TI 2 to pass through. An enlargement at the beam stopper just before UJ22 is mandatory. Depending on the required safety concept, compartment doors will be installed along the HE-LHC tunnel every 550 m, requiring local breakouts in the lining.

Detector considerations

For the HE-LHC energy of 27 TeV, the kinematics and topology of SM processes do not change significantly with respect to the HL-LHC energy of 14 TeV. The HE-LHC uses a value of $l^* = 23$ m, equal to the LHC and assumes only minimal changes to the civil engineering infrastructure of the LHC caverns. In terms of acceptance and overall size, the detectors at the HE-LHC therefore need to be compared to the HL-LHC detectors rather than to detectors at the FCC-hh, which assume significantly increased instrumentation in the very forward region. The HE-LHC luminosity of 16×10^{34} cm^{-2} s^{-1} is however, significantly higher than the HL-LHC luminosity. The resulting pile-up of 500 is about 3.4 times larger than at HL-LHC and about half the number at the FCC-hh. It can therefore be assumed that detectors at the HE-LHC are ATLAS/CMS class detectors with challenges related to radiation, pile-up, trigger and readout rate that are closer to the FCC-hh detector concepts.

Cost and schedule

The construction cost for HE-LHC amounts to 7200 million CHF for the entire project. All particle collider and injector related investments amount to 6100 million CHF or 85% of the total cost. The major part of the accelerator cost corresponds to the 1250 Nb$_3$Sn 16 T main dipole magnets, totalling 2900 MCHF, at a cost target of 2.3 MCHF/magnet. The collider cost also includes 260 MCHF for LHC disposal. The cost for construction of a new superconducting SPS injector and associated transfer lines amounts to about 1100 million CHF according to current estimates. However, a detailed, dedicated study would be needed to confirm this cost. Civil engineering works account for 4% (300 million CHF). The capital cost for the technical infrastructure is 800 million CHF. The operation costs are expected to remain at current levels. The electricity consumption remains constant and the evolution from LEP to LHC today shows a steady decrease in the effort needed to operate, maintain and repair the equipment. The cost-benefit analysis of the LHC/HL-LHC programme reveals that a research infrastructure project of such a scale and hi-tech level has the potential to pay for itself in terms of socio-economic value throughout its lifetime.

The overall HE-LHC project schedule is dominated by accelerator and technology R&D, in particular by the time needed to develop and industrialise 16 T Nb$_3$Sn superconducting magnets. Another key input is the anticipated stop of HL-LHC. The HE-LHC programme will commence with a preparatory phase of 8 years, followed by the construction phase from the stop of the HL-LHC operation (dismantling of existing SPS and LHC, civil engineering works and technical infrastructure, machines and detectors including commissioning) lasting 8 years. Then a period of 20 years is

needed to execute the currently envisaged physics programme. This makes a total of almost 30 years for construction and operation.

Outlook

The technology for constructing a High-Energy LHC can be brought to the technology readiness level required for construction within the next ten years through a committed and focused R&D programme. The concept comprises a power-saving, low-temperature superconducting magnet system based on an evolution of the Nb_3Sn technology pioneered at the HL-LHC, an energy-efficient cryogenic refrigeration infrastructure based on a neon-helium (nelium) light gas mixture, a high-reliability and low loss cryogen distribution infrastructure based on Invar, high-power distributed beam transfer using superconducting elements and local magnet energy recovery and reuse technologies that are already being gradually introduced at other CERN accelerators. Reuse of the LHC underground civil infrastructure worth about 500 million CHF at the time of its construction, extension of the surface sites and use of the existing injector chain that also serves a concurrent physics programme are all levers to come to a sustainable research infrastructure at the energy frontier.

Strategic R&D for HE-LHC aims at minimising construction cost and energy consumption, while maximising the socio-economic impact. The programme needs to mitigate technology-related risks and ensure that industry can benefit from an acceptable economic utility. For implementation, a preparatory phase of about eight years is both necessary and adequate to establish the project governing bodies and organisational structures, to build the international machine and experiment consortia, to develop a territorial implantation plan accounting for the constraints emerging from the use of the existing infrastructure and the host states' requirements, optimising the use of land, resources and preparing the construction project.

Such a large-scale, international fundamental research infrastructure, tightly involving industrial partners and providing training at all education levels, will be a strong motor of economic and societal development in all participating nations. The FCC study has implemented a set of actions towards a coherent vision for the worldwide high-energy and particle physics community, providing a collaborative framework for topically complementary and geographically well-balanced contributions. This conceptual design report lays the foundation for a subsequent infrastructure preparatory and technical design phase.

1 Physics opportunities and reach

1.1 Introduction

At the heart of the HE-LHC project is a pp collider, designed to operate at a centre of mass energy $\sqrt{s} = 27\,\mathrm{TeV}$, and to collect of the order of $15\,\mathrm{ab}^{-1}$ of data during 20 years of operation. The collider will use the current LHC tunnel and rely on the 16 T magnet technology being developed for FCC-hh. The overall scientific context and goals of the HE-LHC are by and large the same as those of the FCC-hh and are therefore reviewed in Volume 1 of this CDR. While 27 TeV is well below the 100 TeV target of the FCC-hh, the increase of energy and luminosity w.r.t. the HL-LHC nevertheless represents a significant improvement over the HL-LHC reach. The discussion of the HE-LHC physics potential, therefore, should not be done through a direct comparison with the obviously more powerful and ambitious FCC project, but in consideration of the expected costs and benefits that it will bring after the HL-LHC has finished operation.

For this discussion, it helps to group the specific potential returns of the HE-LHC in four areas:

1. Extending the HL-LHC reach in direct searches for new particles, approximately doubling the reach in mass.
2. Establishing the structure of the symmetry-breaking Higgs potential, which lies at the heart of the Standard Model's (SM) electroweak (EW) sector.
3. Improving the precision of the HL-LHC measurements in the EW and flavour sectors, with a consequently better indirect sensitivity to new physics at high mass scales, and better direct sensitivity to elusive final states such as dark matter (DM).
4. Exploring in greater detail the properties of possible future LHC discoveries, confirming preliminary signs of discovery from the LHC, or identifying the underlying origin of new phenomena revealed indirectly (e.g. the flavour anomalies currently under discussion) or in experiments other than those of the LHC (e.g. DM or neutrino experiments).

The first three classes of results offer guaranteed deliverables, with targets that can be defined today. On the other hand, only future data will allow qualifying and quantifying the relevance of the fourth area in the planning for the HE-LHC. Currently, only a few scenarios can be considered as examples.

The assessment of the full HE-LHC physics potential started in the context of the Workshop on "The physics of HL-LHC, and perspectives at HE-LHC" [12]. The results of this activity will be documented in its final report, due by the end of 2018, and the reader should refer to that document for a more complete overview, the main results documented so far are summarised here.

1.2 The boundary conditions for the HE-LHC physics studies

The studies done by the FCC-hh detector working group, which led to the baseline detector design documented in Volume 3, are relevant to the definition of an HE-LHC detector. In particular, most radiation issues will be comparable to FCC-hh, since the pp cross sections and track densities at 27 and 100 TeV only differ by $\sim 20\%$ and the pile-up conditions are assumed to be similar. In spite of this, it is premature to propose a detector design specifically for HE-LHC. For FCC-hh, one can assume that the design and construction of the detectors will start from scratch, with complete freedom to explore optimum solutions in terms of technology, machine-detector interface and the corresponding civil engineering. In the case of HE-LHC, one cannot avoid the tight constraints set by the existing cavern size, the infrastructure and the presence of the current detectors. The study of possible upgrade, refurbishing or replacement options for the ATLAS and CMS detectors, following the HL-LHC, is an extremely complex challenge, which would require the direct engagement of the experiments, and cannot be addressed at this time. As a result, ongoing HE-LHC physics studies make reference, at best, to an extrapolation of the ATLAS and CMS HL-LHC detector configurations, modelled via Delphes [13] simulation parameters reproducing the HL-LHC performance projections at 27 TeV and neglecting the impact of the much higher pile-up expected at HE-LHC. In many cases, the physics studies are simply of a phenomenological nature, with basic cuts and resolution/efficiency assumptions. The integrated luminosity benchmark will be set at $15\,\mathrm{ab}^{-1}$, consistent with the accelerator projections and with the possibility to combine the results of two experiments.
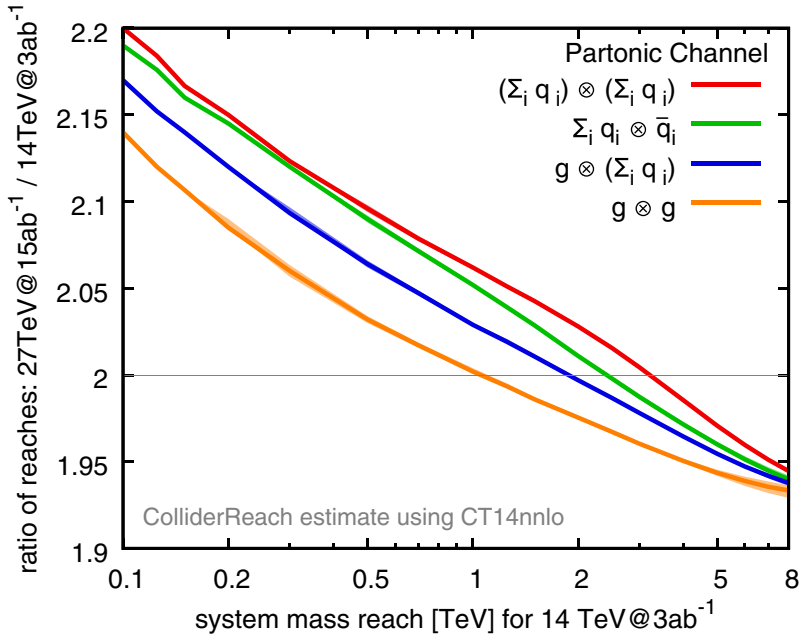
Fig. 1.1. Estimate of the system mass (e.g. $m_{Z'}$ or $2m_{\tilde{g}}$) that can be probed in searches for new particles at HE-LHC, given an established reach at HL-LHC.

1.3 The discovery reach potential of HE-LHC

The HE-LHC is expected to extend the mass reach for the discovery of new particles by a factor of ~ 2 with respect to HL-LHC. While the study of individual scenarios must account in detail for the possibly different evolution of signals and backgrounds with beam energy and include the new analysis opportunities offered by the larger statistics and kinematic reach available at $27\,\mathrm{TeV}$, it is possible to provide general estimates of the improved sensitivity by extrapolating the partonic luminosities that are relevant for the production of various final states. This is shown in Figure 1.1, obtained with the Collider Reach tool [14]. The thick green line includes the lines corresponding to the various possible initial states ($q\bar{q}$, gg etc.), showing that the improvement in mass reach is rather independent of the specific type of particle(s) produced and only depends on the estimated reach at the HL-LHC. For example, new gauge bosons such as a Z', whose reach at the HL-LHC is estimated to be in the range of $6\,\mathrm{TeV}$, could be observed by the HE-LHC up to a mass of $\sim 12\,\mathrm{TeV}$. This qualitative conclusion is verified in the more detailed studies done so far.

In several BSM scenarios, like for generic models of new Z' gauge bosons, the extension of the reach by a factor of 2 relative to the LHC is just a small extra dent in a large range of possible masses. But there are interesting scenarios where the doubling of the reach can cover an important fraction of the relevant parameter space. A few concrete examples are given here and many more will be found in [12].

1.3.1 Supersymmetry

The first studies of the discovery reach for supersymmetry at HE-LHC have recently appeared [15,16]. One of the key questions is to what extent classes of "natural" supersymmetric models are within its reach and can definitely be discovered or excluded.
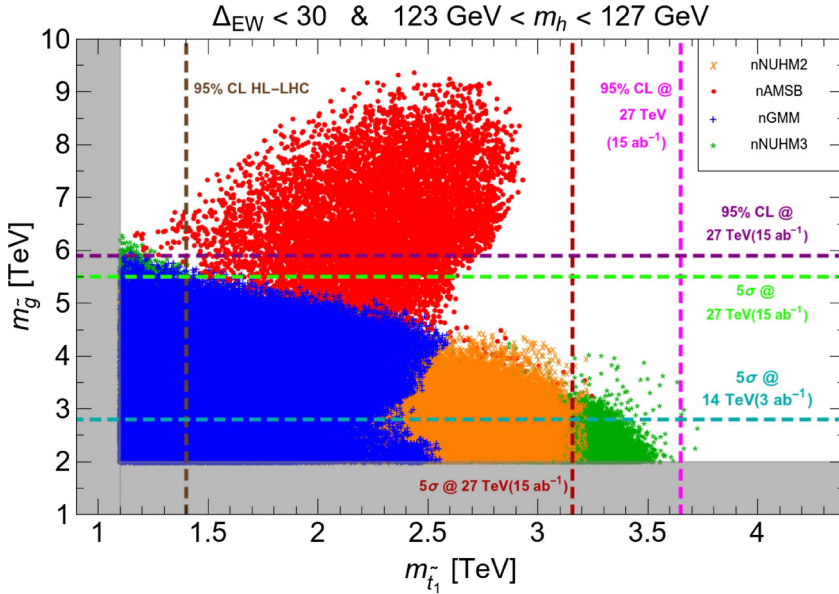
Fig. 1.2. Discovery reach at the HE-LHC for gluinos and stops in various supersymmetric models, compared to the HL-LHC reach and to the expectations of several classes of natural supersymmetric models. The relevant areas lie under the horizontal lines (for the gluino) and to the left of the vertical lines (for the stop).

An example of the added value of a higher-energy option for the LHC [15] is given in Figure 1.2. The points in the plots correspond to parameter configurations of several supersymmetric models inspired by the requirement of a natural solution to the hierarchy problem, including constraints such as the proper Higgs mass. The models considered are described in [15], and include generalised mirage mediation (nGMM) and non-universal Higgs mass (NUHM) models. What clearly emerges from these plots is that, while HL-LHC can only cover part of the parameter space of the illustrated models, HE-LHC covers it entirely. With the exception of the models labeled by red (green) dots, where the gluino (stop) mass is typically larger than the HE-LHC reach, all other models would allow the 5σ discovery via the observation of both gluino and stop.

1.3.2 WIMP searches

A study was presented [17] of the search for weakly-interacting massive particles (WIMPs) as dark matter (DM) candidates. The study follows the pattern of similar ones discussed in Volume 1 at 100 TeV, and also includes a comparison with the 100 TeV (and HL-LHC) results. From their conclusions, a disappearing charged track analysis at the HE-LHC can probe Higgsino-like (wino-like) DM mass of up to 600 GeV (2.1 TeV) at the 95% confidence limit (C.L.). These results, shown in Figure 1.3, improve on the expected reach of HL-LHC, namely 300 GeV (900 GeV). While these results at the HE-LHC come short of saturating the full range of masses for possible DM WIMPs (a goal that requires the power of the full FCC-hh, as shown by Fig. 1.3 and as discussed in Vol. 1), the mass range accessible to HE-LHC greatly extends the HL-LHC potential and can be complementary to the indirect detection probes using gamma rays from dwarf-spheroidal galaxies [17].
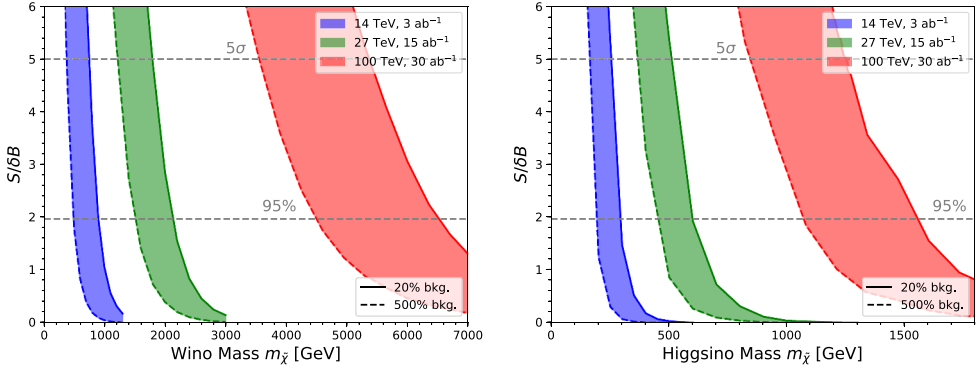
Fig. 1.3. The reach of HE-LHC in the search for a wino (left) or higgsino (right) DM WIMP candidate, using a disappearing charged track signature [17]. The bands limited by the solid and dashed lines show the range obtained by modifying the central value of the background estimate by a factor of five. The results are compared to the reach of HL-LHC and FCC-hh.
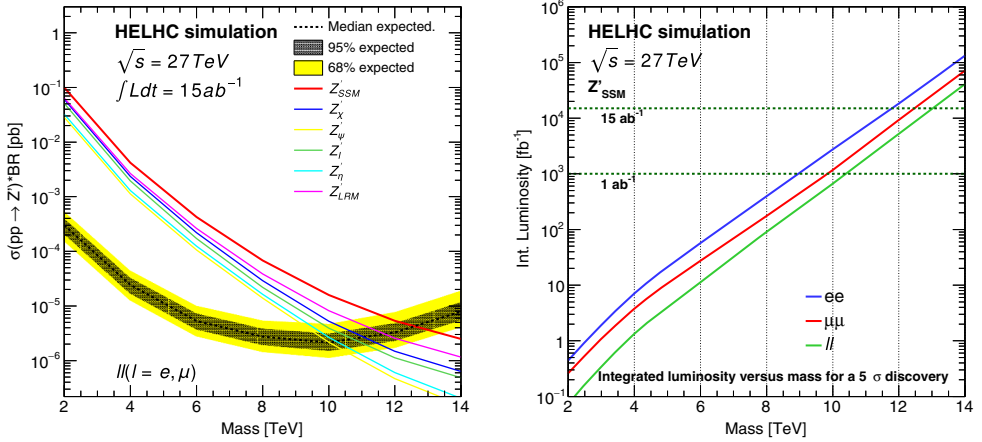
Fig. 1.4. Limit versus mass for the di-lepton channel (left) and luminosity for a 5σ discovery (right) for the ee and $\mu\mu$ combined channels.

1.3.3 Resonance searches

The search for resonances produced in the s channel explores the highest energies kinematically reachable at a collider and provides a good benchmark for the detector performance, since the invariant mass resolution in the resonance reconstruction is a key factor to enhance the search sensitivity. Several models and decay channels have been considered in detailed simulations [18], based on the Delphes detector parameterisation. For leptonic decays, the 95%CL sensitivity of various Z′ models (see [19] for details) is shown in Figure 1.4 (left panel). The 5σ discovery reach, as a function of the integrated luminosity, is shown in the right panel of Figure 1.4, for the so-called sequential SM Z′, Z'_{SSM}, whose couplings to SM fermions are identical to those of the Z boson in the SM. Some further results, for decays to τ leptons, to WW and to di-jets, are given in Table 1.1. Here Q* refers to excited-quark resonances [20], G_{RS} is a Randall–Sudrum massive graviton [21], Z'_{FA} provides a potential explanation to the current flavour anomalies [22], Z'_{TC} arises in top-assisted technicolor models [23].

Table 1.1. Limits and discovery reach at 5σ for various decay modes of resonance models mentioned in the text, at HE-LHC and FCC-hh.

Process	HE-LHC (FCC-hh)		
	95%CL limit (TeV) 15 (30) ab^{-1}	5σ reach (Tev) 1 (2.5) ab^{-1}	5σ reach (TeV) 15 (30) ab^{-1}
$Z'_{\mathrm{SSM}} \to e^+e^-/\mu^+\mu^-$	13 (40)	10 (33)	13 (43)
$Z'_{\mathrm{SSM}} \to \tau^+\tau^-$	6 (14)	3 (12)	6 (18)
$Z'_{\mathrm{FA}} \to \mu^+\mu^-$	4 (25)	$-$ (10)	2 (19)
$Z'_{\mathrm{TC}} \to t\bar{t}$	10 (28)	6 (16)	8 (23)
$G_{\mathrm{RS}} \to WW$	8 (28)	5 (15)	7 (22)
$Q^* \to jj$	14 (43)	10 (36)	12 (40)

Table 1.2. Higgs production event rates for selected processes at $27\,\mathrm{TeV}$ (N_{27}) and statistical increase with respect to the statistics of the HL-LHC ($N_{27} = \sigma_{27\ \mathrm{TeV}} \times 15\ \mathrm{ab}^{-1}$, $N_{14} = \sigma_{14\ \mathrm{TeV}} \times 3\ \mathrm{ab}^{-1}$).

	$gg \to H$	WH	ZH	$t\bar{t}H$	HH
N_{27}	2.2×10^9	5.4×10^7	3.7×10^7	4×10^7	2.1×10^6
N_{27}/N_{14}	13	12	13	23	19

All the results above can be shown to be consistent with the doubling of sensitivity relative to HL-LHC, suggesting that HL-LHC-like detectors are in principle properly scaled to preserve a suitable resolution for energies and muon momenta event at the higher energies of HE-LHC.

1.4 Measurements of Higgs properties

The main targets of the Higgs measurement programme at the HE-LHC include:

– improving the sensitivity to the Higgs self-coupling relative to the HL-LHC;
– further improving the precision on all major Higgs couplings to the percent level;
– continue increasing the sensitivity to possible invisible Higgs decays, and to other rare, forbidden, or elusive decays (e.g. H→c$\bar{\mathrm{c}}$).

The statistics expected for some reference production processes, and the increase with respect to the HL-LHC, are shown in Table 1.2. The Higgs samples will typically increase by a factor between 10 and 25, as a result of the 5 times larger luminosity, leading to a potential reduction in the statistical uncertainties by factors of 3–5. Fortunately, the biggest improvements arise for the channels where the HL-LHC will be statistics limited, such as ttH and HH.

In the study of precision Higgs measurements at FCC-hh, documented in Volumes 1 and 3 of the CDR, Higgs bosons produced at large p_T, above $100\,\mathrm{GeV}$, were considered. It was verified that the reduction in rate is largely compensated by better systematics, and often by an improved S/B ratio. The selection of fiducial regions in p_T and rapidity, furthermore, allows measurements of the ratios of rates for different final states, free from uncertainties related to the production dynamics and to luminosity. The use of large p_T final states, is also expected to mitigate the impact of pile-up.

A similar analysis has been performed for the HE-LHC, studying the rare decays H→$\gamma\gamma$, $\mu\mu$, Zγ and 4ℓ in the range $p_T > 50\,\mathrm{GeV}$. Some results, relative to the precision in the measurement of ratios of different decay modes, are shown in Figure 1.5.
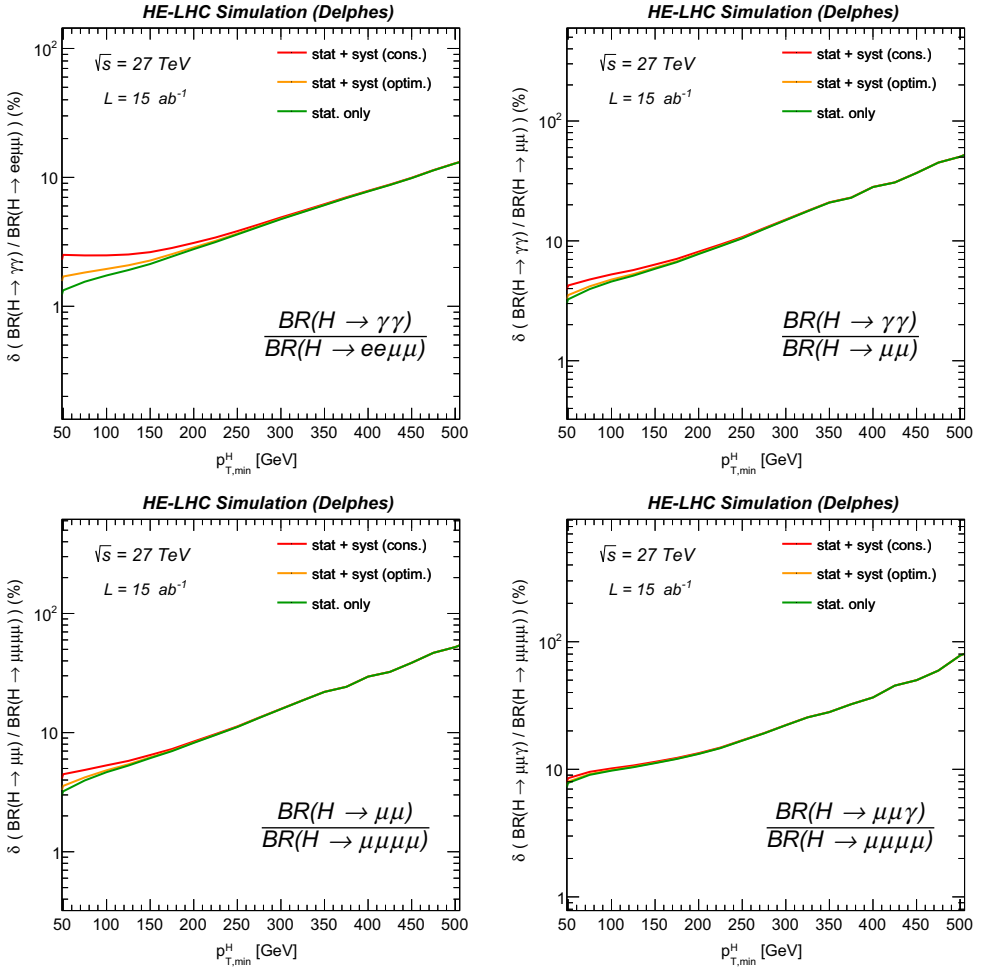
Fig. 1.5. Projected precision for the measurement of ratios of rates of different Higgs final states, in the gg→H production channel. The label "lumi" indicates the inclusion of a 1% overall uncertainty. The systematic uncertainty "syst" is defined in the text. The systematics of conservative scenario (cons) is twice as large as the reference one (optim).

The detector simulation is based on Delphes, with parameters drawn from the projected performance of the HL-LHC detectors. The uncertainties include the systematics on the detection efficiency for the various final state objects, and a 1% luminosity uncertainty. It is assumed that, as for the FCC-hh, processes like pp→Z→ $\ell\ell$ will be calculable with 1% precision and can be used for a precise liminosity determination. More details on the analysis are given in Volume 1 and in [24].

In contrast to FCC-hh, the uncertainty in the high-p_T range is statistics dominated for the rate-limited final states H→$\mu\mu$ and H→ $\ell\ell\gamma$. The study of these channels will therefore require an optimisation of the selection cuts, to include lower p_T Higgses. In the low-p_T domain, the Higgs precision studies at 27 TeV will resemble those carried out at HL-LHC. A fair comparison between HL-LHC and HE-LHC would therefore require much more detailed studies, accounting for the larger pile-up, and based on a concrete detector design. Taking the results of Figure 1.5 at face value, a precision in the range of 2–4% is projected for the ratios BR(H→$\mu\mu$)/BR(H→$\gamma\gamma$) and
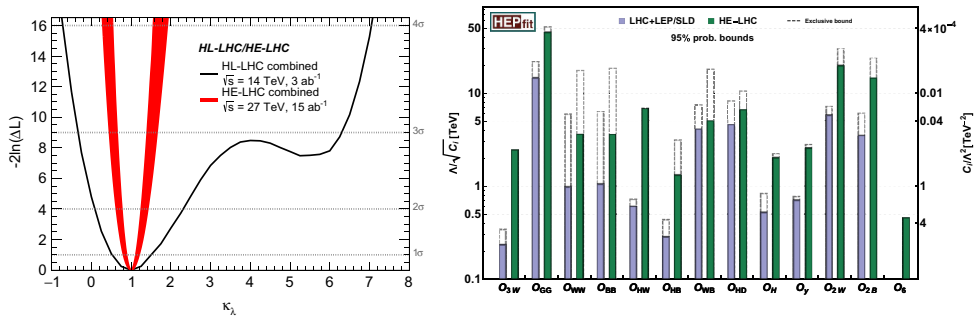
Fig. 1.6. Left: projected precision for the measurement of the Higgs trilinear coupling, from gg→ HH. Right: summary of constraints on the EFT operators considered. The shaded bounds arise from a global fit of all operators, those assuming the existence of a single operator are labeled as "exclusive".

BR(H→ 4ℓ)/BR(H→γγ), and therefore of order 1–2% for the ratios of the relevant Higgs couplings.

The projection for the Higgs self-coupling measurement at HE-LHC, performed in the context of the HL/HE-LHC Physics Workshop, are shown in Figure 1.6 (left). A precision in the range of 10–20%, at 68%CL, is expected. This result, which would significantly improve over the HL-LHC reach, is consistent with other phenomenological studies reported previously (see Refs. [25,26]).

Precision measurements provide an important tool to search for BSM physics associated to mass scales beyond the LHC direct reach. The EFT framework, where the SM Lagrangian is supplemented with higher dimension operators $\sum_i c_i^{(6)} \mathcal{O}_i^{(6)}/\Lambda^2 + c_i^{(8)} \mathcal{O}_i^{(8)}/\Lambda^4 + \cdots$, allows one to systematically parametrise BSM effects and how they modify SM processes. These operators can either modify SM amplitudes, or generate new amplitudes. In the former case, the best LHC probes are, for example, precision measurements of Higgs branching ratios. In the case of the operator $\mathcal{O}_H$, for example, the constraints in Figure 1.6 translate into a sensitivity to the Higgs compositeness scale $f > 2\,\text{TeV}$, corresponding to a new physics mass scale of $25\,\text{TeV}$ for an underlying strongly coupled theory.

Effects associated with new amplitudes grow quadratically (for dimension-6 operators) with the energy. The higher centre-of-mass energy and larger dataset of HE-LHC make it possible to greatly extend the measurable range in the Higgs transverse momenta, providing a new opportunity: a 10% measurement at $1\,\text{TeV}$ energy corresponds roughly to a permille precision measurement at the Higgs mass. In the context of EW physics this will allow to test, via Drell–Yan processes and the operators $\mathcal{O}_{2W,2B}$, energy scales of order $25\,\text{TeV}$; or, via WZ diboson processes, mass scales of roughly 6 (100) TeV if the underlying new physics is weakly (strongly) coupled. Figure 1.6 (right) shows the results of a global fit to observables in Higgs physics, as well as diboson and Drell–Yan processes at high energy.

Another important high-energy measurement concerns the scattering of longitudinally polarised vector bosons: departures from its SM value could betray a composite nature of the Higgs. The decomposition of measurements of VBS cross-sections into the polarised components based on the decays of the individual vector bosons is experimentally challenging. Preliminary studies show that, thanks to pile-up mitigation techniques that retain Run-2 performance of hadronically decaying W/Z-boson tagging, the precision on the VBS cross section measurement in the semileptonic $WV + \text{jj} \to \ell\nu + \text{jjjj}$ channel can be reduced from 6.5% (HL-LHC) to about 2% at HE-LHC. From this measurement and from the measurement of the EW production
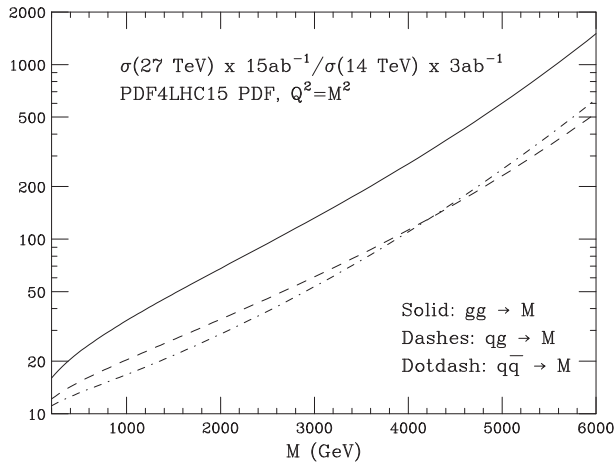
Fig. 1.7. Statistics increase at HE-LHC, relative to HL-LHC, for the production of a system of mass M, in the three production channels gg, qg and q$\bar{\text{q}}$.

of a Z boson pair, the purely longitudinal final state of the WW and ZZ scattering processes can be extracted with a significance of 5σ or more. Similarly, the reach for vector-boson-scattering will be extended by roughly a factor of two in the energy scale of BSM physics, i.e. the sensitivity of the HE-LHC to Wilson coefficients, f/Λ^4, of dimension eight operators, which describe anomalous quartic gauge couplings, improves by a factor 10–20.

FCC-hh provides great flexibility in designing analyses that optimise the balance between statistics and systematics, thanks to the large Higgs production rates, the lever arm in the production kinematics and the existence of big control samples to validate the modeling and reduce the systematics on backgrounds. This justifies optimism in the projections for precision Higgs physics at FCC-hh, as documented in Volume 1. At HE-LHC, the rate increase and the kinematic range extension are more limited and the FCC-hh analysis strategies considered so far offer more limited advantages, as suggested by the results shown here. This leads to considering analyses much closer to those established for the LHC. Detailed comparative studies, properly taking into account both the increase of pile-up and the opportunities to improve the LHC detectors' performance, will therefore be required for a reliable assessment of the improvements in the Higgs physics programme that will be possible at HE-LHC.

1.5 Further exploration of LHC discoveries at HE-LHC

In this section the potential of HE-LHC to further the understanding of possible future discoveries at the LHC is explored. Should future runs of the LHC find evidence of new phenomena, the HE-LHC would increase the statistics of these signals and make it possible to analyse their properties in more detail, or to provide conclusive evidence of unconfirmed deviations from the SM. Many interesting scenarios of new physics, e.g. supersymmetry, present a spectrum of multiple states distributed over a broad mass range and the doubling of LHC's energy would be the minimum necessary step to complement an LHC discovery.

Starting from general cases, Figure 1.7 shows the expected increase in statistics at the HE-LHC relative to HL-LHC, for final states of a given mass M produced through various partonic initial states (gg, qg and q$\bar{\text{q}}$), as a function of M. This growth in the rate takes into account an increase by a factor of 5 in integrated luminosity

Table 1.3. Mass reach at HL-LHC (in TeV) for various Z$'$ models discussed in [19,27].

Model	95%CM	3σ	5σ
SSM	6.6	6.1	5.6
LRM	6.4	5.9	5.4
ψ	6.1	5.6	5.1
χ	6.2	5.7	5.3
η	6.2	5.6	5.2
I	6.0	5.5	5.1

(15 versus $3\,\mathrm{ab}^{-1}$), in addition to the partonic luminosity increase. It is clear that the higher energy of HE-LHC is particularly beneficial in the case of the heaviest objects, where the gain can reach several orders of magnitude, whereas, for the study of low mass systems, the luminosity is the key factor. In this latter case, a careful study of the overall experimental conditions (backgrounds and pile-up) is necessary for a more reliable estimate of the actual gain obtained with the HE-LHC.

1.5.1 Characterisation of a Z$'$ gauge boson

As a specific example, the case of a new Z$'$ gauge boson, observed at the HL-LHC in the di-lepton channel with a 3 or 5σ significance is considered. While these observations are sufficient to support evidence or claim a discovery, typically, they would be insufficient for a complete identification of the properties of the new particle (e.g. defining the nature of the underlying gauge theory in terms of its couplings to quarks and leptons).

Table 1.3 shows the exclusion, evidence and discovery reach, at HL-LHC, for various Z$'$ models considered in the literature [19,27] (SSM, for example, is the sequential SM, where all Z$'$ couplings to fermions match those of the SM Z boson). The exclusion or observation reach are obtained by searching for a peak in the di-lepton mass distribution. In all these cases, the statistics are insufficient to differentiate the various models. The model discrimination requires a higher-statistics study of angular and rapidity distributions. This can be done at HE-LHC, using for example A_{FB}, r_y and $\sigma \times \mathrm{BR}$. Here $r_y = N(\mathrm{Z}', |y| < 0.5)/N(\mathrm{Z}', 0.5 < |y| < 2.5)$, while A_{FB} is defined as the asymmetry between the number of events in which the lepton moves forward or backward (in the Z$'$ rest frame) relative to the Z$'$ longitudinal direction. The left plot in Figure 1.8 shows the correlation between A_{FB} and r_y for the Z$'$ of different models, with a common mass of $6\,\mathrm{TeV}$. The interference between the signal and the SM DY amplitude is included, and events within a mass window of $200\,\mathrm{GeV}$ around the resonance peak are used. Our studies indicate that for such high mass and narrow window around the Z$'$ even a large uncertainty on the background normalisation has no impact. Therefore the left plot in Figure 1.8 assumes no uncertainties. A further handle to discriminate among different models is the study of hadronic decays to light, b and t quarks. The expected precision of the measurements is shown in the right plot of Figure 1.8. For the hadronic decays, a 50% uncertainty on the various background normalisations are considered as nuisance parameters in the profile likelihood. These systematics are not the dominant effect reported, but are likely to increase slightly for dedicated analyses, for example including real detector effects, or modelling of the underlying physical processes. With the exception of the η and ψ models, whose predictions for all variables considered are rather degenerate, all other models can be separated through a combination of different observations. For example, the SSM and ψ models, which have very close predictions for r_y and A_{FB}, have measurably different fractions of b or t final states.
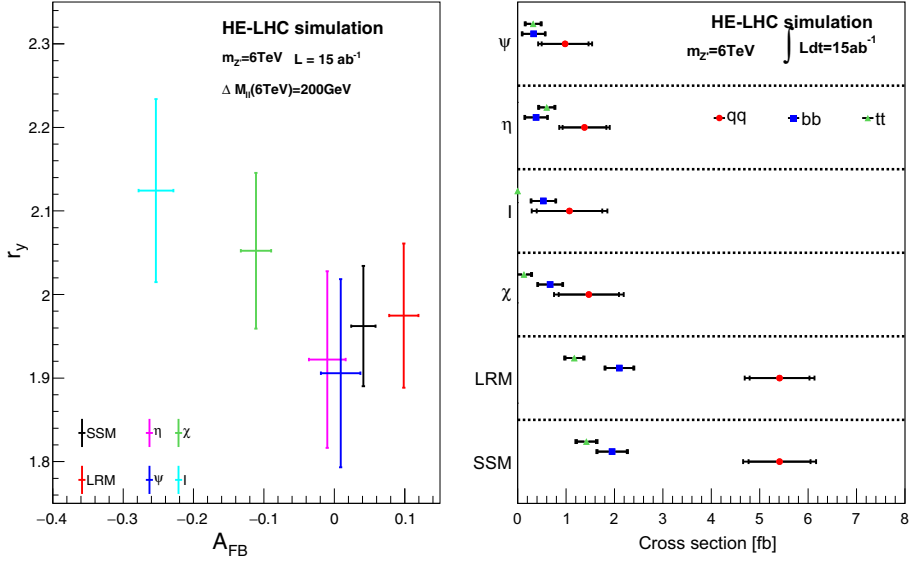
Fig. 1.8. Left: correlation between the observables r_y and A_{FB}, described in the text, for various Z′ models. Right: fitted cross section of the three hadronic analyses. Statistical and full uncertainties are shown for each point.
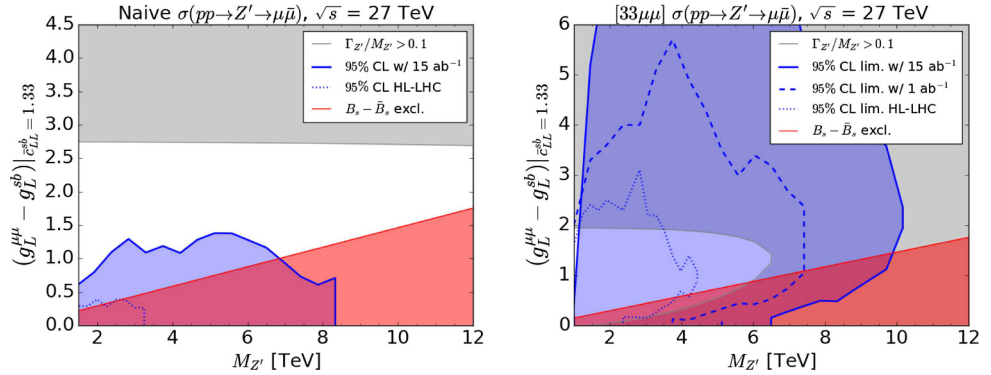
Fig. 1.9. Projected 95%CL sensitivities at HE-LHC (blue regions) for Z′ models explaining the $R_{K^{(*)}}$ anomaly, assuming narrow-width resonances ($\Gamma < 0.1 M_{Z'}$). The red region is excluded from $B_s - \bar{B}_s$ mixing measurements. See [22] for details.

1.5.2 Flavour anomalies

A set of current anomalies present in flavour physics [28], if confirmed, would revolutionise particle physics and open the search for their microscopic origin. While waiting for the final word on their existence, work has started on their possible interpretations, identifying the relevant classes of new physics models, and of model-parameter ranges. This work has been accompanied by the first studies of the potential of the LHC and of future accelerators to conclusively test these models, via the direct discovery of their new particles. An example is the work in [22], where possible scenarios, relevant to the so-called $R_{K^{(*)}}$ anomaly, are considered. The anomaly shows a deviation from the SM prediction for the ratio of branching ratios $R_{K^{(*)}}$=BR($B^0 \to K^{(*)}\mu^+\mu^-$)/BR($B^0 \to K^{(*)}e^+e^-$) and, as possible explanations, points to a Z′ gauge boson,

coupling to b$\bar{\text{s}}$ and to $\mu^+\mu^-$, or to a leptoquark, coupling to bμ and to sμ (see e.g. [29]). The corresponding couplings and masses are primarily constrained by the measured value of $R_{K^{(*)}}$ and by $\text{B}_s^0 - \overline{\text{B}}_s^0$ oscillations. For the case of the Z$'$ models, Figure 1.9 shows the coupling/mass domains that the HE-LHC would be sensitive to, at 95%CL. The left plot is for a minimal case, in which the only Z$'$ coupling to quarks involves the b$\bar{\text{s}}$ pair. The reach is limited by the low production rate for b$\bar{\text{s}}$(s$\bar{\text{b}}$) $\to$ Z$'$. The right plot corresponds to models where the Z$'$ couples to quarks via the current $\sum_{q,q'} V_{tq} V_{tq'} \bar{q} \gamma_\mu q'_L$ (q,q$'$ = d,s,b). In this case, the production channel d$\bar{\text{s}}$(s$\bar{\text{d}}$) $\to$ Z$'$amplifies the signal, giving full coverage of the allowed parameter space. Should the anomaly be confirmed, other flavour observables could add additional constraints to pin down the allowed classes of models more precisely and make more definite projections for the potential of the HE-LHC (the projections for FCC-hh are discussed in Chap. 14 of Vol. 1).

2 Collider design and performance

2.1 Requirements and design considerations

The HE-LHC should provide pp collisions at about twice the collision energy of the LHC, using the existing LHC tunnel infrastructure, without any increase of the tunnel cross section. Reaching a target beam energy of 13.5 TeV relies on the FCC-hh magnet technology. The existing LHC dipole magnets with a nominal field of 8.33 T will be replaced by FCC-type 16 T dipole magnets. Achieving a centre-of-mass energy close to 27 TeV with 16 T magnets requires a dipole filling factor similar to that of the LHC. Following a preliminary design optimisation of compact high-field dipole magnets, the inter-beam distance for the HE-LHC is set to be 250 mm, significantly larger than the 194 mm of the LHC. The lengths of the magnet interconnects are chosen in the same way as the inter-beam distance – equal to those of FCC-hh. However, the HE-LHC dipole magnets are curved, those of FCC-hh straight.

An integrated luminosity exceeding 10 ab^{-1} is within reach over about 20 years of operation of the HE-LHC. After the LHC Injector Upgrade (LIU) [10], scheduled to be completed in 2020, an extremely bright proton beam will be available for injection into the HE-LHC. The luminosity evolution during HE-LHC physics is determined by the combined effects of proton burn-off and significant radiation damping.

In the HE-LHC, both the synchrotron radiation power and, in particular, the photon flux, are much higher than in the LHC. The FCC-hh beamscreen design offers an adequate solution for the challenging cryogenic beam-vacuum system. In addition, the HL-LHC R&D effort [30] provides several novel elements essential for the HE-LHC, such as crab cavities and low-impedance collimators, as well as possible add-ons such as electron lenses, long-range beam–beam compensation and new optics solutions.

Combining advanced technological systems and beam-dynamics solutions developed for the LHC, HL-LHC, FCC-hh and the LIU, facilitates the formulation of a robust accelerator design for the HE-LHC with an excellent performance forecast.

Section 2.2 presents key parameters of the HE-LHC and 2.3 examines the primary challenges. Optics design, collimation, longitudinal parameters, and beam dynamics issues are presented in Section 2.4. In Section 2.5 the proton–proton physics operation and luminosity performance are reviewed.

In addition to delivering pp physics at the energy frontier, the HE-LHC could operate as the world's highest-energy heavy-ion and ion-proton collider. The corresponding performance parameters are discussed in Section 2.6. By adding a 60 GeV electron beam from a multi-pass energy-recovery linac, as proposed for the LHeC,

the HE-LHC could also provide high-energy lepton-proton and lepton-ion collisions. This "HE-LHeC" option is reviewed in Section 2.7.

2.2 Parameter choices

The HE-LHC design assumes essentially the same beam parameters as HL-LHC. Beams meeting the HL-LHC requirements will be available from the upgraded LHC injector complex. Adopting the beam parameters of HL-LHC, the HE-LHC bunch population is taken to be 2.2×10^{11} and the normalised transverse rms emittance at the start of a store to be $2.5\,\mu$m. The bunch spacing of 25 ns is chosen to be the same as in the LHC and HL-LHC.

The baseline design parameters are summarised in Table 2.1, which also presents a comparison with the corresponding values for LHC, HL-LHC and FCC-hh [9]. It is assumed that HE-LHC will accommodate two high-luminosity interaction-points (IPs) 1 and 5, at the locations of the present ATLAS and CMS experiments. IPs 2 and 8 could host secondary experiments, e.g. with a lepton-hadron collision point, combined with injection, as for the present LHC, or the available space could be exploited to serve other needs, e.g. for an extended high energy injection section or for collimation.

At present, optics solutions with a short-term (10^5 turns) dynamic aperture exceeding 10σ only exist for an injection energy above 1 TeV. An injection energy of 1.3 TeV, as could be provided by a superconducting SPS (scSPS), is the current baseline. The creation of artificial pinning centres (APCs) in the Nb_3Sn superconductor might potentially enable an injection energy of 900 GeV or below. The possibility of 450 GeV injection requires further studies.

2.3 Design challenges and approaches

Key design challenges include:

1. The handling of high levels of synchrotron radiation inside the cold arcs;
2. The choice of injection energy in view of significantly decreased physical aperture, greatly enhanced field errors for Nb_3Sn magnets at low energy and a possibly larger energy swing;
3. The event pile-up in the experiment detectors;
4. Achieving the required high dipole packing density in the arcs; and
5. Developing optics for the experiment insertions, beam extraction and for collimation, all of which must fit into the existing straight sections, without the possibility of applying any of the length scaling used for the FCC-hh.

The optics design challenges for the arc and IRs, beam extraction and collimation will be addressed in Section 2.4.

2.3.1 Synchrotron radiation

The synchrotron radiation power and photon flux are both much higher than those of the LHC and, remarkably, the flux is even higher than for FCC-hh (see Tab. 2.2).

The FCC-hh beamscreen [31], illustrated in Figure 2.1, offers an optimum solution for the HE-LHC cryogenic beam vacuum system. Compared with an LHC-type beamscreen, this beamscreen developed for the FCC-hh features greatly enlarged cooling capillaries for increased helium mass flow, a large surface area of shielded

Table 2.1. Key parameters of HE-LHC compared with FCC-hh, HL-LHC and LHC, for operation with proton beams.

Parameter	Unit	FCC-hh		HE-LHC	(HL-)LHC
Centre-of-mass energy	TeV	100		27	14
Injection energy	TeV	3.3		1.3 (0.9, 0.45)	0.45
Peak arc dipole field	T	16		16	8.33
Circumference	km	97.8		26.7	26.7
Straight-section length	m	1400		528	528
Beam current	A	0.5		1.12	(1.12) 0.58
Bunch population	10^{11}	1.0		2.2	(2.2) 1.15
Number of bunches/beam	–	10 400		2808	(2760) 2808
RF voltage	MV	32		16	(16) 16
RMS bunch length	mm	~ 80		90	(90) 75.5
Bucket half height	10^{-3}	0.16		0.21	0.36
RMS momentum spread	10^{-4}	0.5		0.85	1.129
Longitudinal emittance ($4\pi\sigma_z\sigma_E$)	eVs	~ 8		4.2	2.5
Bunch spacing	ns	25		25	25
Norm. transv. rms emittance	μm	2.2		2.5	(2.5) 3.75
IP beta function $\beta_{x,y}^*$	m	1.1	0.3	0.45	(0.15) 0.55
Initial rms IP beam size $\sigma_{x,y}^*$	μm	6.7	3.5	9.0	(7.1 min) 16.7
Half crossing angle	μrad	37	100	165	(250) 142.5
Piwinski angle w/o crab cavities	–	0.42	2.16	1.7	(2.7) 0.65
Peak luminosity per IP	$10^{34}\,\mathrm{cm}^{-2}\,\mathrm{s}^{-1}$	5	30	16	(5, levelled) 1
Total cross section	mbarn	153		126	111
Inelastic cross section	mbarn	108		91	85
Peak no. of events/crossing	–	170	1000	460	(135) 27
RMS luminous region	mm	53	49	57	(68) 45
Stored energy/beam	GJ	8.4		1.4	(0.7) 0.36
Energy loss per proton per turn	keV	4600		93	6.7
SR power/beam	kW	2400		100	(7.3) 3.6
SR power/length	W/m/aperture	29		4.6	(0.33) 0.17
Transv. emittance damping time	h	1.1		3.6	25.8
No. of high-luminosity IPs	–	2	2	2	(2) 2
Initial proton burn-off time	h	17	3.4	4.3	(15) 40
Allocated physics time/year	days	160	160	160	160 (160)
Average turnaround time	h	5	4	5	4 (5)
Optimum run time	h	11.6	3.7	5.3	(18–13) $\sim$10
Accelerator availability	–	70%	70%	75%	(80%) 71%
Nominal luminosity per day	fb^{-1}	2.0	8.0	4.5	(1.9) 0.4
Luminosity per year (160 days)	fb^{-1}	$\geq$250	$\geq$1000	500	(350) 55

Notes. All values, except for the injection energy itself, refer to the collision energy.

Table 2.2. Synchrotron radiation (SR) characteristics in the arcs of LHC, HE-LHC and FCC-hh.

Parameter	LHC	HE-LHC	FCC-hh
Linear SR power (W/m)	0.25	5.5	35
Linear photon flux (10^{16} photons/m/s)	5	27	15
Critical photon energy (eV)	44	320	4300
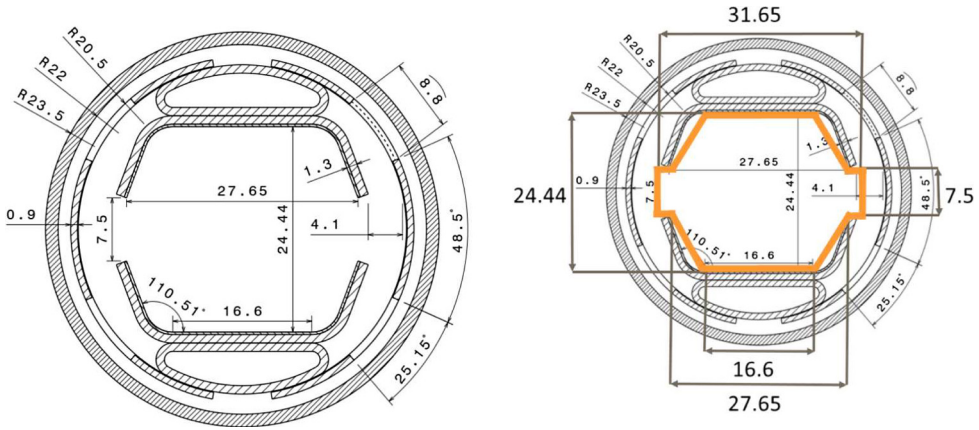
Fig. 2.1. Beamscreen proposed for FCC-hh and HE-LHC [32] (left); and the approximation used for aperture calculation [33] (orange line, right).
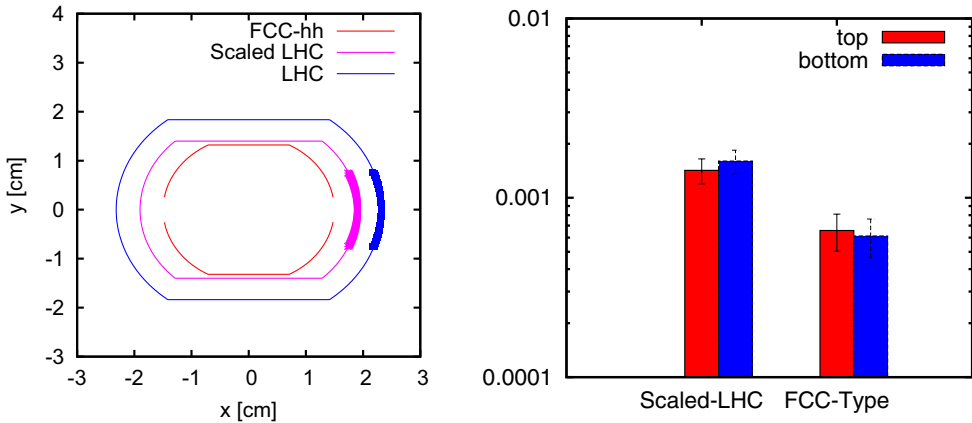
Fig. 2.2. Vacuum chamber cross sections for FCC-hh, LHC and scaled LHC beamscreens, where the thicker line represents the sawtooth on the wall and the transparent region is an opening slot (left); and the fraction of photons absorbed with a 95% confidence interval at the top and bottom of the two vacuum chambers proposed for HE-LHC [34] (right).

pumping slots for reduced impedance and high pumping speed and a kind of "folded antechamber" to minimise the number of photo-electrons generated in the beam pipe itself.

The FCC-hh and HE-LHC beamscreens operate at an elevated temperature of 50 K instead of the LHC's 5–20 K because the higher temperature improves the Carnot efficiency. The large pumping speed is appropriate for the high out-gassing rates caused by the extremely high photon flux from synchrotron radiation. In addition, the FCC-hh type beamscreen reduces the fraction of photons reflected towards the top and bottom of the vacuum chamber by a factor 2–3 compared to an LHC-type beamscreen [34], as is illustrated in Figure 2.2. This helps suppress the initiation of electron-cloud build up due to photo-electrons.

2.3.2 Dynamic and physical aperture at injection

Injection into the HE-LHC could be accomplished from a new fast ramping superconducting (SC) synchrotron in the SPS tunnel (scSPS). SC magnets with double-layer

coils would allow an injection energy of 1.3 TeV, which provides an adequate dynamic and physical aperture at injection and has been chosen as a solid baseline. Alternative injector scenarios include injection at 900 GeV from a single-layer coil SC synchrotron in the SPS tunnel, or injection from the existing warm SPS at 450 GeV. The injector scenarios are detailed in Section 6.

A large number of possible arc optics for the HE-LHC collider were surveyed. The two best performing optics are being developed further. One of these optics is LHC-like with 23 cells per arc, and 90° phase advance per cell, and is the design baseline. The other optics features fewer (18), longer cells, which results in a higher dipole filling factor and hence energy reach. With reference to the number of optical cells per arc and to their betatron phase advance per cell, these two optics are called 23×90 and 18×90, respectively.

At an injection energy of 1.3 TeV, the dipole field would be 1.59 T with the LHC-like 23×90 optics (or 1.53 T with the 18×90 optics). At an injection energy of 900 GeV the field would be about 1.1 T and at 450 GeV about 0.55 T.

Linear optics perturbations would significantly degrade the design performance if the quadrupole component of the dipole magnets (opposite for the two apertures) was too large. The b_2 errors of the dipole magnets are kept below 30 units (10^{-4} at 16.7 mm) at all energies and are therefore acceptable, thanks to the increased inter-beam distance of 250 mm, with respect to the 194 mm in the LHC [35].

The primary nonlinear field error affecting the dynamic aperture is the sextupole component of the dipole magnets. Another relevant error is the decapole component. At injection energy, both types of multipole error are dominated by persistent currents in the superconducting (SC) cable. To obtain an acceptable field quality at injection energy for the HE-LHC Nb$_3$Sn magnets, the effective filament size of the SC wire is chosen as 20 μm, to be compared with a larger filament diameter of 50 μm being used for the HL-LHC conductor. The smaller filament size greatly lowers the field errors at injection related to persistent currents. A further improvement of the field quality at injection is expected from the addition of artificial pinning centres (APCs) [11]. For a given fixed value of critical current density at high field, the addition of APCs decreases the corresponding critical current at low field levels and, thereby, the strength of the persistent current effects. A realistic target value for the flux pinning efficiency is 50%. Figure 2.3 shows the sextupole and decapole multipole errors as a function of the dipole field strength without any artificial pinning centres, with an ideal pinning efficiency of 100%, and with the baseline 50% flux pinning efficiency.

It is common to distinguish systematic ($b_{n,S}$, $a_{n,S}$), uncertainty ($b_{n,U}$, $a_{n,U}$), and random multipole errors ($b_{n,R}$, $a_{n,R}$) of order n. Here, the b coefficients refer to normal field errors and the a components to skew errors. For example, b_2 refers to a normal quadrupole field, b_3 to a normal sextupole, a_2 to a skew quadrupole and b_5 to a normal decapole. In the following, the values of the various multipoles are given in units of 10^{-4} relative to the main field (e.g. dipole field), at a reference radius r_0 (for HE-LHC, $r_0 = 16.7$ mm). The field error b_n of a magnet is calculated as [36]

$$b_n = b_{n,S} + \frac{\xi_U}{1.5} b_{n,U} + \xi_R b_{n,R}, \tag{2.1}$$

where the second term on the right-hand-side represents the difference between production lines (ξ_U is a random number chosen per magnet production line, cut at 1.5σ) and the last term models the random variation from magnet to magnet (a new random number ξ_R, cut at 3σ, is selected for each individual magnet).

Table 2.3, displays some of the predicted systematic, uncertain and random multipole errors for a filament size of 20 μm and 50% pinning efficiency at an injection energies of 1.3 TeV, 900 GeV and 450 GeV.
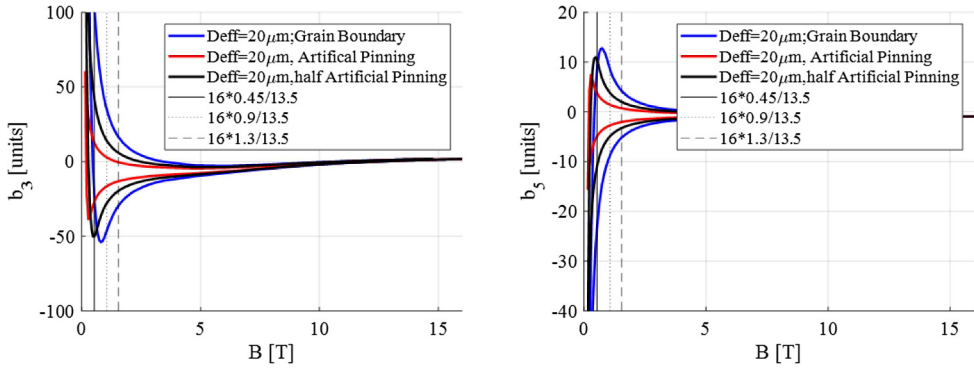
Fig. 2.3. Sextupolar and decapolar multipole errors b_3 and b_5, in units of 10^{-4} at a reference radius of 16.7 mm, for the 16 T dipole magnets as function of field strength, for an effective Nb$_3$Sn filament size of 20 μm, without (blue), with 100% artificial pinning (red), and with a realistic 50% pinning efficiency (black). Three different injection energies are indicated.

Table 2.3. Normal and skew multipole errors in the main arc dipoles up to dodecapole components for injection energies of 1.3 TeV, 900 GeV and 450 GeV, in units of 10^{-4} at a reference radius of 16.7 mm with 20 μm filament size and 50% pinning efficiency [37].

Multipole	Systematic	Uncertainty	Random	Multipole	Syst.	Unc.	Random
1.3 TeV							
b_2	4.79	0.93	0.93	a_2	0.00	1.10	1.10
b_3	-16.20	0.67	0.67	a_3	0.00	0.75	0.75
b_4	0.85	0.47	0.47	a_4	0.00	0.47	0.47
b_5	3.19	0.28	0.28	a_5	0.00	0.33	0.33
b_6	0.54	0.19	0.19	a_6	0.00	0.21	0.21
900 GeV							
b_2	5.61	0.93	0.93	a_2	0.00	1.10	1.10
b_3	-24.86	0.67	0.67	a_3	0.00	0.75	0.75
b_4	0.80	0.47	0.47	a_4	0.00	0.47	0.47
b_5	5.11	0.28	0.28	a_5	0.00	0.33	0.33
b_6	0.67	0.19	0.19	a_6	0.00	0.21	0.21
450 GeV							
b_2	7.83	0.93	0.93	a_2	0.00	1.10	1.10
b_3	-50.76	0.67	0.67	a_3	0.00	0.75	0.75
b_4	0.64	0.47	0.47	a_4	0.00	0.47	0.47
b_5	12.26	0.28	0.28	a_5	0.00	0.33	0.33
b_6	1.08	0.19	0.19	a_6	0.00	0.21	0.21

Comparing the field errors for different energies in Table 2.3 reveals that with 50% pinning efficiency, the absolute value of the b_3 field error at 900 GeV is about two times smaller than the one at 450 GeV (25 versus 51 units). This is consistent with the hysteresis curves in the left picture of Figure 2.3 and is explained by the fact that, for 50% pinning efficiency, at 450 GeV the field has just about penetrated all of the conductor; the maximum b_3 is reached at around 0.55 T (or at a beam energy of 450 GeV).

Table 2.4 and Figure 2.4 illustrate the off-momentum dynamic aperture (DA) due to all multipole errors, simulated by tracking with the SIXTRACK code [38] over 10^5 turns, for an initial relative momentum offset equal to 3/4 of the RF bucket height, and including correctors for the systematic b_3, b_4 and b_5 in each arc (b_3 correctors at each dipole, and b_4/b_5 correctors on every second dipole). Independent simulations

Table 2.4. Simulated minimum dynamic aperture due to all nonlinear multipole errors, up to 20-poles, as obtained by tracking over 10^5 turns, for 5 angles in x–y space, 60 random error seeds, fractional betatron tunes of 0.28 (H) and 0.31 (V) and a chromaticity $Q'_{x,y}$ corrected to $+2$ units.

Optics	Parameter	450 GeV	900 GeV	1.3 TeV
23 × 90	RF voltage (MV)	10.4	10.5	10.6
	momentum offset $\Delta p/p$	8.27×10^{-4}	5.84×10^{-4}	4.86×10^{-4}
	DA w/o APCs	2.7σ	8.0σ	12.1σ
	DA w. 50% flux pinning	5.4σ	12.3σ	15.9σ
	+ sorting	6.2σ	13.9σ	18.1σ
18 × 90	RF voltage (MV)	10.7	10.8	10.8
	momentum offset $\Delta p/p$	6.53×10^{-4}	4.61×10^{-4}	3.84×10^{-4}
	DA w/o APCs	1.5σ	4.2σ	7.6σ
	DA w. 50 flux pinning	2.7σ	7.4σ	11.2σ
	+ sorting	3.8σ	9.0σ	14.4σ

Notes. The systematic, random and uncertainty field errors assumed are those for $20\,\mu$m filament size (the corresponding error values at 1.3 TeV, 900 GeV, and 450 GeV, for APC with 50% pinning efficiency, are given in Tab. 2.3). The systematic part of the b_3 errors was corrected using one sextupole spool piece at each dipole; the systematic b_4 and b_5 errors were compensated with octupole and decapole correctors installed after every second dipole [40].

with a different program (LEGO) yield similar values for the dynamic aperture [39]. Requiring a dynamic aperture of at least 12σ, as for the LHC design, means that at present, the only solution is the 23×90 optics with an injection energy of 900 GeV or above. The 18×90 optics with an injection energy of 1.3 TeV could also be marginally acceptable.

Using two b_3 correctors, i.e. one corrector on each end of each dipole magnet, symmetrises the correction across each optical half cell and thereby improves the 1000-turn dynamic aperture by at least one σ and in many cases by a few σ [39]. Similarly, b_3 correction along the entire magnet or other symmetrical set ups (e.g. one out of three or four dipoles with two correctors, the others with one corrector) should yield dynamic apertures comparable to the two-corrector-per-dipole scheme. Whichever correction scheme is chosen, the alignment tolerances for the b_3 correctors will be an important concern.

The high random sextupole component in the main dipoles was identified as the limiting factor of the dynamic aperture, particularly in the case of no APCs and lower injection energies. For this reason, the effect of sorting via b_3 was examined. Assuming that the field errors of all dipole magnets are measured prior to installation and that no other restrictions exist on the placement of the dipoles, magnets with a similar level of b_3 were grouped together in the same arc section, for both beams, using an adapted K-means clustering algorithm. The resulting improvement of the dynamic aperture for beam 1 (the magnets were sorted for both beams simultaneously) is illustrated in Figure 2.5. The dipole-magnet sorting increases the lowest values of dynamic aperture by about 1σ. Other sorting strategies, sorting with higher order components, and the case of a limited pool of available dipoles for installation in a given slot could be explored in the future.

In summary, with $20\,\mu$m filaments and 50% flux pinning the dynamic aperture at 1.3 TeV is comfortable. Lower injection energies, around 1 TeV, could also be considered; presently the field quality at 450 GeV would be far from adequate. Adding magnetic iron shims [41] or high-temperature-superconductor (HTS) persistent current shims [42] could further reduce the b_3 field errors at all beam energies [35].
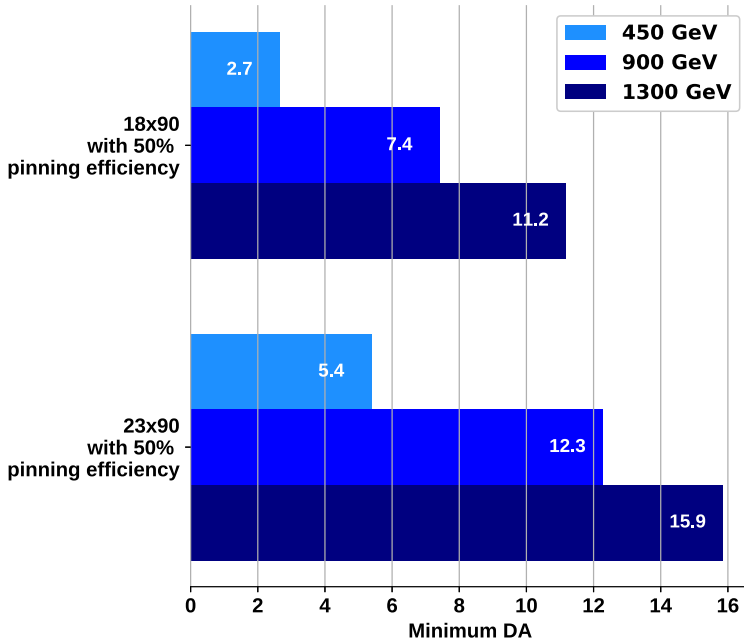
Fig. 2.4. Simulated minimum off-momentum dynamic aperture (10^5 turns) due to all non-linear multipole errors, up to 20-poles, assuming $20 \, \mu$m Nb_3Sn filament diameter with 50% flux pinning, as obtained by tracking over 10^5 turns, for 5 angles in x–y space, 60 random error seeds, fractional betatron tunes of 0.28 (H) and 0.31 (V) and a chromaticity $Q'_{x,y}$ corrected to +2 units. These results are a graphical representation of Table 2.4. The systematic part of the b_3, b_4 and b_5 errors was corrected using one sextupole spool piece next to every main dipole and one nested octupole/decapole spool piece at every second dipole [40].
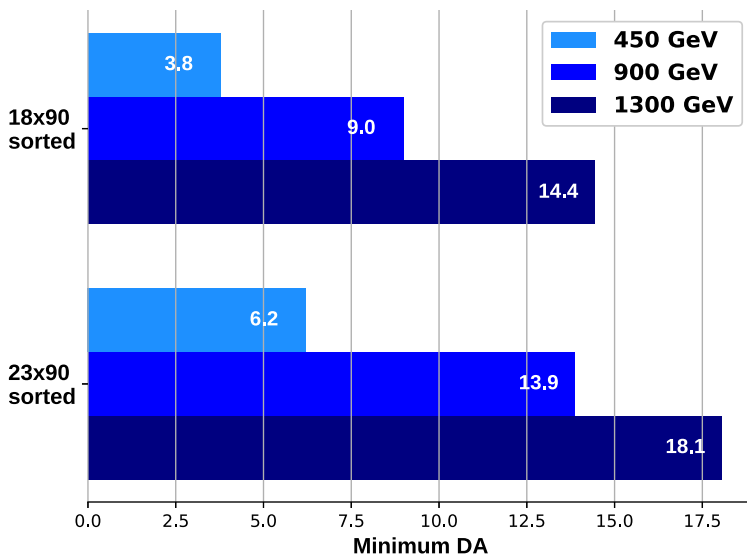
Fig. 2.5. Simulated minimum off-momentum dynamic aperture as in Figure 2.4, demonstrating the improvement obtained by sorting the dipole magnets according to random b_3 component for both beams.
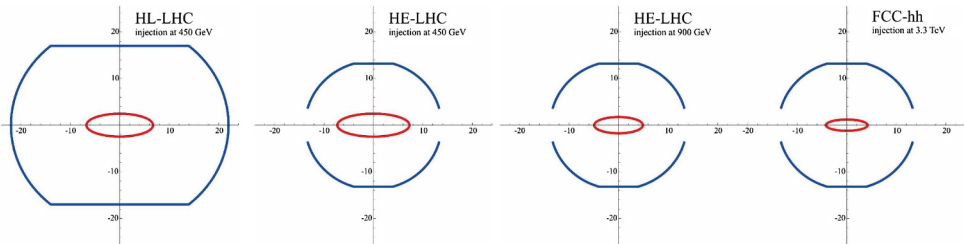
Fig. 2.6. Beam envelope (6σ) at injection energy inside the (approximate) beamscreen at a regular arc QF quadrupole for HL-LHC and for HE-LHC with two alternative injection energies (450 and 900 GeV), assuming the 23×90 optics, and for FCC-hh (at 3.3 TeV), without any b_2 field error.

The rms beta-beating induced by the random b_2 component of each dipole alone, specified in Table 2.3, would amount to 3.9% in the 23×90 arc optics and 4.9% in the 18×90 arc optics (either 23 or 18 cells per arc with a betatron phase advance per cell of 90°), the higher beta-beating in this option being attributed to the larger number of dipoles and, mostly, to the larger beta functions. This assumes that the systematic quadrupole component common to all main dipoles in one arc is well corrected and will not contribute to beta-beating. Another significant contribution to beta-beating could come from the sextupole spool pieces attached to each dipole. For a horizontal misalignment of these b_3 correctors with respect to the magnetic axis of the dipole, the b_2 component generates an additional linear optics perturbation via feed-down. To limit this effect, the alignment tolerances of the spool pieces can be specified by imposing the criterion that the b_2 from feed-down should not exceed the random b_2 of the dipoles. With this condition, the alignment of the spool pieces is required to be below 0.1 mm for the case of 450 GeV injection energy with the highest systematic b_3. Due to the decreased systematic sextupole component (and hence weaker corrector strength) for the higher injection energies of 900 GeV and 1.3 TeV, the alignment tolerances increase to 0.28 mm and 0.43 mm, respectively.

Figure 2.6 compares the 6σ beam size at a focusing arc quadrupole (QF) inside the beamscreen (LHC or FCC type) for the HL-LHC at 450 GeV, the FCC-hh at its nominal injection energy of 3.3 TeV, and the HE-LHC at either 450 or 900 GeV, for the 23×90 optics. At 450 GeV the physical aperture normalised to the beam size is smaller than for any other existing or proposed hadron collider. For the alternative 18×90 optics with only 18 cells per arc, which offers a higher energy reach, the beam size is larger and, accordingly, the normalised physical aperture lower by about a further 2σ. A b_2 field error of 50 units would further reduce the physical aperture at 450 GeV by $\sigma/2$, as is illustrated in Figure 2.7. The latest, asymmetric magnet design ensures that b_2 remains smaller than 5 units at all energies and for both apertures [37].

2.3.3 Event pile-up

For the design bunch spacing of 25 ns the peak pile-up in the experiments is about 460 events per bunch crossing, i.e. more than three times higher than the HL-LHC design value of 140. If necessary, the peak pile-up could be reduced by levelling, as is planned for HL-LHC [43,44]. A reduction of the peak pile-up by a factor of two, to about 200, might lead to a loss of integrated luminosity of about 20%. Another option is to reduce the bunch spacing with a simultaneous decrease in transverse emittance. Halving the bunch spacing from 25 ns to 12.5 ns would also halve the pile-up. However, it may be difficult to produce beams with even smaller bunch spacing
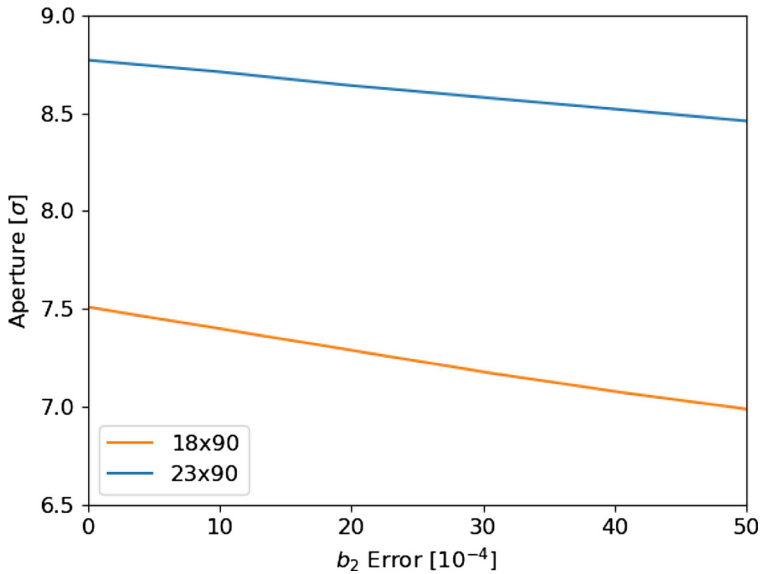
Fig. 2.7. Physical aperture in units of rms beam size (σ) as a function of the magnitude of the systematic b_2 error in the arc dipoles for the 23×90 and 18×90 optics.

in the present LHC injector complex and the experiments may not necessarily benefit from such a short spacing.

2.4 Optics design and beam dynamics

2.4.1 Arc optics

The choice of the arc optics must be a compromise between maximising the energy reach, fitting within the existing tunnel geometry and possibly allowing injection from the existing SPS at a beam energy of only 450 GeV. While a higher dipole packing factor is achieved with fewer and longer cells, injection at lower energy would require stronger focusing and a larger number of shorter cells.

As indicated in Section 2.3, two alternative optics have been developed in detail, both with 90° phase advance per cell. The first one (18×90), features only 18 FODO cells per arc, which maximises the dipole filling factor and energy reach of the collider. The second optics (23×90), consists of 23 cells per arc, similar to the present LHC optics. For the 23×90 optics, the collision energy at a dipole field of 16 T is more than 1 TeV lower than for the 18×90 optics.

At 450 GeV, with the new FCC-hh type beamscreen, for both optics the physical aperture appears unacceptably small and, for the currently expected field errors, the dynamic aperture is also insufficient. However, the 23×90 optics might potentially offer a chance for injection at 450 GeV from the existing SPS, provided that the magnet field quality can be improved sufficiently and the issues of collimation and machine protection can be adequately addressed: even with this 23×90 optics, at 450 GeV the physical aperture would still be less than 9σ (see Fig. 2.16 below).

While the field of the dipole magnets is almost twice that in the LHC for this second optics, the maximum quadrupole strength is increased by less than 50% (assuming single coil Nb$_3$Sn magnet technology). Consequently, the length of the arc quadrupoles has to be about 15% higher than in the LHC. Both HE-LHC optics

Table 2.5. Arc optics parameters for LHC (scaled to a beam energy of 13.5 TeV) and the two HE-LHC optics designs (23×90 and 18×90).

Parameter	Unit	LHC	HE-LHC 23×90	HE-LHC 18×90
Arc cell phase advance	degree	90	90	90
Arc cell length	m	106.9	106.9	137.33
Normalised quadrupole gradient K	m^{-2}	0.009	0.00819	0.00746
Quadrupole gradient at 13.5 TeV	T/m	405	352	336
Quadrupole length	m	3.1	3.3	2.8
Dipole length	m	14.3	13.73	13.94
Dipole-dipole distance	m	1.36	1.5	1.5
Max., min. beta function	m	181, 32	177, 32	230, 40
Max., min. dispersion	m	2.2, 1.1	2.2, 1.1	3.6, 1.8
Momentum compaction α_C	10^{-4}	3.22	3.5	5.8
Arc filling factor	%	0.80	0.77	0.81
Dipole field for 13.5 TeV	T	16.05	16.72	15.82
C.M. energy for 16 T dipole field	TeV	26.91	25.83	27.24
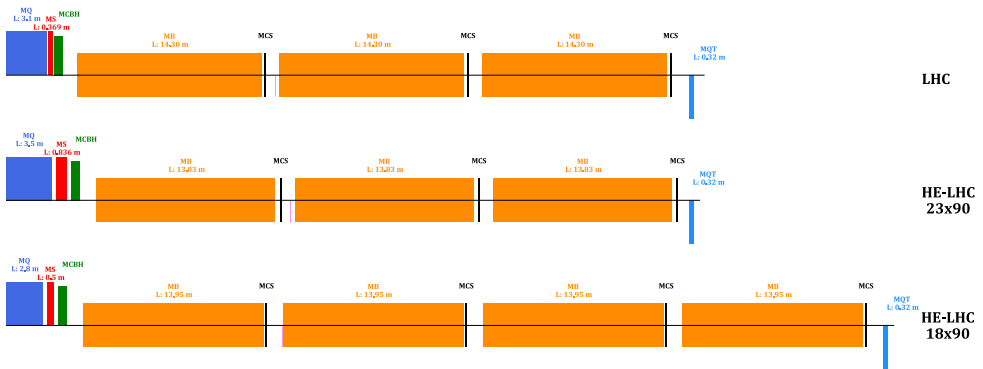
Fig. 2.8. Layout and longitudinal dimensions for the regular arc cell of the present LHC (top), for the HE-LHC 23×90 optics with 23 cells per arc similar to the LHC (centre) and for the alternative HE-LHC 18×90 optics, with 18 cells per arc and longer cells (bottom).

respect the additional requirements from the Nb₃Sn magnet design, i.e. they accommodate the increased inter-magnet distances of the FCC-hh.

Table 2.5 presents key parameters for the 23×90 and 18×90 arc optics along with those of the present LHC. Figure 2.8 compares the two alternative arc cell layouts with those of the LHC. Figure 2.9 shows the optical functions and magnet configuration for the two proposed HE-LHC arc cells. As indicated in the figure, in addition to 8 or 6 main bending magnets (MB), respectively, two main quadrupoles (MQ), and two main sextupoles (MS), each cell comprises decapole and octupole correctors (MCD and MCO, nested) on every second dipole, two trim quadrupoles (MQT), two orbit correctors (MCB), and two beam-position monitors (BPMs). Sextupole spool-piece correctors (MCS) are attached to each dipole magnet. Depending on the location in the arc, the short straight sections (SSS) at the end of each optical half cell accommodate octupole magnets (MO), tuning quadrupoles (MQT) or skew quadrupoles (MQS) next to a main quadrupole (MQ). Specifically, in the first five arc cells on each side (those located nearest the IRs), two MQTs are installed per cell; each arc features four MQS; MOs are placed at all quadrupoles without any adjacent MQS or MQT.
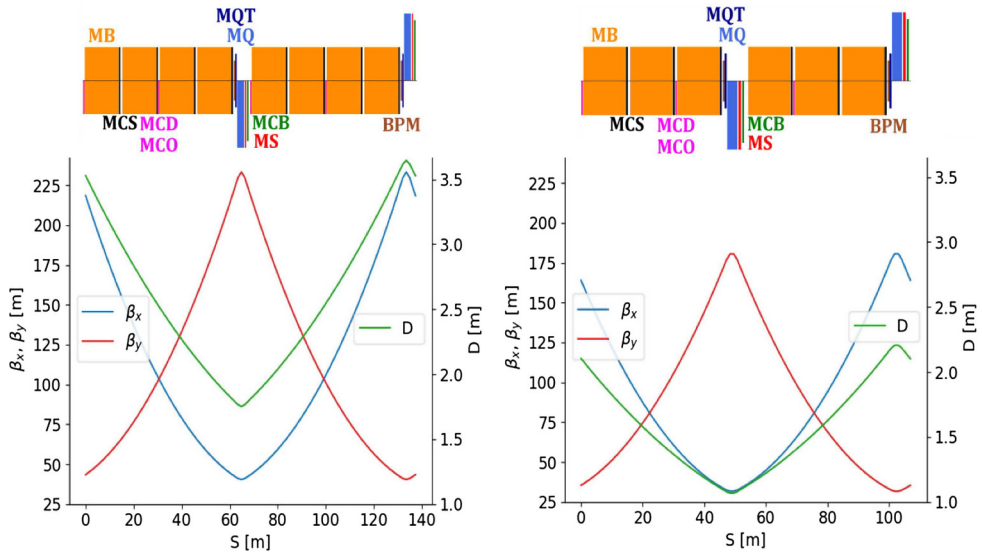
Fig. 2.9. Optics and magnet layout for the regular arc cell of the 18×90 optics with 18 cells per arc (left) and for the 23×90 optics with 23 cells per arc and longer cells (right).

2.4.2 Dispersion suppressors and geometry

The transition between arcs and dispersion-free straight sections is made by means of a so-called dispersion suppressor (DS). Each LHC dispersion suppressor comprises four individually powered quadrupole magnets which are separated by two (instead of three, as in the arcs) dipole magnets. This arrangement of 4 quadrupole and 8 dipole magnets is referred to as two missing dipole cells in the following text. Reducing the dispersion at the IPs to zero requires special powering of two more quadrupole magnets on each side of the arc. In terms of the machine optics, the dispersion suppressor, therefore, refers to the two missing "irregular" dipole cells plus one additional "regular" arc cell. The regular part of the DS is identical to the first FODO cell of its respective arc. The irregular portion of the DS is made of two cells with a total number of eight dipoles which are presently chosen to be identical to the arc dipoles. The irregular part is located closest to the IR and is connected to the regular part by a drift space varying in length between 10 m and 20 m. All of the six quadrupoles in the DS are powered individually.

Three different DS layouts, shown in Figure 2.10 for the 23×90 lattice, are integrated depending on the IR. In the DS next to IR3 and IR7, presented in the middle of Figure 2.10, every quadrupole (MQ) is followed by one or two trim quadrupoles (MQTLI). Both quadrupole types are used for matching. An orbit corrector (MCB) is located next to every quadrupole. The trim quadrupoles as well as the orbit correctors used in the irregular part of the DS are longer than their respective counterparts in the arc. Next to IR1 and IR5 6 m long quadrupoles are needed to ensure sufficient matching flexibility [45]. This configuration is shown in the top plot of Figure 2.10. Finally, the bottom picture of Figure 2.10 illustrates the DS integrated next to IR2, IR4, IR6 and IR8. For the 18×90 lattice the irregular part of the DS is schematically identical to the 23×90 lattice, while the regular part equals the respective regular arc cell of the 18×90 lattice. A modified layout of the DS at all odd-number IRs [46] enables the installation of two DS collimators (TCLD) for improved cleaning efficiency (see Sect. 2.4.6).
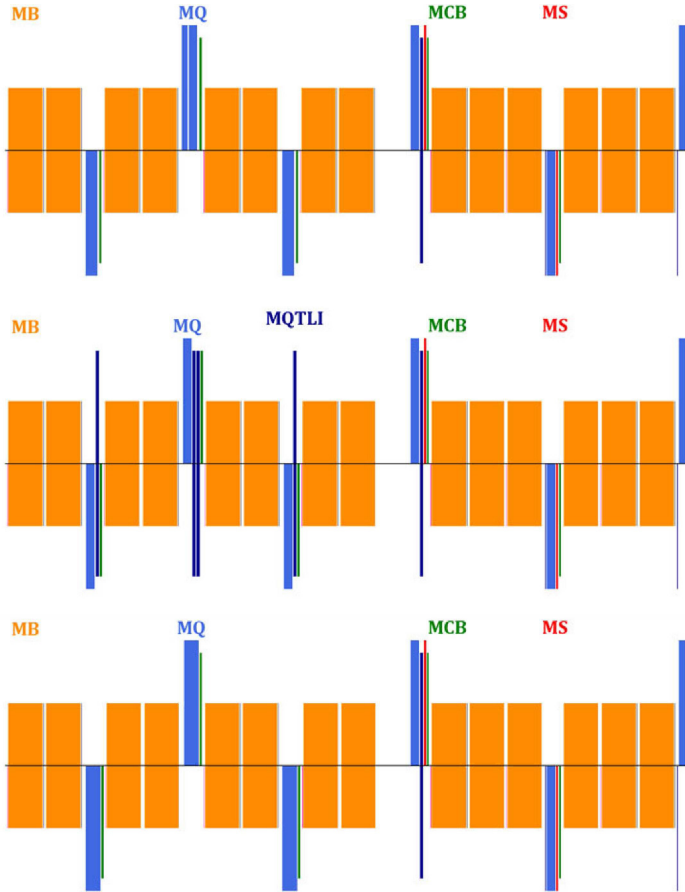
Fig. 2.10. Dispersion suppressor layout for the HE-LHC 23×90 arc optics, in IR1 and 5 (top), IR3 and 7 (centre), and IR2, IR4, IR6 and IR8 (bottom) [33].

The LHC design optics had been matched to the footprint of LEP, with a maximum offset of less than 6 cm, as is illustrated in Figure 2.11. The overall geometrical offset of the HE-LHC lattice with respect to either LEP or LHC may be divided in two parts: arcs, and dispersion suppressors. The offset of the arcs may generally be reduced to about 2 cm peak-to-peak by adjusting the arc cell length to adapt the global bending radius to the curvature of the tunnel, and by centring the bends with respect to the IPs in the same way as in the present LHC. On the other hand, reducing the offset of the DS needs to be done "by hand" and requires more effort.

The geometrical offset of the HE-LHC or LHC dispersion suppressors with respect to LEP depends strongly on the total deflection of the 8 bends in each DS (8A–11B; see Fig. 2.14), which is equal to $16\pi/N_{\mathrm{bend}}$ if all N_{bend} bends in the ring are chosen to be identical. This offset has a minimum amplitude if the DS deflections of LEP (or LHC) and HE-LHC are approximately equal, i.e. in the range $1230 < N_{\mathrm{bend}} < 1237$. A bend scheme of 1232 (a multiple of 16) identical bends was chosen for the present LHC (23 cells per arc), resulting in the footprint difference of Figure 2.12 (right picture). Previous design versions (25 cells, 24 cells) used very different bend schemes, and in those lattices one or more bends in each DS needed to be different from the ones in the regular arc cells in order to follow the LEP geometry.
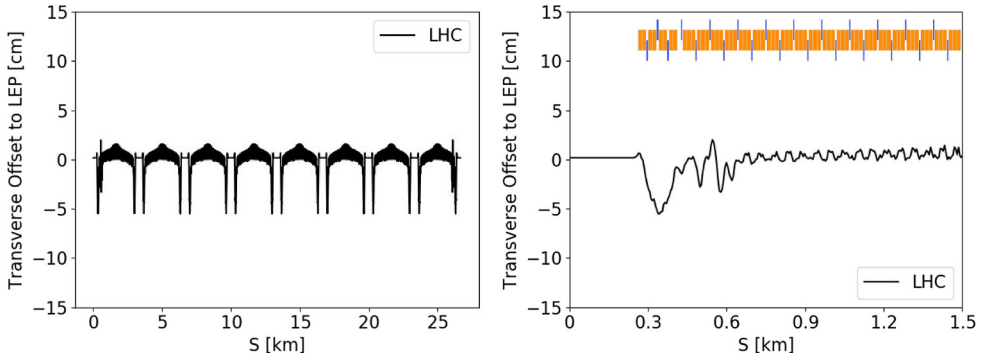
Fig. 2.11. Horizontal difference of the LHC from the LEP footprint all around the ring (left) and in the region of the dispersion suppressor (right).
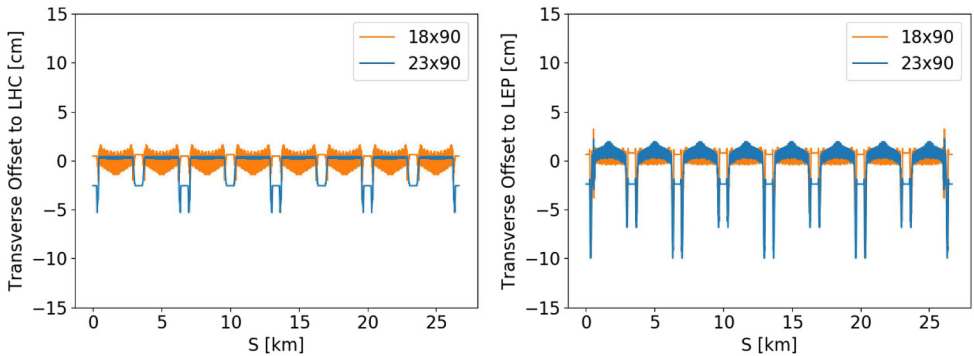
Fig. 2.12. Horizontal difference from the LHC (left) and LEP footprint (right) all around the ring for both the 23×90 with collimators (TCLDs) in the dispersion suppressors of IRs 1, 3, 5 and 7, and for a preliminary 18×90 HE-LHC optics without space for TCLDs.

In the proposed HE-LHC 23×90 lattice N_{bend} is also equal to 1232, and a reasonable offset value of 78 mm peak-to-peak w.r.t. LEP (compared to 69 mm for the peak-to-peak offset of the present LHC w.r.t. LEP) could easily be obtained. However, going away from the number of 1232 bends (e.g. with a cell scheme like 18×90) it becomes more difficult to limit the DS offset. Changing the number of bends in each DS is excluded with such moderate ($\sim$50) changes of N_{bend}, as this would produce a too large an imbalance between the deflections of the DS and the arcs. If the main bends are to remain all identical the only solution left is to move some bends longitudinally. An offset of only 64 mm could recently be achieved in an 18×90 test lattice ($N_{bend} = 1280$), but at the expense of fine tuning the geometry with many bend displacements.

The horizontal offset corresponding to both HE-LHC optics from the LHC and LEP machines is illustrated in Figure 2.12. In the arcs the maximum offset allowed from the LHC or LEP line is about 3 cm. A better fit to the LEP footprint implies a larger difference from the LHC, especially in the DS region. A zoomed view of the offset in this region is shown in Figure 2.13. It is thought that the tunnel wall in the dispersion suppressors follows the LEP footprint. Either optics can be matched to comply with the geometrical constraints.

Two special collimators (TCLDs) are needed in each DS of the collimation straights 3 and 7 and of the high-luminosity straights 1 and 5. It is proposed to displace the dipole pairs 8 and 11, to make room for these collimators, as is
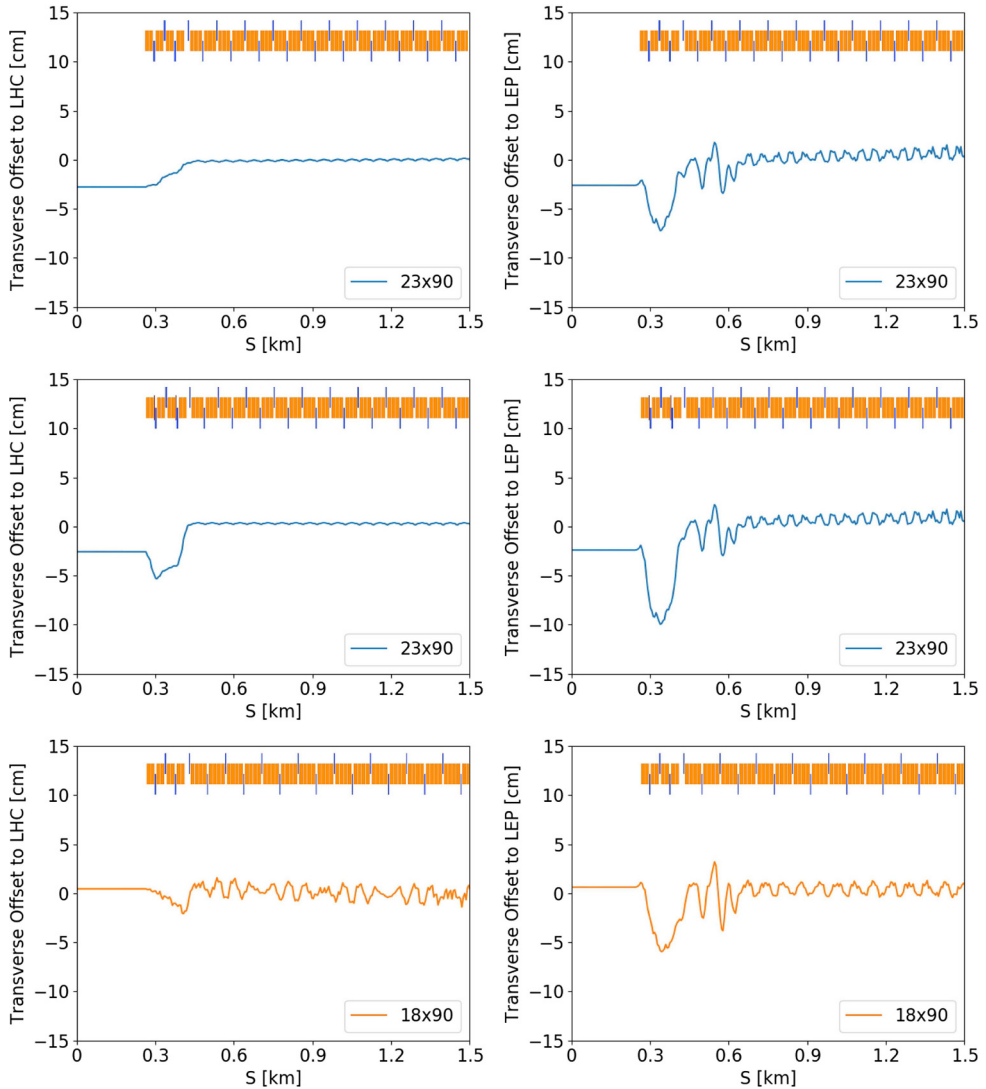
Fig. 2.13. Zoomed view of the horizontal difference from the LHC (left) and LEP footprint (right) in the region of the dispersion suppressor, for the 23×90 optics without (top) and with space for TCLDs (centre), and for a preliminary 18×90 HE-LHC optics without TCLDs (bottom). The 23×90 optics without TLCDs features the correct minimum distances between magnets, and it has been matched both at injection and for collision. The other two optics are being finalised.

illustrated in Figure 2.14. Figure 2.15 sketches how such a dipole displacement by, e.g. 3 m pushes the reference orbit towards the centre of the ring by 30 mm locally around Q9, increasing the peak-to-peak survey offset by the same amount [46]. The resulting larger deviation from the reference footprints in the straight sections with TCLDs can be seen by comparing the top and centre pictures of Figure 2.13.

2.4.3 Physical aperture

The aperture is most critical at injection, in particular for an injection energy as low as 450 GeV. Figure 2.16 presents the expected aperture with errors in units of
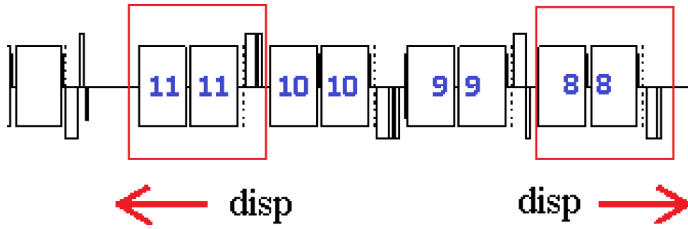
Fig. 2.14. Displacement of the DS dipole pairs 8 and 11 for the installation of TLCD collimators in IRs 1, 3, 5 and 7 [46].
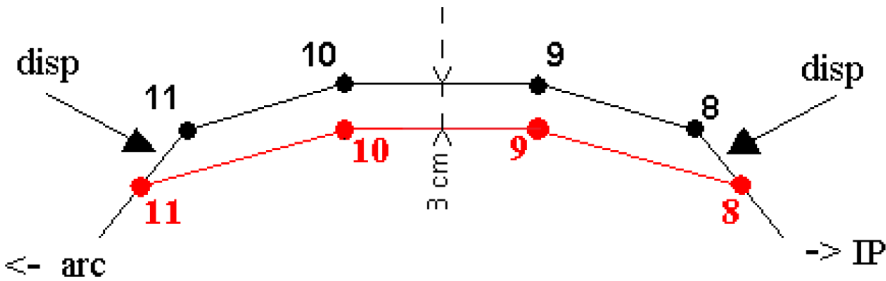
Fig. 2.15. Effect of displacing the DS dipole pairs 8 and 11, to make space for TCLD collimators, on the local footprint [46].

σ, related to the so-called "$n1$" parameter [47], in a regular arc cell at injection. The aperture was calculated assuming the same tolerances as for the HL-LHC [48] (energy 450 GeV, normalised emittance 2.5 μm, closed orbit error 2 mm, beta-beating coefficient 1.05, relative momentum offset 8.6×10^{-4}, relative parasitic dispersion 0.14 and misalignment error $\sim$1 mm [49]). It is assumed that the HE-LHC dipole magnets are bent and follow the curved beam design trajectory, in contrast to the (otherwise identical) straight magnets of the FCC-hh. The minimum aperture in every arc cell is about 9σ, for the 23×90 optics. This is smaller than the minimum aperture of 12.6σ required for the HL-LHC for the same beam emittance [48]. It should be studied whether this reduced aperture for HE-LHC could be rendered acceptable by a stricter control of the injection oscillations, adequate machine protection measures and tighter primary collimator settings. For example, with primary collimators set at 5σ, about 4.5σ space is available to preserve the collimator hierarchy between primary, secondary, dump-protection and tertiary collimators and the arc aperture.

2.4.4 Optics and shielding in the experiment insertions

In the experiment insertions the higher energy beams must be focussed and separated within the limited length of the existing straight section. Figure 2.17 compares the layout of the HE-LHC final focus with those of the present LHC and the HL-LHC upgrade. The triplet for the HE-LHC is noticeably longer than either of the other two. As is already the case for the HL-LHC, the HE-LHC separation dipoles are all superconducting, with a strength of 9.7 (D1) and 7.7 T (D2). Both dipoles, D1 and D2, are about 50% longer than for the HL-LHC. Technical parameters of the final triplet quadrupoles and separation dipoles are presented in Section 3.2.9.

Both the HE-LHC and HL-LHC layouts feature an empty space of about 20 m for the installation of crab cavities and orbit correctors between D2 and the next quadrupole upstream, Q4. With an average beta function β_{crab} in this region of at
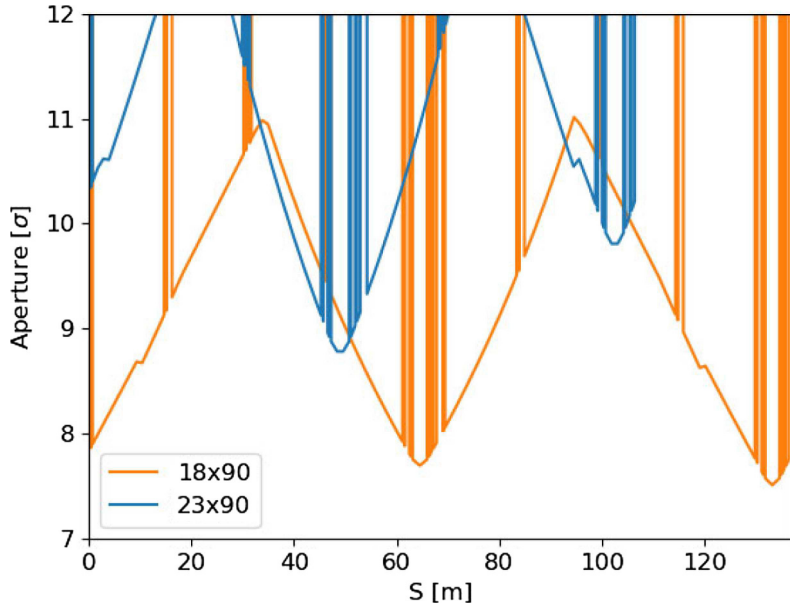
Fig. 2.16. Minimum aperture with canonical errors, in units of σ, along a regular arc cell of the HE-LHC 23×90 and 18×90 optics, for an injection energy of 450 GeV. At 1.3 TeV the aperture in units of σ would be $1.7 \times$ larger.

least 1500 m for an IP beta function β^* of 0.45 m, a crab RF frequency of 400 MHz and at a half crossing angle $\theta_c/2 = 165\,\mu$rad, the crab-cavity voltage required is $V_{\text{crab}} \approx (\theta c/2)(cE_{\text{beam}}/e)/(2\pi f_{\text{rf}})/\sqrt{\beta^* \beta_{\text{crab}}} \approx 10$ MV per side of the interaction point and per beam, to be compared with an HL-LHC crab-cavity voltage of 6 MV. The strength specification for the HL-LHC crab cavities is 2.26 MV/m, so that a 10 MV total crab voltage for HE-LHC implies about 2 cryo-modules with a length of 3 m each per beam, plus perhaps another 2 m for the vacuum interconnections. Therefore, the total crab-cavity system for two beams can be made to fit in the available space.

Figure 2.18 shows the optics and aperture of the squeezed optics at collision energy for the experiment insertions in IRs 1 and 5. The matching section has been adjusted with longer quadrupoles. At the proposed half crossing angle of 165 μrad (16.8σ separation) the physical aperture, including 2 mm shielding of the triplet quadrupoles, is more than 20σ. Potentially much more shielding is possible in the first quadrupole, Q1.

Dynamic aperture studies were performed at collision energy with triplet-quadrupole nonlinear field errors only together with sextupole (a_3/b_3), octupole (a_4/b_4) and dodecapole (b_6) correctors located left and right of IP1 and IP5 [50]. The errors for the triplet quadrupoles are based on the error table for the HL-LHC triplet [51], determined from 60 different random seeds. Only with the nonlinear field errors of the triplet and no correction, the dynamic aperture at $\beta^* = 0.45$ m and a half crossing angle of 165 μrad, corresponding to 16.8σ separation, is about 8σ. It can be increased to 20σ or above, by applying the non-linear correctors, as is illustrated in Figure 2.19. Further improvements are expected from optimising the half-ring phase advances between IR1 and IR5 ("double tuning") [52]. Spurious dispersion correction is working well.

The magnets around the collision points will be subject to high radiation levels, which may degrade their performance over time. It is currently assumed that
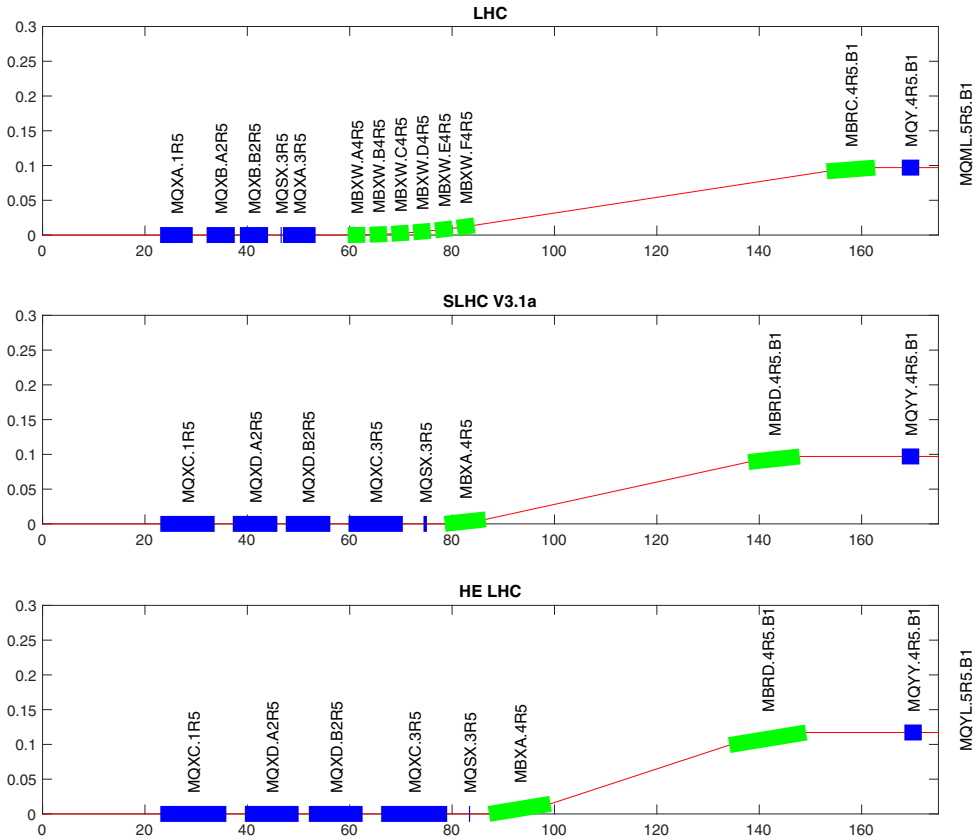
Fig. 2.17. Geometric layout of the HE-LHC final focus system (bottom) compared with the present LHC (top) and the HL-LHC final focus (centre).
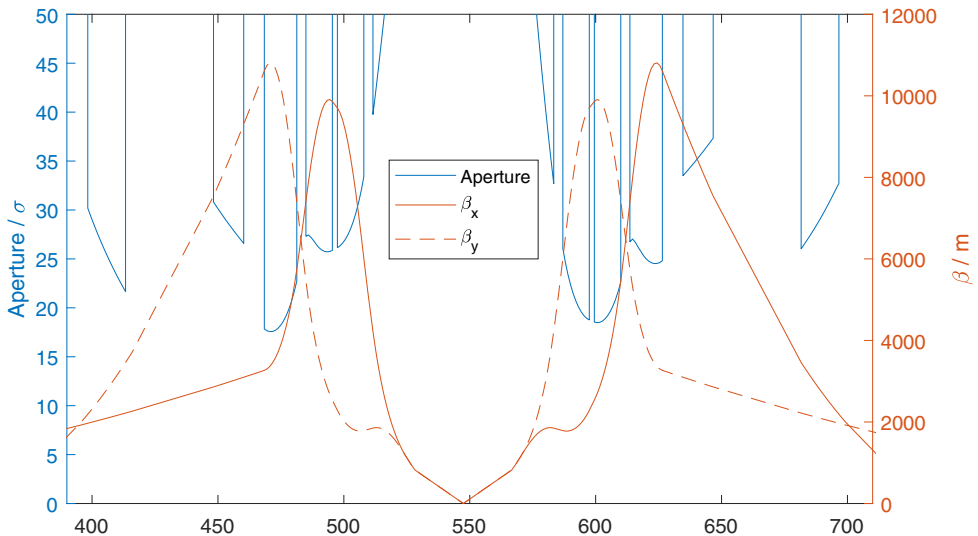
Fig. 2.18. Beta function and aperture for the squeezed optics at collision energy in IRs 1 and 5, for $\beta^*_{x,y} = 0.45$ m, and a half crossing angle of 165μrad (16.8 σ). The aperture includes a 2 mm closed-orbit uncertainty.
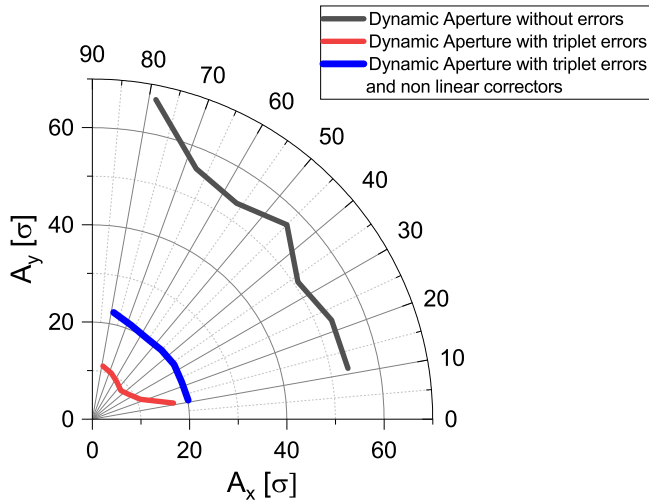
Fig. 2.19. Dynamic aperture without or with corrected and uncorrected triplet errors for $\beta_{x,y}^* = 0.45$ m, a momentum offset of $\Delta p/p = 1.7 \times 10^{-4}$, and a half crossing angle of $165\,\mu$rad.
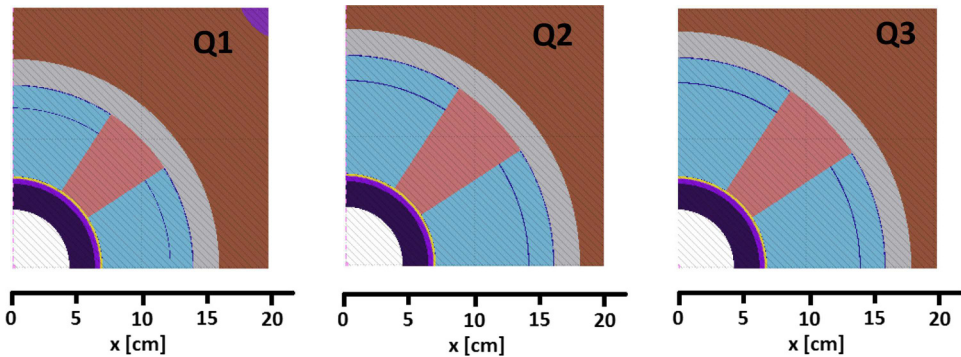
Fig. 2.20. FLUKA model of the final triplet quadrupoles.

the Nb_3Sn conductor performance can be maintained until a displacement-per-atom (DPA) value of 2×10^{-3} is reached and that the magnet insulation can withstand an accumulated radiation dose of 30 MGy.

Over the machine lifetime, if a tungsten shield is used, the limiting values for the DPA and insulation damage cited above may be exceeded after accumulating peak doses of 40–50 MGy in the coils of the magnet.

The impact of the radiation on the HE-LHC final quadrupole triplet and its mitigation by shielding was studied in simulations with the FLUKA code [53]. Figure 2.20 illustrates the FLUKA model of the three types of final quadrupole. Each quadrupole contains a 2 cm layer of tungsten shielding. The free half apertures are 44.6 and 44.8 mm and the magnet coils start at a radius of 70.4 and 70.6 mm, for Q1/Q3 and Q2, respectively. The peak dose simulated inside the magnet coil for an integrated luminosity of $10\,\text{ab}^{-1}$ is shown as a function of the longitudinal position in Figure 2.21. The peak at the beginning of Q2A could be suppressed by installing shielding in the magnet interconnects. With this caveat, the peak dose stays below 30 MGy everywhere, which suggests that the final quadrupole triplets may survive the entire life span of HE-LHC operation. Also the peak power density remains
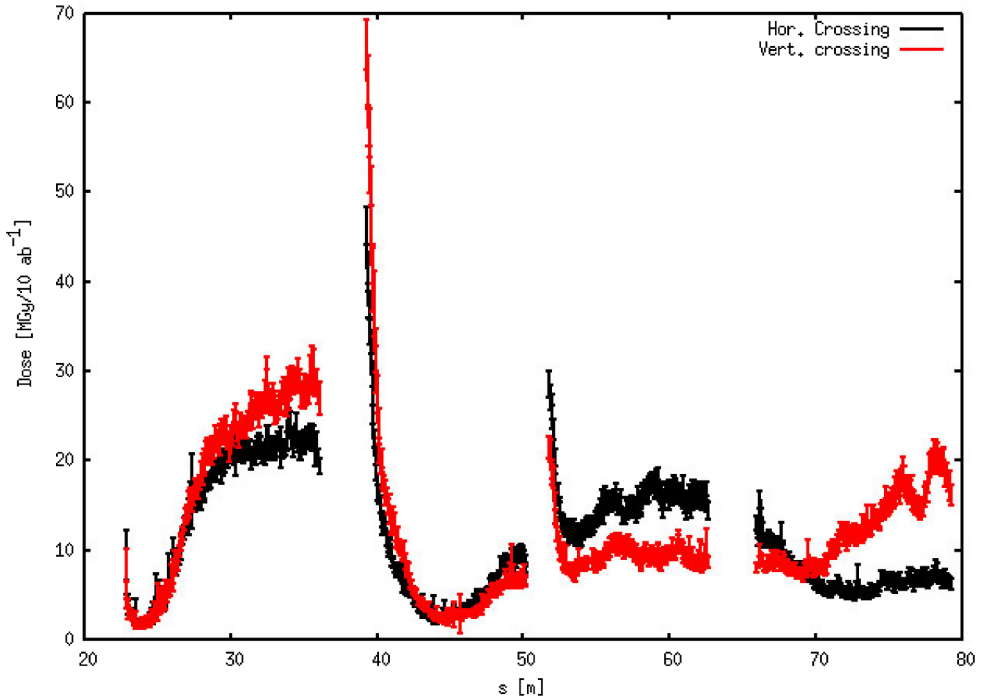
Fig. 2.21. FLUKA simulated peak dose along the final quadrupole triplet for a total integrated luminosity of $10\,\mathrm{ab}^{-1}$ and a horizontal or vertical half crossing angle of $165\,\mu\mathrm{rad}$, with an inner W shielding of $2\,\mathrm{cm}$, in each of the quadrupoles, and without any shielding in the interconnects.

comfortable: at a luminosity of $2.5 \times 10^{34}\,\mathrm{cm}^{-2}\,\mathrm{s}^{-1}$ it stays below $3\,\mathrm{mW}\,\mathrm{cm}^{-3}$. Figure 2.22 shows the simulated energy deposition in the first separation dipole magnet D1.

Figure 2.23 shows the experiment IR optics and aperture at injection with a β^* of 11 m. The maximum value of beta has been limited to 275 m, similar to the peak value in the arcs.

2.4.5 RF and diagnostics insertion

As in the LHC, IR4 will host the radiofrequency (RF) accelerating systems and beam diagnostics. For the 23×90 and 18×90 optics, the RF voltage required will not exceed the value already available in the LHC. Separation dipoles need to be stronger and hence longer, to work at twice the LHC energy. The IR4 optics is also used to tune the machine and to change the phase advance between experiments, which is important for the dynamic aperture. To help with this functionality, a tuning quadrupole has been added. Figure 2.24 compares the HE-LHC IR4 optics with that of the present LHC. The local optics in IR4 can be used to make global tune changes of up to half an integer in both planes, without changing the optics anywhere else in the ring.

2.4.6 Collimation

The collimator system of a hadron collider fulfils multiple functions, in particular: (1) it must minimise beam loss in the cold parts of the machine during periods of
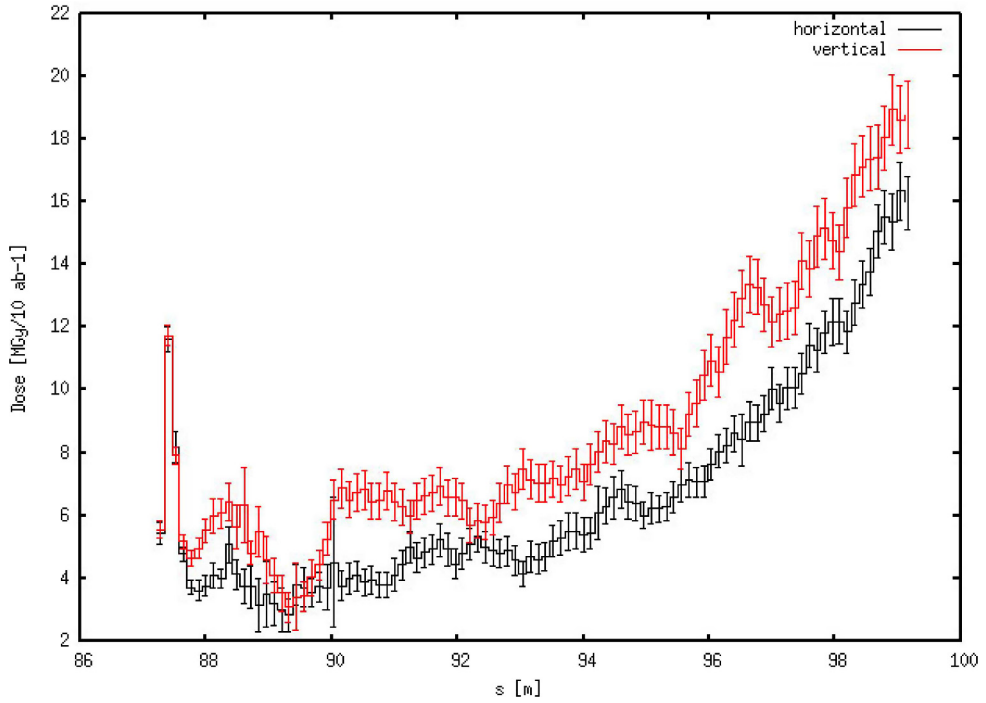
Fig. 2.22. FLUKA simulated peak dose along the separation dipole D1 for a total integrated luminosity of $10\,\text{ab}^{-1}$ and a horizontal (black) or vertical half crossing angle (red) of 165 μrad, with an inner W shielding of 2 cm.
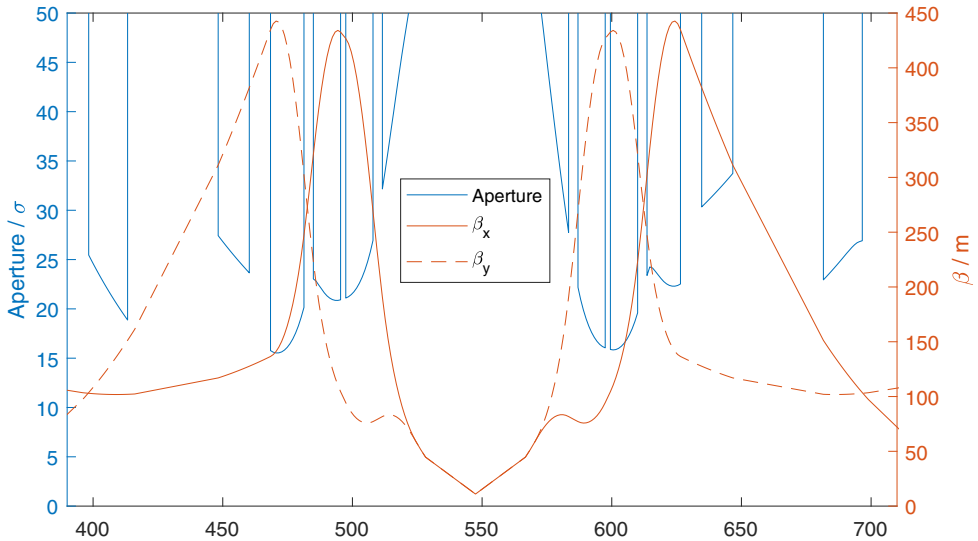
Fig. 2.23. Beta function and apertures for the injection optics at 450 GeV in the experiment IRs 1 and 5, with $\beta^* = 11$ m, including a 2 mm closed-orbit uncertainty, with beam–beam separation at the IP and a half crossing angle of 180 μrad (both separation and angle corresponding to 16.8σ).
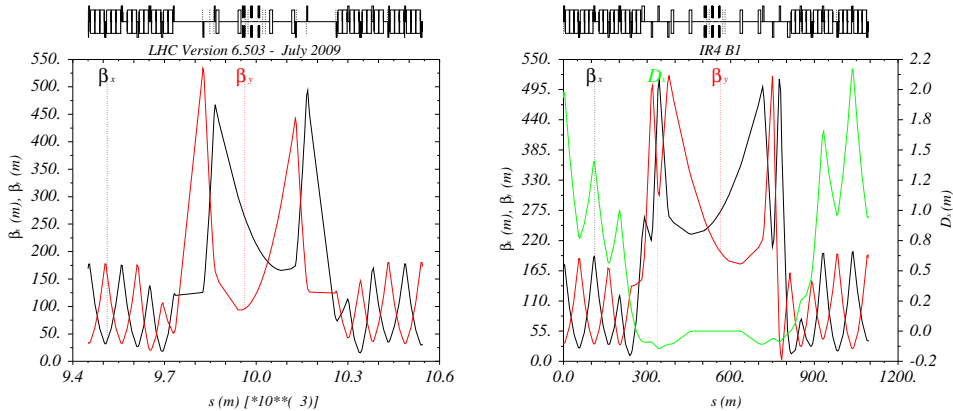
Fig. 2.24. Optics for the RF and diagnostics insertion IR4 in the present LHC (left) and with longer RF section and longer separation dipoles for the HE-LHC (right).

minimum beam lifetime (assumed to be 12 min) to prevent quenches of superconducting magnets; (2) it must protect the machine from failures (e.g. in case of injection errors or an asynchronous beam abort) by intercepting bunches which would otherwise destroy machine components; (3) it must keep experiment backgrounds at an acceptable level. To achieve the second task, the collimators need to be made from highly robust materials. Furthermore, the collimators are the closest elements to the beam and significant sources of impedance. Development of novel, robust, low-impedance collimators is ongoing as part of the HL-LHC effort [54,55]. It is likely that such new low-impedance collimators will be required for the HE-LHC.

With the reduced physical aperture at injection and smaller beams at higher energy, collimating the HE-LHC beams is significantly more challenging than for the HL-LHC. The baseline solution is to use the HL-LHC collimation layout as a starting point [56,57], building on the well-tested LHC collimation system [58,59], with the necessary modifications. As is already the case for the LHC and HL-LHC, the collimator system will be multi-staged, consisting of primary, secondary and tertiary collimators, plus others, such as those used for protection of the extraction system or capturing collision debris.

The betatron collimation straight in IR7 and the momentum collimation straight in IR3 are challenging from an optics/magnet point of view. Due to the intrinsically high beam losses in these regions, the LHC collimation straights can only accommodate warm magnets. The HE-LHC design strategy has been to maintain or approximate the LHC optics with its carefully optimised collimator locations [60] and phase advances between collimators. Keeping exactly the same optics would require a doubling of the integrated bending and focussing fields. Minimising longitudinal gaps, eliminating any weakly excited quadrupoles and spare collimator slots and increasing the length of all magnets to the maximum extent possible, all help accomplish this goal. For IR3 the remaining lack of integrated magnet strength in the region hosting the primary and secondary collimators was compensated by length scaling, leading to beta function values that are increased by the same scaling factor. For IR7 such a length scaling was not necessary.

The introduction of dispersion-suppressor (DS) collimators requires additional space in the DS. The solution adopted for HL-LHC, which relies on replacing one standard dipole by two shorter and stronger dipoles with space for the collimator in between [61–63], can probably not be applied to the HE-LHC, since the standard dipoles already have a field of 16 T. Therefore an alternative solution which implies
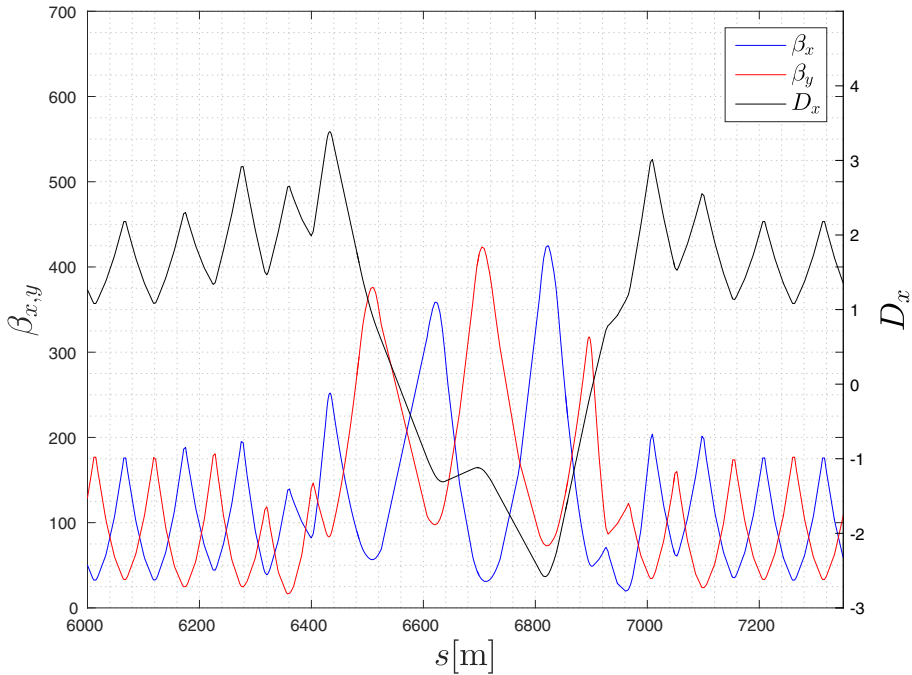
Fig. 2.25. Optics of the HE-LHC momentum collimation section in IR3.

moving several dipoles to create space, has been adopted. This layout uses ideas previously considered for HL-LHC [64].

Based on these considerations, a layout and optics design were established for the two cleaning insertions of the HE-LHC. The optics for IR3 and IR7 are shown in Figures 2.25 and 2.26, respectively.

Possible future improvements include the following three points:

1. Empty areas inside the cross section of the warm twin quadrupoles MQW could be filled with shielding material, if this reduces the radiation levels downstream.
2. To make the most efficient use of the space available in the IR7 and IR3 straight sections, the outer dipoles of the separation doglegs, which are subject to fairly low radiation levels, could be replaced by shorter superconducting dipoles.
3. In addition, since for HE-LHC the inter-beam separation in the arcs is increased to 250 mm, compared with 194 mm at the LHC, the necessity and optimum size of the IR7/3 dogleg (and, hence, the integrated strength of the corresponding dipoles) need to be re-examined.

The hierarchy must be preserved in the presence of errors, which requires a minimum transverse distance of 1–2σ between the different levels of collimators, taking into account machine imperfections, optics and orbit stability, injection oscillations and possible failure modes. Table 2.6 compares the settings planned for the HL-LHC [48,65] with settings for the HE-LHC at two different injection energies, for the 23×90 optics. For injection, LHC-like settings in units of σ are chosen to protect the (reduced) aperture, noting that the HE-LHC emittance is about 30% smaller than the LHC design emittance. Injecting at 900 GeV would allow the same settings and margins to be used as for the LHC or HL-LHC. In view of the larger triplet aperture in units of σ compared with the HL-LHC, the HE-LHC top-energy settings in Table 2.7 are based on the HL-LHC collimation settings, but result in a slightly smaller physical half gap of 0.82 mm. In addition, since the HL-LHC DS collimator
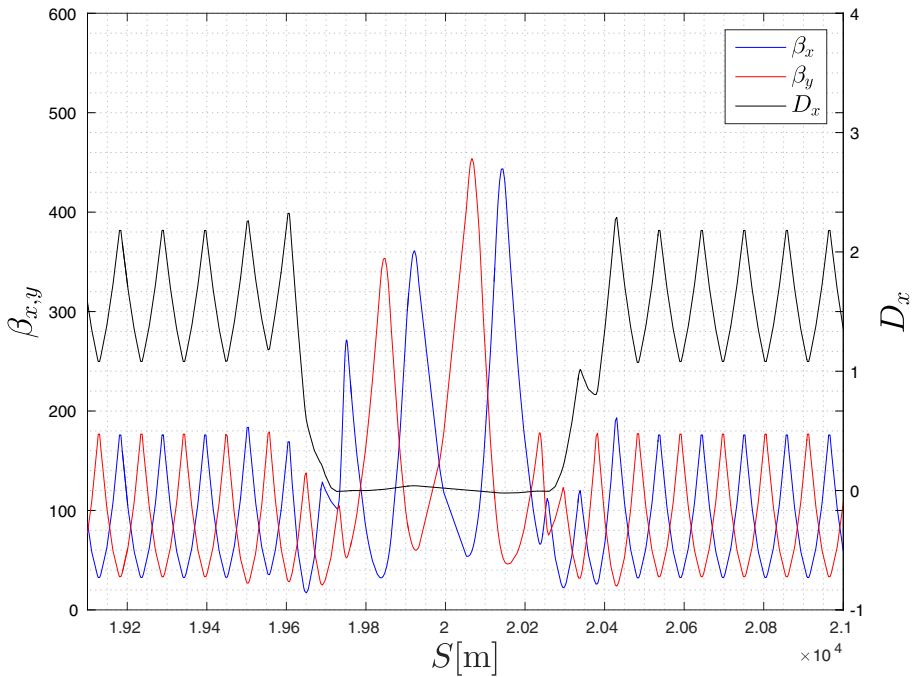
Fig. 2.26. Optics of the HE-LHC betatron collimation section in IR7.

Table 2.6. LHC/HL-LHC and preliminary HE-LHC collimator settings at two different injection energies for a reference emittance of $2.5\,\mu$m, and the 23×90 optics.

	HL-LHC		HE-LHC			
Beam energy	450 GeV		450 GeV		1.3 TeV	
Aperture (half gap)	(σ)	(mm)	(σ)	(mm)	(σ)	(mm)
Primary collimator TCP	6.7	4.3	5.7	3.81	9.7	3.81
Secondary collimator TCS	7.9	4.75	6.7	4.21	11.4	4.21
Active absorber TCLA	11.8	5.9	9.0	4.45	15.3	
Dump protection TCDQ	9.5	15.0	8.0	11.96	13.6	11.96
Tertiary collimator TCT	15.4	7.5	13.0		22.1	
DS collimators TCLD in IR7	>20	n/a	10 and 12	3.55 and 5.33	17 and 20.4	3.55 and 5.33
Machine aperture	12.6	–	9.5	–	16.2	–

Notes. The collimator gaps in mm refer to the minimum gap per family.

gaps would result in an extremely tight physical gap of less 0.8 mm, for the HE-LHC the two TCLD's were opened to $18.1/22.2\sigma$, respectively, without any loss in cleaning efficiency. Some further optimisation of these settings could be done to reach an optimum balance between machine protection and minimum impedance.

Injection at 450 GeV will be significantly more challenging, due to a physical aperture below 10σ, and the feasibility of high-energy operation with the 5.7σ primary cut in Table 2.6 remains to be demonstrated, as well as the tight margin between the primary collimators and the machine aperture.

Table 2.7 presents a similar comparison for the collision optics at top energy, where the aperture and settings are determined by the experiment insertions and not by the arcs. At top energy, the triplet aperture remains large enough that the collimation settings can be chosen similar to the HL-LHC, either in units of beam size or, alternatively, even in physical dimensions. Indeed, for the same number of σ the

Table 2.7. LHC/HL-LHC and preliminary HE-LHC collimator settings at top energy in collision for a reference emittance of $2.5\,\mu$m.

	HL-LHC		HE-LHC	
Beam energy	**7 TeV**		**13.5 TeV**	
Aperture (half gap)	(σ)	(mm)	(σ)	(mm)
Primary collimator TCP	6.7	1.1	6.7	0.82
Secondary collimator TCS	9.1	1.4	9.1	1.32
Active absorber TCLA	11.8	1.6	11.5	1.04
Dump protection TCDQ	10.1	4.0	10.1	2.75
Tertiary collimator TCT	10.4	3.6	10.5	0.94
DS collimators TCLD in IR7	18.1	1.78	18.1 and 22.2	1.17 and 1.54
Machine aperture	11.9*	–	$\sim$12.5**	–

Notes. The collimator gaps in mm refer to the minimum gap per family. *After β*-levelling, **Bottleneck at triplet.
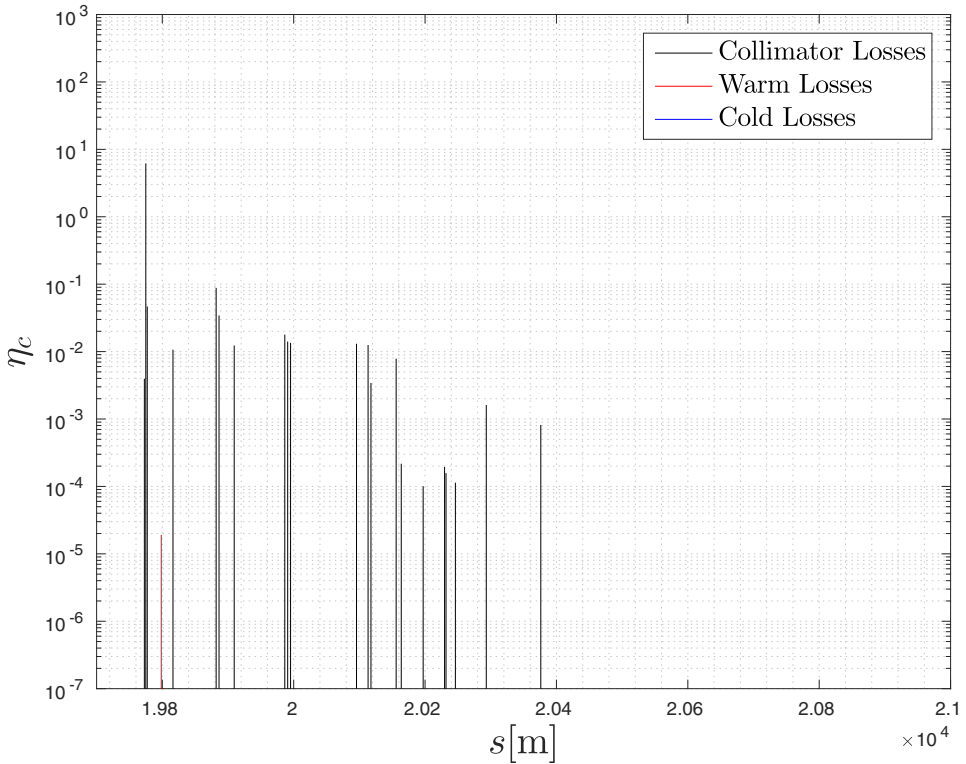
Fig. 2.27. Simulated cleaning efficiency around IR7 at collision energy with primary collimators, TCP, set at 6.7σ and secondary collimators TCSG at 9.1σ, for the 23×90 arc optics.

gap size shrinks by roughly $\sqrt{2}$, so for example, a gap of $140\,\mu$m at HL-LHC becomes $100\,\mu$m at the HE-LHC. The retraction between the dump protection (TCDQ) and the tertiary collimators (TCT) imposes constraints on the phase advance from the extraction kickers to the TCTs, as it does also for the LHC and HL-LHC [66].

Figures 2.27 and 2.28 present simulated cleaning inefficiencies at collision energy and at an injection energy of $450\,$GeV for the 23×90 optics based on the collimation
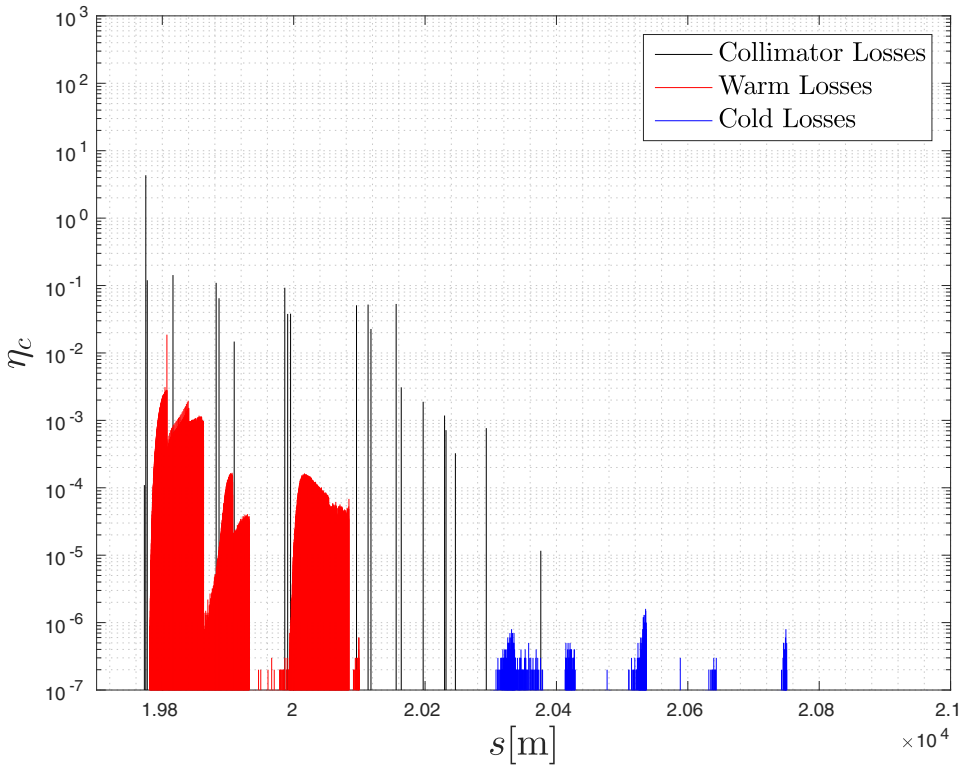
Fig. 2.28. Simulated cleaning efficiency around IR7 at an injection energy of 450 GeV, with the primary collimators, TCP, set at 5.7σ and secondary collimators, TCSG, at 6.7σ, for the 23×90 arc optics. The TDI and TCLI injection protection collimators are set at 6.8 and 8.0 σ, respectively (LHC setting would be 6.8σ, HL-LHC setting 8σ).

settings of Tables 2.6 and 2.7. The cleaning efficiency of the collimation system with this layout and optics was studied using SIXTRACK [38,67,68], using the setup and assumptions described in [59]. The local cleaning inefficiency is excellent, significantly less than 10^{-5}, for all cold sections (shown in blue, while losses in warm areas are displayed in red). The cleaning simulations also include two IR7 dispersion-suppressor (DS) collimators set at 10 and 14σ at injection, respectively, and to 18.1 and 22.2σ at collision. The second DS collimator has a larger opening in order not to affect the momentum cleaning at IR3. As can be seen in Figure 2.28, the DS collimators intercept practically all protons that otherwise would have been lost on the cold magnets in the DS. This is a highly promising result. Nevertheless, FLUKA simulations of the full shower development are still needed to fully validate this design, i.e. to judge the risk of quenches or of any damage to the collimators themselves. In addition, further studies are needed to finalise the collimator settings outside IR7, in particular for the injection protection.

2.4.7 Extraction

Extraction will be hosted in IP6, as in today's LHC. Since the beam energy is almost doubled, a stronger extraction kicker and septum system is required. This can be achieved through a combination of (1) increasing the lengths of kicker and septa, (2) reducing their gap size (easier for a higher injection energy), and (3) improved
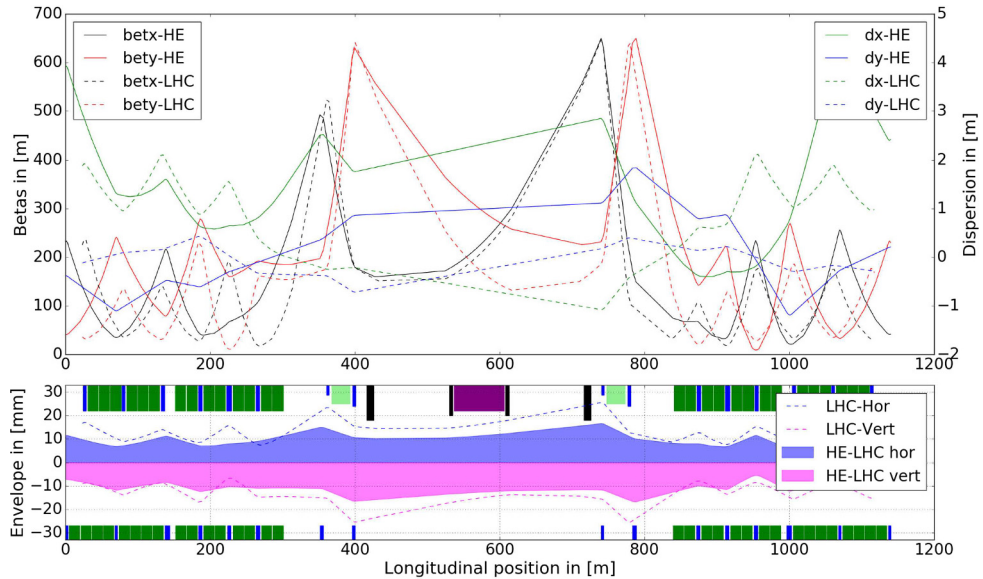
Fig. 2.29. Optics for the extraction insertion in IR6 compared with the present LHC optics (top) and the corresponding beam envelopes for HE-LHC at 1.3 TeV and LHC at 450 GeV (bottom). The envelopes represent 10 RMS betatron beam sizes plus 4 mm.

technology. Peak β-functions are constrained with the help of matching quadrupoles in the DS; this will also allow the kicker gap size to be minimised. The space between Q4 and Q5 is lengthened to generate more space for the kickers. An optimum Q4 and Q5 distance is constrained by the β-functions which increase as the magnets are moved apart. The optics and beam envelopes in the extraction straight are illustrated in Figure 2.29. In Section 3.5.3, the technical parameters for the extraction kickers and septa are summarised and compared with those of the present LHC.

2.4.8 Injection

The HE-LHC injection system strongly depends on the injection energy. With regard to the injection hardware (e.g. kicker and septa) and the local optics, injecting at 450 GeV is obviously possible; indeed, for 450 GeV the optics in the injection region could be quite similar to, if not the same as, the present LHC optics. Injection at 900 GeV requires more space if the rise time has to remain at 1 μs; some impact on the experiment optics becomes inevitable, as shown in Figure 2.30.

At twice the rise time, a 900 GeV beam could be injected with essentially the present kicker design in short-circuit mode, without any impact on length. However, this would affect the overall filling efficiency of the HE-LHC machine. The septum would need to be SC, or else a passage through the cryostat is required in the upstream quadrupole. Injecting at 1.3 TeV, the present baseline, needs more space even in short-circuit mode and, for the same rise time (filling pattern), four times more installed length is required, which has a significant impact on any secondary experiment sharing the same IP (length reduction by 40 m). An intermediate solution with 1.5 μs rise time would reduce the length for the experiment by only 20 m. Injection-kicker parameters for 1 μs rise time are presented in Section 3.5.2. In short, injection is feasible for all energies, but injection energies above 450 GeV impact the
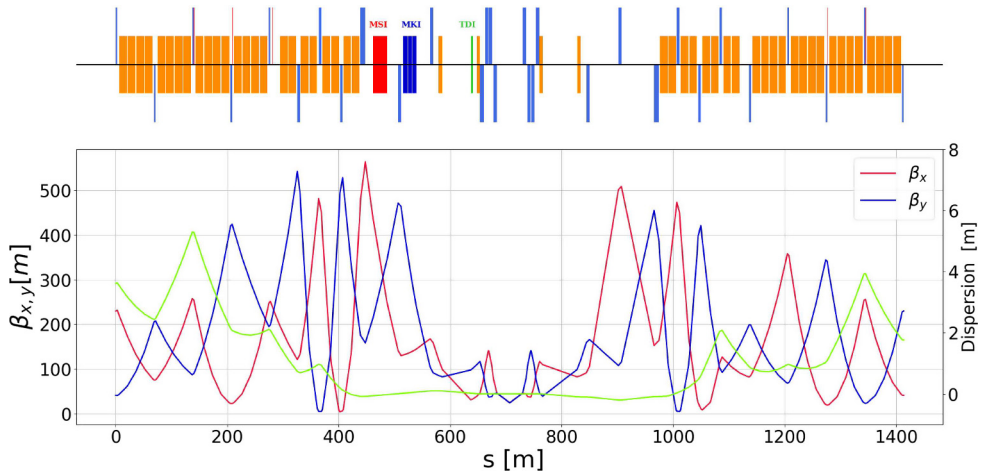
Fig. 2.30. Optics for the IR2 injection insertion for 900 GeV transfer energy with increased space for the injection kickers (6 modules instead of 4).

optics for potential experiments in IR2 and 8, whose corresponding β^* reach remains to be quantified.

The filling pattern of the collider will be affected by the choice of injection energy not only through the corresponding kicker rise time, but also by the maximum number of bunches for safe beam transfer at injection, which is determined by the robustness of the injection protection.

2.4.9 Longitudinal parameters and RF profile on the ramp

The requirement of longitudinal beam stability determines the minimum longitudinal emittance and RF voltages at all energies. Different scenarios considered include the two alternative arc optics, three possible injection energies (0.45, 0.9 and 1.3 TeV), beam parameters in collision, as well as the RF and beam parameters during acceleration.

The longitudinal emittance is defined as the area in longitudinal phase space circumscribed by the trajectory of a particle oscillating between $-2\sigma_z$ and $+2\sigma_z$. The emittance on the 13.5 TeV flat top is obtained by scaling from the value needed to ensure beam stability (Landau damping) at 7 TeV with the HL-LHC intensity (3 eVs). Longitudinal parameters for HE-LHC at 13.5 TeV (during physics) are presented in Table 2.8, for the two proposed optics. The HE-LHC values were obtained by scaling from the 7 TeV values of the HL-LHC baseline, assuming the same effective impedance of $\mathrm{Im}(Z/n)_{\mathrm{eff}} = 0.11\,\Omega$. In case, for the HE-LHC, $\mathrm{Im}(Z/n)_{\mathrm{eff}}$ increases by a factor F compared with the HL-LHC, the bunch length in physics would need to be approximately a factor $F^{1/5}$ longer.

The RF voltage profile and the emittance evolution during a 20 min acceleration to 13.5 TeV are shown in Figure 2.31 (solid line), for three different injection energies and the two arc optics. Controlled emittance blow-up (dashed line) can be achieved applying band-limited phase noise (the method currently used in LHC operation).

Longitudinal parameters at four different HE-LHC beam energies, including three possible injection energies, are presented in Tables 2.9 and 2.10, for the LHC-like baseline optics and the alternative optics, respectively.

The initial emittance of 0.76 eVs at injection for the LHC-like (23×90) optics corresponds to the minimum necessary for beam stability in the LHC when scaled

Table 2.8. Longitudinal parameters for HE-LHC at 13.5 TeV compared with the HL-LHC.

Beam energy (TeV)	Optics	γ_t	Bunch population (10^{11})	400 MHz RF voltage (MV)	Bunch length ($4\sigma_t$) (ns)	Emittance (2σ) (eVs)	Momentum spread ($2\sigma_\delta$) (10^{-4})
7.0	HL-LHC	53.8	2.3	16.0	1.2	3.03	2.36
13.5	23×90	53.8	2.3	16.0	1.2	4.20	1.70
13.5	18×90	42.1	2.3	16.0	1.2	3.30	1.33
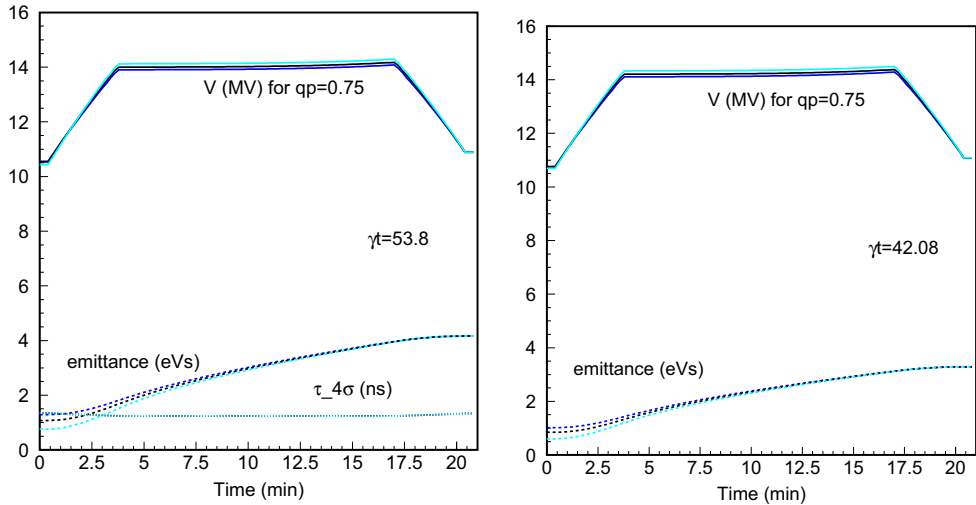
Fig. 2.31. RF voltage (solid line) and emittance with controlled blow up (dashed line) during the ramp from 450 GeV, 900 GeV or 1.3 TeV to 13.5 TeV. A transition energy γ_t of 53.8 ($\alpha_C = 3.5 \times 10^{-4}$, 23×90 optics, left) or 42.1 ($\alpha_C = 5.8 \times 10^{-4}$, 18×90 optics, right) is assumed [69]. For all cases the minimum emittance required for longitudinal beam stability scaled from the HL-LHC at 7 TeV and a total ramp time of 20 min are assumed.

Table 2.9. Longitudinal parameters for HE-LHC with $\gamma_t = 53.8$ ($\alpha_C = 3.45 \times 10^{-4}$) after capture for a bunch population N_b of 2.3×10^{11}, at different beam energies.

Beam energy (TeV)	400 MHz RF voltage (MV)	Emittance (2σ) (eVs)	Bunch length ($4\sigma_t$) (ns)	Momentum spread ($2\sigma_\delta$) (10^{-4})
0.45	10.4	0.76	1.35	8.27
0.90	10.5	1.08	1.35	5.84
1.3	10.6	1.29	1.35	4.86
13.5	10.9	4.16	1.34	1.52

Notes. All emittances are defined by longitudinal stability in LHC and scaled from the 7 TeV value. The SPS (even after LS2) cannot produce 0.76 eVs with 1.65 ns bunch length (288 bunches). RF voltage is calculated for 0.75 bucket filling factor in momentum. Bunch length is after capture and filamentation.

from the top energy value. However, this emittance can only be obtained in the SPS with the Q22 optics, which is currently being considered for the LHC Injector Upgrade (LIU) project, for a different reason.

For the Q20 optics, which has been used in SPS operation so far, the emittance corresponding to 1.65 ns long bunches ($4\sigma_z$, LIU baseline) for 10 MV RF voltage at 200 MHz on the SPS flat top would only be 0.6 eVs. This turns out to be the minimum

Table 2.10. Longitudinal parameters for HE-LHC with $\gamma_t = 42.08$ ($\alpha_C = 5.646 \times 10^{-4}$) after capture for a bunch population N_b of 2.3×10^{11}, at different beam energies.

Beam energy (TeV)	400 MHz RF voltage (MV)	Emittance (2σ) (eVs)	Bunch length $(4\sigma_t)$ (ns)	Momentum spread $(2\sigma_\delta)$ (10^{-4})
0.45	10.7	0.60	1.35	6.53
0.90	10.8	0.85	1.35	4.61
1.3	10.8	1.02	1.35	3.84
13.5	11.0	3.29	1.34	1.2

Notes. All emittances are defined by longitudinal stability in LHC and scaled from the 7 TeV values. RF voltage is defined by 0.75 bucket filling factor in momentum. Bunch length is after capture and filamentation.

emittance required for the alternative 18×90 optics, but it is too small a value for the 23×90 optics. An RF voltage of 10 MV should be available after the SPS RF power upgrade during the LHC Long Shutdown 2 in 2019/2020.

The voltage during acceleration has been determined for an RF bucket filling factor in momentum of 75%, similar to that for current LHC operation. An RF voltage of 11 MV at 13.5 TeV corresponds to a total bunch length of 1.2 ns for either HE-LHC optics. Indeed, the RF voltage V_{RF} required for the same filling factor of the bucket area scales with beam energy E_b, longitudinal emittance $\varepsilon_{||}$, and gamma-transition as $V_{\mathrm{RF}} \propto \varepsilon_{||}^2/(E_b\gamma_t^2)$. For beam stability the emittance must be varied as $\varepsilon \propto E_b^{1/2}\gamma_t$. Therefore, the RF voltage is similar for different values of γ_t.

The RF power requirements do not exceed those of the HL-LHC. The full-detuning scheme can be used on the HE-LHC flat top, in the same way as for the planned RF operation mode at the HL-LHC.

For all injection energies, the minimum longitudinal emittance is defined by beam stability in the HE-LHC, obtained by scaling from the HL-LHC at 7 TeV. However, at 450 GeV the present SPS cannot produce the required emittance within the nominal bunch length of 1.65 ns prior to filamentation. As an example, for $\gamma_t = 53.8$ ($\alpha_C = 3.5 \times 10^{-4}$, 23×90 optics), the minimum longitudinal emittance required for stability at 450 GeV is 0.76 eVs, which is larger than the maximum value of 0.6 eVs achievable in the SPS after upgrades, with a "nominal" extracted bunch length of 1.65 ns. So either the injected bunch length will be 12.5% larger (1.85 ns), leading to higher capture losses and possibly satellites, or, after injection into the HE-LHC, the beam will be below the limit of stability. The second case is actually encountered in the present LHC, where injection oscillations are not damped for a long time (even surviving the ramp and the controlled emittance blow-up), but have no dramatic impact on the collider operation.

2.4.10 Beam–beam effects and crossing angle

The crossing angle and aperture available in the triplet depend on the choice of β^* and on the strength of the long-range beam–beam effects [70–73].

To determine the minimum acceptable beam–beam separation at the location of parasitic encounters in the HE-LHC, the same criteria as used to develop the LHC and HL-LHC collision schemes [63] are applied. In particular, the target value for the one-million-turn DA should be at least 6σ with the HE-LHC normalised emittance of $2.5\,\mu$m. This choice is based on the initial LHC experience with long-range beam–beam effects [74] and the subsequent successful strategy of LHC Run 2 [73,75,76].
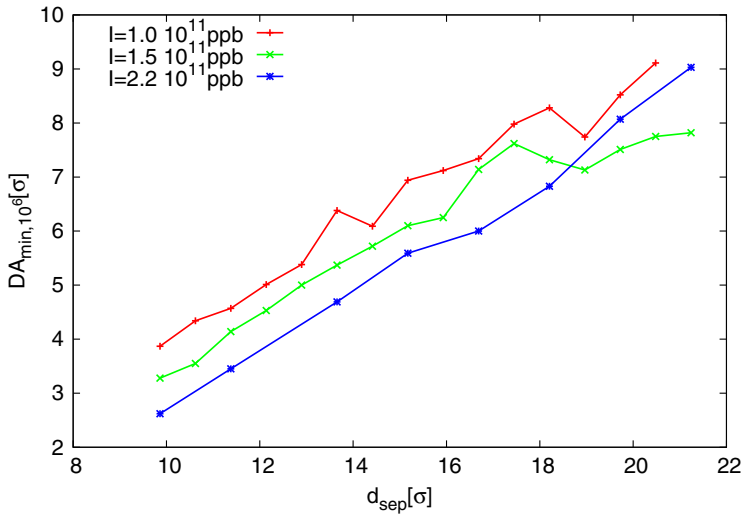
Fig. 2.32. Long-term dynamic aperture as a function of the beam–beam separation in units of the transverse beam size for different bunch intensities at collision.

The beam-to-beam separation at the first long-range encounter is given by $d_{\mathrm{sep}} = \alpha \cdot \sqrt{\beta^* \gamma / \varepsilon_N}$, where ε_N denotes the normalised emittance. Based on LHC operation experience and dedicated beam studies, with an HE-LHC beam–beam separation d_{sep} of approximately 17σ, the dynamic aperture due to the long-range beam–beam encounters is 6.0σ, as shown in Figure 2.32. This appears to be sufficiently large to keep the long-range beam–beam effects under control during collisions. Figure 2.32 presents the dynamic aperture as a function of d_{sep} for the nominal intensity (blue line) and for bunches of lower intensity. To maintain a minimum DA of 6σ a full crossing angle of $230\,\mu$rad is required at the two primary IPs for $\beta^*_{x,y}$ of 0.45 m.

The crossing angle could potentially be reduced in view of the strong radiation damping at 13.5 TeV, which introduces additional operational margins not considered in the tracking simulations. This radiation damping can partially compensate for the nonlinearities of the machine. The crossing angle might also be lowered, or the dynamic aperture could be further improved, if beam–beam compensation techniques, i.e. bunch-to-bunch electron lenses [77] or a wire compensator [78], are applied.

Figure 2.33 compares the normalised beam–beam separations at the various long-range encounters for the HE-LHC crossing scheme with those of the HL-LHC baseline and ultimate configurations, as defined in [79]. The corresponding beam–beam footprints are shown in Figure 2.34, together with those for the LHC configurations of 2012 and 2016. Based on experience gained from LHC Run 1 and 2 [80,81], the total head-on beam–beam tune shift Q_{bbho} is limited to 0.02–0.03. The diagonal extent of the HE-LHC footprint closely resembles that of the HL-LHC, while the long-range wings are smaller than those probed during the LHC 2012 run [75].

2.4.11 Space charge, bunch-to-bunch tune variation, intrabeam scattering, Touschek effect

Space charge effects during injection at 450 GeV will be similar to those at the HL-LHC, with a maximum direct space-charge tune shift of 2–3×10^{-3}. At injection the direct space charge tune spread contributes to Landau damping of higher-order
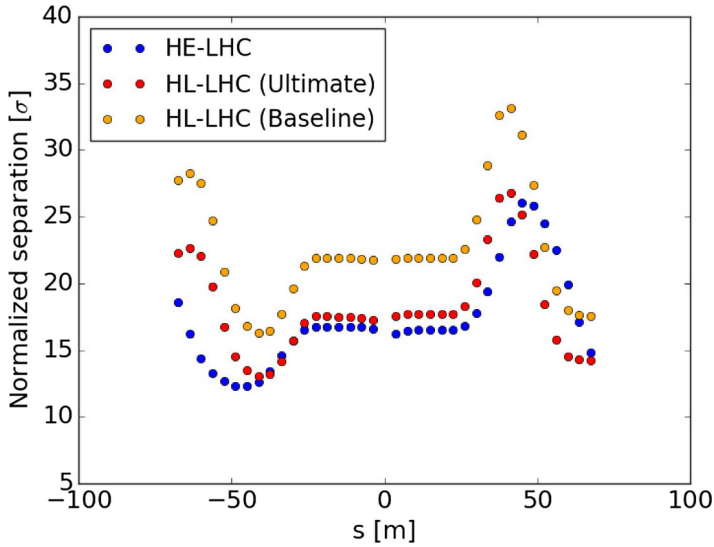
Fig. 2.33. Beam–beam separations at long-range encounters in units of the transverse beam size σ for the HE-LHC, compared with the HL-LHC ultimate (red dots) and baseline configurations (yellow dots).
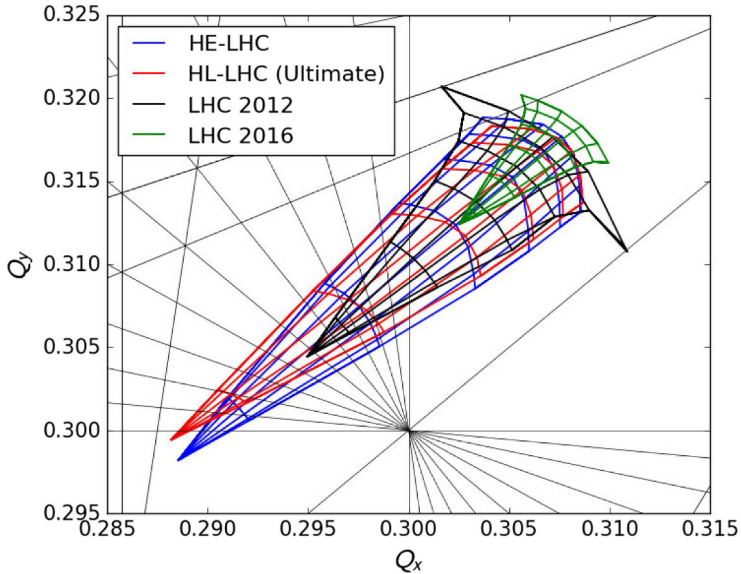
Fig. 2.34. Beam–beam tune footprint up to 6σ in transverse amplitude for the HE-LHC with $165\,\mu$rad half crossing angle, compared with the HL-LHC and the LHC configuration of 2012.

single-bunch head-tail modes [82]. At collision energy the direct space charge tune shift shrinks to 10^{-4} and direct space-charge effects should be negligible.

The smaller chamber size will cause the indirect space charge effects to be enhanced compared to the LHC and HL-LHC. Extrapolating from [83], the vertical Laslett tune shift at $450\,$GeV will be about $\Delta Q_{\text{Laslett}} \approx -0.07$. Although the average tune shift can be corrected by adjusting the arc quadrupoles as a function of

Table 2.11. Collimator gap sizes assumed for the impedance simulations, in units of the rms beam size σ for a normalised transverse emittance of $2.5\,\mu$m, at three different injection energies and at top energy.

Parameter	Unit	450 GeV	900 GeV	1.3 TeV	13.5 TeV
Primary (TCP) in IR7	σ_{coll}	5	5.7	5.7	5
Secondary (TCSG) in IR7	σ_{coll}	6	6.7	6.7	6
Injection protection (TDI)	σ_{coll}	7.3	8	8	900
Dump protection (TCDQ)	σ_{coll}	8	8	8	8

total beam intensity, some leakage of the AC magnetic field in the 10 kHz frequency range during filling of the machine could lead to significant bunch-to-bunch tune variation [83].

Another source of filling-pattern dependent bunch-to-bunch tune variation is the resistive-wall effect. Applying the results of [84] for the injection plateau, the resistive-wall transient could lead to a tune variation along the HE-LHC bunch trains of order 10^{-3}.

With the LHC-like baseline optics, and using the longitudinal parameters of Section 2.4.9, the intrabeam-scattering (IBS) emittance growth time at injection amounts about to 8 h in both the horizontal and longitudinal plane [85]. For the alternative 18×90 optics the IBS rise time is 9 h longitudinally and 6 h horizontally. Therefore, an emittance growth of about 5–6% longitudinally and 6–8% horizontally is expected to occur during 30 min at injection energy. This emittance growth could be reduced by means of a lower frequency RF capture system (e.g. 200 MHz), allowing for a larger longitudinal emittance and larger bunch length at injection. At top energy all IBS rise times exceed 25 h; hence, they appear negligible compared with the radiation damping [85].

For the same longitudinal parameters of Section 2.4.9, the Touschek lifetime is about 1500–2000 h at injection, and 4000–5000 h at top energy, depending on the optics. The higher values refer to the 23×90 baseline optics [85].

2.4.12 Impedance model

An HE-LHC impedance model has been built based on the HL-LHC model with a few modifications [86] to examine the single-beam stability.

The FCC-hh beamscreen impedance [87] is used for the cold arcs, scaled to the HE-LHC length and β-function. This impedance is larger than the beamscreen impedance in the present LHC due to the smaller half aperture (12 versus $\sim$18 mm in the vertical plane) and higher temperature (50 K for HE-LHC versus 5–20 K for LHC). On the positive side, there is no contribution from the pumping holes to be considered because they are effectively shielded by the beamscreen [87]. The impedance for the room temperature beam pipes is taken from the LHC [88].

The collimators are a major contributor to the transverse impedance budget since they are operated with small gaps. The HL-LHC collimation layout is assumed [88], with primary (TCP) and secondary collimators (TCSG) in IR7 assumed to be made from MoGr, with and without a $5\,\mu$m Mo coating, respectively. Table 2.11 shows the collimator gaps assumed for the impedance calculations, in units of transverse rms beam size at the respective collimator, σ_{coll}. The collimator settings used for the top energy case are based on a preliminary HE-LHC optics [82], dating from October 2017. For the injection energy, the simulations are based on the HL-LHC optics and impedance model.
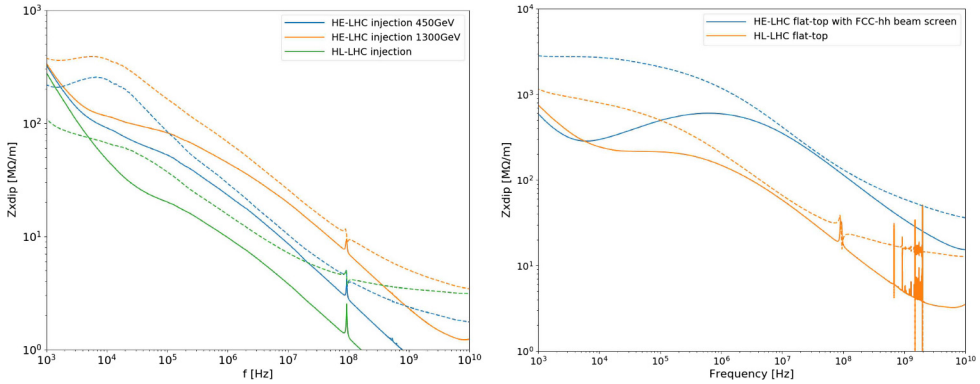
Fig. 2.35. Real (solid curves) and imaginary part (dashed curves) of the HE-LHC transverse impedance at two different injection energies (left) and at top energy (right) compared with the HL-LHC transverse impedance, as a function of frequency [86].

The physical gaps scale with the beam energy and with the normalised emittance. Consequently, the physical gap sizes become tighter as the beam energy increases. Thus, the collimation system already becomes the main impedance contributor at an energy of 1.3 TeV and it remains the dominant source of impedance up to top energy.

The collimator settings of Table 2.11 represent a worst-case impedance scenario. At an injection energy of 450 GeV the gap sizes reported in Table 2.11 are about 10% tighter than those of Table 2.6. At top energy, the gap sizes of primary and secondary collimators used for the impedance calculation are even 30%–40% tighter than the settings of Table 2.7. The latter was considered for simulating the cleaning efficiency. The top-energy settings of Table 2.11 would protect the final-triplet aperture even for $\beta^*_{x,y}$ values two times smaller than the nominal value.

The beamscreen in the impedance model has been replaced by the FCC-hh type beamscreen [89], both at injection and top energy. Also included in the impedance model are the broadband (BB) impedance and higher-order modes from the main RF cavities. The number of cavities included in the model is the same as for the LHC. The experiment vacuum chambers of ATLAS, CMS, ALICE and LHCb are also taken into account. The impedances from the recombination chambers, the shielded bellows and the arc BPMs are also accounted for and represented by a broadband resonator. Crab cavities are not included in this first version of the impedance model and therefore the transverse beam stability is assessed without them. When these cavities are added to the model, the cavity HOMs which would drive instabilities, need to be attenuated. The values for all these elements are derived from simulations or analytical estimates made for the LHC and HL-LHC [88]. For instability estimates, the HL-LHC injection or flat-top optics are assumed.

The transverse impedance model [86] is illustrated in Figure 2.35 (left) for two different injection energies; the HL-LHC impedance is also shown for comparison. At 450 GeV the HE-LHC impedance is about a factor of 2–3 higher than the HL-LHC impedance, due to the changes in the beamscreen. At 1.3 TeV the HE-LHC impedance is even larger because of the tighter collimator gaps assumed here (Tab. 2.11).

Figure 2.36 shows the relative contributions to the real and imaginary impedance at an injection energy of 450 GeV, as a function of frequency. Over a wide range of frequencies, the resistive wall effect of the collimators and of the beamscreen are the two main contributors to the overall impedance. At 1.3 TeV, the collimators alone are the dominant contributors to the impedance, due to their tighter settings, as is illustrated in Figure 2.37.
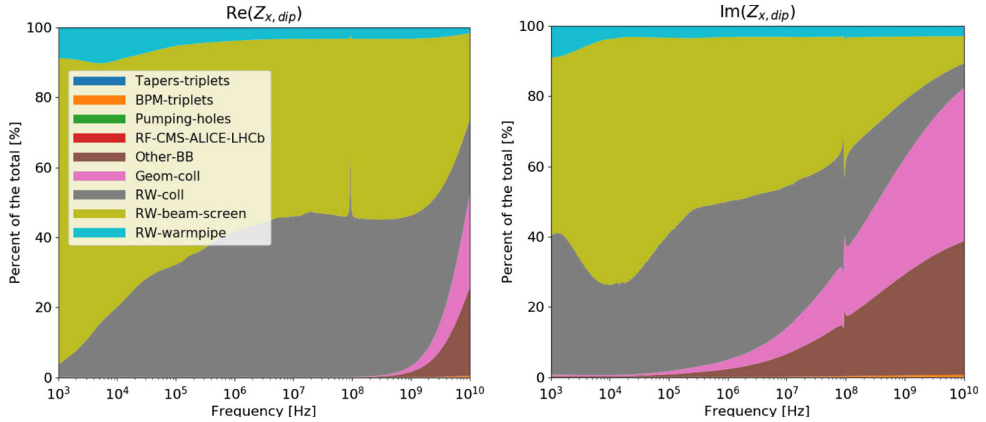
Fig. 2.36. Fractional contribution to real (left) and imaginary part (right) of the HE-LHC transverse impedance at 450 GeV, as a function of frequency [86].
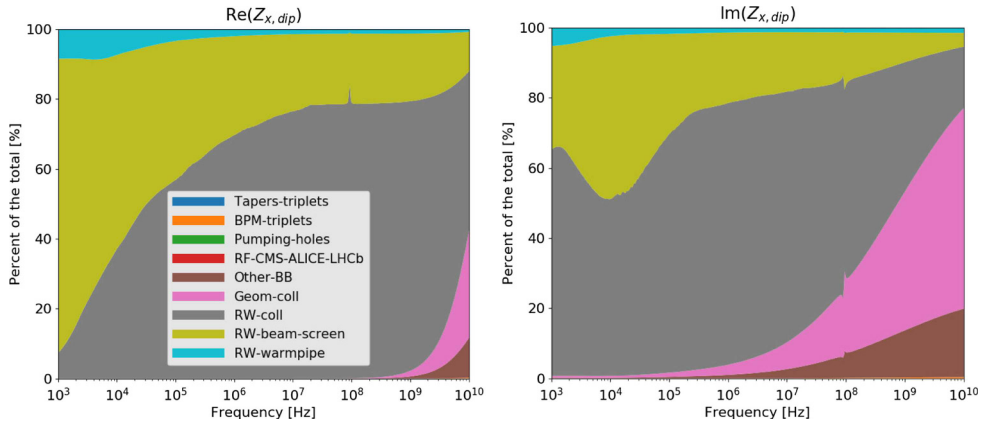
Fig. 2.37. Fractional contribution to real (left) and imaginary part (right) of the HE-LHC transverse impedance at 1.3 TeV, as a function of frequency [86].

Figure 2.35 (right) shows the total transverse impedance as a function of frequency at top energy. Here the impedance is higher still because of the even tighter collimator gaps. Operation with tight collimator gaps is being tested in beam studies at the LHC [90]. Figure 2.38 presents the relative contributions to the top energy impedance. The collimators dominate the impedance over the entire frequency range.

2.4.13 Single-beam coherent instabilities

In general, the transverse impedance drives both single and coupled-bunch beam instabilities. In the LHC the beam is stabilised by a combination of the transverse feedback system, chromaticity settings and Landau octupoles. The stability limits can be explored with a Vlasov solver, such as the Nested Head-Tail (NHT) Vlasov solver [91] or DELPHI [92]; the results of the two codes are consistent. The codes compute coherent intra-bunch and coupled-bunch impedance-driven modes, neglecting the effect of space charge. Different modes are assumed to be independent and a weak head-tail approximation is used to estimate the amount of octupole detuning required to provide Landau damping of the unstable modes.
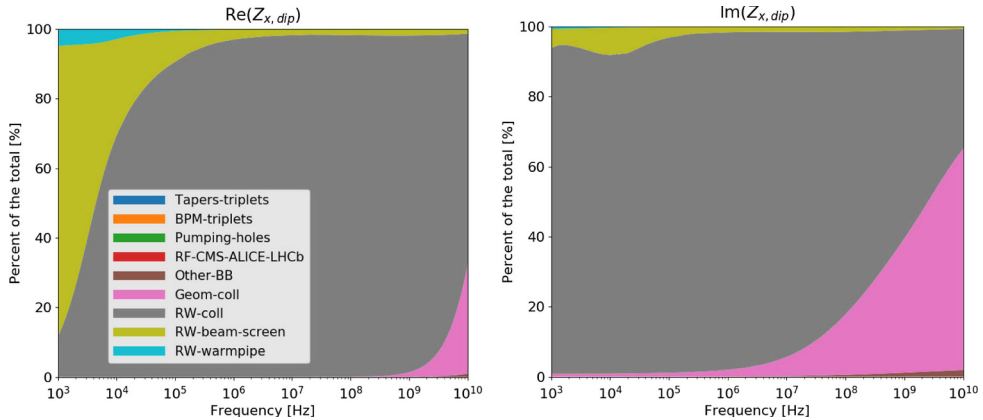
Fig. 2.38. Fractional contribution to real (left) and imaginary part (right) of the HE-LHC transverse impedance at top energy (13.5 TeV), as a function of frequency [86].

The chromaticity is scanned in the range $-20 < Q' < 20$, the bunch intensity N_b from 0 to 10^{12} protons per bunch and the damping rate between 0 and $1/25$ turn^{-1}. For the purpose of this study the damper gain g and the coherent mode shift $\Delta\omega$ are defined in units normalised to the angular synchrotron frequency ω_s. The three injection energies were studied, as well as the top energy of 13.5 TeV. The key beam and machine parameters are listed in Tables 2.1, 2.6, and 2.7.

Figure 2.39 (left) shows the instability growth rates computed at injection energy as a function of chromaticity and damper gain at 450 GeV (top) and 1.3 TeV (bottom). For the 450 GeV injection energy the damping time has to be 50 turns or smaller to ensure beam stability at the nominal intensity. For a 50-turn damper gain the safety margin in intensity is less than a factor of two (Fig. 2.39, top right). The stability region is wider for a higher injection energy. For 1.3 TeV, the damper gain has to be 75-turn or stronger at the nominal intensity (Fig. 2.39, bottom right) and for a 50-turn damper the safety margin in beam intensity is again slightly less than a factor of two.

The small intensity margin can be explained by the effect of the coupled-bunch modes, which lowers the single bunch instability threshold (see, e.g., [93]). For a single bunch at an energy of 450 GeV the threshold of the transverse mode-coupling instability (TMCI) is around 7×10^{11} protons per bunch. Including coupled-bunch motion lowers the intensity threshold by a factor of nearly two to around 4×10^{11}. Nevertheless, the TMCI threshold in the coupled bunch case is about two times higher than the design bunch intensity. Thus, for all injection energy options studied, a negligible amount of octupole detuning is needed to stabilise the unstable modes by Landau damping, provided that there is a sufficiently high damper gain.

Since the collimators are brought closer to the beam at higher energies to follow its shrinking physical size, the impedance reaches its maximum at top energy (Fig. 2.38). Here, a significant amount of octupole detuning is required to stabilise the beam. Figure 2.40 illustrates the effect of chromaticity and damper gain on the instability growth rate at the top energy. In order to stabilise the beam, around 2000 A of negative polarity would be required for the present LHC octupole system, which is only capable of delivering 550 A. In HE-LHC, passive damping of coupled-bunch modes at top energy [82] will be ensured by FCC-type octupole magnets (264 units per ring, each 0.32 m long, with a maximum gradient of 220 000 T/m^3). The resulting total effective octupole strength is about 3.4 times larger than for the Landau octupoles in the LHC [95], bringing the stabilising octupole currents required

450 GeV

1.3 TeV
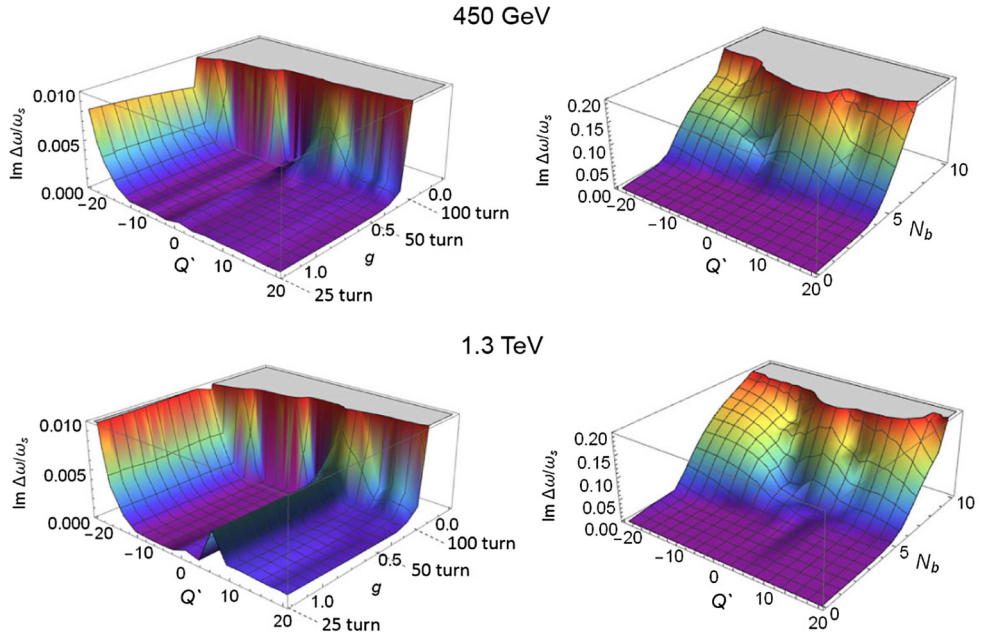
Fig. 2.39. Growth rate of the most unstable mode Im $\Delta\omega/\omega_s$ for $N_b = 2.2 \times 10^{11}$ protons per bunch and 2748 bunches as a function of chromaticity Q' and damper gain g (left) and as a function Q' and N_b with a 50-turn damper (right) for different injection energies [94].
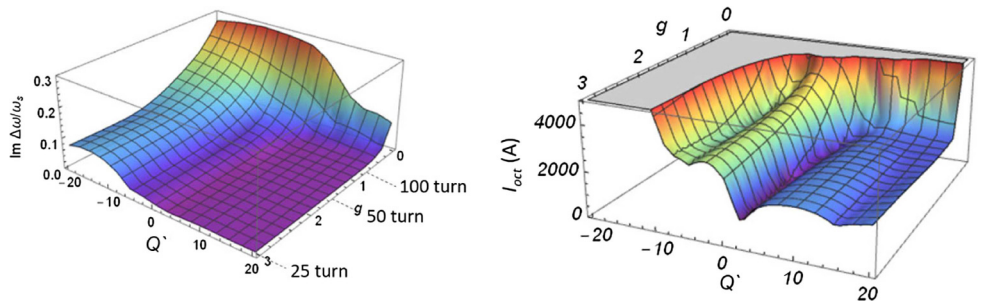
Fig. 2.40. Growth rate of the most unstable mode Im $\Delta\omega/\omega_s$ at top energy as a function of chromaticity and damper gain (left) and the corresponding octupole current, required to stabilise the mode with the HL-LHC octupole system (right), considering $E = 13.5\,\text{TeV}$, 2748 bunches of 2.2×10^{11} protons each, a Gaussian beam profile, $\varepsilon_N = 2.0\,\mu\text{m}$, and the HL-LHC octupole system with negative polarity [94].

close to the levels of LHC and HL-LHC. Alternative passive damping mechanisms are also under study, such as the possibility of using electron lenses [96]. In this configuration, an electron lens powered with a current of about 350 mA will easily stabilise coupled-bunch modes over the chromaticity range $-5.6 < Q' < 20$ with an ADT gain of 50 turns.

2.4.14 Electron cloud

The build-up of electron clouds may lead to coherent beam instabilities, through the interaction between the beam and the electrons. The effect of two proposed

beamscreen options on electron-cloud build-up in the arc dipoles with a field of 16 T has been studied. The two beamscreen designs are:

– An LHC-type beamscreen with a sawtooth structure in the synchrotron radiation impact area for reduced photon reflection [97] with half apertures scaled to 14 and 19 mm in the vertical and horizontal planes, respectively.
– The FCC-hh type beamscreen with antechambers for the synchrotron radiation and shielding of the pumping slots [98,99].

Photo-electrons produced by the impact of synchrotron radiation can play an important role in seeding the cloud build-up [100]. Their effect could be even greater in the HE-LHC, where the number of synchrotron photons produced would be nearly four times that of the present LHC and, moreover, a larger fraction of the photons would have an energy above the work function of copper and could produce photo-electrons.

In the HE-LHC dipoles, where the magnetic field lines confine the electron cloud build-up to vertical stripes around the beam, it is mainly the photo-electrons produced at the top and bottom of the beamscreen that can contribute to the build-up. The transverse distributions of absorbed photons in the arcs have been simulated with the SynRad3D code [101] for both beamscreen options [34]. The fraction of photons absorbed on the top and bottom of the beamscreen corresponds to less than one percent of the total number of absorbed photons for both beamscreen options. For the FCC-type beamscreen the fraction is roughly a factor of ten smaller than for the LHC-type beamscreen. The number of photo-electrons depends on the photoemission yield of the absorbed photons and in the absence of an experimental estimate of this yield, the number of absorbed photons can be used as an upper limit for the number of photo-electrons.

Electron cloud build-up simulations with photo-electron seeding were used to assess the effect of the beamscreen design. The resulting central electron densities as a function of the secondary electron yield (SEY) of the chamber surface are shown in Figure 2.41. The threshold electron density for inducing single-bunch instabilities has been estimated from both analytical calculations [102] and from beam dynamics simulations to be around $10^{12}\,\mathrm{m}^{-3}$ at flat top energy [103], assuming that the electron cloud is distributed over the entire ring. For typical SEY values, the simulated electron density lies below the instability threshold for both chamber options. However, the FCC beamscreen has a lower density, as a result of the lower photoelectron seeding. The heat load produced by the electron cloud, shown on the left in Figure 2.41, is lower for the FCC beamscreen.

Electron cloud build-up has been studied for the preferred beamscreen (FCC-type) in the main arc dipoles and in the arc quadrupoles, at both injection energy (in this case for an elevated energy of 1.3 TeV) and at flat-top energy with dipole and quadrupole fields of 16 T and 220 T/m, respectively. The actual arc quadrupole gradients at top energy are 336–352 T/m; the lower field gradient corresponds to a pessimistic scenario. In addition to the nominal beam parameters, two alternative beam options with lower pile-up were considered: namely a beam with 12.5 ns bunch spacing, a bunch intensity of 1.1×10^{11} protons and normalised transverse emittance of $1.25\,\mu$m and a beam with 5 ns bunch spacing, bunch intensity 0.5×10^{11} and normalised transverse emittance of $0.5\,\mu$m. The estimated central densities for these three beam options at 1.3 TeV are displayed in Figure 2.42. At injection, the beam is more prone to instabilities. For an injection energy of 450 GeV, the threshold electron density for single-bunch instability has been estimated to be at about $10^{11}\,\mathrm{m}^{-3}$ [103]. For a beam energy of 1.3 TeV, the threshold will only be slightly higher [103]. Taking into account that dipoles and quadrupoles cover around 80% and less than 10% of the machine circumference, respectively, the nominal beam option could suffer from
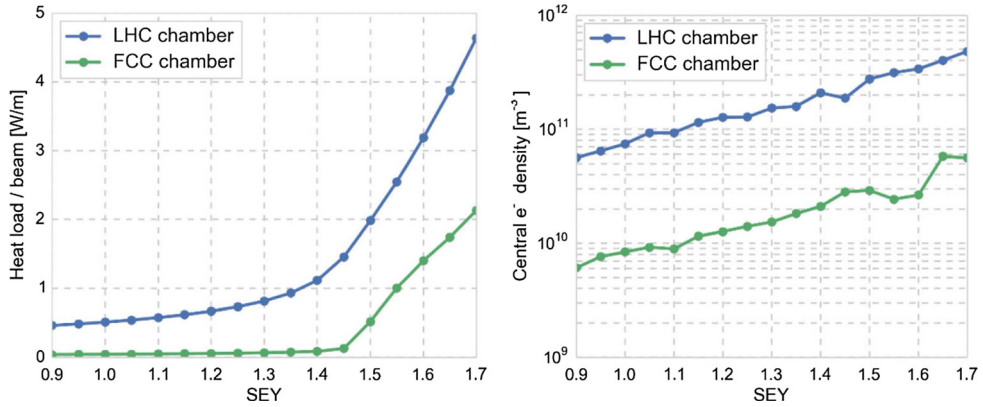
Fig. 2.41. Simulated heat load (left) and central electron density (right) at 13.5 TeV as a function of peak secondary emission yield (SEY), for the scaled LHC beamscreen and the FCC beamscreen. The single-bunch instability threshold is expected to be at 10^{12} m^{-3}.
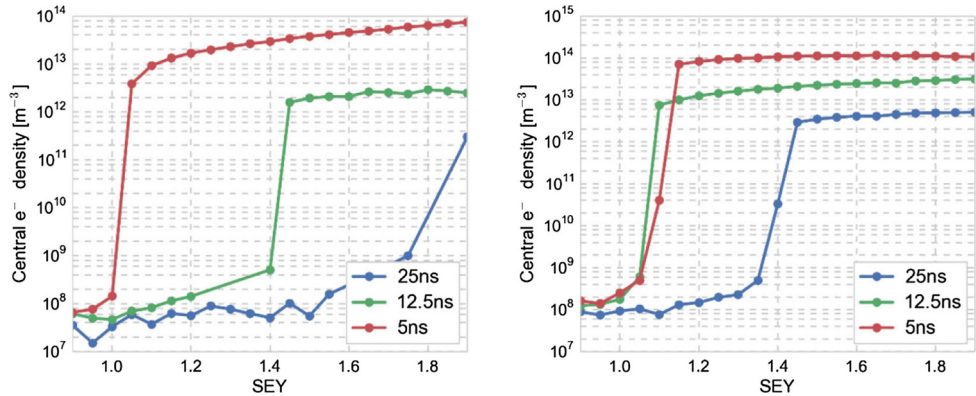
Fig. 2.42. Simulated central electron density as a function of peak secondary emission yield (SEY) at an injection energy of 1.3 TeV for three different beam options in arc dipoles (left) and arc quadrupoles (right). The densities in the dipole should be multiplied with a factor $\sim$0.8 and the ones in the quadrupole with $\sim$0.1, to compare them with the expected single-bunch instability threshold of about 10^{11} m^{-3}.

electron cloud induced instabilities if the SEY of the surface is above 1.4. Suppressing the electron cloud build-up with a low-SEY surface treatment, such as an amorphous carbon coating or laser processing, would efficiently mitigate the occurrence of such instabilities. For the 12.5 ns beam option, electron densities above the threshold can be avoided by keeping the SEY at 1.1 or below, which is quite challenging. With the 5 ns beam, densities above the threshold can even build up for lower values of the SEY – this beam can only be a viable option for the machine with a surface treatment that guarantees an SEY no larger than unity.

Since electron cloud effects do not necessarily scale linearly with the bunch intensity, their evolution can change with the burn-off from luminosity production during a fill. This effect has been estimated with build-up studies, for decreasing bunch intensity and emittance. The central densities for the corresponding bunch intensities in dipoles and quadrupoles are shown in Figure 2.43. Only a mild dependence with intensity can be seen in dipoles whereas in the quadrupoles, the multipacting threshold is seen to decrease and the central density to increase with decreasing
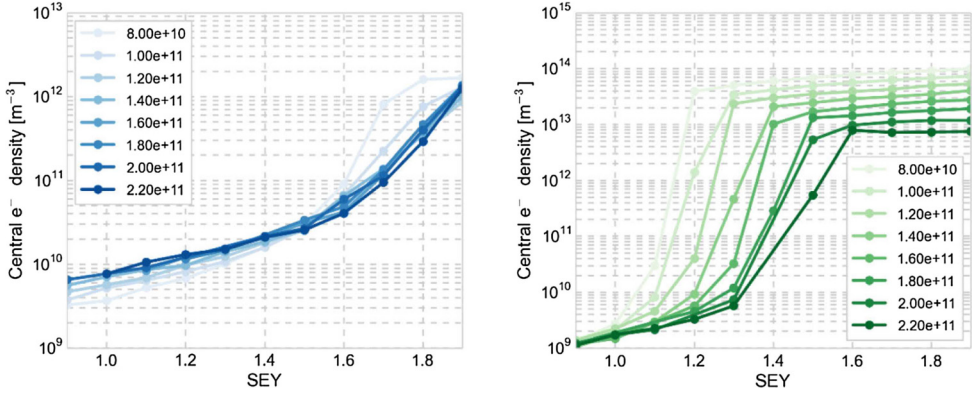
Fig. 2.43. Central electron densities as a function of the SEY for the nominal beam at top energy with decreasing bunch intensity and emittance in arc dipoles (left) and arc quadrupoles (right).

bunch intensity. In the absence of a surface treatment, instabilities could occur due to this effect during fills. However, a low-SEY surface treatment would be sufficient to prevent build-up even for lower bunch intensities.

The decrease of the electron multipacting threshold in the quadrupoles at lower bunch intensity is explained by the associated change in the energy spectrum of electrons hitting the wall, along with the non-monotonic energy dependence of the secondary emission yield. In dipole magnets, changing the bunch intensity shifts the horizontal location of the characteristic electron stripes, which form in the region where the effective secondary emission yield is maximum. In quadrupoles, the dynamics is more complex, but several simulations predict that higher bunch intensities lead to a suppression of multipacting, in particular at low SEY. This suppression of electron cloud at higher bunch intensity is an important feature also for the HL-LHC. The prediction of the simulations will be benchmarked against measurements as soon as bunches of sufficiently high intensity can be injected into the LHC, after the LHC Injector Upgrade in 2020.

2.5 Operation and performance

The longitudinal emittance needs to be kept constant by using controlled noise excitation during the physics store, in order to maintain longitudinal Landau damping. The transverse emittance shrinks due to the strong radiation damping, while the proton intensity rapidly decreases as the result of the high luminosity. At the HE-LHC the proton burn-off time is slightly shorter than the radiation damping time. This situation is qualitatively different from the LHC (negligible radiation damping), HL-LHC (negligible radiation damping and luminosity levelling) and FCC-hh (radiation damping faster than proton burn-off, requiring transverse noise excitation to control beam–beam tune shift or pile-up). The luminosity optimisation for these machines is discussed in [9]. For the HE-LHC, there is almost a natural levelling, while the beam–beam tune shift decreases during the store as the intensity drops.

Following a derivation similar to those in [9], the integrated luminosity per interaction point (IP) at time t during the fill is

$$\int_0^t L(t)\mathrm{d}t = \frac{f_{\mathrm{rev}}N_{b,0}^2 n_b}{4\pi\varepsilon_0\beta_{x,y}^*}\frac{\tau}{B}\left(1 - \frac{1}{1 - B + B\exp\left(t/\tau\right)}\right). \qquad (2.2)$$
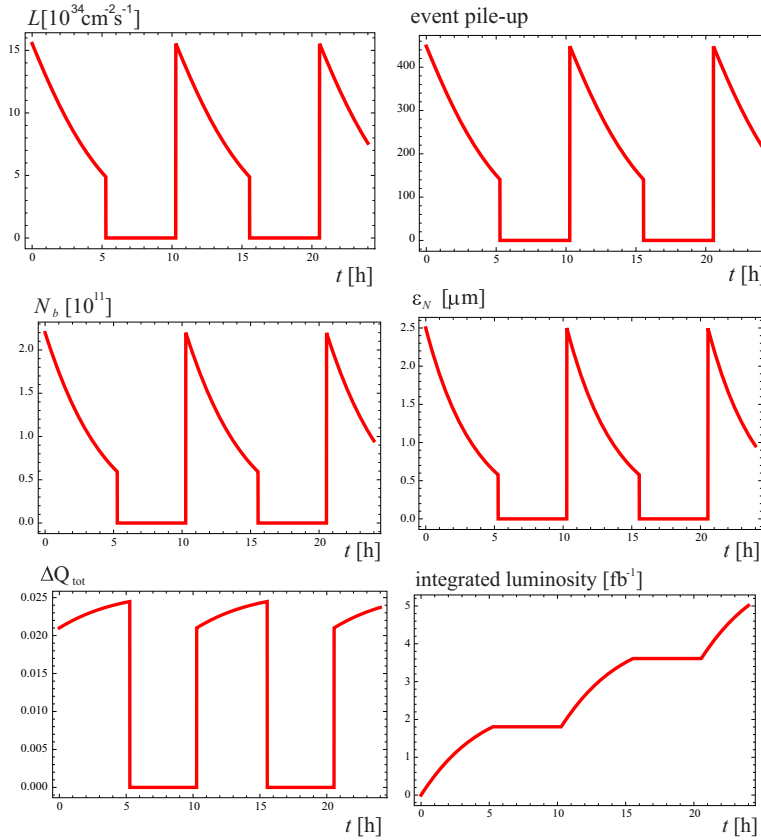
Fig. 2.44. Instantaneous luminosity, pile-up, bunch population, normalised transverse emittance, total beam–beam tune shift, and integrated luminosity as a function of time during 24 h, for the HE-LHC for 100% machine availability.

The optimum run time $t_{r,\text{opt}}$ then follows from

$$[(1-B)\exp(-t_r/\tau) + (2B-1) - B\exp(t_r/\tau) + t_r/\tau + t_{\text{ta}}/\tau]_{t_r=t_{r,\text{opt}}} \overset{!}{=} 0, \quad (2.3)$$

with

$$B \equiv \frac{\sigma_{\text{tot}} n_{\text{IP}} f_{\text{rev}} N_{b,0} \tau}{4\pi \beta^*_{x,y} \varepsilon_0}. \quad (2.4)$$

Here, t_{ta} denotes the average turnaround time, ε_0 the initial geometric rms emittance, $N_{b,0}$ the initial bunch population, f_{rev} the revolution frequency, n_{IP} the number of high-luminosity collision points, σ_{tot} the total cross section, and τ the transverse emittance damping time.

Figure 2.44 shows the evolution of peak luminosity, pile-up, bunch intensity, transverse normalised emittance, total head-on beam–beam tune shift and integrated luminosity over 24 h for 100% availability, without any levelling, just holding the bunch length constant.

The typical optimum run time of HE-LHC is about 5 h. This figure appears attainable in view of the LHC experience, and given a planned HE-LHC ramp-up time of about 20 min. For comparison, the actual average turnaround time of the LHC in 2017 was about 5 h (not counting technical faults, which would enter in the availability

annual luminosity [fb⁻¹]
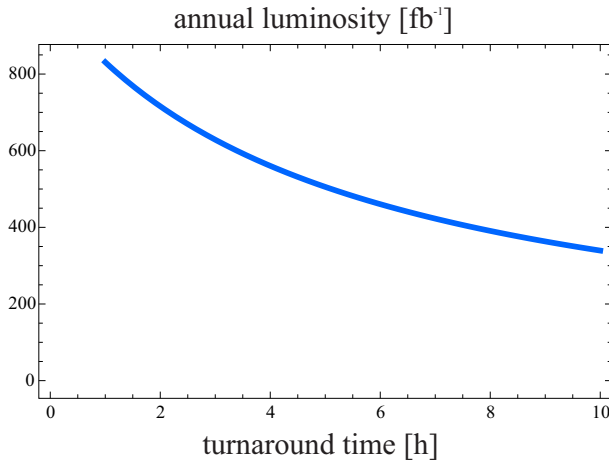
Fig. 2.45. Average annual luminosity versus average turnaround time for the HE-LHC, assuming 70% machine availability and 160 calendar days scheduled for physics operation per year.

figure), while the design average turnaround time for the HL-LHC is 4 h, and for the FCC-hh 5 (initially) and 4 h (baseline). The HE-LHC turnaround time should not be much longer than 5 h. Otherwise the integrated luminosity performance significantly decreases, as is illustrated in Figure 2.45.

2.5.1 Levelling at constant IP divergence

As the transverse beam size shrinks due to radiation damping, the IP beta function $\beta_{x,y}^*$ could be further reduced, in proportion to the shrinking emittance, while keeping the IP divergence, the normalised long-range beam–beam separation and the physical aperture in the final triplet constant. Such a levelling scenario and the corresponding performance is illustrated in Figure 2.46 and summarised in Table 2.12.

The instantaneous luminosity increases slightly until the maximum is reached after 0.61 h or 0.33 h for the 27 TeV and the 26 TeV option, respectively. At the end of the fill the instantaneous luminosity has decayed to $5.8 \times 10^{34}\,\mathrm{cm}^{-2}\,\mathrm{s}^{-1}$ and $5.5 \times 10^{34}\,\mathrm{cm}^{-2}\,\mathrm{s}^{-1}$. The number of events decreases from 425 at the start to 166 at 27 TeV, and from 410 to 160 at 26 TeV. The pile-up shows a behaviour identical to the instantaneous luminosity. In particular, the peak of the pile-up coincides with the peak of the instantaneous luminosity. The pile-up reaches maxima of 435 and 415 events per bunch crossing, respectively. During operation at 27 TeV, about 3.35 collisions per mm and about 980 collisions per ns occur at the start of the fill and the peak values of the pile-up densities are 3.48 collisions per mm and 1010 collisions per ns. In case of colliding at 26 TeV, 3.22 collisions per mm and 945 collisions per ns take place initially. At its maximum the pile-up densities reach 3.27 collisions per mm and 955 collisions per ns.

The value of $\beta_{x,y}^*$ is computed at every step to compensate for the decreased normalised emittance. Therefore, these two parameters show identical behaviour. The initial β^* decreases from 45 cm to about 13 cm. The horizontal and vertical emittances decay from initial 2.5 μm in both planes to about 1.0 μm horizontally and to about 0.7 μm vertically. Using an ATS scheme a minimum β^* of about 15 cm seems feasible, which is about 2 cm greater than the minimum β^* reached in these simulations. Improved simulations will be required in order to avoid falling below
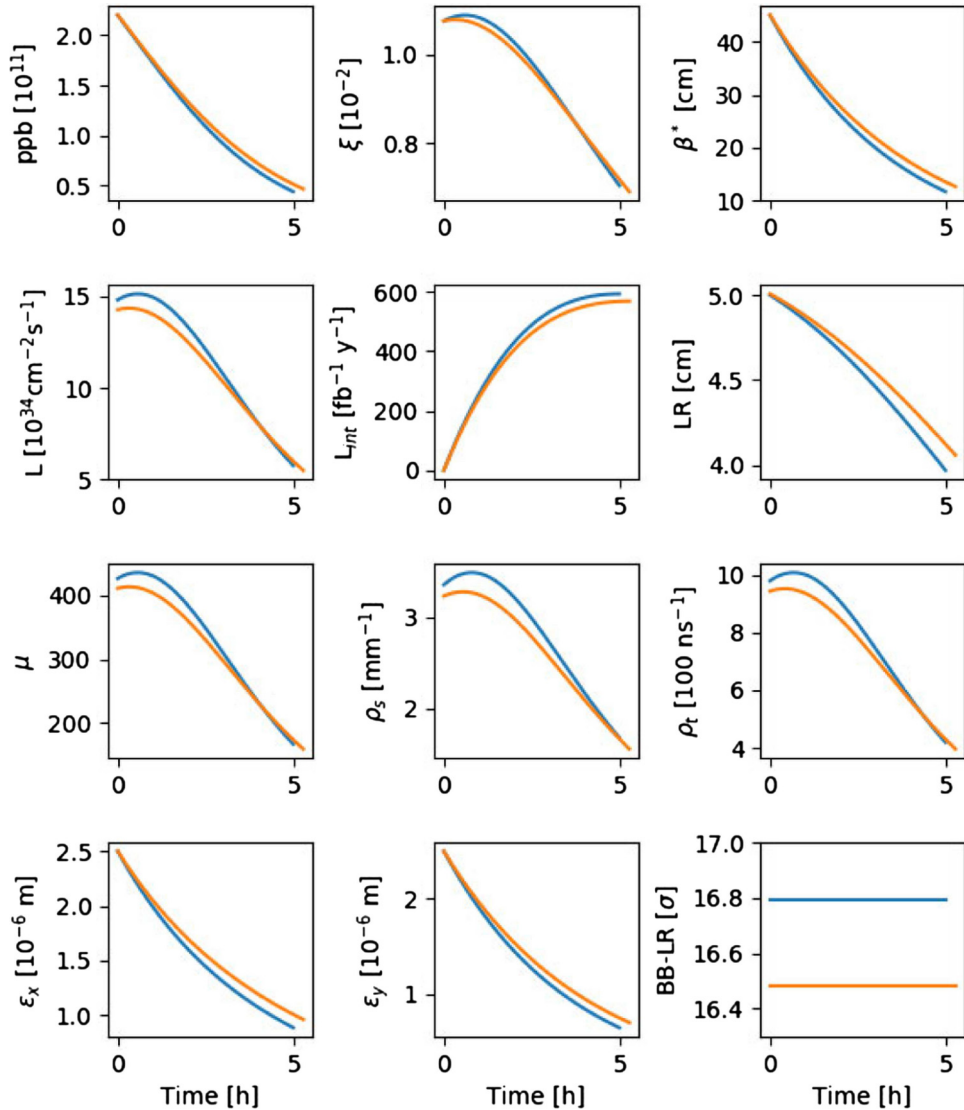
Fig. 2.46. HE-LHC luminosity levelling at constant beam divergence at collision energies of 27 TeV (blue line) and 26 TeV (orange line).

this limit. The number of intermediate optics sets required at 27 and 26 TeV collision energy is 160 and 155, respectively, and accurate commissioning of over 100 optics may be a challenge. In the case of 27 TeV collision energy with a fill time of 4.99 h and 160 different β^* values, one can conclude that the optics needs to be changed every 2 min. Alternatively one could make larger steps and use each of the (remaining) fewer intermediate optics over a longer period of time. The beam–beam parameter does not increase significantly over the fill. It does not exceed 1.1×10^{-2} per interaction point and is therefore in the order of the maximum acceptable beam–beam tune shift of 1.0×10^{-2} to 1.5×10^{-2} per interaction point [104–106].

The main benefit of this mode of operation is the possibility of harvesting a higher integrated luminosity while keeping a constant crossing angle and a constant

Table 2.12. Initial (I) and final (F) performance parameters for constant IP divergence at 27 and 26 TeV.

Parameter	Unit	27 TeV		26 TeV	
		I	F	I	F
L	$10^{34}\,\mathrm{cm}^{-2}\,\mathrm{s}^{-1}$	15	5.8	14	5.5
L_{int}	$\mathrm{fb}^{-1}\mathrm{y}^{-1}$	–	590	–	570
ppb	10^{11}	2.2	0.44	2.2	0.46
β^*	cm	45	12	45	13
LR	cm	5.0	4.0	5.0	4.1
BB-LR	σ	16.795	16.795	16.485	16.485
μ	–	425	166	410	160
ϱ_s	mm^{-1}	3.35	1.69	3.22	1.56
ϱ_t	$100\,\mathrm{ns}^{-1}$	980	420	945	395
ϵ_x	$\mu\mathrm{m}$	2.5	0.9	2.5	1.0
ϵ_y	$\mu\mathrm{m}$	2.5	0.6	2.5	0.7
t_{fill}	h	4.99		5.27	

long-range beam–beam separation in units of σ. With respect to the baseline scenarios the integrated luminosity is increased by 25% for both collision energies.

The potential impact that design changes driven by such considerations would have on operation and production can be evaluated with accelerator availability modelling based on Monte Carlo simulations [107]. These analyses allow the integrated luminosity for different operating scenarios to be predicted and the availability budgets for individual systems to be derived and these can then be used as input to their design. Such models should be maintained and updated as the machine design evolves. The aim should globally optimise the machine design while taking into account constraints like costs and technical feasibility of the different options. An approach for collider availability modelling has been established for these analyses [108,109].

2.6 Heavy ion operation

It is assumed that HE-LHC will use the same Pb beams as the HL-LHC, in terms of charge and normalised emittance. In the high-luminosity burn-off regime, the integrated luminosity per fill is given by the ratio of the total number of Pb nuclei in one beam to the total cross section, $N_{\mathrm{Pb}}/\sigma_{\mathrm{tot}}$. For only 2 experiments taking luminosity (rather than 3 or 4 at HL-LHC), at roughly twice the energy, one can estimate that the Pb–Pb integrated luminosity per experiment would be about a factor of 2–3 better than for HL-LHC because of the higher energy, fast radiation damping and shorter fills. The expected integrated luminosity then amounts to around 10 nb^{-1} per one-month run. The peak luminosity could be well over $2 \times 10^{28}\,\mathrm{cm}^{-2}\,\mathrm{s}^{-1}$, but would probably be levelled to something lower. For p–Pb collisions a similar rough scaling would lead to integrated luminosities of order 2 pb^{-1} per one-month run and a peak luminosity around $2 \times 10^{30}\,\mathrm{cm}^{-2}\,\mathrm{s}^{-1}$. These values fall between those for HL-LHC and FCC-hh.

Heavy-ion operation of the HE-LHC will also have more power than HL-LHC in the losses from bound-free pair production and electromagnetic nuclear dissociation. A first analysis of the locations of these losses [110] indicates that the solutions adopted for LHC could also be applied to the HE-LHC. Indeed space has already been allocated for collimators in the HE-LHC dispersion suppressors close to the interaction points (Sect. 2.4.6). Such a solution, compatible with ion beam operation,

must be included in the layout and implemented from the beginning in HE-LHC. As shown in Section 2.4.6, the DS collimators are also beneficial, if not essential, for proton operation. Without these collimators, heavy-ion operation should still be possible if it is limited to species with lower Z than Pb (which could also provide higher nucleon-nucleon luminosity). Asymmetric collisions, such as p–Pb, would not be affected in this way.

2.7 Lepton–Hadron operation

Lepton-proton collisions can be achieved by colliding protons circulating in the HE-LHC with a 60 GeV polarised electron beam [111]. This option is known as the High-Energy Large Hadron electron Collider (HE-LHeC). The electron beam would be provided by a dedicated 3-pass recirculating energy-recovery linac (ERL), similar or identical to the configuration of the LHC-based LHeC machine [112], as is illustrated in Figure 2.47. This machine is not in the (HE-)LHC tunnel and so it minimises any interference with the main hadron beam infrastructure. To a large extent the electron accelerator may be built independently from the operation of the proton machine. For HE-LHC this ERL may already exist, and may need to be upgraded, if the LHeC is built in the 2030's.

The same ERL machine could be used for the LHeC in combination with the HL-LHC, for the HE-LHeC and later on for the FCC-eh, presenting a potential large return on the initial investment. Furthermore, in periods without hadron beams, the recirculating electron linac of the LHeC could be configured as a photon-collider Higgs factory, "SAPPHiRE" [113,114], as a driver for the world's most powerful X-ray Free Electron Laser (FEL) [115] or as a 45–80 GeV injector for the FCC-ee and/or the FCC-e booster synchrotron [116].

The energy chosen (60 GeV) leads to a circumference of the electron racetrack of 8.9 km. This length is a fraction $1/n$ of the HE-LHC circumference with $n = 3$, which is required to match the bunch patterns. This particular circumference was chosen following a cost optimisation, looking at the fraction of the circumference in the straights covered by superconducting RF versus the fraction in the return arcs.

It appears possible to locate the LHeC electron beam tangentially to the HE-LHC, on its inside, for eh collisions at IP2.

In a simplified model, the luminosity L of the HE-LHeC is given by

$$L = \frac{N_p N_e f \gamma_p}{4\pi \epsilon_p \beta_p} \cdot H_{\mathrm{geom}} H_{b-b} H_{\mathrm{coll}}, \tag{2.5}$$

where, N_p is the number of protons per bunch and ϵ_p and β_p are the proton emittance and beta-functions. It is assumed that the proton beam parameters N_p and ϵ_p are governed by the main experiments that collide protons on protons because the baseline is for concurrent ep and pp operation. For the proton β-function in the ep collision point a challenging target value of $\beta_p = 15$ cm is assumed. This may be achievable because only one proton beam needs to be focussed, which is a simplification compared to the pp case. The bunch frequency, denoted by $f = 1/\Delta$, is 40 MHz for the default bunch spacing of $\Delta = 25$ ns. N_e is the number of electrons per bunch which determines the electron current $I_e = eN_e f$. The electron current for HE-LHC is assumed to be $I_e = 20$ mA, a slight increase compared to the 15 mA assumed for the LHeC in the HL-LHC phase and triple the value of 6.4 mA defined in the LHeC CDR. A value of 20 mA has already been surpassed with DC photocathodes. This intensity will produce a total synchrotron radiation power of about 40 MW in the return arcs. To compensate this power loss from the beam, a grid
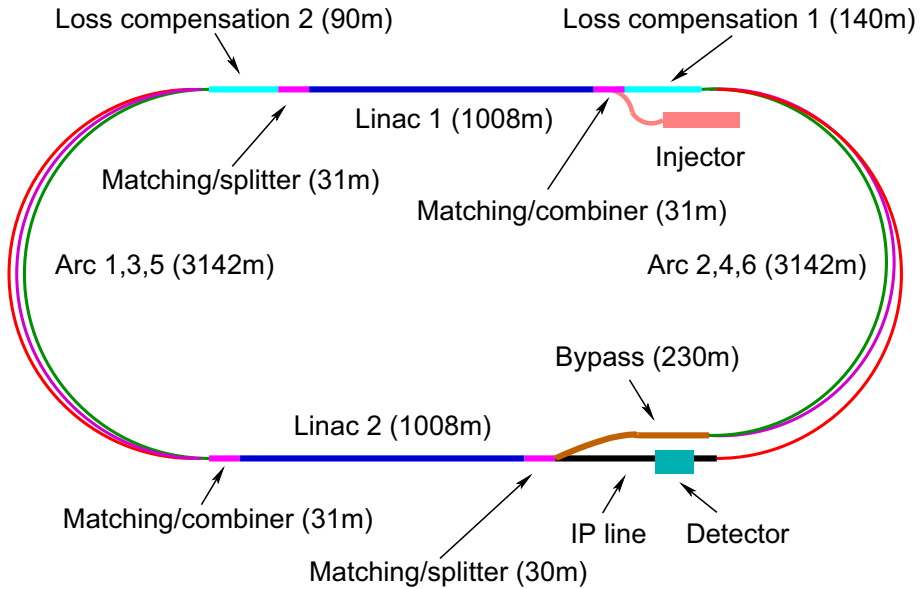
Fig. 2.47. Schematic view of the default (HE-)LHeC configuration [112]. Each SC linac consisting of 60 cavity-cryo-modules accelerates the beam by 10 GeV, which leads to an electron energy of 60 GeV at the interaction point after three passes through the diametrically opposed linac structures. The arc radius is about 1 km. The beam is decelerated to recover the beam power after passing through the IP.

power of the order of 65 MW may be required. Since, however, a cavity has to withstand six times I_e due to the acceleration and deceleration over three turns each, the choice of I_e should not to be too large. The numbers for the electron current quoted hold for unpolarised electron beams. One may currently expect a polarised electron source to provide half of that current. R&D efforts like those ongoing at MESA in Germany, for example, aim to reach the LHeC/FCC-eh target intensity. In order to achieve luminosities of order $10^{33}\,\mathrm{cm}^{-2}\,\mathrm{s}^{-1}$ with positrons, significant developments are required. For positrons, dedicated operation at very high luminosity may be a particularly attractive option as the loss in lepton intensity is compensated by a gain in proton intensity and operational performance as indicated below.

The factors H_{geom}, H_{b-b} and H_{coll} are geometric correction factors with values typically close to unity. H_{geom} is the reduction of the luminosity due to the hourglass effect, H_{b-b} is the increase of the luminosity by the strong attractive beam–beam forces and H_{coll} is a factor that takes the filling patterns of the electron and proton beams into account. Estimates for these parameters are shown in Table 2.13. Unless discussed above, further parameters used for the four ep collider configurations considered can be found (i) for the LHeC as evaluated in its conceptional design in [112], (ii) for the high luminosity version of the LHeC in references [30,117,118], (iii) for the energy doubler of the LHC, the HE-LHC in [119,120] and for the FCC-he in [119,120]. One observes that, compared to the CDR of the LHeC from 2012, it seems possible to achieve peak luminosities near to or larger than $10^{34}\,\mathrm{cm}^{-2}\,\mathrm{s}^{-1}$, which makes these future ep colliders efficient machines for the study of new physics at the accelerator energy frontier.

Table 2.13 summarises the current choices of the parameters for the energy frontier ep collider configurations at CERN, including HE-LHeC. All are based on the racetrack, multi-turn ERL as the electron accelerator and in each case it is assumed

Table 2.13. Baseline parameters and estimated peak luminosities of future ep collider configurations based on an electron ERL, esp. HE-LHeC, when used in concurrent ep and pp operation mode [111].

Parameter (unit)	LHeC CDR	ep at HL-LHC	ep at HE-LHC	FCC-he
E_p (TeV)	7	7	13.5	50
E_e (GeV)	60	60	60	60
$\sqrt{s}$ (TeV)	1.3	1.3	1.7	3.5
Bunch spacing (ns)	25	25	25	25
Protons per bunch (10^{11})	1.7	2.2	2.5	1
$\gamma\epsilon_p$ (μm)	3.7	2	2.5	2.2
Electrons per bunch (10^9)	1	2.3	3.0	3.0
Electron current (mA)	6.4	15	20	20
IP beta function β_p^* (cm)	10	7	10	15
Hourglass factor H_{geom}	0.9	0.9	0.9	0.9
Pinch factor H_{b-b}	1.3	1.3	1.3	1.3
Proton filling H_{coll}	0.8	0.8	0.8	0.8
Luminosity (10^{33}cm^{-2} s^{-1})	1	8	12	15

Table 2.14. Baseline parameters of future electron–ion collider configurations based on the electron ERL, in concurrent eA and AA operation mode [111].

Parameter (unit)	LHeC (HL-LHC)	eA at HE-LHC	FCC-he
E_{Pb} (PeV)	0.574	1.03	4.1
E_e (GeV)	60	60	60
$\sqrt{s_{eN}}$ electron–nucleon (TeV)	0.8	1.1	2.2
Bunch spacing (ns)	50	50	100
No. of bunches	1200	1200	2072
Ions per bunch (10^8)	1.8	1.8	1.8
$\gamma\epsilon_A$ (μm)	1.5	1.0	0.9
Electrons per bunch (10^9)	4.67	6.2	12.5
Electron current (mA)	15	20	20
IP beta function β_A^* (cm)	7	10	15
Hourglass factor H_{geom}	0.9	0.9	0.9
Pinch factor H_{b-b}	1.3	1.3	1.3
Bunch filling H_{coll}	0.8	0.8	0.8
Luminosity (10^{32} cm^{-2} s^{-1})	7	18	54

that ep and pp are operated at the same time. The ERL technology is under intense development worldwide and a design concept is about to be published [121], presenting the main choices for the ERL configuration which is the base for the ep colliders mentioned here. A total integrated luminosity of the order of $1\,\text{ab}^{-1}$ appears to be a realistic, ultimate goal for a decade of operation with HE-LHeC. An interesting option is the possibility of achieving luminosities of $\sim 10^{35}\,\text{cm}^{-2}\,\text{s}^{-1}$ in dedicated ep operation with the enhanced proton beam lifetime resulting from the absence of pp collisions.

There could be an interest in dedicated ep operation to profit from possible significant gains in the instantaneous and integrated luminosity performance: first estimates indicate tenfold higher proton beam brightness and a reduced β-function, by perhaps a factor of two, with only one beam present and squeezed and with fewer aperture constraints. A factor of two may also be obtained from the much enhanced efficiency of operation in dedicated mode, mainly because the proton beam lifetime would be hugely increased without pp collisions, which leads to $\tau_{\text{p}} < 5\,\text{h}$. Therefore, dedicated ep runs could typically be a day long and overall, in dedicated mode, luminosities in excess of around $10^{35}\,\text{cm}^{-2}\,\text{s}^{-1}$ appear to be realistic. An integrated annual

luminosity of $1\,\text{ab}^{-1}$ would be possible to achieve. Such a scenario could be specially relevant for taking a large amount of positron-proton data in a short period of operation, since the e^+ currents will be one or even two orders of magnitude lower than the e^- currents.

The heavy ion beams that the CERN injector complex can provide to the HE-LHC also are a unique basis for high energy, high luminosity deep inelastic electron–ion scattering physics. Combining the intense beams of $^{208}\text{Pb}^{82+}$ nuclei that have to be provided for HL-LHC and HE-LHC, with the default $60\,\text{GeV}$ electron ERL, yields the eA parameter set of Table 2.14.

Radiation damping of Pb beams in the hadron rings is about twice as fast as for protons and can be fully exploited. For the HE-LHC and FCC-hh cases, the emittance values in Table 2.14 are estimates of the effective average values during a fill in which Pb–Pb collisions are being provided at one other interaction point [122].

3 Collider technical systems

3.1 Overview

Many of the LHC systems can be reproduced or reused for the HE-LHC. This section presents details of those technical systems which require particular attention and substantial R&D efforts: higher-field magnets, suitably modified cryogenics, RF, beam transfer from a possibly new superconducting SPS, the beam-vacuum system adapted for the much enhanced synchrotron radiation, magnet powering, beam diagnostics, etc. The section also addresses the radiation environment in which the various systems will have to perform.

3.2 Main magnet system

3.2.1 Introduction

The magnetic system of the HE-LHC will profit a great deal from the experience gained with the LHC, which has demonstrated the feasibility and effectiveness of operating a large number of superconducting magnets cooled by superfluid helium at $1.9\,\text{K}$. The number of HE-LHC magnets will be about the same as those of the LHC, but the field amplitude produced by the arc dipoles will be increased by almost a factor of two, whilst maintaining a similar beam aperture and twin configuration. The field increase will be enabled by using Nb_3Sn superconductor instead of the Nb–Ti used in the LHC arc dipoles. With respect to the conductor properties, the HE-LHC magnets will operate in a similar condition as the LHC magnets, with 14% of margin on the load line and at about 60% of the maximum upper critical field B_{c20}. It is believed that with an appropriate R&D programme and if all magnets are cold tested before installation, this margin will be sufficient to achieve the nominal energy of the HE-LHC with limited magnet training. This technology, though not yet used in particle colliders, is being implemented for dipoles and quadrupoles of the HL-LHC project, where they will be operating at peak fields of between 11 and $12\,\text{T}$. It is estimated that this technology will be ready to start mass production of $16\,\text{T}$ magnets within a decade from the manufacture of a first long model.

3.2.2 Superconducting main dipole

The main dipoles (MD) of the HE-LHC are twin-aperture magnets of cosine-theta layout assembled in a helium-tight cold mass (CM) structure, integrated in a cryostat:
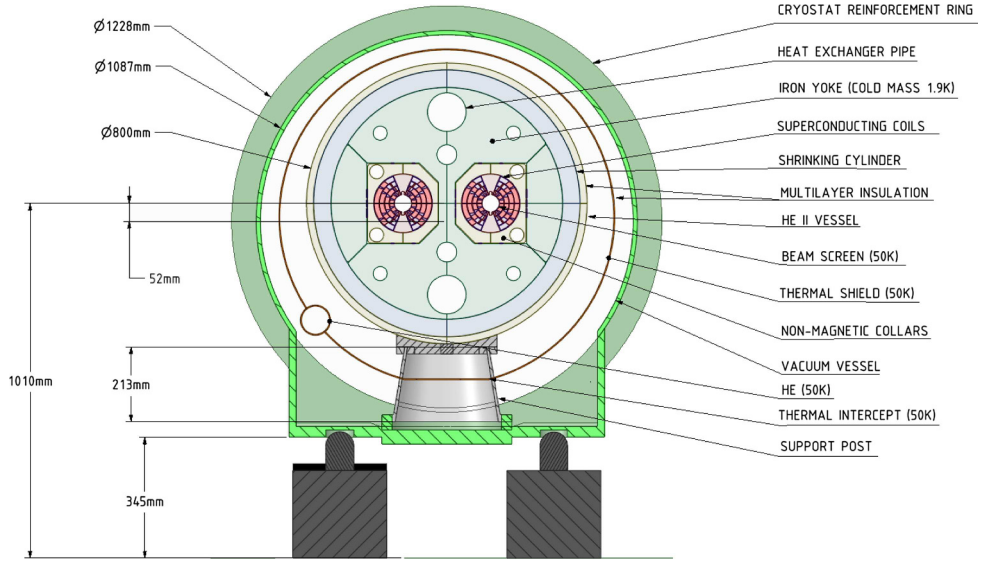
Fig. 3.1. Main dipole magnet cross section.
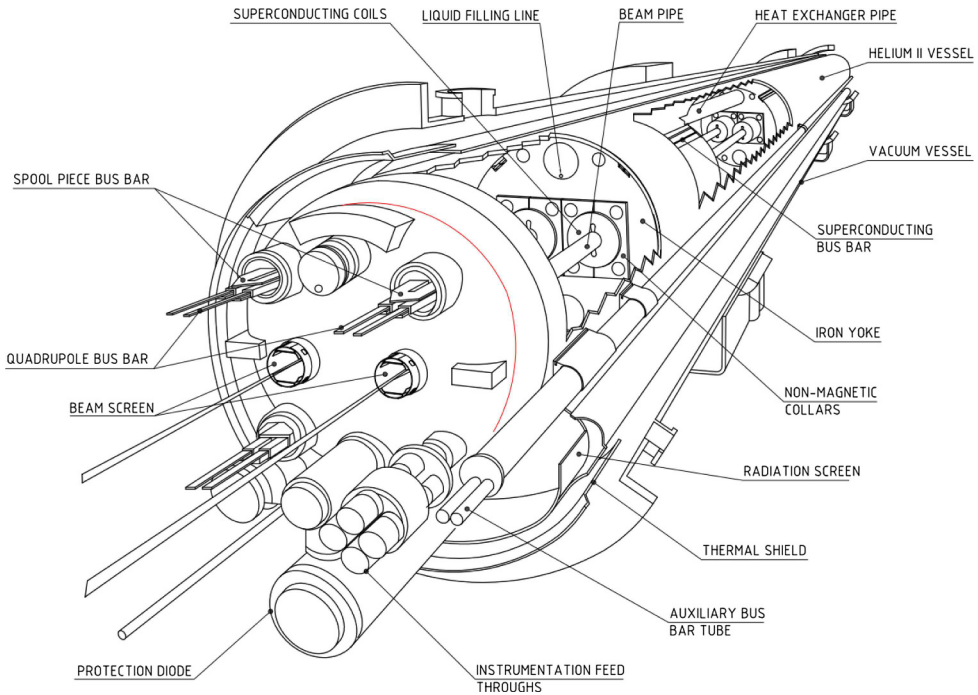
Fig. 3.2. 3D view of main dipole magnet cold mass assembly.

a cross section of the system is presented in Figure 3.1 and a 3D of the assembly is shown in Figure 3.2.

Unlike for the FCC-hh, the cold mass for the HE-LHC main dipole must be curved with a bending radius of about 2 800 m, with a sagitta of 9 mm, or a deviation from a straight line of 3.5 cm over about 14 m. The HE-LHC main dipole cold mass has a magnetic length of 13.73 m for the 23 × 90 optics and 13.94 m for the 18 × 90 optics,

Table 3.1. Main dipole parameters, for the 23×90 optics at $12.9\,\mathrm{TeV}$, and the 18×90 optics at $13.5\,\mathrm{TeV}$ beam energy.

Item	Unit	Value
Number of units		1,232 (23×90), 1,280 (18×90)
Operating field	T	16.0 (23×90), 15.82 (18×90)
Coil physical aperture	mm	50.0
Operating current	A	11 390
Operating temperature	K	1.9
Magnetic length @ 1.9 K	mm	13,730 (23×90), 13,940 (18×90)
Stored energy at 16 T (entire magnet)	MJ	36
Self-inductance at 16 T (entire magnet)	mH	560
Field margin on the load line at 16 T	%	14
Magnetisation losses (two apertures) over a full excitation cycle	kJ/m	5
Distance between aperture axes at 1.9 K	mm	250
Number of coil turns per aperture		200
Surface of conductor (2 apertures)	cm^2	131
Cold mass length beam pipe flange-to-flange at 1.9 K	m	15.8
Mass of the cold mass	t	54
Mass of the cryostat	t	6
Geometric field harmonics b_2, b_3, b_4, b_5	units	3.7, −2.4, 1.0, 0.3
Contribution of persistent currents b_2, b_3, b_4, b_5 at 1.3 TeV	units	1.1, −13.8, −0.1, 3.0
Contribution of persistent currents b_2, b_3, b_4, b_5 at 900 GeV	units	1.9, −22.5, −0.2, 4.8
Contribution of persistent currents b_2, b_3, b_4, b_5 at 450 GeV	units	4.1, −48.4, −0.3, 12.0
Contribution of saturation b_2, b_3, b_4, b_5	units	−3.7, 2.5, −0.6, −0.1
Total field harmonics b_2, b_3, b_4, b_5 at 1.3 TeV injection (1.54 T)	units	4.8, −16.2, 0.9, 3.2
Total field harmonics b_2, b_3, b_4, b_5 at 900 GeV injection (1.07 T)	units	5.6, −24.9, −0.2, 4.8
Total field harmonics b_2, b_3, b_4, b_5 at 450 GeV injection (0,53 T)	units	7.8, −50.8, 0.6, 12.3
Total field harmonics b_2, b_3, b_4, b_5 at nominal field (16 T)	units	0.025, 0.11, 0.31, 0.18
Random harmonics b_2, b_3, b_4, b_5	units	0.93, 0.67, 0.47, 0.28
Random harmonics (skew) a_2, a_3, a_4, a_5	units	1.1, 0.75, 0.48, 0.33

resulting in a total length between the two extermities of the beam pipe flanges of 15.46 m and 15.67 m respectively. The cold mass external diameter is 800 mm. It is installed in a cryostat structure composed of a radiation shield, a thermal screen and a vacuum vessel. It is supported on three feet made from a composite material and there is a flange bolted to the vacuum vessel. All parts between the beam pipe and the shrinking cylinder, which defines the outer envelope of the cold mass, are immersed in superfluid helium at atmospheric pressure and cooled by a heat-exchanger tube, in which two-phase low-pressure helium circulates. The next temperature stage is that of the beamscreen, cooled at a reference temperature of 50 K, which also corresponds to the temperature level for cooling the thermal screen and the support posts. The fact that the additional intermediate temperature level used in the LHC, in the range between 4 to 20 K is missing, results in larger static losses from the cold mass and the support posts than in the LHC. The total heat loads of a cryodipole operating in steady state mode are estimated to be about 0.5 W/m at 1.9 K and about 10 W/m at 50 K. The target losses during a full cycle from nominal field, down to injection and up to nominal field again, which mainly come from the magnetisation of the superconductor, are set to 5 kJ/m at 1.9 K for the two apertures. The operating field of 16 T is generated by a current of 11 390 A in a coil which has a physical aperture of 50 mm and the distance between the axis of the two apertures is 250 mm. The magnet design is described in [123]. The main parameters of the main dipole magnet, including the expected field quality, are listed in Table 3.1.
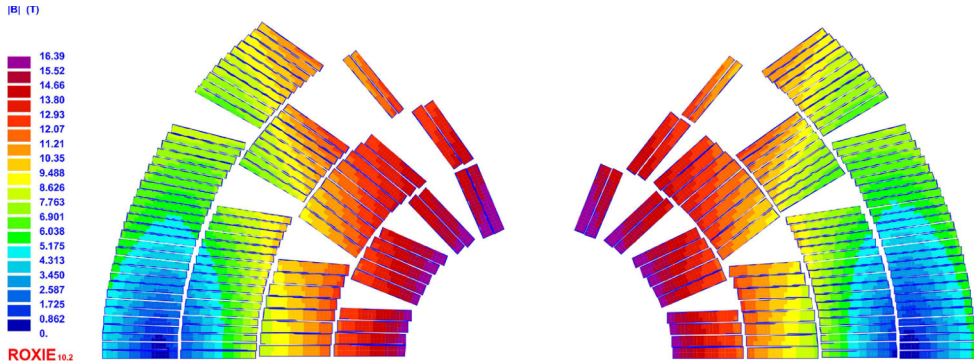
Fig. 3.3. Conductor distribution and field amplitude in the coil (one quarter of the aperture).

Each main dipole aperture has 200 cable turns distributed in one upper and one lower pole, and each pole comprises two double layer (inner and outer) coils. Since the magnetic flux density varies considerably in the coil (it is much higher in the inner than in the outer pole), the design exploits the principle of grading (see below). The inner pole comprises 32 turns of a 0.5° keystoned Rutherford cable, made from 22 strands of 1.1 mm diameter, the outer pole has 68 turns of a 0.5° keystoned Rutherford cable, made from 37 strands of 0.7 mm diameter (see Tab. 3.2). The conductor distribution and the field amplitude in the coil is shown in Figure 3.3, where one quarter of an aperture is pictured. The coil cross section is asymmetric, to compensate the quadrupole component of the magnetic field coming from the interaction between the two magnet apertures.

The current density in the outer coil is larger than that in the inner coil because the two coils are connected in series and the cable in the inner layers has a larger conductor area than that in the outer layers. This design exploits the so-called grading concept, which consists of increasing the current density where the magnet field is lower, resulting in a considerable saving of conductor for a given margin on the load line, which for the HE-LHC MD has been set to 14%. The structure is based on the so-called key and bladders concept together with the use of an aluminium cylinder surrounded by a stainless steel welded shell. The aluminium shell provides the increase of coil loading required from assembly to the operational temperature and during magnet powering. The stainless shell, as well as adding stiffness to the structure, provides helium tightness, alignment fiducials and support for the magnet end covers. The CM assembly and its main components are shown in Figure 3.4.

The field distribution in the magnet cross section for a central field in the magnet aperture of 16 T is shown on the left side of Figure 3.5, and the von Mises stress distribution in the structure at the same field of 16 T is shown on the right side of the same picture. The detail of the stress distribution in the coil cross section is shown in Figure 3.6. It can be seen on the electromagnetic section that the ferromagnetic yoke is saturated which produces a stray field of about 0.1 T at the boundary of a non-magnetic cryostat. Structurally, the coil remains entirely under azimuthal compression (with a minimum pressure of 6 MPa) up to the 16 T field amplitude. In these conditions the peak stress on the coil does not exceed 180 MPa. The stress in the other part of the structure remains well below the limits of the components of the magnet.

Prior to installation in the tunnel, each magnet will be cold tested. Depending on its training performance, the magnet may also be submitted to a thermal cycle to confirm that, once installed, the magnet can be powered up to nominal field without
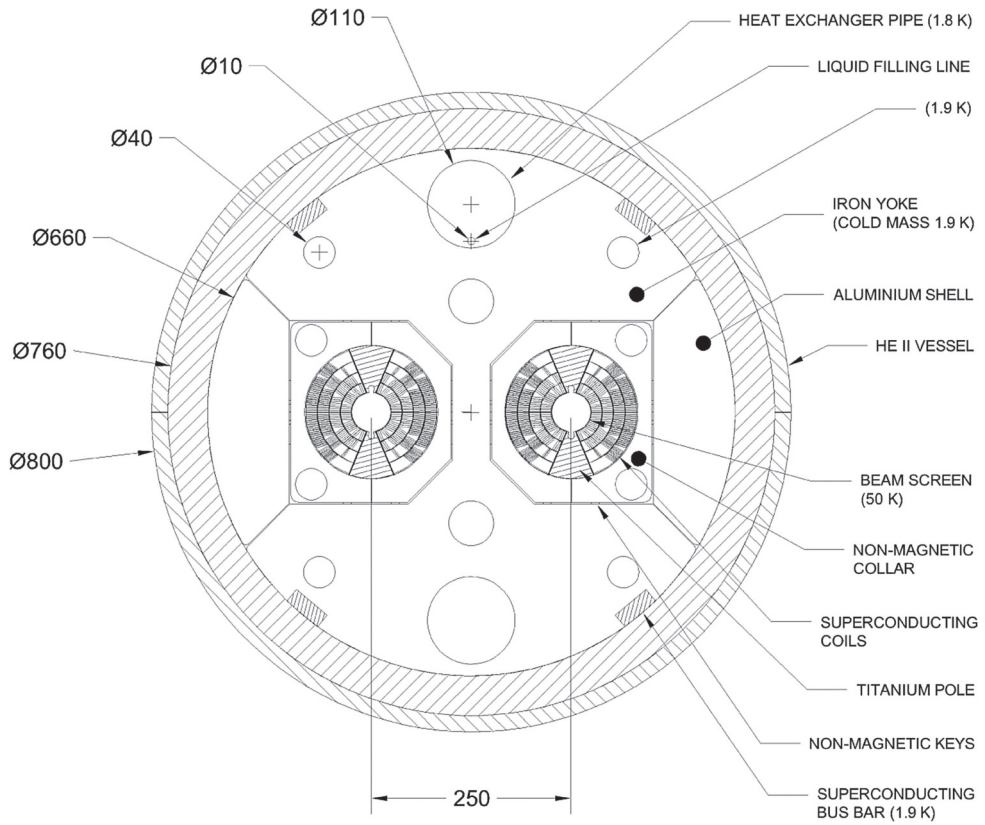
Fig. 3.4. Main dipole cold mass.
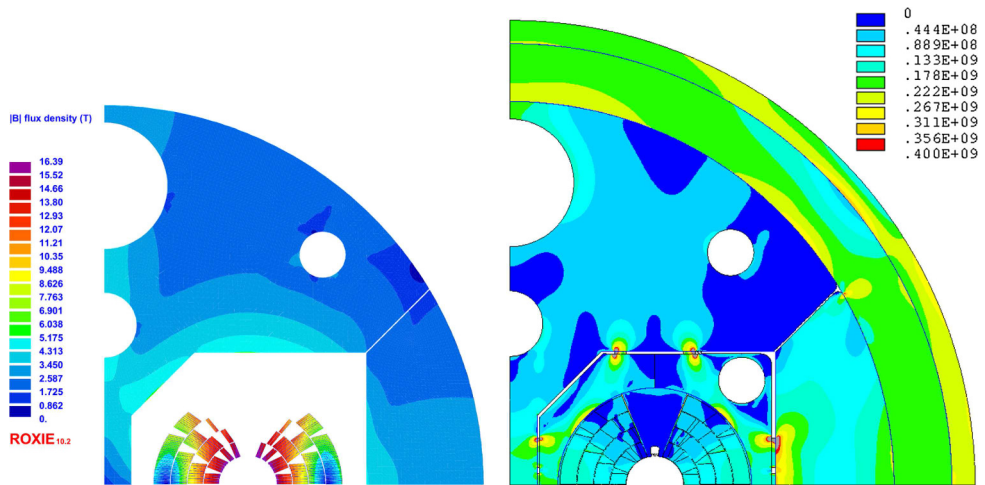
Fig. 3.5. Electromagnetic (left) and structural (right) cross section for a central field of 16 T.
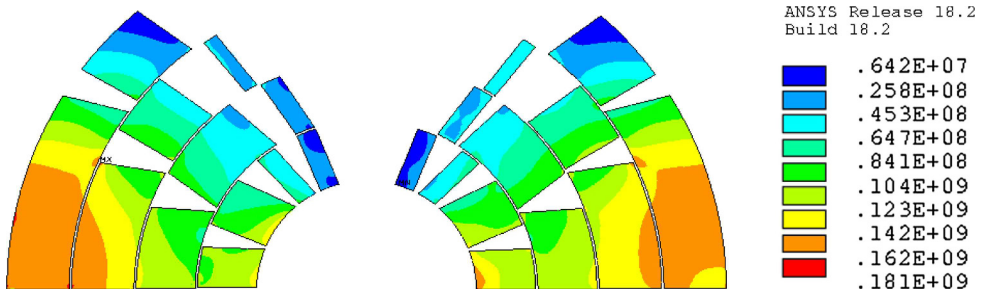
Fig. 3.6. Stress distribution (von Mises) in the coil for a central field amplitude of 16 T.

experiencing training quenches. As was successfully done for the LHC, a warm-cold magnet measurement correlation will be established, based on the statistics from pre-series magnets. All series magnets will be magnetically measured warm and only a small percentage of them also measured at operating (cryogenic) temperatures.

3.2.3 Field quality

The field error naming convention follows the one adopted for the LHC [124]. The systematic field error values are deterministic and computed with ROXIE: they comprise a geometric contribution, a contribution coming from persistent currents and the effect of saturation of the ferromagnetic yoke. The contribution from the persistent currents [125] has been computed using the conductor parameters of Table 3.3 and assuming that artificial pinning, which allows the critical current (thus the magnetisation) at low fields to be reduced, has been implemented. Considering that it is very unlikely that a perfect point pinning can be achieved, the contribution reported in Table 3.1 has been obtained assuming 50% of perfect point pinning. The random values are due to the spread of the geometric and persistent current contributions. The geometric random errors have been determined by means of Monte-Carlo simulations which include a random displacement of the coil blocks with a root-mean-square (RMS) amplitude $d = 50\,\mu$m. The uncertainty errors are linked to the production line, at this stage it is assumed, as was done for HL-LHC, that there is uniform production and therefore the uncertainties are equal to the random values. Further optimisation is on-going to passively correct the b_3 error from persistent currents by using iron shims. The yoke shape will also be further optimised to minimise the saturation effects.

3.2.4 Magnet protection

The magnet and its protection system are conceived to limit the hot spot temperature to below 350 K in case of a quench and the peak voltage to ground in the coil below 2.5 kV. This voltage limit comprises up to 1.2 kV due to the quench evolution in the magnet itself and up to 1.3 kV from the circuit. The protection system can be based on the coupling-loss-induced quench method (CLIQ), on quench heaters alone or on a combination of both. On paper all options effectively protect the magnets within the above limits [126]. Experiments on HE-LHC models and prototypes will demonstrate if, in real conditions, CLIQ can be implemented with the required reliability and redundancy for every quench situation. For the reasons above, though it is believed that CLIQ has the potential to quench the entire magnet in 30 ms after the initiation
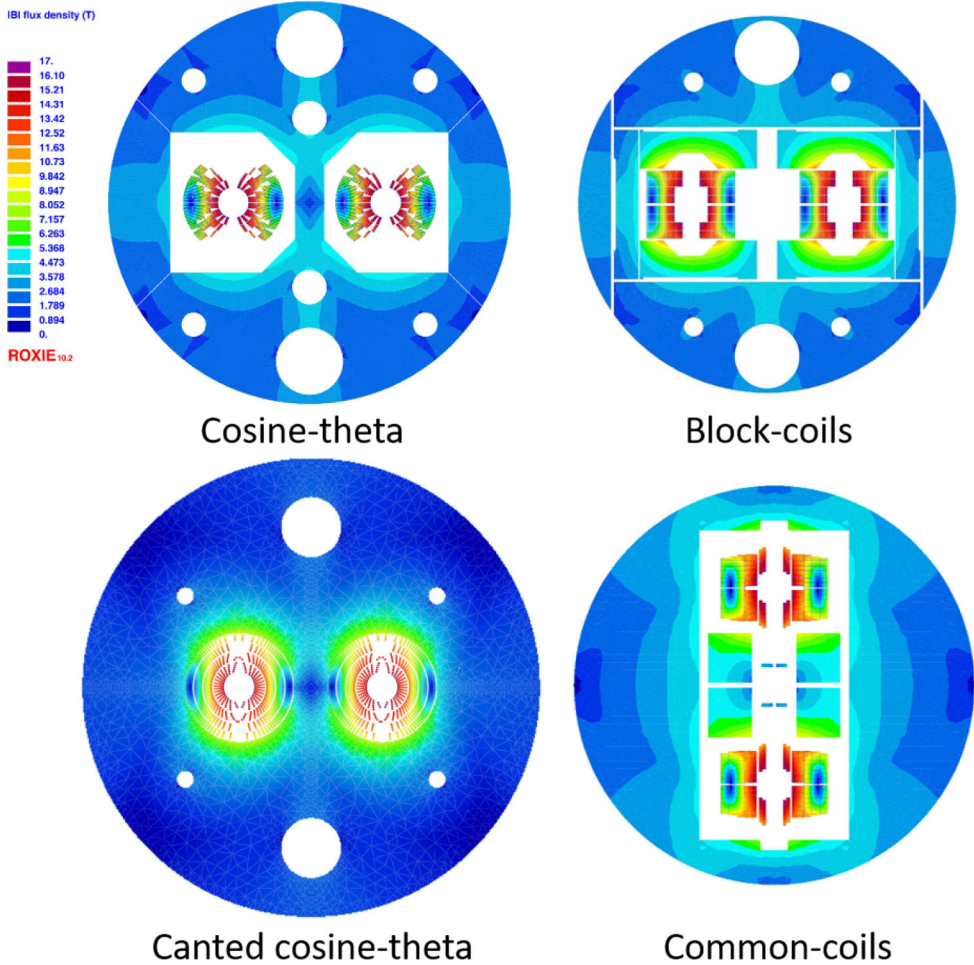
Fig. 3.7. Electromagnetic cross sections of the 16 T dipole design variants.

of a quench (time delay), the 16 T magnets have been designed assuming a time delay of 40 ms, which is compatible with the use of quench-heaters.

3.2.5 Other design options

In addition to the baseline design of the cosine-theta type, other design options have been studied in detail and will be tested experimentally in the coming years. These other designs are the block-type [127], the common-coil [128] and the canted-cosine-theta (CCT) [129] configurations. All options have been explored under the same assumptions, in particular concerning the magnet aperture (50 mm), the field amplitude (16 T), the conductor performance (assuming the availability of a conductor with a target critical current density of 1500 A/mm^2 @ 4.2 K @ 16 T corresponding to 2300 A/mm^2 @ 1.9 K @ 16 T), the margin on the load line (>14%) and the allowed mechanical constraints on the superconducting coil (<150 MPa at warm and <200 MPa at cold). The electromagnetic cross section of each of these options is shown in Figure 3.7. Their salient features, with respect to the baseline cosine-theta, are shown in Table 3.2.

Table 3.2. Salient features of design options for 16 T magnets.

Parameter	Cos-theta	Block-coil	CCT	Common-coil
Peak field on conductor (T)	16.40	16.73	16.35	16.57
Operating current (A)	11 441	10 176	18 135	15 880
Inductance @ 16 T (mH/m)	38	48	18	26
Outer yoke diameter (mm)	660	616	750	650
Mass of conductor (kg/m)	115	120	148	145

Each of these alternatives features some interesting characteristics which may have the potential to become competitive with the baseline cosine-theta design in terms of performance, in particular if they would allow operation at a lower margin on the load-line, thus reducing the required amount of conductor.

3.2.6 Low temperature superconductors

The 16 T dipole magnets for the HE-LHC rely on Nb_3Sn. Experience has been gained in the use of this technology in both the USA and Europe, not only on R&D magnets but, more recently, thanks to the HL-LHC project, also on accelerator magnets. Both the electrical performance and filament size are beyond state-of-the-art Nb_3Sn wire. A dedicated R&D programme has been launched worldwide, with some promising results already [130]. This programme has three phases: in the first phase, the focus is on increasing the critical current by 50% with respect to HL-LHC (1500 A/mm^2 at 4.2 K and 16 T), maintaining high RRR (150). This requires a major breakthrough and work on novel methods, such as artificial pinning centres (APC), grain refinement and architectures. In the second phase, the conductor will be optimised for the reduction of magnetisation, in particular at low fields, by modifying the effective filament diameter and possibly using APC. The third phase can be considered the preparation for industrialisation, focusing on achieving long unit length (5 km) and competitive cost (5 Euro/kAm at 4.2 K and 16 T). As reported in [130], despite the short time since the start of the programme, high-performing Nb_3Sn conductors have been already produced by new collaborating partner institutes and companies, achieving a J_c performance of the order of the specification for HL-LHC. Work performed on grain refinement and APC has shown promising results, nearly doubling the J_c at 12 T, 4.2 K on small samples. Finally, to improve the training of magnets, the introduction of materials with high heat capacity (Gd_2O_3) directly within the Nb_3Sn wire is being considered.

Two distinct conductors are used for the 16 T dipoles: a high-field (HF) conductor used for the inner pole and a low-field (LF) conductor used for the outer pole. The parameters of the HF and LF conductors are summarised in Table 3.3. It is assumed that the insulated conductor can be subjected to pressures of up to 150 MPa at ambient temperature and 200 MPa when cold, without experiencing an irreversible degradation. Based on the information coming from tailored experiments and from magnet tests, these values are considered to be challenging but realistic. Finally, due to the high J_c, the large filament diameter and the large amplitude of a magnet cycle, the magnetisation losses of these magnets have a considerable impact on the design of the cryogenic system, which assumes 5 kJ/m at 1.9 K for the two apertures. This limit can be respected with filament diameters of around 20 μm and if new manufacturing techniques have been developed, e.g. the afore-mentioned APC, and if the reset current during the machine powering cycle has been optimised.

Table 3.3. Target parameters for the main dipole conductor.

Property	Unit	Value
Critical current density at 16 T and 1.9 K	A/mm^2	1500
Strand diameter HF conductor	mm	1.1
Strand diameter LF conductor	mm	0.7
Filament size HF conductor	μm	20
Filament size LF conductor	μm	20
Cu/nonCu HF conductor		0.8:1
Cu/nonCu LF conductor		2.1:1
Number of strands HF cable		22
Number of strands LF cable		38
Width of HF cable	mm	13.2
Width of LF cable	mm	14.0
Keystone angle of HF/LF cable	degrees	0.5
Average thickness of HF cable	mm	1.950
Average thickness of LF cable	mm	1.265

3.2.7 Superconducting main quadrupole

The main quadrupoles (MQ) of HE-LHC are twin-aperture magnets based on a cosine-2theta coil configuration assembled in a 20 mm thick helium II vessel. The cooling system and the cryogenic features in the iron yoke are linked to MD magnet characteristics. Like the MD magnet, the inter-beam distance is 250 mm and the physical aperture is 50 mm in diameter. Each aperture is mechanically independent from the other due to the use of a collar and key mechanical assembly. The main parameters of the MQ are listed in Table 3.4. Each double pancake is made of 18 turns of Nb$_3$Sn Rutherford cable with a 0.4° keystone angle, as is illustrated in Figure 3.8. The cable consists of 35 strands, 0.85 mm in diameter, the filament size is 20 μm. The CLIQ system protects the magnet with a hotspot limited to 350 K and a peak voltage to ground below 900 V.

3.2.8 Other magnets in the arcs

For the baseline HE-LHC optics, the FODO cell length in the arc is chosen to be 106.9 m, roughly the same length as for the LHC. The HE-LHC has 8 equally long arcs, each with 23 FODO cells. Each FODO cell has 6 dipoles and 2 Short Straight Sections (SSS). As in the LHC, each SSS contains one MQ, and sextupole (MS) and dipole corrector magnets (MC). Depending on the SSS location in the arc, there may be in addition, octupole corrector magnets (MO), tuning quadrupoles (MQT) or skew quadrupoles (MQS). It is planned to have 800 MB-MB, 416 MB-SSS and 416 SSS-MB interconnections in the arcs. The magnet types and their main parameters are listed in Table 3.5. The space required for the interconnections and the magnet extremities is summarised in Table 3.6, which shows the target distance between the magnetic ends of the various magnets.

3.2.9 Low-beta quadrupoles and separation dipoles

The low-beta triplets are composed of quadrupole magnets and corrector magnets. There are two types of low-beta triplets for installation in the high and low luminosity interaction regions respectively. The magnet parameters of the final triplet quadrupoles and separation dipoles for the high-luminosity insertions in Points

Table 3.4. Main arc quadrupole parameters for the 23×90 optics at $12.9\,\mathrm{TeV}$, and 18×90 optics at $13.5\,\mathrm{TeV}$ beam energy.

Item	Unit	Value
Number of regular units		376 (23×90), 296 (18×90)
Total number of units		424 (23×90), 344 (18×90)
Operating gradient	T/m	352 (23×90), 336 (18×90)
Coil physical aperture	mm	50.0
Peak field	T	10.51
Operating current	A	22500
Operating temperature	K	1.9
Magnetic length @ $1.9\,\mathrm{K}$		3300 (23×90), 2800 (18×90)
Stored energy at $16\,\mathrm{T}$ (entire magnet)	MJ	1.7, 1.5
Self-inductance at $16\,\mathrm{T}$ (entire magnet)	mH	6.7, 5.7
Field margin on the load line at nominal	%	20
Temperature margin at nominal	K	4.6
Distance between aperture axes at $1.9\,\mathrm{K}$	mm	250
Number of coil turns per aperture		72
Mass of the cold mass	t	8, 7
Total field harmonics at nominal b_6, b_{10}	units	-0.47, 0.41
Total field harmonics at injection b_6, b_{10}	units	-22.3, 2.40

Notes. Each optics contains 48 "irregular" quadrupoles in the dispersion suppressors, consisting of four different types: 12 MQMXL (DS of IR1 and IR5), 12 MQ (DS of IR3 and IR7), 8 MQML (DS of IR2, IR4, IR6 and IR8), and 16 MQM (DS of IR2, IR4, IR6 and IR8).
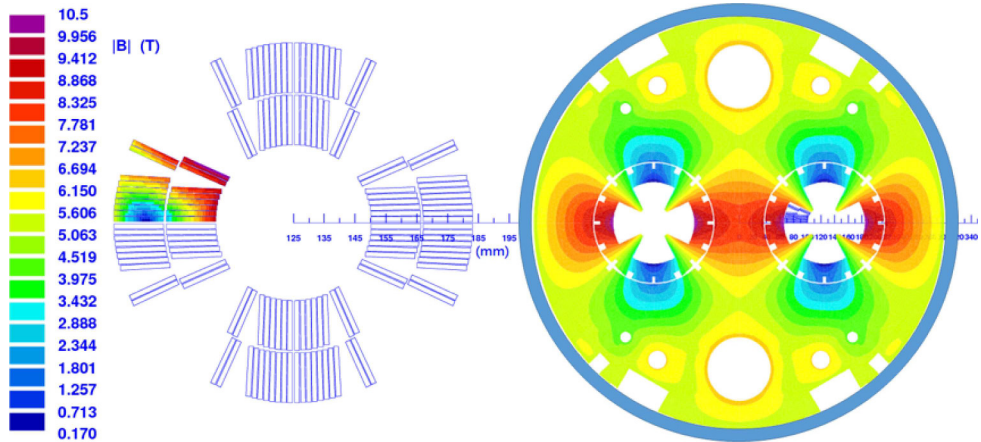
Fig. 3.8. Left: conductor distribution and magnetic field [T] in the quadrupole coil. Right: iron yoke, steel collar layout and HeII vessel.

Table 3.5. Other magnets, and BPMs, in the arcs and in the dispersion suppressors (DIS), for the 23×90 and the 18×90 optics.

Optics	23×90			18×90		
Magnet type	No.	Strength	Length	No.	Strength	Length
Lattice Sextupole (MS)	376	$7000\,\mathrm{T/m^2}$	0.836 m	296	$7000\,\mathrm{T/m^2}$	0.5 m
Lattice Octupole (MO)	168	$200\,000\,\mathrm{T/m^3}$	0.32 m	104	$200\,000\,\mathrm{T/m^3}$	0.32 m
Dipole Corrector (MCB)	376	4 T	0.647 m	296	4 T	0.647 m
Trim Quadrupole (MQT)	160	$220\,\mathrm{T/m}$	0.32 m	160	$220\,\mathrm{T/m}$	0.32 m
Skew Quadrupole (MQS)	32	$220\,\mathrm{T/m}$	0.32 m	32	$220\,\mathrm{T/m}$	0.32 m
Sextupole Corrector MCS	1232	$3000\,\mathrm{T/m^2}$	0.11 m	1,280	$3000\,\mathrm{T/m^2}$	0.11 m
Octupole Corrector MCO	616	$14\,000\,\mathrm{T/m^3}$	0.06 m	640	$14\,000\,\mathrm{Tm^3}$	0.06
Decapole Corrector MCD	616	$4.4 \times 10^6\,\mathrm{T/m^4}$	0.06 m	640	$4.4 \times 10^6\,\mathrm{T/m^4}$	0.06
Beam-Position Monitor	424	–	0.15 m	344	–	0.15 m
DIS Quadrupole (MQ)	12	$360\,\mathrm{T/m}$	3.5 m	12	$360\,\mathrm{T/m}$	3.5 m
DIS Quadrupole (MQM)	8	$360\,\mathrm{T/m}$	3.4 m	8	$360\,\mathrm{T/m}$	3.4 m
DIS Quadrupole (MQMC)	8	$360\,\mathrm{T/m}$	2.4 m	8	$360\,\mathrm{T/m}$	2.4 m
DIS Quadrupole (MQML)	16	$360\,\mathrm{T/m}$	4.8 m	16	$360\,\mathrm{T/m}$	4.8 m
DIS Quadrupole (MQMXL)	12	$360\,\mathrm{T/m}$	6.0 m	12	$360\,\mathrm{T/m}$	6.0 m
DIS Trim Quadr. (MQTL)	32	$220\,\mathrm{T/m}$	1.3 m	32	$220\,\mathrm{T/m}$	1.3 m

Table 3.6. Distances between magnets (magnetic lengths).

Magnet types	Distance (m)	Remarks
MB-MB	1.5	may be longer if stronger MCS are required
MB-SSS	1.3	does not include BPMs
MQ-Other	0.35	Other magnetic elements in SSS
Other-Other	0.35	

Table 3.7. Parameters for the superconducting inner-triplet quadrupoles.

	Q1	Q2	Q3	Comment
No. of submagnets	1	2	1	
Submagnet length (m)	12.9	10.5	12.9	
Coil radius (mm)	70.4	70.4	70.4	Empirical formula
Cold bore radius (mm)	64.4	64.6	64.6	Coil radius -5.44%, $-2\,\mathrm{mm}$ LHe & insulation
Shielding thickness (mm)	20	20	20	
Free aperture (mm)	40.5	40.5	40.5	With 2.05 mm beamscreen and 2 mm insulation
Gradient (T/m)	145.8	145.4	145.7	

1 and 5 are presented in Tables 3.7 and 3.8. The target distance between the magnetic length of each of these magnets is two meters, ignoring the corrector magnets.

The magnets around the collision points will be exposed to high radiation levels which may affect their performance negatively. It is assumed that the conductor performance can be maintained until a displacement-per-atom (DPA) value of 2×10^{-3} and that the magnet insulation can withstand an accumulated radiation dose of 30 MGy. These values are unlikely to be exceeded over the machine lifetime, assuming the use of the baseline 20 mm thick tungsten shield (Sect. 2.4.4). Some optimisation by adding shielding in the interconnects is ongoing, as is the development of a more radiation resistant impregnation system in the magnets. Furthermore, the estimated static heat load using the baseline shield and at the nominal operation conditions is

Table 3.8. Parameters for the superconducting separation dipoles in IRs 1 and 5.

	D1	D2
Type	Single aperture	Double aperture
Length (m)	12	15
Field (T)	9.7	7.7

about $5\,\text{mW/cm}^3$, which corresponds to a temperature increase of the coil of about $0.5\,\text{K}$.

3.2.10 Other magnets

Depending on their location, the matching and dispersion suppressor quadrupoles have a similar cross section to the MQ but have apertures increased to up to $70\,\text{mm}$. Around 154 matching quadrupoles are distributed as follows: 96 in the dispersion suppressors, 16 in the high-luminosity experiment insertions, 16 in the low-luminosity experiment insertions and injection, 4 in the extraction section, 6 in the RF section and 16 in the collimation section. Furthermore, 64 trim quadrupoles are installed in the 16 dispersion suppressors. The same type of magnets as those in the LHC are required in the collimation insertion. However, the radiation load in the betatron collimation region is large. Normal-conducting dipole magnets with bedstead coils would reduce the radiation dose by one order of magnitude compared to magnets with racetrack coils.

3.3 Cryogenic beam vacuum system

3.3.1 Overview

Vacuum stability at cryogenic temperature is a key element for the design of the HE-LHC. Significant levels of synchrotron radiation are produced in this machine that result in heat power depositions of the order of 5 W/m. Early analysis has revealed that it is unlikely to be possible to design a beamscreen akin to the one in the LHC that can cope with the operational conditions expected. A novel design is needed that can effectively shield the cold bore of the superconducting magnets operating at $1.9\,\text{K}$ from the heat load. The concept must also help mitigating electron cloud, resistive and impedance effects from the beginning. The proposed design is currently being validated experimentally.

3.3.2 Beamscreen

Synchrotron radiation, impedance and cryogenic considerations

The synchrotron radiation (SR) power and flux are higher than those of the LHC. Figure 3.9 shows a comparison between the LHC, HE-LHC, and FCC-hh flux spectra from $4\,\text{eV}$ to $1\,\text{MeV}$. A 4 eV cut-off has been chosen because photons below $4\,\text{eV}$, the typical value of work-function for metals, are incapable of extracting photo-electrons and producing molecular desorption from the walls of the beamscreen. While the linear photon flux for HE-LHC is only a factor of 4 times higher than that of the LHC, the linear SR power density at $13.5\,\text{TeV}$ is about 30 times higher than that of

SR Photon Flux Spectra for LHC 7, 7.3, 7.54 TeV,
HE-LHC 13.5 TeV and FCC-hh 50 TeV

E (TeV)	P' (W/m)
7	0.21
7.3	0.26
7.54	0.29
13.5	5.55
50	35.5

E (TeV)	E_{crit} (eV)
7	43.8
7.3	49.7
7.54	54.8
13.5	305.1
50	4269

Beam Currents: LHC:584 mA; HE-LHC: 1120 mA; FCC-hh: 500 mA
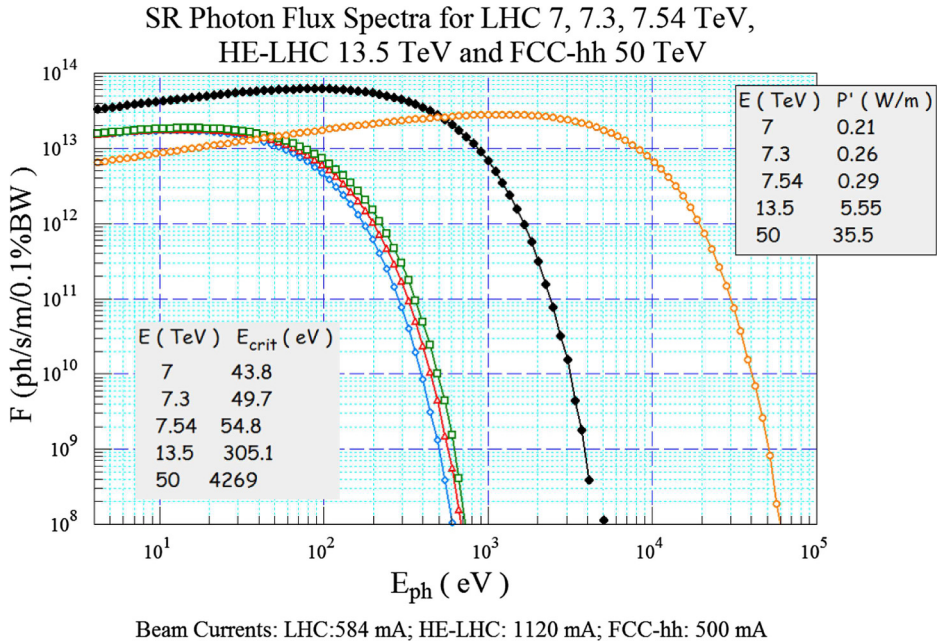
Fig. 3.9. Comparison of the SR flux spectra for LHC at three energies, HE-LHC and FCC-hh.

the LHC, ruling out a scaled version of the LHC beamscreen. Calculations [131] have also ruled out the possibility of using LHC sized capillaries (<4 mm) because the supercritical helium flow rate would not be sufficient. The required number of pumping slots would also affect the impedance budget too much [132]. For these reasons the design concept has longitudinal slots along the external part of the beamscreen in the plane of the orbit, where the highly collimated SR photon fan is directed.

Beamscreen design

Figure 3.10 shows the conceptual beamscreen design. With respect to initial designs, the height of the two longitudinal slots has been increased to limit effects on the impedance budget. This improvement is also beneficial for vacuum quality, since it captures a larger fraction of the primary SR photon fan during the acceleration phase. At lower beam energies the rms vertical aperture of the SR photon fan is bigger, as it depends on the reciprocal of the relativistic factor [133]. The number and position of the pumping slots has been optimised taking into account the leakage of scattered SR power reaching the magnet cold-bore. The internal surface of the beamscreen could be treated using Laser-Ablated Surface Engineering (LASE), creating μm sized patterns on the surface. This treatment has proven [134] to greatly reduce the secondary-electron yield (SEY) of the bare surface. Experimental validation of LASE treated surfaces on the resistive wall impedance to reduce SEY and photo-desorption yield are ongoing in the EC funded EuroCirCol project [134]. Details of the measurements on 3 variations of the beamscreen were reported at the 2018 FCC week [135]. If HTS coatings are chosen for improved impedance reduction, e-cloud mitigation would be provided by an a-C (amorphous carbon) coating.
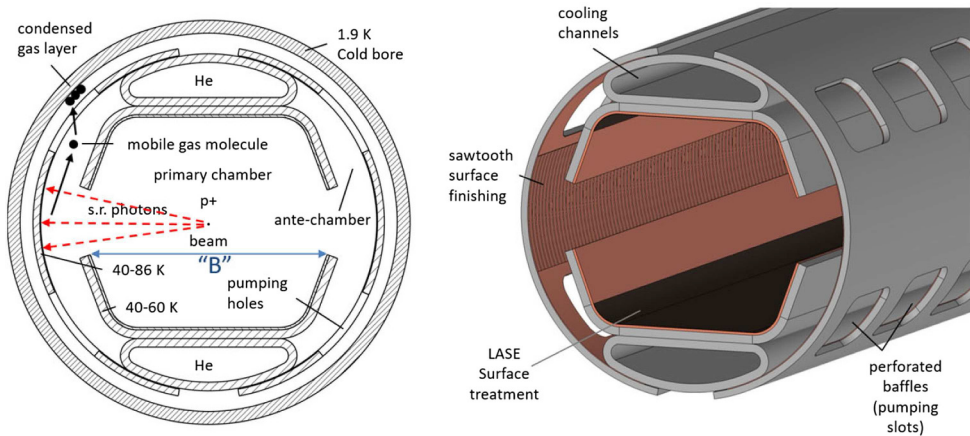
Fig. 3.10. Design of the HE-LHC beamscreen. The main functions and parts are indicated together with details of the temperature distribution. The internal part has a height of 26.9 mm and a width "B" of 27.55 mm. The large pumping slots provide an effective pumping speed for H_2 inside the beamscreen of ∼860 l/m/s at 50 K (LHC: ∼480 l/s/m at 15 K, as derived from [136]). The thickness of the copper layer on the inside of the ante-chamber areas, including the saw-tooth, is reduced to 80 μm.

The HE-LHC main dipole magnets are curved. The dipole beamscreens must, therefore, either be produced curved, or be flexible enough that they can be slid into the cold bore of the bent dipole magnets, guided by the sagitta of the magnet.

Beamscreen temperature

The total SR load is ∼100 kW/beam. If the SR power were to be dumped on a beamscreen at a temperature between 5 K (inlet) and 20 K (outlet) as in the LHC arc cells, then given the Carnot efficiency, the corresponding cryo-compressor electric power input at room-temperature would be more than 10 MW [131]. A detailed analysis has determined the most appropriate operating temperature for the beamscreen for a workable system. The temperature range for cryogenic cooling at the inlet and outlet of each cell should be between 40 K and 60 K. A reference temperature of 50 K is close to the optimum working point for a cryogenic refrigeration system when considering the temperature-dependent resistivity of Cu [137] and also ideal for the option of deploying HTS coatings [138]. This temperature range is also advantageous for the vacuum system: it leads to higher conductance, which is proportional to the square root of the absolute temperature. It also guarantees that no particular vapour pressure instability is excited [139].

Heat load to cold bore

Table 3.9 gives an overview of all beamscreen heat load sources, assuming that the beamscreen is mounted using elastic springs in the cold-bore [140] and excluding electron cloud contributions. The results show that the total heat load is below the allowed threshold of 300 mW/m [141].

Table 3.9. Cold bore heat load sources.

Source	HE-LHC cold bore heat load 13.5 TeV 1.1 A
Beam-gas scattering for baseline MD	∼100 mW/m
Thermal conduction BC 50 K–CB 1.9 K	100 mW/m
Grey body thermal radiation from 50 K BS	3 mW/m
Leaked radiation power through pumping holes	0.5 mW/m
Total heat load	**200 mW/m**

Residual gas density

The requirements for the residual gas density are similar to those at the LHC. At the LHC the acceptable level was specified for an H_2-equivalent gas density of about $10^{15}\,\mathrm{m^{-3}}$ for a 100 h beam-gas nuclear scattering lifetime, i.e. a gas density of a mixture of gases usually released by SR irradiation, consisting of H_2, CO, CO_2, CH_4, each weighted with its radiation length and percentage molecular content and referred to that of 100% H_2 [142]. A scaling has been performed for a hadron beam of higher energy [136]. Given the higher beam energy of HE-LHC and the less-than-linear increase of the nuclear scattering cross section with beam energy, it has been estimated that a factor of ∼2 decrease of the H_2-equivalent density will ensure the same 100 h lifetime contribution as for the LHC. The target is to remain below 5×10^{14} H_2-equivalent $\mathrm{m^{-3}}$.

A 3D CAD model of the arc dipole and interconnect area, based on the LHC, has been created [142]. It takes into account the new requirements of SR photon flux and linear power densities. It has been found that the RF fingers installed after each dipole and quadrupole, compensating displacements and thermal contraction during cool-down, need to be shielded from the primary SR photon fan. Otherwise these could be damaged by the 5 W/m power density. A symmetric SR absorber upstream of the RF contact fingers, as used in modern light sources, mitigates that risk. The absorber intercepts and concentrates up to 85 W of SR power, casting a shadow downstream for about 2–3 m, up to the subsequent beamscreen. Along the shadowed area, the racetrack shaped beamscreen gradually merges into the circular shape which is needed for the LHC-style RF contact fingers and, eventually, for the beam-position monitor (BPM) button blocks.

Figure 3.11 shows a cut-away view of the interconnect area. The residual gas density profile for HE-LHC would look similar to the one calculated for FCC-hh (FCC CDR Vol. 3, Fig. 3.12). The density profile would have density bumps localised at each interconnect area, generated by the large SR photon flux and power intercepted by the end absorbers. The actual density values would depend upon the integrated photon flux, as per experimental data [142]. Considering the much larger photon flux of HE-LHC compared to that of the LHC, the integrated photon dose necessary to have an operationally-safe residual gas density should be reached in a rather short time, of the order of few hundred hours at nominal beam current.

Electron cloud mitigation

There are a number of different proposals for electron cloud mitigation. One path currently being considered is using amorphous carbon (a-C) coating, which has been successfully tested in the SPS at CERN. Another option is LASE treatment (see Fig. 3.10), which is also being assessed experimentally. Figure 3.12 shows the areas which would need to be treated, the corresponding percentage of copper-coated
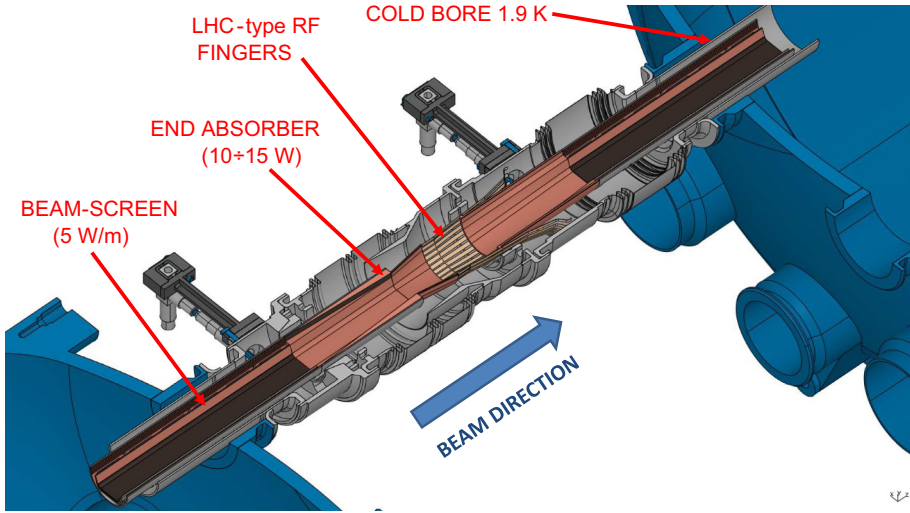
Fig. 3.11. Cut-through, in the plane of the orbit, of the dipole-to-dipole short interconnect area model. This model does not show the BPM block, which is under design in another work package.
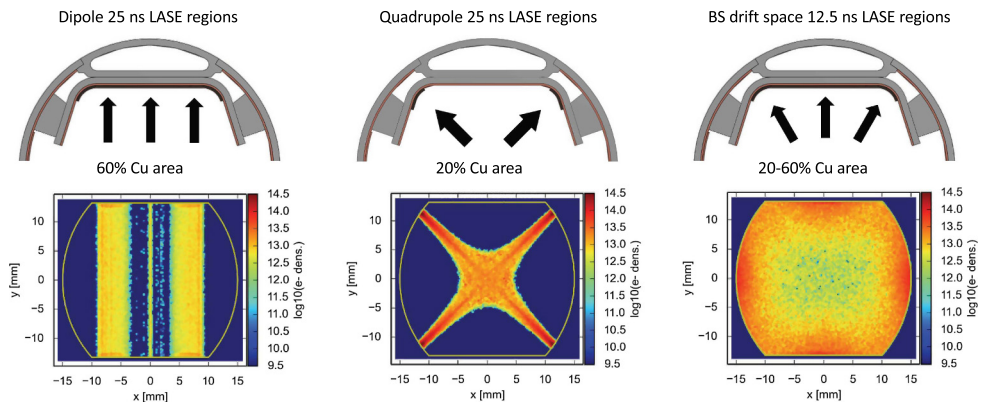
Fig. 3.12. The transverse density of the electron cloud in different components of the collider arc. The location of the surface coating in each component is also shown. These simulation results were obtained for FCC-hh beam parameters. The situation for HE-LHC is expected to be very similar.

beamscreen area and the electron cloud distribution for each type of magnetic element: dipole, quadrupole and field-free drift [143].

3.3.3 Vacuum

Insulation vacuum design

The insulation vacuum system creates a vacuum barrier between the magnet cryostat and the cryogenic distribution lines. The design will be based on the LHC system [131], which has been operating successfully for more than ten years. By-passes will be possible. Mobile, rough pumping groups will evacuate the large volumes, starting from atmospheric pressure level. Permanent turbo-molecular pumping groups

installed at the vacuum barrier by-pass will be used to reach the required target pressure levels and will evacuate helium gas if there are leaks in the cryogenic pipes.

Equipping the arcs with turbo pumps at a spacing comparable to the LHC's appears possible and straightforward. The permanent turbo-molecular groups will also make pumping during thermal transients of the cryostat possible, which lead to excessive gas release from the absorbers.

Helium absorbers

The absorber material, its shape and its assembly in the cryostat are under investigation. The current conceptual design is based on compacted nano-porous materials fixed in thermal contact with the cold-mass support cooling pipes at $4.5\,\mathrm{K}$ (the C' line in LHC terminology).

The development of the He absorbers can benefit from the large spectrum of studies performed over the last ten years, in particular for the ITER project [132,137,142]. He pumping has been measured for activated charcoal fixed on metallic surfaces. Surface areas available for absorption regularly exceed $3000\,\mathrm{m}^2$ per gram of absorber; this means that 30 g of activated charcoal would have the same surface area available as the total multi-layer insulation (MLI) in a 400 m long vacuum sector. In the coming years, the focus will be to develop a material with a well defined porous structure for He pumping at affordable cost for quantities around $\sim100\,\mathrm{kg}$. The activation of the absorbers in the cryostats is also currently under investigation.

3.4 Radiofrequency system

3.4.1 Overview

The injected beam will be captured, accelerated and stored using a 400 MHz superconducting cavity system, which is also used to damp the longitudinal injection errors. A system of electrostatic deflectors will be used to damp the transverse injection instabilities/errors and thus ensure transverse stability. The radiofrequency (RF) and beam feedback systems are located in point 4, as in the present LHC.

HE-LHC requires an RF voltage of between 10 and 11 MV per beam (Sect. 2.4.9). The HE-LHC RF system could be based on 400 MHz single-cell Nb/Cu cavities and be quite similar to that of the LHC, or HL-LHC, but with higher quality factors.

A 200 MHz capture system for injection could also be considered, or even be mandatory, should the possibility of injection at 450 GeV from the present SPS be pursued, as highlighted in Section 2.4.9.

Crab cavities are mandatory for the HE-LHC and their operation at 400 MHz is preferred, as for the HL-LHC crab cavities. A total deflecting voltage of 10 MV is required for each beam on each side of each primary collision point (see Sect. 2.4.4), therefore, a crab cavity system with a total deflecting voltage of 80 MV is needed.

The RF power requirements for the main 400 MHz RF system are similar to those of the HL-LHC (Sect. 2.4.9): up to about 2 MW total RF power will be required during acceleration. More efficient RF power sources are under development and would help to lower the overall electric power consumption.

3.4.2 Superconducting accelerating cavities

The frequency of 400 MHz naturally calls for the Nb/Cu technology operated at $4.5\,\mathrm{K}$. It is anticipated that a vigorous R&D programme on Nb/Cu films will eventually decrease the surface resistance by a factor two to three, and hence further
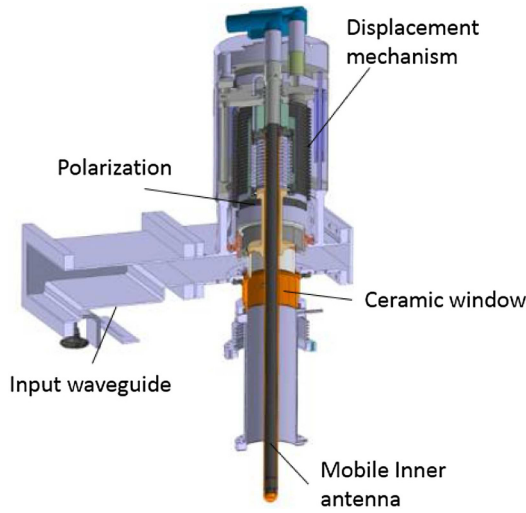
Fig. 3.13. Schematic of the LHC power coupler.

increase the advantage of this technology [144]. Efforts are ongoing to push the cavity construction technology beyond existing limits to produce seamless cavities within the very tight tolerances required [145]. Such cavities will no longer suffer from performance limitations related various defects induced by the presence of welds and have less scatter in their electro-magnetic performance [146].

The A15 compounds have the potential to outperform niobium as their BCS surface resistance is much lower due to the higher critical temperatures. Nb_3Sn cavities obtained by thermal diffusion of Sn in bulk Nb have similar performance at $4.5\,K$ to state of the art bulk Nb cavities at $2\,K$. A programme aimed at the synthesis of Nb_3Sn films on copper substrates is ongoing at CERN and has already produced high quality films on small samples [147,148].

RF power couplers

Fundamental power couplers for superconducting cavities are among the most important and most complex auxiliary systems. They must deliver RF power to the beam and simultaneously separate the cavity ultra-high vacuum, ultra-low temperature environment from air-filled, room temperature transmission lines, as illustrated in Figure 3.13. A wide variety of techniques is involved in achieving these goals: RF design, cryogenic and mechanical engineering, materials science, vacuum technology, and electromagnetic field modelling.

3.4.3 Crab cavities

Crab cavities are used to increase the luminosity by tilting the bunches to maximise their overlap at the collision point. In HE-LHC, the limited impedance budget calls for new concepts and innovative developments. Unlike the existing HL-LHC crab cavity prototypes [149], the design for HE-LHC crab cavities is based on Nb/Cu superconducting technology. As illustrated in Figure 3.14a, it consists of a ridged waveguide resonator with wide open apertures to make the Nb coating process possible and also optimise the RF performance.
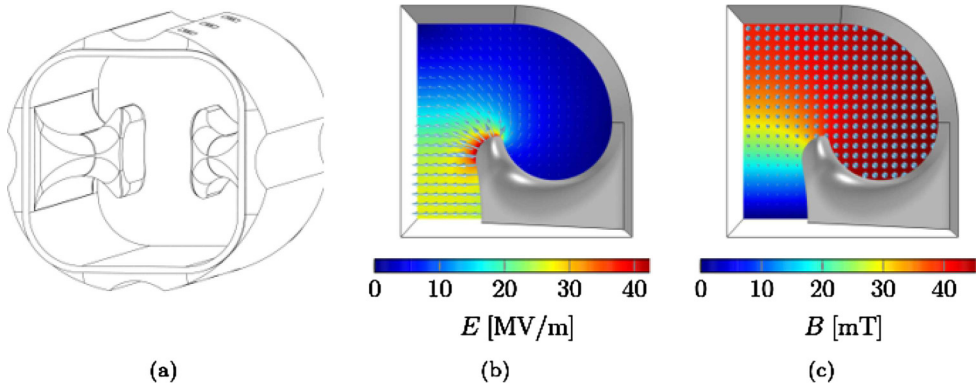
Fig. 3.14. (a) Design of the wide-open-waveguide crab cavity. The electric (b) and magnetic (c) fields of the fundamental mode are scaled to the nominal deflecting voltage of $V_\perp = 3$ MV.
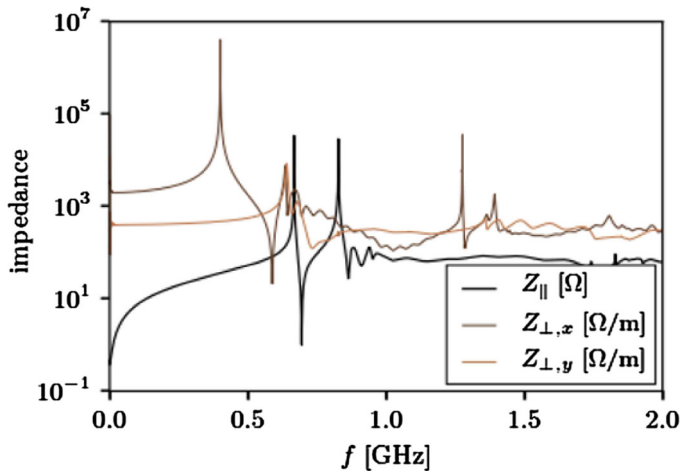
Fig. 3.15. Longitudinal and transverse beam coupling impedances.

Figures 3.14b and 3.14c show one quarter of the transverse cross section at the cavity centre together with the electric and magnetic field distributions, respectively. The particle deflection is caused by the transverse electric field of the TE111-like fundamental mode between the two mushroom-shaped ridges (see Fig. 3.14a). Details of the optimised cavity design and the relevant RF parameters can be found in [150].

This design has good performance; the simulated beam coupling impedances are shown in Figure 3.15. It has only half the effective impedance of the double quarter wave and one third of the RF dipole crab cavity [151]. Since the number of HE-LHC crab cavities will be higher than for the HL-LHC this impedance reduction is important.

3.4.4 RF power generation

The RF power requirements for the main 400 MHz RF system are similar to those of the HL-LHC (Sect. 2.4.9). Up to about 2 MW total RF power will be required during acceleration. More efficient RF power sources are under development and these would help to lower the overall electric power consumption.

Improving energy efficiency and reducing energy demand is absolutely crucial for any future big accelerator and the development of high-efficiency RF power sources must be at the core of the R&D programme [152]. The High Efficiency International Klystron Activity (HEIKA) was initiated at CERN in 2014 [153] to evaluate and develop new klystron bunching technologies for high efficiency klystrons [154–156]. In the light of these developments, efficiencies are expected to rise from 65% to potentially above 80%. Gaining efficiency also means reducing costs [156].

3.4.5 Low-level RF

Strong feedback around the cavities will be required for high intensities. A direct RF feedback will be supplemented by a one-turn delay feedback giving extra impedance reduction around the revolution frequency sidebands. Transient power requirements can be kept to a minimum by the use of a cavity phase modulation scheme as in LHC.

Controlled longitudinal emittance blowup to maintain stability by Landau damping, both during the ramp and in physics, is achieved by the injection of band-limited RF phase noise.

Most of the low-level RF issues have been addressed in LHC [157], or studied for HL-LHC [158]. Modern designs implement most of the signal processing in the digital domain and even better performance will be achieved in the future with the continuous growth of processing power.

Transverse damping and feedback system

With bunch intensities of 2×10^{11} protons per 25 ns, a strong transverse feedback system similar to the feedback already operating in LHC and HL-LHC will be needed to damp injection errors and to cure transverse instabilities caused by the resistive wall impedance. The impedance is dominated by the beamscreen impedance and details are given together with the required transverse feedback performance in Section 2.4.13.

From the technological point of view, the transverse feedback system needed to cure the coupled bunch instabilities at 25 ns bunch spacing will resemble the ADT system deployed in LHC. The bandwidth of this system has to be at least 20 MHz to cover all possible coupled bunch modes and – similar to LHC – with bunch lengths of the order of ns, the choice is for a system to operate in the base-band, i.e. from the lowest betatron frequency up to 20 MHz, half the bunch repetition frequency.

The baseline system for 25 ns bunch spacing can be easily scaled from the parameters of LHC. From a technological point of view it can be implemented using tetrode power amplifiers directly installed under the kicker tanks, which contain electrodes to supply kicks in the horizontal and vertical planes. The advantage of this system over a matched 50 Ω strip-line system is that the tetrode amplifier can deliver strong kicks at low frequencies in the multi-kV range essentially because it is a high impedance device (≈ 1 kΩ load in the case of LHC). It is not straightforward to replace this tetrode based system by a system using solid-state devices. Solid-state devices can usually provide high currents at low impedance determined by their internal capacitances and are therefore not suitable for this application. A strip-line kicker system with long strip-lines can be considered as an alternative to a tetrode-based system.

Table 3.10. Main parameters for HE-LHC beam transfer.

Parameter	Unit	HE-LHC		HL-LHC
injector		SPS	scSPS	
Beam injection energy	TeV	0.45	1.3	0.45
Beam injection rigidity	T·km	1.50	4.33	1.50
Beam top energy rigidity	T·km	45.0	45.0	23.3
Beam current	A	1.12	1.12	1.12
Bunch population	10^{11}	2.2	2.2	2.2
Bunches per ring		2808	2808	2808
Bunches per injection		288	~100	288
Stored beam energy	GJ	1.3	1.3	0.7
Injected beam energy	MJ	4.6	~5	4.6
Norm. emittance	μm	2.5	2.5	2.5
Max. injection $\sigma_{x,y}$	mm	1.11	0.66	0.98
Injection gap	μs	0.9	0.57	0.9
Abort gap	μs	3.0	3.0	3.0

3.5 Beam transfer systems

3.5.1 Overview

The relevant parameters assumed for injection and extraction from HE-LHC are listed in Table 3.10, with the values for HL-LHC given for comparison. The resulting total energy per transfer (injection or extraction) and beam sizes are also included. The parameters for the present LHC injection energy and for an assumed 1.3 TeV injection energy are given, and compared with those of the HL-LHC. At injection the transferred energy limits the number of bunches injected, which requires the 570 ns injection kicker gap to reach the full number of bunches if the injection energy is 1.3 TeV.

3.5.2 HE-LHC injection system

For 1.3 TeV and a similar injection trajectory, the beam rigidity increases by a factor 2.9 for septa and kickers. The kicker and septum elements can profit from reduced gaps, depending on the details of the insertion optics and impedance constraints. Part of the increase in $\int$B.dl can be provided by proportionally increasing the space in the insertion for septa and kickers similar to the existing LHC designs, which will limit the β* reach of any experiment sharing the straight section: this option will work for 1.3 TeV injection, but lattice space can be regained by introducing new hardware concepts under development for FCC-hh: superconducting septum, short-circuit mode for kickers, higher dI/dt (switch voltage) and fast solid-state generator topologies. The eventual solution will be a compromise between aperture, rise-time (filling pattern) and space in the lattice (β* reach).

The layout requires either a 4 T superconducting septum or a cryostat passage for the upstream quadrupole, to allow the septum to be accommodated. The beam size at the absorbers may limit the number of bunches per injection.

Injection subsystems

The 1.3 TeV injection kicker will be a terminated transmission line system, with a flat-top length of 2.5 μs, based on inductive adder solid-state pulse generators. Impedance

Table 3.11. Key parameters of LHC and HE-LHC injection kickers in IR2 and IR8.

Parameter	Unit	450 GeV	900 GeV	1300 GeV	1300 GeV
Rise time	ns	900	750	570	1500
Deflection angle	mrad	0.8	0.8	0.8	0.8
Magnet length	m	2.7	2.3	1.7	2.7
Aperture height	m	0.054	0.044	0.040	0.040
Gap field	T	0.11	0.15	0.185	0.215
dI/dt	kA/μs	4.7	7.0	10.3	4.6
Voltage	kV	47.3	59.7	65.1	45.7
No. kicker modules		4	7	11	6
Total installed length		15.3	22.4	26.2	22.6

Notes. The 450 GeV configuration is for the present LHC.
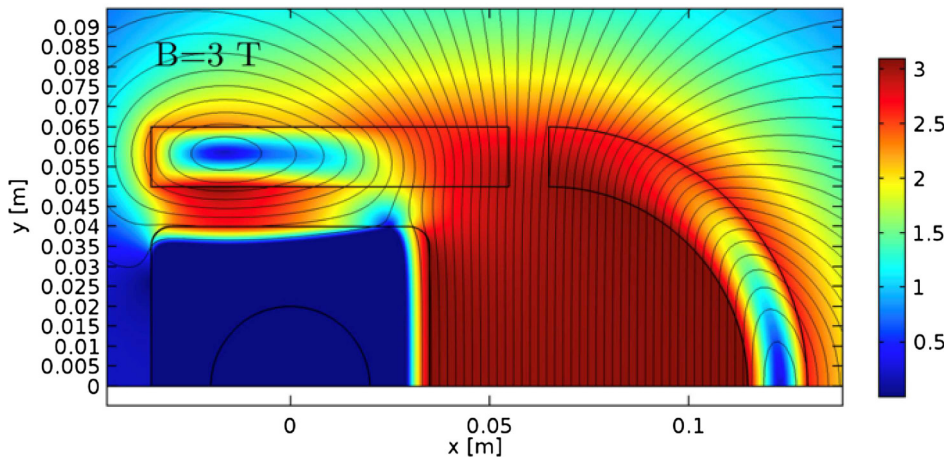
Fig. 3.16. Superconducting 3 T septum cross section, based on superconducting shield concept. The septum shield could be MgB$_2$ or multilayer NbTi/Nb/Cu.

shielding will need to be equivalent to that developed for HL-LHC, with the added complication of a faster rise time. Injection kicker parameters for 570 ns rise time are presented and compared with those of the LHC, in Table 3.11. As an alternative, a kicker system with 1500 ns rise time is shown. In this case the optics and integration of a side experiment is feasible at the expense of a reduction of the maximum number of bunches in the machine. Figures for 900 GeV have also been included.

A septum field of 3 T is required and tentative parameters are given in Table 3.14. The technology will be based on the SC septum developments currently under way for FCC-hh extraction, where both superconducting shield, Figure 3.16, and $\cos\theta$ topologies are being investigated. The septum dipole is being designed as a canted-$\cos\theta$ magnet, as already under development for HL-LHC.

The other key element of the injection system is the protection device to intercept mis-kicked beam, which can either be the injected beam or the circulating beam, depending on the specific kicker failure. The robustness limits of the jaw material will limit the number of injected bunches, with only about 100 bunches possible at 1.3 TeV. R&D into advanced materials will be required to increase this number – sacrificial jaws are not considered for this particular device, since LHC experience has shown that it is struck by the beam several times per year.

Table 3.12. Parameters of LHC and HE-LHC injection septa in IR2 and IR8.

Parameter	Unit	450 GeV	900 GeV	1300 GeV
Deflection angle	mrad	12	12	12
Magnet length	m	4.0	4.0	4.5
Aperture height	mm	25	22	20
Gap field	T	0.76/1.13	3.0	3.0
Number of magnets		5	3	4
Total installed length	m	22	16	23

Notes. The 450 GeV configuration is for the present LHC.

Table 3.13. Key parameters of LHC and HE-LHC extraction kickers in IR6.

Parameter	Unit	LHC now	HE-LHC inj. 1.3 TeV	HE-LHC inj. 0.9 TeV	HE-LHC inj. 450 GeV
Rise time	μs	3	2	2	2
Deflection angle	mrad	0.27	0.27	0.27	0.27
Magnet length	m	1.42	0.75	0.75	0.75
Aperture height	m	0.072	0.054	0.062	0.072
Gap field	T	0.323	0.49	0.49	0.49
dI/dt	kA/μs	6.2	10.5	12.1	14.0
Current	kA	18.5	21.1	24.2	28.1
Voltage	kV	29.7	35.7	35.7	35.7
No. kicker modules		14	33	33	33
Total installed length	m	25.6	32.6	32.6	32.6

3.5.3 HE-LHC beam dump system

The beam dump system concept for HE-LHC is based on that of the present LHC, which uses a sequence of extract – dilute – absorb to abort the ~700 MJ beam in a loss-free way. For HE-LHC the dumped beam energy increases to 1.3 GJ. It is assumed that the existing tunnel and caverns are reused without significant civil engineering works, which fixes similar horizontal and vertical extraction trajectories and therefore similar kicker and septum angles. The sweep radius is limited to a maximum of ~300 mm, to avoid enlarging the TJ62 and TJ68 junction caverns.

Extraction kicker magnets

Twice the present LHC integrated strength is required for the extraction kickers, while a reduction in rise time is strongly motivated by the limits expected on the absorber. Doubling the kick per magnet and retaining the present layout of 15 magnets would result in an unrealistically high switch voltage of 60 kV. The voltage could be reduced to 30 kV if the rise time were relaxed to 6 μs; however, this will further increase the already difficult challenge of surviving an asynchronous beam dump at 13.5 TeV. The magnet length therefore needs to be halved to allow faster rise time. Smaller aperture and a more reasonable system would be possible with 1.3 TeV injection – parameters for the extraction kicker are shown in Table 3.13. With 33 modules, the space needed in the lattice will nevertheless increase from the present 26 m to about 33 m, for a rise time of 2.0 μs with 1.3 TeV injection energy. The kicker parameters for an injection energy of 450 GeV (largest gap size) are the most challenging – a higher dI/dt will complicate the switch design, whilst a higher voltage increases the probability of erratic functioning.

Table 3.14. Options for HE-LHC beam dump extraction septa configurations.

Parameter	Unit	Baseline	Option
New units		3	6
New septum type		superconducting	MSDC
New septum field	T	3.0	1.24
Total $\int$B.dl	Tm	108	108
Deflection angle	mrad	2.4	2.4
Septum unit length	m	4.3	4.46
Additional total length	m	17	35
Δ_S Kick centre	m	14.9	18.1
Δ_v trajectory	mm	−36.3	−43.5

Extraction septa

Extraction of the beam is made vertically, above the continuous cryostat. The HE-LHC layout would keep the same entrance location. The deflection angle of 2.4 mrad needs to be maintained, which requires $\int$ B.dl = 108 Tm. With the field increased to the maximum possible values a total of 70 Tm is available. The 5 units each of MSDB and MSDC would be retained. The remaining deflection would be provided either by additional MSDC units, or by three new 3 T, 4.3 m long superconducting septa [159] occupying an additional ~17 m. The SC version has the advantage of keeping the kick centre closer to the original location at the centre of LSS6, which reduces the vertical trajectory difference with respect to the reference. This version is assumed as the baseline: the parameters for the two options are compared in Table 3.14. The vertical trajectory is moved downwards by about 36 mm,

For the SC septum the details of the integration and susceptibility to beamloss need to be addressed in detail – the SC septum will need to be located either adjacent to the present TCDS septum protection device, or a further 10 m downstream, which changes the kick centre and moves the vertical offset another ~25 mm downwards (which could in turn pose a problem for the extracted beam passage past the Q4 cryostat).

3.5.4 Dilution and dump

The dumping system of the LHC consists of extraction kickers (MKD), extraction septa, dilution kickers (MKB), a long transfer line, and a beam dump block, consisting of graphite core with a graded density, varying between 1.77 and $1.2\,\mathrm{g/cm^3}$. The beam dilution and beam dump system for the HE-LHC at 13.5 TeV beam energy looks possible using a similar concept and layout to the present LHC system.

The survival of the dump block in case of a beam abort is of paramount concern. In order for the dump block to withstand the impact of an extracted HE-LHC beam, the dilution sweep length has to be increased, compared with the LHC, as is illustrated in Figure 3.17.

A promising option in terms of kicker aperture and length is raising the sweep frequency, along with a smaller sweep radius. Increasing the dilution sweep length to around 3 m, as shown, requires a higher dilution-kicker frequency f_0, additional kickers with about 4 times the present number of modules and twice the space, to produce the 2.6 turn spiral. Lowering the density of the inner graphite core from 1.2 to $1.0\,\mathrm{g/cm^3}$, while increasing the length of this low-density portion to 4 m, seems feasible and could provide additional margin.
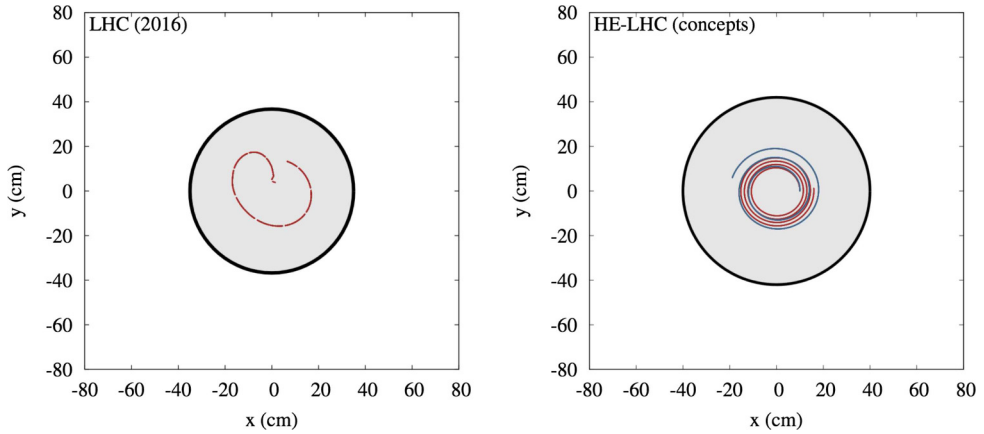
Fig. 3.17. Spiral dilution pattern of extracted bunches at the entrance of the beam dump absorber block for the present LHC (left) and the HE-LHC (right).

Table 3.15. Key parameters of HE-LHC vertical and horizontal dilution kickers in IR6.

Parameter	Unit	MKBV	MKBH
Frequency	kHz	44.4	44.4
Deflection angle	mrad	0.33	0.32
Magnet length	m	0.70	1.0
Coil turns		2	1
Aperture height	mm	36	32
Aperture width	mm	66	58
Gap field	T	0.88	1.02
Current	kA	23.2	26.1
Voltage	kV	28.6	28.9
Number of kicker modules		24	14
Total installed length	m	23.7	17.9

The tape-wound grain-oriented $50\,\mu$m Si steel cores used for the dilution kickers of the LHC show a high saturation field $(1.5\,\mathrm{T})$ and acceptable losses up to frequencies of $\sim$50 kHz. Higher frequencies could require nanocrystalline steel. The aperture of MKB(V) will be a limit; a higher injection energy allows for smaller aperture.

The possible addition of a SC dilution quadrupole in the extraction line was also studied, but found to be unattractive, since such a quadrupole promises little gain, but instead causes integration issues.

Tentative parameters of the HE-LHC dilution kicker systems are given in Table 3.15. The total of 38 modules should be compared to 10 for the present LHC.

The performance of the system could be further improved by use of a modified beam dump. For a standard absorber the maximum energy deposition of all bunches occurs at the same longitudinal position inside the beam dump. This region experiences a much higher temperature rise than the surrounding parts of the beam dump. An improved type of beam absorber would spread out the deposited energy over different longitudinal positions from the front surface of the absorber, thereby reducing the maximum temperature. One potential implementation is a "mosaic absorber", i.e. composite dump blocks made transversely from sets of different materials or portions of the same material with varying densities. Such a mosaic beam dump can redistribute the deposited energy since the penetration depth of the energy deposition varies for different materials and densities. A mosaic beam dump was first studied for the FCC-ee [160].

Table 3.16. Basic HE-LHC beam parameters that are relevant for the specifications of diagnostic devices.

Particle type	Bunch spacing (ns)	N. emittance (μm)	Bunch charge (e)	Number of bunches	Transverse Size (μm) ($\beta = 2$ m) $E = 1.3$ TeV	$E = 13.5$ TeV
p$^+$	25	$2.5(\rightarrow 0.9)$	$5 \rightarrow 220 \times 10^9$	$1 \rightarrow 2760$	600	$185 \rightarrow 110$
	12.5	$1.3(\rightarrow 0.5)$	$5 \rightarrow 110 \times 10^9$	$1 \rightarrow 5520$	430	$135 \rightarrow 80$

3.5.5 Conclusion

The HE-LHC injection system is strongly dependent on injection energy. At 1300 GeV there is an impact on experimental β* reach, and the kicker and septum performance are pushed, with SC septa as the baseline. For the dump system, the extraction is feasible if the number of modules is doubled. More space in the lattice is needed for the extraction kickers, and advances in technology are assumed. Detailed studies of the (protection) absorber limits and extraction kicker rise time are needed, with trade-off between failure probability and consequences. The septa require SC technology and/or a cryostat passage, and to reach the required performance, the dilution kicker system will be the most challenging.

3.6 Beam diagnostics

3.6.1 Requirements and concepts

The beam diagnostic requirements for HE-LHC are, to a large extent, defined using the experience gained from LHC operation [161]. These requirements are compared to what is achievable with the state-of-the-art technologies used for modern beam instrumentation systems. A baseline suite of beam diagnostics for HE-LHC is proposed based on the outcome of this comparison. Areas where further research and development is required to fulfil specifications that cannot be met using existing technologies are highlighted.

The operational scenarios considered for HE-LHC beam diagnostics are:

- Initial beam commissioning, including the need for beam threading to establish circulating beams, the first ramp and squeeze cycle and optics measurement and correction. All typically using a low intensity, single pilot bunch.
- Machine protection validation for injection and beam dump systems, collimator set-up and loss-map validation, all using a single, nominal intensity, set-up bunch.
- Operation with nominal beams.

The LHC notion of a set-up beam is defined as a beam with an intensity that can never harm machine components as a result of total loss. For LHC, the set-up beam is defined as 5×10^{11} protons at 450 GeV and 1×10^{10} protons at 7 TeV. Assuming an HE-LHC top energy of 14 TeV, with a nominal transverse beam size of 0.36 mm (1σ at 1.3 TeV) and 0.18 mm (1σ at 14 TeV) for a typical $\beta = 200$ m in the HE-LHC arc, the HE-LHC set-up beam is estimated to be 1×10^{11} and 5×10^9 protons at injection and top energy respectively. This sets the lower intensity limit for the operation of all beam diagnostic devices. The HE-LHC beam parameters relevant for the beam diagnostics are presented in Table 3.16.

3.6.2 Beam position monitoring

The requirements for HE-LHC beam position monitoring are similar to those of LHC [162]. It is therefore proposed to maintain all quadrupoles with dual plane

beam position monitors (BPMs) as this significantly improves the global measurement capabilities of the system and makes it less susceptible to single BPM failures. This results in a total of ∼1000 BPMs (∼500 per beam). It remains to be seen if the significant synchrotron radiation emitted at high energy requires that the BPM sensors will need to be placed at 45° (as is done in synchrotron radiation facilities). This has a slight impact on availability compared to an orthogonal arrangement as the loss of a single sensor results in the in-operability in both planes. Having this angle to avoid the synchrotron radiation fan would also reduce the BPM sensor area available, making the BPM less sensitive.

The system will be capable of providing measurements of the closed orbit with sub-micron resolution and a fill-to-fill reproducibility of better than $20\,\mu$m. This data will be provided in real-time to allow orbit and radial position feedback.

The system will also be capable of providing turn-by-turn data for injection oscillation and optics measurements and post mortem analysis. A few special BPMs will provide sub-micron resolution bunch-to-bunch and turn-by-turn data for special purposes such as instability observations or interlock purposes.

A modern, state-of-the-art BPM acquisition system will be able to meet all of these requirements. The sensor and front-end electronics, comprising analogue signal shaping and digitisation circuitry, would be located in the tunnel. A radiation-hard, bi-directional, fibre optic link [163] will connect each station to the processing electronics located on the surface away from the radiation environment. The challenge will be to design a cost effective solution, where the front-end electronics can function in the tunnel's radiation environment.

3.6.3 Beam loss monitoring

A lack of data on the quench behaviour of the $16\,$T dipoles planned for HE-LHC means that an in-depth analysis of the beam loss monitor (BLM) requirements is not possible. It is therefore assumed that a copy of the LHC BLM system [164] would be adequate for machine protection purposes.

The latest magnet design has compact $16\,$T dipoles with a reduced iron yolk, which could lead to the stray field on the outside of the cryostat reaching $0.2\,$T. The detectors and electronics used for loss monitoring would therefore need to work in such an environment. Ionisation chambers can meet this requirement and magnetic shielding could be installed around them if necessary.

3.6.4 Beam current and intensity measurements

The beam current and intensity measurement systems will provide the total circulating current and the relative bunch-to-bunch intensities with an accuracy better than 1%. These systems should also provide the overall beam and bunch-by-bunch lifetimes.

For the total circulating current, the main challenge is the large dynamic range to be covered, from $10\,\mu$A (single bunch of 5×10^9 charges) to 1.1 A (2760 bunches of 2.2×10^{11} charges). LHC experience shows that better than 1% accuracy is required for medium to high current operation (to allow accurate luminosity calibration), but this is significantly relaxed for lower current operation. Nevertheless, for machine protection purposes an interlock on the beam intensity during set-up is needed and this requires a system that has an accuracy and resolution of at least ∼20% of this lower limit (∼2 A). While direct current – current transformers (DCCTs) are suitable for the accurate measurement of medium to high currents, they have an intrinsic

noise floor at around the 1 A level, believed to result from properties of the magnetic core material (Barkhausen noise). This makes them unsuitable as machine protection devices for HE-LHC. A cryogenic current comparator [165] could therefore be considered to provide this functionality.

A wall current transformer coupled to fast digitisation electronics is proposed for the bunch-by-bunch measurement. A recent upgrade of the LHC system using such technology, combined with numerical integration, has already reached the required performance for 25 ns beams [166].

3.6.5 Tune, chromaticity and coupling

The requirements for tune, chromaticity and coupling measurements are the same as for LHC. The principal problem to be overcome (and which is already present in the LHC) is the incompatibility of tune measurements with a high gain active transverse damping system. Study of the possible implementation of a non-linear transfer function for the transverse damper is therefore proposed. This may lead to some self excitation of betatron oscillations at low amplitudes which will result in slow emittance growth, but this may be fully compensated by the radiation damping in HE-LHC.

3.6.6 Transverse profile measurements

The target accuracy for normalised emittance (ε) derivation in HE-LHC is 1%. This folds in both the error from measurement of the beam size (σ) and knowledge of the beta function (β) at the measurement location. If a similar contribution from both is assumed ($\varepsilon = \beta\sigma^2$), then this translates into an admissible error of 0.7% on the beta function and 0.5% on the beam size. For the beam size, this is certainly a challenge towards the end of the fill, where the average size in the arcs is expected to be in the 100 μm range. In addition to this absolute emittance requirement, a bunch-to-bunch emittance with a relative accuracy of 1% (0.5% on the transverse bunch size) is required. Both the absolute emittance measurement and the bunch-to-bunch measurement will be continuous, i.e. capable of providing measurements from injection, throughout the ramp and during physics.

Due to the high energy density contained in most operational beams, non-intercepting devices will be required to measure the beam size. A synchrotron light monitor is the instrument of choice for such a high-energy hadron accelerator [167], because there is sufficient visible light generated from a standard bending dipole at all energies (1.3 TeV injection to 14 TeV collision). The variety of sources required to generate synchrotron radiation in the LHC (undulator at injection, edge radiation during the ramp and dipole radiation at top energy), along with the difficulties in reliable calibration that this poses can therefore be avoided. Nevertheless, measuring the small beam size at top energy will be a challenge and requires the synchrotron radiation instrument to be placed in a high beta-function location. Since the visible radiation observed is close to the diffraction limit for a large part of the energy range, cross calibration with other instruments is mandatory to ensure reliable measurements. This cross calibration is currently provided by intercepting devices (wire scanners), which can only work with a low number of nominal bunches. Alternative, non-intercepting calibration devices, such as gas jet scanners [168] or a beam gas vertex detector, as are being developed for HL-LHC [169], should therefore be studied.

3.7 Element support, survey and alignment requirements, and concepts

The HE-LHC accelerator elements and their alignment tolerances, discussed in Section 5.9, are similar to those of the existing LHC. Therefore, the concepts, methods and tools of the LHC should be suitable and sufficient for the HE-LHC, although some improvements may be expected from technological developments.

The alignment of the HE-LHC can be based on the geodetic network of the LHC or an updated version thereof. The LHC geodetic network is composed of about 500 points sealed in the tunnel floor. Their position was determined by the alignment of the main quadrupole magnets (MQ) of the Large Electron Positron Collider (LEP), in operation between 1989 and 2000 and located in the same tunnel as the LHC [170]. The MQ position was determined initially from a surface network of geodetic points using GPS, their co-ordinates being transferred to the tunnel via eight civil engineering shafts and propagated on tripods along the tunnel. The network was gradually improved during the LEP shutdowns and in 2000, before LEP dismantling, it was considered by the survey team and the physicists, as the best that could be achieved and, therefore, a good reference for the alignment of the LHC. Levelling measurements, horizontal angles, offsets with respect to a stretched wire, gyroscopic measurements as well as mekometer range-finder were combined, and compensated, in order to determine the co-ordinates of the LHC geodetic network. The absolute 1σ accuracy of the geodetic points in horizontal and vertical planes is considered to be ± 2 mm for points close to the shafts and ± 4.5 mm for those located at the mid-point between two shafts. In the longitudinal direction, the 1σ accuracy is ± 2 mm [170]. The LHC components were aligned with respect to this geodetic network and then a smoothing was performed in order to detect any remaining significant relative misalignments. The relative accuracy obtained after smoothing was better than 0.15 mm rms. The excellent initial alignment of the LHC facilitated fast threading of the beam and limited the number of corrector magnets necessary to establish circulating beams in 2008. Regular re-alignments are performed during the LHC winter shutdowns. Quite similar conditions and procedures are expected for the HE-LHC.

The HE-LHC magnet supports could also resemble those of the LHC, except that they must be able to sustain the greater weight of the HE-LHC cryo-magnets.

3.8 Architecture and powering of magnet circuits

Use of FCC magnet technology for the HE-LHC means that the stored energy in the superconducting magnet system will be about 41 GJ. In order to handle such energies safely, the magnets must be powered in several independent powering sectors. In today's LHC, the energy stored in the 154 dipole magnets of one of the eight sectors is in the order of 1.1 GJ. In order to maintain the powering and magnet protection system similar to that of the LHC (including the cold by-pass diode ratings), a baseline of the HE-LHC powering with a subdivision into 32 independent dipole circuits, as detailed in Table 3.17, is proposed. This will also allow the voltage and nett power requirements for the power converters to be maintained at a comparable order of magnitude, while obviously adding additional complexity due to the synchronisation required for 32 power supplies instead of the previous 8.

The subdivision into 32 independent circuits will furthermore allow the voltages to ground to be maintained within acceptable limits during energy extraction. This will also avoid excessive insulation requirements for the magnets and the associated circuit powering components, in particular during a fast discharge of the energy after e.g. magnet quenches. If a circuit powering scheme as depicted in (Fig. 3.18) is adopted, a single energy extraction system per dipole circuit could be envisaged.

Table 3.17. HE-LHC versus LHC dipole circuit parameters.

	LHC	HE-LHC
Number of circuits N_{cir}	8	32
Nominal current	11.9 kA	11.4 kA
Magnets in series	154	38 or 39
Energy	1.1 GJ	1.4 GJ
Apparent inductance	15 H	22 H
Ramp up time	20 min	$\sim$20 min
Inductive boost voltage required from PC	150 V	230 V
Max PC net power during ramping	1.8 MW	2.6 MW
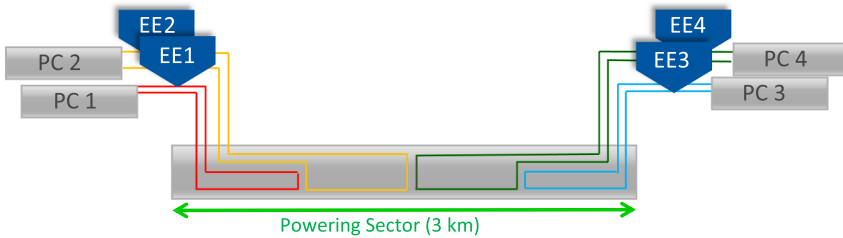
Fig. 3.18. Schematic of the dipole circuit architecture for HE-LHC. Each power converter (PC) is connected to an energy extraction (EE) system.

Table 3.18. Fast power abort of HE-LHC dipole circuit compared with LHC.

	Half of EE voltage	Discharge time constant	MIITs	Busbar copper cross section
LHC	0.45 kV	100 s	7×10^3 MA^{2}s	270 mm^2
HE-LHC	1.3 kV	106 s	7×10^3 MA^{2}s	235 mm^2

The extraction time could be further reduced compared with a resistor-based system by performing the extraction at constant maximum voltage, reducing operational losses as well and therefore resulting in a smaller environmental impact. On the contrary, the cold busbars and bypass diode ratings will have to be carefully reconsidered as shown in (Tab. 3.18). Protection of quadrupole and corrector magnets is well within the capabilities of the current LHC protection hardware. The insertion of a second energy extraction system in the middle of the arc cryostat is possible, but would require the creation of an additional small alcove in the mid-arc region or alternatively the connection of the mid-point to the underground galleries at the arc extremities via a long superconducting link or cold busbar system.

The core strategy for evolution of the quench detection system for the HE-LHC is the concept of a centralised data processing and quench detection. This enables considerable simplification of the instrumentation units located in the tunnel (QS), thus reducing their susceptibility to the expected levels of ionising radiation. Central data processing units (QPU) will be located outside the LHC tunnel and interconnected with high speed and highly deterministic data links to the intelligent instrumentation sensors. The centralisation facilitates data acquisition from multiple sources, which allows novel quench instrumentation technologies to be employed. These technologies improve noise suppression and accuracy by performing correlation across multiple channels of the superconducting circuits. A considerable challenge for the development of a global protection scheme is to design a digital system that enables

Table 3.19. Maximum voltage, $\mathrm{d}i/\mathrm{d}t$ and active power requirement for the two ramp-up strategies and the two ramp-up durations.

Ramp strategy	Ramp-up time	Max. voltage	Max. $\mathrm{d}i/\mathrm{d}t$	Power requirement
Constant voltage	20′	234 V	9.50 A/s	2.66 MW
Constant voltage	30′	160 V	6.33 A/s	1.83 MW
Constant power	20′	300 V	12.84 A/s	1.52 MW
Constant power	30′	300 V	12.84 A/s	0.90 MW

the adaptation of a software-defined approach for fast and reliable quench detection and to deal with the resulting large data volumes.

3.8.1 Power converters for magnet powering

The principal challenge for the powering of the magnets is the high peak power during ramp-up and the energy return during ramp-down. The system can be optimised by eliminating or reducing these large power swings and at the same time, the energy consumption minimised.

Power requirements for the main dipole converters

With four circuits per power sector, there will be 38 or 39 magnets per circuit, resulting in a stored energy in these magnets of about 1.4 GJ. The rated current for the dipole magnets is 11.39 kA and the estimated equivalent resistance for each magnet circuit is 1 mΩ. There are two options for the ramp-up strategy:

– Constant voltage: a fixed output voltage is applied to the magnets and the current ramps up with a constant slope ($\mathrm{d}i/\mathrm{d}t$). The main drawback of this option is that the power requirement during the end of the ramp up is very high. This can be seen from the solid curves in Figure 3.19a.
– Constant power: the output voltage applied to the magnets is controlled in order to limit the maximum power during ramp-up. A higher voltage is applied in the first part of the ramp and it is reduced as the current increases (see the solid curves in Fig. 3.19b).

The duration of the ramp has a significant influence on the power converter requirements: the shorter the ramp, the higher the power requirements. The difference in power ratings of the converters for a 20′ ramp up and a 30′ ramp up is shown in Figure 3.19 where the solid lines are for a 20′ ramp and dashed lines for a 30′ ramp. The main parameters corresponding to these ramps are given in Table 3.19.

If the total number of dipole circuits is 32, the total power requirements for all dipole circuits would be 32 times the power requirements given in Table 3.19 and therefore reducing the power requirements of each power converter is extremely important. In conclusion, to limit the power consumption from the AC network as much as possible, the ramp-up should be as long as possible and the strategy selected for the converter topology should be the most appropriate.

Topology and ratings of main dipole converters

The LHC uses twelve-pulse thyristor rectifier technology (13 kA at 190 V) in the dipole magnet power converters. For the HE-LHC, it is proposed to use switch-mode converters which will provide several advantages over thyristor converters:
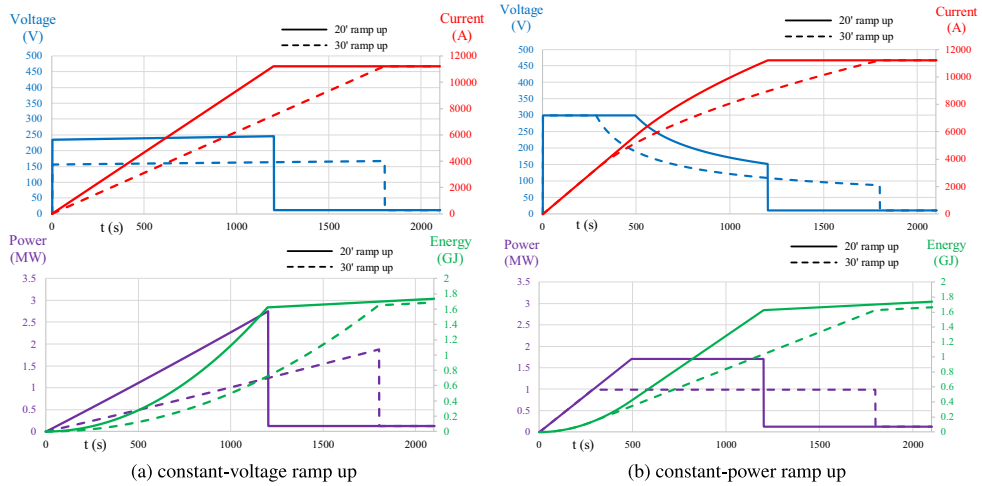
Fig. 3.19. Voltage applied to the dipole circuit, current in the dipole circuit, power requirement and energy supplied to the magnets for: (a) constant-voltage ramp; (b) constant-power ramp. Solid lines correspond to the 20′ ramp and dashed lines are for the 30′ ramp.

- Fewer harmonics will be injected into the AC network;
- There is no need for reactive power compensation;
- DC storage can be incorporated, which offers the possibility of storing part or all of the peak energy for the dipole magnets and to discharge it during the ramp up;
- It is possible to downsize the AC connection if energy storage is integrated in the converters since the AC network will only have to compensate the system losses.

The power supply for the dipole circuits will be rated for 12 kA @ 300 V. Each power supply will be composed of four 6 kA @ 150 V converters, connected two in parallel in series with another two in parallel (2P2S) as shown in Figure 3.20. Each converter will be composed of 4 bricks of 1.5 kA @ 150 V in parallel. The modularity of this converter topology provides excellent availability ($N + 1$) and easy repair and maintenance.

3.8.2 Energy storage in power converters

The main challenge for the powering of the dipole circuits is to provide the peak power during ramp-up. In order to minimise the power consumption from the AC network, it is essential to integrate energy storage systems (ESS) in the power converters.

At CERN, the use of energy storage in power converters has been implemented in numerous power supplies and it is becoming the general practice for all new projects e.g. POPS, POPS-B or the recently developed SIRIUS converter series for projects CERN-wide. Today, these converters use energy-storage capacitors. For FCC-hh, HL-LHC and HE-LHC, the cycles are much slower than in the injectors however they require much more energy due to the superconducting magnets. In this case, the capacitors cannot be used as energy storage units due to their volume. Alternative energy storage technologies are under consideration, of which only two technologies were identified as suitable:

- Super-capacitors: this type of capacitor is characterised by a much greater energy density than electrolytic capacitors. Within this family, electrical double layer
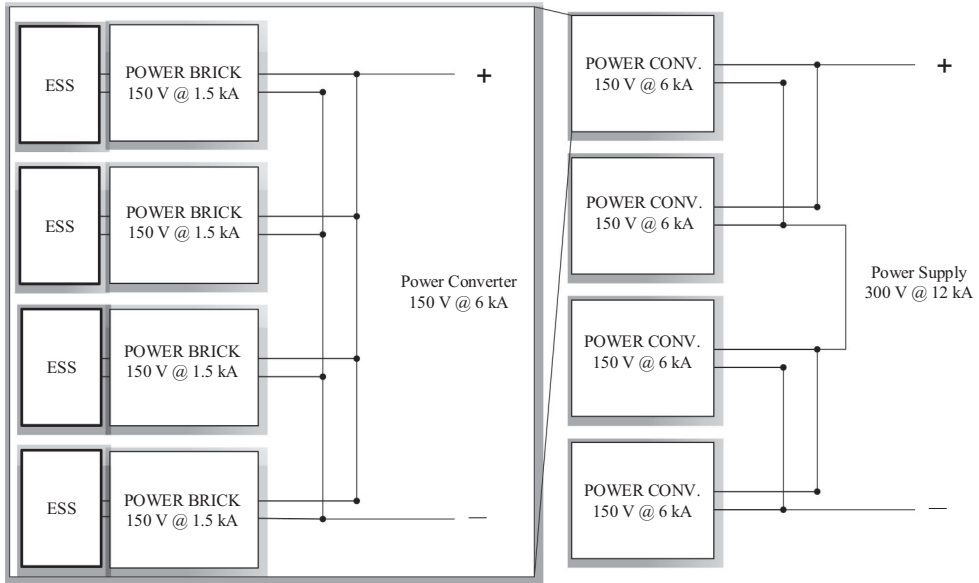
Fig. 3.20. Simplified diagram of a dipole power converter circuit.

capacitors (EDLCs) are the most interesting. However, for large-scale energy storage this technology is still very expensive: they are at least ten times more expensive than the equivalent lithium-ion batteries.

– Batteries: due to their superior energy density, battery storage seems to be the best technology. Significant developments in this area, driven by the automotive sector, are expected in the coming years.

Battery systems have been analysed in detail for magnet powering applications. The most suitable battery technology is based on lithium batteries and in particular the lithium titanium oxide (LTO) type. The main issue with lithium batteries is their limited lifetime, which is typically a maximum of 3000 charge-discharge cycles. For LTO batteries, the lifetime ranges from 5000 up to 20 000 cycles, which would be suitable for HE-LHC, as well as for the FCC-hh and HL-LHC. For the new inner triplet magnets of HL-LHC, the ESS needs to be able to recover 55 MJ from the magnets, which requires only one 19″ rack of LTO batteries. This solution seems very promising, since the ESS is very compact and cheap. For HE-LHC, the energy to manage is two orders of magnitude higher. The dipole magnets require an energy of 1.5 GJ, which means an effective energy of 417 kWh which corresponds to about 520 kWh in the energy storage system. Two options are proposed for the ESS:

– One common storage system for each power sector: this system of 1040 kWh (2 × 520 kWh/circuit) would be placed on the surface and linked to the converters in the tunnel by a common DC cable passing down the shaft. This configuration implies high transmission losses and the need for a DC breaker with high switching capability;

– Distributed amongst all power bricks: the energy storage systems would be installed in the tunnel, in separate racks or even integrated in the converter racks. This option requires more space in the tunnel (approximately 25–30% more than the space requirements for the converters alone), however, it provides the best performance and reliability.

Using current LTO batteries, the energy for each circuit (520 kWh) could be easily installed in the equivalent volume of ten 19″ racks, weighing a total of 6.5 t. Nevertheless, research on energy storage is currently intense and significant improvements in energy density, size and weight are expected in the near future.

3.9 Machine protection concepts

The increase in the centre of mass energy for HE-LHC implies a factor of 4 higher stored energy in the particle beams than in today's LHC, for which the damage limit can be derived from detailed energy deposition studies [171]. At a top beam energy of 13.5 TeV and assuming similar beam sizes to today's LHC, a localised loss of only 1.6×10^{10} protons (equivalent to about 7% of a nominal HE-LHC bunch) would already damage accelerator equipment. As for the LHC, the machine protection system (MPS) should therefore be designed to prevent any uncontrolled release of energy stored in the magnet system and the particle beams. In view of the reduced quench margin in the superconducting magnets, the protection system must also be able to prevent or at least minimise beam induced quenches of the superconducting magnets. The main principles of the LHC MPS design are still valid for HE-LHC, namely to define the aperture limitation in the ring and transfer lines by collimators, to detect abnormal equipment and beam conditions with fast and reliable instrumentation, to provide passive protection for specific fast failures by beam absorbers and collimators and to provide – wherever possible – diverse redundancy for the detection of the most critical failures.

If the injection energy for HE-LHC remains 450 GeV, a modest upgrade of the current injection protection system should be adequate while an increase of the injection energy (to 900 GeV or 1.3 TeV) requires reviewing the robustness of the absorbers and collimators concerned or limiting the number of bunches per injection. To survive an asynchronous dump at the nominal beam energy of 13.5 TeV, various techniques are being explored such as decreasing the kicker rise-time, modifying the optics around the extraction region and upgrading the robustness of the absorbers which receive the impact.

Similar studies to those already conducted for the HL-LHC are required for the HE-LHC to determine the acceptable level of halo population for which the collimators and absorbers can survive these most critical failure cases. The installation of dedicated fast beam loss monitors with nano-second resolution close to the injection and extraction absorbers would facilitate understanding of the processes and possibly reduce and mitigate some of the ultra-fast losses.

To mitigate changes in the beam trajectory during main magnet quenches, the protection and interlock systems have to ensure that the particle beams are dumped before the current discharge in the quench heater is triggered. In order to provide further, diverse redundancy for the detection of fast beam losses, a global protection system should be implemented. A good candidate for such a system, which has already proven its efficiency in HERA, is the fast beam current change monitor [172].

3.10 Controls requirements and concepts

With the ever larger particle accelerator facilities that have been constructed over the last two decades [173–176] and the entry of versatile particle accelerators in industry and healthcare, the development of control systems for particle accelerators has become a well understood task. The work of companies worldwide towards an Industry 4.0 architecture [177] extends the traditional architecture with enterprise
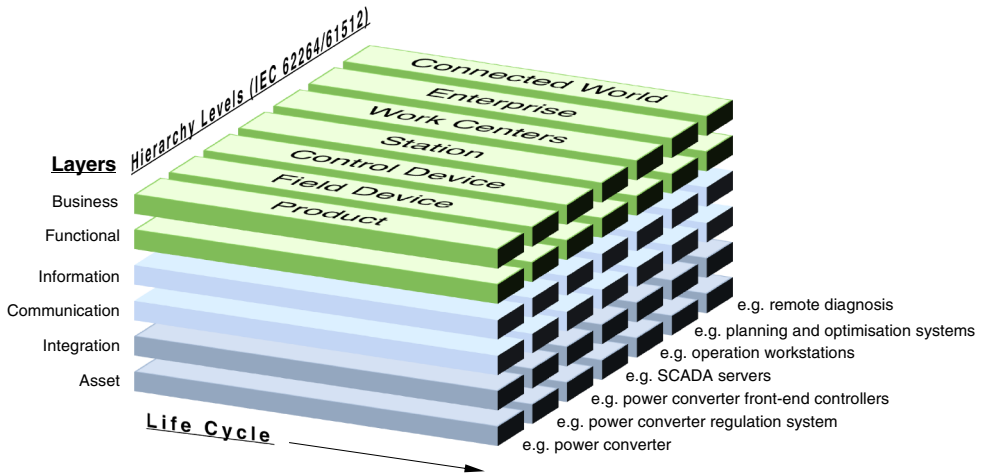
Fig. 3.21. The "Industry 4.0 reference architecture" can serve as a model for an integrated particle accelerator and experiment control ecosystem. For each system tier (connected world, enterprise, work centers, station, control device) that is needed to integrate the accelerator and detector equipment (field device and product tiers), services, interfaces and integration guidelines are currently being conceived by industry players at the different functional levels (business, functional, information, communication, integration and asset). Together with a lifecycle management framework that spans from concept over requirements, design, implementation/procurement, transition to operation, operation, maintenance/repair and retirement, this model represents an ideal reference for establishing a control and data acquisition architecture for the entire project, limiting project-internal developments to those parts, which cannot be covered by existing products, services, standards and guidelines.

resource planning and intelligent device tiers in the hierarchy and includes life cycle and functional layers (see Fig. 3.21).

With a steady increase of computing and communication technology capacities, a move to wireless communication including safety-related data exchange and ever more flexible embedded computing systems and re-programmable hardware, functionality is shifting from the upper tiers of the system architecture to the lower ones. Front-end systems that are cooperating more autonomously can overcome the constraints that result from centralised control over long distances. Scalable synchronisation and the reliable coordination of actions on a timescale of nanoseconds to support acquired data correlation will soon be widely available [178–182]. Femtosecond timing distributions over kilometer distances, as are currently used in free electron lasers [183,184], demonstrate that the performance of timing systems are up to FCC collider (hh, ee, and HE) demands today. An ever better understanding of how to adapt off-the-shelf designs to radiation environments is leading to more affordable intelligent controls in equipment that has to be close to the accelerator [185]. Industry is asking for greater use of COTS in mission-critical applications [186–190] and the factory of the future [191] has comparable requirements and these facts will drive the development of commercially available technologies within a few years [192].

Although the system sizes are gradually increasing (see Tab. 3.20), the main challenges for a control system infrastructure are gradually shifting from technical to organisational domains. On the time scale of a future collider project, the key persons who conceived CERN's accelerator complex operation and control concepts may no longer be available. This potential loss of expertise needs to be mitigated by establishing a systems engineering process [193,194] with adequate documentation

Table 3.20. Number of front-end control units in different systems.

Category	System	Number of front-end control units
Particle accelerator	CERN PS Booster	81
Particle accelerator	CERN PS	115
Particle accelerator	XFEL	ca. 200
Particle accelerator	CERN SPS	257
Particle accelerator	CERN LHC	525
Aerospace	International Space Station	660
Particle accelerator	Future Circular Collider	ca. 1500
Fusion research	ITER	ca. 5000 expected

support to capture operation requirements, architecture and design components as well as end-to-end test scenarios, well before a new facility is constructed.

Developers of industrial embedded systems have understood that traditional programming is a time consuming, costly and error prone activity [195]. Particle accelerators are no exception and therefore new development paradigms are needed to come to a sustainable long-term operation concept, reducing loss of knowledge, easing the management of software and its evolution and facilitating working with external partners in a cost effective way. Medical particle accelerator facilities have been successfully applying this approach for several years [196–201]. The need for continuous operation of CERN's particle accelerator complex calls for a gradual modernisation that has to be mastered from a managerial perspective. Such a scheme indicates a gradual evolution towards a new generation of accelerator control systems. It allows suitable concepts to be assessed early using the existing accelerators as test beds for new concepts.

Although fault-tolerant designs can help to meet the reliability requirements of these geographically extended machines, automated and remote maintenance/repair will play a role in ensuring the overall availability of a particle accelerator. As embedded systems become more powerful and flexible they also become more vulnerable to intentional and unintentional misuse. Cybersecurity became an important activity during the development of the control systems for the LHC [202]. For a future facility, this topic needs to be included from the beginning in the systems engineering process in close cooperation with the planning for the IT infrastructure. A well coordinated, complex-wide information and communication technology management environment covering requirements, planning, procurement, maintenance and upgrades will help accelerator groups to focus on the provision of the core control functionality. This approach will ease the transition towards the concept of "Controls as a Service" which can evolve and scale with the underlying technology platforms, focusing on technology independence as much as is reasonably possible.

As is the case in other domains [203], support for closed-loop settings optimisation and including an accelerator physics point of view towards controls will help to improve the efficiency of the accelerator complex [204]. This will become possible with the higher computing power and data exchange capacities, more flexible analysis using big-data approaches, the introduction of machine learning, model driven approaches and an end-to-end cost/benefit sensitivity analysis.

3.11 Radiation environment

3.11.1 Introduction

Radiation levels in the collider scale with energy and, as LHC has shown, degradation of components exposed to radiation can become a show stopper. A structured

approach for radiation hardness assurance (RHA) will ensure that the electronics and materials developed perform to their design specifications after exposure to the radiation in the collider environment. Two complementary approaches are needed: the reduction of the dose to equipment by shielding and developing fault tolerant or radiation resistant electronics and equipment.

3.11.2 Reference radiation levels

Radiation to electronics (R2E) is an issue in the design of any high energy and high intensity machine [205]. Radiation effects in electronic devices can be divided into two main categories: cumulative effects and stochastic effects (Single Event Effects – SEE). Cumulative effects are proportional to the total ionising dose (TID) – the damage induced by ionising radiation, and the 1 MeV neutron-equivalent fluence which concerns displacement damage. On the other hand, SEE, which are proportional to the high energy hadron fluence (HEH, i.e. hadrons with energies >20 MeV), are due to the direct or indirect ionisation by a single particle which is able to deposit sufficient energy to disturb the operation of the device. SEE can only be defined by their probability to occur and the effect strongly depends on the device, the intensity and the kind of radiation field. An accurate specification of the radiation levels in areas critical for electronics is essential for the design of the accelerator.

Monte Carlo (MC) simulation is an indispensable tool to evaluate the impact of radiation on the machine equipment, but it relies on both a refined implementation of physics models of the particle interaction with matter and an accurate 3D-description of the region of interest. In this context, FLUKA [206,207] which is widely employed at CERN, is a well benchmarked, multi-purpose and fully integrated particle physics MC code for calculations of particle transport and interactions with matter. For a high intensity and high energy machine like the HE-LHC, typical sources of radiation are luminosity debris, direct losses on collimators and dumps and beam interactions with the residual gas in the vacuum [208].

A FLUKA model of the HE-LHC arc, for both optics solutions (18×90 and 23×90) is currently under development. Although FLUKA simulation allows a detailed study of the radiation environment, taking the infrastructure around the accelerator into acount, the order of magnitude of the radiation levels can be estimated from the measured and calculated values from LHC. Scaling with the beam energy, beam current and assuming the maximum residual gas-density design value of 1.0×10^{15} H_2/m^3 (corresponding to beam lifetime of 100 h), the annual HEH fluence and absorbed dose distribution at the locations where electronic racks are typically placed below the magnets in the arc are expected to be $\sim 4 \times 10^{10}$ cm^{-2} y^{-1} and ~ 80 Gy y^{-1} respectively. These values are about a factor 2.5 lower than FCC-hh, assuming the same residual gas-density. Such values impose serious constraints on the selection and qualification of electronic components for operation in distributed systems in the machine arc.

It is important to underline that the values reported above refer to an extreme situation in which the residual gas-density represents an upper limit which should not be exceeded. LHC experience has shown that the residual gas-density can be factors of several hundreds lower, leading to a better vacuum quality and therefore to lower radiation levels.

Finally, the residual gas-density plays an important role in the HE-LHC design because of the infrastructure, which is fixed by the current machine layout. Indeed, in the case of FCC-hh, ad-hoc shielded alcoves for electronics were designed to ensure adequate protection of all the electronic systems from the severe radiation levels expected in the arc, even for a residual gas-density of 1.0×10^{15} H_2/m^3. With regard

to HE-LHC, the existing RE alcoves need to be studied with FLUKA simulations, to verify that the shielding already available provides adequate protection and, potentially, to support civil engineering studies for the redesign of these areas.

3.11.3 Radiation hardness

Radiation hardness assurance (RHA) comprises all if the activities undertaken to ensure that the electronics and materials perform to their design specification after exposure to the HE-LHC radiation environment. Several strategies are being developed.

As is the case for the present LHC machine, the power converters, beam position and beam loss monitors (BPM and BLM) and quench protection system (QPS) have to be close to the accelerator itself. Such equipment is mainly based on commercial-off-the-shelf (COTS) components and therefore the equipment needs to be qualified for use in the radiation environment. CERN's current irradiation facilities are an essential means to independently assess the radiation hardness of electronic components, assemblies and systems in the collider environment. An analysis of the main shortcomings of CERN's facilities and possible solutions has been carried out and the main conclusions are outlined elsewhere [209]. For cumulative TID effects, facilities such as the CC60 [210] and GIF++ [211] will have to be upgraded with more powerful sources. This will allow higher doses to be reached in shorter times and it has the potential of running more users in parallel. For the assessment of the single event effects, the CHARM facility [212] can be upgraded by increasing the beam intensity and the space available for the users to make parallel and multiple testing possible. The extensive qualification programme required needs the upgrade of existing and well-known irradiation facilities, by collaboratively exploiting the expertise and test capacity worldwide.

The HE-LHC RHA strategy is founded on a full-availability approach based on: (i) remote control, moving the processing tasks away from the equipment under control and (ii) failure self-diagnosis, online hot swapping and remote handling. Therefore system designs are based on a modular approach that will allow switching to a redundant sub-system without any impact on operation. This will be particularly beneficial for transient errors, which can typically be corrected with a reset. The approach will also relax the constraints on the error qualification limits, which will be obtained through accelerated radiation testing. In the case of events which cause permanent effects such as hard SEEs (occurring stochastically) or cumulative damage, online hot-swapping will need to be complemented by the substitution of the faulty board. This procedure will need to be carefully optimised, especially for cumulative damage, where similar sub-systems exposed to similar radiation levels are expected to fail at around the same time. Remote handling and the possibility of replacement of faulty units with spares which have been stored in radiation-safe areas, is one way to mitigate the risk.

The proposed scheme will bring benefits from the use of a selected set of semiconductor components that can be used in different sub-systems. The related procurement and qualification processes can be optimised and the impact of variability in sensitivity across batches and deliveries can be reduced. In specific cases, the use of radiation-hardened solutions at component level (e.g. FPGA) can be considered in combination with the use of COTS devices.

Finally, intensive work on radiation hardening of electronics, components, materials and detectors, as it is currently happening for HL-LHC, will continue in parallel to technology scouting and early technology analysis to cope with the rapid advance of electronics development and market trends. Key technology areas for HE-LHC include, to name but a few, the development of radiation-hard, fast and

high-bandwidth communication links [213], as they allow reduction of the burden and complexity of the systems deployed in radiation areas, improved radiation performance and the accompanying miniaturisation of on-detector Application-Specific Integrated Circuits (ASICs) [213], and development of novel concepts for Ultra High Radiation Dosimetry [214].

4 Civil engineering

4.1 Requirements and considerations for upgrade of the existing infrastructure

To house the HE-LHC in the LHC tunnel, several modifications to the existing infrastructure will be required. The current infrastructure was built in two phases: initial construction for the LEP project took place from 1983 to 1989, involving the majority of the shafts and tunnels. This was followed by the LHC works, which included additional large span caverns, shafts and surface sites for the ATLAS and CMS experiments, built between 1998 and 2005. Further civil engineering activities began in 2018, at points 1 and 5, to construct new shafts and tunnels for the HL-LHC project. Figure 4.1 shows these structures, with HL-LHC-related works highlighted in blue and HE-LHC highlighted in red.

The existing tunnel, located in the Geneva basin, is 27 km long. The majority of the tunnel is located in variable sedimentary deposits, collectively known as *molasse.* These deposits comprise a complex, alternating sequence of almost horizontally bedded sandstones and marls, with a range of composite marly sandstones and sandy marls [215]. These deposits are generally impermeable and stable, and hence favourable for tunnel boring machine (TBM) excavation. However, the sector between points 3 and 4 was constructed in the Jura limestone. The Jura limestone is characterised by karst features, which include instances of chemically formed voids acting as water conduits. During the construction of sector 3–4, considerable water ingress was observed.

In order to keep as much of the underground structures as possible in the molasse, and to limit the overburden at point 4 close to the Jura, the entire ring was placed on an inclined plane with a slope of 1.4% (Fig. 4.2). Three TBMs were used for excavation in the molasse. Sector 3–4 was created using the drill-and-blast method [216].

Figure 4.3 shows a typical cross section for the tunnel constructed in molasse, which comprises a 100 mm thick primary concrete segmented lining and a 150 mm thick secondary cast in-situ lining. A waterproofing system sits between the two linings.

4.2 Lifetime of the existing tunnel infrastructure

The underground structures for LEP were designed for a lifespan of 50 years. They were completed in 1989 and will thus reach the end of their specified lifetime around 2040. Refurbishment, continuous monitoring and maintenance is therefore necessary to extend their lifetime for use with a future particle collider. Such activities have already started to meet the requirements of the HL-LHC project.

4.3 New civil engineering infrastructure

The existing infrastructure will be reused as much as possible to accommodate new equipment required for HE-LHC. All equipment from the LHC tunnel has to be
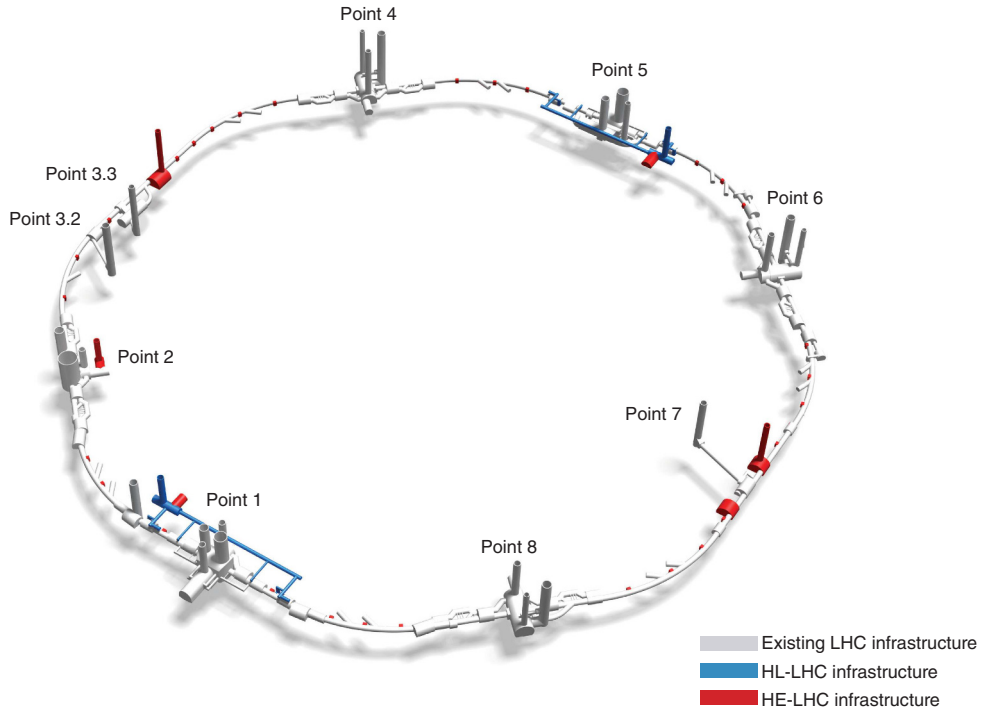
Fig. 4.1. Schematic drawing of the existing LHC underground structures including HL-LHC and HE-LHC upgrades.
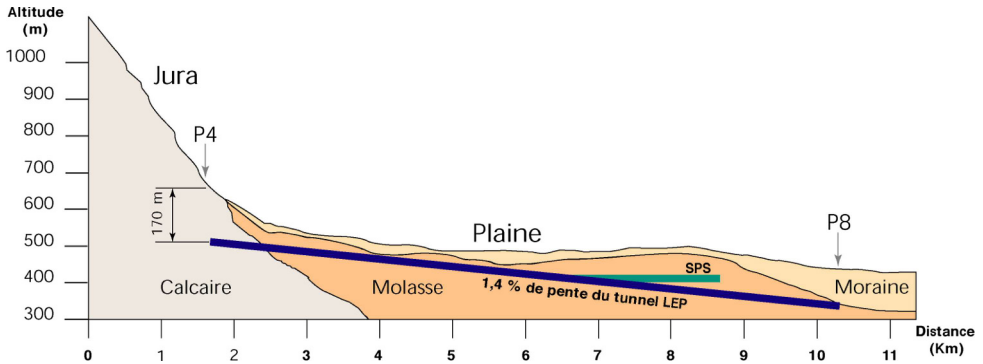
Fig. 4.2. Profile of LHC tunnel.

removed before the new particle collider can be installed. In addition, some new infrastructures will be constructed to accommodate new equipment for cryogenics, electricity and ventilation systems. Figure 5.11a shows additional cryogenic refrigeration plants required at each point.

4.3.1 Underground structures

New caverns are required for cryogenic equipment at points 3 and 7. Different options have been evaluated regarding the location of the new caverns. A new shaft is mandatory at point 3.3, since the existing shaft PZ33 is used for access of personnel
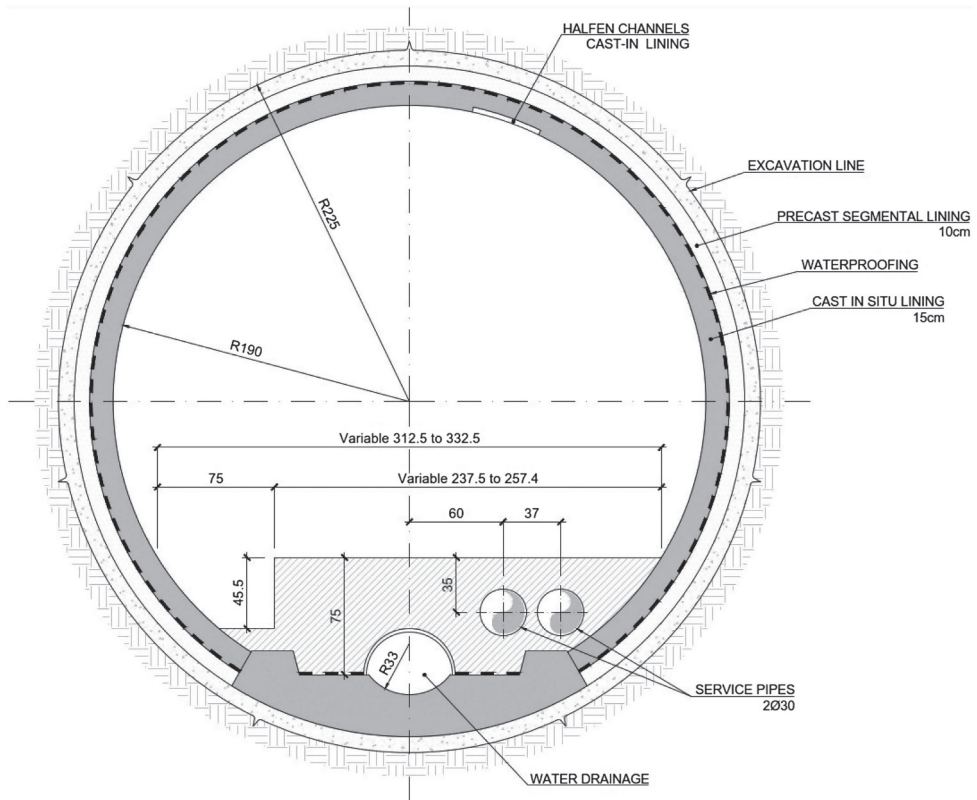
Fig. 4.3. Typical LHC tunnel cross section.

only and its diameter would not allow lowering of the 7 m long cryogenics cylinders. Figure 4.4 shows the proposed location for the access shaft and the cryogenic caverns.

At point 7, two caverns of size $10 \times 13 \times 9$ m (W $\times$ L $\times$ H) are proposed at the mid-point of the straight section, each cavern accommodating one 1.8 K refrigeration unit. A new shaft in the proximity of the UJ76 cavern would provide access for the installation of the new equipment into the underground structures (Fig. 4.5). Alternatively, the existing PM76 shaft and the connection tunnel TZ76 can be used for access, if all equipment is removed. One advantage of providing a new shaft is that it would allow cavern construction to start while the LHC machine is in operation. This is the same approach as adopted for the HL-LHC project.

A more detailed analysis remains to be performed for point 2 to confirm that the existing caverns can be used to accommodate the new equipment. If the space is not sufficient, a new cavern has to be constructed. To transport the new equipment into the tunnel at point 2, either the existing shafts, PM25 and PMI2, can be used or a new shaft needs to be created. As mentioned in Section 4.1, new caverns and shafts are being constructed at points 1 and 5 for HL-LHC, and these could be used to install the additional cryogenics equipment. New alcoves for electrical equipment are required to supply the cryogenic installations at points 3 and 7. Depending on the power consumption and the reliability required from the existing network, additional upgrades might be needed at other locations. Additional space in the underground caverns has been allocated for cooling equipment. Table 4.1 shows the dimensions of the underground structures required.
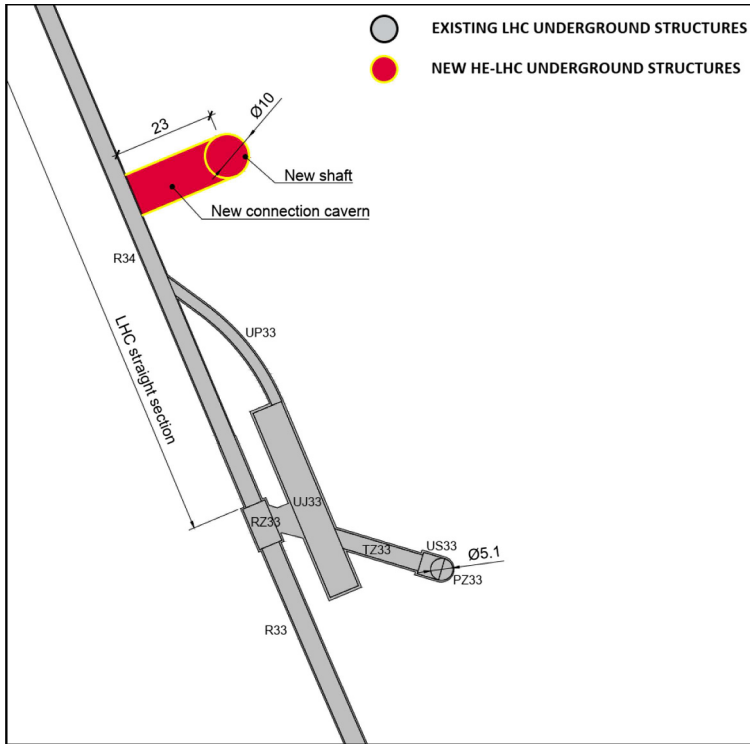
Fig. 4.4. Proposed cryogenic caverns and access shaft at point 3.3.

At some locations, parts of the tunnel lining will be broken out to facilitate the excavation of the new spaces. This activity introduces the risk of water ingress and structural damage. Temporary propping in the vicinity of the breakouts will be required. Excavating in the Jura limestone should be avoided, since the risk for water ingress is very high in this location. This affects the works required at point 3. Additional ground investigations may be necessary to precisely determine the geology in certain areas.

Figure 4.6 shows an example of such a breakout for the Brisbane Airport Link project. It is important to note that, in that project the lining was designed to be opened at a later stage which is not the case for the LHC tunnel. A thorough structural investigation is required to assess if the risks associated with creating openings in the tunnel lining is acceptable. The caverns will be created using mining techniques. The lining will then either be cast in-situ or by using shotcrete. Both options will have to be assessed during the detailed design phase.

4.3.2 Surface points

New buildings are required at each point of the LHC as listed in Table 4.2 and where possible, existing buildings will be used. Where new access shafts are needed, head shaft buildings will be added. New noise insulated buildings to accommodate cryogenic and electrical equipment are necessary at points 3 and 7. New turbo-Brayton refrigerators need to be installed in existing or new buildings at points 1.8, 2, 4, 6 and 8. A refurbishment of the existing tunnel ventilation and additional ventilation systems are necessary to provide supply and extraction units for each sector. Hence,
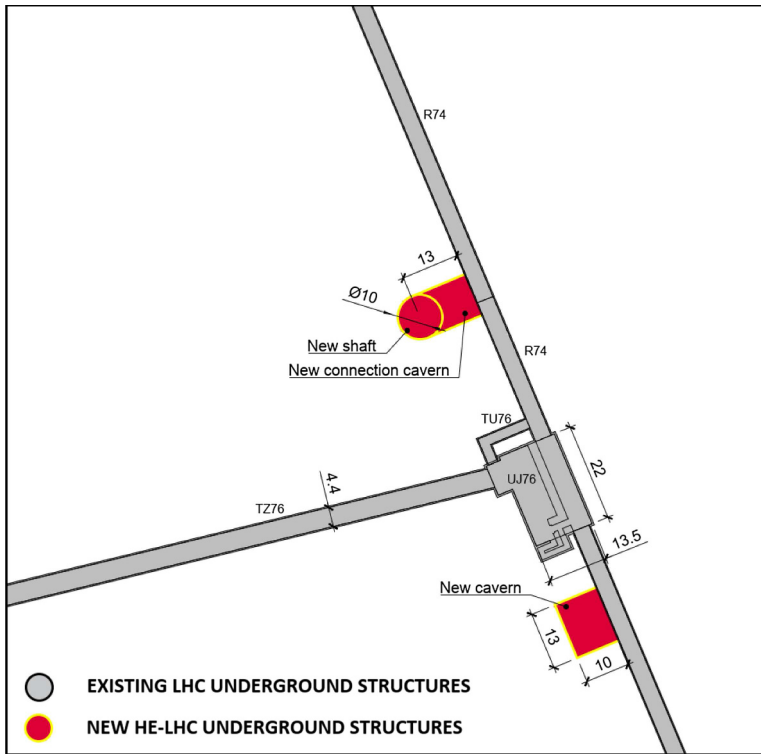
Fig. 4.5. Proposed cryogenic caverns and access shaft at point 7.

Table 4.1. List of underground structures.

Point	Structure description	Dimensions (W × L × H)
1	Cryogenic cavern	5 × 13 × 9 m
2	Cryogenic cavern	5 × 13 × 9 m
3	Cryogenic cavern	10 × 23 × 9 m
	Electrical alcove	6 × 25 × 6 m
5	Cryogenic cavern	10 × 23 × 9 m
7	Cryogenic cavern	10 × 13 × 9 m
	Cryogenic cavern	10 × 13 × 9 m
	Electrical alcove	6 × 25 × 6 m

new surface buildings are required for ventilation equipment at each point. Indicative dimensions of the proposed surface buildings are given in Table 4.2.

The existing SDI2/SMI2 building has to be replaced to accommodate a higher-capacity crane to lower the new accelerator magnets. Access to the sites is also a key constraint for the works presented above. New access roads will be required at locations where new shafts and buildings are planned.

4.4 Tunnel enlargements

Separation walls need to be installed every 548 m to create fire compartments to implement the new fire safety concept. Given the size of the magnets, it is not possible to fit the doors of these separations in the existing tunnel envelope, as shown in
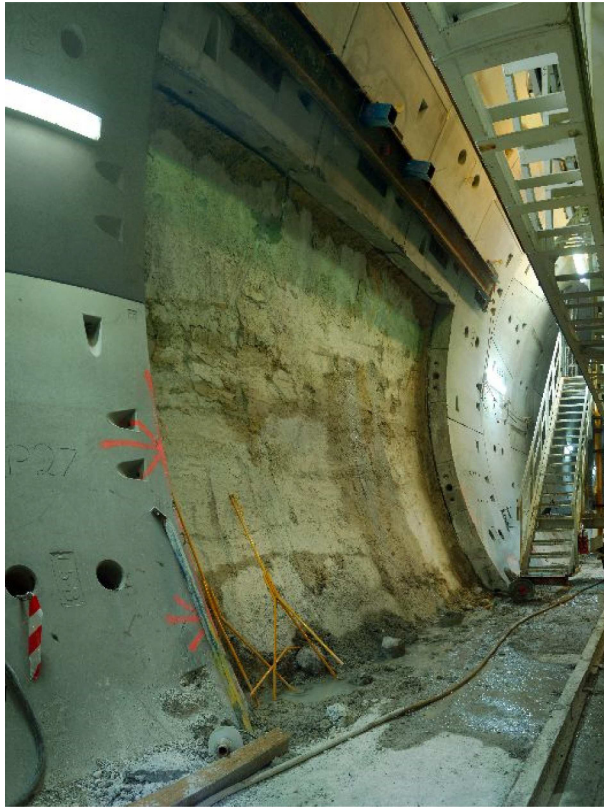
Fig. 4.6. An example of lining breakout from the Brisbane Airport Link, Australia (Arup).

Table 4.2. Exemplary list of buildings and constructions at the surface points in order to illustrate the scope of the project required to adapt the LHC infrastructures.

Point	Structure description	Structure type	Dimensions (W × L × H)
1	Cryogenic building	Concrete	$10 \times 20 \times 12$ m
	Ventilation building	Steel frame	$30 \times 30 \times 10$ m
1.8	Cryogenic building	Concrete	$9 \times 18 \times 12$ m
2	Cryogenic building	Concrete	$10 \times 20 \times 12$ m
	Cryogenic building	Concrete	$9 \times 18 \times 12$ m
	Ventilation building	Steel frame	$20 \times 25 \times 10$ m
	Shaft head building	Steel frame	$20 \times 35 \times 25$ m
3	Cryogenic building	Concrete	$16 \times 23 \times 12$ m
	Ventilation building	Steel frame	$30 \times 30 \times 10$ m
	Electrical building	Steel frame	$10 \times 20 \times 6$ m
	Shaft head building	Steel frame	$20 \times 35 \times 25$ m
4	Cryogenic building	Concrete	$12 \times 18 \times 12$ m
	Ventilation building	Steel frame	$20 \times 25 \times 10$ m
5	Cryogenic building	Concrete	$16 \times 23 \times 12$ m
	Ventilation building	Steel frame	$30 \times 30 \times 10$ m
6	Cryogenic building	Concrete	$12 \times 18 \times 12$ m
	Ventilation building	Steel frame	$20 \times 25 \times 10$ m
7	Cryogenic building	Concrete	$16 \times 23 \times 12$ m
	Ventilation building	Steel frame	$30 \times 30 \times 10$ m
	Electrical building	Steel frame	$10 \times 20 \times 6$ m
	Shaft head building	Steel frame	$20 \times 35 \times 25$ m
8	Cryogenic building	Concrete	$12 \times 18 \times 12$ m
	Ventilation building	Steel frame	$20 \times 25 \times 10$ m
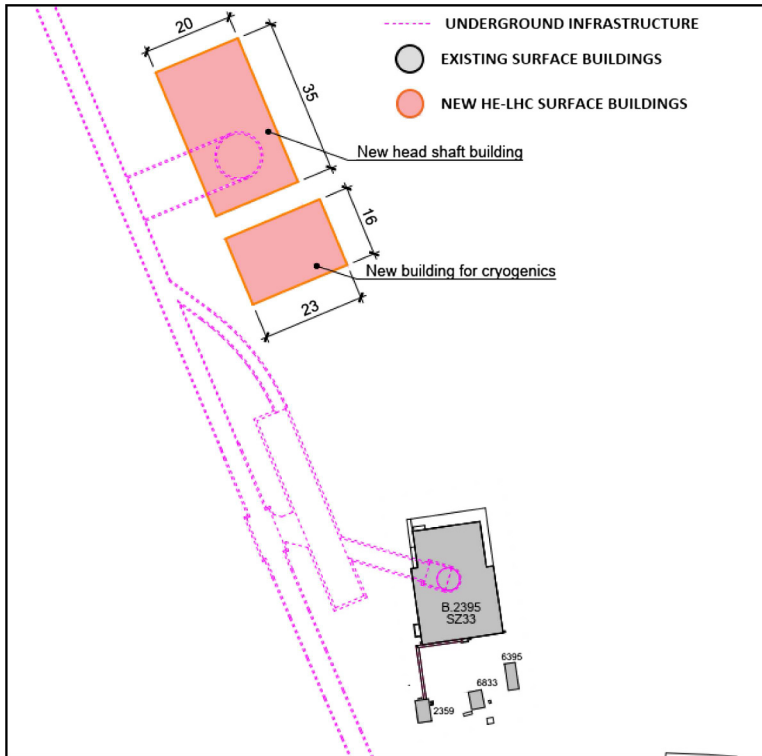
Fig. 4.7. Proposed surface buildings for cryogenics at point 3.3.

Figure 4.9. Therefore, parts of the lining must be broken out. Techniques similar to those for the cryogenic caverns, in terms of temporary support and breaking out of the concrete, will need to be used. A structural feasibility assessment has to be carried out along the entire tunnel circumference during the detailed design phase to confirm that the risks associated with such civil engineering works can be appropriately controlled. Alternatively, a different safety concept may have to be developed.

The vault height of UJ22 will have to be increased by $\sim$1 m, to allow the HE-LHC magnets to be lifted from TI 2 into the HE-LHC tunnel once the HE-LHC machine is installed (see Sect. 5.7). Parts of TI 2 may need to be locally enlarged by $\sim$30 cm to allow certain magnet groups of TI 2 to pass through. An enlargement at the beam stopper just before UJ22 is mandatory.

4.5 Sector 3–4 refurbishment

Technical challenges were encountered during the construction of sector 3–4 of the LEP tunnel, when excavating though the limestone formations of the Jura massif. Fault zones and karstic features in this region precluded the use of a full-face TBM, hence the drill-and-blast method was used for this sector. During excavation through a faulted passage in the limestone, high-pressure water inflow containing sand-silt material occurred in the invert section of the tunnel (Fig. 4.10). A large part of these inflows was treated by grouting before lining and waterproofing of the tunnel [216].

Increased hydrostatic pressure jeopardised the tunnel structural integrity after tunnel completion. One incident was reported in 1990, when the built-up water pressure behind the tunnel crown led to the failure of a small section of the concrete lining
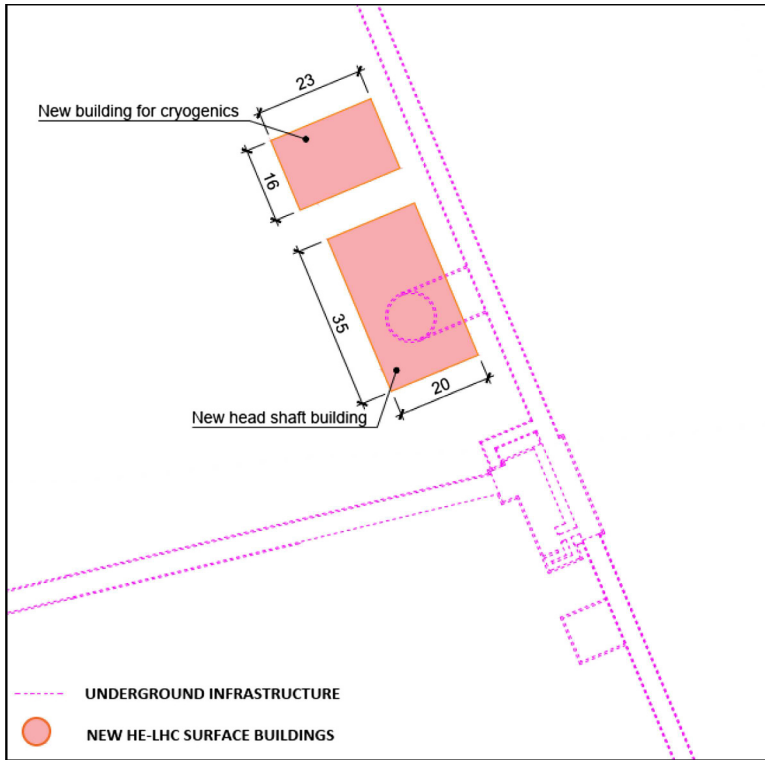
Fig. 4.8. Proposed surface buildings for cryogenics at point 7.

(Fig. 4.11). A shutdown of the LEP machine for a period of 14 days was necessary to carry out repair works. The collapse also caused damage to the LEP machine. On two other occasions in 1990 and 1993, the tunnel was flooded after drains were blocked by sand deposits [97].

Following several episodes of water inflow, external consultants were engaged to develop a solution. Their studies showed that critical areas were situated in the Thoiry limestone, more specifically between positions PM1450 and 1836 and between PM2735 and 3242.

The first proposal was the "600 m submarine". This solution foresaw heavy steel lining of the tunnel along 680 m between PM2610 and 3290 combined with local reinforcement of the tunnel in the areas where increase in hydrostatic pressure could lead to loss of structural integrity. The submarine option was eventually rejected because of the potentially high cost, impacts on the research programme and reduction of the tunnel inner diameter by 16 cm [217].

It was decided instead, to improve the existing drainage system, including the installation of a 6 inch stainless steel pipe in the tunnel. In addition, the tunnel vault was locally reinforced by fixing steel mesh panels. The cost was significantly lower compared to the submarine option. However, this solution demands a commitment to regular maintenance. Several interventions were necessary after completion of the works, to treat water ingress and repairs of the concrete [218]. A monitoring system was installed in sector 3–4, comprising manometers and pressure release valves. Further maintenance activities are planned during the LHC long shutdown 2 (LS2), including clearing of blocked drains, replacement of pressure valves and installation
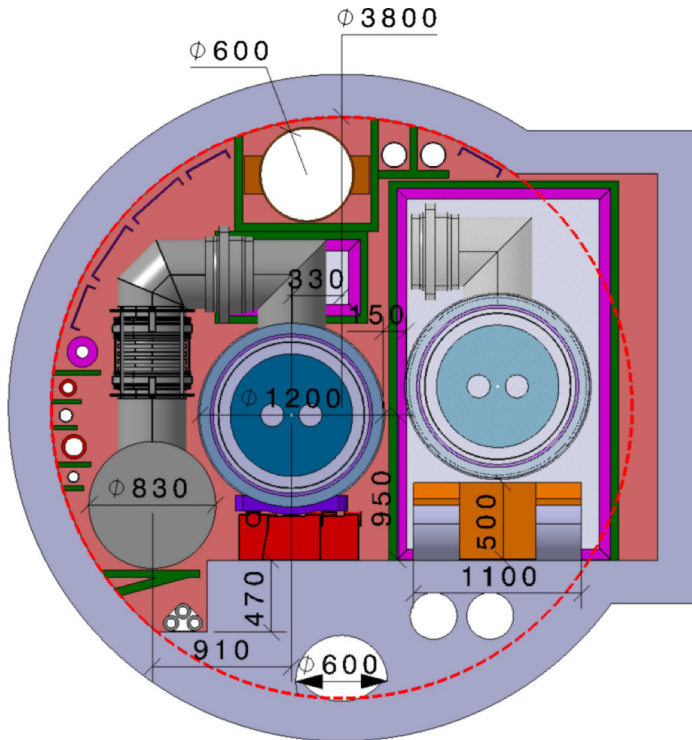
Fig. 4.9. Tunnel cross section at fire compartment separation wall.

Fig. 4.10. Water inflows during LEP tunnel construction.

Fig. 4.11. Failure of tunnel concrete lining in 1990.

of new equipment to control the water flow. Continuous maintenance is needed for sector 3–4 but a refurbishment of the sector would lead to lower maintenance costs and improve the availability of the infrastructure.

5 Technical infrastructure

5.1 Requirements and design considerations

The technical infrastructure comprises a large and diverse set of services to enable and support the operation of the collider and the experiments. These include the supply of electrical energy and cryogens, the air and water cooling systems, facilities to transport people and material, the geodetic network, survey and alignment, control of accelerator equipment, data acquisition, computing and networking, as well as access control and other safety related functions.

As is customary for other facilities at CERN, the HE-LHC will make as much use of the existing chain of pre-accelerators as possible. Some of the infrastructure, like computer networks, will integrate with the existing infrastructure; others, like the additional electrical infrastructure, cryogenic refrigeration and cooling, will extend existing facilities.

A large research infrastructure which crosses borders in a densely populated area like the Geneva basin requires that a wide range of conditions and regulations are respected to ensure environmental and socio-cultural compatibility. The whole HE-LHC, including its technical infrastructure, must be designed and built for safe, high-performance operation, with high reliability and availability in mind. The equipment must generally be energy- and cost-effective. Future-oriented, yet technically solid approaches must be chosen to ensure enduring high performance and affordable operation.

5.2 Piped utilities

5.2.1 Introduction

The piping systems are for the various water systems for the machine and its infrastructure. Accelerator and detector equipment such as electronic racks, cryogenics plants and conventional magnets will require industrial and demineralised water. Chilled water will be needed for the air handling units of the ventilation systems. Raw water will be used in primary cooling circuits and for fire fighting purposes. Drinking water will be needed for sanitary purposes as well as for the make-up of raw water cooling circuits. There will also be a drainage network for the waste water which comprises the rejected and drained water from the surface facilities and the underground areas. The other main piped utility is for compressed air which will be used both underground and on the surface.

In most cases, the existing systems for piped utilities will be adapted to the HE-LHC requirements; no major structural change is planned. Present technical choices ensure that there will be satisfactory operational conditions for the HE-LHC. Most of the work will consist of extending the distribution circuits as required and replacing existing cooling equipment with new equipment dimensioned to cope with the HE-LHC working parameters.

5.2.2 Water cooling plants

The cooling plants will use raw water to remove most of the heat generated by the accelerator equipment, the detectors and in the technical areas. The basic layout of the cooling systems is inherited from LHC. The accelerator and its related equipment are cooled by cooling towers located at the even points and points 1 and 5. Additional cooling towers at points 1 and 5, separate from those mentioned above, are dedicated to the cooling of experiments and associated equipment. At point 1.8, the cooling towers are mainly for the test areas on the surface; a separate circuit is dedicated to cryogenic equipment underground.
The water cooling plant will consist of:

 – A primary circuit, using raw industrial water and cooled by means of open wet cooling towers. Some equipment, in particular cryogenic systems, will be directly cooled by the primary circuit.
 – A secondary circuit, connected via a heat exchanger to the primary system, which in most cases will use demineralised water in a closed loop.

Distribution circuits will be grouped according to the typology of the equipment to be cooled and the equipment pressure rates. As for the LHC, given the height difference between surface and underground premises of about 100 m, cooling stations in the underground caverns will allow the separation via heat exchangers of the circuits coming from the surface from the distribution circuits in the underground. Wherever possible, this split will correspond to the separation between the primary and secondary circuit but it will also be applied for other circuits such as those of the underground cryogenic equipment. The decoupling of the surface from the underground circuit will allow safer operation of the underground circuits. For safety reasons, underground cooling stations will not be accessible during accelerator running; part of the operational activities will be performed remotely using the control system.

A cooling area in the underground caverns at points 1, 2, 4, 5, 6 and 8 will house the secondary circuit stations which cool the adjacent sectors as well as equipment

such as the cryogenics and the experiment. The secondary circuit in each sector will also cool the air handling units in the alcoves.

Primary circuits will use raw industrial water with a make-up from drinking water to compensate for evaporation, losses and blow-down. Continuous water treatment against legionellae, scaling and proliferation of algae will also be included. The drinking water make-up is provided from Lake Geneva via a pipeline embedded in the concrete floor of the tunnel.

Secondary circuits will use demineralised water with a maximum conductivity of $0.5\,\mu S/cm$ in a closed loop. A set of demineralisation cartridges will be installed in each circuit to control the conductivity. The demineralised water will be produced by the central station on the Meyrin site and distributed to all points for refill through a pipe in the LHC tunnel.

To ensure continuous operation if one plant stops, the level of redundancy of the primary and secondary circuits is set at an $(N + 1)$ level for pumps, chillers and cooling towers. No redundancy is needed for plate heat exchangers, power or control cubicles. The safe power supply is currently only planned for systems related to safety. No equipment needs continuous cooling to prevent damage. Some cooling towers with a lower capacity will be installed to backup the main towers in order to allow essential cryogenic equipment to be kept at low temperature during mandatory stops for maintenance and cleaning.

Point 1 will include a plant to concentrate the chemicals in the rejected water and to recycle most of it. This will allow the amount of make-up water to be reduced, compared to today, by about 50% and the rejected volume by more than 70%.

5.2.3 Operational parameters

The design parameters for the cooling plants are:

– primary circuit: 40°C at the inlet of the cooling towers and 25°C at their outlet;
– secondary circuit: 42°C at the inlet of the heat exchanger and 27°C at its outlet.

The temperature difference between inlet and outlet is 15 K with a tolerance of about 0.5 K. Tables 5.1 and 5.2 list the total power and the nominal diameter for the circuits in the underground area and at the surface of each point, respectively. The chilled water load is not taken into account in the total power needed in points 3 and 7, since the chillers will be air cooled.

With regard to the flow rates needed in the cooling circuits, it is not planned to replace the existing pipework in the tunnel.

5.2.4 Chilled water

The cooling for ventilation plants (dehumidification or air cooling) will require the installation of chilled water production stations at each surface point and some distribution circuits for the air handling units on the surface and in the underground areas. Additional cooling power might be needed by the experiments. No chilled water is needed in the machine sectors.

For ventilation purposes, the chilled water will be produced at a temperature of 6°C and return at 12°C. The ventilation of HL-LHC areas will be an exception as it will use water between 12°C and 18°C. The chillers will be water cooled and connected to the cooling towers at each point, with the exception of points 3 and 7 where they will be air cooled since no cooling towers are planned.

The redundancy level for the cooling circuits ensures continuous operation in case of a breakdown of one element (chiller or distribution pump). In the case of a general

Table 5.1. Cooling power and pipe diameter for circuits in the HE-LHC underground areas.

Point		Cryogenics	Experiment	RF	Tunnel left	Tunnel right	TI	Total underground
1	P (MW)	0.1	1	1.6				**2.7**
	ND (mm)	50	100	125				**150**
1.8	P (MW)	0.4						**0.4**
	ND (mm)	80						**80**
2	P (MW)	0.4	6.9		4.4	4.9	2.2	**18.8**
	ND (mm)	80	250		250	250	150	**400**
3	P (MW)	0.06						**0.06**
	ND (mm)	25						**25**
4	P (MW)	0.8		20	3.6	3.9		**28.3**
	ND (mm)	100		2*350	200	200		**500**
5	P (MW)	0.1	1	1.6				**2.7**
	ND (mm)	50	100	125				**150**
6	P (MW)	0.8			4.6	4.6		**10**
	ND (mm)	100			250	250		**300**
7	P (MW)	0.06						**0.06**
	ND (mm)	25						**25**
8	P (MW)	0.8	5		4.6	4.3	3.5	**18.2**
	ND (mm)	100	200		250	250	200	**450**

Notes. "Tunnel left" designates the counter-clock-wise adjacent machine tunnel sector; "Tunnel right" the clock-wise adjacent machine tunnel sector.

Table 5.2. Cooling power and pipe diameter for circuits at HE-LHC surface sites.

Point		Cryo-genics	Experiment	Power Converters	Gen. Services	Chilled Water	Total Underground	Total Point
1	P (MW)	5.6	4	1.5	1	10.5	2.7	**25.4**
	ND (mm)	250	200	125	100	500	150	**500**
1.8	P (MW)	5.8			7.9		0.4	**14.1**
	ND (mm)	250			300		80	**350**
2	P (MW)	6.3	0.46	1.5	1	9.4	18.8	**37**
	ND (mm)	250	80	125	100	450	400	**500**
3	P (MW)	0.9		1.5	0.5	(0.6)	0.06	**3**
	ND (mm)	100		125	80	125	25	**200**
4	P (MW)	12		1.5	0.5	2.8	28.3	**45**
	ND (mm)	300		125	80	250	500	**600**
5	P (MW)	6.1	4	1.5	1	10.5	2.7	**25.9**
	ND (mm)	250	200	125	100	500	150	**500**
6	P (MW)	12		1.5	0.5	2.8	10	**26.7**
	ND (mm)	300		125	80	250	300	**500**
7	P (MW)	0.9		1.5	0.5	(0.9)	0.06	**3**
	ND (mm)	100		125	80	150	25	**200**
8	P (MW)	12	0.8	1.5	1	4.7	18.2	**38.2**
	ND (mm)	300	100	125	100	350	450	**550**

Notes. "Total Underground" is identical to the last column of Table 5.1.

power failure, a buffer tank in each production circuit will ensure sufficient autonomy of part of the plant. The distribution pumps will therefore be connected to the secure electrical network.

Table 5.3 presents the total power and the main characteristics of the chilled water circuits at each point.

5.2.5 Drinking water

Drinking water will be used for human consumption only. In all LHC points it is provided by local water suppliers and only feeds sanitary premises.

Table 5.3. Main characteristics of chilled water circuits.

Point	Cooling power (kW)	Flow rate (m³/h)	Number of chillers	Cooling power/ chiller (kW)
1	7900	1134	5	2000
2	7100	1019	5	2000
3	450	65	2	450
4	2100	301	3	1000
5	7900	1134	5	2000
6	2100	301	3	1000
7	700	100	2	700
8	3500	502	3	2000

5.2.6 Raw water

Raw water is used for the make-up of cooling towers. Its quality is similar to that of drinking water. However, since it is not certified, it cannot be used for human consumption. It circulates in a non-drinking water circuit. The raw water is pumped by a dedicated pumping station located in point 1 and supplied to the various points through two half-loops placed in the concrete floor slab of the tunnel. The half-loops are connected by means of a valve between point 4 and point 5 in order to allow supply from two directions. Valves allow isolation part of the network without affecting the availability of water in the remaining part. Dedicated pumps in the underground caverns at each point pump the water to the surface.

5.2.7 Fire fighting network

The existing fire fighting network in all LHC points is fed by the raw water half-loops with a dedicated branch in the underground caverns of each point. At present, the underground service and experiment caverns are equipped with fire hoses as well as the part of the tunnel close to each point. No fire fighting pipework exists in the middle of each sector. If it is needed for HE-LHC, the existing pipework will be extended accordingly.

Surface premises will be protected by a hydrant network and by dedicated water hoses inside the buildings where necessary. Most of the surface hydrants are fed by the raw water circuit. One of them is fed by the local water network in order to ensure a minimum availability if the raw water loop fails. An additional volume of water is available from the cooling towers basins, where they exist. The fire brigade can connect flexible hoses to the network via Storz connections.

If the water pumping station for LHC stops, the fire fighting requirements will be met by the drinking water station dedicated to the Meyrin and Prevessin sites acting as a backup. All stations are on the secure electrical network which mitigates power supply failures.

5.2.8 Reject water

Two separate pump systems to lift sewage are installed underground at each point. They are connected to the local drainage network of the point. Retention basins are located in points 7 and 8 to separate natural hydrocarbons which have infiltrated the tunnel before release into the local network. The clear water reject network, which also takes the blow-down from the cooling towers, is composed of two half-loops, parallel to the raw water ones, embedded in the concrete floor of the tunnel. Water is pumped to the surface of point 1 and then it is released in the local clear water

drainage. In order to decrease the volume of discharged water, a treatment plant will be specifically implemented at point 1 for all rejected water; the residue will then be discharged in the sewage. All underground equipment (tunnel and caverns) must be redundant in order to avoid affecting operation if there is a breakdown. Alarms for "high level" and "level too high" will be implemented in all basins.

In sector 3–4, a continuous water inflow, mixed with sand from an underground water conduit made the installation of a dedicated system in point 3.2 of LHC necessary. A pit is equipped with a set of pumps to continuously lift the mix of sand and water to the surface. The pit is divided into two separate volumes in order to allow maintenance in one of them without stopping the evacuation of water. The redundancy level of the pumps in each volume of the pit is $3 \times N$ and the power can be provided by 3 different sources to avoid any stop. A settling basin on the surface is used to separate water from the sand before releasing it into the nearby stream. The main parameters (e.g. temperature, pH) of the rejected water are monitored before release.

5.2.9 Compressed air

The compressed air for all equipment and actuators will be provided by compressed air stations located in the surface and underground areas at each point. It is planned to have a level of redundancy of $N + 1$ to ensure the reliability and maintainability of the plant.

5.3 Heating, ventilation, air condition, cooling

5.3.1 Overall design concept

The installations have to provide fresh air for personnel working within the facilities as well as heating for the working environment. At the same time, the ambient temperature has to be suitable for the accelerator equipment. It is important that the air supplied has been dehumidified in order to prevent condensation on equipment and structures. In addition to being able to purge the air in the tunnel before access is allowed, the extraction systems have to be capable of removing smoke and gases. The extracted volumes have to be filtered before release.

5.3.2 Interior conditions

The indoor conditions to be maintained by the ventilation system are the following:

– Tunnels (with maximum heat load): max 25°C;
– Experiment caverns: 18/30°C – from floor to ceiling;
– Surface buildings with controlled temperature: 18°C during winter, 25°C during summer.

The values for surface buildings are mean values at heights where people and equipment are expected.

The relative humidity does not need to be regulated except for some specific areas which might require it (Faraday cage, clean rooms or other laboratories). If needed, such systems will be designed at a later stage. The dew point will be kept below 12°C to avoid condensation. A specific treatment is required for sector 3–4; details are provided below.

The outdoor conditions for the Geneva region which were used to specify the air handling equipment are 32°C for dry bulb temperature and 40% for relative humidity during summer and −12°C and 90% during winter.

As a general principle, a free cooling and air recycling approach will be adopted in order to reduce the electrical consumption, unlike what is presently implemented in the LHC (the term "free cooling" refers to the use of outside air at ambient temperature to cool equipment or areas, instead of using artificial air cooling).

5.3.3 Ventilation of underground areas

The LHC complex has separate ventilation systems according to their function, the area concerned and the operational needs of the area. More generally, the main areas are:

- the LHC tunnel;
- the safe areas around the lifts;
- the LHC service tunnel (UAs);
- the LHC experimental area:
- the experimental caverns (UXs);
- the service caverns (USs).

The ventilation systems for the LHC tunnel and ancillary premises are independent and separate from the ventilation systems for the experiment areas. This makes the management of the pressure cascade between tunnel and caverns easier. Other underground facilities such as RE alcoves, UW, RR and dump areas are equipped with air cooling units to remove the heat load locally.

The underground areas are generally ventilated by air handling units located on the surface, which are therefore accessible at all times. It is planned to have redundant units (level $N + 1$) everywhere to avoid affecting accelerator operation if there is a breakdown. One of the two units dedicated to air extraction will not be equipped with filters since these units will be used to extract smoke, which could clog the filters. All systems related to safety will be powered by the secure electrical network.

5.3.4 Machine tunnel

The existing layout for the ventilation of the accelerator tunnel will be modified to improve the safety in case of a helium leak or fire. Air is currently supplied to each sector from the even points and extracted at the odd points. The HE-LHC will have supply and extraction units dedicated to each sector installed at each point; this will allow air to be recycled from a sector to the adjacent one (Fig. 5.1). In addition, unlike the current situation, the tunnel will be split into fire sectors by fireproof walls and doors in order to handle the propagation of smoke or helium in a better way. During normal operation, the doors will be kept open and air can flow from one extremity of the sector to the next (Fig. 5.2). In case of an alarm, the doors of the compartments concerned will automatically close and air will be supplied to each side of the compartment by the air handling units located at both points (Fig. 5.3).

As mentioned before, the ventilation of sector 3–4 is different, since the humidity level is extremely high due to water infiltration from an underground conduit. In order to avoid condensation and consequent corrosion in the tunnel in this area, the air supplied is dehumified at a wet bulb temperature of −20°C by a de-humidification wheel located in point 4.
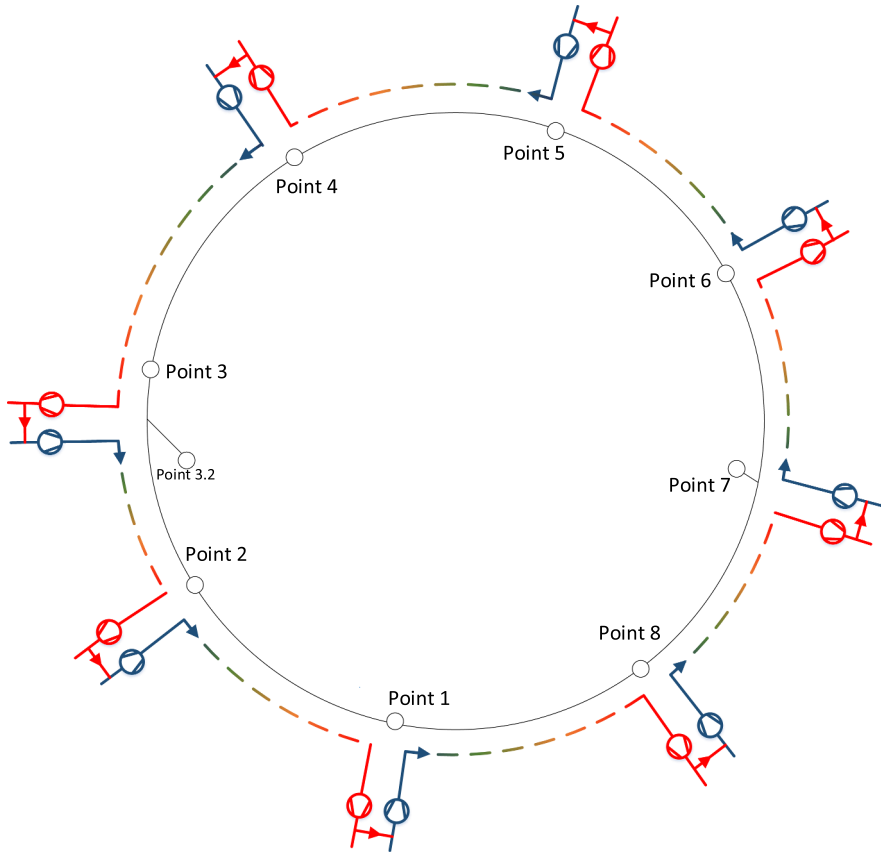
Fig. 5.1. Operation of the ventilation in the machine tunnel.
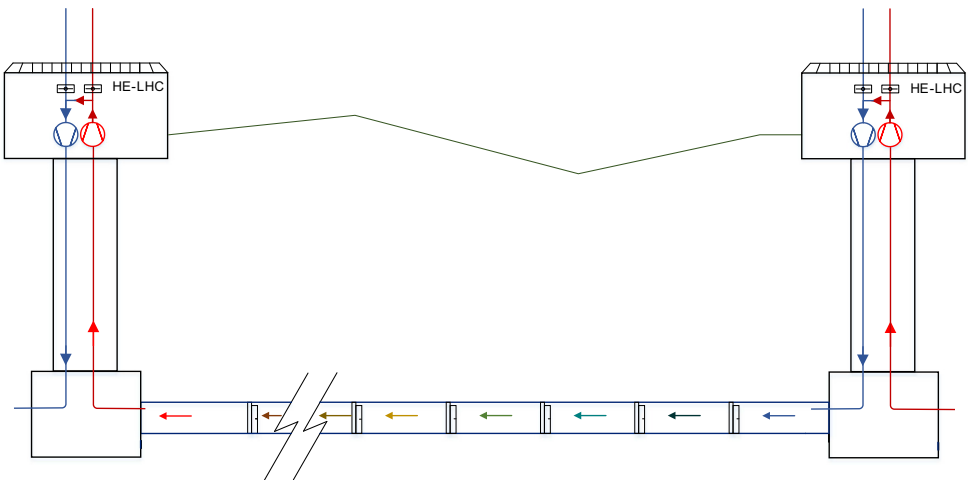
Fig. 5.2. Operation of the ventilation elements in one sector of the machine tunnel during normal operation.
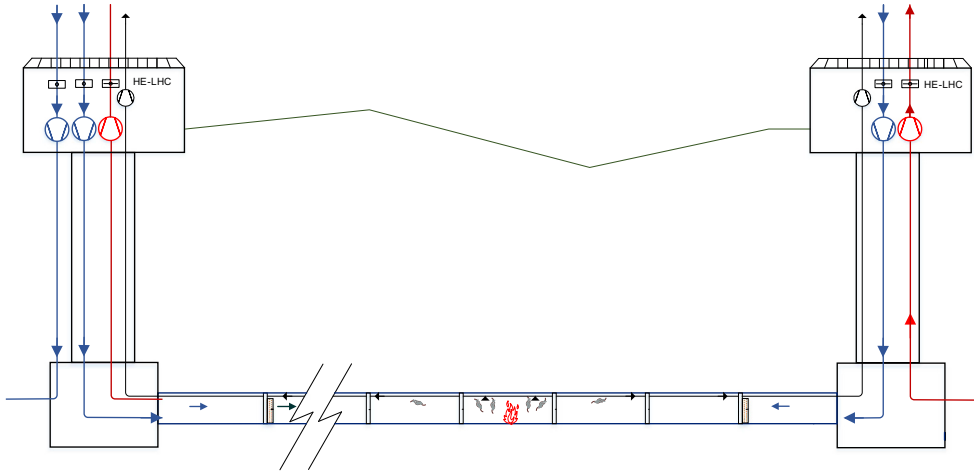
Fig. 5.3. Operation of the ventilation elements in one sector of the machine tunnel in an emergency situation (in this case a fire).

Table 5.4. Operating modes and conditions for ventilation systems.

Mode	Conditions
Run	No access, accelerators running and equipment powered, full air recycling
Shutdown	Open access, accelerator stopped, maintenance interventions, fresh air/partial recycling
Purge	Where needed, before allowing access to personnel, accelerator stopped fresh air.

5.3.5 Experiment caverns

For the ventilation of the experiment caverns, the air is blown in through diffusers at floor level (or the different floor levels) and extracted through one or more ducts located on the ceiling. Dedicated gas extraction systems will be installed where needed.

5.3.6 Other areas

Local air handling units will be added in areas housing equipment with particularly high heat dissipation. These units will be fitted with coils cooled by chilled water produced on the surface.

5.3.7 Operating modes

It is planned to have different modes for the ventilation systems depending on the machine operating conditions; these are presented in Table 5.4. All motors for ventilators will be equipped with variable speed drives in order to adjust the flow rates, to adapt the working conditions to the operational needs and to achieve the dynamic confinement between adjacent areas, where requested.

5.3.8 Working parameters

Table 5.5 shows the main ventilation parameters of an HE-LHC tunnel sector. The parameters of the ventilation plants for the underground points are presented in

Table 5.5. Working parameters for the ventilation of one machine tunnel sector.

Parameter	Flow rate (m³/h)	Air speed (m/s)
Air flow in run and shutdown modes	18 000	0.7–1
Air flow in purge mode	64 000	2–3

Table 5.6. Working parameters of air handling units for underground areas.

Underground area	Nominal flow rate (m³/h)	Nominal duct diameter (mm)	Air recycling
Point 1 Experiment cavern	30 000	1450	Yes
Point 2 Experiment cavern	45 000	1500	Not at present
Point 4 Cavern	45 000	1500	Not at present
Point 5 Experiment cavern	22 500	1400	Yes
Point 6 Cavern	45 000	1500	Not at present
Point 8 Experiment cavern	22 500	1500	Not at present
Shaft and safe area pressurisation (PM, PX)	8000–12 000	600–700	No
Fresh air to service caverns at accelerator points (US, UL and UA)	22 500	900	No

Table 5.6. In areas where a supply and an extraction system are installed, the air can be recycled according to the operating mode.

The level of filtering of the exhaust air before its release to the atmosphere will be mainly determined by the radiation protection requirements.

5.3.9 Ventilation of surface buildings

Each surface building will be ventilated by a dedicated air handling unit. Where accelerator equipment is installed, the ventilation system will remove the heat load. In all the other industrial halls, the ventilation system will ensure air renewal and heating during the cold season. Where the building size requires, it is planned to have several units in the same building, each of them taking care of a part of the building.

At present, no redundant units are installed in the LHC buildings; should this be needed, redundancy can easily be implemented. All surface buildings will be equipped with a mechanical system on the roof to extract smoke, designed and certified for operation at 400°C for a minimum period of 2 h.

For all new buildings, free cooling will be available whereas, for the existing ones, a financial evaluation will be made of whether or not to modify the present systems to allow free cooling.

5.3.10 Safety

In general, smoke extraction exists in all facilities where there is a risk due to fire loads or where it is necessary to ensure the safety of personnel. If there is a fire, in addition to the automatic actions, the fire brigade will be able to manually switch off or reconfigure the ventilation system.

All supply air handling units are equipped with smoke detection sensors downstream of the ventilator in order to avoid injection of smoke into underground areas.

The concrete module for the lift and staircase in the shafts is kept over-pressure with respect to the surrounding underground areas and will therefore be used as a safe area in emergencies.

In compliance with safety norms, a pressure cascade exists to prevent the passage of activated air from areas with higher levels of activation to areas with lower levels. Therefore the machine tunnel is at a lower pressure with respect to the experiment caverns and adjacent areas. Volumes with higher activation risk are separated from less activated areas by airlocks kept pressurised by fans installed in the less activated areas.

Exhaust air ducts will have branches to connect air monitoring equipment for radiation monitoring of the air before its release into the atmosphere.

All ventilation systems related to safety of personnel or equipment will be powered from the secure electrical network.

5.4 Electricity distribution

5.4.1 Conceptual layout

The concept for the design of the HE-LHC electrical network is driven by four factors:

- The existing electrical infrastructure that is used to supply the LHC and its extension for HL-LHC;
- The estimated electrical power requirements of HE-LHC (Tab. 9.1 in Sect. 9.2);
- The location and type of equipment to be supplied;
- The expected level of electrical network availability and operability.

The electrical network is composed of a transmission and a distribution level. The transmission level transmits the power from one source to all 8 of the HE-LHC points at voltages of 400 kV and 66 kV. The distribution level distributes the power from the transmission level to the end users at medium and low voltage levels comprised between 18 kV and 400 V.

5.4.2 Source of electrical energy

The estimated 213 MW electrical power requirement will be supplied from the European grid through the existing 400 kV connection to the Bois Tollot electrical substation. The source is self-redundant and, according to French network provider RTE (Reseau Transport Electricité), is capable of providing 200 MW on top of its current load by the year 2035 (the present maximum daily load by CERN on source I is 191 MW).

5.4.3 Transmission network topology

The transmission network includes:

- The 400 kV transmission line connecting the 400 kV source on the European grid to the incoming substation;
- The existing 400/66 kV transformer substation on the CERN Prévessin campus;
- Six existing 66 kV transmission lines connecting the transformer substation radially to six points;
- A new 66 kV transmission ring composed of 8 segments connecting each of the 8 points to its two neighbouring points.
- A 66/18 kV transformer substation at each point;
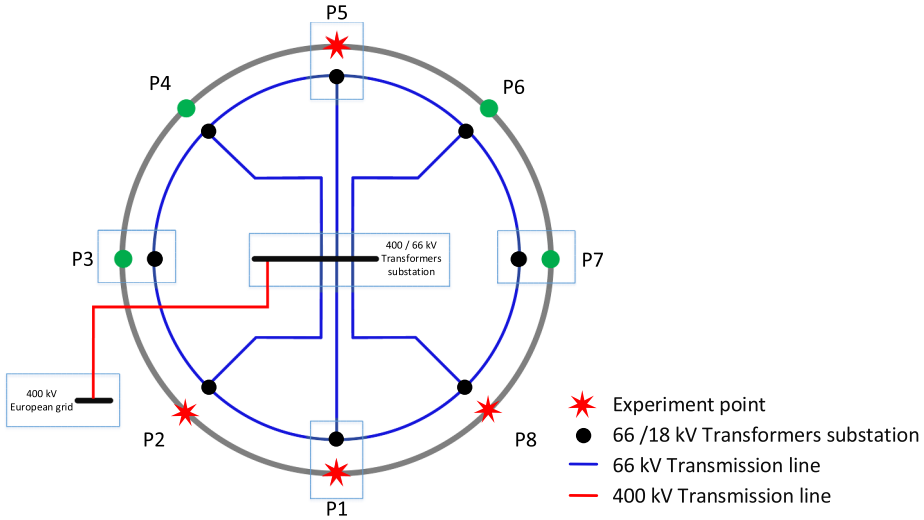
Fig. 5.4. Schematic representation of the transmission network.
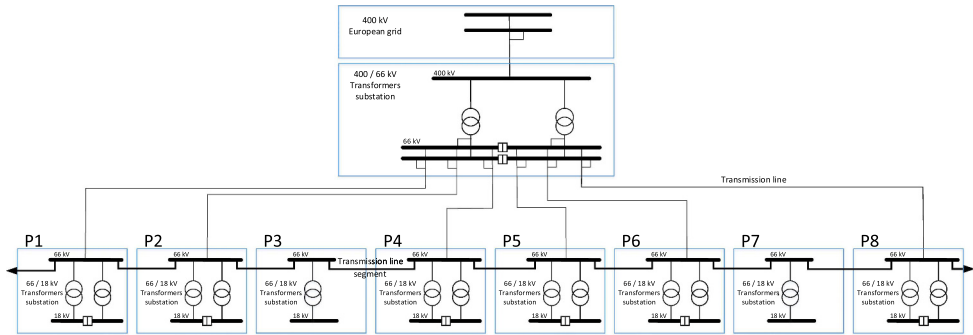
Fig. 5.5. Simplified scheme of the 400 kV incoming substation and the connection to the step-down transformers.

Figure 5.4 shows a schematic view of the transmission network.

Analysing the power requirements of the machine for each point and nominal operation with beam, the highest power demands occur in 6 points (1, 2, 4, 5, 6 and 8) where the cryogenic and RF systems are located, each requiring between 12 and 31 MW. These points are radially connected to the main substation. The remaining points 3 and 7 only host cryogenic systems requiring 7 MW each. They are powered through one of the adjacent points via the transmission line segments.

This transmission network layout provides full redundancy, enhanced availability and operability in case of a fault on one of the transmission line segments. A redundant scheme of 400/66 kV voltage step-down transformers supplies the transmission line segments connecting two adjacent points. In points 1, 2, 4, 6 and 8 a substation will receive the incoming 66 kV transmission line segments. In all points 66/18 kV step-down transformers supply the distribution networks level. Redundant step-down transformers and switchgear provide the required level of availability and maintainability. Figure 5.5 shows a simplified scheme of the 400 kV incoming substation and the connection to a point with the corresponding step-down transformers.
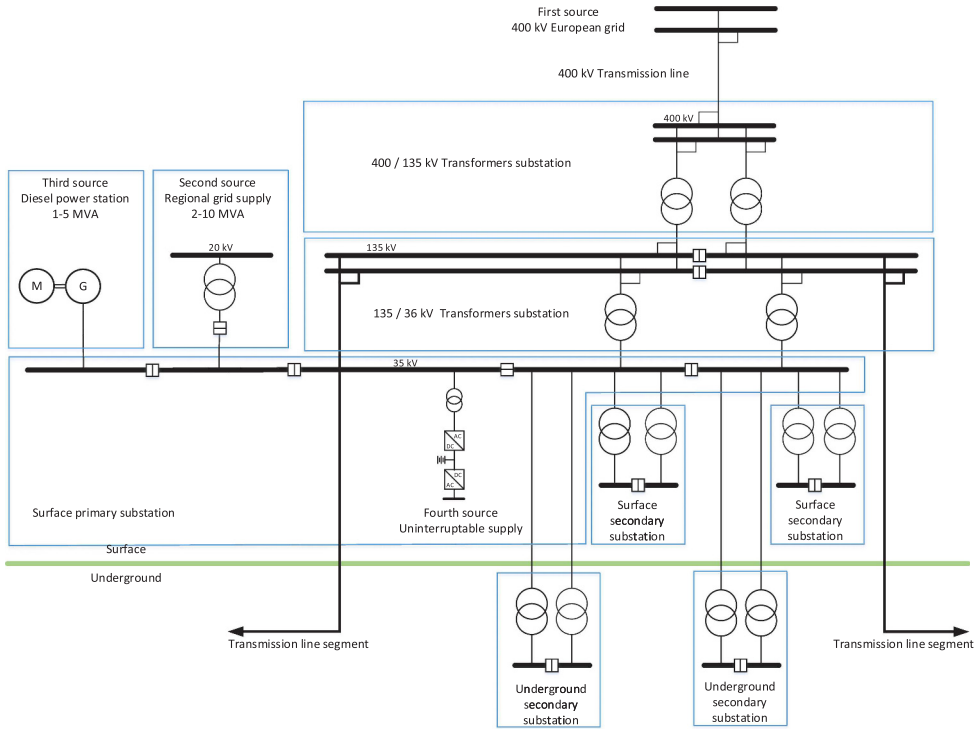
Fig. 5.6. Diagram of the baseline distribution network of one HE-LHC point including the alternative power sources.

5.4.4 Distribution network topology

The distribution networks connect the transmission network to the surface and underground equipment and systems. During normal operation, the transmission network supplies the distribution network. Alternative sources of supply are needed to meet the required level of network availability and to cope with a degraded scenario such as a disruption of the general or local power supply. Therefore, the distribution network includes a second supply that already exists, rated between 2 and 4 MVA, fed from a regional grid node, a third source of supply rated 1–3 MVA from local, diesel-powered generator power stations and a fourth source which provides uninterruptable power. Figure 5.6 shows the single line diagram of the baseline distribution network of one point including the alternative power sources.

The distribution network is composed of a primary indoor substation comprising five bus bars located on the surface. The incoming feeders are the two redundant 66/18 kV transformers supplied from the transmission network, the second supply from a regional source and the third supply from the local diesel power station. The outgoing feeders supply secondary substations. These are located either on the surface or underground, near the load. The operating voltage of the distribution network is 18 kV corresponding to the current operating voltage of the LHC. This voltage is used for the power distribution over distances greater than 750 m. Voltage step-down transformers feed end users from the secondary substations over a maximum cable length of 750 m. End users are supplied from the secondary substations at voltage levels between 400 V for wall plug equipment and 3.3 kV for high power motors for cooling, ventilation and cryogenic systems.
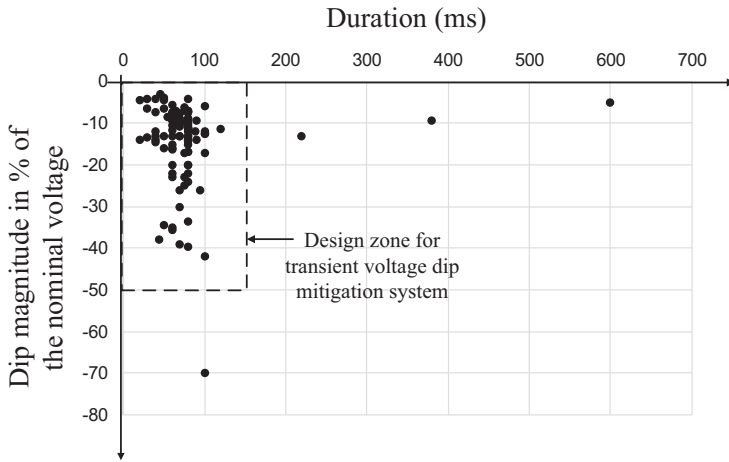
Fig. 5.7. Typical distribution of transient voltage dips recorded within the existing CERN network (collected between 2011 and 2017); the design zone covers most of the transient voltage dips, which are within 0–150 ms and 0–50% magnitude.

5.4.5 Power quality and transient voltage dip mitigation

The main issues concerning power quality are voltage stabilisation, harmonic filtering and reactive power compensation as well as the mitigation of transient voltage dips. Transient voltage dips as shown in Figure 5.7, which are typically caused by lightning strikes on the 400 kV network overhead lines, often cause undesired stops of CERN's accelerators. The powering system design must include mitigation measures against these.

The following mitigation measures are being studied:

– Dynamic Voltage Restorer (DVR) technology: the voltage will be restored by dynamic series injection of the phase voltage between the distribution network and the loads. An integrated energy storage system provides the required energy to restore the load voltage during transient voltage dips (Fig. 5.8a).
– High-Voltage DC (HVDC) back-to-back link: HVDC is a well-established technology for long distance transmission of large powers and for decoupling different high voltage networks. Combined with energy storage, an HVDC system provides performance similar to a very large uninterruptable power supply (UPS). Such a system would prevent transient voltage dips in the 400 kV transmission network from entering the collider network. In addition it would allow the reactive power (Fig. 5.8b) to be controlled.
– Static Synchronous Compensator (STATCOM): this technology is already used for reactive and active power compensation. STATCOM would fully restore the load voltage during transient voltage dips by dynamic shunt (parallel) injection, combined with an integrated energy storage system (Fig. 5.8c).
– Motor-Generator Set: such a system would decouple the network from the load. During transient voltage dips, the load voltage is restored by using the energy stored in a rotating mass (Fig. 5.8d).
– Medium-Voltage DC (MVDC) distribution network: the principle of this approach is the distribution of power using DC. In combination with energy storage, this technology mitigates transient voltage dips, eliminates the reactive power, reduces the distribution losses and, compared to AC distribution, permits a larger spacing between electrical substations in the tunnel. This promising technology is still in
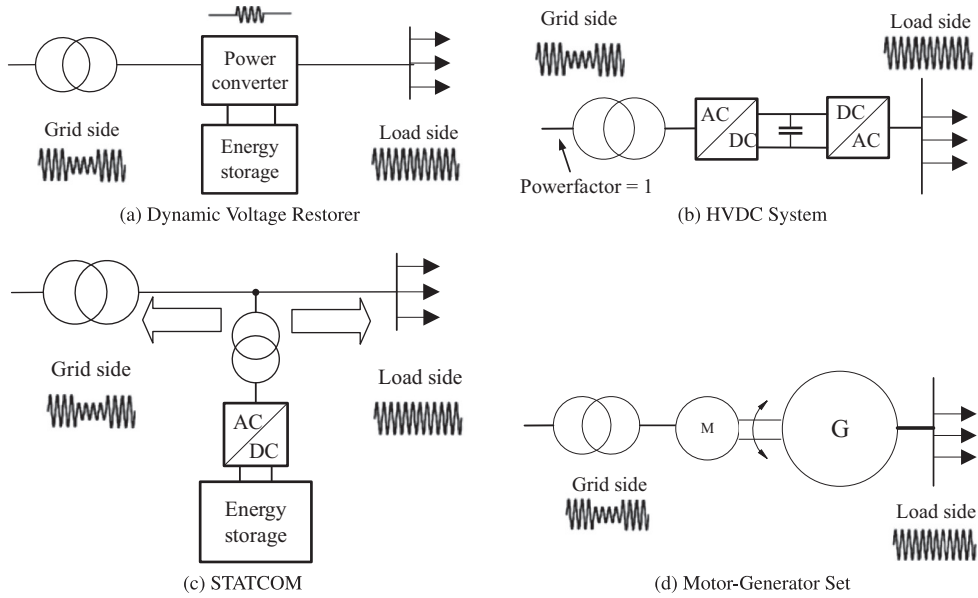
Fig. 5.8. Simplified layout of various methods for transient voltage dip mitigation.

its early stage of development and would require considerable R&D efforts before its use (see Sect. 12.10).

5.5 Emergency power

The emergency power concept is based on the requirement to keep essential parts of the accelerator infrastructure operational if the regular power source fails. Particular emphasis is put on maintaining personnel and machine safety related functions during degraded situations. The various load classes and types are shown in Table 5.8. The main ranking parameters are the acceptable duration of the power interruption and whether the load is part of a personnel or accelerator safety function or not.

Machine loads are energised from the transmission network through the distribution network and do not have a second source of supply. The general services loads typically accept power cuts of several minutes to hours. They can switch to an alternate source or wait until the main source is restored. Secured loads include personnel and machine safety equipment or systems that can only accept short power cuts up to a duration of 30 s. They require three staged supplies. In a degraded situation, the first backup is implemented by a generator power station, which typically starts up within 10 s. If the power station is unavailable, the second backup is implemented by supplying power from the regional grid.

High availability loads require true uninterruptable power supply. The network scheme is composed of two redundant uninterruptable power supply (UPS) systems that are supplied from the distribution network in the two adjacent points. Downstream of the redundant UPS systems, a doubly redundant network delivers two independent sources, each coming from an adjacent point to the end-user plug. Each piece of end-user equipment has two entries and will manage the double source of supply. To meet safety and access requirements, UPS and batteries are located outside the tunnel and above ground. Figure 5.9 shows the functional scheme of the general services loads network and the doubly redundant uninterruptable load network.

Table 5.7. Power quality and transient voltage dip mitigation.

	DVR	Back-to-Back	DC grid	STATCOM	Motor-Generator Set
Transient voltage dips	Covered	Covered	Covered	Covered	Covered
Compensation of reactive power on the load side	Not covered, although the resulting voltage deviations on the load side can be compensated	Covered	Covered	Covered	Covered
Compensation of active power on the load side	Not covered	Covered	Covered	Covered	Covered
AC Harmonic filtering capability	Yes (although additional HF filter required)	No (additional harmonic filtering required)	No (not necessary)	Yes	No (additional harmonic filtering required)
Steady-state power losses	Very low	High	Medium	Very low	Medium
Technology readiness level	Available in industry	Available in industry	Design and standardisation phase	Available in industry	Available in industry
Protection aspects	Bypass is needed	Bypass is needed	Under development	Bypass is needed	Very high protection

Table 5.8. Load classes and main characteristics.

Load class	Load type (non-exhaustive list)	Power unavailability duration in case of degraded scenario
Machine	Power converters, radio frequency, cooling pumps, fan motors	Until return of main supply
General Services	Lighting, pumps, vacuum, wall plugs	Until return of main or secondary supply
Secured	**Personnel safety:** lighting, pumps, wall plugs, elevators	10–30 s
Uninterruptable	**Personnel safety:** evacuation and anti-panic lighting, fire-fighting system, oxygen deficiency, evacuation **Machine safety:** sensitive processing and monitoring, beam loss, beam monitoring, machine protection	Interruptions not allowed; continuous service mandatory

5.6 Cryogenic system

5.6.1 Overview

The HE-LHC is assumed to use the superconducting magnet technology planned for the FCC-hh, based on Nb_3Sn windings operating at a temperature below 2 K. An effort is made to reuse as much of the existing LHC and HL-LHC infrastructure as possible.

Functions and constraints

The superconducting magnet windings will be immersed in a pressurised bath of superfluid helium at about 0.13 MPa (1.3 bar) and a maximum temperature of 1.9 K.
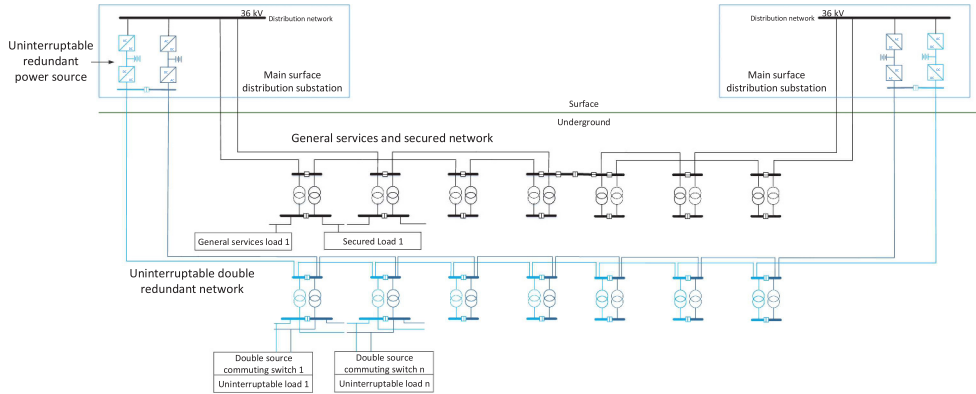
Fig. 5.9. Functional scheme of the general services load network and the doubly redundant uninterruptable load network.

This provides a sufficient temperature margin for heat transfer across the electrical insulation. This cooling requirement applies during stored beam operation. The temperature excursion during a magnet current ramp-up must remain below 2.1 K. During pre-cycles the temperature excursion may be larger but must still remain below the helium II/helium I phase transition (lambda line).

The cryogenic system must cope with load variations and the large dynamic range induced by operation of the collider. The system must also be able to fill and cool down the huge cold mass of the HE-LHC, 60×106 kg, in less than 20 days, while avoiding thermal gradients higher than 50 K in the cryo-magnet structure. This limit in thermal gradient and time also applies to the forced emptying and warm-up of the machine prior to shutdown periods. The cryogenic system must be able to cope with resistive transitions of the superconducting magnets, which will occasionally occur in the machine, while minimising the loss of cryogen and system perturbations.

The cooling power will be produced by 8 refrigeration plants at 5 technical sites and will be distributed to the adjacent sectors over distances of up to 3.3 km. To simplify the magnet string design, the cryogenic headers distributing the cooling power along a machine sector as well as all remaining active cryogenic components in the tunnel are contained in a compound cryogenic distribution line (see Fig. 5.10). The cryogenic distribution line runs alongside the cryo-magnet strings in the tunnel and feeds each lattice cell in parallel via a jumper connection. The LHC tunnel is inclined at 1.4% with respect to the horizontal plane, giving rise to elevation differences of up to 120 m across the ring diameter. This will generate hydrostatic heads in the cryogenic headers and could generate flow instabilities in two-phase, liquid-vapour, flow. Ideally, to avoid these harmful instabilities, all fluids should be transported over large distances in the mono-phase state, i.e. in the superheated-vapour or supercritical region of the phase diagram. Local two-phase circulation of saturated liquid, in a controlled direction, can be tolerated over limited distances. Equipment is installed above ground as much as possible to avoid the need for excavation of further large underground caverns. However, certain components, which must be close to the cryostats, will be installed underground. To limit the effect of the gravity (hydrostatic head and relative enthalpy variation) in the deep access shafts (up to 150 m), the cold part of the helium cycle, including cold compressors, must be located in underground caverns. In order to reduce the size of the cryogenic distribution system and to integrate it within the existing LHC tunnel, active cryogenics must also be installed at both sides of the HE-LHC sectors.
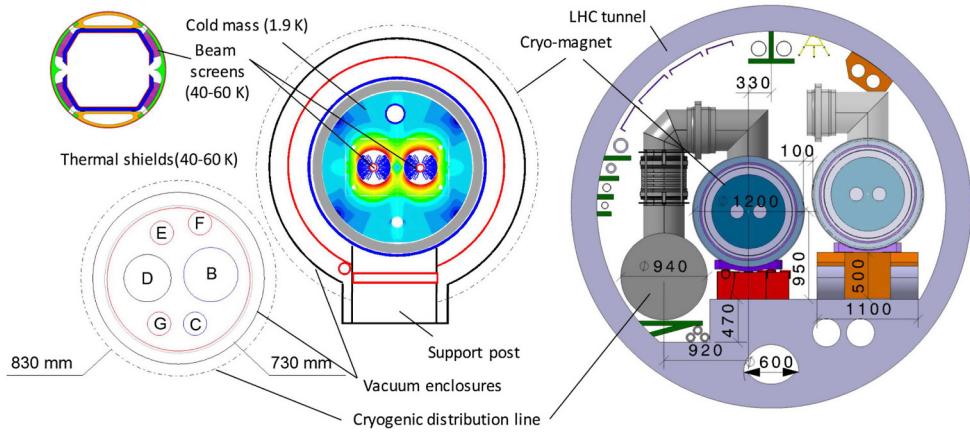
Fig. 5.10. Cross section of the LHC tunnel and main HE-LHC cryogenic components.

For safety reasons, nitrogen is not used in the tunnel and the discharge of helium is restricted to small quantities. These safety aspects are reflected in specific design features of the system, such as a large acceptance cold recovery header inside the distribution line. The cryogenic system is designed for fully automated operation. Maintenance will be performed during shutdown periods.

Layout and architecture

A direct consequence of the site constraints is the cryogenic layout of the machine (Fig. 5.11a), with 5 cryogenic "islands" at points 1.8, 2, 4, 6 and 8 where the main refrigeration and ancillary equipment is concentrated. Equipment at ground level includes an electrical substation, a warm compressor station (WCS), cryogen storage (helium and liquid nitrogen), cooling towers and cold-boxes (UCB and TBB). The lower cold-boxes (LCB), interconnecting lines and interconnection boxes are underground. Each cryogenic island houses one or two refrigeration plants that feed adjacent tunnel sectors, requiring distribution and recovery of the cooling fluids over distances of 3.3 km underground. Figure 5.11b shows the general architecture of the cryogenic system. A refrigeration plant comprises one helium refrigerator including two 1.8 K refrigeration units (CCB) and one turbo-Brayton refrigerator (TBB) for the efficient production of cooling capacity above 40 K. The two 1.8 K refrigeration units are located at either side of the HE-LHC sectors and pump on a half-sector length, thus reducing the required pumping line diameter from 340 mm to 220 mm. At each cryogenic island, an interconnection box couples the refrigeration equipment to the cryogenic distribution line. Where possible, they also provide redundancy between the refrigeration plants. To limit the environmental impact as well as the pressure build-up during helium discharge in case of a sector quench helium storage is provided at all 8 surface sites.

In addition, at points 1 and 5 where high luminosity insertions are required for the two large detectors, the HL-LHC cryogenic plants will be reused for cooling the insertions. Each unit's capacity is equivalent to 18 kW at 4.5 K.

5.6.2 Proximity cryogenics and heat loads

Temperature levels

In view of the high thermodynamic cost of refrigeration at 1.8 K, the thermal design aim of the cryogenic components is to intercept the largest fraction of heat loads at
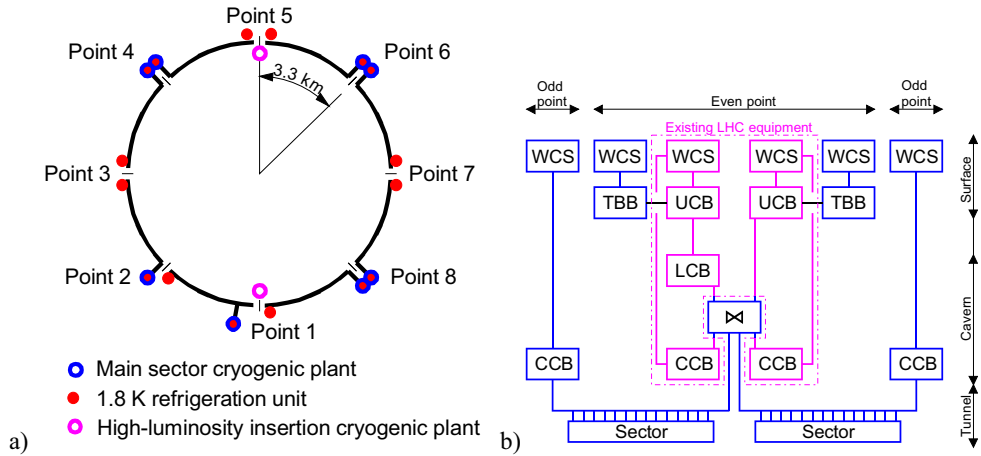
Fig. 5.11. (a) General layout. (b) Cryogenic plant architecture.

higher temperature, hence the multiple, staged temperature levels in the system. The temperature levels are:

- 40 K–60 K for the thermal shield as a first major heat intercept, shielding the cold mass from the bulk of heat in-leaks from the environment;
- 40 K–60 K to cool the beamscreens which protect the magnet cold bore from beam-induced loads;
- 1.9 K quasi-isothermal superfluid helium to cool the magnet cold mass;
- 4 K at very low pressure (VLP) to transport the superheated helium coming from the distributed 1.8 K heat exchanger tubes across the sector to the 1.8 K refrigeration units;
- 4.5 K normal saturated helium for cooling superconducting radiofrequency cavities and the lower sections of high temperature superconducting (HTS) current leads;
- 40 K–300 K cooling for the resistive upper sections of the HTS current leads.

The cryostats and cryogenic distribution line combine several low temperature insulation and heat interception techniques which will have to be implemented on an industrial scale. These techniques include low-conduction support posts made of non-metallic fibreglass/epoxy composite, low impedance thermal contacts under vacuum for heat intercepts and multi-layer reflective insulation for wrapping about $1.2\,km^2$ of cold surface below 60 K.

The beam-induced heat load on the beamscreens is dominated by the synchrotron radiation power of about 190 kW of the total 300 kW in nominal conditions. This beam induced load has to be intercepted at a temperature well above that of the magnet. A thermodynamic optimisation which takes into account the exergetic costs of the beamscreen and cold mass cooling gives an optimum operating temperature of around 50K, which corresponds to the average value of the cooling range (40–60 K).

Heat loads

Static heat in-leaks are a function of the design of the cryostats and originate in the ambient temperature environment. Thermal calculations for the cryostats and the distribution system are based on LHC thermal performance data with appropriate scaling of the geometry (for radiation terms) and mass (for solid conduction).

Table 5.9. Distributed steady-state heat loads in HE-LHC (nominal conditions).

Temperature level		40–60 K	1.9 K	4 K VLP
Static heat in-leaks (W/m)	Cold mass supporting system	2.4	0.13	
	Radiative insulation		0.13	
	Thermal shield	3.1		
	Feedthrough and vacuum barrier	0.2	0.1	
	Beamscreen		0.12	
	Distribution	3.0	0.1	0.1
	Total static	**8.7**	**0.58**	**0.1**
Dynamic heat loads (W/m)	Synchrotron radiation	8.0	0.08	
	Image current	4.5		
	Resistive heating in splices		0.3	
	e-clouds	0.2	–	–
	Beam-gas scattering		0.18	
	Total dynamic	**12.7**	**0.56**	
Total		**21.4**	**1.1**	**0.1**
Dynamic range		2.5	2	1

Electrical resistive heating is caused by the non-superconducting sections of the magnet excitation circuits, essentially in splices of the superconducting cables and in current leads. The heat load due to magnet splices has to be absorbed by the cold mass helium bath. Resistive heating in current leads has to be absorbed by cooling circuits in the electrical feed boxes.

Beam induced loads are deposited in the cryo-magnets through several processes and by the circulating and colliding proton beams themselves. These loads strongly depend on the energy, the bunch intensity and on the number and length of the circulating bunches. The various beam induced loads are:

– Synchrotron radiation from the bending magnets, mostly absorbed by the beam-screens;
– Resistive dissipation of beam image currents induced in the resistive walls and geometrical singularities of the beam channel, mostly absorbed by the beam-screens;
– Impinging photo-electrons accelerated by the beam potential (e-clouds), mostly absorbed by the beamscreens;
– Nuclear inelastic beam-gas scattering corresponding to a continuous distributed loss of particles from the circulating beam, mostly absorbed by the cold mass helium bath.

Table 5.9 lists the distributed steady-state heat loads in HE-LHC for nominal conditions.

Ramping the magnetic fields up and down generates transient heat loads in the superfluid helium due to eddy currents in the superconducting cables and in the mechanical structure of the magnets. Raising the current to its nominal value in 1600 s is expected to dissipate 5 kJ per metre of main dipole. This represents a power of approximately 3 W/m. This power corresponds to 2 times the total steady-state heat load at 1.9 K and cannot be extracted in real time. The only practical way to absorb these transient heat loads and to keep the temperature below 2.1 K during ramping up and below the lambda line during a pre-cycle (ramping up followed by a ramping down: 2×5 kJ/m), is to use the heat capacity of the liquid helium contained in the magnet cold masses. About 33 l of liquid helium per metre length is sufficient to cope with the energy to be buffered. To extract the energy deposited in a time
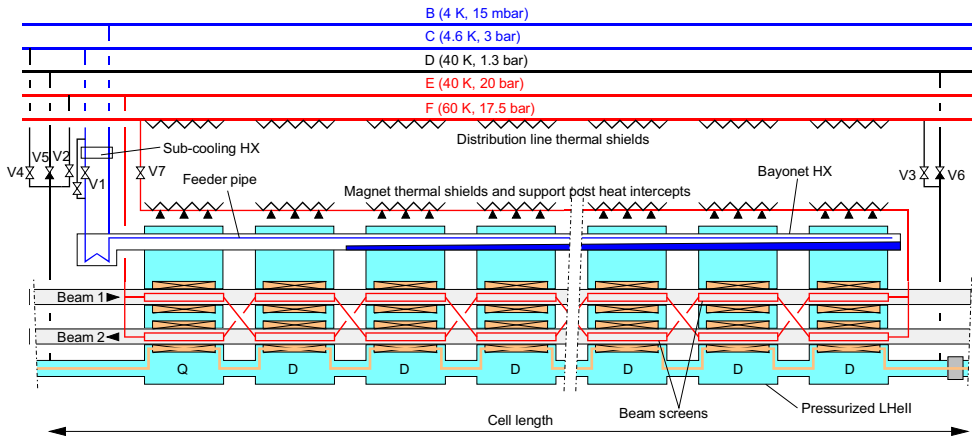
Fig. 5.12. Cryogenic flow scheme of an HE-LHC cell.

compatible with high-luminosity beam operation (<2 h) an extra cooling capacity of 1.1 kW at 1.8 K per refrigerator is required.

Cooling scheme and cryogenic distribution

The cryogenic flow scheme of an HE-LHC cell is shown in Figure 5.12. The pressurised superfluid helium bath at 1.9 K, in which the superconducting magnets are immersed, is cooled by saturated two-phase helium flowing in a bayonet heat exchanger (HX) tube extending along the string of magnets and supplied by line C through expansion valve V1 and a sub-cooling heat exchanger. The low saturation pressure is maintained by pumping the vapour through line B. Table 5.10 gives the main superfluid helium cooling loop parameters (LHC parameters are also given for comparison).

Cool-down and warm-up are achieved by forced circulation of high-pressure gaseous helium supplied at variable temperature by line E, tapped through valve V2 and returned to the cryogenic plant by valve V3 and line F. At the end of the cool-down, the liquid helium filling is done by valve V4.

In case of a magnet quench, the resulting pressure rise is contained below the 2 MPa design pressure by discharging the liquid helium inventory of a half-cell into line D through the V5 and V6 safety relief valves; the low hydraulic impedance of this 200 mm diameter pipe, normally maintained at 40 K, is very helpful in containing the helium discharge and buffering the gas storage vessels.

The beamscreens are cooled by forced circulation of high pressure helium, tapped from line E and returned to line F by valve V7, after cooling the magnet thermal shields and support-post heat-intercepts. Table 5.11 gives the main beamscreen cooling loop parameters (LHC parameters are also given for comparison).

The weak points of conventional stainless steel tube cryogenic distribution lines are their compensation units based on bellows and their inherent risk of leaks and buckling. The HE-LHC design is based on Invar tubes. Invar, an iron-nickel alloy, exhibits a very low thermal contraction coefficient and the corresponding cool-down stresses can be handled without compensation units. In order for this technology to be used, dedicated R&D needs to be carried out. Efficient transport of the refrigeration capacity between 40 and 60 K for the beamscreen and thermal shield cooling can be achieved with an operating pressure of 20 bar. Table 5.12 gives the dimensions of the main lines and vacuum jackets of the cryogenic distribution line in the tunnel.

Table 5.10. Main superfluid helium cooling loop parameters.

Parameter	Unit	LHC	HE-LHC
Unit cooling length	m	106.9	106.9
Sector cooling length	m	2900	2×1450
Number of parallel cooling loops (total)	–	216	216
Average nominal heat load	W/m	0.40	1.10
Bayonet heat exchanger inner diameter	mm	53.4	83.1
Feeder pipe inner diameter	mm	10.0	15.0
Wall thickness of bayonet heat exchanger	mm	2.3	5.0
Joule-Thomson valve inlet temperature	K	2.18	2.18
Free longitudinal cross section area	cm^2	60	156
Δ T max pressurised saturated HeII	mK	50	50
Cold mass operating pressure	bar	1.3	1.3
Pumping line (B) diameter	mm	270	220
Helium supply line (C) diameter	mm	100	100
Heat load on pumping line	W/m	0.11	0.10
Pumping pressure at cryogenic plant interface	mbar	15	15
Maximum cold mass helium temperature	K	1.9	1.9

Table 5.11. Main beamscreen cooling loop parameters.

Parameter	Unit	LHC	HE-LHC
Unit cooling length	m	53.4	106.9
Sector cooling length	m	2900	2900
Number of parallel cooling loops (total)	–	432	216
Average beamscreen nominal heat load	W/m	1.6	21
Supply pressure	bar	3	20
Supply helium temperature	K	5	40
Max. allowed BS temperature	K	20	60
BS helium outlet temperature (nominal)	K	20	57
Minimum BS temperature (nominal)	K	5	41
BS pressure drop (nominal)	bar	0.5	1.0
ΔP control valve (nominal)	bar	0.8	1.0
ΔP supply and return line (nominal)	bar	0.4	0.5
Total cooling loop pressure drop	bar	1.7	2.5
Supply/return header(E/F) diameter	mm	100/150	100/100

Table 5.12. Dimensions of the main cryogenic distribution line components.

Component	Diameter (mm)
Line B	220
Line C	100
Line D	200
Line E	100
Line F	100
Vacuum jacket of pipe elements	730
Flanges and bellows of pipe elements	830
Vacuum jacket of service modules	880

5.6.3 Cryogenic plants

Table 5.13 gives the heat loads per sector of the main tunnel users. An operational margin of a factor of 1.3 has been included to allow for the heat loads at the different temperature levels apart from the 1.9 K level, for which extra capacity of 1.1 kW has already been added to take care of magnet transients. At Point 4, heat loads at

Table 5.13. Heat loads per sector of main tunnel users (without HL insertions).

Temperature level	>40 K		<40 K		
	40–60 K (kW)	40–300 K (g/s)	1.9 K (kW)	14 K VLP (kW)	4.5 K (kW)
Cold mass steady-state load	–	–	3.3	–	–
Additional load for transient mode	–	–	1.1	–	–
Beamscreen load	36.6	–	–	–	–
Magnet thermal shield load	15.3	–	–	–	–
Distribution thermal shield load	9.3	–	–	–	–
Pumping line (line B) load	–	–	–	0.31	–
Current leads cooling	–	50	–	–	–
RF cavity modules (only at Point 4)	–	–	–	–	0–1.5
Total w/o operational margin	61.2	50	4.4	0.31	0–1.5
Operation margin factor (–)	1.3	1.3	1	1.3	1.3
Total with operational margin	81	65	4.4	0.4	0–2
	7	2	16		0–2
Total entropic load (kW @ 4.5 K)	9		16–18		
	25–27				

Table 5.14. Electrical power to cryogenic plants.

Point	Installed power				Nominal power			
	Main	1.8 K unit	HL insertion	Total	Main	1.8 K unit	HL insertion	Total
Point 1	–	0.5	4.2	4.7	–	0.4	3.6	4.0
Point 1.8	5.4	–	–	5.4	4.7	–	–	4.7
Point 2	5.4	0.5	–	5.9	4.7	0.4	–	5.1
Point 3	–	1.0	–	1.0	–	0.8	–	0.8
Point 4	11.7	–	–	11.7	10.2	–	–	10.2
Point 5	–	1.0	4.2	5.2	–	0.8	3.6	4.4
Point 6	10.8	–	–	10.8	–	0.8	–	0.8
Point 7	–	1.0	–	1.0	–	0.8	–	0.8
Point 8	10.8	–	–	10.8	9.4	–	–	9.4
Total	**44.1**	**4.0**	**8.4**	**56.5**	**38.4**	**3.2**	**7.2**	**48.8**

4.5 K are added for the cooling of superconducting RF cavities. The total entropic load per sector varies from 25 to 27 kW equivalent at 4.5 K, which is definitely too large with respect to the existing LHC plants which have an installed entropic load of 18 kW at 4.5 K. However, the entropic load for the temperature level below 40 K is compatible with the size of the existing LHC cryogenic plants. Therefore, it is proposed to upgrade the LHC plants with turbo-Brayton refrigeration units, which will be used for all the refrigeration requirements above 40 K. This proposal allows the existing LHC infrastructure to be reused as much as possible. However, by 2040, some plants will be 50 years old. The ageing issue must be studied carefully. As in FCC-hh, the turbo-Brayton refrigeration units can also be used for the pre-cooling of the existing LHC plants as well as for production of the cool-down capacity from 300 to 40 K.

Table 5.14 gives the electrical power to the cryogenic plants including the plants in the high-luminosity (HL) insertion. The electrical power installed per point varies from 1 to 12 MW and the total installed electrical power for HE-LHC cryogenics is about 57 MW. The electrical consumption during nominal operation will be about 50 MW.

5.6.4 Cryogen inventory and storage

With respect to the present LHC helium inventory (135 t), the main increase for HE-LHC comes from the magnet cold mass inventory which increases from 25 to 33 l/m. The total helium inventory will increase by 28 t. To store this, 2 additional liquid

helium storage tanks with a unit capacity of $120\,\text{m}^3$ are required. Nitrogen will only be used for the regeneration of absorbers and dryer beds. Consequently, the existing LHC infrastructure will be sufficient.

5.7 Equipment transport and handling

The concepts for magnet transport are based on the LHC situation and strategy, having a single access shaft (PMI2) for cryo-magnets. To be able to handle the much heavier HE-LHC magnets, the structure of the shaft head building SMI2 needs to be reinforced for the installation and operation of an electrical overhead travelling (EOT) crane with 75 t capacity.

The part of the transfer tunnel TI 2 between the shaft PMI2 and the junction chamber UJ22 needs to be emptied to give more clearance during the initial installation of HE-LHC magnets. When a magnet needs to be replaced, other magnets may need to be removed before being able to pass through TI 2. Alternatively, parts of TI 2 could be locally enlarged by $\sim$30 cm. This enlargement is mandatory at the beam stopper just before UJ22. As discussed in Section 4.3, it is also necessary to increase the height of UJ22 by $\sim$1 m, to allow HE-LHC cryo-magnets to be lifted from TI 2 into the HE-LHC tunnel once the HE-LHC machine is installed (Fig. 5.13).

Because of the magnet diameter and weight and due to the LHC tunnel space constraints, transport and installation is considered a challenge. Installation must start from point 7 clockwise and anti-clockwise towards TI 2, to avoid having to move past magnets which have already been installed. Magnets must be installed strictly sequentially because there is insufficient clearance, leading to a high collision risk.

The LHC principle for transport, unloading and lateral transfer will be applied for HE-LHC: tractors, trailers and lifting tables will be used. Because of the restricted space it will be necessary to install either lifting anchors or a lifting rail all along the LHC tunnel ceiling. These will be used to lift the magnets from the trailer and to lower them onto the transfer tables for lateral transfer onto the support jacks for final positioning.

The vehicles will be custom-made due to the heavy load and space constraints and their main features will be:

– Battery powered;
– Autonomous driving;
– 3D guiding system;
– Speed:
  • In machine tunnel: 3 km/h (loaded) during the initial installation; <1 km/h during replacement of an installed cryo-magnet;
  • In TI 2 tunnel: 1 km/h (loaded) during the initial installation (significant slope); <1 km/h during replacement of an installed magnet.

5.8 Personnel transport

No changes are planned for the transport of personnel with respect to the LHC. People can either be transported collectively with wagons pulled by electric tractors or use individual transport means like electric tractors or (electric) bicycles.
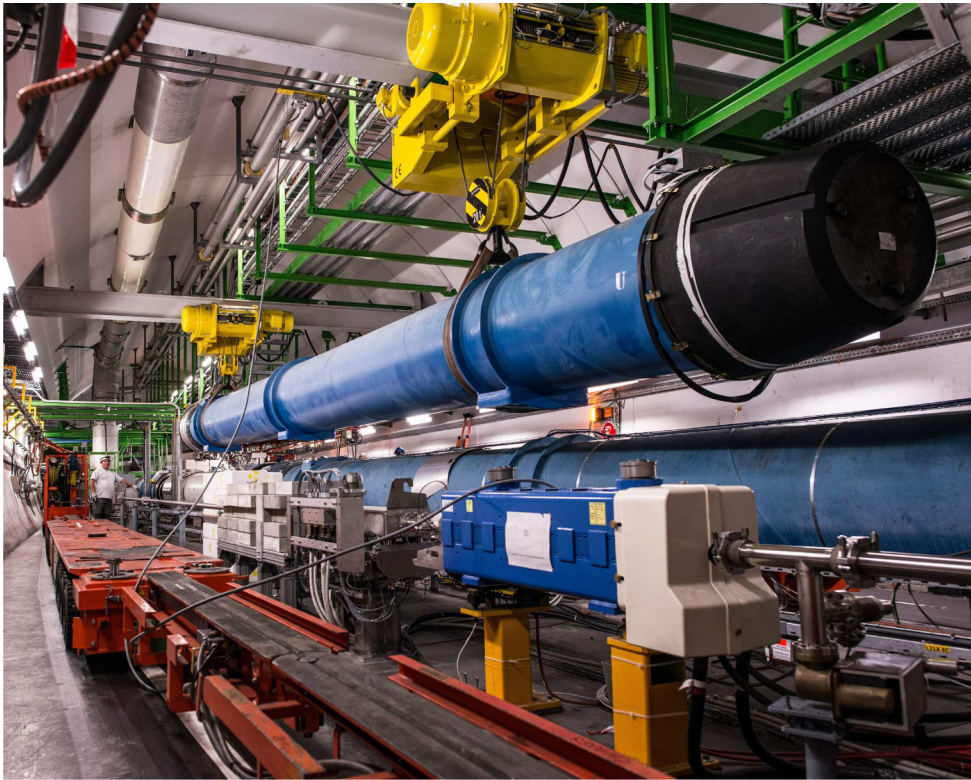
Fig. 5.13. Transfer of an LHC cryo-magnet between the transfer tunnel TI 2 (foreground/left, with the beam line arriving from the right) and the LHC main tunnel (background/right).

5.9 Geodesy, survey and alignment

It is assumed that the demands in terms of positioning accuracy will be the same as those for the LHC. Present technical possibilities have to be compared to future physics requirements, to define which developments are required.

5.9.1 Alignment tolerances

The alignment precision requirements will drive any survey study. The absolute accuracy in the vertical direction is the deviation from the theoretical plane of the collider, whilst in the transverse plane it is the variation of its radius with respect to the theoretical value. The differential variations between several consecutive magnets is the relative accuracy. This latter type of error has a more direct effect on the closed orbit of the particles. A value of several mm has been assumed as the requirement for the absolute accuracy (this was achieved for the LEP and LHC). A relative misalignment of 0.5 mm (1σ) between consecutive quadrupoles and 0.1 mrad (1σ) for the roll angle are the values achieved for the LHC. This error budget has to be shared between mechanical errors, due mainly to the assembly process and alignment errors, including misalignments due to ground motion or mechanical constraints.

5.9.2 Geodesy

As the area covered by the HE-LHC is the same as that of the LHC, only an upgrade of the mean sea level equipotential surface of gravity (also called the geoid) will be necessary. The LHC was aligned using a geoid determined in 1985, but a new determination performed at the beginning of the 2000's for the CNGS project showed differences with a maximum amplitude of ±40 mm, which therefore justifies a redetermination before starting the project. The current geodetic network could be kept, but with additional points located in the vicinity of the shafts, hosting permanent Global Navigation Satellite Systems (GNSS) antennas. To achieve the absolute accuracy, GNSS measurements will be used, possibly complemented by electro-optical distance measurements. The transfer of the geodetic network points from the surface to the tunnel will be performed using the standard techniques, which were already used at the time of the LEP. The underground network will require gyro-theodolite traverses, as well as accurate distance and angle measurements, and possibly offsets with respect to a stretched wire.

5.9.3 Metrological aspects

Metrological checks and alignments have to be integrated at different times in the manufacturing and assembly processes. This includes the fiducialisation, which determines the survey reference points with respect to the reference axes of a component. The techniques proposed are similar to those used for the LHC, i.e. laser trackers and photogrammetry. New sensors such as frequency scanning interferometry (FSI) [219] will be used for monitoring elements inside cryomodules and elsewhere when justified by the accuracy required. The positioning of the alignment targets (fiducials) has to take into account the survey needs and the experimental cavern or accelerator tunnel constraints. As the magnets will have a larger diameter than the LHC magnets, but the height of the beam with respect to the floor will be kept the same as that of the LHC, the design of the equipment supports will be challenging in order to comply with the available space, the weight of the magnets and the alignment specifications and constraints.

5.9.4 Alignment of accelerator components

The alignment of the accelerator components will be done in two steps:

- The first "absolute" alignment from the underground network will be performed using standard digital level and total station measurements.
- The "relative" alignment or smoothing. As the length of the cell is not yet fixed, the values for the LHC have been assumed. The levelling technique of offset with respect to a stretched wire will be used again. If tunnel access time is limited, measurements and realignments will have to be performed rapidly and the development of survey and alignment trains will have to be considered.

5.9.5 Interaction regions and collimators areas

The alignment accuracy for the interaction regions is assumed to be the same as for the LHC, i.e. 0.1 mm for the triplets located on the same side of the IP, 0.2 mm from left side of the IP to the right side and 0.5–1.2 mm from the triplets line to the detector (all values given at 1σ). To achieve these specifications, the survey galleries

Data and Computing Services Scope				
General IT services and infrastructures				
Particle Collider Experiments	Worldwide Research Community	Particle Accelerators and Collider	Infrastructure Services	Administration
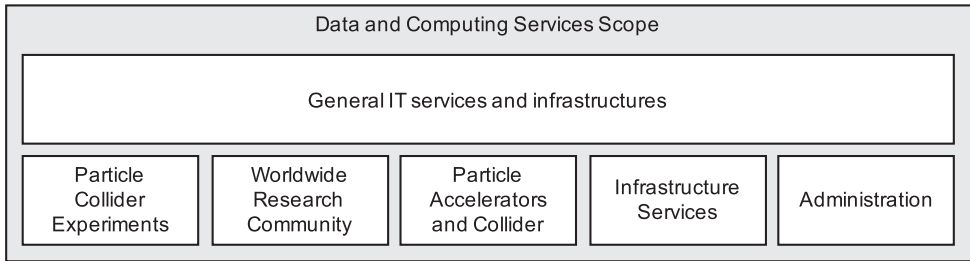
Fig. 5.14. Scope of the IT services found in a high-energy physics research facility.

will be used to host part of a permanent monitoring system based on the latest sensor technology available.

Due to the high level of radiation in the collimator areas, a permanent monitoring system, or an automatic measuring solution using a survey train, will be used together with a remote controlled re-alignment system. Such systems will be evolutions of the developments that will be implemented for the HL-LHC project. A solution must also be developed to maintain, dismantle and re-install the permanent survey systems.

5.9.6 Experiments

The alignment accuracy for assembly of the experiment is assumed to be similar to those of ATLAS and CMS i.e. 0.5 mm. The positioning of the experiment with respect to the beam line is done using a geodetic network for the experiment derived from the underground network. It is composed of points distributed across the whole cavern volume on the walls and floor. It is used at all stages of the assembly and positioning of the detectors. It is measured once the cavern has been delivered and is still empty, using mainly distances, angles and levelling measurements. The use of 3D laser tracker technology is appropriate for this type of 3D network. From this network, only the outer skin of the experiment is visible and therefore the position of the inner detectors will be reconstructed from the position of the external fiducials and the fiducialisation and assembly measurements.

5.10 Communications, computing and data services

During the LHC operation era computing for particle accelerators and the experiments has evolved into a service for a world-wide user community. Adopting products and best practices that emerge from an ever-growing Information and Communication Technologies (ICT) industry has proven to be a cost and performance effective path to serve the community. Large-scale science projects used to be a driver of IT infrastructure developments [220–225]. A future particle collider research facility can again be a case and a driving force for advanced ICT developments in areas that go beyond the hardware and software domains, which dominated the particle accelerator projects of the 1980's and 90's.

A set of general services comprising wired and wireless networks, desktop, mobile and centralised computing for all users, various storage system tiers, software and data provisioning, authentication and authorisation, assistance and consultancy, training and much more, form the backbone of services for individual business units (see Fig. 5.14). Depending on the activity type, different levels of quality of service apply. The particle collider experiments require an elastic data communication and

processing infrastructure for data acquisition and high-level event filtering. The data need to be made accessible for a world-wide research community together with data organisation, archiving, retrieval and the management of a dynamically evolving federation of participating organisations. The provision of openly accessible information and the engagement of the public through services to develop citizen-science projects are additional functions for this domain. Computing for the particle accelerator, on the other hand, involves various different networks for data, voice and video communication as well as infrastructures comprising embedded and real-time computing facilities.

Service units of the facility such as the fire brigade and medical services, security and site protection, environmental monitoring, safety-related systems and industrial installations require dedicated IT services. In particular, remote monitoring and intervention has become an important means to reduce service level agreement costs for industrial plants over the last ten years. Finally, administration units ranging from human resources and finance to different types of workflow systems need to be appropriately served whilst taking into account the length of the construction and operation phases which will last for decades. For all domains, resilience, data protection, cyber-security, technology evolution and migration and long-term data accessibility are topics that call for a dedicated organisation to ensure proper coverage with an appropriate mix of in-house personnel, external suppliers and industry/academia partnerships.

The geographical extent of the services and long-term sustainability of a new large-scale particle-collider research facility call for a shift of activities, traditionally covered by individual detector and accelerator engineering groups, to a business oriented scientific IT unit. This approach allows tenders, contracts and operation to be optimised at an organisation-wide scale as well as influencing the value of member state contributions favourably for the member countries, the organisation and the world-wide community. In particular, this approach for the construction and operation of data centres can be beneficial for experiment users, accelerator engineers and users with generic needs.

Computing and interconnect technologies are evolving rapidly and generation changes need to be expected. At the same time the optimum cost effectiveness is continuously swinging between buying and leasing. This ever changing IT environment can best be accommodated by a continuous cost/benefit analysis considering all users in the organisation, carried out by a team which is working closely with industry on one side and with the users on the other.

Embedded and real-time computing including programmable logic controllers are also a concern for a technology infrastructure that is characterised by its longevity and thus dominated by operating costs. Given the significant increase in the number of devices for a future collider, further standardisation, coordinated testing and certification and procurement and maintenance/repair services, available to all users of the organisation, will help to improve the cost effectiveness. A large-scale particle accelerator building on decades of engineers' experience presents an ideal case for an openly available architecture and platform for supervisory control to integrate the diverse subsystems. A system that can evolve with emerging "Internet of Things" (IoT) products and yet unanticipated device technologies can create impact far beyond the particle accelerator community.

Cyber-security plays an increasingly important role in IT systems and embedded computing is no exception to this. The use of processors, operating systems and embedded Web servers in the majority of programmable laboratory equipment such as simple digital I/O devices, measurement instruments, oscilloscopes and autonomous robots already require a well organised infrastructure. This is supported by a process that leads to a secure environment on one side and which has the least

possible impact on usability on the other side. For example, it should allow the possibility of developing and deploying across network boundaries, create islands and sandboxes to limit potential harm, have transparent virus and malware checking and isolation, have system updates that have little or no impact on work efficiency, provide coordinated rollback and much more. This evolution is expected to continue and the IoT approach will also require an organisation wide vertical integration of services across the horizontal user domains [177].

Cooperation on IT standards, technology developments and organisation with other research facilities which have similar requirements (e.g. DESY, ESRF, ESS, Fermilab) needs to be strengthened. Synergies with other scientific domains (e.g. astronomy and radioastronomy facilities, material sciences with light sources and FELs, astrophysics installations such as neutrino and gravitational wave observatories, particle accelerators for medical applications and nuclear fusion experiments) can be developed to lead to more effective operation of world-wide IT services for research. Activities spawned by DESY on front-end computing hardware [226] and CERN's openlab [227] are good examples for such initiatives.

Possible services include not only fibre optics and data centres that can be shared with external partners but can also include mobile communication and the cooperation with emergency and rescue services in a cross-border context. CERN's activities concerning the establishment of the TETRA radio communication system in the region are a first step in this direction [228]. CERN's particular status as carrier-neutral Internet eXchange Point (CIXP) [229] will gain importance in a technology ecosystem that becomes ever more dominated by profit making organisations which are building and operating global communication infrastructures. These collaborations may help to ensure that non-profit making organisations continue to operate independently and become less dependent on infrastructure operator priorities, which may favour financially stronger commercial clients.

Beyond the regional scale, the LHC programme has shown the value of a world-wide computing and communication infrastructure to make the research data available to scientists in all participating countries [230]. The success of a future particle collider programme will rely even more on international participation. Many potential participating countries are not part of CERN's global vision today and some are still technologically underserved. The SESAME light-source under the auspices of UNESCO is a great example of such an initiatives [231]. The capacity to plan, develop and implement a world-wide inclusion policy goes beyond the scope of the high energy physics community and is therefore also a good opportunity to establish a common strategy with other scientific disciplines. A timely development of such an initiative will help raising the interest and acceptance level of large-scale investments in an infrastructure focusing on fundamental scientific research.

Considering the fast evolution of information technologies in all domains [232], the long term cost impact of in-house technology developments and their potentially limited large scale impact, it is prudent to base architectures for the particle accelerator and the experiment data processing environments on industrial hardware, software and service infrastructures. The particular needs of an FCC-scale facility may, however, also represent attractive test-beds for emerging technologies. Co-innovation projects with industrial partners during the early construction phase, permitting pre-commercial procurement initiatives that can lead to high-performance infrastructure services at a competitive cost are one way to optimise this situation [233].

A preliminary cost-benefit-analysis of the LHC/HL-LHC programme [234] revealed that more than the impact value generated by training coresponds to more than one third of the infrastructure's cost (sum of captital and operation expenditures). The ICT sector represents an ideal case for training at large with ever growing societal and industrial demands. Early stage researchers and engineers are

much appreciated participants in CERN's technology programmes, which give them opportunities to acquire skills that are also high on the wish list of industry. It would be possible to extend these training programmes to participating industrial partners, generating value for industry directly. The CERN openlab public-private partnership already demonstrates the validity of this approach. Further industrial cooperation can focus on field testing of pre-commercial products and services, common optimisation, development of standards and best-practices and co-innovation with the research infrastructures as a demonstration case. These activities would be carried out in low risk environment for industrial partners of any size. The scaling up of the open, industrial SCADA platform PVSS around the year 2000 is one example of the success of this approach [235]. Eventually, the company was integrated in the SIEMENS group and the software has been re-branded as WinCC OA to become the SIEMENS flagship SCADA system on the global scale.

Finally, long-term data availability [236] has become an important aspect of ensuring the lasting impact of the facility [237]. The accessibility of several decades worth of raw LHC data, all metadata and previous analysis results has turned out to be a major topic for the ICT community. With a future particle collider, the time span will extend to the end of the 21st century, calling for evolving data storage and management systems that serve the worldwide particle physics community for more than 100 years. Considering the continuous evolution of data formats, the ever-changing particle detectors and a highly dynamic user community, data quality management is a primary topic. The value of a particle collider research facility depends directly on its quality and long term world-wide accessibility for as large a community of scientists as possible.

5.11 Safety and access management systems

A safety management system (SMS) for a future large-scale particle collider will be based on an industry best-practice system which integrates, in a uniform and regulatory-compliant way, everything which contributes to safe operation. This system also includes the procedures associated with the different operating conditions encountered during the lifetime of the collider. A high-level computer-based safety management system integrates underlying safety related functions, including fire detection, oxygen deficiency detection, smoke and helium extraction systems, fire extinction systems, access and authorisation management, door supervision and control, video surveillance, radiation monitoring, conventional environmental monitoring, evacuation signalling, supervision and control of lifts, communication with people in underground zones, emergency lighting and acoustics and communication with emergency services (fire fighting, rescue, healthcare providers, public and private security forces). The sub-systems function autonomously.

There are two complementary systems for personnel protection in the underground areas: the access safety system and the access control system. During machine operation, the access safety system protects personnel from the hazards arising from the operation of the accelerator and from the beams. It acts through interlocks on important safety elements of the accelerator. By interlocking these elements it is possible to establish the right accelerator and equipment conditions in order to allow authorised personnel to access the underground installations or to allow the restart of the accelerator equipment when access is finished. When the accelerator is not operating with beam and is in access mode, the access control system allows the positive identification of any person requesting access and ensures that all pre-requisites and authorisations for that person are valid. For operational and/or safety reasons, the access control system also limits the number of people present simultaneously in the underground areas.

Table 5.15. Examples for typical safety management system solutions for large-scale applications.

Supplier	Product
Advancis Software & Services	PSIM
ATS Elektronik	AES5000, DLS4000
Bosch Security Systems	Building Integration System
CENARIO solutions	CENARIO
digivod	CRISP PSIM
ETM/SIEMENS	WinCC OA
Genetec	Security Center
GEOBYTE	Metropoly BOS
Honeywell	Enterprise Buildings Integrator, WINMAG plus
KÖTTER Security	LENEL OnGuard
PKE	AVASYS
Scanvest	ScanVis.Pro
Securiton	Universal Management System SecuriLink UMS, IPS
SIEMENS	GMA-Manager, Siveillance Vantage
Tyco Integrated Fire & Security CKS Systeme	CELIOS, C-cure 9000
WAGNER Group	VisuLAN X3

An automatic fire detection system consisting of detectors and air sampling networks to detect the presence of smoke is connected to control and monitoring equipment located in one of the surface buildings at each point. If fire or smoke is detected, the system launches automatic safety functions and alerts the fire and rescue service. Fire detection is installed in all underground areas and will allow accurate location of a fire. An automatic oxygen deficiency detection system warns users of the danger and alerts the fire and rescue service. Underground areas will also be equipped with communication channels to allow a user to contact the fire and rescue service directly.

The SMS launches safety functions if there is a fire or oxygen deficiency is detected. These functions include compartmentalisation, evacuation and smoke extraction. The CERN fire brigade has the possibility to trigger these functions remotely and to broadcast safety instructions in the various areas of the facility.

The emergency evacuation system is a part of the automatic protection system. It broadcasts audible evacuation signals triggered either automatically by a safety system, such as fire or oxygen deficiency detection, or manually by pushing one of the emergency evacuation buttons installed within the area in question.

The SMS provides prioritised and homogeneous visualisation of the status of all safety relevant parameters, allows the supervisory control of all sub-systems and handles the sub-system interconnections. The SMS communicates with the sub-systems through fail-safe protocols, over a dedicated communication infrastructure. It guarantees that critical alarms are automatically transmitted to the competent services (e.g. fire brigade, radiation protection team) and that all incidents are recorded and suitably documented for potential internal and external examination (auditing). Furthermore, the SMS ensures that any condition which is incompatible with safe beam operation (e.g. intrusion) is detected and the beam is aborted.

Such supervisory systems are in daily operation in most large-scale plants (e.g. particle-accelerator-based ion therapy facilities, oil and gas rigs, manufacturing and processing plants). Examples for typical Safety Management System solutions are listed in Table 5.15.

The future system must be compliant with international norms, be open and extensible and be configurable to the specific application (e.g. GIS and CAD

integration, user interface designer). Processing speed is generally not critical, but the system must work extremely reliably, be highly scalable and be open to the integration of a continuously growing set of diverse subsystems from different suppliers. Implementation details (e.g. positioning of a central supervision point, the number and position of decentralised facilities to interact with the system, hard- and software choices, rights management, means to identify people requesting access, or locating people in the machine) will be subject to a requirements specification phase, once the detailed design of the infrastructure and its individual technical systems are well known.

6 Injector scenarios

6.1 Requirements and basic assumptions

The HE-LHC injector chain needs to be able to fill the HE-LHC with the 2808 nominal 25 ns proton bunches in around 10 min, as is possible at present (at least on paper) for the LHC. The bunch intensity required is 2.2×10^{11} protons in a normalised emittance of $2.5\,\mu$m, as is needed for the HL-LHC.

The pre-injector chain is assumed to be the present LHC injector chain consisting of Linac 4, PSB, PS and SPS (see Fig. 6.1). The performance is assumed to be the same as after the LHC Injector Upgrade (LIU) project (see Tab. 6.1), for which the expected performance at 25 ns is the one required by HE-LHC.

The HE-LHC injection energies under study are 450 GeV when using the unmodified LHC injector chains and and 1.3 TeV when using a new High Energy Booster (HEB) that replaces the existing 6.9 km long SPS. A higher injection energy is favourable in terms of impedance, beam stability, aperture and energy (field) swing, but for transfer to HE-LHC, simplicity and cost of the injector complex, a lower energy is preferred. The overall project optimisation needs to take into account all these factors, as well as the capital and operation costs.

An intermediate energy around 900 GeV may be the optimum, but at this conceptual design stage the 1.3 GeV version is the only new HEB machine to have been studied, leveraging a synergy with the study for the FCC-hh injectors.

It is assumed that today's TI 2 and TI 8 transfer line tunnels are used, although for energies above 450 GeV new superconducting transfer magnets are mandatory.

Due to the need to avoid damage to the injection protection absorbers, the number of bunches which can be safely transferred to HE-LHC is determined by the injection energy. This limit scales non-linearly with beam energy, as the energy deposition in the absorber also depends on the secondary shower development. It is assumed that 320 bunches per transfer are possible at 1.3 TeV, corresponding to around $8\,\mu$s of the $23\,\mu$s SPS tunnel circumference. Therefore, as for the LHC today, around 10 extractions are needed to fill each HE-LHC ring.

Any new HEB should have a high degree of operational flexibility. In addition to filling the HE-LHC several times per day, it will also be serve multiple users e.g. beams for material test facilities and fixed target (FT) experiments using slow extraction. Another important requirement is high availability for the entire injector chain. The HEB should be considerably easier to operate than the collider.

Other HEB options, such as a 27 km superferric HEB in the LHC tunnel, have been considered in the past (see e.g. [238]), but they are not described in more detail here. Specifically this option would not be suitable to also serve fixed-target operation and it would be difficult if not impossible to integrate a dual-ring accelerator with the HE-LHC machine in the small LHC tunnel. This scenario would also require additional by-passes around the experiments.
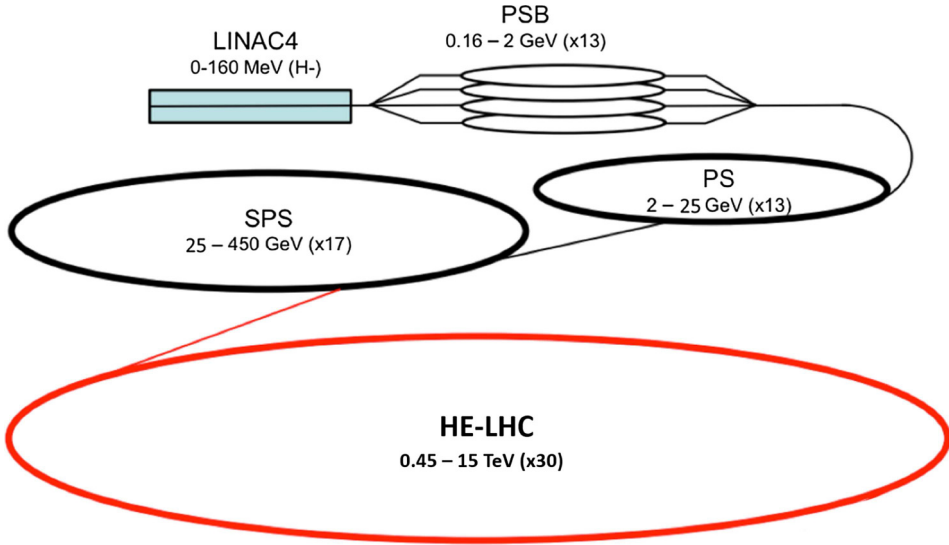
Fig. 6.1. HE-LHC injector chain, based on the existing LHC injector chain. Replacing the SPS by a 1.3 TeV HEB would reduce the energy swing in HE-LHC to only ×10, but would increase it in superconducting SPS to ×52.

Table 6.1. Planned beam parameters at LHC top energy, after the LIU and HL-LHC upgrades.

Parameter	Bunch pop. (10^{11} p/b)	$\epsilon_{x,y}$ (μm)	ϵ_z (eVs)	Bunches/injection
Standard 25 ns	2.3	2.08	0.56	288
BCMS 25 ns	2.3	1.6	0.56	240

Notes. The maximum number of bunches per injection from the SPS is quoted.

6.2 Superconducting SPS as 1.3 TeV HEB

A new superconducting SPS (scSPS) in the existing 6.9 km tunnel with 1.3 TeV extraction energy has been studied as an alternative HEB scenario for FCC-hh [239]. This machine is also interesting as HEB for HE-LHC, where an injection energy higher than the 450 GeV available from the existing SPS could be necessary for field quality, aperture and impedance reasons. For future fixed target programmes in CERN's North Area, the possibility of slow extracted beams at energies above 1 TeV could open new physics and detector test beam possibilities [240], especially if a relatively fast-ramping concept can deliver large numbers of protons on target per year.

The main parameters of an scSPS can be found in Table 6.2. These values are based on the parameters of a 12 m long, 6 T superconducting dipole magnet. The interconnects between two neighbouring magnets were assumed to have a length of 1.25 m.

The circulating beam would contain ∼33 MJ energy, requiring beam dump and collimation systems which will resemble those of the LHC more than those of the SPS. To respect ∼10 min filling time, the average ramp rate should be 0.35–0.5 T/s, with 10 ramps needed to fill both HE-LHC rings.

Using the PS as injector, the scSPS injection energy would be 25 GeV, giving a very large energy swing of ×52. This is likely to be a challenge for the magnet field

Table 6.2. Main parameters of a new 1.3 TeV superconducting SPS.

Parameter	Unit	Value
Injection energy	GeV	25
Extraction energy	GeV	1300
Maximum dipole field	T	6
Dipole field at injection	T	0.12
Dipole magnet length	m	12.12
Cold bore inner diameter	mm	80
Number of dipoles		372
Number of quadrupoles		216
Ramp rate	T/s	0.35–0.5
Cycle length	min	1
Number of bunches per cycle		640
Number of injections into scSPS		8 (8 × 80 b)
Number of protons per bunches		$\leq 2.5 \times 10^{11}$
Number of extractions per cycle to HE-LHC		2 (2 × 320 b)
Number of cycles per HE-LHC filling		10
FCC filling time	min	10
Max stored beam energy	MJ	33

quality and dynamic aperture. These aspects could be eased by injecting at higher energy, but this would pose its own challenges, either of integration if retaining the SPS in the same tunnel, or of the need for a new high-field (or larger circumference) machine to replace the PS. At present the challenge of a ×52 energy and magnetic field swing in scSPS is maintained as the target.

In this study, the present SPS tunnel geometry was maintained and locations for the existing long straight section (LSS) functionalities were kept, where possible. The injection remains in LSS1 with the beam circulating in a clockwise direction, keeping the slow extraction and transfer lines to the North Area in LSS2. The RF system stays in LSS3. The fast extractions towards HE-LHC P8 and P2 are located in LSS4 and LSS6, respectively. Note that for beam transfer to FCC-hh these extractions should be located in LSS3 and LSS5 [239]. The external beam dump system either remains in LSS5, combined with a new collimation system, or re-located as an external system to LSS6, leaving LSS5 for the collimation system. An overview of the layout is shown in Figure 6.2.

Although the detailed design study of the different straight sections remains to be done, the basic feasibility has been confirmed. This assumes the improved performance from the technological developments in kickers and septa already under study for FCC-hh beam injection and extraction, such as 4 T septa [159], which are needed to extract beams with three times the rigidity in the same 120 m long LSS.

A first scSPS lattice has been developed, similar to the present SPS with a missing-magnet dispersion suppressor. A half-cell of 2 main dipole magnets is assumed, with 372 dipoles in total, each with a bend angle of 16.89 mrad. These would need to be curved to avoid a huge sagitta. The current SPS access shafts would need to be rebuilt as they restrict the length of components which can pass through them horizontally to a maximum of 6.9 m. Peak β values are 107 m in the centres of the quadrupoles, and peak dispersion functions 4.3 m, for an integer tune of 26 in both planes and 89.96 degree phase advance per cell. A plot of beta function and dispersion in one sextant is shown in Figure 6.3.

The 6 T peak field was chosen to have relatively simple, fast-ramping dipoles designed with a single layer NbTi Rutherford cable – in the case of 900 GeV energy, lower fields of around 4 T would result in an even simpler dipole magnet. The
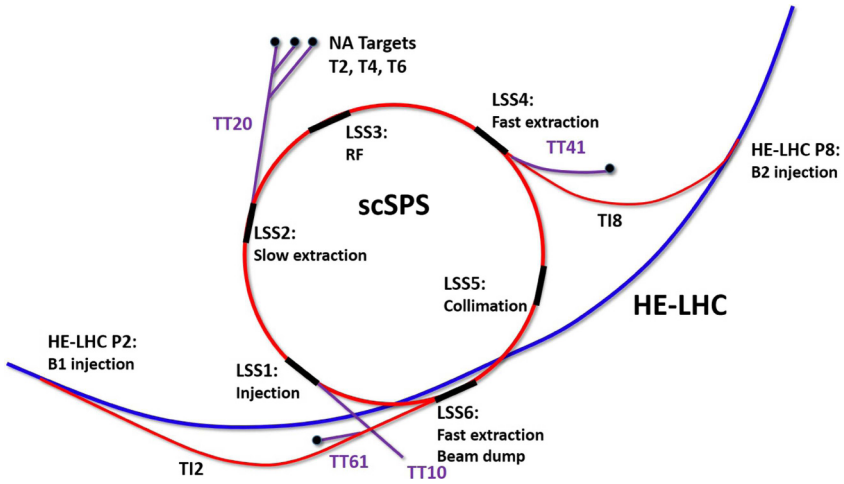
Fig. 6.2. Layout of a superconducting SPS showing the overlap with HE-LHC.
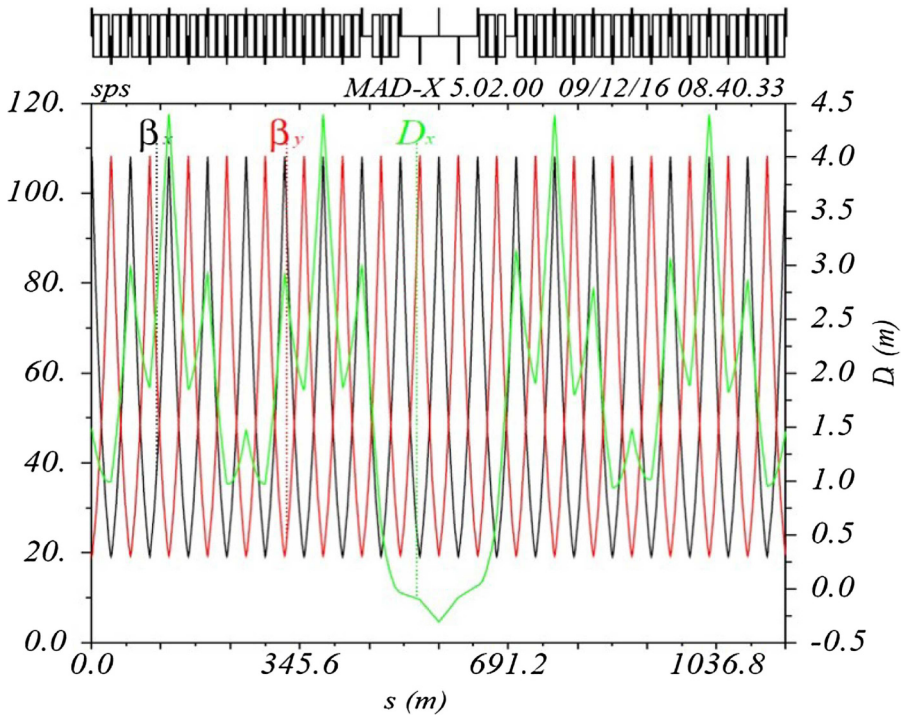
Fig. 6.3. Optics for superconducting SPS with 32 m half-cell length and 12 m long dipoles.

maximum quadrupole gradient assumed is $67\,\mathrm{T/m}$, again feasible with NbTi technology. The magnet aperture was chosen to accommodate both HE-LHC beams and also a low-emittance $(2.2\,\mu\mathrm{m})$ fixed target beam. For 25 GeV injection the inner diameter of the circular cold-bore is 80 mm, which is rather large. This value could be reduced for a higher injection energy. The vertical aperture required is slightly smaller because the vertical dispersion is taken as zero and the injection oscillations are assumed to be only in the horizontal plane. The main parameters concerning the aperture are summarised in Table 6.3.

Table 6.3. Main parameters of superconducting SPS concerning aperture.

Parameter	Unit	Value
Max. beta $\beta_{x,y}$	m	107
Max. dispersion D_x	m	4.3
Orbit + alignment tolerance $O_{x,y}$	mm	2.5
Max inj. oscillation	mm	1.5
Emittance $\epsilon_{x,y}$ (1 σ, norm.)	m	2.2×10^{-6}
$\delta p/p$		5×10^{-4}
A_x/A_y 25 GeV	mm	76/69
Coldbore diameter 25 GeV injection	mm	80

A superconducting RF system can be placed within one straight section, assumed to be LSS3. A detailed study of the optimum frequency (or frequencies) and parameters (also to debunch the beam for slow extraction) is needed. The beam dump could possibly remain in LSS5 but has to be combined with the collimation system and probably also converted to an external system. Alternatively, LSS5 could be dedicated to collimation, while LSS6 is used for both fast extraction and dumping. TT61, presently used for HiRadMat, would be modified to serve as a beam dump line, with dilution kickers and an absorber block similar to the LHC concept [97]. Civil engineering to create a cavern would be needed in either case.

For fixed target experiments and test beams for experiments, a slow extraction in the milli-second to several seconds range is needed. The machine should be able to deliver around 10^{19} protons-on-target (PoT) per year. To avoid increasing the machine aperture dramatically, innovative solutions for slow extraction will need to be developed. At present a crystal-based extraction with low losses is assumed [241], with non-resonant transverse excitation of the beam to avoid large excursions caused by the resonant-extraction separatrices. The impact of high loss levels and additional local protection elements needed for the integration of the slow extraction with the collimation system needs to be studied. For other test facilities like HiRadMat [242] fast extracted beams will be needed. This type of extraction and beamline does not pose any major additional technical challenge, aside from the conversion of the beamlines to superconducting magnets.

6.3 Injection chain summary

The existing 25 ns LHC injectors will form the baseline of the HE-LHC injector chain to 450 GeV. A new 6 T superconducting magnet based scSPS together with new transfer line magnets is required to reach 1.3 TeV. A 900 GeV version would only require 4 T superconducting dipoles. A more drastic alternative of a 1.5 T, 27 km long, superferric HEB in the LHC tunnel has been considered in the past, but has not been explored in more detail. It lacks flexibility because it will not allow fixed-target operation and integration with the HE-LHC in the current LHC tunnel is considered highly challenging.

The main parameters and performance aspects of the different options are compiled in Table 6.4. The potential integrated number of protons on target for FT operation is $\sim 1 \times 10^{19}$ PoT/y for both scSPS options, if a maximum extracted flux of 10^{13} ps^{-1} is assumed for 180 days of operation at 80% efficiency.

Power consumption depends on whether the injector complex is used only for injecting into the HE-LHC or also for a separate fixed-target programme. Various

Table 6.4. Main parameters and performance comparison of the different HEB options for HE-LHC, including the existing 450 GeV SPS.

Parameter	450 GeV nc SPS	900 GeV sc SPS	1.3 TeV sc SPS	1.3 TeV sc LHC
Circumference (km)	6.9	6.9	6.9	26.7
Injection energy (GeV)	25	25	25	450
Extraction energy (TeV)	0.45	0.90	1.3	1.3
Energy swing factor	18	36	52	2.9
Maximum field (T)	2.0	4.0	6.0	1.5
Injection field (T)	0.11	0.11	0.11	0.52
Dipole length (m)	6.2	12	12	12
Number of dipoles	744	372	372	1768
Number of quads	216	216	216	410
HEB injection time (s)	10.8	25.2	25.3	284
Ramp rate (T/s)	0.35	0.35	0.35	0.005
HEB cycle length (s)	19.2	39.6	45.6	510
HEB stored energy (MJ)	5.6	23	33	291
Total bunches	320	640	640	5600
Cycles to fill HE-LHC	20	10	10	1
HE-LHC filling time (m)	6.3	6.5	7.5	8.0

Notes. All machines except the 1.5 T normal conducting HEB in the LHC tunnel are considered to be single aperture machines (nc means normal-conducting and sc means superconducting).

Table 6.5. Estimated average electrical power consumption of the HE-LHC injector complex with a supercondcuting SPS, compared to the present injector chain, in dedicated injector operation only or with a concurrent fixed-target programme (sc means superconducting).

Injector Subsystem	Unit	2017 as LHC injector	2017 total	sc SPS as LHC injector	sc SPS total
SPS magnets	MW	11	34	2	6
SPS cryogenics	MW	–	–	3	10
SPS RF	MW	2	3	2	3
SPS other services	MW	4	11	4	11
North area	MW	0	23	0	23
PS complex	MW	16	30	16	30
Total	**MW**	**33**	**101**	**27**	**83**

scenarios are compared in Table 6.5, which shows that the power consumption for the superconducting SPS complex is expected to be significantly lower than the one of the present normal-conducting SPS.

7 Experiments and detectors

Table 7.1 shows the collision environment and some key parameters for the different hadron machines LHC, HL-LHC, HE-LHC and FCC-hh. For the HE-LHC c.m. energy of 27 TeV, the total inelastic pp cross section, multiplicity and average p_T of charged particles increase by less than 20% with respect to LHC. The rapidity distribution of benchmark SM objects like b-jets, VBF jets, H$\rightarrow 4l$ is slightly increased by ≈ 0.3 with respect to LHC. The HE-LHC uses a value of $L^* = 23$ m, equal to the LHC and assumes only minimal changes to the civil engineering infrastructure of the LHC

Table 7.1. Key values relating the detector challenges at the different accelerators.

Parameter	Unit	LHC	HL-LHC	HE-LHC	FCC-hh
E_{cm}	TeV	14	14	27	100
Circumference	km	26.7	26.7	26.7	97.8
Peak $\mathcal{L}$, nominal (ultimate)	$10^{34}\,\mathrm{cm^{-2}\,s^{-1}}$	1 (2)	5 (7.5)	16	30
Bunch spacing	ns	25	25	25	25
Number of bunches		2808	2760	2808	10 600
Goal $\int \mathcal{L}$	$\mathrm{ab^{-1}}$	0.3	3	10	30
σ_{inel} [243]	mb	80	80	86	103
σ_{tot} [243]	mb	108	108	120	150
BC rate	MHz	31.6	31.0	31.6	32.5
Peak pp collision rate	GHz	0.8	4	14	31
Peak av. PU events/BC, nominal (ultimate)		25 (50)	130 (200)	435	950
RMS luminous region σ_z	mm	45	57	57	49
Line PU density	$\mathrm{mm^{-1}}$	0.2	1.0	3.2	8.1
Time PU density	$\mathrm{ps^{-1}}$	0.1	0.29	0.97	2.43
$\mathrm{d}N_{ch}/\mathrm{d}\eta|_{\eta=0}$ [243]		6.0	6.0	7.2	10.2
Charged tracks per collision N_{ch} [243]		70	70	85	122
Rate of charged tracks	GHz	59	297	1234	3942
$\langle p_T \rangle$ [243]	GeV/c	0.56	0.56	0.6	0.7
Bending radius for $\langle p_T \rangle$ at $B = 4\,\mathrm{T}$	cm	47	47	49	59
Total number of pp collisions	10^{16}	2.6	26	91	324
Charged part. flux at 2.5 cm, est.(FLUKA)	$\mathrm{GHz\,cm^{-2}}$	0.1	0.7	2.7	8.4 (10)
1 MeV-neq fluence at 2.5 cm, est.(FLUKA)	$10^{16}\,\mathrm{cm^{-2}}$	0.4	3.9	16.8	84.3 (60)
Total ionising dose at 2.5 cm, est.(FLUKA)	MGy	1.3	13	54	270 (300)
$\mathrm{d}E/\mathrm{d}\eta|_{\eta=5}$ [243]	GeV	316	316	427	765
$\mathrm{d}P/\mathrm{d}\eta|_{\eta=5}$	kW	0.04	0.2	1.0	4.0
90% $\mathrm{b\bar{b}}$ $p_T^{\mathrm{b}} > 30\,\mathrm{GeV/c}$ [244]	$|\eta|<$	3	3	3.3	4.5
VBF jet peak [244]	$|\eta|$	3.4	3.4	3.7	4.4
90% VBF jets [244]	$|\eta|<$	4.5	4.5	5.0	6.0
90% $\mathrm{H} \to 4l$ [244]	$|\eta|<$	3.8	3.8	4.1	4.8
$\mathrm{b\bar{b}}$ cross-section	mb	0.5	0.5	1	2.5
$\mathrm{b\bar{b}}$ rate	MHz	5	25	250	750
$\mathrm{b\bar{b}}$ $p_T^{\mathrm{b}} > 30\,\mathrm{GeV/c}$ cross-section	μb	1.6	1.6	4.3	28
$\mathrm{b\bar{b}}$ $p_T^{\mathrm{b}} > 30\,\mathrm{GeV/c}$ rate	MHz	0.02	0.08	1	8
Jets $p_T^{\mathrm{jet}} > 50\,\mathrm{GeV/c}$ cross-section [243]	μb	21	21	56	300
Jets $p_T^{\mathrm{jet}} > 50\,\mathrm{GeV/c}$ rate	MHz	0.2	1.1	14	90
$\mathrm{W^+ + W^-}$ cross-section [245]	μb	0.2	0.2	0.4	1.3
$\mathrm{W^+ + W^-}$ rate	kHz	2	10	100	390
$\mathrm{W^+} \to l + \nu$ cross-section [245]	nb	12	12	23	77
$\mathrm{W^+} \to l + \nu$ rate	kHz	0.12	0.6	5.8	23
$\mathrm{W^-} \to l + \nu$ cross-section [245]	nb	9	9	18	63
$\mathrm{W^-} \to l + \nu$ rate	kHz	0.1	0.5	4.5	19
Z cross-section [245]	nb	60	60	100	400
Z rate	kHz	0.6	3	25	120
$\mathrm{Z} \to ll$ cross-section [245]	nb	2	2	4	14
$\mathrm{Z} \to ll$ rate	kHz	0.02	0.1	1	4.2
$\mathrm{t\bar{t}}$ cross-section [245]	nb	1	1	4	35
$\mathrm{t\bar{t}}$ rate	kHz	0.01	0.05	1	11

tunnel and caverns. In terms of acceptance and overall size, the detectors at the HE-LHC therefore are more similar to HL-LHC than to those of the FCC-hh, which assume significantly increased instrumentation in the very forward region.

The HE-LHC luminosity of $\mathcal{L} = 16 \times 10^{34}\,\mathrm{cm^{-2}\,s^{-1}}$ is however, significantly higher than the HL-LHC luminosity. The pile-up of 500 is about 3.4 times larger than at HL-LHC. It can therefore in a first approximation be assumed that detectors at the HE-LHC are ATLAS/CMS type detectors with challenges related to radiation and pile-up. Trigger and readout rates are closer to the FCC-hh detector requirements. To what extent the magnet systems of ATLAS and CMS can be reused will depend on the specific new subdetector concepts and also on the expected lifetimes of these magnets.

The hadron fluence in the innermost silicon layers is one of the key challenges for such a high luminosity hadron detector. The value is about four times larger than the HL-LHC at the same radius, and will increase with $1/r^2$ if the first layer is moved closer to the collision point. Since the fluence for the HL-LHC already poses a significant challenge to the phase II upgrades of ATLAS and CMS, dedicated R&D on radiation hard silicon sensors that can withstand hadron fluences in excess of $10^{17}\,cm^{-2}$ for the inner tracking layers is essential.

The increased radiation load is also a concern for the calorimetry. Cryogenic noble liquid calorimeters, as employed by the ATLAS experiment or silicon calorimeters, as planned in the forward region of the CMS phase II upgrade, are candidates for a detector at the HE-LHC. The rates in the muon systems permit the use of large area gas detectors similar to those used at the LHC.

To deal with the large pile-up of about 500, a high precision timing detector with a resolution of $<10\,ps$, as discussed for the FCC-hh detector, is an essential enabling technology. The total rate of charged tracks is about 4 times larger than that of the HL-LHC and about 3 times smaller than that at the FCC-hh. The rate of high energy jets is about 12 times larger than at HL-LHC and 6 times smaller than at the FCC-hh. The readout and trigger challenges are therefore more similar to the FCC-hh than to the HL-LHC.

As is the case for the FCC-hh reference detector, it is highly likely that the signals from the calorimeters and muon detectors can be digitised at the full bunch crossing rate of 40 MHz and sent to a first level trigger processor over optical fibres. Whether the tracker information can also be digitised and read out at 40 MHz or whether a dedicated trigger will have to reduce the tracker readout rate to a few MHz will depend on the communication technologies available in the future.

For HE-LHC physics studies, the performance of the ATLAS/CMS detectors for a pile-up of 1 is assumed. It is therefore assumed that there will be an ATLAS/CMS type detector with a rate capability and technology for pile-up rejection that allows detector performance equal to the present low pile-up performance of the LHC detectors.

8 Safety

8.1 Safety policy and regulatory framework

The concept study aims at demonstrating that hazard and risk control for a future collider is possible with best practices and industrial standards, which are complemented, where necessary, with techniques specific for a particle accelerator facility. The approach is introduced below by first presenting CERN's legal context and then the hazard and risk management in place for the existing accelerator complex. The subsequent sections show how occupational health and safety topics are addressed, which are specific for a particle collider, and how the risks associated with ionising radiation are managed. For the conceptual design, a two-stage process has been chosen: first, a hazard register lists the safety hazards that will be present at the facility and identifies those, for which standard best practices can be applied to control the associated risks. Second, a detailed analysis will be carried out, for the remaining safety risks, to assess the risk levels and to identify mitigation measures.

8.1.1 Legal context of CERN

CERN's status as international organisation requires that it defines a safety policy in a pro-active and consensus-based process with the host states (see Art. II 2

de l'accord de statut de 1973 entre le CERN et la France [246]). This approach is applicable for non-standard installations like the accelerators, the experiments and the technical infrastructure needed to operate these facilities. Where standard infrastructure dominates (e.g. offices, car parks and workshops), CERN ensures uniformity in the safety conditions across its sites, taking into account the laws and regulations of the host states and EU regulations and directives. Where uniformity cannot be achieved or where compliance is not required to ensure the proper functioning of the organisation, a dedicated risk management process is applied, including the planning, implementation and verification of risk mitigation measures.

8.1.2 Hazard register and safety performance based design

A systematic collection of safety hazards associated with the construction and operation of the accelerator complex is the starting point of the safety assessment. Hazard registers are an established technique in industry. To compile the register, a process-centred approach has been used [247]. In a first step, a systematic description of the processes during the life cycle of the accelerator facility has been established, based on the Project Breakdown Structure (PBS). Each process is characterised by *activities*, *equipment* and *substances* used or released. Hazards may emerge from these activities, equipments and substances at different locations.

As an example, the process of providing electrical power to accelerator magnets is active during commissioning and operation of the accelerator. It relies on transformers and power converters (equipment) at the surface and in underground locations. This equipment is at the origin of electrical hazards, noise and potential environmental pollution in case of dispersion of insulating fluids.

It is assumed that the relevant risks associated with the hazards will be mitigated by standard best practices, implementing compliance with laws and regulations of the host states, EC regulations and directives, international regulations, standards and directives and recommendations from technical or prevention organisms.

Where standard best practices cannot be applied or would affect the proper operation of the organisation, a performance-based design approach is used [248]. It is proposed to use a standard method like "Failure Mode, Effects and Criticality Analysis" (FMECA) [249] to identify those risks which remain unacceptable. From this starting point, the performance based approach is used. In this process, essential safety objectives, such as preservation of human lives or prevention of environmental damage, are defined. The safety performance of design choices is evaluated for different incident scenarios. If the objectives are met, the design can be retained as mitigation measure.

8.2 Occupational health and safety

The study has initiated a methodological approach in tackling occupational health and safety aspects. The hazard registry classifies relevant sources of risks to permit identifying those, which can be addressed by standard approaches and those, for which project-specific assessments need to be performed, followed by a definition of mitigation measures against residual risks. This preliminary activity has identified that two main hazards are present in underground areas: fire and oxygen deficiency (ODH). The latter is a residual risk that emerges after applying "safety-by-design" to cryogenic hazards, such as the avoidance of cold surfaces and functional measures such as combined vacuum and superinsulation blankets. This report, focusing on the feasibility and concept elements of a future particle accelerator research infrastructure does not permit the technical risk management files to be presented in a

Table 8.1. Safety objectives in the design-oriented study.

Life safety	Environmental protection	Property protection	Continuity of operation
Safety of authorised occupants (O1)	Limited release of pollutants to air (O4)	Continuity of essential services (O6)	Limited downtime (O9)
Safe evacuation or staging of injured occupants (O2)	Limited release of pollutants to water (O5)	Incident must not cause further incidents (O7)	
Safe intervention of rescue teams (O3)		Limited property loss (O8)	

Table 8.2. Fire scenarios in the design-oriented safety study.

Scenario	Description	Ignition source
Fire 1	Cable tray fire	Electrical fire
Fire 2	Cable drum fire	Hot work
Fire 3	Transport vehicle fire	Battery malfunction

comprehensive manner. It therefore only focuses on the presentation of the approach for the two main hazards (fire and oxygen deficiency). The results of the studies [250–252] are summarised in the following sections. The agreed safety objectives for these two hazards are listed in Table 8.1.

To create safe zones along the entire perimeter of the particle collider, smoke and fire resistant compartment walls are recommended to be installed every four accelerator lattice cells, each 548 m. Under normal conditions, their doors are open. The ventilation system is based on a pull-push scheme between adjacent shafts to create a longitudinal unidirectional flow. Smoke and ODH detectors initiate localised mitigation measures. A dedicated 350 mm diameter extraction duct traverses all compartments and can extract smoke or helium. The extraction for each compartment can be controlled individually. It is planned to have a fire fighting pipeline with an outlet at each compartment door.

8.2.1 Fire hazard

The most critical phases for a fire hazard are (1) the operation with beam, (2) a long shutdown and (3) a technical stop. During operation, all electrical systems are powered and potential ignition sources. During other periods, personnel are present and they may inadvertently cause a fire, e.g. during welding. Table 8.2 shows the three fire scenarios studied.

Following the performance based design methodology, the current LHC tunnel equipped with the planned safety measures was challenged with three different fire scenarios representing credible incidents in the HE-LHC underground tunnel structure. For consistency, the fire scenarios considered were the same as those considered for FCC-hh [253].

Only the life safety goal for occupants was evaluated during this initial study (O1–O3 in Tab. 8.1). For the sake of consistency, the same performance criteria used for the FCC-hh study were set to ensure tenability limits for the evacuees. These criteria comprised incident heat flux, temperature, visibility and exposure to toxic materials accounted for by means of fractional effective dose (FED).

Upon fire detection, the four doors delimiting the fire compartment and the adjacent ones will shut and the smoke/helium extraction duct dampers will only open in the fire compartment to create the highest possible extraction flow.

The smoke/helium extraction duct, always kept at a pressure below normal to optimise the reaction time, will start extracting smoke and creating a pressure cascade to reinforce smoke confinement. For the rest of the tunnel, air will be extracted via both shafts, maintaining evacuation paths over-pressured with respect to the fire compartment and clear from smoke.

This strategy was evaluated within the fire compartment by means of CFD simulations of the three accidental scenarios investigated. The simulation program is the Fire Dynamics Simulator (FDS) V 6 [254]. The pre-movement time and walking speed were defined according to standard recommendations [255] (British Standard PD 7974-6) and were further improved by adding some degree of uncertainty. The results showed that the heat flux, temperature and FED values to which evacuees are exposed are well within the acceptable thresholds stated in the performance criteria. However, for a single evacuation location visibility is locally reduced to below 10 m at 2 m height. The stratification is still maintained and visibility is unimpeded at 0.5 m height.

Based on the outcome of the simulations, it can be stated that the current design meets the life safety objective for occupants in case of fire. However, there is a very limited safety margin and it is strongly recommended that additional safety measures aiming at increasing the robustness of the design should be incorporated. The other safety objectives will be evaluated at a later stage.

Protection of the environment calls for a careful selection of fire-fighting agents (e.g. water, foam) which will be done at a later, detailed design stage. The system configuration will help keeping the release of smoke, chemical and radioactive contaminants to quantities as low as reasonably possible.

8.2.2 Oxygen deficiency hazard

An oxygen deficiency hazard arises from the release of asphyxiating cryogenic liquids (He, Ar, N_2) in closed environments, where they may displace oxygen during a sudden evaporation of the fluids. Commissioning and maintenance are the most critical phases concerning this hazard because of the presence of personnel in the underground areas.

The scenario considered for the oxygen deficiency hazard (ODH) study was an accidental and uncontrolled release of helium into the LHC tunnel, including the most critical commissioning and maintenance phases. Based on the current access restrictions in the LHC for operational periods where large helium release flows cannot be excluded, it is assumed that similar measures would be in place during the life of the HE-LHC. Therefore, the accident scenario chosen for the analysis was a release of 340 g/s gaseous helium into the LHC tunnel.

The evaluation of these studies linked to the cryogenic hazards were based on an initial safety assessment made for the "Release of Gaseous Helium in Tunnels" [256]. The major change is linked to the magnet technology and the requirement to have compartment walls in the tunnel every 548 m. The objective of the study was to determine whether an accidental release of 340 g/s produces a helium layer at the ceiling of the tunnel that is large enough to prevent successful evacuation of occupants.

The helium release is localised within one compartment. The compartment doors will remain open during a helium release. Gaseous helium rapidly warms up and rises to the compartment ceiling. In order to simplify the estimation, it is assumed that the longitudinal ventilation does not have an influence of the stratification of helium and that all helium is in the ceiling layer shortly after release. The maximum thickness

Table 8.3. Input data for the evaluation of an accidental release of helium in the tunnel.

Q_{He} $(\mathrm{kg\,s^{-1}})$	0.34
$V_{He}(\mathrm{m^3\,s^{-1}})$ @300K	2.12
a (m)	2
h (m)	0.8
A $(\mathrm{m^2})$	1.65
L (m)	548
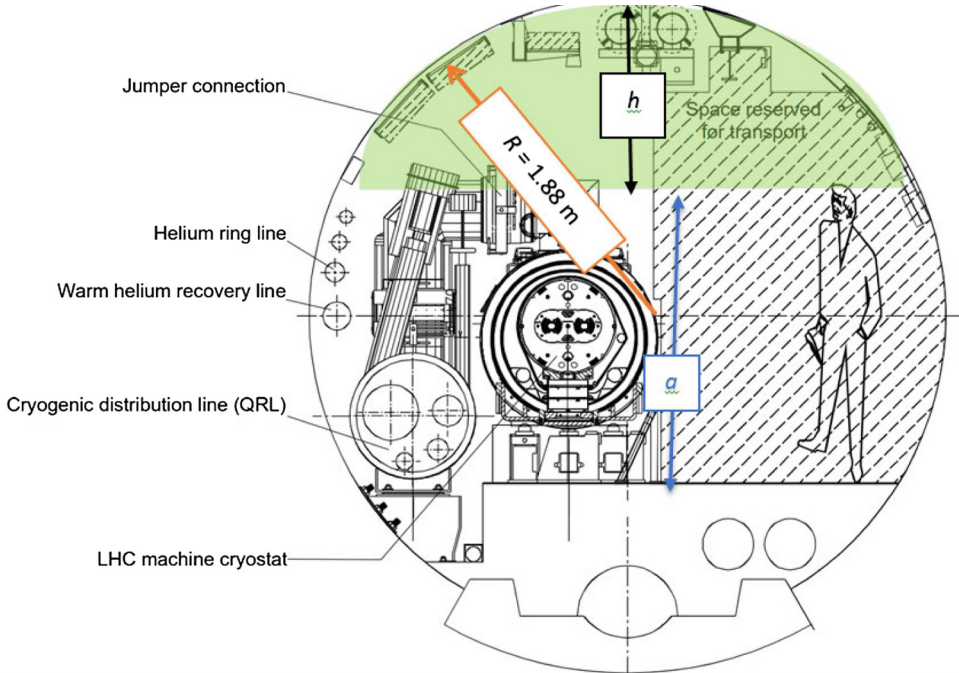
Fig. 8.1. Cross-section of the LHC Tunnel. The green area indicates the helium ceiling layer with cross-section area A and depth h. a is the height of the compartment doors and h the remaining height until the tunnel ceiling, 0.8 m.

of the helium layer at the ceiling is 80 cm, when its lower edge reaches the upper edge of the compartment doors and it can spill over to the adjacent compartments. Table 8.3 shows the input data used for the evaluation (see also Fig. 8.1).

It can be seen from Figure 8.2 that it would take seven minutes to fill a compartment with a helium layer of 0.8 m, for a gas temperature of 300 K. For a temperature of 273 K it takes almost eight minutes. Based on the data used for the FCC-hh magnet concept, the estimated volume to empty the helium inventory can be determined (c.f. Tab. 8.4).

If the extraction duct was also used for the management of the released helium, it would be operational at full capacity in the sector concerned for four minutes after the ODH alarm. The capacity of the system is estimated at 2200 m³/h, with an extraction efficiency of 80%. The remaining 20% of the volumetric flow rate is air.
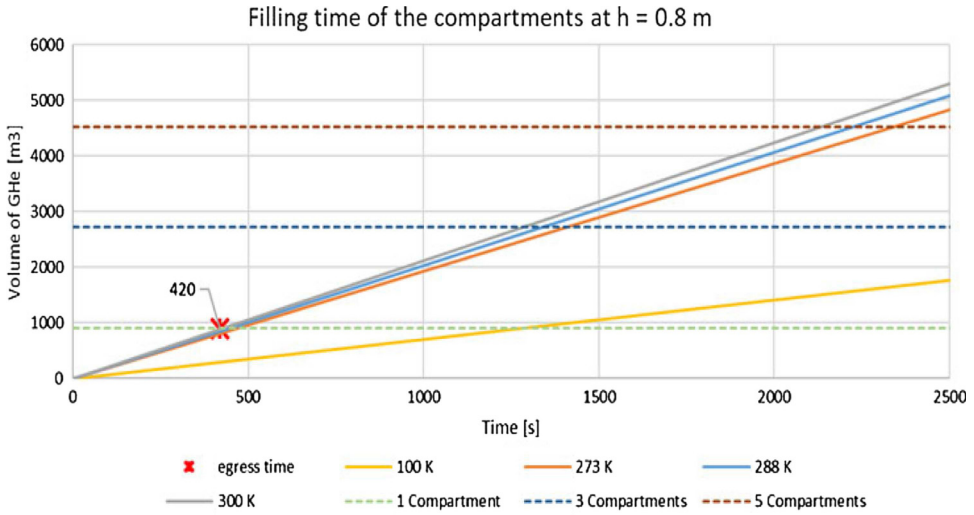
Fig. 8.2. Volume of gaseous helium in the compartments as a function of the gas temperature and time. The crossing of the dashed horizontal lines mark the time from the beginning of the release to when the helium penetrates the next adjacent compartments.

Table 8.4. Parameters used for FCC-hh dipole magnets.

$V_{\mathrm{LHe}}(\mathrm{lm}^{-1})$	33
L (m) Sectorisation (corresponding to 1 cell)	137
V_{GHe} (kg)	670

Main conclusions

– Personnel access to the underground areas is forbidden in operational phases where the potential helium release exceeds 340 g/s. In LHC, this is the case for powering phase 2. A similar assessment of possible helium release rates must be conducted for the HE-LHC magnets.
– Assuming the tunnel occupants are not in the "turbulent zone" of the helium release [256], they would be minimally affected by the helium released, which is accumulated at the ceiling of the tunnel. Safe evacuation from the tunnel is necessary. As an additional precautionary measure, personnel are equipped with self-rescue masks.
– The temperature of the gas (between 273 and 300 K) does not have a major effect on the time to fill the 0.8 m deep volume at the ceiling of one compartment.
– If the mass flow of the release is constant, it would take about 30 min to empty the helium inventory. By that time, three compartments in a sector would have been filled with helium to a level of 0.8 m from the ceiling.
– The addition of the He extraction would only be considered as a compensatory safety measure for flow rates above 6000 m^3/h.
– Further studies on the dynamics and influences of the boundary conditions in such an environment are necessary. A simulation with a Computational Fluid Dynamics (CFD) program is recommended.

At this stage, the ODH analysis uses a simplified approach on a qualitative engineering level, mainly due to the level of technical detail at this stage of the study. A quantitative approach will be used for the technical design report.

8.3 Radiation protection

For the mitigation of risks associated with ionising radiation, the standard prescriptive methods of the existing CERN radiation protection rules and procedures have been used. Risks resulting from ionising radiation must be analysed from a very early design phase onwards and mitigation approaches must be developed. Design constraints will ensure that the doses received by personnel working on the sites as well as the public will remain below regulatory limits [257,258] under all operation conditions. A reliable and continuously operating radiation monitoring system will therefore be an essential part of the system implementing risk control measures.

The HE-LHC will be comparable in terms of radiological hazards to the LHC after its high luminosity upgrade. These are reliable sources of experience to take into account when planning the radiation protection measures during the design phase. The main difference for the HE-LHC compared to the HL-LHC is the higher beam energy which will eventually lead to higher activation levels in some sections of the accelerator and experiments.

Radiation protection is concerned with two aspects: protection of personnel operating and maintaining the installations and the potential radiological environmental impact. The second topic is addressed in Section 10.2.1. To enable the assessment of the potential radiological risks to the personnel working on the sites, the radiological hazards are classified by their sources: (1) particle beam operation, (2) activated solids, liquids and gases.

The HE-LHC will be housed in a modified version of the existing LHC tunnel and infrastructure. As parts of the LHC tunnel will be radioactive, dismantling, civil engineering and installation works in the tunnel will require specific attention and planning. Decommissioning and dismantling of the LHC is a project that requires separate planning. Intervention techniques and waste management must be adapted to the radioactive environment. Standard operating procedures and technologies will be adequate to address this topic.

8.3.1 Particle beam operation

Radiation hazards from high energy particle beams arise from their interaction with matter and other particles. Shielding protects personnel by absorbing the primary radiation and the subsequently generated stray radiation. An access control system prevents people from accessing hazardous areas. An interlock system prevents beam operation in the case of an unauthorised access. An emergency stop system ensures that the operation with beam is terminated quickly and in a controlled way if needed.

The LHC is currently operated with access to underground areas prohibited, with the exception of the experiment service caverns. For the HE-LHC, these access conditions will be sufficient to protect against undue stray radiation levels from particle beam operation in accessible areas.

A detailed reassessment to be performed during a detailed technical design phase needs to reconfirm or adjust the delimitation between radiation and non-radiation areas underground (mainly service caverns of the experiments) and to redefine the accessible and non-accessible radiation areas during beam operation. This analysis will take into account the energy and intensity increase, as well as the design objectives adopted in terms of doses mainly for incident scenarios.

The only locations where radiation can possibly stream to the surface are at the existing shafts above the experiments. They can be equipped with additional top shielding if required. However, it is expected that no additional top shielding compared to the current LHC situation is required, given the scaled shielding effect of the experiments at HE-LHC.

8.3.2 Activation of solids

Activation of solids represents a potential hazard to persons through exposure to gamma radiation during interventions inside the accelerator tunnel such as in-situ maintenance or handling of radioactive parts. The radiation levels differ considerably amongst the various sectors of the accelerator and depend on the type of beam operation and on the time that has passed since the machine was stopped. Locations close to the interaction points, the beam cleaning insertions as well as the absorbers of the beam dumping system, will exhibit the highest radiation levels from activation, exceeding those at the LHC. Compared to the nominal LHC operation, an average increase by a factor 4 of induced radioactivity concentrations and residual dose rates is currently assumed as a result of the energy and intensity increase. Optimisation of activation levels can be achieved through an appropriate choice of materials in the design phase of the new accelerator components.

The main arc sections of the LHC are exposed to very low radiation levels. The expected increase for HE-LHC will remain low enough to apply current maintenance intervals and techniques. Further use of automated and remotely controlled interventions are one way to reduce the exposure of personnel and these are are already being considered for the HL-LHC. These techniques will become even more important at the HE-LHC, especially in the sections next to the high luminosity interaction points and the collimation regions.

Activated materials are routinely removed from the accelerator tunnel and experiment caverns for maintenance or disposal. The operations expected for the HE-LHC will generate a similar amount of materials to that currently handled within the existing infrastructure at CERN [259]. Corrosion and machining of activated materials can produce dispersed activated solids in the accelerator and workshop areas. Experience from high energy accelerators at CERN shows that this does not lead to relevant radiation risks; therefore, standard procedures apply.

8.3.3 Activated or contaminated liquids

Infiltration water and leakage water from closed water circuits will be collected by the tunnel drainage system. The water will be pumped to the surface sites for collection and further treatment before being cleared and released. Continuous monitoring and confinement will ensure that no activated and/or contaminated water will be released. The demineralised water filtering units collect and concentrate radioactive particles and will be treated through standard procedures.

Ventilation cooling units for the tunnel and experimental areas can, under certain operational conditions, concentrate airborne radioactivity in their condensates, mainly in the form of tritiated water. This liquid waste water will be collected and treated according to standard procedures. The activation of liquid helium in the superconducting circuits results in the production of small amounts of tritium. Sufficient storage capacity for slightly activated helium will be installed at the various sites.

8.3.4 Activated or radioactive gases and radioactive aerosols

Air in the accelerator and experiment areas will become radioactive during beam operation. The energy and intensity increase for HE-LHC and the required safety margin calls for the implementation of an air recycling system. The main LHC ventilation system must be refurbished and complemented to operate in full or partial recycling mode to limit releases to the environment. Areas will be ventilated with fresh air before allowing access to avoid undue exposure of personnel. Areas with different activation potentials will be separated, such that only those areas are vented where access is required, thus avoiding unnecessary releases of radioactive air. Experience shows that outgassing from activated concrete or radon decay products will only be present in small concentrations in the tunnel air because they are continuously removed by the ventilation system. Dust activation and airborne corrosion products are no relevant sources of exposure to intervening personnel, since aerosols are continuously removed by the air treatment systems.

9 Energy efficiency

9.1 Requirements and design considerations

Energy efficiency is a topic which is high on the societal agenda in general and must consequently also be a core value of any future research facility, especially energy-intensive facilities like particle accelerators. It concerns the availability and cost of electricity, the reduction of climate-relevant emissions, and other side-effects linked to energy production, transmission and conversion. Operating the HE-LHC in an energy efficient way will enhance its public acceptance. Moreover, the HE-LHC is an opportunity to drive the evolution of energy-efficient technologies leading to socio-economic benefits. A sign of the importance of the topic is the "Energy for Sustainable Science" workshop series [260] established several years ago. Concerted efforts are being made in the framework of the EuCard2 Project [261] (Work Package 3 – Energy efficiency of particle accelerators [262]) and the ARIES Project [263] in the EC Horizon 2020 Research and Innovation Programme. An overview of activities in view of greater energy efficiency of particle accelerators can be found in [264].

Energy-efficient approaches can be categorised in three levels. The first level, with the highest priority, is to consume less energy by making appropriate design choices. Using Nb_3Sn based superconducting magnets is the appropriate choice if this machine has to follow the HL-LHC programme without a gap. The second level aims at using energy more efficiently while providing the same level of service or performance. Examples are the use of high-efficiency klystrons and a more efficient cryogenic refrigeration infrastructure, such as one based on a neon-helium light gas mixture. Finally, recovering and reusing energy for other purposes, ranks third. A typical example is to recover waste heat from cooling circuits, using it within the research infrastructure and feeding it into an energy storage system from which it can be used later for district heating purposes.

Applying fine-grained monitoring of energy use will help to raise energy-awareness, control the peak power and energy losses and allow better predictions of energy use to be made. All equipment or facilities not currently in use will be switched off or ramped down. Any new surface buildings will be constructed to follow high environmental standards, bearing in mind that by far the dominant share of the energy consumption comes from the operation of the accelerator. As far as possible, electrical energy will be purchased from renewable sources. Generally, it should be noted that reconciling the demand for highest performance of the facility
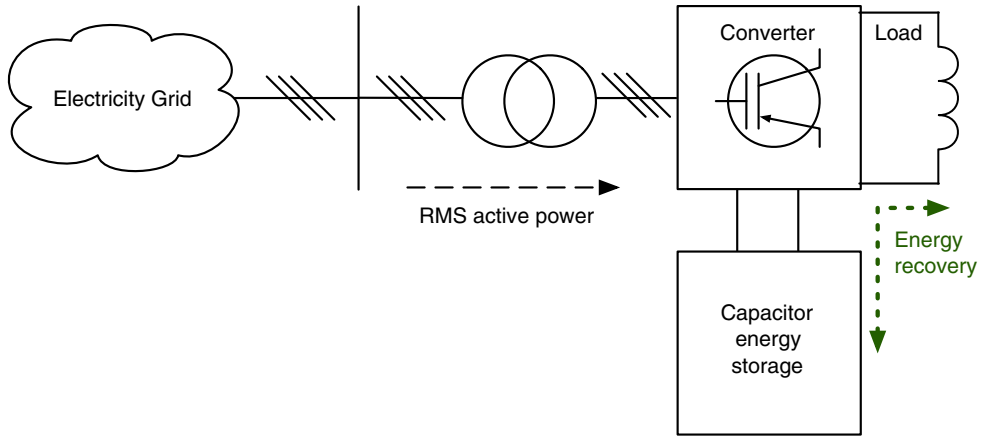
Fig. 9.1. Simplified schematic of the principle of combining switch-mode converters with energy storage.

over extended running periods with sustainability and reasonable/acceptable energy use is not a simple task. Experts specialising in matters of energy efficiency or energy saving will be consulted to devise a comprehensive and coherent concept from the outset.

The collider will be operated like the injector complex in a cyclic way, creating a cyclic peak power demand from the power grid. Different ways of supplying power are considered:

– *Supply of peak power from external network*: by the external network. This is the simplest solution; it might, however, require partial reinforcements of the external network, which is operated by Réseau de transport d'électricité (RTE).
– *Use of energy storage systems*: this concept uses a combination of switch-mode power converters (Fig. 9.1) and local energy storage systems to power magnet circuits. Peak demands during the ramp-up are fully or partially provided by the storage system. During the ramp-down the energy is recovered and fed back into the storage system. This principle is already being used to power the PS magnets (POPS system) and will also be used to power the PS Booster (PSB) at CERN after its upgrade to 2 GeV (POPS-B). The energy storage system can be based on a set of different energy buffering technologies such as high voltage DC capacitors and batteries. This concept eliminates the positive power peak during ramp-up and the negative during ramp-down, thus resulting in a flat power profile seen by the grid. As a consequence, the external power transmission and the machine internal distribution networks can have lower component ratings for substations, cables and transformers, and will also cause less distribution losses.

9.2 Power requirements

The HE-LHC will be operated according to the operational model discussed in Section 2.5. The electrical power requirements of the various systems during physics operation at the highest energy are listed in Table 9.1.

The overall collider peak power requirement of about 135 MW of this particle collider with its experiments during the flat top phase of each cycle has to be compared to the LHC electricity consumption of 98 MW and the estimates for the HL-LHC power consumption of about 110 MW. The LHC delivers beams with half the collision

Table 9.1. Power requirements of accelerator subsystems for the highest performance operation period during the luminosity production phase at the flat top of the cycle.

Subsystem	LHC (MW)	Electrical needs (approx. MW)
Cryogenics	39 (+ 11 for HL-LHC)	49
Radiofrequency	7.7	7
Magnets	7.1	20
Cooling and ventilation	9.4	11
General services	10	11
Four experiments	20.5	21
Data centres for four experiments	3.5	16
Injector complex	60 (with SPS)	27 (with superconducting SPS)
Total	**157** (168 for HL-LHC)	**162**

energy and 15 (LHC) to 3 (HL-LHC) times lower peak luminosities. This electrical power requirement is the result of a combination of energy-efficient designs and the use of novel, energy savings technologies in numerous accelerator subsystems.

The power requirement figure for the cryogenic system includes the cooling of the main ring magnets, the beamscreen, the insertion-region quadrupoles, the superconducting link to distribute the power for the magnet system and the RF system. To minimise the overall cryogenics power required for the main ring magnets the temperature of the beamscreen was optimised to about 50 K, as compared with 5–20 K used for the LHC beamscreen, in view of the much higher synchrotron radiation heat load (see Sect. 3.3.2). This allows the synchrotron radiation heat load of 200 kW to be extracted with a total electric power of 4 MW. A comparable amount of heat may arise from magnetisation effects during the ramp.

Losses of the order of 5–7% in the electrical distribution chain (e.g. magnetisation losses in transformers) have to be added to calculate the power to be supplied by the grid.

Using similar data for other significant phases in the HE-LHC operation cycle (injection, ramping) and incorporating the projected yearly operation programme, one obtains an energy consumption that is comparable to CERN's energy consumption today (about 1.2 TWh in 2016).

9.3 Energy management and saving

One of the principal challenges of the 21st century will be to develop solutions for the sustainable use of energy. In this context, one of the key design aspects of HE-LHC must be a strict focus on energy efficiency, energy storage and energy recovery. This project can and must be used as a technology driver, pushing towards more efficient ways to use electrical and thermal energy.

The foundation for sustainable energy management is real-time energy monitoring, for example using smart meters. This opens the possibility to precisely predict and optimise the overall powering profile, with the objective of reducing the peak power as well as the electrical losses. For the reduction of the peak power demand, cyclic loads of the injector chain also need to be taken into consideration.

By systematically applying the concept of energy storage for the powering of the magnet circuits, the HE-LHC will be able to recover a significant part of the energy stored in the magnets. When combining energy storage with complementary measures such as optimisation of the power cycles, the costs for the electrical infrastructure as well as for electrical losses can be greatly reduced.

Electricity transmission over long distances and voltage step-down or step-up leads to power losses. The overall losses of a conventional transmission and distribution network range between 5% and 7%. Power line losses are resistive losses due to the Joule effect. Transformers contribute with load losses which will vary according to the load on the transformer and no-load losses which are caused by the magnetising current needed to energise the transformers and which are steady losses. The proposed baseline transmission and distribution scheme aims to provide the required level of availability, maintainability and operability from the early concept phase onwards. As an example, where needed, two 66/18 kV transformers are operated on access points in parallel, each at a nominal load level of 50%. Such a configuration responds to the above mentioned, non-functional requirements, but it is not optimised for energy efficiency. Alternative schemes aiming at improving the overall efficiency of the transmission and distribution network while maintaining the required level of availability, maintainability and operability therefore need to be studied. Industrial partners will lead the development, potentially demonstrating the technology in a pilot scheme at CERN's LHC so that a system at acceptable cost and with the required level of reliability can be obtained from market suppliers when needed.

The power demand is particularly high during ramping-up of magnets. With the proposed powering layout (see Sect. 3.8) and the baseline ramp-up time of 20 min, the main dipoles would require a peak power of 85 MW. This value can be reduced by having a different ramp shape, ramping the circuits up with constant power instead of constant voltage. Extending the time of the ramp is another way to reduce the peak power. For instance, using a constant-power ramp over 30 min, the peak power for the main dipole circuits will be reduced to 25 MW.

If the power for ramping up the collider were to be drawn from the external supply, the power grid would need to be significantly reinforced. Despite this additional equipment, impacts on the grid would still occur. Instead of drawing the power directly from the grid, it could also be taken from local storage, typically in the form of batteries, high-voltage DC capacitors, or a combination of different technologies. Examples of this have already demonstrated and are being gradually implemented in the new power converter systems of PS and PSB at CERN. This has the advantage that the energy stored in the magnets can be recovered and fed back into the storage media, from where it can be drawn again during the next ramp. 1232 magnets each returning 37 MJ per cycle can provide ∼38 MW to significantly reduce the peak power needed during the next acceleration cycle. Depending on where the local energy storage is located, this approach would also reduce the cross section of the cables supplying the power converters and the dimensions of the sub-stations and transformers.

The RF system energy efficiency can be improved by optimising the electrical to RF power conversion efficiency and the cryogenic refrigeration system energy consumption. With new bunching technologies for high-efficiency klystrons, efficiencies are expected to rise from 65% to above 80%. These improvements reduce the water cooling requirements by the same amount. The cryogenic losses can be reduced by improving the static and dynamic losses of the cavity cryomodule. The static losses in an optimised cryomodule are expected to be up to 40% lower than in the LHC. Recent findings on alternative cavity materials promise real progress in cutting the dynamic losses [144].

A future particle collider will use a cryogenics system based on a neon-helium mixture (nelium), which leads to electrical energy savings of about 8% with respect to the LHC-type infrastructure. Further electrical power savings leading to about 10% savings with respect to the LHC can be achieved by improving the efficiency of the 40–60 K cooling stage. This includes improvements in the technology of turbo-expanders and recovering energy from the system. Additional improvements may be achieved

with centrifugal compressors on the helium cycle. However, such developments are on a long time-scale and are, therefore, not considered at this stage.

9.4 Waste heat recovery

Currently, a project is being implemented to connect the cooling system of LHC at Point 8 to a "thermal energy exchange" loop which will supply a new industrial zone near Ferney-Voltaire (France) with warm and cold water circuits for both heating and refrigeration purposes (see Fig. 9.2) [265]. This is a hybrid system, consisting of waste-heat recovered from cryogenic machinery that is stored by heating the ground and which is made available via geothermal probes. Similarly, plans have been developed to feed waste heat from LHC Point 1 into CERN's distributed heating system. Installations of this type can also be envisaged for the (other) HE-LHC sites. However, the waste heat can also be supplied directly or through storage in dedicated buffers rather than in the ground. Although a significant potential for waste heat recovery from HE-LHC exists, the needs and opportunities and the infrastructure conditions need to be evaluated for the specific site situation (e.g. whether a distributed heating system exists already, or whether it could be implemented for a new industrial or housing area close to a surface site) and for each specific technical system. Potential applications of such recuperated heat are being envisaged. The definitive energy recovery potential depends on the developments planned in the vicinity of the surface sites and must be studied in collaboration with the host states.

The amount of recoverable energy increases with the proximity to the consumer and also with the temperature of the medium, typically water which is at 10–15°C above ambient temperature. How much this can be increased, by e.g. operating specific equipment at higher temperatures, will be studied. The most promising candidates for waste heat recovery are the cryogenic plants, which are the top electrical energy consumers, and the conventional cooling systems. The host states have requested that an effort is made to reduce the water consumption with respect to today's operating installations.

It should be noted that the host state representatives expect that project owners develop a plan in cooperation with industrial and public partners to ensure that ongoing efforts on a transition towards a sustainable and circular society are given priority. This is comparable to approaches which are currently being developed in the frame of smart-city projects.

Another potential area of interest is the return to the supplier of cooling water after use for subsequent heating purposes. GeniLac[1], a 280 MCHF investment project close to the United Nations district (Geneva, Switzerland) with a total cooling capacity of 280 MW, can be further investigated with a view to optimising the overall energy balance. The cooling water could also be transported to remote points through the tunnel. This study should take the distances from potential consumers and the evolution of urban areas up to the middle of the century into consideration. Potential consumers include, first of all, public institutions such as healthcare providers, schools, public buildings and industrial zones. Next, innovation potential such as indoor farming, health care centres and support for private district heating can be considered.

A third concept involves a step increase of the water temperature in the outer circuits such that the heat supplied becomes an interesting resource for industries such as chemical and food processing. Systems for vapour generation stepping up

---

[1] https://www.genie.ch/project/h/genilac-une-innovation-energetique-majeure-et-durable-pour-geneve.html
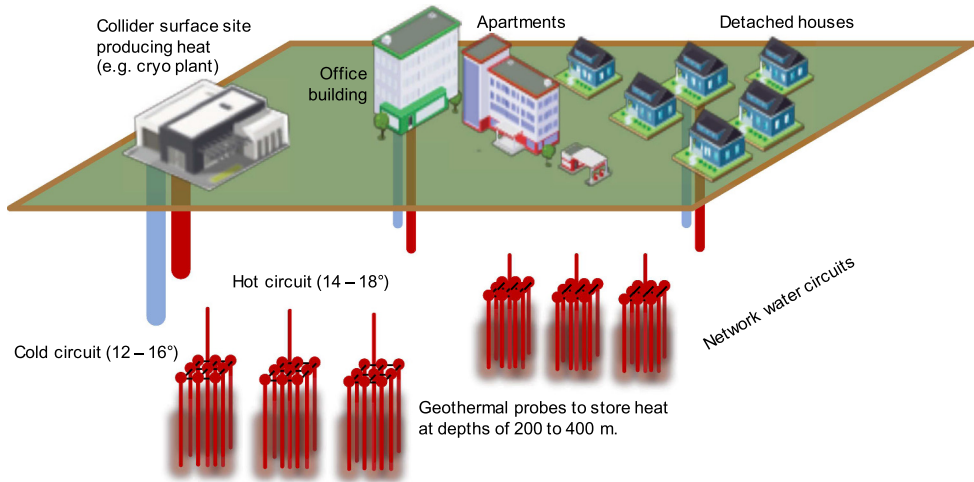
Fig. 9.2. Concept of a heat recovery facility based on a thermal network. The concept is similar to a project, which is currently under construction in the vicinity of CERN. In that project, waste heat is supplied from LHC point 8 to consumers in an industrial zone in Ferney-Voltaire, France. The distance between the LHC surface point and the industrial zone is 2 km.

from 25°C quickly become economically feasible [266], but a client needs to be close to the heat production source and willing to engage in a project that does not require the research infrastructure to function as a reliable energy supplier.

Eventually, direct power generation from waste heat can also be envisaged. Today, the effectiveness of such systems is still low, in the few percent range, but industrial interest [267] in increasing the efficiency of industrial plants is driving R&D activities, for instance via ORC [268] devices. For a large-scale research facility with a system that generates of the order of 100 MW of heat, even modest gains from converting heat into electrical or mechanical energy can be beneficial, particularly considering technological advances on a time scale of twenty years.

10 Environment

10.1 Requirements and approach considerations

10.1.1 Legal requirements

For the correct operation of CERN's facilities, its status as an international organisation requires that it establishes the requirements and constraints concerning the management of its environmental impact in a pro-active and consensus-based process with the host state on whose territory the installation lies (see Art. II 2 of "L'accord de statut de 1972 entre le CERN et la France" [269]). Where there is standard infrastructure on the surface sites (e.g. office buildings, car parks, ordinary workshops), CERN implements the national laws and regulations that apply at the location where the facility is located (see also "Art. II Convention entre la France et la Suisse de 1965" [270]). A specific process is necessary for the non-standard installations like the accelerators, the experiments and the technical infrastructure needed to operate these facilities. Different rules apply to a project with underground infrastructure which crosses the international border and which has surface sites in both Switzerland and France:

Underground infrastructure. In Switzerland, underground volumes below a depth that is considered *useful* for the land owner is not subject to the acquisition of rights-of-way and the law applying to private property. A communication from the Département Fédéral des Affaires Étrangères (DFAE) on 16 July 1982, informs CERN that it is exempt from right-of-way acquisition regulations for the LEP/LHC underground structures. In France, land ownership extends to the centre of the earth. Therefore either a process to acquire the underground volumes or to acquire the rights-of-way needs to take place. For both host states, CERN remains liable for any potential impact on the population and the environment resulting from the construction and operation of underground and surface installations.

Surface sites. The land plots for surface sites need to be acquired or leased in both host countries. According to a preliminary study carried out with an environmental impact assessment contractor [271], in Switzerland, an environmental impact assessment needs to be performed when new car parks with more than 500 places are constructed or if per year more than 10 000 t of excavation material are processed on Swiss territory with the purpose to reuse that material [272]. The "Ordonnance relative á l'étude de l'impact sur l'environnement (OEIE, Oct. 1988 and 2016)" and the manual "L'étude de l'impact sur l'environnement (EIE) (2009)" [273] define the scope and contents of the assessment. In France, a recent law revision[2] introduced a new environmental impact management process [274]. This new process explicitly requires a public consultation process on the scope, objectives, socio-economic potential and the impact on the development of the territory that needs to take place well before a specific technical design is developed and before a decision to construct is taken[3]. The host countries require an early and continuous involvement of the population in the project development and construction preparation phases that goes beyond information exchange. It calls for an active participation, giving people the possibility to contribute in well-defined and limited ways in shaping the project and in particular in developing the potential for added value. Consequently, France and Switzerland require that the initial assessment process is carried out from the early design phase onwards, followed by regular reviews of the effectiveness of the mitigation measures and assessment of residual or new impacts which become apparent during the construction and operation phases.

Both host states have regulations and laws concerning the continuous assessment and limitation of environmental impact for a variety of different topics. While the processes comprise very similar topics, the organisation of the information and the reporting templates are different for the two host states. In Switzerland the impact study may be limited to certain topics depending on the project needs, whereas in France all topics need to be discussed. In Switzerland the reporting is topically structured and in France the reporting is chronological across the entire project life cycle.

Since the project is international, the Espoo agreement applies [275]. CERN has to ensure that both host states are informed about the effects of any new infrastructure project in their country and the effects on the neighbouring countries. This includes for instance the use of energy, consumption of water, traffic and the management of waste across the borders.

---

[2] https://www.ecologique-solidaire.gouv.fr/levaluation-environnementale.
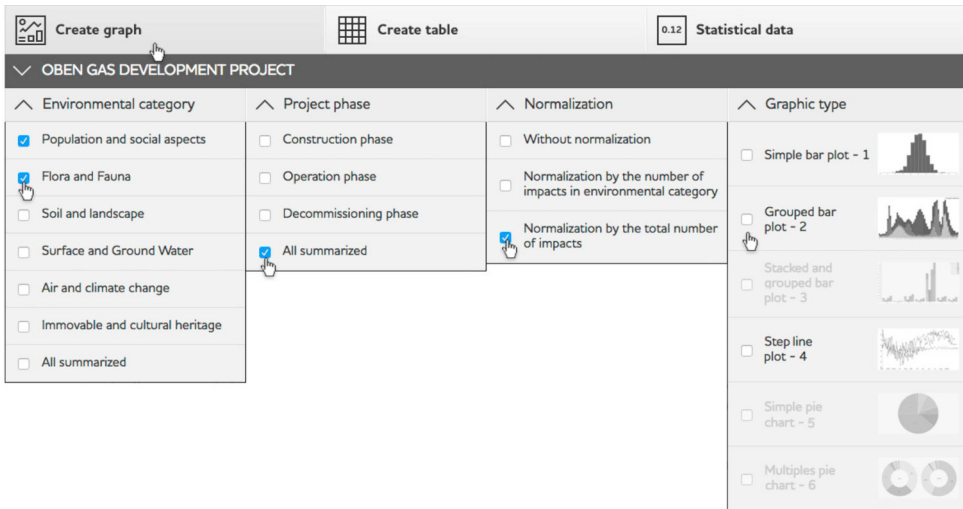[3] See also Art. L121-15-1 of law 2018-148 of 2 March 2018.

Fig. 10.1. Example of a continuous environmental impact assessment system supported by an information system.

10.1.2 Environmental compatibility management concept

The international nature of the project and the similarity of the surface points suggest a uniform and streamlined framework to carry out an environmental impact assessment across both host states. This approach splits the project into locations (e.g. underground structure, individual surface points, associated infrastructures), topics relevant for the impact assessment (e.g. water, air, noise) and the life cycle phases of the project (e.g. construction, operation, maintenance and retirement). Different requirements and constraints apply to the various locations and phases. For some it may be necessary to meet the standard national guidelines of the relevant host state or, for some particular installations, the guidelines need to be agreed between CERN and the host state on a case-by-case basis.

It is planned to have a central, uniform platform to manage the analysis, the assessment of proposed mitigation measures, the follow up of the effectiveness of mitigation measures and the analysis of the residual impact. This platform will permit the extraction of information according to the specific needs of the individual host states. Specialised companies and software solutions exist and should be used whenever possible (e.g. Envigo by eon+, see Fig. 10.1). A market survey and competitive selection process should be performed in cooperation with the host state partners in order to ensure that a suitable set of experts and tools are selected for this process. It is considered good practice in Switzerland that the owner of a large-scale project delivers a "Notice d'Impact sur l'Environement (NIE)", which is more comprehensive than the minimum required environmental impact assessment. The uniform framework mentioned here permits this approach.

The need to perform the environmental impact assessment and management process before a decision to construct is made, calls for the preparation of the assessment framework with the help of experienced consultants and the host state authorities in the years 2018–2020. Given some basic infrastructure, consultants and authority partners who know the project vision and goals can work with the scientific and engineering team until the design has reached maturity by 2023. By this time, CERN must have reached consensus with the authorities and the population that permits the formal initiation of a public consultation process as required in both host states.

The process is considered lengthy in both countries and is expected to require a few iterations. The goal is to obtain clearance to submit a request for construction permits by 2026, i.e. before an international consortium (e.g. the CERN member states or an international consortium bound by a memorandum, a letter of intent or a similar type of collaboration agreement) takes a formal decision to build the facility.

10.2 Environmental impact

10.2.1 Radiological impact

The hadron collider will operate at twice the beam energy of the LHC, causing higher radiation and activation levels in some parts of the accelerator and experiments. The potential radiological environmental impact comprises (1) dose from stray radiation emitted during beam operation, (2) dose from radiation emitted by radioactive materials and waste, (3) operation of ion sources and X ray emitting devices and (4) the dose from release of activated water and air. Safeguards will be included in the design of the accelerator infrastructure to control the impact on the environment. Dedicated monitoring systems and procedures will ensure continuous parameter recording and auditing throughout the entire operational phase of the facility and will facilitate control of the impact. LHC operational experience shows that the radiological impact on the environment and population are well below the legal limits. Since the beginning of the operation of the LHC, levels of stray radiation measured on surface sites remain negligible. The effective dose received by the public exposed to atmospheric and effluent releases of the existing particle collider remain below $10\,\mu$Sv/year. Release levels and dose values are regularly reported to the host states [276]. This experience provides confidence that the particle collider described in this report can indeed be operated in compliance with the host-state laws and regulations.

Like the LHC, the accelerator will be located at least 50 m below the surface and the experiment interaction points will be around 100 m below ground level. There will be no publicly accessible underground infrastructure. Therefore sufficient shielding against stray radiation from beam operation exists at all times. Two scenarios need to be considered to estimate the environmental impact: continuous beam losses during the operation and the effect of a total loss of the stored, high energy particles. In both cases, 15 m of lateral shielding by rock is sufficient to ensure a negligible impact on the environment and population [277,278]. Muon radiation emitted from losses in the plane of the accelerator will be attenuated by hundreds of meters of rock. The shafts are the only direct connections to the surface. At the interaction points they are sufficiently deep to exclude radiological impact from stray radiation [279]. Additional concrete slabs could be placed on top of the shafts to exclude residual impact from scattered radiation.

Activities involving handling, transport and storage of radioactive materials and the operation of X-ray emitting equipment on the surface sites are well regulated and are no different from current operations at CERN. The standard procedures in place within the current framework of radiation protection at CERN are well developed and proven to effectively control the radiological impact.

Beam operation activates air and potentially water close to the machine. The potential environmental impact originating from these sources is addressed as follows:

– *Air activation*: redundant, partially or fully recycling ventilation systems will limit the release of gaseous isotopes (mainly short-lived) during beam operation. This operation scheme is different from the LHC and has the potential to help achieve annual doses to members of the public lower than those with LHC [276].

Aerosol releases are expected to be insignificant due to the low activity content and efficient air filtration at the release points, similar to the LHC. Long term experience at many accelerator installations confirms this estimation [276].

– *Water activation*: drain water, raw water and demineralised water in the accelerator tunnel can become activated during beam operation and can carry trace amounts of radioactive corrosion products. Demineralised water circuits will be operated in a filtered, closed circuit. Leakage and infiltration water will be collected in the tunnel and will be pumped to retention and treatment basins at the surface. The water will be continuously monitored so that release will only occur after clearance. Experience shows that radioactivity in water is not a relevant source of radiological impact on the environment at the LHC [276]. The production rate of radioactivity in water at the future collider is expected to be lower or equal to the LHC, given the possibility to optimise pipe routing and avoid high activation areas [277].

– *Ground activation and migration of radioactivity towards the biosphere*: a limited amount of rock around the tunnel will be activated. Along the arcs, the largest part of the collider ring, activation remains at very low levels, well within the set limits [277]. Sections with higher activation potential (e.g. collimation regions, regions close to the high luminosity interaction points) will be located in rock with negligible water migration risk so that transfer to the biosphere can be avoided. Detailed ground investigations at an early design stage phase must be carried out to optimise the tunnel placement. Considering the low levels of concentrations produced [277] and the small residual risk, no radiological impact is expected. Effective mitigation measures to limit the rock activation, such as additional wall shielding can be implemented, if necessary.

– *Solid materials*: equipment and solid materials removed from the accelerator area can be radioactive. Their handling, transport, storage and elimination is subject to regulations and processes already in place for the operating installations at CERN. No radiological exposure is expected in the environment from these tasks.

The impact of ionising radiation on personnel during operation and maintenance phases, as well as the management of radioactive waste are described in Section 8 (Safety) and Section 10.3 (Waste Management), respectively.

10.2.2 Conventional impact

A preliminary review of underground and surface sites has been performed with expert organisations in France and Switzerland [271,280] for the scenario of a particle collider in a new, 100 km long tunnel. The findings of these investigations summarise host state requirements and constraints, which are also applicable to the new surface and underground structures that are needed for a HE-LHC scenario.

No conflicts with geothermal boreholes, seismic activities, underground technical features such as pipelines, critical power and communication lines could be found so far. Also, no relevant conflicts with underground water layers could be identified. However, existing underground and surface site infrastructure constrains the possibilities for the additional infrastructure required. Therefore, a further detailed iteration is needed if the HE-LHC scenario is the preferred scenario for a next particle collider infrastructure project. In particular, some surface sites require further optimisation in the design phase. Swiss law requires the reservation of a certain surface area for agricultural activities in order to remain self-sufficient in case of crisis [281]. This constraint imposes the launch of a declassification and ground/right-of way acquisition process in the subsequent design phase. Working groups are currently being established with representatives of the Swiss confederation and the relevant offices

of the Canton and State of Geneva in order to facilitate this multi-year process. The legal framework in both countries requires further detailed information in order to jointly develop a scenario that is compatible with the existing LHC infrastructure, the needs of the project and adequate compensation actions that need to be developed together with the Canton of Geneva and the Swiss federal government. The environmental impact during the construction phase, which extends over many years, needs to be studied. The reuse of the excavated material, even if the quantities are limited, (in order of priority: on-site use, processing and reuse, landscaping, storage), construction site traffic, noise and dust are all elements which also need to be considered.

Official bodies of both host countries (Secrétariat Generale de la Région Auvergne-Rhône-Alpes and Département de l'aménagement, du logement et de l'énergie de la République et Canton de Genève) have informed the study management that for emerging urban areas and where there is a region with high-value natural assets, early participation of the authorities and representatives of the population in the further development of the project plans is required. Surface sites need to blend into the landscape. Synergies with local and regional activities that profit from the infrastructure in the host countries need to be developed. Examples include cooling via the GeniLac [282] water project, waste-heat recovery for residential districts and healthcare providers, possibilities for temporary energy storage and release in cooperation with neighbouring industries. For the construction phase, particular attention needs to be given to noise, dust and traffic. For the operation phase, topics include the consumption of water, electricity, the emission of noise and the increased need to provide all kinds of infrastructure for an ever growing community of scientists, engineers and visitors.

The immediate subsequent design phase of the project will focus on the further optimisation of the collider and surface site placement, based on the findings already obtained in cooperation with the host state authorities and their nominated technical advisory bodies for the concept phase. This work will, in compliance with the regulations of both host countries, involve representatives of the local population in order to ensure a seamless evolution of the project design towards a later construction decision.

10.3 Waste management

10.3.1 Radioactive waste management

CERN has a radioactive waste management system which has been implemented in agreement with its host states [259]. The production, temporary storage, processing and elimination of radioactive waste is performed according to the processes defined in the radioactive waste management system. The production of waste from the HE-LHC and its provisional classification will be addressed and quantified during the technical design phase. It is estimated that the de-commissioning and dismantling of the LHC is a project that will last about three years with a cost in the lower percentage range of the LHC construction expenditure. Since radioactive waste will be generated by the dismantling of the LHC and its experiments, an agreement with the host states needs to be concluded so that the quantities of waste produced will be accepted by the host states for a specific duration from a particular point in time. In addition, a "fair-share" approach needs to be agreed in the scope of the CERN-France-Switzerland tripartite framework concerning the distribution of the different classes of radioactive waste. Consequently, the temporary storage and treatment facilities required will be evaluated in detail if the HE-LHC is considered

Table 10.1. Estimates of radioactive waste for HE-LHC.

	TFA	FMA
Construction phase		
New SPS as injector	$5000\,\mathrm{m}^3$	$200\,\mathrm{m}^3$
LHC as injector	$300\,\mathrm{m}^3$	$900\,\mathrm{m}^3$
Operation phase		
Injectors (including LHC)	$650\,\mathrm{m}^3$/year	$30\,\mathrm{m}^3$/year
Collider	$1450\,\mathrm{m}^3$/year	$70\,\mathrm{m}^3$/year

as the preferred next particle collider infrastructure project. The choice of materials to be used in terms of their isotope production and known elimination pathways will be optimised during the design phase.

During operation, the HE-LHC will produce similar types of radioactive waste to LHC. Given the similarity in materials used, the radionuclide inventory is not expected to change significantly. The expected beam loss rate per metre is comparable to the LHC. The increase in beam energy will account for an increase in activity concentration, and it is assumed that the fraction of medium level radioactive waste (classified in the French system as "faible et moyenne activité", FMA, and "très faible activité", TFA) with respect to the total volume, will not change significantly compared to LHC. The higher luminosity in HE-LHC will lead to higher activation levels in the detectors of the high-luminosity experiments at points 1 and 5, in the final focusing regions next to the interaction points, as well as in the regions with beam cleaning, collimation system and dumps. The dose rates are expected to increase compared to the levels in the LHC. In terms of handling and waste processing, technical developments will be required. These are already planned and will be implemented for the High Luminosity LHC (HL-LHC) project.

HE-LHC will reuse the existing LHC injector chain. As an alternative, a superconducting SPS could serve as an injector. During the construction, parts of the existing accelerator chain need to be upgraded. As the components of these accelerators are already activated, the material to be removed from those areas will be radioactive. Both of the scenarios above have been taken into account in the estimation of radioactive waste production during the construction phase of the HE-LHC.

The full replacement of the SPS by a superconducting accelerator would generate an estimated total volume of $5000\,\mathrm{m}^3$ (TFA) and $200\,\mathrm{m}^3$ (FMA) [283]. In the case of a complete decommissioning of SPS, the temporary storage space required for the radioactive waste during the decommissioning remains to be evaluated in terms of the disposal capacity per elimination pathway.

During the operation phase of the accelerator complex, radioactive waste will be produced from the collider and the injectors, mostly during the long shutdown periods. As for the LHC, about 87% of the waste generated will be TFA type and 4% FMA. The remaining 9% of the volume could be considered as a candidate for release from regulatory control via the clearance procedure. The average volume produced per year is estimated to be $2100\,\mathrm{m}^3$ (TFA) and $100\,\mathrm{m}^3$ (FMA) [283], which corresponds to a considerable increase with respect to the current capacities of reception, treatment and disposal of radioactive waste (average $400\,\mathrm{m}^3$ per year). The volumes given above take into account the accelerator components themselves, but not the associated infrastructure like cables and cable trays inside the tunnel. It is expected that these other elements would add less than 20% to the total volume.

Table 10.2. Examples for conventional waste.

Class	Description	Subsequent reuse
Inert waste	Excavation materials	Use on construction site, processing for create raw materials for industry and construction and isolation materials, landscaping, environmental protection measures, addition to construction material, final disposal (e.g. quarries)
Inert waste	Construction materials	Recycling, final disposal (e.g. quarries)
Inert waste	Polluted excavation materials (e.g. from drill & blast)	Final disposal in dedicated sites
Wood (treated)	Cable drums, palettes, construction wood, packaging materials	Taken back by supplier
Wood (untreated)	Cable drums, palettes, construction wood, packaging materials	Recycling, incineration
Plastics	Packaging materials	Taken back by supplier, recycling
Metals (low quality)	Construction	Recycling
Metals (high quality)	Wires, cables, machinery, sheets	Taken back by supplier for re-integration into production cycle
Electronics	Cards, computers, outdated devices	Recycling
Insulation materials	Construction, machine construction	Taken back by supplier, reuse
Paint, solvents, glue	Construction, maintenance	Residuals from construction taken back by suppliers, recycling after stabilisation
Chemicals	De-mineralised water production, cooling tower cleaning and anti-legionella treatment	Favour bio-degradable products and processes involving less or no chemicals
Paper and cardboard, textile, filters, glass	Packaging	Recycling
Plaster, coating, gypsum, tiles	Residual construction materials	Taken back by contractors
Oil	Hydraulics, cooling, insulation, lubrication	Taken back by contractors with obligation to decontaminate and recycle

10.3.2 Conventional waste management

A large-scale research facility produces conventional waste during the construction and operation phases. Typical classes of waste produced during construction are shown in Table 10.2.

While plans for the management of waste during both phases need to be established, the regulatory frameworks of both host countries require the development of waste prevention plans for the construction phase as part of a preparatory phase. In France, the "Plan régional de prévention et de gestion des déchets" [284] requires the project owner to include approaches that work towards a circular economy, taking into account the possibilities offered by the regional infrastructures. Waste reduction targets are documented in the "Loi relative à la transition énérgetique et a la croissance verte" [285]. In Switzerland, the "Ordonnance relative à l'étude d'impact sur l'environnement (OEIE)" [272] specifies the activities related to the planning of how conventional waste is managed. In the Canton of Geneva, the "Plan directeur cantonal 2030" documents the specific waste reduction targets [286].

The management of waste follows three priorities: (1) keeping the amount of conventional waste as low as reasonably possible, (2) develop a plan to reuse the waste locally and regionally and (3) keep the impact of residual waste transport low.

Today, excavation material is still considered waste by law, but the legislation is evolving in many European countries. Excavation material can be a valuable primary resource and even for the limited quantities to be expected in the scope of the HE-LHC project, the host states require a plan for the use of this material. The FCC study has launched a research activity with the French tunnel design center (CETU), the Geneva based "Service de géologie, sols et déchets" (GESDEC) and Montanuniversität Leoben (Austria) on this subject. The study will serve as an input to the environmental impact assessment. Furthermore, detailed plans for the construction phase, including the identification of waste, its collection, treatment, reuse and disposal in compliance with the individual national laws have to be developed as part of the environmental impact assessment process. This plan should include measures that can be included in procurement procedures and in the agreements concerning in-kind contributions from collaboration members. The procedures should address the sharing of the responsibility between project owner and suppliers for dealing with conventional waste.

11 Education, economy and society

11.1 Implementation with the host states

11.1.1 Overview

Assuming a start of operation around ten years after the end of the HL-LHC programme, a decision point for a project in 2026 and start of the project towards the end of 2028, a number of administrative processes need to be set up with the two host states and to be carried out during a preparatory phase although the HE-LHC project is limited in terms of new construction. Work with the host state authorities has been launched in order to develop a workable schedule for the available time window. The results of this work so far show that an eight-year preparatory process is required, in cooperation with both host states and involving a diverse set of administrative processes with public engagement. The main reasons of a process with host-state representatives and involving public stakeholders are the need to extend existing surface sites in both countries, to create new surface site installations, to de-commission and dismantle the LHC, to construct a new particle accelerator and experiment detectors and therefore to create installation activities in the region for a significant time period and to increase the quantities of resources needed, such as water and electricity to operate the new collider. The procedures required on French territory are less demanding than for FCC-hh and FCC-ee. However, the national public debate committee still needs to be involved for any project with an investment larger than 300 million Euro, including research projects. Even if limited, new plots of land on the surface and underground volumes need to be acquired and made available to the organisation. According to the current state-of-understanding the declaration of public utility is still required.

The preparatory phase schedule, which has been developed jointly by CERN, government representatives of France and Switzerland for the FCC-hh and FCC-ee scenarios applies in general terms, but certain elements such as detailed underground investigations are not necessary. On the other hand, a refurbishment of the existing underground infrastructure is needed and an agreement on the reception of radioactive waste needs to be concluded and implemented with both host states. Figure 11.1
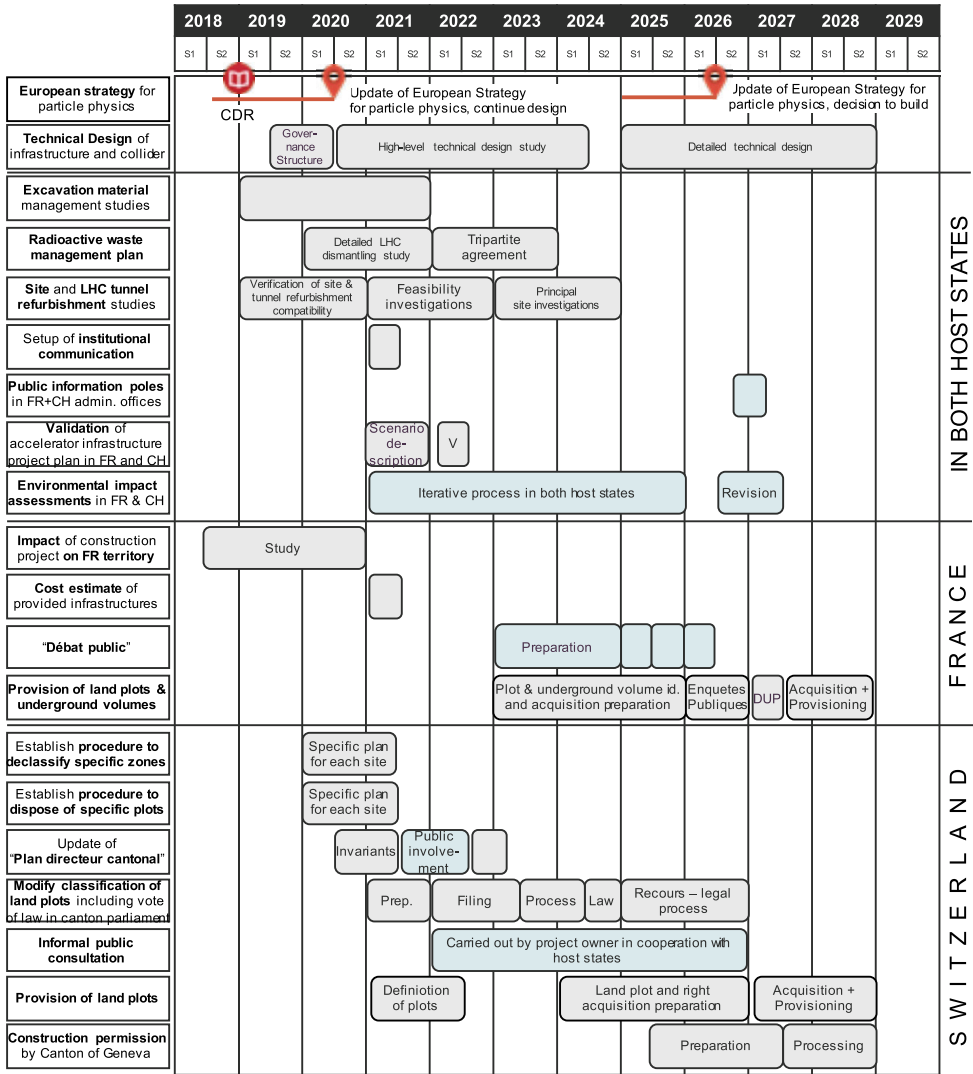
Fig. 11.1. Schema for the administrative processes required in both host states including those needed during the preparatory phase, before a decision to construct is taken.

shows an adapted version of the FCC-ee/FCC-hh administrative preparatory phase schedule for the HE-LHC scenario. The same start date as for the FCC-hh and FCC-ee scenarios is used. The key time-determining factor is the necessity to re-classify non-constructible zones, which are subject to quota restrictions in Switzerland and to acquire the rights to these plots. This process is expected to take about eight years and needs to be completed before a decision to construct is taken. The process is owned and steered by the project owner, which is an international consortium, represented by CERN, including its member states and, potentially, additional project partners from non-member states.

The host state authorities recommend working with locally experienced contractors for tasks that relate to the development of an implementation scenario in the region, to benefit from their knowledge concerning territorial specificities and to set up a working environment that permits putting workforce and contracts in place

quickly and to be able to adjust to the evolving requirements in a timely manner. Both host states have demonstrated their will to accompany CERN throughout the preparatory phase in order to ensure a coherent development of the project, thus increasing the likelihood of success when a decision to move forward with construction is taken by the research community. Although the legal frameworks and government structures in the two host states differ and different types of actors need to be involved on each side of the border, the goals and scope of the individual processes are similar. Some specific elements have to be planned and carried out in an international framework. An environmental impact assessment according to the Espoo "Convention on Environmental Impact Assessment in a Transboundary Context" [275] needs to be planned, set up with appropriate tool support and carried out as a co-operative activity with the host states. The dismantling of the LHC calls for a tripartite agreement among CERN, France and Switzerland on the acceptance of the different classes of activated materials by the two host states. It is therefore prudent to plan the establishment of an international agreement between France and Switzerland for the purpose of preparing, implementing and operating an upgrade of CERN's current particle accelerator infrastructure in the two territories as foreseen for the FCC-ee and FCC-hh scenarios.

11.1.2 France

The Auvergne-Rhône-Alpes regional government is headed by a *prefect* who is supported by an office (Secrétariat Général de la Région Auvergne-Rhône-Alpes, SGAR) located in Lyon. Within this administration, the prefect is the representative of the French Republic. The SGAR and the prefect's office work together on all development activities in the area. In 2016 the SGAR launched an analysis so that the prefect, and in turn the French national administration, could be informed about a significant extension of CERN's infrastructure and to estimate the associated administrative and financial impacts for France. This activity led to the establishment of a series of regular meetings with CERN for the development of the preparatory phase. France promotes a "participative democracy" [287–289], calling for a process to find a consensus through open discussions amongst all stakeholders in the project from the conceptual stage onwards. The process starts with the development of the basic concept, a feasibility study concerning the infrastructural challenges, a proposal for the governance and funding and a socio-economic cost-benefit analysis. The infrastructural changes concern a wide range of topics: the use of excavation material, a concept for managing conventional waste during all project phases, an energy management plan that can be integrated with the territorial energy balance plan, plans for the consumption of resources such as water, proposals for synergies with the host state to contribute to the territorial development, the development of traffic and mobility concepts and further topics. CEREMA[4], a public entity associated with the ministry of ecologic transition and solidarity and the ministry of territorial cohesion, has produced a report for the SGAR and the prefect on the impact of an FCC for the host state concerning administrative processes and the associated financial engagements [290].

Initially, a specific project scenario needs to be produced since government offices cannot work on concrete preparatory tasks based on generic processes, but need to base their actions on so called *project invariants* that need to be considered in the update of regional development plans. This scenario description will cover a wide range of subjects including for instance, the purpose of the research facility, an

---

[4] http://www.cerema.fr

initial proposal for the placement of the underground and surface sites, known technical infrastructure requirements including the resources and services (e.g. electricity, water, communication, transport, emergency and security services), the high-level construction and operation project plans, a catalogue of initial risks and benefits, a list of known uncertainties, a construction and operation cost estimate, a cost-benefit analysis, a first realisation plan, a governance and management structure and a preliminary analysis of the administrative impact on the host states. Once the scenario is validated by the office of the President of the Republic, which is where the regional and national stakeholders come together, the preparation of the legally required process for the public to participate in the project ("débat public") [291] can begin. The goal of this process is to develop an acceptance and appreciation of the project amongst the population, which forms the basis for a governmental clearance for the project owner to continue with the preparation. A commission defines which topics are relevant for the population and where there can be reasonable involvement in this process. The formal procedure lasts six months, but it requires about two years of preparation and is concluded with a one-year phase for its implementation.

After this internal preparatory phase, the project owner in close cooperation with the public debate commission, prepares information material (documents, databases, Web contents, booklets, videos, travelling information stands, town meetings), organises the process with a reach defined by the commission (regional or national), employs consultants and companies experienced with this process, sets up the required technical infrastructure and finally, defines a schedule that will allow relevant public representatives to be involved. This takes about one year. According to the law revised in 2017 [292], the three-year period also involves the publication of summaries of the environmental impact assessment. At the end of the formal "débat public" phase, a follow-up consultation process, which continues until the end of the construction phase, must be put in place. Its findings need to be integrated in an iteration of the technical design and the project documents.

Once the national committee of the public enquiry (CNDP) [291] agrees that the documentation is mature, the formal open discussion can be launched. This milestone is associated with a certain risk. If the process is insufficiently mature, an extension of the preparatory period will be required. During this consultation phase, the plan for the project is presented and discussed with representatives of the population at local, regional and national levels during formal, recorded and audited sessions [293]. The project owner is asked to collect all questions and provide answers in a secure and auditable way. The findings lead to another iteration of the required project documentation (e.g. environmental impact assessment, plan for the management of excavation material and waste, energy management plan, traffic and mobility concept, land and rights-of-way acquisition plan, final land plot valuation). After the successful completion of this phase, acquisition of rights-of-way and surface plots can start.

A public enquiry ("Enquête publique") concludes the process by confirming the agreed infrastructure design which emerged from the public debate phase. If the tribunal has no objections, the French government issues an approval of the infrastructure project's utility for the nation ("Déclaration d'utilité publique") [294]. In any case, after successful completion of the public enquiry process, the project owner can proceed with the preparation of a construction project. The acquisition of the rights-of-way and land plots can take place concurrently with the civil engineering calls for tender.

11.1.3 Switzerland

Switzerland is a republic, federating significantly autonomous "Cantons"; this system of semi-direct democracy which has been in place since 1848, is unique. The country

has a long standing tradition of involving the population at all levels (municipal, cantonal and federal) and at all phases of infrastructure projects. The procedures differ substantially in the different Cantons. Therefore, a workable process has been developed with the assistance of the Canton and State of Geneva, the Swiss permanent mission for international organisations in Geneva, the representatives of the Swiss Confederation and a consultant for public construction project administrative procedures.

Although CERN's primary communication partner for administrative matters in Switzerland is the permanent mission and the ministry of foreign affairs (DFAE), the common work so far revealed that for the preparatory phase of a new particle collider requiring additional land plots and surface site facilities, the majority of processes will be carried out together with the State Office of Geneva. The federal government will be involved in the entire process with respect to the approval of applicable federal laws, regulations and financial contributions. In 2017, the "Structure de Concertation Permanente" (SCP) was established for this purpose. It includes Swiss government representatives at federal and cantonal level, experts from different administrative domains on an "as-needed" basis and representatives of CERN for various development areas, including future projects.

The schedule, which has been developed in the frame of the SCP takes note of the status of CERN as an international organisation developing research instruments on a global scale, which are technically and organisationally unique. Several years before initiating the cantonal formal processes to obtain permission to construct, the acquisition of rights of way on land plots and the declassification of those agricultural zones needed for construction have to be launched and successfully completed. The authorities assume that CERN also carries out a set of informal processes which include a public consultation process. Duration and contents of such a process will be chosen according to the expected impact of the project. It may include a public information booth, information materials and events, a public hearing, the establishment of an office to collect questions and to develop responses. In addition, the engagement of a diverse set of stakeholder groups at municipal, cantonal and federal levels is required, with an initial institutional communication strategy and plan which will be developed in close cooperation with the cantonal and federal authorities.

Two major preparatory actions have been identified by the representatives of the Swiss Federation and the Canton of Geneva that need to be initiated as soon as possible and which are independent of the amount of required land plots and the nature of the new technical facilities at the surface: a working group needs to develop a procedure in cooperation with the representatives of the Swiss Federation and the Canton of Geneva that permits CERN to request the Canton of Geneva to process the re-classification of agriculturally reserved, green-belt zones, called "Surface d'assolement" (SDA) [295,296]. The working group needs to tackle the process based on concrete, yet preliminary and non-binding assumptions of surface sites in order to develop concrete plans for the de-classification process, which will include mitigation and compensation measures. This process goes along with the development of a re-classification plan for a concrete set of potential plots of land that need to be acquired or rented long-term, for the construction project at a later stage. At the same time, another working group needs to develop the procedures to obtain the rights of way or the acquisition of those specific plots of land on behalf of CERN. The procedures are expected to differ for the different specific plots and involve the development of negotiation and, if needed, acquisition strategies and the drawing up of plans to provide the sites to the international organisation. Some areas may be used only for limited periods of time, for instance during the construction and commissioning periods. Expropriation of land in the interest of the public is generally avoided in Switzerland and therefore negotiation with the owners of needed land

plots or current users of CERN non-fenced areas should be started in the preparatory phase. This work goes along with an evaluation of the market value of the land plots, notification of the cantonal authorities of the intent to use the plots for an infrastructure project and pre-agreements with land owners or current land users. These processes have to be managed by CERN or a mandated project consultant and rely on the active participation of a number of federal and cantonal offices.

Although an environmental impact assessment is formally only required for the creation of parking spaces for more than 500 cars and for the processing of excavation materials of more than 10 000 t per year on a site [272], it is seen as good practice and in agreement with the Espoo Convention that the project owner pro-actively carries out this process. A specific framework needs to be developed to be able to perform one single integrated environmental impact assessment of the project across the two host states with the possibility to provide information in a way that is accepted by the relevant administration offices in the two nations.

In order to get started with a number of different federal and cantonal offices efficiently, CERN is asked to initially put emphasis on the establishment of an institutional communication plan and its implementation. This will inform all officials who have to support the work of CERN about the project scope, goals, scale and schedule. Regular informal meetings with the regional population, their representatives and various interest groups are welcomed from the initial design phase, since transparency is considered the most efficient aspect of activities for the preparation of a potential project.

Authorisation for construction can be requested after successful completion of the necessary steps and before a decision to build takes place. The French authorities ask for a Cost-Benefit-Analysis (CBA). The Swiss authorities encourage the idea of aiming at creating added value from training, tourist development, creation of a technology pole and synergies concerning transport and energy recovery in the Geneva region.

11.2 Socio-economic opportunities

11.2.1 Introduction and motivation

Cost-Benefit-Analysis (CBA) [297] for conventional infrastructures such as roads, power plants, energy distribution networks and public transport systems is a useful tool to identify, quantify and communicate the potential value, in addition to the gain of scientific knowledge, that a new research facility can bring to society.

A preliminary, quantitative study of the LHC/HL-LHC project using this method has been carried out [234]. This work serves as a foundation for a dedicated Cost-Benefit-Analysis of one particular future collider scenario that needs to be carried out at an early stage of the preparatory phase. The study has been performed by three independent organisations: University of Milan, University Roma Tre and the Centre for Industrial Studies (CSIL), Italy. The result reveals that the estimated Net Present Value (NPV) for the entire, combined LHC/HL-LHC programme over a period of 45 years (from 1993 to 2038) is positive, taking into account an annual social discounting rate of 3%. The likelihood of generating benefits of up to 5 billion CHF over the life of the programme is 80% [234]. This shows that a research facility like the FCC can generate added value for both industry and society. Despite the significant investment for constructing a new particle-collider infrastructure (CAPEX), the overall costs are dominated by operational expenditure (OPEX).

CBA has become a requirement for the preparatory phase of research facilities. The upcoming ESFRI roadmap includes a specific request [298] for it and the EC

staff working document on sustainability of research facilities asks for it. In 2018 an EC supported H2020 project, RI Impact Pathways [299], was launched with CERN's participation to develop a uniform CBA method for research facilities in the European Research Era (ERA). Here, the results from the study on the combined LHC/HL-LHC programme are presented. The results of the investigations so far triggered a set of complementary surveys and studies by the university of Milan in cooperation with CSIL in order to establish a set of solid input parameters and assumptions for a CBA of a post-LHC particle collider scenario.

So far, the studies of the LHC/HL-LHC programme revealed six economically relevant benefits: (1) the value of scientific publications, (2) technological spillover, (3) training and education, (4) cultural effects, (5) services for industries and consumers and (6) the value of knowledge as a public asset. There are two direct socio-economic benefits that stem from the dissemination of scientific information [300–302] (publications, reports, conference presentations): first, the direct value of scientific products is conservatively estimated to be equivalent to their production costs [303,304]. Second, the value of publications produced by an additional tier of scientists which cite the scientific products directly emerging from the research infrastructure is equivalent to the cost of their production. For the LHC/HL-LHC project, this added value is around 2% of the total benefits [301]. This report focusses on the findings concerning training, impact on industry and cultural effects in the following sections.

11.2.2 The value of training

The value of education and training is the single largest socio-economic benefit of a large-scale, hi-tech research facility. The impact is high, if the project is carried out in an open, international environment with strong cooperation between educational institutes, research centres and industrial partners (the "knowledge triangle") [305]. A conservative estimate of the net present value added to the lifetime salary of early stage researchers (master's degree, doctoral degree and post-doctoral researcher) after leaving the LHC/HL-LHC project has been estimated. The lifetime salary premium for people who perform research and development in the scope of the LHC/HL-LHC project at CERN ranges between 5% and 13% in excess of the salary premium of the academic degree acquired. This translates into an absolute lifetime salary premium of about 90 000 Euro to 230 000 Euro per person with an average added value of ca. 160 000 Euro for a doctorate degree obtained during a research period at CERN (2018 currency value) [306,307]. Based on CERN's current training programme capacity, during a 15 year construction phase and an initial operational phase of 20 years. 40 000 individuals would generate more than 6 billion Euros for the economies of the participating nations. The training value potential depends significantly on the possibility to acquire intersectoral and transferable skills [308] and the number of supervisors that are available to ensure the quality of the training provided.

These results triggered a process with the two host states [309] to find how the value of training can be further increased. Proposals include extending the training to non-academic teaching levels (apprentices, technical schools), continuous professional training (partnerships with companies in the frame of maintenance and upgrades as well as the increasing exploitation of under-used equipment), partnerships with public services (healthcare providers, public security and emergency services) and the continued enlargement of the training opportunities for non-technical domains (e.g. management, finance, economy, law, business administration). Also, joint academic education through partnerships with universities and industry should be further strengthened. The EASITrain H2020 Marie Skłodovska Curie Action Innovative Training Network project [310], launched by 11 institutes collaborating in the FCC

study and 13 industry partners is a first step in this direction. It includes as goal the development of a European joint doctorate in applied superconductivity.

11.2.3 Opportunities for industries and technological spillover

The industrial activities that emerge from physics research projects are important for the European economy [311]. The "utility factor" is a key figure on which all estimates of industrial impacts are based. It indicates that every Swiss franc spent on co-development and customisation projects with industrial partners generates, on average, three Swiss francs worth of follow-up sales revenues for the industrial partner [312]. The LHC/HL-LHC CBA study provides quantitative evidence that companies participating in the project and exhibiting medium to high levels of innovation also benefit from a measurable increase of their earnings before interest and taxes (EBITDA) [313,314]. The relevance of this effect has been tested using the accounting figures of 669 companies involved in CERN procurements worth more than 10 000 CHF and a control group [315]. The majority of companies report that the main benefit stems from the learning experience in such a project.

The LHC/HL-LHC CBA also reveals that there is added economic value due to improved products, services and operation models including information and communication technologies (ICT) of ∼10 billion CHF: more than 40% of the total cost (capital and operation expenditures). Further intensification of industrial involvement in core R&D activities in the framework of a well-planned industrialisation strategy can increase this share, so that a payback of 50% of the total costs can become realistic. The most prominent example for such research-induced industrialisation is the development of Nb–Ti superconducting wires for the Tevatron collider which triggered the mass production of medical magnetic resonance imaging (MRI) devices [316]. Another noteworthy example is the development of large-scale cryogenic refrigeration plants – the architecture and machinery developed for helium liquefaction for use in particle accelerators has been the industry standard for almost 40 years [317].

For a future particle collider, the benefits emerging from procurement and co-innovation depend on (a) the investment volume, (b) the potential for innovation related to the individual subsystems and (c) on the value of the utility factor. It is not yet possible to reliably quantify the overall impact for industry. A dedicated study for a specific accelerator scenario needs to be carried out, once the detailed technical design starts. Technologies that lead to innovation on a broader scale for the different particle collider scenarios include superconducting radiofrequency systems for a lepton collider, superconducting wires for a hadron collider, construction and testing of superconducting magnets for a hadron collider and large-scale cryogenic refrigeration infrastructure for a hadron collider. Initial estimates of the economic impact values have been performed, based on the expected captial expenditures of the lepton and hadron particle collider scenarios in a new, 100 km long tunnel. For a high-energy LHC, the benefits would be less, since the benefits from industrial spillovers directly correlate with the investment volumes. Section 11.2 in Volumes 2 and 3 of the FCC CDR give a glimpse of the estimated benefits.

An earlier study [318] has shown that hi-tech companies can transfer the knowledge and experience acquired during work with CERN to new products and services easier than companies who offer off-the-shelf products and services. Therefore, it is crucial to make an effort to cooperate with industry on increasing the potentials for other fields, such as civil engineering.

The introduction of Information and Computing Technologies (ICT) [319] are also important levers. One topic is the development of open source software and

open ICT specifications that can be used in other scientific domains or for business. The HTML and HTTP specifications that form the basis of the World Wide Web are prime examples [320]. However, since its value for society cannot be reliably quantified, this invention was not considered in the LHC/HL-LHC CBA study. Selected cases for which the impact is currently being estimated include: software tools used in other physics research (ROOT[5]), software tools used in medical imaging (GEANT4[6]), collaborative tools (Indico[7]), library software (INVENIO[8]), scalable storage systems (EOS, cernbox [321]), scalable modelling and simulation tools needed to devise reliable and energy efficient industrial systems (ELMAS [108][9]), measurement and control systems (for instance add-on components and extensions for SIEMENS WinCC OA and National Instruments Labview).

11.2.4 Cultural effects

The creation of cultural activities generates economic value and helps to involve the public in research. With 130 000 visitors[10] per year [301], CERN is Geneva's leading tourist attraction. The travel-cost method [322–324] estimates the value of this activity to be ∼120 million CHF per year [325]. Designing future surface sites with this in mind and gradually transferring the responsibility for public involvement to a dedicated operation and marketing organisation leads to a sustainable concept, which can increase this figure. A preliminary investigation of such a concept by one of the FCC collaboration members led already to the award of a prestigious architecture prize [326]. First estimates for the net benefits from 180 000 visitors (to a dedicated visitor centre at the main site) and 280 000 visitors (with an additional visitor centre on French territory) per year suggest additional annual societal benefits of 25–80 million CH [327]. This initial estimate includes annually assumed costs of 1 million CHF for the operation of these services. NASA's approach for a self-sustaining and independently operated visitor centre, which has been operating since 1967, is evidence for the success of this model [328].

Web and social media have become key communication platforms and their importance is expected to grow quickly with the introduction of new features and full coverage, high-speed mobile networks. The value of the contents directly produced by CERN and the LHC experiment collaborations, measured by the time people spend on average consuming the contents, is estimated to be in the order 120 million CHF per year [327], with videos being the largest contributor in the order of 90 million CHF per year. Channels combining different types of media have the highest impact (text interleaved with short videos, interactive info-graphics, apps, functions that encourage the reader to provide interactive feedback and to participate in collective tasks to shape opinion and to create new contents). The documented impact suggests that investing further in the provision of complementary, media-rich contents permits multiplying today's measured impacts many times. If technology evolutions such as augmented reality, tailored contents for different audiences, multi-language support and high-resolution virtual reality are adopted quickly, the research facility can significantly leverage the cultural effects.

In all cases, the research infrastructure operator should ensure that the content is made available by independent Web and social media content producers via

---

[5] https://root.cern.ch

[6] https://geant4.web.cern.ch/applications

[7] https://getindico.io

[8] https://invenio-software.org

[9] http://www.ramentor.com/products/elmas/

[10] See also at https://visit.cern/tours/guided-tours-individuals

well-working communication networks to achieve high technical quality and user satisfaction. Other powerful cultural products are computer programs ("apps") which engage their users in the research. Higgs Hunters [329] is a good example of such a citizen science project – it attracted 32 000 volunteers in a single year. The strong use of this technology by other research communities [330] motivates the development of further cases in the particle accelerator and high-energy physics domains. Computational physics applications as needed for the lepton collider FCC-ee and data analysis challenges as created by the hadron collider are ideal topics to create citizen science and public engagement programmes that also help disseminating the concepts of modern physics ("the Standard Model of Particle Physics"), which have so far not reached a wide audience.

Exhibitions such as *Extreme* [331] in Italy and *Begin* [332] in Austria, combined with interactive sessions and public events are an effective way to introduce the public to the research carried out in their countries in their own language. Their value, measured by the number of visitors and the time visitors dedicate, has been estimated to be in the order of 4.4 million CHF per year. The most successful item is the travelling LHC interactive tunnel, which alone creates about 1.1 million CHF of societal benefit per year, because it engages a large number of people for substantial amounts of time. When designed and created in cooperation with experienced museums and science exhibition centres in the member states and when accompanied by Web and social media contents that help to amplify the impact, the concept is a powerful vehicle to create a lasting awareness and promote the vision of a future particle collider facility.

The value of numerous books, TV shows, films and music produced by people not directly participating in the research programme undoubtedly has a further economic impact. It is a challenge to provide evidence for a causal relationship between a particular communication product and the research facility's activity. Therefore it is difficult to quantify the impact and the study is ongoing, focussing on video productions, TV and journal coverage and books.

CERN builds an image amongst the population of all member states through its communication activities. Because it exists and deals with questions that touch everybody, CERN has a value for everybody. This value has been estimated with "Willingness To Pay" (WTP) [297] surveys in CERN's member states specifically targeting the topic of a future particle collider. An initial LHC/HL-LHC CBA study suggested a total discounted value of 3.1 billion CHF for the total project period from 1993 to 2038. It is based on the assumption that the average annual voluntary contribution per year and person is 1.5 Euro. For the LHC/HL-LHC programme this very conservative, lower-bound discounted estimate represents about ∼12% of the total forecast impact [234]. However, a recent survey among French taxpayers [333], that has been performed to establish solid assumptions for a CBA of a post-LHC particle collider infrastructure, suggests a much higher WTP of around 4.7 CHF per taxpayer and year. In comparison, French taxpayers contribute to space research through funding of CNES with 35 Euro per year [334]. A number of eligible contributors in CERN member states of the order of 350 million people, needs to be considered for future WTP estimates.

11.2.5 Impact potential

An initial set of recommendations to increase the impact of a post-LHC particle collider beyond the science community was developed in the frame of the CBA work carried out during the FCC study. It involved the University of Milano, the Centre for Industrial Studies and the University Roma Tre in Italy, a field study carried

Table 11.1. Opportunities to further strengthen the reuse of a large-scale particle collider infrastructure.

Domain	Actions
Training	Common inter-sectoral education programmes with universities world-wide, extension of trainee programmes with industry, extension of adult training in the scope of development and service contracts, strengthening of the involvement of non-STEM domains in the training programmes. Reliable reporting of the research infrastructure induced salary premium will require periodic surveys via the CERN Alumni network, HR offices of collaborating universities and research centres as well as cooperation with national and international statistics institutes and selected industrial partners.
Industry	Technological competence leveraging projects to increase the probability of creating products and services from leading-edge technologies developed in the framework of the new particle accelerator, strengthening of the participation in the development of standards and specifications, develop technological spillover for conventional project domains such as civil engineering, increase the focus on the development of information technologies, open specifications and open source software with use cases outside the particle accelerator and high-energy physics domain, closer work with national ministries of economy and industry interest groups to create denser networks with industrial partners.
Cultural goods	The channels with the highest impact potential are social media and online content. It makes sense to further strengthen the presence in this domain, to complement it with media-rich contents (videos, interactive applications, augmented reality, citizen engagement). Creation and operation of high-quality and high-capacity visitor centres by an independent profit-making organisation that continuously involves the scientists, citizen science projects in collaboration with academic partners worldwide, promoting exhibitions developed by professional organisations in the member states, particular projects in other areas of the world (Africa, Asia, South America).

out by the company "iddest", which specialises in public consultation processes [335] and finally the common working groups with French [309] and Swiss [336] host state representatives. Some impact pathways are outlined in Table 11.1.

All consultants for relations with the public recommended the creation of a *future collider ambassador programme*. A dedicated communication plan, regular training and support material for target groups at different levels (institutional, local, regional, national, international) should make project members at all levels and from all sectors effective advocates of a future project. In the member states, this source of information will be the first and most effective communication channel to promote future research, to explain its benefits and challenges and to explain its purpose in simple terms. It is important that this programme also addresses common concerns. It should include a balanced set of ambassadors with different professional, cultural and personal backgrounds. The narratives should focus on what stimulates people's imagination like the origin of the universe, the nature of the matter which we are made of and where we come from.

12 Strategic research and development

12.1 Introduction

The information presented in this volume presents a concept for a future circular collider. The level of detail corresponds to the conceptual development stage

requirements as defined in the European Strategy for Research Infrastructures (ESFRI) methodology roadmap [337,338]. At this level, a number of concepts are presented that can be screened by experts in the domain, funding agencies and other stakeholders. It forms the basis for an implementation project of one of the scenarios and prepares the ground for developing a funding concept. The subsequent preparatory phase will focus on the development of the implementation plans, relying on credible designs that need to be based on a set of technologies that enable the research infrastructure to be built.

At this stage, any project of such scale, ambition and with a long-term vision spanning many decades, comprises a number of uncertainties with different probabilities and potential impact. Appendix A compiles the most relevant uncertainties for the specific collider scenario presented in this volume. Before a decision to build is taken, the most relevant technical uncertainties require investments in research and development to bring the technologies to readiness levels that permit the construction and subsequent operation with acceptable project risks. Therefore, the immediate next step, the design phase, will include the development of a technically achievable and coherent blueprint, which successfully responds to the requirements and concepts presented at this first stage.

The R&D topics presented in this section are considered "strategic", since they represent those key elements, which are considered necessary prerequisites to come to a technical design that can actually be implemented within acceptable time and cost envelopes. The topics are not ranked in any way and many more research topics need to be addressed before arriving at a particle collider technical design, which can meet the physics goals and which can be operated in a sustainable fashion throughout the planned operational period. However, additional topics which are not considered decisive in terms of technical feasibility or operational sustainability are not presented in this volume. This allows the scenario to be screened whilst remaining focused on the physics opportunities, the long-term importance for the worldwide particle and high energy physics community and on the most essential technical feasibility questions. It is assumed that also the existing diverse and vibrant set of R&D activities in the field of particle accelerator technology will continue and will lead to a converging programme for a future particle collider, nourished by cross-fertilisation of different particle acceleration technologies, design studies and the continuous optimisation of facilities in operation. Some of the enabling technologies are equally important for all three particle collider scenarios (FCC-hh, FCC-ee and HE-LHC). The following subsections present R&D plans for these topics:

- 16 Tesla superconducting high-field, dual aperture accelerator magnet
- Cost-effective and high-performance Nb_3Sn superconducting wire at industrial scale
- Energy efficient, large-scale cryogenic refrigeration plants for temperatures down to $40\,K$
- Invar based cryogenic distribution line
- Superconducting septum magnet
- High-speed, high-power switching system for beam transfer elements
- Efficient radiofrequency power sources
- Decentralised, high-capacity energy storage and release
- Particle detector technologies
- High-power solid state amplifiers
- Efficient and cost-effective DC power distribution.

12.2 16 Tesla superconducting magnet

Motivation

At the design stage of the LHC, the dipole field level was chosen to give the highest collision energy possible with Nb–Ti technology, cooling the magnets to 1.9 K and operating them with a 14% margin on the load line. For the future hadron collider a similar approach is used. The goal is to develop magnets that can provide the highest achievable field using the technology which provides the best cost/performance ratio. With Nb_3Sn superconductors, a nominal field of 16 T can be reached. This is about twice the 8.3 T generated by the Nb–Ti magnets in the LHC and about 5 T higher than the 11 T of the Nb_3Sn-based dipole magnet of the high-luminosity LHC upgrade. With this technology, a beam energy of almost twice the LHC one can be delivered. The cost of such superconducting magnets is dominated by the amount of conductor. The cost increases rapidly when the operation parameters are approaching the conductor's critical surface. Consequently, to be able to exploit the full potential of the conductor in order to achieve the required field and quality, the smallest possible margin on the load line needs to be chosen.

Objectives

The goal is to develop a viable design for a superconducting 16 T, dual-aperture magnet. The design needs to be verified using simulations first and then with short (∼1.5 m) models. Eventually, full-scale models need to be built to validate the design. This programme depends on a separate R&D programme for the development of a high-performance, cost-effective Nb_3Sn superconducting wire. For the R&D phase, it is assumed the FCC-hh will work with the same 14% margin on the load line as was adopted for the LHC. The programme aims at achieving a margin, which is lower than at today's state-of-the-art Nb_3Sn HL-LHC magnets, where the margin ranges between 20 and 22%. A main concern is to achieve reliable operation with a margin of 14% and to reduce it further to 10%. It is also necessary to reduce the amount of superconducting magnet training needed, so that initial test times are shorter and consequently fewer resources are needed. Eventually, operation during the nominal thermal cycle must be demonstrated.

Description of the work

The programme spans three distinct domains:

1. The development of magnets based on different designs and manufacturing technologies.
2. The design, construction and verification of magnet components and partial magnets for R&D purposes.
3. The verification and validation of model magnets.

The design studies aim to develop various feasible concepts for a high-field accelerator magnet. The designs will be verified and compared using electromechanical performance simulations including their behaviour under mechanical stress. The design process includes the identification and specification of new structural components for the ferromagnetic yoke and the coil end spacers and wedges. It also includes the development and specification of new resin impregnation systems and the development of advanced internal splicing techniques for the superconducting cables. The design process will also lead to the development of an in-depth understanding of the

mechanical conductor and coil stack properties corresponding to the various manufacturing processes (insulation materials and layout, heat treatment and impregnation).

The construction of magnets for R&D purposes is based on the study of short model coil (SMC), enhanced racetrack model coil (ERMC) and racetrack model magnet (RMM) assemblies. The SMC is used as an intermediate stage to determine the effectiveness of the technologies developed for training improvements, conductor insulation and impregnation resins, as well as specific production steps, in particular the adhesion conditions between coil and poles. ERMCs are developed in two variants with non-graded and with graded coils. They facilitate the assessment of strategies for coil manufacture and assembly, namely the interface between conductor and end spacers or conductor and pole, heat treatment and impregnation conditions (volume, stress), internal splices for the graded versions, loading conditions to minimise degradation and training and finally, the management of transitions (layer jump, ends). Eventually, ERMCs will demonstrate that the field level of 16 T can be achieved with some margin and with limited or no training. The RMM and the ERMC share the same structure but the insertion of an additional coil between the two pancakes of the ERMC creates an aperture of 50 mm over a straight section of 470 mm in addition to a 250 mm layer jump. The structure will be designed to contain large longitudinal rods made of stainless steel or aluminium, tightened in different ways to explore various conditions of longitudinal loading, including extreme situations of nearly rigid boundaries. These magnets will enable the training performance for a straight section of a real accelerator magnet to be determined. In addition, the measurement of the magnetic field in the aperture will be possible, even in the absence of free access from the ends. Finally, the magnetisation effects over the powering cycle, including reproducibility from cycle to cycle as a function of the injection field will be recorded.

By building short models of all the viable options explored by the EuroCirCol H2020 project the cosine-theta, block coils, common coils and canted cosine-theta designs can be verified under realistic conditions. Eventually, full-scale models of the most promising designs have to be constructed to validate the approach before a decision to launch a construction project for a high-energy hadron collider can be taken.

Collaboration with universities and research institutes

From the beginning this R&D programme has been a collaborative endeavour which builds on the committed involvement of universities and research centres from around the world. The EuroCirCol H2020 project initiated a worldwide consortium to develop and explore designs of different high-field accelerator magnets. Research institutes with established track records in the design and development of superconducting high-field magnets need to intensify their contributions further. Model magnets are already planned to be constructed by CERN (international organisation), CEA (France), CIEMAT (Spain), INFN (Italy), PSI (Switzerland) and Fermilab (USA). The design, construction and testing activities include the cooperation of well-known institutes and universities such as EPFL (Switzerland), KEK (Japan), Technical University of Tampere (Finland), Karlsruhe Institute of Technology (Germany), University of Patras (Greece), University of Twente (The Netherlands), University of Geneva (Switzerland), National High Magnetic Field Laboratory (USA), Brookhaven National Laboratory (USA) and Berkeley Lab (USA). In particular, the high-field magnet development programme led by the Department of Energy (USA) will be a crucial factor on the way to determine a viable design for a 16 T magnet. In the near future, the consortium needs to be enlarged with additional academic partners, in particular universities and institutes in Russia with a track record in the development of high-field superconducting magnets. The consortium also needs the involvement

of academic partners in Asia and more regional partners in North America, including Canada.

Collaboration with industrial partners

The design and development of the 16 T magnet relies strongly on the capability to manufacture, install and operate a large number of devices. Therefore, industrial partners will be included at all stages of the R&D programme, from the development of fundamental technologies from assembly and process-related activities to quality management, installation, maintenance and repair concepts. Co-development with industrial partners during the R&D phase prioritises the following key topics: automated winding systems with integrated quality control, quality improvements and resource optimisation of impregnation and heat treatment, the optimisation of assembly, the optimisation of internal and external interfaces to improve assembly, testing, installation, maintenance and repair. These activities will include the definition of collaborative, EC co-funded, projects to increase the impact of transferring technological developments from research to industry.

Milestones and deliverables

The following Table 12.1 outlined initial milestones and deliverables for this R&D activity.

Table 12.1. Milestones and deliverables for 16 T magnets.

Title and description	Year
4 different electro-mechanical magnet designs studied	2019
SMC tested	2019
ERMC tested	2019
15 T cos-theta model (US) tested	2020
RMM tested	2021
SMC, ERMC, RMM results	2022
3 short 16 T models validated	2023
1 long 16 T model validated	2025

12.3 Nb$_3$Sn wire

Motivation

The feasibility of a 16 T superconducting accelerator magnet with two apertures of 50 mm each depends on the availability of an affordable conductor that can deliver a current density (Jc) of at least 1500 A/mm^2 at 4.2 K and 16 Tesla [339]. If a high-energy hadron collider was to be built as an immediate next step after the LHC/HL-LHC programme, Nb$_3$Sn is seen today as the only superconducting material that can be produced at the rate and in the quantity needed for a series production of thousands of magnets by 2030 [340]. This material is being produced for use in the magnets of the HL-LHC upgrade project, the first application of Nb$_3$Sn technology in a particle accelerator. Industrial production of such wire is presently with one leading company in the field (Bruker) that has mastered two processes: internal tin (RRP©) and powder-in-tube (PIT). Performance of up to 1200 A/mm^2 at 4.2 K in

a field of 16 T is available and is therefore considered to be the current state-of-the-art. The push to reach higher critical current density to meet the target requires extensive material science research effort and the development of new manufacturing technologies.

High critical current density is necessary, but not sufficient. Dynamic and adiabatic stability, field quality and protection considerations as well as a need for high-current in compact Rutherford cables call for small superconducting sub-elements, low resistivity of the matrix stabiliser and good mechanical properties. The conductor research and development programme launched by the FCC study aims to develop a Nb_3Sn that can meet all these requirements exactly. This programme is based on a set of academic institutes and industrial partners worldwide that are tied together by an FCC R&D agreement. This nucleus has started to investigate routes to reach the performance goals [130], first aiming to verify different approaches and then aiming to validate a viable technology in a full-scale magnet. For the series production of the particle collider magnets, about 2000 t of superconducting material will be needed. Therefore, the initiative is also a first step in the direction of preparing the ground for a credible large-scale supply chain at global scale. Affordable wire cost is a third goal of the conductor programme. Since the early research and development phase, effort has been focused on production processes that appear promising in terms of scalability and that have a potential for industrial low-cost production. The target maximum cost, derived from magnet design and conductor analysis, is 5 Euro/kA at 4.2 K and 16 T.

Objectives

The main objective is to achieve a performance of $1500\,A/mm^2$ at 4.2 K and 16 T for a J_c of at least to $2300\,A/mm^2$ at 1.9 K and 16 T – the latter are the operating conditions set for the magnet. The full set of objectives are outlined in Table 12.2.

Table 12.2. Target parameters for the conductor of 16 T magnet series production.

Parameter	Value	Unit
Wire diameter	ca. 1	mm
Non-copper J_c (4.2 K, 16 T)	≥1500	A/mm^2
Copper to non-copper ratio	0.8 : 1	
Sub-elements effective diameter	20	μm
Magnetisation – $\mu o\ \Delta M$ (4.2 K, 1 T)	≤150	
Residual Resistivity Ration	≥150	
Wire unit length	≥5	km
Cost (4.2 K, 16 T)	≤5	Euro/kAm

Smaller sub-element diameters are important to limit losses in coils during transients (acceleration ramp), to ensure dynamic and adiabatic stability and to achieve the required field quality. State-of-the-art Nb_3Sn wires have sub-element diameters of about $50\,\mu m$. Obtaining smaller sub-element size together with higher J_c and high RRR are requirements that conflict with each other. This is a challenge facing the conductor development programme.

Description of the work

The main focus of the work is the development of a high-performance Nb_3Sn wire via the internal tin process. Different wire layouts have to be developed and studied in collaboration with industry, including both common and separated barrier designs.

Industrial partners will produce R&D billets in order to encourage continuation of the developments by industry, to consider industrial production from the beginning and in order to produce wire that industry can also test for applications beyond research applications.

The conductor programme needs to be in parallel with the magnet development programme, accompanying the development and verification of short and long model magnets. The programme focuses on three main themes:

1. Development of novel wire layouts and compositions;
2. Industrial production of medium size billets;
3. Development of cost-efficient, large-scale industrial production of large billets.

Task (1) to study and develop novel wire layouts and compositions aiming to improve the critical current and high RRR properties. However, the development of a suitable Nb_3Sn wire for the HL-LHC upgrade project does not indicate a way to achieve the target performance through further, gradual optimisation. Therefore, the development of novel processes are highlighted in this activity. "Internal oxidation" is considered as one route towards a substantial improvement of the conductor in-field performance. Only limited work has been performed by the community to date, but preliminary results are promising. Both industry and research laboratories have taken up this challenge, which requires fundamental research calling for a combined effort of industrial and academic partners.

Task (1) spans from understanding the fundamental material properties in model system configurations to the production of small amounts of wire for research purposes. The development needs to also include wire performance indicators such as the effective filament diameter. The test samples are produced in simplified configurations (e.g. material layers, mono-filaments) up to small-size billets of a few kilometres for selected routes. Independent academic partners will perform extensive analysis of electro-magnetic, mechanical and thermal properties, as well as advanced analysis such as SEM, TEM and XRD. This research is an iterative process, during which results from wire manufacturing and testing provide feedback for improved designs. Optimisation of heat treatments, study of tin diffusion and wire composition, in-depth microstructural analysis, study of phase transformations, preliminary evaluation of mechanical properties, measurement of electrical and magnetic in-field properties are typical investigations that need to be performed to evaluate progress and to indicate the viable paths for further developments. Experimental work, material analysis and testing/analysis are at the core of this activity.

Task (2), the production of medium-sized billets by industrial partners aims to reproduce the experimental billets on a larger scale and to increase the technological readiness of the most promising designs that emerge from the wire R&D activity. The goal is to produce a few tens of kilometres of wire. The development of industrial processes will be accompanied by further wire design improvements to be able to meet all additional requirements: stable and controlled magnetisation, filament diameter, mechanical properties. Achieving this objective will require further progress in wire design and layout. It is therefore an iterative development loop. At this stage the qualification of Rutherford cables made from the wires is starting in addition to wire measurements and testing. Short cable samples will be tested and, according to the results, will be used for short model coils. For each wire layout, production of Rutherford cables requires a specific development, with iterative studies, production runs, optimisation of cable geometries and heat treatments and electro-mechanical and magnetic measurements.

The time necessary to perform tasks (1) and (2) is expected to cover a period of about ten years. During these phases, the production of about 1.5 t of conductor per year is needed to be able to meet the requirements for testing, development of cables

and short model coils and to build short magnet models. This activity is needed to provide essential feedback to the conductor programme. Conductor and magnet R&D therefore proceed in a synchronised manner and are closely interlinked.

Task (3), covers the development of industrial lines for the cost-efficient, large-scale production of large billets. The production processes need to be developed and validated for the wire architectures that meet all objectives and meet the target performance. This part of the programme aims to show the feasibility of the production of long conductor lengths of up to 5 km in a cost-effective manner. Ultimately, large billets up to hundreds of kilometres of the material with the target characteristics, required to feed the optimised Rutherford cable production for the long model magnets and prototypes need to be produced.

Cooperation with universities and research institutes

From the beginning this R&D programme has been a collaborative endeavour that requires the committed involvement of world-wide universities and research centres. The EuroCirCol and EASITrain H2020 projects catalysed the establishment of a solid set of committed academic partners to make progress in fundamental materials research.

At the nuclear reactor institute, the Technical University of Vienna (Austria) is leading the effort concerning the material characteristics using SEM and FIB techniques and the investigation of the creation of artificial pinning centres. CERN is complementing the work on characteristics with TEM analysis.

In its fundamental material research programme, the University of Geneva (Switzerland) is exploring ways of reducing the grain size using an internal oxidation method, thus advancing wire performance. TU Bergakademie Freiberg (Germany) has launched a project to investigate the phase formation in the ternary Cu-Nb-Sn system. The Bochvar Institute (Russia) is experimenting with various layouts of internal tin wires which show a significant performance increase, currently reaching $1200 \, \mathrm{A/mm^2}$ at 16 T and 4.2 K.

In the near future, the consortium will be enlarged with additional academic partners, for instance with the Applied Superconductivity Center at Florida State University in the USA.

Cooperation with industrial partners

The establishment of a representative set of industrial partners who participate in the improvement of Nb_3Sn wire performance is vital for the preparatory phase of a high-energy hadron collider project. Therefore, in 2016 the FCC collaboration launched a conductor R&D programme involving industry. To date JASTEC and Furukawa in Japan, KAT in South Korea, Bochvar Institute associated with TVEL in Russia and Luvata Pori in Finland have joined the effort. A joint R&D project with Bruker in Germany is being developed.

Milestones and deliverables

The joint research initiative with the HL-LHC project and the progress in conductor development during the FCC study period (2014–2018) has created confidence that the performance target can be achieved. A dedicated workshop at CERN in March

2018[11], federating a large and active group of participants from academia and industry reported on preliminary, encouraging results from the work performed so far. The commitment of the participating industrial partners and the confident enthusiasm to be able to achieve the target performance led to the definition of well-focused plans for the continuation of this R&D initiative on an international scale.

Table 12.3. Milestones and deliverables for Nb$_3$Sn wire.

Title and description	Year
Multi-phase R&D initiative set up on an international scale	2019
Routes to develop performance improvements identified	2021
Methods and processes to increase the current density towards the target performance	2024
Target performance demonstrated	2025
Industrial process for large scale production developed	2028
Scale-up and preparation of series production achieved	2030
Procurement start	2030

12.4 Efficient and cost-effective cryogenic refrigeration

Motivation

Satisfying the cryogenic refrigeration requirements of a future hadron collider with the traditional technologies in use today at the LHC is not possible. The FCC study therefore launched a long-range R&D programme at an early stage to develop an alternative approach. The current machinery for helium refrigeration is based on warm screw compressors which have a unit capacity more than 10 times smaller than that required for the FCC-hh and they have a poor isothermal efficiency of about 50%. Since pure helium cannot be compressed easily, a novel concept based on a mixture of about 75% light helium and 25% heavier neon (known as nelium) is being developed for cooling down to 40 K in a scalable and cost-effective way. The light gas mixture together with a high isothermal efficiency centrifugal compressor reduces the number of cooling stages required from 20 to 14, leading to power and cost savings of ~16%. This translates into savings in operating expenditure of almost 20 MCHF per year. Building on recent advances, a novel turbo compressor with fewer moving parts, less lubrication and a sealed design for light gas mixtures will boost reliability and efficiency.

Objectives

The primary objective is to showcase a full scale nelium cryogenic refrigeration system. The nelium cycle has been studied conceptually but the practical feasibility remains to be demonstrated. In order to do this, the core components, centrifugal compressors with up to 80% of isentropic efficiency and with larger unit capacities, need to be introduced as an alternative to the screw-based compressors.

Description of the work

In parallel with the simulations of a nelium cycle-based refrigeration architecture, design studies and a limited-scale test bed for turbo-compressor machinery is

---

[11] See https://indico.cern.ch/event/698917

currently being established in the framework of the EASITrain H2020, EU funded project. To demonstrate that the nelium cycle is viable, a dedicated test bed must be built with the smallest centrifugal compressor available today. Such a machine would be about one third of the size of the full-scale system required for FCC-hh and will consume about 5 MW of electrical power. The project goals are:

– validating the concept,
– determining the optimum helium/neon mixture,
– optimising the overall efficiency,
– determining the availability of such a system,
– identifying the turndown capacity of the machinery.

Cooperation with universities and research institutes

In the last few years a set of academic partners including the Technical University of Dresden (Germany), the Technical University Stuttgart (Germany) and CEA Service Basses Temperatures Grenoble (France) has been formed to push this technology forward. As the R&D progresses, further academic partners will be attracted and they can become involved in additional activities such as materials for machinery, dedicated system simulation including fluid dynamics, reliability and availability engineering, business case development, automation technologies, mechanical engineering and much more.

Cooperation with industrial partners

As the development of the technology advances towards general implementation, it becomes an interesting test bed for the industrial partners who drive compressor machinery technology forward (e.g. MAN Turbo and ATLAS-COPCP). Eventually, when the programme approaches the practical demonstration of the nelium-cycle, companies who are leaders in cryogenics such as Linde and Air Liquide will be interested in the developments for their own use.

Impact potential

The main impact of this technology is the produce a large-scale cryogenic refrigeration system, which makes the FCC-hh feasible. Beyond that goal, the development of an entirely novel refrigeration technology could have a substantial economic impact. The potential extends to hydrogen liquefaction, considered the most difficult liquefaction process but a key technology to enable a shift to clean energy production. In general, any application that requires highly efficient and reliable compressors will directly profit from this R&D. Examples include the production of liquid oxygen for space transport systems, industrial production of metal, natural gas production and transport.

Milestones and deliverables

The milestones and deliverables are presented in Table 12.4.

Table 12.4. Milestones and deliverables for cryogenic refrigeration.

Title and description	Year
Nelium cycle modelling and simulation results available	2019
Test station and compressor prototype design and specifications available	2020
Test station operational	2021
Results from experience with test station available	2023
Architecture for a demonstrator with optimised machinery available	2024
Designs of the machinery for a demonstrator available	2025
Demonstrator operational	2026
Results available for co-design of full-scale nelium plant with leading industries	2027

12.5 Cryogenic distribution line

Motivation

The state-of-the-art large cryogen distribution systems deploy stainless steel headers equipped with compensation units and fixed/sliding points in order to accommodate the 3 mm/m contraction during the cool-down phase. The new cryogen distribution line requires the compensation of a total thermal contraction of more than 90 m. In the conventional design, the compensation units and the sliding points are the main source of failure (buckling, leaks). In order to achieve a feasible technical design and good reliability, R&D for a new approach is required.

Objectives

Designing the internal cold headers based on Invar is one way to have a system that is technically feasible and is sufficiently robust. Invar is a nickel-iron alloy, invented in 1896, notable for its uniquely low coefficient of thermal expansion. Its inventor, physicist Charles Edouard Guillaume received the Nobel prize for his discovery in 1920. Using this material, compensation units and sliding points are not required and consequently, the overall reliability of the system increases.

Description of the work

In order to validate the approach, a 100 m long demonstration example of a compound cryogenic distribution line needs to be designed and studied under realistic operating conditions. This project comprises the proof of feasibility of production (e.g. definition of welding procedures), the development of a mechanical and thermal design that suits the various operation modes (cool-down, steady-state, warm-up) and the gathering of detailed information about the reliability of the system over long periods of operation.

Cooperation with universities and research institutes

Several universities who are active in the field of low temperature engineering are candidates for this project. In particular, Wroclaw University of Technology (Poland) has a background in this domain. The possibility to set up a large-scale test facility is also an ideal opportunity for universities of applied sciences, higher technical schools and apprentices to participate in an international technological research project which has industrial collaboration.

Cooperation with industrial partners

The nature of this project with its close links to industry creates a favourable environment for a collaborative project with industry. In addition to the leaders in cryogenic systems, Air Liquide (France) and Linde (Switzerland), other companies such as Alstom (Switzerland), Kraftanlagen (Germany), Messer-Griesheim (Germany), Nexans (Germany), Nordon (France), as well as ancillary equipment providers such as Criotec (Italy) can all contribute to the project.

Impact potential

The large-scale demonstration of the Invar based approach can translate into direct benefits for the industries which deliver cryogenic refrigeration plants and infrastructure. In addition, the knowledge gained by participating universities, schools, apprentices and industrial engineers is a notable facet of this R&D. The outcome should be an expansion of the market and an increase of competitiveness through the adoption of this validated advanced technology.

Milestones and deliverables

Table 12.5 outlines initial milestones and deliverables for this R&D activity.

Table 12.5. Milestones and deliverables for the cryogenic distribution line.

Title and description	Year
Requirements and design	2019
Prototype specification and test-bed definition	2020
Test bed operational	2022
Prototype built and installed	2023
Tests complete	2024
Concept validated and recommendations formulated	2025

12.6 Superconducting septum magnets

Motivation

The extraction system is a key component of the collider, ensuring safety of operation. Conventional normal conducting septa are limited to magnetic fields of around 1.5 T. For transferring beams with very high energies at the FCC-hh or HE-LHC this limitation would lead to power-intensive systems which occupy a large amount of space. Superconducting septa reaching field levels of 3 to 4 T will allow significantly more compact injection and extraction systems, will simplify straight section and overall system design and will also greatly reduce the operating cost by having a lower electrical power consumption. The development of such an accelerator device is therefore considered a key research topic in enabling technologies.

Objectives

This specific R&D project aims to design, build and validate a short (∼0.5 m), accelerator-quality prototype magnet based on the flux-shield principle. It can be

used to demonstrate the validity of the concept and will have the following target parameters: 20 mm aperture for the circulating beam, 30 mm aperture for the extracted beam, 3.2 T field, 1% field homogeneity and an apparent septum thickness of 25 mm.

Description of the work

The project consists of the following steps:

- Design of the shield, including simulation of the element
- Investigation of quench protection aspects and design of a viable quench protection system
- Construction of a 700 mm long, MgB_2-based, superconducting half-moon shield
- Test of shield performance in an HL-LHC CCC corrector prototype
- Design of a dedicated CCT septum magnet incorporating the half-moon shield
- Construction and test of a CCT magnet
- Construction of a Ni-Ti/Cu multilayer shield (optional)
- Test of shields in the CCT septum magnet
- Assessment of the septum system performance.

Cooperation with universities and research institutes

This well-defined and self-contained R&D package is an ideal candidate for a collaborative research activity. Wigner Institute (Hungary), having already accumulated experience in this field of superconducting technologies, would lead the design and simulation activities as well as the manufacture of the CCT magnet. CERN would provide essential components, expertise in superconducting magnet design and quench protection systems as well as a cryogenic test facility (SM18). The project is open to further academic partnerships in the fields of superconducting magnets, instrumentation and field testing, electronics and software development.

Cooperation with industrial partners

Potential industrial partners for this topic are in the process of being identified. Engious Ltd. (Hungary) for instance, is an advanced manufacturing company that could develop the precision tooling and mechanical assembly methods for the shield and magnet. Additional high-tech companies could be partners for the provision of services for ancillary equipment components and the testing facility.

Impact potential

In addition to the design of a viable extraction system of the FCC-hh or the HE-LHC, applications include the FAIR facility at GSI (Germany) and a new extraction system at the potential new superconducting SPS accelerator at CERN. The co-development with a fast growing high-tech manufacturing company would provide the partner with the possibility of gaining experience in an international project and thus to build a reputation and enter new markets. In particular the acquisition of expertise in the handling of the superconducting material MgB_2, which is increasingly used in medical imaging devices, and in the domain of lossless power transmission will help to improve the competitiveness of the R&D partners.

Milestones and deliverables

Table 12.6 outlines initial milestones and deliverables for this R&D activity.

Table 12.6. Milestones and deliverables for superconducting septum magnets.

Title and description	Year
700 mm MgB_2 shield manufactured	2019
Shield tested in HL-LHC CCT corrector in SM18 at CERN	2019
Design of CCT septum dipole available	2019
CCT septum dipole constructed	2020
Septum assembly tested in SM18 at CERN	2020
Ni-Ti/Cu multilayer shield manufactured	2020
Ni-Ti/Cu septum assembly tested in SM18 at CERN	2021
Assessment of superconducting septum documented	2022

12.7 Solid state generators

Motivation

Modular, scalable, fast and affordable high-power switching systems are key components of beam transfer systems. The current gas-filled thyratron switches are becoming increasingly outdated and their future commercial availability is already uncertain. In addition, they suffer drifts in performance and have high operational complexity. Solid-state switches are the ideal technology for large systems and for systems with high operational availability requirements. However, such high-performance systems are not yet commercially available.

Objectives

This R&D programme progresses along three well-aligned paths:

1. Fundamental research on switches aims to increase the performance of individual switching SiC, dynistor and GTO modules. This activity includes the development of the associated high-speed, reliable triggering methods such as impact ionisation, laser and potentially other optical methods, which are robust against spurious activation. The developments aim to operate reliably in radiation environments, therefore one part of the work will deal with understanding and increasing the radiation-related performance limits. Finally, this package needs to carefully cover all protection-related issues.
2. A novel inductive adder generator with fast rise-time and high-voltage for short-pulses for use with terminated and short-circuit loads needs to be developed.
3. A Marx generator for slower rise time, lower voltages and longer pulses for use with terminated and short-circuit loads, needs to be developed.

Description of the work

The project consists of the three steps described below.
For fundamental research and development on switches, the following activities are needed:

- Evaluate the basic performance of single devices such as MOSFET, SiC, dynistor and GTO.
- Improve the performance of stacked arrays and single-switch applications. Verify the switching time, voltage, current and resistance.
- Establish the potential performance reach of the individual technologies from the technology assessment and improvement activities.
- Develop appropriate triggering methods that match the individual device characteristics, stacking topologies, EMC and performance needs. In particular, drive the development of laser triggering and investigate the potential of impact ionisation triggering for GTOs.
- Determine the characteristics of the different switching modules for use in radiation environments. To achieve this, advances in the measurement techniques for radiation-related performance analysis are required.
- Develop fast, scalable, modular systems that meet the new protection requirements of single and stacked switches, especially in view of adaptation to short-circuit loads.

The following activities are needed for the inductive adder generator development:

- Design and build an inductive adder generator with a target pulse length of $1\,\mu$s to be evaluated in the PS complex at CERN (e.g. test on the ion injection kicker).
- Set up a demonstration device consisting of a series of generators to gain experience with the operational behaviour of a large distributed system.
- Based on the findings, develop the detailed specifications for a complete system including non-functional requirements such as operation, maintenance and repair, safety and industrial supply.

For the Marx generator, the following activities are needed:

- Identify institutes for a collaborative project for the construction of a Marx generator with a target pulse length of $10\,\mu$s.
- Design and build the generator. Deploy it in the PS complex at CERN to gain experience in operating such a system.
- Based on the findings, develop the detailed specifications for a complete system including non-functional requirements such as operation, maintenance and repair, safety and industrial supply.

Cooperation with universities and research institutes

The individual, well-defined and self-contained parts of this R&D package are ideal candidates for collaborative research activities. Several institutes such as ETH Zürich (Switzerland), various Helmholtz Gesellschaft institutes (Germany), the Institute of Electrophysics (Russia), the University of Manchester (UK) and Lisbon University (Portugal) have already been identified as partners in this programme. The project is open to further academic partners in the fields of high-power semiconductor technology, electronics and embedded systems development.

Cooperation with industrial partners

Potential industrial partners are in the process of being identified. ABB (multinational with headquarters in Switzerland) is a potential co-innovation partner for switches and EnergyPulseSystems (Portugal) for modulators. Additional high-tech companies could be partners to provide services for ancillary equipment and for system integration.

Impact potential

In addition to ensuring the long term future of kicker systems for particle accelerator laboratories (e.g. ALBA-CELLS, ESRF, INFN labs, ISIS, SOLEIL, GSI, PSI, FNAL, BNL, JPARC to name but a few), developing this innovative technology with industrial partners has many potential applications in industry: wherever high-energy (voltage and current) pulses are needed, the technology can be deployed. Examples include high-speed forming systems, such as electro-hydraulic magnetic forming and magnetic pulse forming, which has become wide-spread in the automotive and aerospace industries, and for metallic forming processes of commodity goods, radar power supplies and medical x-ray devices.

Milestones and deliverables

Table 12.7 outlines initial milestones and deliverables of this R&D activity.

Table 12.7. Milestones and deliverables for solid state generators.

Title and description	Year
Establishment of a consortium comprising academic and industrial partners	2019
Technology survey available	2020
Procurement of components for test systems completed	2020
Laboratory test benches operational	2021
Radiation tolerance assessment complete	2022
Performance limitations for device triggering evaluated	2022
Switch and adder system designs and test procedures complete	2023
Prototype systems ready for deployment in a particle accelerator	2023
Experience from practical operation documented	2025
System specifications available (requirements, architecture, design)	2026

12.8 Energy storage and release R&D

Motivation

The development of novel energy storage systems has seen impressive progress over recent years, mainly driven by the automotive sector and the increasing use of renewable energies. Batteries appear to be the most promising solution to store the energy recovered from superconducting magnets at the end of a cycle to support the powering of the accelerator during the subsequent ramp phase. This approach could significantly reduce the requirements for peak-power and would keep the overall energy consumption and cost of the electrical infrastructure within the limits that have been established based on average power consumption estimates. Batteries are the focus of the R&D programme due to the continuing developments towards ever higher energy storage densities. Today, the most suitable battery technology for this application are lithium batteries, in particular lithium titanium oxide (LTO). On a longer time scale, other technologies can also be considered and a targeted R&D initiative would feature an ongoing assessment of technology options in cooperation with academic and industrial partners.

Objectives

This R&D initiative aims to develop a suitable battery-based energy storage and release system to recover the energy stored in superconducting magnets, to temporarily buffer the energy and to provide the energy to magnet power converters to support the accelerating phase of the cycle. Such a system would required batteries capable of at least 20 000 charge-discharge cycles suitable for the power profile of the magnet cycles. Due to the underground space limitations, energy density and volume reduction are additional requirements to be considered. The system must comply with the safety requirements for underground installation and operation. Maintenance, reliability and total-cost-of-ownership (TCO) need to be part of the investigation from the beginning.

Description of the work

The first stage of this programme consists of drawing up a battery-supported powering system concept for a particular particle collider. This scheme will be used to develop requirements specifications for a battery-supported energy storage and release system that can be used with a superconducting magnet/power converter circuit. An essential part of this work is the definition of the interface and the interplay between the battery storage system and the power converter, which is part of the magnet circuit. The second stage focuses on the technical design studies for the energy storage systems, including the co-development activities with industrial partners for all major system components. A third stage would focus on a demonstration of a battery-based energy storage system at an existing particle accelerator, such as the HL-LHC.

Collaboration with universities and research institutes

The cooperation with universities and research institutes focuses on the requirements finding process and on the development of a concept for energy recovery, buffering and release in the particle accelerator domain. The work on developing a concept for a future circular collider will also be carried out as a cooperative effort with universities and research centres. The construction of the HL-LHC upgrade, in particular an energy recovery system for the inner triplet magnets, opens an ideal opportunity and time window for this activity.

Collaboration with industrial partners

The cooperation with industrial partners focuses on the design, development, testing and co-innovation of major system components to build an energy recovery system for a particle accelerator. The following equipment components would be candidates for such an activity: battery-cells and modules that can meet the operation and deployment conditions and the reliability requirements, and a battery management system and protection systems. Finally, cooperation on assessing the total cost of ownership, that permits a cost-benefit analysis to be carried out, will be included in the work with industry.

Milestones and deliverables

Table 12.8 outlines initial milestones and deliverables for this R&D activity.

Table 12.8. Milestones and deliverables for the energy recovery demonstrator project.

Title and description	Year
Definition of a demonstration case for an existing particle accelerator	2019
Documentation of requirements and constraints for an energy recovery system	2020
Creation of a consortium for the research project	2021
System concept specification and architecture definition	2022
Key component definition and start of research work with industry	2023
Development of test bed complete	2024
Testing of key components performed	2026
Demonstrator operational	2028

12.9 Particle detector technologies

Motivation

The particle detectors at future circular lepton and hadron colliders will require significant performance advances and the development of cost-effective devices using new detection technologies. Since this is an ongoing process of improvements that have to be validated in operating environments with a continuous effort to develop ever more precise and faster particle detection, a significant amount of preparative R&D will already be performed within the LHC/HL-LHC experiment upgrade projects.

A targeted detector R&D programme needs to be defined once a particular particle collider scenario is selected for in depth design and when the corresponding experiment projects have been defined.

Therefore, the focus here is on a brief description of the ongoing effort and initiatives which underline the continuing need to support collaborative particle detection research in programmes at academic institutes worldwide. Such initiatives will lead to the development of technologies which will be used in the LHC/HL-LHC experiments and will therefore create lasting impacts beyond individual efforts. Proof-of-concept and fundamental technology research will accompany these developments and the results will flow into the development of technical proposals for specific projects. These proposals will become part of a focused particle detector research programme following the selection of a specific particle collider scenario.

Objectives

At CERN, a strategic R&D initiative, to define and organise the detector technology related research activities for the coming years, was launched in 2017 [341]. It covers the following topics:

1. Silicon sensors
2. Gas detectors
3. Calorimetry and light based detectors
4. Mechanical supports for detectors
5. Integrated circuits
6. High-speed data links
7. Simulation and analysis software
8. Detector magnets.

These technological aspects will be accompanied by detector performance studies in order to have a clear understanding of the improvement potential for various detection technologies and to be able to quantitatively document the further improvement potential and to identify potential limits of the various technologies.

It is only at this stage the detector concepts that have been developed for the hadron and lepton particle colliders can be simulated with a sufficient degree of fidelity. The results will give a better understanding of the physics performance that can be expected and will identify the technological gaps and how they can be overcome. This activity will eventually lead to the specification of the function, performance, reliability and other qualitative requirements that form the foundation of the technical design of the experiments.

Description of the work

The CERN coordinated detector technology research initiative spans a five-year period. Regular workshops are already taking place (e.g. [342]) to develop the detailed research programme and to prioritise the work together with an open, international consortium of academic institutes. The programme also aims to identify possible involvement of industrial partners from a very early stage so that it can be understood which technologies can eventually be produced on an industrial scale and which technologies industry is particularly interested in.

The initiative is structured in several working groups (WG), each one focusing on a particular technological domain. This setup forms the nucleus of a converging activity of international research institutions and universities which provides the opportunity to involve partners from all over the world.

The depleted CMOS technology attracts a lot of interest in the domain of silicon detectors (WG 1), as it allows low-mass and high-resolution sensors, which have the potential to cover large areas at affordable cost, to be built. In recent last years, substantial progress was achieved in terms of radiation hardness, a key requirement for all future experiments. Another trend is in low gain avalanche detectors (LGAD), which have achieved timing precision in the range of a few tens of picoseconds. Finally, there is also a strong need to continue the development of classic silicon detectors (pixels, strips and pads) and the associated electronics.

Gas detectors (WG 2) will continue to play an important role in future experiments as they can cover large areas at moderate cost. Micro pattern technologies have boosted their performance and a wealth of new ideas in terms of materials, production techniques and readout methods, show how this success story can be pursued. An important question concerns the choice of the gases and their compatibility with environmental standards.

Working group 3 deals with calorimetry and light based detectors, two topics often closely linked. One focus is on highly granular calorimeter concepts which allow the decomposition of jets into their individual particles ("particle flow calorimetry"). The requirements are manifold as are the options in terms of active media (e.g. scintillators, noble liquids, silicon), absorbers and readout concepts. Accurate and high-precision timing is a key topic, too. In recent years, photosensors have been evolving rapidly. The silicon photomultiplier (SiPM) has matured and has become a standard tool for many applications. However, its high dark count rate and moderate radiation hardness limit its use when it comes to the detection of low light levels, e.g. in Cherenkov detectors. This is still the domain of vacuum tubes, where emerging, finely segmented multi-anode devices, micro-channel plate tubes (for ultra-fast timing) and completely new concepts go far beyond the classic PMT.

Working group 4 on detector mechanics pursues the use of advanced materials, design tools and production technologies, which have the potential to change the way detectors are built and help to boost their performance. Ultra-light, precise and large size carbon-fibre components have become accessible and permit the development of solutions which were inconceivable ten years ago. Environmentally friendly cooling

technologies, combined with 3D printing and micro-fabrication technologies reduce the amount of material in vertex and tracking detectors. Close cooperation with industrial partners is seen as the best way forward.

Working groups 5 and 6 deal with the development of application-specific electronics and high-rate, high throughput, data transmission for applications with severe constraints (radiation, power consumption, heat dissipation and space limits, accessibility, cable path limitations and more). The numbers of custom made chips in the LHC experiments is counted in millions and the high energy physics community is considered to be an expert customer with very special requirements. The ever-decreasing size feature in the CMOS manufacturing processes leads to benefits (higher functionality), but also to emerging behaviour (higher sensitivity to radiation, challenging cooling needs) and much higher costs (the number of transistors that can be obtained levelled out in around 2012 and since then it has started decreasing again. As a result of consolidation in industry fewer suppliers of very high density integration devices exist and the competition across the market has decreased. The main challenges remain the strongly increasing ionising doses and the necessity to read and transfer continuously increasing amounts of data.

Found at the other end of the data acquisition systems are the event filtering farms with their advanced software for pattern recognition, track reconstruction and other event selection processes. This is the topic covered by WG 7. New approaches to cope with the track reconstruction challenge at event pile-up rates of 1000 and more (FCC-hh scenario) need to be developed. Machine learning is one topic that needs to be investigated as a possible support technology for such challenges. Already more than ten thousand physicists world-wide use the software frameworks and algorithm toolkits produced by such software development initiatives. The Exabyte era, which is appearing on the horizon, calls for new concepts to manage such amounts of data on a global scale throughout several decades of research.

Last but not least, WG 8 pursues the development of sustainable concepts for large high-field magnets for the experiments. There is a study for FCC-ee of an ultra-thin 2 T magnet with a free bore of 4.4 m and 6 m lengths and a target material budget below 1 radiation length. The FCC-hh baseline design has a main solenoid with a free bore of 10 m and a length of 20 m and forward solenoids at both ends. All of these magnet developments require progress in superconducting wire technology.

Milestones and deliverables

The second workshop scheduled for autumn 2018 [343] concerns the writing of a report that summarises the focus and the priorities of the R&D programme. This roadmap will include the milestones and deliverables for the initial five-year period.

12.10 Efficient power distribution infrastructure

Motivation

Power quality is a primary concern for all three of the colliders studied (FCC-hh, FCC-ee and HE-LHC). Achieving adequate availability to ensure efficient use of the new infrastructure, to avoid costly downtimes and to achieve energy-efficient operation by reducing the need for recovery and restore actions is closely linked to the parameters that determine power quality: transient voltage dip mitigation, reactive power control, harmonic filtering and voltage stability. Switching from an alternating current (AC) distribution network to a direct current (DC) power distribution in

combination with local energy buffering addresses several of the key impact factors. Frequent transient power dips can be tolerated, active and reactive power can be compensated on the load side, AC harmonic filtering is not needed, distribution losses are significantly reduced and larger spacing between electrical infrastructures compared to AC distribution is permitted which leads to reduced infrastructure component investments.

Today, this technology is still in its infancy, mainly lacking adequate standardisation of operating parameters and the availability of a set of equipment from different vendors due to its lack of widespread adoption. Viable designs of electrical components for DC current and voltage switching, short-circuit current switching, fault detection and protection system selectivity remain to be developed and still represent technical challenges.

Objectives

The objective is to raise the readiness level of medium-voltage DC distribution network technology by demonstrating its merits at CERN in close-cooperation with an industry-driven demonstrator project. This case serves as a platform for a consortium of industrial partners to develop standards for this grid technology and to trigger the development of market-ready equipment. Technical challenges that still remain to be addressed mainly concern electrical components for current and voltage switching and protection elements such as short-circuit current switching, the detection of faults and an appropriate approach to implement selective protection for the network (e.g. a fast fault-detection and protection communication system to isolate the faulty element, maintaining overall high system reliability). This project aims at facilitating the acceptance of the technology among potential end-users in the commodity market. Eventually, if this technology becomes wide-spread it will be available to large-scale research infrastructure customers at the time when a future particle accelerator is to be installed.

Description of the work

The first phase to be carried out during a particle collider preparatory phase aims to establish a stable consortium of companies who are active in standardisation bodies and who actively study the market opportunities of commodity sectors, companies who have an interest in the development of key components and integrating them in a demonstrator at one of CERN's accelerators. Universities and research centres that develop solutions for the technical challenges and who have the necessary experience should also be part of this consortium. The first phase of the work consists of analysing a specific use case to provide power for one of CERN's accelerators, the capture of the requirements and a detailed technical gap analysis in cooperation with academic and industrial partners. In a second phase, consortium members draw up an architecture and propose a design for a demonstrator that includes the development of novel components to address the most critical technical challenges. In a third phase, prototypes of the technical components are developed by different contributors, fostering the co-development of academia and industry. Finally, a demonstrator that can also serve as a showcase for industries to raise the acceptance of the technology at large scale should be installed at CERN. This work programme needs to be accompanied with the conceptual and technical design of a DC network for a specific particle collider scenario. This work can be based on the recommendation of the next European Srategy for Particle Physics update.

Collaboration with universities and research institutes

MVDC distribution systems are an active area of academic research that spans various sectors including electrical engineering, electronics, information and computing technologies, reliability engineering, functional safety, economics and business analysis. Consequently, this is an ideal application to bring academic partners with complementary competencies from different geographical regions together at CERN in a concrete technological research project with tangible impact potential at academic levels, with high-educational value and with opportunities to work in a close-to-market environment. Specifically, EPFL (Lausanne, Switzerland), a technical university, has an active programme on the development of MVDC power distribution networks with support of the Swiss Federal Office of Energy (SFOE).

Collaboration with industrial partners

With the increasing availability of modern power electronics technologies such as switch-mode converters with higher power ratings, DC networks are being increasingly considered for high voltage transmission lines (HVDC). DC networks start to be deployed for specific applications such as the supply of power for trains in underground metro transport facilities.

In addition to point to point and residential collection grids, MVDC is an interesting solution for industrial applications due to its efficient operation, the small footprint and the low installation and operating costs. Companies like Hyundai, ABB, Siemens and Rolls-Royce are investigating the suitability of this technology for offshore and maritime vessel applications as well as for heavy industries (e.g. aluminium manufacturing) and DC microgrids like those found in shopping centres, office blocks and in particular ever power hungry data centres, smart residential areas and also rural electrification. Since the technology is also ideal for integrating environmentally friendly power sources such as photovoltaic panels (PV) and to a lesser extent fuel cells, companies that are active in the power generation market are also starting to have an interest in this technology. The "EMerge Alliance" (www.emergealliance.org) built around this elusive technology is a mirror of who-is-who in the electrical industry and also the world's most important standardisation organisations IEEE and ISO are involved in the ongoing activities. Hence, this is an ideal opportunity for an international community with a vision for a large-scale research infrastructure to provide a test-bed for academia and industry world-wide with the potential of large benefits for society and at the same time preparing the path for large-scale science infrastructures to be operated in a sustainable fashion.

Initially, the focus can be on designing and standardising components, such as DC current breakers, rectifiers, rectifier-transformer solutions and protection systems. The co-developments should leverage existing application development efforts, such as DC railway systems.

Milestones and deliverables

A preliminary set of milestones and deliverables for this research activity is outlined in Table 12.9.

Table 12.9. Milestones and deliverables for MVDC demonstrator project.

Title and description	Year
Definition of demonstration case for an existing particle accelerator	2019
Creation of a consortium for showcase project	2020
Definition of requirements and corresponding sub-projects complete	2021
Testbed design and key challenges documented	2022
Component prototyping complete	2024
Development of key components for test bed complete	2026
Testing of key components performed	2026
Design iteration of test bed complete	2027
Demonstrator operational	2028

Trademark notice: All trademarks appearing in this report are acknowledged as such.

Appendix A: Uncertainties

This section summarises those uncertainties, which have the highest potential of leading to adverse impacts on the project. They are grouped by technological and implementation-related elements, depending on their origin. The preliminary information provided in this volume is a non-exhaustive, simplified assembly of risks, risk origins, impacts and mitigation measures. It merely serves to give a glimpse of the comprehensive risk management process, which has been set up and which is currently ongoing in the Future Circular Collider study. A risk assessment database is maintained by the study group in order to establish an early warning and mitigation process that is expected to grow into a comprehensive project risk management scheme during the project preparatory phase.

A.1 Accelerator and technologies

Table A.1. Technological uncertainties with decisive impact potentials on the project.

Uncertainty	Impacts	Mitigation Measures
Nb_3Sn wire performance not achievable within the available time window.	Target field level and field quality of dipole magnets cannot be reached. Collision energy will be lower than designed and consequently the collider performance is lower than expected.	Increase the intensity of the low-temperature superconducting wire R&D programme.
Cost target of Nb_3Sn wire not reachable or not reachable within the available time window.	Project not affordable or particle collider performance targets need to be adjusted.	Increase the intensity of the low-temperature superconducting wire R&D programme. Invest in building up a co-development with industries worldwide in an R&D programme to avoid a *vendor-locked-in* situation and to prevent price limitation.
Vendor locking for superconducting wire.	Project not affordable or project schedule cannot be met.	Consider an R&D initiative with academic partners to ensure in-house expertise on the technology and open standards and designs that can be licensed to different types of companies including those established in metallurgical processing and manufacturing.

Table A.1. (Continued.)

Uncertainty	Impacts	Mitigation Measures
Inefficient magnet series manufacturing and limited availability of companies with comparable manufacturing throughput and adequate quality management.	Project not affordable, reduced performance and reliability of the machine, possible need to lower the collision energy in order to adapt to lower field and field quality, lower overall collider performance leading to a longer operation schedule. Project implementation delayed. Excessive growth of project cost due to the need to re-manufacture or exchange magnets. Unsustainable operation due to lower than foreseen reliability that causes substantial downtime for repair or maintenance.	Invest in R&D to develop magnet designs that are easier to manufacture, in particular aiming at streamlined production, testing and installation. Optimise the internal system interfaces with respect to number and simplicity as well as the external system interfaces, including test points for total quality management. Launch studies to improve the efficiency of assembly, considering interfaces, simplification and speed-up of individual production and processing steps. Invest in automation of production, assembly, testing and the integration with a total quality management system which takes into account a geographically distributed production process.
Magnet is incompatible with limited LHC tunnel dimensions and operation environment.	Trade off between constraints imposed by existing underground and technical infrastructure and attainable performance (lower field leading to lower collision energy). Lower availability due to need to work with accelerator cycles that are compatible with the magnet performances and cryogenic refrigeration infrastructure capacities that can be implemented. Project delayed due to a longer design phase.	Perform a HE-LHC specific superconducting magnet design study during the technical design phase.
Capacity of cryogenic refrigeration system insufficient.	Lower particle collider performance due to the need to adjust operating parameters (e.g. longer cycles, lower peak field, lower intensity).	Invest in bringing the more efficient, nelium-based cryogenic refrigeration technology to a higher technological readiness level in cooperation with industrial partners through dedicated R&D.
Electrical supply peak power requirement is too high.	Cost of classical electrical infrastructure and installation becomes prohibitive.	Invest in bringing more efficient cryogenic refrigeration with less electrical energy requirements for the same cooling performance to higher technology readiness level in cooperation with industrial partners through dedicated R&D. Invest in R&D to develop a system that can recover energy from the accelerator subsystems, buffer that energy temporarily and use it during the subsequent cycle to reduce the peak power needs during the ramp phase. Invest in R&D on more efficient electricity distribution systems which exhibit lower equipment costs and reduced losses.
High amplitude thermal contraction and expansion of conventional cryogenic distribution system during cool down and warm up.	Complicated design of a conventional cryogenic distribution system to absorb thermal contraction and expansion can result in significant cost increase, lower reliability and thus unsustainable operating costs. In addition, high loss rates and excessive maintenance and repair can cause unacceptable downtimes and drive the cost of operation up.	Bring a cryogenic distribution system based on a low-thermal expansion material to industrial production grade through focused R&D and a co-innovation approach with industrial partners. This activity, which will also reduce the number of equipment components and lead to a simpler design will also help to control the total cost of ownership through reduced losses and reduced requirements for maintenance and repair.

Table A.1. (Continued.)

Uncertainty	Impacts	Mitigation Measures
Conventional systems may not be adequate to extract the high-energy beams reliably and with acceptable electrical consumption.	Unreliable extraction can lead to equipment damage and consequently to substantial downtimes. This situation results in the loss of investments and unsustainable operation of the infrastructure. Conventional systems consume too much electrical energy leading to high operating costs.	Through targeted R&D, develop a highly distributed, reliable and high-performance extraction system that can cope with the high beam energies. The research has two facets: a novel superconducting septum, requiring less energy, space and system complexity and secondly, scalable, fast and affordable high-power switching devices. Accompanying this equipment R&D, and in cooperation with external partners, there should be the development and validation of fast, modular and reliable control system technologies that can meet the safety and reliability requirements.
Depending on the particle collider scenario and the foreseen research programme, particle detection technologies do not meet the performance, reliability and cost needs.	Under-use of the potential of the particle collider can lead to the physics programme goals not being met or not meeting the goals within the planned schedule and cost envelope. Excessive costs of experiment detectors. Low maintenance intervals and long repair times as well as equipment replacement costs that lead to unsustainable operation of the research facility. Loss of interest of the worldwide science community due to limited physics research reach, loss of a science vision within an achievable time frame and within state-of-the-art scientific research methods and tools.	Definition of a world-wide coordinated strategic R&D initiative focusing on detector technologies that, with the selection of a preferred particle collider scenario, becomes more specific as technical designs advance, research communities become organised and the specification of experimental physics investigations are developed in greater detail.

A.2 Implementation

Table A.2. Project implementation related uncertainties with decisive potential impact.

Uncertainty	Impacts	Mitigation Measures
Decommissioning and dismantling of LHC. Concrete examples include the development of technologies to dismantle the accelerator magnets, to remove and dismantle activated equipment, to store and treat large quantities of activated material in a short time. An open item to be agreed with the two host states is the distribution of the activated waste after dismantling according to a "fair share" approach.	Decommissioning and dismantling of the LHC is a project for which schedule, cost and risks remain to be analysed. The costs of dismantling, treating and disposal of the resulting waste can be estimated as a small percentage of the machine's construction cost. Due to the various classifications of the radioactive materials resulting from decommissioning, cost and duration of the work are today difficult to estimate. Skilled personnel are needed to develop, plan and carry out the dismantling project. Depending on these factors, the overall HE-LHC project cost may increase and the time for construction and brining it into operation may need to be extended.	Perform a thorough study for the decommissioning and dismantling of the collider and all the technical infrastructure equipment. As soon as possible perform an in depth study for the treatment of the radioactive waste, including temporary storage and develop agreements with the two host states to accept the material within the necessary time span and at the appropriate point in time. Technologies and processes are available on the market today. Therefore, cooperate with industrial partners to evaluate the appropriate technologies that can help to speed up the process and limit the need for personnel in radiation areas. Develop technologies in cooperation with experienced external partners with a view to reducing the amount of material classified as radioactive-waste.

Table A.2. (continued.)

Uncertainty	Impacts	Mitigation Measures
Limited capacity for handling excavation materials in the host states, relevant for all particle collider scenarios, including the HE-LHC due to the need for new underground facilities.	Delay of construction phase start or increase of construction costs due to unplanned waste disposal needs. Non-acceptance of project plan by host-state representatives with or with- out public opposition.	Early start to develop a territorial waste management plan that takes into account the current legal situation in the host states and the transnational context of the project, contributing through the involvement of relevant experts at international level to the evolution of the current initiatives on moving towards a circular economy at European scale. Through the work at a stage in which a detailed project design remains yet to be developed, invest in R&D, e.g. through EC funded projects on circular economy and infrastructure construction efficiency, to identify novel separation and processing techniques, identify existing and so far not considered use cases and bring them to credible technology readiness levels. Develop a territorial concept for the logistics of tracing and transporting the excavation materials with the support of ICT systems, involving the host states, potentially relevant industries and consumers throughout the entire process.
Cost of the underground infrastructure consolidation and upgrade.	Cost uncertainty leads to unexpected project cost increase and extended project schedule.	Perform a HE-LHC project specific, detailed underground infrastructure upgrade and consolidation study to obtain a more specific cost and schedule estimation. Through more detailed studies of subsystems that require electronics equipment close to the accelerator confirm or disprove the need of additional alcoves.
Timely availability of the rights of way on required land plots, mainly in Switzerland, but also to a limited extent in France.	Delay of the project preparatory and construction phases. Excessively growing project costs due to real-estate speculations. This can lead to a delay of the start of collider operation beyond 2050 and to the need for substantial re-scoping of the project and unacceptable project goal compromises. Consequently, the world-wide research community may loose interest in the project, which in turn, can adversely impact the project implementation.	Early optimisation of the layout and placement of the collider and surface sites as a cooperative effort between project owner and named governance bodies, involving public stakeholder representatives. Apply the strategy of "avoid – reduce – compensate" to prevent the need for excessive socio-environmental impact mitigation as far as reasonably possible. Inclusion of a project scenario in the territorial development plans of both countries from 2020 onwards to anticipate the needs and to avoid conflicts of use with other development projects.

Table A.2. (continued.)

Uncertainty	Impacts	Mitigation Measures
Uncontrolled resource usage during the operation phase (examples include, but are not limited to, water for conventional cooling, in particular if intake and reject occur in different countries, electricity consumption, generation of waste-heat, cryogens, potentially harmful chemicals, introduction of sealed surfaces on the land – asphalt, concrete etc.)	Project-specific regulatory requirements imposed early during the preparatory phase (e.g. in the frame of the development of the law for the unique project procedure in France) can lead to unsustainable operating costs. Alternatively, project acceptance by public stake-holder representatives may be delayed, leading to the project preparation, construction and commissioning period being longer than acceptable, potentially also requiring technical modifications at a stage where such interventions in the design can be costly.	Timely work with the host-state representatives on establishing a communication culture between administration offices, external experts and project engineers has started during the conceptual design phase. Subsequent early common work in the form of a partnership can on one hand help developing a technical project with reduced resource needs and on the other hand trigger targeted investigations to identify alternative approaches to cope with the resource needs. Consequently, a number of design studies dealing with resource-related questions during the preparatory phase, including experience from the LHC and HL-LHC projects is indicated. Examples include applications for making the waste-heat available, studying alternative cooling and ventilation technologies, studying surface site designs that correspond to the ecological needs and that can fit with the cost envelopes, identify approaches to limit losses and to recover energy.
Low cost-effectiveness and quality of materials and services supplied due to excessive constraints on public tendering processes. This includes the limitations of a well-defined cost/performance based procurement scheme for the project, ineffective international networks with industries and potential suppliers of all sizes, too much generic focus on either in-house or out-sourced services, insufficient personnel (in-house or contracted) resources for procurement, contract follow up and inadequate business processes as well as during peak periods a lack of legal advisers with extensive industrial experience.	High effort required for administrative procedures resulting in lengthy and costly procurement processes which have an impact on the duration of the project preparation and construction phases. These can lead to the selection of under-performing suppliers which in the long run leads to potentially unacceptable high total costs of ownership (re-construction of subsystems, high repair or maintenance costs, high operating costs).	Timely preparation of an adequate procurement and academia/industry co-development framework. Timely investment in preparing the basis of a well staffed project procurement system, taking into account the changing needs during various phases of the project (preparation, CE construction, machine construction, commissioning). Timely development of an appropriate concept for in-kind participation of member- and non-member states with a corresponding project governing and management structure that includes effective levers to proceed with the implementation of the project (early stall warning, re-prioritisation, re-scheduling, re-assignment).

Table A.2. (continued.)

Uncertainty	Impacts	Mitigation Measures
Availability of stable and effective governing and management structures driving forward the technical design of a collider, the associated experiment detectors, the host state activities and the financial strategy.	The lack of a vision of the priorities, which is propagated in the framework of a governing and management structure with adequate resource assignment, leads to a stall in the progress of the technical design and the development of mitigation measures for the uncertainties. This fails to strengthen the momentum, which is a prerequisite of a project of such scale, of an ever growing international community. Consequently, investments made so far and being made for limited activities cannot have lasting impacts. Consequently the research community may choose to re-orient towards alternative projects.	With the next update of the European strategy for particle physics, an adequate governing and management structure for the preparatory project phase needs to be established for the accelerator and infrastructure project and for a particle detector design project. This should be well anchored in CERN's structure and mission programme, which has the financial and personnel resources to carry out the planned tasks before a decision to build is taken. Consequently, the successful preparation of a new research infrastructure for high-energy particle physics relies on the unambiguous recommendation emerging from the next strategy update, permitting the available resources to be focused on the tasks which need to be accomplished with highest priority.

Appendix B: Communities

The impact on the community can be presented in terms of an "onion" type model, starting with the innermost layer comprising the core scientific communities, which need, conceive and use such a facility. Further communities in the European Research Area and beyond, which will benefit throughout the entire lifecycle, starting with the early design phase, include: other sciences, engineering communities, higher education, industrial partners, researchers from non-technical domains, and ultimately all members of society.

Particle physics

The HE-LHC increases the physics discovery potential. It will address the high energy frontier, electroweak, Higgs, Dark Matter and heavy flavour physics communities as well as the heavy ion and lepton-hadron communities, presently working on the LHC, flavour factories, Dark Matter experiments and other particle collider experiments worldwide.

The theory community is needed to develop scenarios that can be tested well at this future collider. Together with the experimental physics community, they need to define a comprehensive programme for such a frontier collider.

Experimental physics

The detectors for this machine will have to be highly versatile. Requirements include the measurement of multi-TeV jets, leptons and photons with masses up to 12 TeV. At the same time, detectors must be highly sensitive to known SM processes. Precision tracking and calorimetry are further fields of activity. The high occupancy and pile-up calls for unprecedented time resolution and advances in data reduction. The need for high spatial resolution due to boosted objects needs novel approaches for particle identification techniques and precision tracking.

Additional experimental physics communities will be attracted by this research infrastructure through the concurrent fixed target and heavy ion operation programmes.

Accelerator physics

With its unprecedented collision energy and luminosity, the HE-LHC will attract a world-wide community of accelerator physicists. Fully automated operating procedures ensuring the concurrent operation of CERN's injector complex and the future high-energy collider, integrating luminosity optimisation, are topics that call for the integration of diverse domains of competence.

Other physics communities

The research at the HE-LHC will have implications for astrophysics and cosmology, offering an unprecedented opportunity to federate these scientific fields.

Technology, engineering, computing

The project will drive the development of superconductors for high-field magnet applications including large series production and precision machinery. The collider requires a novel approach to cryogenic refrigeration on a large-scale. The project also involves the development of systems for higher efficiency radio-frequency power generation. The development of cost-effective, high-performance thin-film coated, superconducting cavities needs material scientists and requires expertise from manufacturing experts. Specific engineering areas include precision mechanics, surface treatment, superconductivity, novel materials, electronic and reliability engineering to improve the particle accelerator efficiency.

Electrical engineering communities will be involved in bringing medium voltage DC technology to the market, to conceive lower loss electricity distribution systems which are more reliable and develop environmentally friendly and sustainable energy recovery and buffering systems. Designers will be needed for the development of waste heat recovery and reuse systems.

To design and construct the underground infrastructure in a cost-effective way, the civil engineering community is needed to make advances in tunnelling technologies and to develop ways for the recovery and reuse of excavation materials. This work will be carried out as a joint endeavour with material scientists, geologists and chemists.

Information and communication technology communities will be involved everywhere. Their activities include simulation algorithms and software infrastructure; parallel and high-performance computing; distributed computing; real-time and embedded systems; mechatronics to conceive new standards and technologies for low-maintenance and easy-to-repair systems in the areas of protection, access, remote handling and autonomous interventions; data acquisition, data visualisation, modelling and operation optimisation; the introduction of artificial intelligence in machine and detector operation; radiation and fault tolerant systems; environmental information systems; data mining technologies; wireless communications including safety-related functions; data and document management facilities; world-wide computing infrastructures; long term data stewardship; open access data models and infrastructures and much more.

Higher education

The design and construction of the accelerator and the detectors will offer many opportunities for science teachers and students at master, doctorate and post-doc levels.

Eventually the findings from all the scientific activities will enrich the academic curricula: state-of-science today will become state-of-the art tomorrow. This project will enlarge the impact potential of higher education to highly qualified personnel and apprentices.

Industry

A project of such scale must be designed, constructed, operated and maintained with strong involvement of industrial partners from all of the participating nations. Where reasonably possible, a gradual shift towards co-development will lead to a research infrastructure which is on one hand sustainable in the long-term and which has greater impact for industry on the other. A specific initiative during the detailed design phase will focus on identifying the fields of cooperation, also elucidating where companies can best profit from enhanced learning to increase their competitiveness and improve the quality of their product and internal processes.

Non-technical sciences

This project will engage a variety of scientific communities, beyond physics, technology and engineering domains. Examples include, but are not limited to research in logistics and systems engineering around the world-wide production chain for the accelerator and detectors (logistics, operations, sales, HR, procurement, accounting, management and organisation, business administration). Media and visual arts as well as museums and marketing experts are needed to efficiently engage the public and to communicate with institutional stakeholders.

Radiation protection, technical risk management and waste management experts will facilitate the control of hazards and risks in all areas throughout the entire life cycle. Environmental and urban sciences will help avoiding, reducing and mitigating impacts.

Economics, innovation management and political sciences form another group of non-technical sciences, which have already shown during the FCC study phase that they are essential for the successful preparation of a future project.

Members of the global society

The continued deep exploration of our universe tackles fundamental questions that intrigue everyone: What is the origin of the universe? What is the nature of the matter that we are all made of? Where do we come from? Why is there something and not nothing?

This project addresses these questions directly and created opportunities to engage everyone who is interested. During the preparatory phase, an effort will be made to intensify such involvement through community science and a modern communication plan.

The conceptual study phase has revealed that the greatest challenge is, however, to create interest among the majority of people who are unaware. HE-LHC needs to address the challenge and raise awareness on a global scale and strengthen the support for continued investment in this research by policy makers, funding agencies and ultimately, by every member of society.
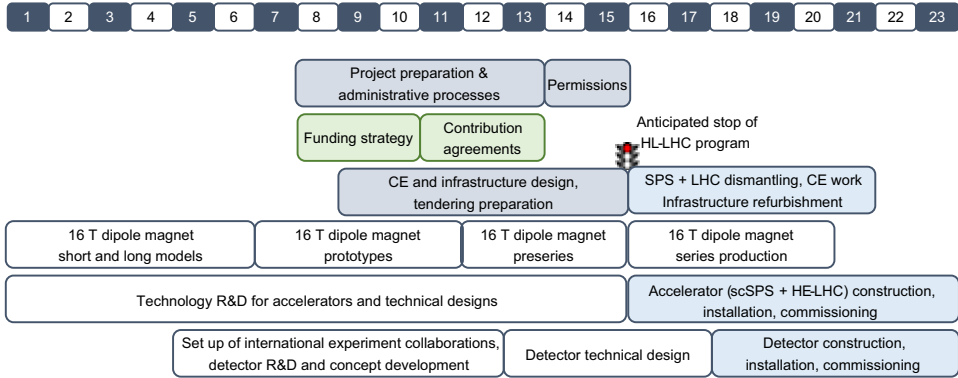
Fig. C.1. Overview of the HE-LHC implementation timeline starting in 2020. Non technical tasks marked in grey and green are compulsory for any new particle collider project and precede the actual construction. Numbers in the top row indicate the year. Physics operation would start in the mid 2040ies according to this schedule.

Appendix C: Timeline

The overall project schedule is dominated by accelerator and technology R&D, in particular by the time needed to develop and industrialise 16 T Nb_3Sn superconducting magnets. Another key input for the HE-LHC schedule is the anticipated stop of HL-LHC. The construction phase then requires at least 8 years, from stop of HL-LHC operation to start of HE-LHC physics.

The preparation phase has to be launched at least 8 years before project start and includes:

– all administrative procedures with the host states, ultimately leading to the construction permits and delivery of the surface and underground rights of way;
– the development of project financing, organisation and governing structures;
– the site investigations, civil engineering design, tendering for consultant and construction contracts.

The construction phase has a duration of 8 years and includes:

– all underground and surface structures;
– technical infrastructure;
– HE-LHC collider and detectors;
– superconducting SPS and associated transfer lines to HE-LHC;
– hardware and beam commissioning.

The implementation timeline for the HE-LHC project is shown in Figure C.1.

Appendix D: Costs

D.1 Construction costs

A cost study was performed for the HE-LHC based on the conceptual design. The cost estimates for the accelerators (collider and injector complex) and the technical infrastructure are based on machine and system inventories. The cost estimate for civil engineering is based on an analysis of construction methods for underground and surface structures, the associated material quantities and unit

Table D.1. Summary of capital cost for the implementation of the HE-LHC project.

Domain	Cost (MCHF)
Collider	5000
Injector complex	1100
Technical infrastructure	800
Civil engineering	300
Total cost	7200
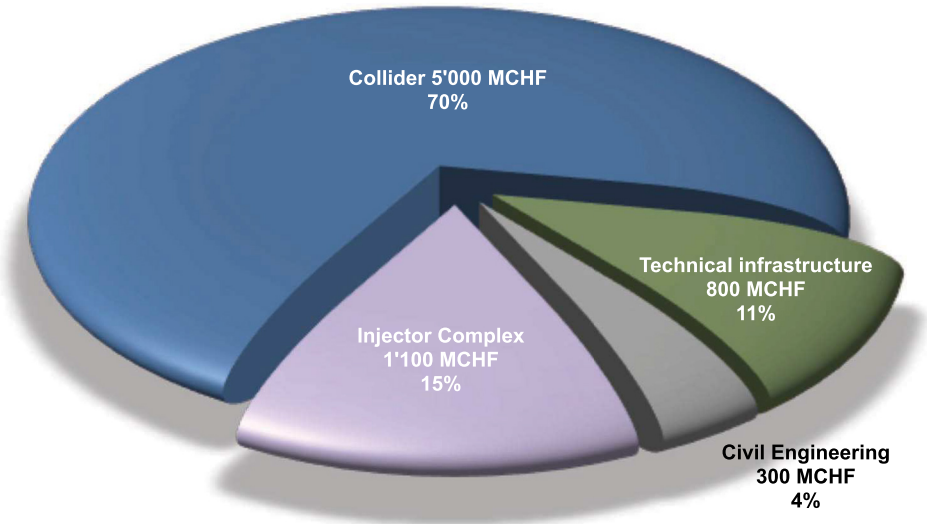
Fig. D.1. HE-LHC capital cost per project domain.

prices, derived from several recent large-scale tunnel and civil engineering projects in Central Europe. The resulting precision of the overall cost estimate is at $\pm 30\%$ level.

The capital cost for construction of the project is summarised in Table D.1. Cost items are indicated in millions of Swiss francs (MCHF) at 2018 values.

The total construction cost amounts to 7200 MCHF as shown in Figure D.1. It is dominated by 69% or 5000 MCHF for the collider. The major part of the accelerator cost corresponds to the 1,250 Nb_3Sn 16 T main dipole magnets, with a cost target of 2.3 MCHF/magnet, totalling 2900 MCHF. The collider cost also includes 260 MCHF for LHC disposal. The cost for construction of a new superconducting SPS, with an energy around 1 TeV, and associated transfer lines (1100 MCHF) was derived from scaling from SPS, LHC and HE-LHC systems and needs to be confirmed by a specific superconducting SPS (scSPS) design study. The construction cost for surface and underground civil engineering modifications and new structures is 300 MCHF or 4% of the total. The capital cost for the technical infrastructures is 800 MCHF corresponding to 11% of the total construction cost.

D.2 Operation costs

The general concept for operation of the HE-LHC will be an evolution of the HL-LHC approach, streamlined to guarantee sustainable operation and maintenance: the machine design will put emphasis on a modular approach while conceiving the individual systems and subsystems so that they can be monitored, maintained and repaired by service suppliers as much as reasonably possible.

The electric power consumption is an important operational expenditure and to arrive at a long-term, sustainable highest-luminosity collider, the HE-LHC conceptual design already integrates a number of energy saving measures:

- Use of power-saving superconducting magnets and circuit layout optimisation.
- A novel beamscreen design with an optimised temperature working point that permits efficient removal of the synchrotron radiation heat and minimises the load on the cryogenic refrigeration infra-structure.
- Use of an innovative cryogenic refrigeration system based on a neon-helium (nelium) light gas mixture, which reduces the electricity consumption and waste heat generation by about 10% with respect to traditional plants.
- Recovery and buffering of the energy stored in the superconducting magnets at the end of the cycle for reuse during the subsequent ramp in order to save energy and to control the peak electricity demand.
- Using medium-voltage DC electricity distribution to optimise the size of the powering infrastructure, enabling the introduction of renewable energy and storage systems and supressing the need for a power quality system.
- Waste heat recovery and reuse inside the facility, and for storage and provision to district services (heating and air conditioning).

The above measures result in a total electrical energy consumption per year of nominal HE-LHC operation of 1.2 TWh/year, directly comparable to the 1.2 TWh/year consumed by CERN today and the expected 1.4 TWh/year for HL-LHC. Based on the CERN electricity prices from 2014/15, the electricity cost for HE-LHC collider operation would be about 55 Meuro per year. Considering the total luminosity production of $15\,ab^{-1}$ over 20 years, about 70 keuro for electricity would need to be invested to produce $1\,fb^{-1}$ of integrated luminosity. With more than 2.5×10^9 Higgs bosons and 5×10^{10} top-pairs produced in total, this translates into an *electricity cost of about 43 cents per Higgs boson and per 20 top quark pair.*

Glossary

Ω The ohm is the SI derived unit of electrical resistance.

4DCHM 4-dimensional composite Higgs model.

A The ampere (symbol: A) is the base unit of electric current in the International System of Units (SI).

A15 A15 is the Strukturbericht notation for the crystal structure of Cr_3Si, originally reported for β-tungsten. This structure is shared by a family of intermetallic compounds with the formula A_3B, where A is a transition metal. Several of these compounds, with $A = Nb$ or V, are superconducting with a critical temperature T_c of around 20 K and an upper critical magnetic field H_{c2} exceeding 20 T. The most commonly applied example is Nb_3Sn.

ab An attobarn corresponds to an area equal to $10^{-46}\,m^2$.

ABCI The azimuthal beam cavity interaction is software which solves the Maxwell equations directly in the time domain when a bunched beam goes through an

axi-symmetric structure on or off axis. An arbitrary charge distribution can be defined by the user.

AC Alternating current.

a-C Amorphous carbon.

ADC Analogue-to-digital converter.

ADT The ADT is a transverse damping system deployed in the LHC to reduce the oscillations of the injected proton beam, to reduce emittance blow-up due to ground motion and magnetic noise or ripple and to stabilise the beam against the resistive wall instability and other possible instabilities caused by narrow band parasitic transverse impedances in the ring.

Alcove An alcove is a recessed area open from a larger room but enclosed by walls, pillars, or other architectural elements.

AMD Adiabatic matching device.

APC Artificial pinning centre: a particle, defect or other feature intentionally introduced to act as a site for flux pinning.

Ar Argon is a chemical element with symbol Ar and atomic number 18.

Arc A circular collider is composed of curved cells called arcs that are separated by straight sections (see LSS). An arc half-cell forms the periodic part of the arc lattice (see lattice).

ARIES A H2020 EC funded research and development project in the area of particle accelerator technologies.

ARMCO American Rolling Mill Company pure iron became synonymous with the purest steel mill produced iron with a purity of more than 99.85% Fe.

ASIC An application-specific integrated circuit is an integrated circuit (IC) customised for a particular use, rather than intended for general-purpose use.

ATLAS A toroidal LHC apparatus is one of the seven particle detector experiments constructed at the LHC.

B The byte is a unit of digital information that most commonly consists of eight bits, representing a binary number.

b The bit, a binary digit, is a basic unit of information used in computing and digital communications. A binary digit can have only one of two values, and may be physically represented with a two-state device.

B_i The dispersion function of a beam line is determined by the strength and placement of dipole magnets. As a consequence, dipole field errors also contribute to the dispersion function. Multipole components corresponding to a magnetic flux distribution, which can be added up are denoted by B_i and A_i. B_1 corresponds to a normal dipole component, B_2 to a normal quadrupole component, B_3 to a normal sextupole component, A_1 to a skew dipole, A_2 to a skew quadrupole and A_3 to a skew sectupole.

barn A barn (symbol: b) is a unit of area equal to $10^{-28}\,\mathrm{m}^2$. It is best understood as a measure of the probability of interaction between small particles. A barn is approximately the cross-sectional area of a uranium nucleus.

BCS Theory named after John Bardeen, Leon Cooper, and John Robert Schrieffer. It is the first microscopic theory of superconductivity since Heike Kamerlingh Onnes's 1911 discovery. The theory describes superconductivity as a microscopic effect caused by a condensation of Cooper pairs into a boson-like state.

Be Beryllium is a rare chemical element with symbol Be and atomic number 4.

Beam pipe Volumes of different shape (e.g. cylindrical, conical, flanges and bellows) and material (e.g. metallic, ceramic) used to transport the beam. The ultrahigh-vacuum within it reduces beam-gas interactions to a level at which the beam lifetime is acceptable.

Beamline A series of functional elements, such as magnets and vacuum pipe, which carry the beam from one portion of the accelerator to another.

Beamscreen Perforated tube inserted into the cold bore of the superconducting magnets in order to protect the cold bore from synchrotron radiation and ion bombardment.

Beta function An optical function proportional to the square of the local transverse beam size. The beta function describes how the beam width changes around the accelerator. There are separate β-functions for the x and y planes.

B-factory A B-factory, or sometimes a beauty factory, is a particle collider experiment designed to produce and detect a large number of B mesons so that their properties and behaviour can be measured with small statistical uncertainty. Tauons and D mesons are also copiously produced at B-factories.

BFPP Bound-free pair production is one of the new types of processes that occur in relativistic collisions of atoms and ions. It is the production of an electron-positron pair with the electron not produced as a free state but as a bound state of one of the ions.

Bhabha scattering The electron-positron scattering process: $\mathrm{e^+e^-} \to \mathrm{e^+e^-}$ There are two leading-order Feynman diagrams contributing to this interaction: an annihilation process and a scattering process.

BHWIDE A Monte Carlo event generator software simulating Bhabha-scattering, developed for linear collider detector luminosity studies.

BIM Building information modeling is a process involving the generation and management of digital representations of physical and functional characteristics of places.

BLM Beam loss monitor.

BPM Beam position monitor.

Bq The becquerel is the SI derived unit of radioactivity. One becquerel is defined as the activity of a quantity of radioactive material in which one nucleus decays per second. The becquerel is therefore equivalent to an inverse second, s^1.

BR In particle physics and nuclear physics, the branching ratio for a decay is the fraction of particles which decay by an individual decay mode with respect to the total number of particles which decay.

BR (machine) The booster ring is an accelerator in the collider tunnel, which provides the particle collider continuously with particles at collision energy.

BRGM Bureau de Recherches Géologiques et Minières, France.

BS Beamstrahlung.

BSCCO Bismuth strontium calcium copper oxide (pronounced "bisko"), is a family of high-temperature superconductors. Specific types of BSCCO are usually referred to using the sequence of the numbers of the metallic ions. Thus Bi-2201 is the n = 1 compound (Bi2Sr2CuO6+x), Bi-2212 is the $n = 2$ compound (Bi2Sr2CaCu2O8+x), and Bi-2223 is the $n = 3$ compound (Bi2Sr2Ca2Cu3O10+x).

BSM Beyond Standard Model.

Bunch A group of particles captured inside a longitudinal phase space bucket.

BX Bunch crossing.

C The coulomb (symbol: C) is the SI (international system of units) unit of electric charge. It is the charge (symbol: Q or q) transported by a constant current of one ampere in one second.

C band The C band is a designation by the IEEE (institute of electrical and electronics engineers) for a part of the microwave band of the electromagnetic spectrum covering frequencies from 4 to 8 gigahertz.

C++ An object-oriented programming language.

CAD Computer-aided design is the use of computer systems to aid in the creation, modification, analysis, or optimisation of a design.

CAF A compressed air foam system is used in firefighting to deliver fire retardant foam for the purpose of extinguishing a fire or protecting unburned areas.

CAPEX Capital expenditures are the funds used to acquire or upgrade fixed assets, such as expenditures towards property, plant, or equipment.

Carnot Efficiency Carnot efficiency describes the maximum thermal efficiency that a heat engine can achieve as permitted by the second law of thermodynamics.

CBA Cost-benefit analysis is a systematic process for estimating and comparing benefits and costs of a project. The purpose of CBA is to facilitate a more efficient allocation of resources, demonstrating the convenience for society of a particular intervention rather than possible alternatives.

CC60 The CC60 facility at CERN uses a ^{60}Co source for the qualification of components against TID effects.

CCT A canted-cosine-theta magnet is an accelerator magnet that superposes fields of nested and tilted solenoids that are oppositely canted.

CDR A conceptual design report completes the first stage of the ESFRI roadmap methodology, permitting concept screening, consortium formation, access policy and funding concept preparation, scientific and project leadership definition.

CEA The French alternative energies and atomic energy commission (Commissariat à' l'énergie atomique et aux énergies alternatives).

CepC The circular electron positron collider is an electron-positron collider proposed by the Chinese high energy physics community, acting as a Higgs-factory in a new tunnel 80–100 km in length.

CEREMA The French "Centre d'Etude et d'Expertise sur les Risques, l'Environnement, la Mobilité et l'Aménagement" is a public administration organisation, governed by the "ministre chargé de l'écologie, du développement durable et de l'énergie" and the "ministre du transport, de l'égalité des territoires et de la ruralité". The organisation works with the territorial state services during all development projects, notably with respect to implement sustainable development goals (urbanism, environment, infrastructures and transport, risk management).

CERN European Organisation for Nuclear Research.

CETU The "centre d'études des tunnels" is a technical service of the French "ministère de l'Écologie, du Développement et de la Mer", a notified body for the safety of tunnels in France.

CFC Carbon fibre composite.

CFD Computational fluid dynamics uses numerical analysis to solve and analyse problems that involve fluid flows.

CH$_4$ Methane is a chemical compound.

CHARM CERN high energy accelerator mixed field facility, located in the CERN east area, supplies a wide spectrum of radiation types and energies.

CHF ISO code of the Swiss franc currency.

Chilled Water Chilled water is a commodity used to cool a building's air and equipment. It's temperature is between 4°C and 7°C.

CIR Circuit.

CIXP CERN internet exchange point.

CL Confidence level.

CLD The CLic detector is a conceptual design for an experiment detector at CLic, which also serves as a design model for an experiment detector at the FCC-ee.

CLIC The compact linear collider (CLIC) is a concept for a future linear electron-positron collider in a new tunnel, ranging from 11 to 50 km, depending on the collision energy.

CLIC-dp The CLIC detector and physics study is an international collaboration currently composed of 30 institutions.

CLIQ The coupling-loss-induced quench method is a superconducting magnet protection approach.

CM Cold mass.

CMM Coordinated measuring machines.

CMOS Complementary metal oxide semiconductor is a technology for constructing integrated circuits patented in 1963 by Frank Wanlass while working for Fairchild Semiconductor.

CMS The compact muon solenoid is one of the seven particle detector experiments constructed at the LHC.

CNDP The French "Commission nationale du débat public" was created in 1995 and is since 2002 an independent administration authority. The organisation ensures that the public participates in the process of construction projects of national interest.

CNES The National Centre for Space Studies is the French government's space agency.

CNRS The French national center for scientific research (Centre National de la Recherche Scientifique).

COL Collimation.

Collimator A device that removes beam particles at large amplitudes. They are used to keep beam-losses low and to protect critical elements of the accelerator.

Collision A close encounter of particles during which dynamic quantities such as energy, momentum, and charge may be exchanged.

Comsol A cross-platform, finite element analysis, solver and multiphysics simulation software developed by private company COMSOL Inc. (Sweden). It allows conventional physics-based user interfaces and coupled systems of partial differential equations.

Cooper pair Two electrons that appear to "team up" in accordance with theory, BCS or other, despite the fact that they both have a negative charge and normally repel each other. Below the superconducting transition temperature, paired electrons form a condensate, a macroscopically occupied single quantum state, which flows without resistance. However, since only a small fraction of the electrons are paired, the bulk does not qualify as being a "Bose-Einstein condensate".

COTS Commercial-off-the-shelf.

CP Charge conjugation parity symmetry is the product of two symmetries: C for charge conjugation, which transforms a particle into its antiparticle, and P for parity, which creates the mirror image of a physical system. The strong interaction and electromagnetic interaction seem to be invariant under the combined CP transformation operation, but this symmetry is slightly violated during certain types of weak decay. Historically, CP-symmetry was proposed to restore order after the discovery of parity violation in the 1950s.

Cr_2O_3 Chromium(III) oxide is an inorganic compound. It is one of the principal oxides of chromium and is used as a pigment. In nature, it occurs as the rare mineral eskolaite.

Critical temperature Temperature T_c below which characteristics of superconductivity appear. The value varies from material to material and depends on the magnetic field.

Cryo magnet Complete magnet system integrated in a cryostat, including main magnet coils, collars and cryostat, correction magnets and powering circuits.

Cryogenic system A system that operates below a temperature set by convention at $150\,\mathrm{K}$ ($-123.15°C$).

CST Computer simulation technology is a computational tool from Dassault Systems for 3D electromagnetic design and analysis.

Cu Copper is a chemical element with symbol Cu and atomic number 29.

CW A continuous wave is an electromagnetic wave of constant amplitude and frequency, almost always a sine wave, that for mathematical analysis is considered to be of infinite duration.

Cybersecurity Cybersecurity is the protection of computer systems from theft or damage to their hardware, software or electronic data, as well as from disruption or misdirection of the services they provide.

DA Dynamic Aperture.

DAΦNE The double annular Φ factory for nice experiments is an electron-positron collider at the INFN Frascati National Laboratory in Frascati, Italy. It has been colliding electrons and positrons at a centre of mass energy of $1.02\,\text{GeV}$ to create φ mesons Since 1999.

DAQ Data acquisition.

Dark matter Invisible matter that makes up 26% of the universe and which can only be detected from its gravitational effects. Only 4% of the matter in the Universe are visible. The remaining 70% are accounted to dark energy.

dB The decibel (symbol: dB) is a unit of measurement used to express the ratio of one value of a physical property to another on a logarithmic scale. When expressing power quantities, the number of decibels is ten times the logarithm to base 10 of the ratio of two power quantities. That is, a change in power by a factor of 10 corresponds to a $10\,\text{dB}$ change in level.

DC Direct current.

DCAL Digital hadron calorimeter.

DCCT A direct current-current transformer is a current-to-voltage transducer, employed when measurement of very high current is required.

DCH Drift CHamber.

DD4hep A detector description toolkit for high energy physics.

DELPHES Delphes is a C++ framework, performing a fast multipurpose detector response simulation. The simulation includes a tracking system, embedded into a magnetic field, calorimeters and a muon system.

DELPHI The detector with lepton, photon and hadron identification was one of the four main detectors of the large electron-positron collider (LEP) at CERN.

DESY The German electron synchrotron (Deutsches Elektronen-Synchrotron).

DFAE The Département Fédéral des Affaires Étrangères is the Swiss foreign ministry.

Dipole A magnet with two poles, like the north and south poles of a horseshoe magnet. Dipoles are used in particle accelerators to keep particles moving in a circular orbit.

DIS Dispersion suppressor.

DM Dark matter.

DN Diametre nominal, the European equivalent of NPS (nominal pipe size) defines a set of nominal pipe sizes in standard ISO 6708. The dimensionless number after the letters DN indicate the physical size in millimetres of the bore.

DOE The United States Department of Energy.

DPA Displacement per atom.

DR A damping ring reduces the emittances produced by the particle source to the small values required for the collider. Emittance reduction is achieved via the process of radiation damping, i.e. the combination of synchrotron radiation in bending fields with energy gain in RF cavities.

DRAM Dynamic random-access memory.

DVR Dynamic voltage restorer.

Dynamic aperture Maximum transverse oscillation amplitude that guarantees stable particle motion over a given number of turns. If the motion amplitude of a particle exceeds this threshold, the betatron oscillation of the particle will not have any bounds, and the motion will become unstable, leading to loss of the particle. It is expressed in multiples of the beam size together with the associated number of turns. Unlike the physical aperture, dynamic aperture separating stable and unstable trajectories is not a hard boundary.

Dynistor A dynistor is an unidirectional thyristor breakover diode. It can be used as switches in micro- and nanosecond power pulse generators.

EASITrain A H2020 EC funded Marie Słodovska Curie innovative training network project to advance superconducting wire and thin film technologies as well as cryogenic refrigeration systems for particle accelerators.

EBITDA A company's earnings before interest, taxes, depreciation, and amortisation is an accounting measure calculated using a company's net earnings, before interest expenses, taxes, depreciation, and amortisation are subtracted, as a proxy for a company's current operating profitability (i.e. how much profit it makes with its present assets and its operations on the products it produces and sells, as well as providing a proxy for cash flow.

EC Electron cloud.

ECal Electromagnetic calorimeter (also ECAL).

ECFA European Committee for Future Accelerators.

Eddy current Eddy currents are loops of electrical current induced within conductors by a changing magnetic field in the conductor due to Faraday's law of induction. Eddy currents flow in closed loops within conductors, in planes perpendicular to the magnetic field.

EDLC Electrical double-layer capacitors.

EES Energy extraction system.

EFT An effective field theory is a type of approximation, or effective theory, for an underlying physical theory, such as a quantum field theory or a statistical mechanics model.

EHF Electrohydraulic forming is a type of metal forming in which an electric arc discharge in liquid is used to convert electrical energy to mechanical energy and change the shape of the workpiece.

EIA Environmental impact assessment.

EIE Étude de l'impact sur l'environnement is the Swiss name for the environmental impact assessment in the scope of the OEIE.

EIR Experimental insertion region.

Electron cloud A cloud of electrons generated inside an accelerator beam pipe due to gas ionisation, photoemission from synchrotron radiation, or "beam-induced multipacting" via electron acceleration in the field of the beam and secondary emission. Electron clouds may cause single- and multi-bunch beam instabilities as well as additional heat load on the beamscreen inside the cold magnets.

electronvolt In physics, the electronvolt (symbol eV, also written electron-volt and electron volt) is a unit of energy equal to approximately 1.6×10^{-19} joules (symbol J) in SI units. By definition, it is the amount of energy gained (or lost) by the charge of a single electron moving across an electric potential difference of one volt. The electronvolt is not an SI unit, and its definition is empirical. By mass-energy equivalence, the electronvolt is also a unit of mass, expressed in units of eV/c^2, where c is the speed of light in vacuum.

Electroweak symmetry breaking Although electromagnetism and the weak force have the same strength at high energies, electromagnetism is much stronger

than the weak force in our everyday experience. The mechanism by which, at low energies, a single unified electroweak force appears as two separate forces is called electroweak symmetry breaking.

EM Electro magnetic.

EMB Electromagnetic barrel calorimeter.

EMEC Endcap electromagnetic calorimeter.

EMF Forward electromagnetic calorimeter.

Emittance The area in phase space occupied by a particle beam. The units are mm-milliradians for transverse emittance and eV·s for longitudinal emittance.

EN European norms are documents that have been ratified by one of the three ESOs (European Standardisation Organisations), CEN, CENELEC or ETSI; recognised as competent in the area of voluntary technical standardisation as for the EU Regulation 1025/2012.

EOT The most common type of overhead crane, found in many factories. These cranes are electrically operated by a control or remote control pendant, or from an operator cabin attached to the crane.

EPFL The École polytechnique fédérale de Lausanne is one of the two Swiss Federal Institutes of Technology.

EPPSU European Particle Physics Strategy Update. See also https://europeanstrategy.cern.

ERL Energy recovery Linac.

ERMC Enhanced racetrack model coil.

ES Electro static.

ESD Electron-stimulated desorption.

ESFRI European strategy forum for research infrastructures.

Espoo Convention The Espoo Convention sets out the obligations of parties to assess the environmental impact of certain activities at an early stage of planning. It also lays down the general obligation of states to notify and consult each other on all major projects under consideration that are likely to have a significant adverse environmental impact across boundaries.

ESPP European Strategy for Particle Physics. See also https://europeanstrategy.cern.

ESRF The European Synchrotron Radiation Facility is a joint research facility situated in Grenoble, France, and supported by 22 countries (13 member countries: France, Germany, Italy, UK, Spain, Switzerland, Belgium, The Netherlands, Denmark, Finland, Norway, Sweden, Russia and 9 associate countries: Austria, Portugal, Israel, Poland, Czech Republic, Hungary, Slovakia, India and South Africa).

ESS Energy storage system.

ETHZ The Eidgenössische Technische Hochschule Zürich is one of the two Swiss Federal Institutes of Technology.

EU European Union.

EuCARD2 A FP7 EC funded research and development project in the area of particle accelerator technologies.

EuroCirCol A H2020 EC funded research and development project to develop the foundations of a future circular hadron collider.

EW Electroweak.

EWPO Electroweak precision observables.

EWPT Electroweak phase transition.

EWSB Electroweak symmetry breaking.

EXP Experiment.

Experiment insertion region Place in the particle collider hosting the interaction region in which the two beams are brought to collision and the surrounding particle physics experiments.

EXT Extraction.

fb A femtobarn corresponds to an area equal to $10-43\,\mathrm{m}^2$.

FCC Future circular collider is a feasibility study aiming at the development of conceptual designs for future particle colliders with energies and intensities at the frontier, based on a technically feasible and affordable circular layout permitting staged implementation.

FCC-ee Future circular intensity-frontier electron-positron collider with multiple centre-of-mass collision energies ranging from the Z peak to $t\bar{t}$ collision energies at luminosities up to almost $5 \times 10^{36}\,\mathrm{cm}^{-2}\,\mathrm{s}^{-1}$ in a new circular tunnel of about 100 km length.

FCC-eh Future circular energy-frontier electron-hadron collider interaction point scenario. The scenario foresees an energy recovery linac (ERL) to generate electron beams and to collide them with high-energetic proton or ion beams of a hadron collider in a new circular tunnel of about 100 km length.

FCC-hh Future circular energy-frontier hadron-hadron collider reaching up to 100 TeV centre-of-mass collision energies at luminosities of $5-10 \times 10^{34}\,\mathrm{cm}^{-2}\,\mathrm{s}^{-1}$ in a new circular tunnel of about 100 km length. Operation with protons and ions is envisaged.

FDS Fire dynamics simulator is a software developed and maintained by the U.S. Department of Commerce National Institute of Standards and Technology for the simulation of smoke and heat transport from fires.

FED Fractional effective dose.

FEM European federation of material handling.

FF Final focus.

FIB An FIB setup is a scientific instrument that resembles a scanning electron microscope (SEM). However, while the SEM uses a focused beam of electrons to image the sample in the chamber, a FIB setup uses a focused beam of ions instead.

FinFET A type of non-planar or "3D" field effect transistor used in the design of modern processors. The transistor architecture uses raised channels called "fins", from source to drain.

FLUKA A particle physics Monte Carlo simulation package for high energy experimental physics and engineering, shielding, detector and telescope design, cosmic ray studies, dosimetry, medical physics and radio-biology.

Flux pinning In practical applications, a type II superconductor in a magnetic field is usually in the mixed state, in which the superconducting material is penetrated by magnetic flux. When carrying a current, a force (the Lorentz force) acts on these flux lines. If this was not opposed, the resulting movement of flux would result in energy dissipation, rendering the material useless for current-carrying applications. Flux pinning is the phenomenon by which defects in a superconducting material immobilise flux lines, producing a pinning force to oppose the Lorentz force. The volumetric flux pinning force effectively defines the J_c of a type II superconductor. The type of defects providing effective flux pinning depend on the material (e.g. grain boundaries in Nb_3Sn.

FMA Radioactive waste of "faible et moyenne activité" (low and intermediate activity), the classification depends on the level of activity and on the radionuclides.

FMECA The failure mode, effects, and criticality analysis is a bottom-up, inductive analytical method which may be performed at either the functional or piece/part level. It is used to chart the probability of failure modes against the severity

of their consequences. The result highlights failure modes with relatively high probability and severity of consequences, allowing remedial effort to be directed where it will produce the greatest value.

FNAL Fermi National Accelerator Laboratory.

FODO The focusing and defocusing cell is a widespread lattice concept for designing a particle accelerator based on a magnet structure consisting alternately of focusing and defocusing quadrupole lenses.

FPC Fixed power coupler.

FPGA A field-programmable gate array is an integrated circuit designed to be configured by a customer or a designer after manufacturing.

Free (air) cooling Free cooling is an economical method of using low external air temperatures to assist in chilling water, which can then be used for industrial processes, or air conditioning systems.

FSI Frequency scanning interferometry.

GB A gigabyte is by definition of the IEC, 10^9 B.

Gd Gadolinium is a chemical element with symbol Gd and atomic number 64.

Gd_2O_3 Gadolinium(III) oxide is an inorganic compound. It is one of the most commonly available forms of the rare-earth element gadolinium, derivatives of which are potential contrast agents for magnetic resonance imaging.

GEANT4 `GEANT4` is a platform for the simulation of the passage of particles through matter using Monte Carlo methods. It is the successor of the GEANT series of software toolkits developed by CERN.

GeniLac A project planned in Geneva to use the water of lake Geneva for cooling and heating of public buildings and international organisations.

GESDEC The "service de géologie, sols et déchets" is the office of the canton and state of Geneva in charge of questions related to excavation materials, ground acquisition and classification, protection of underground volumes and underground water.

GeV 10^9 electronvolt.

Gfitter A generic fitter software for for the statistical analysis of parameter estimation problems in high-energy physics.

GHz 10^9 Hz.

Gif++ The gamma irradiation facility is located in the CERN north area. It combines a 137Cs source with a high-energy particle beam from the SPS H4 beam line.

GIM In quantum field theory, the GIM mechanism (or Glashow-Iliopoulos-Maiani mechanism) is the mechanism through which flavour-changing neutral currents (FCNCs) are suppressed in loop diagrams. It also explains why weak interactions that change strangeness by 2 are suppressed, while those that change strangeness by 1 are allowed, but only in charged current interactions.

GIS Geographical information system.

GNSS The global navigation satellite system is the standard generic term for satellite navigation systems that provide autonomous geo-spatial positioning with global coverage. This term includes e.g. the GPS, GLONASS, Galileo, Beidou and other regional systems.

GRI A global research infrastructure is mandated by the G8+5 and addresses worldwide science and technology challenges, following the "GSO Framework for Global Research Infrastructures". The GSO maintains a list of potential GRIs.

GRN Geodetic reference network.

GSO Group of senior officials mandated by G8+5 to develop GRI concepts.

GTO A gate turn-off thyristor (GTO) is a special type of thyristor, which is a high-power semiconductor device. It acts as a bistable switch, conducting when the

gate receives a current trigger, and continuing to conduct until the voltage across the device is reversed biased, or until the voltage is removed. GTOs, as opposed to normal thyristors, are fully controllable switches which can be turned on and off by their third lead, the gate lead.

Guinea-Pig++ An electron-positron beam-beam simulation software developed at CERN.

GV 10^9 volt.

GV (vacuum) Gate valve.

Gy The gray (symbol: Gy) is a derived unit of ionising radiation dose in the International System of Units (SI). It is defined as the absorption of one joule of radiation energy per kilogram of matter.

H The Higgs boson (symbol: H) is an elementary particle in the Standard Model of particle physics, produced by the quantum excitation of the Higgs field. The particle has a spin of 0.

H2020 Horizon 2020 is an EU Research and Innovation funding programme over 7 years (2014–2020). It is the financial instrument implementing the "Innovation Union", a Europe 2020 flagship initiative aimed at securing Europe's global competitiveness.

H_c The critical magnetic field of a superconductor. For current-carrying and magnet applications of a type II superconductor, in practice the upper critical field H_{c2} must be considered instead.

H_{c2} The upper critical magnetic field of a type II superconductor, above which the material enters the normal state and does not show superconducting behaviour.

ha The hectare is an SI accepted metric system unit of area equal to a square with 100 m sides, or 1 ha = 10 000 m^2.

Hadron A subatomic particle that contains quarks, antiquarks, and gluons, and so experiences the strong force. The proton is the most common hadron.

HB Barrel hadron calorimeter.

HCAL Hadron calorimeter.

HCal Hadron calorimeter.

HEB High energy booster.

HEC Endcap hadron calorimeter.

HEH High energy hadron fluence, i.e. hadrons with energies greater than 20 MeV.

HEIKA The high efficiency international Klystron activity was initiated at CERN in 2014 to evaluate and develop new bunching technologies for high-efficiency Klystrons.

HEL Hollow electron lens.

HE-LHC High-energy large hadron collider. A new particle collider with about twice the LHC collision energy in the existing LHC tunnel, using technologies conceived for the FCC-hh.

HERA The hadron-elektron-ringanlage (English: hadron-electron ring accelerator) was a particle accelerator at DESY in Hamburg. It began operating in 1992. At HERA, electrons or positrons were collided with protons at a center of mass energy of 318 GeV. It was the only lepton-proton collider in the world while operating. HERA was closed down on 30 June 2007.

HF Hadron forward calorimeter.

HFSS A 3D electromagnetic simulation software for designing and simulating high-frequency electronic products from ANSYS.

HIE-ISOLDE The high-intensity and energy upgrade of ISOLDE project incorporates a new linear accelerator (linac) into CERN's ISOLDE facility (isotope mass separator on-line device).

Higgs boson An elementary particle linked with a mechanism to model, how particles acquire mass.

HiRadMat The high-radiation to materials facility at CERN provides high-intensity pulsed beams to an irradiation area where material samples as well as accelerator component assemblies can be tested.

HL-LHC High Luminosity upgrade of the LHC to a levelled constant luminosity of $5 \times 10^{34}\,\mathrm{cm}^2\,\mathrm{s}^{-1}$. A dedicated FP7 design study (HiLumi LHC DS) precedes the implementation of the upgrade.

HLS Hydrostatic levelling system.

HLT High level trigger.

HOM Higher order modes are undesired Eigenmodes parasitically excited in a resonant (accelerating) radiofrequency cavity.

HTML Hypertext markup language.

HTS High temperature superconductors have critical temperatures above $77\,\mathrm{K}$.

HTTP Hypertext transfer protocol.

HV High voltage.

HVDC High voltage direct current power distribution.

HX Heat exchanger.

Hz The hertz (symbol: Hz) is the derived unit of frequency in the International System of Units (SI) and is defined as one cycle per second.

IBS Iron-based superconductors (IBS) are iron-containing chemical compounds whose superconducting properties were discovered in 2006.

IC Integrated circuit.

ICS Inverse compton scattering.

ICT Information and communications technology.

IDEA The international detector for electron accelerator is a conceptual design for an experiment detector at the FCC-ee.

IEEE The Institute of Electrical and Electronics Engineers is is the world's largest association of technical professionals. Its objectives are the educational and technical advancement of electrical and electronic engineering, telecommunications, computer engineering and allied disciplines.

ILC The international linear collider (ILC) is a proposed linear electron-positron particle collider aiming at collision energies of $500\,\mathrm{GeV}$ and an upgrade to $1000\,\mathrm{GeV}$ ($1\,\mathrm{TeV}$).

Impedance A quantity that quantifies the self-interaction of a charged particle beam, mediated by the beam environment, such as the vacuum chamber, RF cavities, and other elements encountered along the accelerator or storage ring.

INFN Istituto Nazionale di Fisica Nucleare.

INJ Injection.

Innovation New ideas that respond to societal or economic needs and generate new products, services, business and organisational models that are successfully introduced into an existing market and are able to create new markets and that contribute value to society.

Invar Invar, also known generically as FeNi36 (64FeNi in the US), is a nickel-iron alloy notable for its uniquely low coefficient of thermal expansion (CTE). The name Invar comes from the word invariable, referring to its relative lack of expansion or contraction with temperature changes. It was invented in 1896 by Swiss physicist Charles Édouard Guillaume. He received the Nobel Prize in Physics in 1920 for this discovery, which enabled improvements in scientific instruments.

Ion An atom or molecule that is not electrically neutral but that carries a positive or negative charge (electrons removed or added).

IP Interaction point.

IPC Incoherent pair creation.

IR Interaction region.

IrCe Iridium-cerium is an alloy used as a photocathode.

ISD Ion-stimulated desorption.

ISO The International Organisation for Standardisation is an international standard-setting body composed of representatives from various national standards organisations.

IT Information technology.

ITER ITER is an international nuclear fusion research and engineering project. It is an experimental Tokamak fusion reactor that is being built next to the Cadarache facility in Saint-Paul-lèz-Durance, in Provence, southern France.

ITS Inner tracking system.

J The joule (symbol: J) is a derived unit of energy in the International System of Units. It is equal to the energy transferred to or work done on an object when a force of one newton acts on that object in the direction of its motion through a distance of one metre. It is also the energy dissipated as heat when an electric current of one ampere passes through a resistance of one ohm for one second.

J_c The scientific notation representing the "critical current density" or maximum current that a superconductor can carry. As the current flowing through a superconductor increases, the T_c will usually decrease.

JLab Thomas Jefferson National Accelerator Facility (TJNAF), commonly called Jefferson Lab or JLab.

K See Kelvin.

Karst Karst is a topography formed from the dissolution of soluble rocks such as limestone, dolomite, and gypsum. It is characterized by underground drainage systems with sinkholes and caves.

kB A kilobyte refers traditionally to 1024 bytes. In december 1998, the IEC defined $2^{10} = 1024$ bytes as 1 kibiyte (KiB).

KEKB KEKB is a particle accelerator used in the Belle experiment to study CP violation. KEKB is located at the KEK (High Energy Accelerator Research Organisation) in Tsukuba, Ibaraki Prefecture, Japan.

Kelvin Unit of measurement for temperature (K) using as null point the absolute zero, the temperature at which all thermal motion ceases. $0\,\mathrm{K} = -273.15°\mathrm{C}$.

keV 10^3 electronvolt.

kg The kilogram or kilogramme (symbol: kg) is the base unit of mass in the International System of Units (SI), and is defined as being equal to the mass of the International Prototype of the Kilogram (IPK, also known as "Le Grand K" or "Big K"), a cylinder of platinum-iridium alloy stored by the International Bureau of Weights and Measures at Saint-Cloud, France.

KLOE A particle physics experiment at the INFN Frascati National Laboratory, Italy

KlyC Software developed at CERN for the optimisation and design of high efficiency Klystrons based on new bunching mechanisms.

Klystron A specialised linear-beam vacuum tube, which is used as an amplifier for high radio frequencies.

Kr Krypton is a chemical element with symbol Kr and atomic number 36.

kW 10^3 Watt.

l The litre (SI spelling) or liter (American spelling) (symbol l in this document) is an SI accepted metric system unit of volume equal to 1000 cubic centimetres or 1/1000 cubic metre.

L* The distance from the IP to the start of the magnetic field of the first magnet closest to the IP. The physical equipment is larger and is closer to the IP.

LAL Laboratoire de l'Accélérateur Linéaire (LAL) of CNRS in Orsay in France.

LAr Liquid argon.

LASE Laser-ablated surface engineering.

Lattice In accelerator physics, a magnetic lattice is a composition of electromagnets at given longitudinal positions around the vacuum tube of a particle accelerator, and thus along the path of the enclosed charged particle beam. Many lattices are composed of identical substructures or cells, which denote a special magnet arrangement that may reoccur at several positions along the path.

LCB Lower cold box.

LCBI Longitudinal coupled bunch instability.

LCCS Local Chromatic Correction System.

LEP The large electron–positron collider, which was operated at CERN until 2000.

LEP3 A concept for an electron-positron collider in the existing LHC tunnel with a centre-of-mass of $240\,\text{GeV}$ and a peak luminosity of $1 \times 10^{34}\,\text{cm}^{-2}\,\text{s}^{-1}$ at each of two experiments.

Lepton A class of elementary particles that do not experience the strong force. The electron is the most common lepton.

LF Low field.

LFV Lepton flavour violation.

LGAD Low gain avalanche detectors.

LHC The large hadron collider is a circular particle collider for protons and heavy ions with a design centre-of-mass energy of $14\,\text{TeV}$ for proton–proton collisions at a peak luminosity of $1 \times 10^{34}\,\text{cm}^2\,\text{s}^{-1}$ at CERN in Geneva, Switzerland.

LHCb The large hadron collider beauty experiment is one of the seven particle detector experiments constructed at the LHC.

LHeC A study to extend the current LHC collider with an energy recovery linac (ERL) to generate electron beams and to collide them with high-energetic proton or ion beams of the LHC.

LIL LEP injector linac.

Limestone Limestone is a sedimentary rock, composed mainly of skeletal fragments of marine organisms such as coral, forams and molluscs. Its major materials are the minerals calcite and aragonite, which are different crystal forms of calcium carbonate ($CaCO_3$).

Linac A linear accelerator for charged particles in which a number of successive radiofrequency cavities that are powered and phased such that the particles passing through them receive successive increments of energy.

Linac4 The linear accelerator 4 at CERN accelerates negative hydrogen ions (H^-, consisting of a hydrogen atom with an additional electron) to $160\,\text{MeV}$ to prepare them to enter the PSB (proton synchrotron booster), which is part of the LHC injection chain.

LIU LHC injector upgrade.

LLRF Low Level RF.

LN$_2$ Liquid nitrogen is nitrogen in a liquid state at an extremely low temperature.

LSP Lightest supersymmetric particle.

LSS Long straight section: quasi-straight segments of a circular collider, which are available for beam interactions or utility insertions (e.g. injection, extraction, collimation, RF).

LTO Lithium titanium oxide.

LTS Low temperature superconductors have critical temperatures below $77\,\text{K}$.

Luminometer A calorimeter inside the detector to precisely measure the luminosity.

Luminosity Luminosity is the rate of collision events normalised to the cross section. It is expressed as inverse square centimetre and inverse second ($cm^{-2}\,s^{-1}$) or barn (1 barn = $10^{-24}\,cm^2$).

LV Low voltage.

MAC The medium access control sublayer and the logical link control (LLC) sublayer together make up the data link layer (DLL). Within that data link layer, the LLC provides flow control and multiplexing for the logical link (i.e. EtherType, 802.1Q VLAN tag), while the MAC provides flow control and multiplexing for the transmission medium. MAC is responsible for the transmission of data packets to and from the network-interface card, and to and from another remotely shared channel.

MAD-X MAD-X is a project and computational physics software to aid particle accelerator design and simulation.

MADX-PTC MAD X polymorphic tracking code.

MAPS Monolithic active pixel sensor. A silicon detector technology for high-energy physics particle detectors.

MB A megabyte are by definition of the IEC, 1 000 000 bytes (10^6 B).

MC Main corrector magnet.

MCHF 10^6 CHF.

MD (magnet) Main dipole.

MDI The machine detector interface refers to the topics and regions where the beamlines of the accelerator overlap with the physics experiment's detector. Key elements include mechanical support of final beamline elements, luminosity monitoring, feedback, background suppression and radiation shielding.

MDISim A tool set developed in the frame of the FCC study for Machine Detector Interface SIMulations using and combining the standard tools MAD-X, ROOT and GEANT4.

MDT Monitored drift tube.

MEG A particle physics experiment at the Paul Scherrer Institute, Switzerland.

MeV 10^6 electronvolt.

MgB$_2$ Magnesium diboride is the inorganic compound. It is a dark gray, water-insoluble solid. The compound becomes superconducting at 39 K.

MGy 10^6 gray.

MHz 10^6 Hz

MI Microwave instability.

MIIT Millions of amp squared seconds. A performance indicator of a superconducting cable that determines two primary factors of the adequate quench protection system: how quickly the current in the magnet must be reduced once a quench is detected and how quickly a quench must be detected, once the initiating spot quenches.

MJ 10^6 J.

MLI Multi layer insulation.

mm 10^{-3} m

MO Main octupole corrector magnet.

Molasse Variable sedimentary deposits comprising sandstones, shales and conglomerates that form as terrestrial or shallow marine deposits in front of rising mountain chains. It is the typical soil type found in the Franco-Geneva basin.

MolfFlow+ Software developed at CERN to calculate the pressure in an arbitrarily complex geometry when ultra-high vacuum condition is met.

MOSFET Metal-oxide-semiconductor field-effect transistor.

MoU Memorandum of understanding.

MP Medium pressure, around 20 bar.

MPGD Micro pattern gas detector.

MQ Main quadrupole.

MQDA Main quadrupole dispersion suppressor magnet.

MQS Main quadrupole skew magnet.

MQT Main quadrupole tuning magnet.

MQTL Main quadrupole trim magnet.

MRI Magnetic resonance imaging.

MRN Metrologial reference network.

MS Main sextupole.

MTE Multi turn extraction.

MTTF Mean time to failure.

MTTR Mean time to repair.

MVDC Medium voltage direct current power distribution.

MW 10^6 Watt

N The newton (symbol: N) is the SI unit of force. A newton is how much force is required to make a mass of one kilogram accelerate at a rate of one metre per second squared.

NASA National Aeronautics and Space Administration.

Nb Niobium, formerly known as columbium, is a chemical element with symbol Nb (formerly Cb) and atomic number 41. It is a soft, grey, crystalline, ductile transition metal, often found in the minerals pyrochlore and columbite, hence the former name "columbium". Niobium is used in various superconducting materials.

Nb$_3$Sn An intermetallic compound of niobium (Nb) and tin (Sn) with the A15 structure, and a type II LTS with with $T_c = 18.3$ K and $H_{c2} = 25$ T.

NbTi Niobium-titanium is an alloy of niobium (Nb) and titanium (Ti) and a type II LTS with $T_c = 9.5$ K. Nb–Ti wires, containing Nb–Ti filaments in an aluminium or copper matrix, are produced industrially and are used in the majority of superconducting magnets.

NEG Non-evaporable getter materials are mostly porous alloys or powder mixtures of Al, Zr, Ti, V and iron (Fe). They help to establish and maintain vacuums by soaking up or bonding to gas molecules that remain within a partial vacuum.

Nelium A light gas mixture made of neon and helium.

NEXTorr A patented flanged vacuum pumping solution, combining NEG and ion pumping technologies by the saes group, Milan, Italy.

NIE The notice d'impact sur l'environnement is an assembly of the results of environmental impact assessments for large projects in Switzerland.

NMR Nuclear magnetic resonance.

NN Neural network.

NPV Net Present Value is a measurement of profit calculated by subtracting the present values (PV) of cash outflows (including initial cost) from the present values of cash inflows over a period of time. It is determined by calculating the costs (negative cash flows) and benefits (positive cash flows) for each period of an investment. After the cash flow for each period is calculated, the PV of each one is obtained by discounting its future value at a periodic rate of return.

NTU The number of transfer units is defined as a ratio of the overall thermal conductance to the smaller heat capacity rate. It may also be interpreted as the relative magnitude of the heat transfer rate compared to the rate of enthalpy change of the smaller heat capacity rate fluid.

NuPECC Nuclear physics European Collaboration Committee.

$\mathcal{O}$ Big O notation is a mathematical notation that describes the limiting behavior of a function when the argument tends towards a particular value or infinity.

OBS Organisation breakdown structure.

ODH Oxygen deficiency hazard.

OEIE The ordonnance relative à' l'étude de l'impact sur l'environnement is the Swiss environmental impact assessment regulation.

OFHC Oxygen-free copper (OFC) or oxygen-free high thermal conductivity (OFHC) copper is a group of wrought high conductivity copper alloys that have been electrolytically refined to reduce the level of oxygen to 0.001% or below.

OPEX An operating expense, operating expenditure, operational expense, operational expenditure or opex is an ongoing cost for running a product, business, or system.

Optics An optical configuration refers to a powering scheme of the magnets. There can be several different optics for a single lattice configuration. Different optics exist for instance, for injection and for luminosity operation corresponding to different β^* values in the experiment insertions.

ORC The organic rankine cycle is named for its use of an organic, high molecular mass fluid with a liquid-vapor phase change, or boiling point, occurring at a lower temperature than the water-steam phase change. The fluid allows Rankine cycle heat recovery from lower temperature sources. The low-temperature heat is converted into useful work, that can itself be converted into electricity.

OSI The open systems interconnection model is a conceptual model that characterises and standardises the communication functions of a telecommunication or computing system without regard to its underlying internal structure and technology.

OSI Model The open systems interconnection model is a conceptual and logical layout that defines network communication used by systems open to interconnection and communication with other systems.

Overburden Material (rock, soil) that lies above an underground structure, e.g. a tunnel or cavern.

Pa The pascal is the SI derived unit of pressure. A common multiple unit of the pascal us the hectopascal (1 hPa = 100 Pa) which is equal to one millibar.

Pandora PFA The pandora particle flow algorithm is an event reconstruction software developed for future linear collider studies ILC and CLIC.

Pb Lead is a chemical element with symbol Pb (from the Latin plumbum) and atomic number 82.

PBR The pre booster ring is an injector to the booster top-up ring (BR), which continuously provides the particle collider with particles at collision energy.

PBS Product breakdown structure.

PCB Printed circuit board.

PCO Power COnverter.

PDF The parton name was proposed by Richard Feynman in 1969 as a generic description for any particle constituent within the proton, neutron and other hadrons. These particles are referred today as quarks and gluons. A parton distribution function is defined as the probability density for finding a particle with a certain longitudinal momentum fraction at a certain resolution scale.

PEDD Peak energy deposition density.

PEP-II The PEP-II facility consists of two independent storage rings, one located atop the other in the at the Stanford Linear Accelerator Center (SLAC). The high-energy ring, which stores a 9 GeV electron beam, was an upgrade of the existing Positron-Electron Project (PEP) collider; it reused all of the PEP magnets and incorporated a state-of-the-art copper vacuum chamber and a new radio-frequency system capable of supporting a stored beam of high current. The low-energy ring, which stores 3.1 GeV positrons, was newly constructed. Injection is achieved by

extracting electrons and positrons at collision energies from the SLC and transporting them each in a dedicated bypass line. The low-emittance Stanford Linear Collider (SLC) beams are used for the injection process. The collider was completed in July 1998.

PERLE Powerful energy recovery Linac for experiments, an envisaged test facility for an energy recovery linac (ERL) at Laboratoire de l'Accélérateur Linéaire (LAL) of CNRS in Orsay in France.

PFL Pulse forming line.

PFN Pulse forming network.

pH A logarithmic scale used to specify the acidity or basicity of an aqueous solution. It is approximately the negative of the base 10 logarithm of the molar concentration, measured in units of moles per liter, of hydrogen ions.

Phase Space A six-dimensional space consisting of a particle's position (x, y, z) and divergence (x′, y′, z′). Phase space is represented in two dimensions by plotting position on the horizontal axis and the corresponding divergence on the vertical axis.

PHY In the seven-layer OSI model of computer networking, the physical layer or layer 1 is the first and lowest layer. This layer may be implemented by a dedicated PHY chip. The physical layer consists of the electronic circuit transmission technologies of a network.

Pile-up The situation where a particle detector is affected by several events at the same time.

PIT The powder-in-tube process is often used for making electrical conductors from brittle superconducting materials such as niobium-tin or magnesium diboride and ceramic cuprate superconductors such as BSCCO.

PLC Programmable logic controller.

PMNS The Pontecorvo-Maki-Nakagawa-Sakata matrix, Maki-Nakagawa-Sakata matrix (MNS matrix), lepton mixing matrix, or neutrino mixing matrix is a unitary mixing matrix which contains information on the mismatch of quantum states of neutrinos when they propagate freely and when they take part in the weak interactions. It is a model of neutrino oscillation. This matrix was introduced in 1962 by Ziro Maki, Masami Nakagawa and Shoichi Sakata, to explain the neutrino oscillations predicted by Bruno Pontecorvo.

PMT Photomultiplier tube.

pNGB Pseudo Nambu-Goldstone boson.

PoT Protons on target.

PPLP Parabolic parabolic linear parabolic.

ppm Parts per million (10^{-6}).

PS The proton synchrotron is a particle accelerator at CERN. It was CERN's first synchrotron, beginning operation in 1959. It has since served as a pre-accelerator for the ISR (intersecting storage rings) and the SPS (super proton synchrotron), and is currently part of the LHC (large hadron collider) accelerator complex. In addition to protons, PS has accelerated alpha particles, oxygen and sulphur nuclei, electrons, positrons and antiprotons.

PSB The proton synchrotron booster at CERN is an accelerator made up of four superimposed synchrotron rings that receive beams of protons from the linear accelerator Linac 2 or 4 at 50 MeV and accelerate them to 1.4 GeV for injection into the PS (proton synchrotron).

PSD Photon stimulation desorption is a phenomenon whereby a substance is released from or through a surface.

PSO In computational science, particle swarm optimisation is a computational method that optimises a problem by iteratively trying to improve a candidate solution with regard to a given measure of quality. It solves a problem by having

a population of candidate solutions, here dubbed particles, and moving these particles around in the search-space according to simple mathematical formulae over the particle's position and velocity. Each particle's movement is influenced by its local best known position, but is also guided toward the best known positions in the search-space, which are updated as better positions are found by other particles. This is expected to move the swarm toward the best solutions.

PU Pile-up.

PV Photovoltaics.

PVSS Prozessvisualisierungs- und steuerungssoftware. A SCADA product from SIEMENS company ETM professional control now called WinCC OA.

Px One of the 12 FCC access points. x can be one of A, B, C, D, E, F, G, H, I, J, K, L, e.g. PA is the access point A close to the CERN Meyrin site.

PyHEADTAIL A macroparticle tracking software designed specifically to simulate collective effects in circular accelerators.

Pythia A Monte Carlo event generator software.

Q The quality factor or Q factor is a dimensionless parameter that describes how underdamped an oscillator or resonator is, and characterises a resonator's bandwidth relative to its centre frequency. Higher Q indicates a lower rate of energy loss relative to the stored energy of the resonator. For an RF cavity it characterises RF losses in the cavity: an RF cavity having a higher Q factor is a more efficient user of RF power.

QC1 First final focus quadrupole next to the IP.

QC2 Second final focus quadrupole, behind QC1.

QCD In theoretical physics, quantum chromodynamics is the theory of the strong interaction between quarks and gluons, the fundamental particles that make up composite hadrons such as the proton, neutron and pion.

QD Defocusing quadrupole.

QED In particle physics, quantum electrodynamics is the relativistic quantum field theory of electrodynamics.

QF Focusing quadrupole.

QFT Quantum field theory.

QGP Quark gluon plasma.

QPS Quench protection system.

QPU Quench processing unit.

QRL Cryogenic distribution line.

QS Quench instrumentation units in the tunnel.

Quench The change of state in a material from superconducting to resistive. If uncontrolled, this process damages equipment due to thermal stress induced by the extremely high-currents passing through the material.

R&D Research and development refers to activities to develop new services and products, or to improve existing services and products. Research and development constitutes the first stage of development of a potential new service or the production process.

R2E Radiation to electronics.

rad The radian (SI symbol rad) is the SI unit for measuring angles. The length of an arc of a unit circle is numerically equal to the measurement in radians of the angle that it subtends; $360°$ correspond to 2π rad.

RAMS Reliability, availability, maintainability and safety. Four non-functional key characteristics that determine the performance and total cost of technical systems.

RD52 A research and development project at CERN, carried out by an international collaboration, to develop a detector technology for a future electron-positron

particle collider using the simultaneous measurement of scintillation light and Čerenkov light generated in the shower development process.

RDC Radiation dependent capacitor.

RDP Resonant depolarisation.

RDR Radiation dependent resistor.

ReBCO Rare-earth barium copper oxide is a family of chemical compounds known for exhibiting high temperature superconductivity.

RF Radiofrequency.

RF cavity An electromagnetically resonant cavity used to convey energy (accelerate) to charged particles as they pass through by virtue of the electric field gradient across the cavity gap(s). Radio Frequency is a rate of oscillation in the range of around 3 kHz–300 GHz.

RH Relative humidity is the ratio of the partial pressure of water vapor to the equilibrium vapor pressure of water at a given temperature. Relative humidity depends on temperature and the pressure of the system of interest. The same amount of water vapor results in higher relative humidity in cool air than warm air.

RHA Radiation hardness assurance.

RI A research infrastructure is a facility, a set of resources and services that are used by research communities to conduct research and foster innovation in their fields. This includes major scientific equipment or sets of instruments, knowledge-based resources such as collections, archives and scientific data, e-infrastructures, such as data and computing systems and communication networks and any other tools that are essential to achieve excellence in research and innovation.

RMC Racetrack model coil.

RMM Racetrack model magnet.

RMS The root mean square is square root of the arithmetic mean of the squares of a set of numbers.

Roadheader Excavation equipment consisting of a boom mounted cutting head with a hydraulic mechanism.

Rockbreaker A hydraulically powered tool used to break up rock during the excavation process.

RoHS The restriction of hazardous substances directive 2002/95/EC, (RoHS 1), short for directive on the restriction of the use of certain hazardous substances in electrical and electronic equipment, was adopted in February 2003 by the European Union.

ROOT ROOT is a modular scientific software toolkit. It provides functionalities needed to deal with big data processing, statistical analysis, visualisation and storage.

ROXIE Software developed at CERN for the electromagnetic simulation and optimisation of accelerator magnets.

RPC Resistive plate chamber.

RRP The restacked-rod restack process is a manufacturing process for Nb_3Sn wires developed by the OST company (Oxford instruments technologies), which has been subsequently acquired by BEST Inc. (Bruker Energy and Supercon. Technologies).

RRR The residual resistivity ratio is defined as the ratio of the electrical resistivity of a material at room temperature and at a chosen cryogenic temperature. For superconducting materials, a cryogenic temperature above T_c must be chosen. RRR serves as a measure of the purity and overall quality of a sample: as electrical resistivity usually increases as defect prevalence increases, a large RRR is associated with a pure sample.

RTE Réseau de Transport d'Électricité is the French electricity transmission system operator. It is responsible for the operation, maintenance and development of the French high-voltage transmission system.

RW The resistive wall impedance is one of the main sources for beam instabilities in synchrotrons and storage rings.

S The siemens (symbol: S) is the derived unit of electric conductance, electric susceptance and electric admittance in the International System of Units (SI). Conductance, susceptance, and admittance are the reciprocals of resistance, reactance, and impedance respectively; hence one siemens is redundantly equal to the reciprocal of one ohm, and is also referred to as the mho.

$\sqrt{s}$ The total centre of mass energy of the colliding particles.

S band The S band is a designation by the IEEE (institute of electrical and electronics engineers) for a part of the microwave band of the electromagnetic spectrum covering frequencies from 2 to 4 gigahertz.

S275JR A structural steel grade according to EN 10025: part 2: 2004.

SAD Strategic accelerator design is a software tool for particle accelerator design developed at KEK since 1986.

SC coating A very thin layer of superconducting material on normal-conducting material (e.g. copper). Used for various purposes such as quench avoidance of a neighbouring superconductor, reduction of production costs due to use of cheaper support material and impedance reduction.

SCADA Supervisory control and data acquisition.

SCP The "Structure de Concertation Permanente" federates representatives of CERN, the Swiss federal and cantonal governments as well as the Swiss permanent mission at the international organisations in order to work in common on adequate administrative frameworks for CERN's operation and future developments on Swiss territory.

scSPS The superconducting SPS is a superconducting synchrotron, replacing the current SPS accelerator at CERN.

SDA The "surfaces d'assolement" are land plots in Switzerland, which are reserved for potential agricultural purposes in the event of crisis. They are not constructible.

SEE Single event effect is a general class of radiation effects in electronic devices. There are two types of effects: those which cause permanent damage to the equipment's functionality and those, which cause a transient fault.

SEM A scanning electron microscope (SEM) is a type of electron microscope that produces images of a sample by scanning the surface with a focused beam of electrons.

SESAME The synchrotron-light for experimental science and applications in the middle east is a third-generation synchrotron light source. SESAME is located in Allan, Jordan (30 km from Amman and 30 km from the King Hussein/Allenby Bridge crossing of the Jordan River).

SEU A single event upset is a change of state caused by one single ionising particle (ions, electrons, photons) striking a sensitive node in a micro-electronic device, such as in a microprocessor, semiconductor memory, or power transistor. It is not considered to permanently damage the equipment's functionality. It is an example of a general class of radiation effects in electronic devices called single event effects (SEE).

SEY Secondary electron yield.

SFOE The Swiss Federal Office of Energy.

SFOPT Strongly first order phase transition.

SGAR The Secretariat Générale de la région Auvergne-Rhône-Alpes assists the prefect of the region in the implementation of the government's policies in the region.

Shotcrete A sprayed concrete lining that is projected at high velocity via a hose onto a surface.

SI The international system of units (SI, abbreviated from the French système international (d'unités)) is the modern form of the metric system, and is the most widely used system of measurement. It comprises a coherent system of units of measurement built on seven base units that are ampere, kelvin, second, metre, kilogram, candela, mole, and a set of twenty prefixes to the unit names and unit symbols that may be used when specifying multiples and fractions of the units. The system also specifies names for 22 derived units, such as lumen and watt, for other common physical quantities.

SiC Silicon carbide (SiC) devices belong to the so-called wide band gap semiconductor group. They offer a number of attractive characteristics for high voltage power semiconductors when compared to commonly used silicon (Si). In particular, the much higher breakdown field strength and thermal conductivity of SiC allow devices to be created which by far outperform the corresponding Si ones. This way previously unattainable efficiency levels can be achieved.

SiD The silicon detector is a conceptual design for an experiment detector at the ILC.

SiPM Silicon photomultiplier.

SIRIUS Sirius is a synchrotron light source facility based on a 4th generation low emittance storage ring that is under construction in Campinas, Brazil.

SITROS A tracking program developed at DESY in 1983 for the simulation of polarising and depolarising effects in electron-positron storage rings.

Sixtrack A single particle 6D symplectic tracking code optimised for long term tracking in high energy particle accelerators.

SLC Stanford Linear Collider.

Slurry shield TBM A TBM fitted with a full face cutterhead which provides face support by pressurizing boring fluid inside the cutterhead chamber. These machines are most suited for tunnels through unstable material subjected to high groundwater pressure or water inflow that must be stopped by supporting the face with a boring fluid subjected to pressure.

SM Standard Model.

SMC Short model coil.

sMDT Small diameter muon drift tube.

SME Small and medium-sized enterprises.

SMEFT The Standard Model effective field theory is a model independent framework for parameterising deviations from the Standard Model in the absence of light states.

SMS A safety management system integrates autonomously working safety-related subsystems for higher-level operation, such as intrusion alarms, entrance and access control systems, fire and smoke detection, communication with public emergency services, public address and evacuation systems and many more.

SPN Support pre-alignment network.

SPS The super proton synchrotron is a particle accelerator at CERN. It is housed in a circular tunnel, 6.9 km in circumference and delivers beams to fixed target experiments and the LHC.

SPT The standard penetration test is an in-situ dynamic penetration test designed to provide information on the geotechnical engineering properties of soil. The test procedure is described in ISO 22476-3, ASTM D1586 and Australian Standards AS 1289.6.3.1.

SR Synchrotron radiation.

SRF Superconducting radiofrequency.

SSM Sequential Standard Model.

SSS Short straight section.

Standard Model The Standard Model explains how the basic building blocks of matter interact, governed by four fundamental forces.

STATCOM Static synchronous compensator.

STFC Science and Technology Facilities Council in the UK.

Storz Storz is a type of hose coupling invented by Carl August Guido Storz in 1882 and patented in Switzerland in 1890, and patented in the U.S. in 1893 that connects using interlocking hooks and flanges. It is widely used on fire hoses in firefighting applications.

Strand A superconducting strand is a composite wire containing several thousand superconducting filaments (e.g. Nb_3Sn) dispersed in a matrix with suitably small electrical resistivity properties (e.g. copper).

Strong force One of four known fundamental forces (the others are the weak force, electromagnetism and gravity). The strong force is felt only by quarks and gluons, and is responsible for binding quarks together to make hadrons. For example, two up quarks and a down quark are bound together to make a proton. The strong interaction is also responsible for holding protons and neutrons together in atomic nuclei.

Superconducting cable Superconducting cables are formed from several superconducting strands in parallel, geometrically arranged in the cabling process to achieve well-controlled cable geometry and dimensions, while limiting the strand deformation in the process. Cabling several strands in parallel results in an increase of the current carrying capability and a decrease of the inductance of the magnet, easing protection.

Superconductivity A property of some materials, usually at very low temperatures that allows them to carry electricity without resistance.

Superferric magnet An iron-dominated magnet based on a magnetic steel structure with a minimal amount of superconductor. The structure is the same as a normal conducting magnet, but the coil is built from superconducting material. The yole is cooled to cryogenic temperature.

SuperKEKB SuperKEKB is a particle accelerator located at KEK (High Energy Accelerator Research Organisation) in Tsukuba, Ibaraki Prefecture, Japan. SuperKEKB will collide electrons at 7 GeV with positrons at 4 GeV. The accelerator is an upgrade of KEKB, providing approximately 40 times higher luminosity, due mostly to superconducting quadrupole focusing magnets.

SUSY Supersymmetry.

Synchrotron A circular machine that accelerates subatomic particles by the repeated action of electric forces generated by RF fields at each revolution. The particles are maintained on constant circular orbits by synchronously increasing the magnetic fields.

Synchrotron Radiation Electromagnetic radiation generated by acceleration of relativistic charged particles in a magnetic or electric field. Synchrotron radiation is the major mechanism of energy loss in synchrotron accelerators and contributes to electron-cloud build-up.

SynRad+ A modified MolFlow+ software developed at CERN to trace photons in order to calculate flux and power distribution caused by synchrotron radiation on a surface.

t The "metric ton" is a unit of measure. It corresponds to 1000 kg in this document.

T_c The critical temperature of a superconducting material, above which material enters the normal state and does not show superconducting behaviour.

Tantalum Tantalum is a chemical element with symbol Ta and atomic number 73. It is a rare, hard, blue-gray, lustrous transition metal that is highly corrosion-resistant. It is part of the refractory metals group, which are widely used as minor components in alloys. The chemical inertness of tantalum makes it a valuable substance for laboratory equipment and a substitute for platinum.

TBA Triple bend achromat.

TBM A tunnel boring machine is a machine used to excavate tunnels with a circular cross section through a variety of soil and rock strata. They can bore through anything from hard rock to sand. Tunnel diameters can range from one metre to more than 17 m to date.

TCLA Active tungsten absorber.

TCLD Dispersion suppression collimator.

TCO Total cost of ownership.

TCP Primary collimator.

TCSG Secondary collimator.

Technology Spillover Technology spillover refers to the unintentional technological benefits to firms coming from the research and development efforts of other organisations without the costs being shared.

TEM Transmission electron microscopy (TEM) is a microscopy technique in which a beam of electrons is transmitted through a specimen to form an image.

Tesla Unit of magnetic field strength. 1 T is the field intensity generating one newton (N) of force per ampere (A) of current per metre of conductor.

TETRA Terrestrial trunked radio, a European standard for a trunked radio system, is a professional mobile radio and two-way transceiver specification.

TeV Tera electron Volts (10^{12} eV). Unit of energy. 1 eV is the energy given to an electron by accelerating it through 1 Volt of electric potential difference.

Tevatron A 2 TeV proton on anti-proton collider that was operated at Fermilab in Batavia, Illinois (USA) until 2011. The top quark was discovered using this collider.

TFA Radioactive waste of "très faible activité" (very low level activity), the classification depends on the level of activity and on the radionuclides.

Thyratron A type of gas-filled tube used as a high-power electrical switch and controlled rectifier. Thyratrons can handle much greater currents than similar hard-vacuum tubes. Electron multiplication occurs when the gas becomes ionised, producing a phenomenon known as Townsend discharge.

TID Total ionising dose.

TileCal TileCal is a hadronic calorimeter covering the most central region of the ATLAS experiment at the LHC.

TLEP A concept for a circular electron-positron collier in a new 80–100 km long tunnel acting as a Tera-Z factory

TM Transverse magnetic modes have no magnetic field in the direction of propagation.

TM$_{210}$ In rectangular waveguides, rectangular mode numbers are designated by two suffix numbers attached to the mode type, such as TM$_{mn}$, where m is the number of half-wave patterns across the width of the waveguide and n is the number of half-wave patterns across the height of the waveguide. In circular waveguides, circular modes exist and here m is the number of full-wave patterns along the circumference and n is the number of half-wave patterns along the diameter.

TMCI Transverse model coupling instability.

TOT The tunnel optimisation tool is software that has been developed under a cooperation contract for CERN by the company ARUP (UK).

TRL Technology readiness levels (TRLs) are indicators of the maturity level of particular technologies. This measurement system provides a common understanding

of technology status and addresses the entire innovation chain. There are nine technology readiness levels; TRL 1 being the lowest and TRL 9 the highest.

TTB Turbo Brayton box.

Tungsten Tungsten, or wolfram is a chemical element with symbol W and atomic number 74.

UFO Unidentified falling object.

UNESCO The United Nations Educational, Scientific and Cultural Organization is a specialised agency of the United Nations based in Paris.

UPS Uninterruptible power supply.

V The volt (symbol: V) is the derived unit for electric potential, electric potential difference (voltage), and electromotive force.

VA A volt-ampere is the unit used for the apparent power in an electrical circuit, equal to the product of root-mean-square (RMS) voltage and RMS current. In direct current (DC) circuits, this product is equal to the real power (active power) in watts. Volt-amperes are useful only in the context of alternating current (AC) circuits.

Vacuum Pressures much below atmospheric pressure.

Variant A variant of a product has a specific set of characteristics that distinguish it from other products in the same product line. All variants are derived from a common base and share common design features. The development of different variants is managed by distinct processes and different variants co-exist at the same time.

VBF Vector boson fusion.

Version A version of a product represents that same product at a different time. It may or may not have undergone some change (revision).

VFET Vacuum field-effect transistor.

VLP Very low pressure.

VSM An established compact shaft sinking technology for all ground conditions for soft and stable soils, originally developed by Herrenknecht AG.

VXD CLD vertex detector.

W (particle) The W and Z bosons are together known as the weak or more generally as the intermediate vector bosons. They mediate the weak interaction. The W bosons have either a positive or negative electric charge of 1 elementary charge and are each other's antiparticles. The particles have a spin of 1.

W (Watt) The watt (symbol W) is a unit of power. In the international system of units (SI) it is defined as a derived unit of 1 joule per second, and is used to quantify the rate of energy transfer.

WBS Work breakdown structure.

WCS Warm compressor station.

Weak force A force carried by heavy particles known as the W and Z bosons. The most common manifestation of this force is beta decay, in which a neutron in a nucleus is transformed into a proton, by emitting an electron and a neutrino. Weak neutral current is a very weak interaction mediated by the Z boson that is independent of the electric charge of a particle. Particles can exchange energy through this mechanism, but other characteristics of the particles remain unchanged.

Willingness To Pay An indicator of how much a person values a product or device, measured by the maximum amount she or he would pay to acquire one.

WIMP Weakly interacting massive particles are hypothetical particles that are thought to constitute dark matter.

WinCC OA WinCC Open Architecture is a SCADA system for visualising and operating processes, production flows, machines and plants in all lines of business. It was formerly called PVSS.

WLS Wave length shifting.

WPS Wire positioning sensors.

Xe Xenon is a chemical element with symbol Xe and atomic number 54.

XFEL A free-electron laser generating high-intensity electromagnetic radiation by accelerating electrons to relativistic speeds and directing them through special magnetic structures.

XRD X-ray powder diffraction (XRD) is a rapid analytical technique primarily used for phase identification of a crystalline material and can provide information on unit cell dimensions. The analysed material is finely ground, homogenised, and average bulk composition is determined.

YBCO Yttrium barium copper oxide is a family of crystalline chemical compounds, displaying high-temperature superconductivity. YBCO is often categorised as a rare-earth barium copper oxide (REBCO).

Z The W and Z bosons are together known as the weak or more generally as the intermediate vector bosons. They mediate the weak interaction. The Z boson is electrically neutral and is its own antiparticle. The particles has a spin of 1.

ZrTiV A zirconium-titanium-vanadium alloy that is used as a coating for a large surface getter pump.

References

1. CERN Council, *European Strategy Session of Council*, CERN-Council-S/106 (May 30, 2013)
2. *Future Circular Collider Study Kickoff Meeting* (University of Geneva, February 12–15, 2014), http://indico.cern.ch/e/fcc-kickoff
3. E. Todesco, F. Zimmermann (eds.), *Proceedings of EuCARD-AccNet-EuroLumi Workshop: The High-Energy Large Hadron Collider – HE-LHC10, Malta*, CERN-2011-003 (October 14–16, 2010), arXiv:1111.7188 [physics.acc-ph]
4. J. Osborne, C. Waaijer, Pre-feasibility assessment for an 80 km tunnel project at CERN, Contribution to the update of the *European Strategy for Particle physics* (July 27, 2012), Vol. 165, http://indico.cern.ch/event/175067/call-for-abstracts/165/file/1.pdf
5. *Joint Snowmass-EuCARD/AccNet-HiLumi meeting "Frontier Capabilities for Hadron Colliders 2013" a.k.a. EuCARD VHE-LHC Day, CERN* (February 21–22, 2013), http://indico.cern.ch/event/223094
6. A. Blondel, F. Zimmermann, A High Luminosity e^+e^- collider in the LHC tunnel to study the Higgs boson (2011), arXiv:1112.2518 [hep-ex]
7. EuCARD LEP3 workshop (June 18, 2012); 2nd EuCARD LEP3 workshop (October 23, 2012); 3rd EuCARD TLEP3 workshop (January 10, 2013); 4th EuCARD TLEP workshop (April 4–5, 2013)
8. The TLEP Design Study Working Group, JHEP **01**, 164 (2014)
9. M. Benedikt, D. Schulte, F. Zimmermann, Phys. Rev. ST Accel. Beams **8**, 101002 (2015)
10. H. Damerau et al. (eds.), *LHC Injectors Upgrade, Technical Design Report, Vol. I: Protons*, CERN-ACC-2014-0337 (2014)
11. X. Peng, M.D. Sumption, X. Xu, Adv. Mater. **27**, 1346 (2015)
12. *The physics of HL-LHC, and perspectives on HE-LHC*, Workshop, https://twiki.cern.ch/twiki/bin/view/LHCPhysics/HLHELHCWorkshop/

13. DELPHES 3 Collaboration, C. Delaere et al., JHEP **02**, 057 (2014)
14. G. Salam, A. Weiler, *Collider Reach*, Website, http://collider-reach.web.cern.ch/
15. H. Baer, V. Barger, J.S. Gainer, H. Serce, X. Tata, Phys. Rev. **D96**, 115008 (2017)
16. A. Aboubrahim, P. Nath, Phys. Rev. D **98**, 015009 (2018)
17. T. Han, S. Mukhopadhyay, X. Wang, Phys. Rev. D **98**, 035026 (2018)
18. C. Helsens, D. Jamin, M. Selvaggi, Search for high-mass resonances at FCC-hh, CERN Document Server (October, 2018), https://cds.cern.ch/record/2642473
19. T.G. Rizzo, Phys. Rev. **D89**, 095022 (2014)
20. U. Baur, I. Hinchliffe, D. Zeppenfeld, Int. J. Mod. Phys. **A2**, 1285 (1987)
21. L. Randall, R. Sundrum, Phys. Rev. Lett. **83**, 3370 (1999)
22. B.C. Allanach, B. Gripaios, T. You, JHEP **03**, 021 (2018)
23. C.T. Hill, Phys. Lett. **B345**, 483 (1995)
24. M. Selvaggi, Higgs measurements at FCC-hh (October, 2018), https://cds.cern.ch/record/2642471
25. D. Gonçalves, T. Han, F. Kling, T. Plehn, M. Takeuchi, Phys. Rev. **D97**, 113004 (2018)
26. S. Homiller, P. Meade, J. High Energy Phys. **2019**, 55 (2019)
27. T. Han, P. Langacker, Z. Liu, L.-T. Wang, Diagnosis of a new neutral Gauge Boson at the LHC and ILC for Snowmass 2013, arXiv:1308.2738 [hep-ph]
28. S. Bifani, S. Descotes-Genon, A. Romero Vidal, M.-H. Schune, J. Phys. G: Nucl. Part. Phys. **46** (2018), DOI: 10.1088/1361-6471/aaf5de
29. G. D'Amico, M. Nardecchia, P. Panci, F. Sannino, A. Strumia, R. Torre, A. Urbano, JHEP **09**, 010 (2017)
30. G. Apollinari et al., *High-Luminosity Large Hadron Collider (HL-LHC): Preliminary Design Report*, Yellow Report CERN-2015-005 (2015)
31. R. Kersevan, Research program on the cryogenic beam vacuum of the FCC-hh, in *Int. Conf. on High Energy Physics, Chicago, 3–10 August 2016* (2016)
32. R. Kersevan, New beam screen design proposal, Presented at *FCC-hh General Design Meeting* (March 22, 2018)
33. M. Benedikt, J. Keintzel, R. Tomas, *Optics Design and Performance Aspects of the HE-LHC*, CERN-THESIS-2018-177 (September 21, 2018), http://cds.cern.ch/record/2640684
34. G. Guillermo, D. Sagan, F. Zimmermann, Examining mitigation schemes for synchrotron radiation in high-energy hadron colliders, Accepted for publication in Phys. Rev. Accel. Beams (2018)
35. D. Schoerling, b_2/b_3 shimming recipe and prospects, HE-LHC Design Meeting no. 26, 8 March 2018 (2018)
36. O.S. Brüning, S. Fartoukh, *Field Quality Specification for the LHC Main Dipole Magnets*, LHC Project Report 501 (2001)
37. S.I. Bermudez, D. Tommasini, *Field quality table update for EuroCirCol 16 T design*, (2018)
38. *SixTrack Code*, Website, http://sixtrack.web.cern.ch/SixTrack/
39. Y. Nosochkov, Dynamic aperture at injection for different lattice options, in *FCC Week 2018, Amsterdam, April 9–13, 2018* (2018)
40. M. Hofer, Dynamic aperture at injection with updated FQ table, in *HE-LHC Design Meeting no. 31, 26 June 2018* (2018)
41. V.V. Kashikhin, A.V. Zlobin, Persistent current effect in 15–16 T Nb$_3$Sn accelerator dipoles and its correction, in *Proceedings of the NAPAC'16* (2016)
42. J. van Nugteren et al., *Persistent Current Shim Coils for Accelerator Magnets*, CERN TE-MSC Internal Note 2016-03, EDMS Nr. 1574002 (2014)
43. W. Scandale, F. Zimmermann, Nucl. Phys. B, Proc. Suppl. **177–178**, 207 (2008)
44. S. Fartoukh, Phys. Rev. ST Accel. Beams **17**, 111001 (2014)
45. L.V. Riesen-Haupt, Unpublished (2018)
46. T. Risselada, Unpublished (2018)
47. J.B. Jeanneret, R. Ostojic, *Geometrical Acceptance in LHC Version 5.0*, LHC-Project-Note **111** (1997)

48. R. Bruce et al., Parameters for aperture calculations at injection for HL-LHC, CERN-ACC-2016-0328 (2016)

49. J.B. Jeanneret, *Geometrical Tolerances for the Qualification of LHC Magnets*, LHC Project Report **1007** (2007)

50. M. Giovanozzi, R. de Maria, and R. Tomàs, Phys. Rev. ST Accel. Beams **12**, 011002 (2009)

51. B. Bellesia, J.P. Koutchouk, C. Santoni, E. Todesco, *Estimating field quality in low beta superconducting quadrupoles and its impact on beam stability*, LHC Project Report **1061** (2007)

52. J.L. Abelleira et al., Nonlinear correction schemes for the phase 1 LHC insertion region upgrade and dynamic aperture studies, in *Proceedings of the IPAC'18, Vancouver, Canada* (2018)

53. *FLUKA*, Website, http://www.fluka.org

54. F. Carra et al., Mechanical engineering and design of novel collimators for HL-LHC, in *Proceedings of the 5th IPAC'14, Dresden, Germany* (2014), p. 369, http://accelconf.web.cern.ch/AccelConf/IPAC2014/papers/mopro116.pdf

55. E. Quaranta et al., Towards optimum material choices for HL-LHC collimator upgrade, in *Proceedings of the 7th IPAC'16, Busan, Korea* (2016), p. 2499, http://accelconf.web.cern.ch/AccelConf/ipac2016/papers/wepmw031.pdf

56. G. Apollinari, I. Béjar Alonso, O, Brüning, M. Lamont, L. Rossi, (eds.), *High-Luminosity Large Hadron Collider (HL-LHC): Preliminary Design Report*, CERN-2015-005, FERMILAB-DESIGN-2015-02 (2015)

57. D. Mirarchi, R. Appleby, A. Bertarelli, R. Bruce, F. Cerutti, H. G. Morales, P. Hermes, R. Kwee-Hinzmann, A. Lechner, A. Mereghetti, E. Quaranta, and S. Redaelli, *Cleaning Performance of the Collimation System of the High Luminosity Large Hadron Collider*, Proceedings of the International Particle Accelerator Conference 2016, Busan, Korea (2016), http://accelconf.web.cern.ch/AccelConf/ipac2016/papers/wepmw030.pdf

58. R.W. Aßmann et al., The final collimation system for the LHC, in *Proceedings of the EPAC'06, Edinburgh, Scotland* (2006), p. 986

59. R. Bruce, R.W. Assmann, V. Boccone, C. Bracco, M. Brugger, M. Cauchi, F. Cerutti, D. Deboy, A. Ferrari, L. Lari, A. Marsili, A. Mereghetti, D. Mirarchi, E. Quaranta, S. Redaelli, G. Robert-Demolaize, A. Rossi, B. Salvachua, E. Skordis, C. Tambasco, G. Valentino, T. Weiler, V. Vlachoudis, D. Wollmann, Phys. Rev. ST Accel. Beams **17**, 081004 (August, 2014)

60. M.K. Craddock, J.B. Jeanneret, D.I. Kaltchev, R.V. Servranckx, *Numerical Optimization of Collimator Jaw Orientations and Locations in the LHC*, CERN LHC-Project-Report-134 and Proceedings of the PAC'97, Vancouver, Canada (1997)

61. R. Bruce, A. Marsili, S. Redaelli, Cleaning performance with 11 T dipoles and local dispersion suppressor collimation at the LHC, in *Proceedings of the IPAC'14, Dresden, Germany* (2014), p. 170, http://accelconf.web.cern.ch/AccelConf/IPAC2014/papers/mopro042.pdf

62. B. Auchmann et al., Power deposition in LHC magnets with and without dispersion suppressor collimators downstream of the Betatron cleaning insertion, in Proceedings of the IPAC'14, Dresden, Germany (2014), p. 112, http://accelconf.web.cern.ch/AccelConf/IPAC2014/papers/mopro021.pdf

63. G. Apollinari et al., High-luminosity large hadron collider (HL-LHC), Technical Design Report V.0.1, in Vol. 4 of *CERN Yellow Reports: Monographs*, CERN, CERN, Geneva, Switzerland, CERN-2017-007-M (2017)

64. R.W. Aßmann et al., *Accelerator physics concept for upgraded LHC collimation performance*, in Proceedings of the PAC'09, Vancouver, Canada (2009)

65. R. Bruce et al., Updated parameters for HL-LHC aperture calculations for proton beams, CERN-ACC-2017-0051 (2017)

66. R. Bruce, C.Bracco, R. De Maria, M. Giovannozzi, A. Mereghetti, D. Mirarchi, S. Redaelli, E. Quaranta, B. Salvachua, Nucl. Instr. Meth. Phys. Res. A **848**, 19 (2017)

67. F. Schmidt, SixTrack user's reference manual, CERN/SL/94-56-AP (1994)

68. G. Robert-Demolaize, R. Assmann, S. Redaelli, F. Schmidt, A new version of SixTrack with collimation and aperture interface, in *Proceedings of the PAC'05, Knoxville, USA* (2005), p. 4084

69. E. Shaposhnikova, HE-LHC: Longitudinal beam parameters, *Unpublished: RF Parameters and Longitudinal Emittance during the HE-LHC Ramp* (July 25, 2018)

70. D.V. Neuffer, S. Peggs, *Beam-beam Tune Shifts and Spreads in the SSC: Head on, Long Range, and PACMAN Conditions* (SSC, Berkeley, CA, USA, April, 1986), http://cds.cern.ch/record/168383

71. J. Irwin, *Diffusive Losses From SSC Particle Bunches Due to Long-range Beam-beam Interactions* (Berkeley, CA, USA, September, 1989), http://cds.cern.ch/record/202623, SSC-233

72. Y. Papaphilippou, F. Zimmermann, Phys. Rev. Spec. Top. Accel. Beams **2**, 104001 (1999)

73. M. Crouch et al., Dynamic aperture studies of long-range beam-beam interactions at the LHC, in *Proceedings of the IPAC'17, THPA056, Copenhagen, Denmark* (2017)

74. W. Herr et al., *Long-range beam-beam effects in the LHC*, in *Proceedings ICFA mini-Workshop on beam-beameEffects in Hadron Colliders, CERN, Geneva, Switzerland*, edited by W. Herr and G. Papotti (March 18–22, 2013), pp. 87–92, CERN-2014-004

75. T. Pieloni et al., Two beam effects, in *Proceedings of the 2014 Evian Workshop on LHC beam operation* (2014), pp. 69–79, http://cds.cern.ch/record/2289585, CERN-ACC-2014-0319

76. T. Pieloni et al., Beam-beam effects long-range ad head-on, in *Proceedings of the 2015 Evian Workshop on LHC Beam Operation, CERN-ACC-2015-0376* (2015), pp. 111–122

77. V.D. Shiltsev, Electron lenses for super-colliders, in *Particle Acceleration and Detection* (Springer, New York, NY, 2016), http://cds.cern.ch/record/2112966

78. J.P. Koutchouk, Principle of a correction of the long-range beam-beam effect in LHC using electromagnetic lenses, CERN LHC-Project-Note 223 (2000)

79. E. Metral et al., Update of the HL-LHC operational scenarios for proton operation, CERN-ACC-NOTE-2018-0002 (2018)

80. T. Pieloni et al., Colliding high brightness beams in the LHC, in *Proceedings of the HB'12: Beijing, China* (2012), p. MOP250

81. J. Barranco García et al., Probing the behaviour of high brightness bunches in collision at 6.5 TeV and the interplay with an external source of noise (MD1433) (April, 2017), https://cds.cern.ch/record/2261037, CERN-ACC-NOTE-2017-0030

82. D. Amorim et al., ICFA Beam Dyn. Newsl. **72**, 151 (2017)

83. F. Ruggiero, Part. Accel. **50**l, 83 (1995)

84. L. Vos, Tune and stability of high intensity bunch trains in the CERN SPS and LHC, in *Proceedings of the EPAC'00, Vienna, Austria* (2000)

85. H. Pikhartova, HE-LHC Touschek Lifetime and Intrabeam Scattering, in *HE-LHC Design Meeting no. 32, 31 July 2018* (2018)

86. D. Amorim et al., Impedance model for HE-LHC, in *HE-LHC Design Review, CERN, 11 December 2017 Meeting 08, CERN, 11–12 December 2017* (2017)

87. S. Arsenyev, Impedance aspects of the beam screen, in *HE-LHC Design Review, CERN, 11 December 2017 meeting 08, CERN, 11–12 December 2017* (2017)

88. D. Amorim et al., *HL-LHC impedance and related effects*, CERN-ACC-NOTE-2018-0087 (2018)

89. *FCC-hh impedance web site*, http://impedance.web.cern.ch/impedance/fcchh/impedances.html

90. D. Mirarchi et al., *MD1878: Operation with Primary Collimators at Tighter Settings*, CERN-ACC-NOTE-2017-0014 (2017)

91. A. Burov, Phys. Rev. Accel. Beams **17**, 021007 (2014)

92. N. Mounet, DELPHI: an analytic Vlasov solver for impedance-driven modes, Talk presented at *HSC Meeting, CERN, 09 April 2014* (2014), https://espace.cern.ch/be-dep-workspace/abp/HSC/Meetings/DELPHI-expanded.pdf

93. J.S. Berg, R.D. Ruth, Phys. Rev. E **52**, 2179 (1995)

94. S. Antipov et al., HE-LHC instability growth rates, in *HE-LHC Design Review, CERN, 11 December 2017 Meeting 08, CERN, 11–12 December 2017* (2017)

95. C. Tambasco, Beam-beam effects, in *HE-LHC Design Review, CERN, 11–12 December* (2017)

96. Y. Alexahin, A. Burov, V. Shiltsev, A. Valishev, Phys. Rev. Lett. **119**, 134802 (2016)

97. O.S. Brüning et al. (eds.), *LHC Design Report v.1: The LHC Main Ring*, CERN-2004-003-V1 (2004)

98. C. Garion, FCC-hh beam screen studies and beam screen cooling scenarios, in *FCC Week 2016, Rome* (2016)

99. I. Bellafont, Studies on the beam induced effects in the FCC-hh, in *EuroCirCol Meeting, CERN, October 2017* (2017)

100. P. Dijkstal et al., Simulation studies on the electron cloud build-up in the elements of the LHC Arcs at 6.5 TeV, CERN-ACC-NOTE-2017-0057 (2017)

101. G. Dugan, D. Sagan, Synrad3D photon propagation and scattering simulations, in *Proceedings of the Joint INFN-CERN-EuCARD-AccNet Workshop on Electron-Cloud Effects, La Biodola, Isola d'Elba, Italy* CERN-2013-002 (June 5–9, 2012), pp. 117–129

102. K. Ohmi, E. Perevedentsev, F. Zimmermann, Phys. Rev. E **65**, 016502 (2001)

103. K. Ohmi, Electron cloud thresholds in HE-LHC, in *HE-LHC Design Meeting 08, CERN, December 2016* (2016)

104. T. Pieloni et al., Colliding high brightness beams in the LHC, in *MOP250, Proceedings of HB Beijing, China* (2012), https://accelconf.web.cern.ch/accelconf/HB2012/papers/mop250.pdf

105. X. Buffat et al., Probing the Behaviour of High Brightness Bunches in Collision at 6.5 TeV and the Interplay with an External Source of Noise (MD1433) (2017), https://cds.cern.ch/record/2261037, CERN-ACC-NOTE-2017-0030

106. S. Furuseth, Head-on beam-beam interactions in high-energy Hadron colliders. GPU-powered modelling of nonlinear effects, Master thesis, https://cds.cern.ch/record/2299580, CERN-THESIS-2017-279 (2017)

107. A. Niemi, A. Apollonio, J. Gutleber, P. Sollander, J.P. Penttinen, S. Virtanen, Phys. Rev. Accel. Beams **19**, 121003 (December, 2016)

108. J. Gutleber, A. Niemi, J.P. Penttinen, *An Open Modelling Approach for Availability and Reliability of Systems – OpenMARS*, CERN-ACC-2018-0006 (CERN, Geneva, Switzerland, January, 2018), Preprint CERN-ACC-2018-0006, https://cds.cern.ch/record/2302387

109. J.-P. Penttinen, A. Niemi, J. Gutleber, K.T. Koskinen, E. Coatanéa, J. Laitinen, Reliab. Eng. Syst. Saf. **183**, 387 (2019)

110. J.M. Jowett, Nuclear beams in HE-LHC, in *FCC Week 2018, Amsterdam, The Netherlands* (2018), https://indico.cern.ch/event/656491/contributions/2923429/

111. O.S. Brüning et al., *Future Circular Collider Study FCC-eh Baseline Parameters*, CERN FCC-ACC-RPT-012, 6 April 2017 (2017)

112. LHeC Study Group Collaboration, J.L. Abelleira Fernandez et al., J. Phys. **G39**, 075001 (2012)

113. S.A. Bogacz et al., *SAPPHiRE: a small gamma-gamma Higgs factory* (2012), arXiv:1208.2827 [physics.acc-ph]

114. O.S. Brüning, M. Klein, F. Zimmermann, The LHeC as a Higgs Boson factory in *Proceedings of the IPAC'13, Shanghai, China* (2013), pp. 1017–1019

115. H. Aksakal, Z. Nergiz, F. Zimmermann, *A High-Brilliance Angstrom-FEL Based on the LHeC* (July, 2018), http://cds.cern.ch/record/2639702, CERN-ACC-NOTE-2018-0061, ARIES 18-001

116. I. Papaphilippou et al., *Conceptual Design of the FCC-ee Injector*, FCC-ee Conceptual Design Report (2018)

117. O. Brüning, M. Klein, F. Zimmermann, The LHeC as a Higgs Boson factory in *Proceedings of the 4th IPAC'13, Shanghai, China* (May 12–17, 2013), p. MOPWO054, http://JACoW.org/IPAC2013/papers/mopwo054.pdf, CITATION = INSPIRE-1338636

118. O.S. Brüning, M. Klein, Mod. Phys. Lett. **A28**, 1330011 (2013)

119. D. Schulte et al., FCC-he parameters, Talk presented at the *FCC Workshop, Rome* (2016)
120. F. Zimmermann, FCC accelerator parameters, Talk presented at the *FCC Physics Week, Geneva, CERN* (2017)
121. PERLE Collaboration, G. Arduini et al., J. Phys. G: Nucl. Part. Phys. **45**, 065003 (2018)
122. A. Dainese et al., Heavy ions at the Future Circular Collider, arXiv:1605.01389 [hep-ph]
123. R. Valente et al., Baseline design of a 16 T costheta bending dipole for the Future Circular Collider, Presented at the *ASC, Seattle, USA* (2018)
124. R. Wolf, Field error naming conventions for the LHC, LHC-M-ES-0001, EDMS90250 (2001), Engineering Specification
125. S. Bermudez, Persistent currents magnetization effects in the 16 T main dipoles for the Future Circular Collider, CERN EDMS 2036614 (2018)
126. T. Salmi et al., Quench protection of the 16 T Nb$_3$Sn dipole magnets designed for the Future Circular Collider, in *Presented at the ASC, Seattle, USA* (2018)
127. C. Pes et al., Magnetic and mechanical design of the block-coil dipole option for the Future Circular Collider, Presented at the *ASC, Seattle, USA* (2018)
128. F. Toral, *Magnetic and mechanical design of a 16 T common coil dipole for FCC*, FCC Week, 2018, https://indico.cern.ch/event/656491/contributions/2920132/attachments/1629665/2597178/FCCweek2018_common_coil_ftoral.pdf
129. B. Auchmann et al., IEEE Trans. Appl. SC **28**, 3 (April, 2018)
130. A. Ballarino et al., The CERN FCC conductor development program: a world-wide effort for the future generation of high-field magnets, Submitted to IEEE Trans. Appl. Supercond., forthcoming on IEEE XPlore
131. L. Tavian, *Cryogenics*, FCC Collider Kickoff Meeting, Univ. Geneva, Switzerland (2014), https://indico.cern.ch/event/282344/contributions/1630775/
132. O. Boine-Frankenheim, FCC-hh Impedances, in *FCC Week, Rome, Italy* (2016), https://indico.cern.ch/event/438866/contributions/1085013/
133. R. Kersevan, Synchrotron radiation & vacuum concepts, in *FCC Collider Kickoff Meeting, Univ. Geneva, Switzerland* (2014), https://indico.cern.ch/event/282344/contributions/1630665/
134. O. Malyshev et al., Laser treatment at STFC, in *FCC-hh impedance and beam screen Workshop* (March, 2017), https://indico.cern.ch/event/619380/contributions/2527422/
135. L.A.G. Gomez, Results on the FCC-hh beam screen prototype at the KIT electron storage ring, in *FCC Week, Amsterdam, The Netherlands* (April, 2018), https://indico.cern.ch/event/656491/contributions/2938816/
136. O.S. Brüning et al., *LHC Design Report*, CERN Yellow Reports: Monographs (CERN, Geneva, Switzerland, 2004), http://cds.cern.ch/record/782076
137. C. Garion, FCC-hh Beam screen studies and beam screen cooling scenarios, *FCC Week, Rome, Italy* (2016), https://indico.cern.ch/event/438866/contributions/1084911/
138. S. Calatroni, IEEE Trans. Appl. Supercond. **26**, 1 (April, 2016)
139. V. Baglin, Cryogenic beam vacuum specificities applicable to FCC hh, in *FCC Week, Washington, DC* (2015), https://indico.cern.ch/event/340703/contributions/802149/
140. J.F. Topham, FCC-hh beam screen design, *WP4 EuroCirCol Coordination Meeting 05, ALBA Light Source* (November 7–9, 2016), https://indico.cern.ch/event/579868/
141. C. Kotnig, Cold mass cooling with supercritical helium, in *2nd FCC Cryogenics Day, Dresden, Germany* (2016)
142. I. Bellafont, Photon tracing and gas-density profile in the FCC-hh, in *FCC Week, Berlin, Germany* (2017), https://indico.cern.ch/event/556692/contributions/2487660/

143. L. Mether, CERN-EPFL, personal communication, and FCC-hh electron cloud, in *FCC Week, Berlin, Germany* (2017), https://indico.cern.ch/event/556692/contributions/2567985/

144. S. Aull, O. Brunner, A. Butterworth, N. Schwerg, *Material Options for the Superconducting RF System of the Future Circular Collider* CERN-ACC-2018-0019 (CERN, Geneva, Switzerland, 2018), Preprint CERN-ACC-2018-0019, http://cds.cern.ch/record/2625126

145. E. Palmieri, C. Pira, Coating studies on 6 GHz seamless cavities, in *Fourth Annual Meeting of the Future Circular Collider Study, Amsterdam, The Netherlands* (2018)

146. W.V. Delsolaro, *Thin film research: CERN experience and possible future applications* (TESLA Technology Collaboration (TTC) Meeting, Milano, Italy, 2018), https://agenda.infn.it/contributionDisplay.py?sessionId=12&contribId=4&confId=13791

147. D.L. Hall, S. Posen, Supercond. Sci. Technol. **30**, 033004 (2017)

148. K. Ilyina-Brunner, Magnetron sputtering of Nb_3Sn thin films on copper for SRF application, in *Fourth Annual Meeting of the Future Circular Collider study, Amsterdam, The Netherlands* (2018), https://indico.cern.ch/event/656491/contributions/2918336/attachments/1628654/2595685/Ilyina_Nb3Sn_FCC2018.pdf

149. G. Apollinari et al., High-luminosity large Hadron collider (HL-LHC), in *Preliminary Design Report. CERN Yellow Report* (2015)

150. K. Papke, A. Carvalho, C. Zanoni, A. Grudiev, Multiphysics simulations of the wide opened waveguide crab-cavity, in *Proceedings of the SRF'17, Lanzhou, China* (2017)

151. J.R. Delayen, S.U. De Silva, Phys. Rev. ST Accel. Beams **16**, 012004 (2013)

152. I. Syratchev, Introduction to HEIKA. Tentative structure and objectives, in *CLIC Workshop 2015, CERN, Geneva, Switzerland* (CERN, 2015), https://indico.cern.ch/event/336335/contributions/789041/

153. C. Marrelli, I. Syratchev, A. Yu, IEEE Trans. Electron Devices **62**, 3406 (2015)

154. I.A. Guzilov, BAC method of increasing the efficiency in Klystrons, in *IEEE Vacuum Electron Sources Conference 2014, St. Petersburg, Russia* (2014)

155. G. Burt et al., Particle-in-cell simulation of a core stabilization method klystron, in *IEEE International Vacuum Electronics Conference, IVEC 2017, London, UK* (2017)

156. I. Syratchev, High efficiency klystron technology, in *Third Annual Meeting of the Future Circular Collider Study, Berlin, Germany, 2017* (CERN, 2017), https://indico.cern.ch/event/556692/timetable/#20170530.detailed

157. P. Baudrenghien, T. Mastoridis, Phys. Rev. Accel. Beams **20**, 011004 (2017)

158. P. Baudrenghien, R. Calaga, E. Shaposhnikova, H. Timko, The main RF system and its implications for HL-LHC, in *7th HL-LHC Collaboration Meeting* (CIEMAT, Madrid, Spain, 2017), https://indico.cern.ch/event/647714/contributions/2646158/attachments/1556707/2453084/HL-LHC_2017_Timko.pdf

159. D. Barna, Phys. Rev. Accel. Beams **20**, 041002 (April, 2017)

160. A. Apyan, B. Goddard, K. Oide, F. Zimmermann, Advanced beam dump for FCC-ee, in *Proceedings of the IPAC'17, Copenhagen, Denmark* (2017) no. CERN-ACC-2017-294 WEPIK001, http://cds.cern.ch/record/2287345

161. O.R. Jones, First years experience of LHC beam instrumentation, in *Proceedings of the IPAC'11, San Sebastian, Spain* (2011)

162. *CERN EDMS Specification*, https://edms.cern.ch/document/327557, LHC-BPM-ES-0004

163. M. Barros Marin et al., JINST **11**, C02062 (2016)

164. B. Dehning et al., The LHC beam loss measurement system, in *2007 IEEE Particle Accelerator Conference (PAC)* (June, 2007), pp. 4192–4194

165. M. Fernández et al., Optimized cryogenic current comparator for CERN's low-energy antiproton facilities, in *Proceedings of the IBIC'16, Barcelona, Spain* (2016)

166. D. Belohrad et al., Upgrade of the LHC bunch by bunch intensity measurement acquisition system, in *Proceedings of the IBIC'16, Barcelona, Spain* (2016)

167. G. Trad et al., Performance of the upgraded synchrotron radiation diagnostics at the LHC, in *Proceedings of the IPAC'16, Busan, Korea* (2016)

168. H. Zhang et al., A supersonic gas-jet based beam induced fluorescence prototype monitor for transverse profile determination, in *Proceedings of the IPAC'17, Copenhagen, Denmark* (2017)

169. S. Vlachos et al., The LHC beam gas vertex detector – a non-invasive profile monitor for high energy machines, in *Proceedings of the IBIC'17, Grand Rapids, Michigan, USA* (August, 2017)

170. D. Missiaen, J.P. Quesnel, R.J. Steinhagen, The alignment of the LHC, in *Proceedings of the PAC'09 Vancouver, Canada* (2009)

171. Y. Nie, R. Schmidt, V. Chetvertkova, G. Rosell-Tarragó, F. Burkart, D. Wollmann, Phys. Rev. Accel. Beams **20**, 081001 (2017)

172. M. Werner, K. Wittenburg, *Very fast beam losses at HERA, and what has been done about it*, Technical report, DESY (2006)

173. Q. Bai et al., J. Instrum. **13**, T04004 (2018)

174. T. Wilksen et al., *The control system for the linear accelerator at the European XFEL: status and first experiences*, in *Proceedings of the 16th ICALEPCS'17, Barcelona, Spain, October 8–13, 2017* (2018), p. MOAPL01, http://inspirehep.net/record/1656098/files/moapl01.pdf

175. R. Ganter et al., *SwissFEL Conceptual Design Report*, PSI Bericht 10–14, (Paul Scherrer Institut, July, 2010), https://www.psi.ch/swissfel/SwissFELCDREN/SwissFEL_CDR_web_small.pdf

176. R. Huhmann et al., The FAIR control system – system architecture and first implementations, in *Proceedings of the ICALEPCS'13, San Francisco, CA, USA* (2013), p. MOPPC097, http://accelconf.web.cern.ch/AccelConf/ICALEPCS2013/papers/moppc097.pdf

177. M. Hankel, B. Rexroth, *The Reference Architectural Model Industrie 4.0 (RAMI 4.0)* Whitepaper Version 1.0 (ZVEI: Die Elektroindustrie, April, 2015), https://www.zvei.org/fileadmin/user_upload/Themen/Industrie_4.0/Das_Referenzarchitekturmodell_RAMI_4.0_und_die_Industrie_4.0-Komponente/pdf/ZVEI-Industrie-40-RAMI-40-English.pdf

178. E.P. Boven, White rabbit in radio astronomy, in *Proceedings of the ICALEPCS'17, Barcelona, Spain* (2017), p. TUCPL03, http://accelconf.web.cern.ch/AccelConf/icalepcs2017/

179. N. Moreira, J. Lázaro, U. Bidarte, J. Jimenez, A. Astarloa, IEEE Trans. Smart Grid **8**, 1932 (2017)

180. R. Excel, G. Gaderer, P. Loschmidt, Comput. Netw. Commun. **2012**, 1 (2012)

181. As-2d2 Deterministic Ethernet and Unified Networking, *Time-Triggered Ethernet* (Standard AS 6802, SAE International, September 11, 2016)

182. J. Allnut et al., Timing challenges in the smart grid, *Natl. Inst. Stand. Technol. Spec. Publ. 1500-08* (US Department of Commerce, January, 2017)

183. C. Sydlo et al., Femtosecond timing distribution at the European XFEL, in *Proceedings of the FEL'15, Daejeon, Korea* (2015), p. WEP047, http://accelconf.web.cern.ch/AccelConf/FEL2015/papers/wep047.pdf

184. A. Aghababyan et al., The large scale European XFEL control system: overview and status of the commissioning, in *Proceedings of the ICALEPCS'15, Melbourne, Australia* (2015), p. MOA3O02, http://tesla.desy.de/doocs/doocs_papers/ICALEPCS2015/moa3o02.pdf

185. A. Dinius, Q. King, B. Todd, S. Uznanski, J. Instrum. **7** (2012), C11012

186. F. Abdi et al., Application and system-level software fault tolerance through full system restarts, in *ACM/IEEE 8th International Conference on Cyber-Physical Systems (ICCPS), Pittsburgh, PA, USA* (April 18–21, 2017), pp. 6505–6519, https://ieeexplore.ieee.org/document/7945009/

187. W. Benjamin et al., An open architecture for embedded systems: hardware open systems technologies, in *IEEE SoutheastCon, Charlotte, NC, USA* (March 30–April 2, 2017), pp. 6505–6519

188. P. Bieth, V. Brindejonc, COTS-AEH – Use of complex COTS in airborne electronic hardware – failure mode and mitigation Research Project EASA.2012.C15 Report

EASA.2012/04 (European Aviation Safety Agency, 2013), `https://www.easa.europa.eu/sites/default/files/dfu/Final20Report20EASA202012-04.pdf`

189. National Instruments, *Considerations When Navigating Build or Buy Decisions for Industrial Embedded Control Projects*, White Paper 54072 (National Instruments, August 30, 2017), `http://www.ni.com/white-paper/54072/en/`

190. L. Yubin, L. Yucheng, High continuous availability digital information system based on stratus Fault-Tolerant server, in *2010 International Forum on Information Technology and Applications* (July, 2010), Vol. 2, pp. 184–187

191. B. Chen, J. Wan, L. Shu, P. Li, M. Mukherjee, B. Yin, IEEE Access **6**, 6505 (2017)

192. I. Dai, P. Oleniuk, B. Todd, A. Voto, J. Instrum. **11**, C01047 (2016)

193. IEEE, *Systems and Software Engineering – System Lifecycle Processes* Standard ISO 15288:2008, IEEE/ISO/IEC (2008), `https://en.wikipedia.org/wiki/ISO/IEC_15288`

194. K. Forsberg, H. Mooz, System engineering for faster, cheaper, better, in *INCOSE International Symposium Systems Engineering Past, Present and Future I, Brighton, England* (June 6–11, 1999), Vol. 9, pp. 924–932

195. European Commission, *Horizon 2020 Work Programme 2016–2017. 5.i. Information and Communication Technologies* European CommissionDecision C(2017)2468 (European Commission, April 24, 2017), `http://ec.europa.eu/research/participants/data/ref/h2020/wp/2016_2017/main/h2020-wp1617-leit-ict_en.pdf`

196. J. Gutleber et al., The MedAustron accelerator control system, in *Proceedings of the ICALEPCS'11, Grenoble, France* (October 10–14, 2011), pp. 9–12, `https://accelconf.web.cern.ch/accelconf/icalepcs2011/papers/mobaust03.pdf`

197. J. Gutleber and R. Moser, The MedAustron accelerator control system: design installation and commissioning, in *14th International Conference on Accelerator and Large Experimental Physics Control Systems, San Francisco, CA, USA* (March 6–11, 2013), p. TUCOAAB04, `https://cds.cern.ch/record/1697002`

198. Cosylab, *Accelerator Control System for PT*, Website (2018), `https://www.cosylab.com/accelerator-control-system-for-pt/`

199. D. Ondreka, U. Weinrich, The Heidelberg ion therapy (HIT) accelerator coming into operation, in *European Physical Society Accelerator Group, Proceedings of EPAC 2008, Genoa, Italy* (June 23–27, 2008), pp. 979–981, `https://accelconf.web.cern.ch/accelconf/e08/papers/tuocg01.pdf`

200. S. Rossi, *The status of CNAO*, S. Eur. Phys. J. Plus **126**, 78 (2011)

201. S. Giordanengo, M.A. Garella, F. Marchetto, F. Bourhaleb, M. Ciocca, A. Mirandola, V. Monaco, M.A. Hosseini, C. Peroni, R. Sacchi, R. Cirio, M. Donetti, Med. Phys. **42**, 263 (2016)

202. P. Bryant, L. Evans (eds.), J. Instrum. **3**, S08001 (2008)

203. B. Kihei, Automotive Doppler sensing: The Doppler profile with machine learning in vehicle-to-vehicle networks for road safety, in *18th IEEE International Workshop on Signal Processing Advances in Wireless Communications, Sapporo, Japan* (July 3–6, 2017)

204. ICFA, *Beam Dynamics Mini-Workshop: Machine Learning Applications for Particle Accelerators. SLAC National Accelerator Laboratory, Menlo Park, CA, USA.*, Indico presentation (27 February–2 March, 2018), `https://indico.fnal.gov/event/16327/other-view?view=standard`

205. R.G. Alia, M. Brugger, S. Danzeca, F. Cerutti, J.P. de Carvalho Saraiva, R. Denz, A. Ferrari, L.L. Foro, P. Peronnard, K. Røed, R. Secondo, Semicond. Sci. Technol. **32**, 034003

206. T.T. Böhlen, F. Cerutti, M.P.W. Chin, A. Fassò, A. Ferrari, P.G. Ortega, A. Mairani, P.R. Sala, G. Smirnov, V. Vlachoudis, Nucl. Data Sheets **120**, 211 (2014)

207. A. Fassò, A. Ferrari, J. Ranft, P.R. Sala, *FLUKA: a multi-particle transport code* Report CERN-2005-10, CERN, Geneva, Switzerland, 2005, Also available as INFN/TC_05/11 and SLAC-R-773

208. R.G. Alia, M. Brugger, F. Cerutti, S. Danzeca, A. Ferrari, S. Gilardoni, Y. Kadi, M. Kastriotou, A. Lechner, C. Martinella, O. Stein, IEEE Trans. Nucl. Sci. **65**, 448 (January, 2018)

209. M. Brugger et al., *Irradiation Facilities at CERN* (October, 2017), https://cds.cern.ch/record/2290629, AIDA-2020-CONF-2017-007

210. P. Carbonez, R. Macián-Juan, F. Pozzi, CERN Radiation Protection (RP) calibration facilities (July 1st, 2016), https://cds.cern.ch/record/2256137, CERN-THESIS-2015-394

211. M.R. Jäkel et al., CERN GIF++: a new irradiation facility to test large- area particle detectors for the high-luminosity LHC program, in *PoS (TIPP2014), 102, Proceedings of the TIPP'14, Amsterdam, The Netherlands* (2014), https://pos.sissa.it/213/102/pdf

212. G. Tsiligiannis, S. Danzeca, R. García Alía, A. Infantino, A. Lesea, M. Brugger, A. Masi, S. Gilardoni, F. Saigné, IEEE Trans. Nucl. Sci. **65**, 1511 (2018)

213. A. Baschirotto et al., GigaRad total ionizing dose and post-irradiation effects on 28 nm bulk MOSFETs, in *Proceedings 2016 IEEE Nuclear Science Symposium, Medical Imaging Conference and Room-Temperature Semiconductor Detector Workshop (NSS/MIC/RTSD)* (October, 2016), pp. 1–4

214. G. Gorine, G. Pezzullo, I. Mandic, A. Jazbec, L. Snoj, M. Capeans, M. Moll, D. Bouvet, F. Ravotti, J.-M. Sallese, IEEE Trans. Nucl. Sci. **65**, 1583 (January, 2018)

215. H. Rammer, *Two New Caverns for LHC Experiments: ATLAS and CMS* (CERN, Chamonix, February, 1998), https://cds.cern.ch/record/357157/files/st-98-005.pdf, 1st ST Workshop

216. C. Laughton, Int. J. Min. Geol. Eng. **6**, 353 (1988)

217. J.L. Baldy, *Commission Tunnel Jura* EDMS 2041211 (CERN, Geneva, Switzerland, June, 1999), Preprint design proposal for refurbishment, Report 2041211

218. J.L. Baldy, *Tunnel LEP Secteur Jura Etudes du renforcement local du revetement en beton* , EDMS 2041211, restricted access. (CERN, Geneva, Switzerland, June, 1999), Preprint Design proposal for refurbishment. Report not publicly accessible

219. P. Brockill et al., *A Novel Multichannel Interferometer System For Absolute Distance Measurements*, Large Volume Metrology Conference (2012)

220. D. Clark, IEEE Comput. Sci. Eng. **5**, 84 (1998)

221. I. Bird, L. Robertson, J. Shiers, Deploying the LHC computing grid – the LCG service challenges, in *2005 IEEE International Symposium on Mass Storage Systems and Technology* (June, 2005), pp. 160–165

222. J.C. Webber, The ALMA telescope, in *2013 IEEE MTT-S International Microwave Symposium Digest (MTT)* (June, 2013), pp. 1–3

223. D. Ding, D. Wu, F. Yu, An overview on cloud computing platform spark for Human Genome mining, in *2016 IEEE International Conference on Mechatronics and Automation* (August, 2016), pp. 2605–2610

224. G. Antchev, E. Cano, S. Chatelier, S. Cittolin, S. Erhan, D. Gigi, J. Gutleber, C. Jacobs, F. Meijers, L. Orsini, L. Pollet, A. Racz, D. Samyn, N. Sinanis, P. Sphicas, IEEE Trans. Nucl. Sci. **47**, 293 (2000)

225. K. Anikeev, G. Bauer, I. Furic, D. Holmgren, A. Korn, I. Kravchenko, M. Mulhearn, P. Ngan, C. Paus, A. Rakitin, R. Rechenmacher, Comput. Phys. Commun. **140**, 110 (2001)

226. DESY, *MicroTCA Technology Lab*, Website (2018), https://techlab.desy.de

227. CERN, *openlab*, Website (2018), https://openlab.cern

228. Sepura, *Case Study: Advancing Safety and Communications at CERN*, Website (January, 2014), https://www.sepura.com/media/166841/cern-case-study.pdf

229. Euro-IX, *Information on Carrier Neutrality*, Website (2018), https://www.euro-ix.net/en/forixps/set-ixp/ixp-models/neutrality

230. CERN, *Documents and Maps of the Worldwide LHC Computing Grid (WLCG)*, Website (2018), http://wlcg.web.cern.ch/documents-reference

231. H. Schopper, Riv. del Nuovo Cimento **40**, 199 (2017)

232. B. Panzer-Steindel, *IT Technology and Markets, Status and Evolution*, Indico presentation (March 26, 2018), https://indico.cern.ch/event/658060/contributions/2889027/attachments/1622791/2583013/tech_market_BPS_Mar2018_v9pptx.pdf

233. A. Di Meglio, M. Girone, A. Purcell, F. Rademakers, CERN openlab white paper on future ICT challenges in scientific research (January, 2018), http://cds.cern.ch/record/2301895

234. A. Bastianin, M. Florio, *Social Cost Benefit Analysis of HL-LHC*, CERN-ACC-2018-0014 (CERN, Geneva, Switzerland, May, 2018), Preprint CERN-ACC-2018-0014, https://cds.cern.ch/record/2319300

235. S. Schmeling, IEEE Trans. Nucl. Sci. **53**, 970 (2006)

236. D. Collaboration, *Data Preservation in High Energy Physics (DPHEP)*, Website (2018), https://hep-project-dphep-portal.web.cern.ch

237. F. Berghaus et al., *CERN Services for Long Term Data Preservation*, CERN-IT-Note-2016-004 (CERN, Geneva, Switzerland, July, 2016), Preprint CERN-IT-Note-2016-004, https://cds.cern.ch/record/2195937

238. G. de Rijk (Chair), *Workshop on a Low Energy Ring in the LHC tunnel as Main Injector*, http://ler06.web.cern.ch/LER06

239. W. Bartmann et al., Conceptual design considerations for a 1.3 TeV superconducting SPS (scSPS), in *Proceedings of the 8th IPAC'17, Copenhagen, Denmark* (May 14–19, 2017), p. WEPVA033, http://inspirehep.net/record/1626398/files/wepva033.pdf

240. B. Goddard et al., CERN Yellow Rep.: Monographs **3**, 693 (2017)

241. A.D. Kovalenko, W. Scandale, A.M. Taratin, Nucl. Instrum. Methods Phys. Res. Sect. B: Beam Interact. Mater. Atoms **355**, 390 (2015)

242. I. Efthymiopoulos et al., *HiRadMat: A New Irradiation Facility for Material Testing at CERN* (November, 2011), http://cds.cern.ch/record/1403043, CERN-ATS-2011-232

243. H. Brooks, P.Z. Skands, P. Eur. Phys. J. C **78**, 963 (2018)

244. J. Alwall, R. Frederix, S. Frixione, V. Hirschi, F. Maltoni, O. Mattelaer, H.-S. Shao, T. Stelzer, P. Torrielli, M. Zaro, JHEP **07**, 079 (2014)

245. M.L. Mangano, *Physics at the FCC-hh, a 100 TeV pp Collider*, CERN Yellow Reports: Monographs (CERN, Geneva, Switzerland, 2017), https://cds.cern.ch/record/2270978

246. Gouvernement de la République française and CERN, *Accord entre le Gouvernement de la République française et l'Organisation Européenne pour la Recherche Nucléaire relatif au statut juridique de ladite Organisation en France*, CERN institutional documents (CERN, Geneva, Switzerland, August, 1973), https://cds.cern.ch/record/436804/files/CM-B00042459.pdf

247. U. Forsblom-Pärli et al., *Connaissez-vous le potentiel des phénomènes dangereux dans votre entreprise?* instruction, système selon commission fédérale de coordination pour la sécurité au travail, SUVA – Protection de la santé (June, 2011), Preprint 66105.1, https://www.suva.ch/materiel/documentation/connaissez-vous-le-potentiel-des-phenomenes-dangereux-dans-votre-entreprise--le--66105.f-25527-25526

248. S.L. Mendola, *FCC Performance-based Safety Design – A Proposal for a Methodology Founded on the SFPE Guideline*, Internal presentation (CERN, June, 2017), Preprint EDMS 1770088, https://edms.cern.ch/document/1770088

249. International Electrotechnical Commission, *IEC 60812:2018 – Failure Modes and Effects Analysis (FMEA and FMECA)*, International Standard (IEC, Geneva, Switzerland, August 10, 2018), https://cds.cern.ch/record/436804/files/CM-B00042459.pdf

250. O. Rios, A. Arnalich, *Quantitative Assessment of Fire Hazard for FCC-hh (and FCC-ee)*, Internal Report (CERN, June, 2018), Preprint EDMS 1975602, https://edms.cern.ch/document/1975602

251. A. Henriques, Private Communication (CERN, Geneva, Switzerland, April, 2018)

252. O.R. Rubiras, A. Arnalich, *HE-LHC Fire Safety Preliminary Analysis: Executive Summary* EDMS 1975608 (CERN, Geneva, Switzerland, 2018), Preprint FCC-INF-RPT-0056 v.1, https://edms.cern.ch/document/1975608/

253. O.R. Rubiras, A. Arnalich, *FCC-hh Fire Safety Analysis: Executive Summary*, EDMS 1982356 (CERN, Geneva, Switzerland, 2018), Preprint FCC-INF-RPT-0060 v.1, https://edms.cern.ch/document/1982356/

254. K. McGrattan et al., *Fire Dynamics Simulator User's Guide*, Special publication (National Institute of Standards and Technology, June, 2018), Preprint 1019, https://pages.nist.gov/fds-smv/;https://github.com/firemodels/fds/releases/download/FDS6.7.0/FDS_User_Guide.pdf

255. British Standards Institute, The application of fire safety engineering principles to fire safety design of buildings: part 6: Human factors: Life safety strategies: occupant evacuation, behaviour and condition (sub-system 6) (British Standards Institute, London, 2004), PD 7974-6

256. T. Otto, *Release of Gaseous Helium in Tunnels* EDMS 1853419 (CERN, Geneva, Switzerland, October, 2017), Preprint EDMS 1853419, https://edms.cern.ch/document/1853419

257. La République française, *Article L1333-1 to L1333-25*, Code de la santé publique (2018), https://www.legifrance.gouv.fr/telecharger_pdf.do?cidTexte=LEGITEXT000006072665

258. L'Assemblée fédérale de la Confédération suisse, *Loi sur la radioprotection (LRaP)*, Recueil officiel du droit fédéral (RO) (2017), https://www.admin.ch/opc/fr/classified-compilation/19910045/index.html

259. L. Bruno, M. Magistris, *Radioactive Waste Management at CERN, Technical Note*, EDMS 1453489 (2017)

260. *Energy for Sustainable Science at Research Infrastructures*, 4th Workshop in Măgurele, Bucharest, Romania (November 23–24, 2017)

261. *EuCard2 (Enhanced European Coordination for Accelerator Research and Development)*, Website, http://eucard2.web.cern.ch/

262. *EuCard2 Work Package 3*, Website, https://www.psi.ch/enefficient/

263. *ARIES (Accelerator Research and Innovation for European Science and Society)*, Website, https://aries.web.cern.ch/

264. M. Seidel, *Energy Efficiency of Accelerators in the European Programs Eucard2 and ARIES*, https://indico.eli-np.ro/event/1/contributions/6/attachments/70/106/4_enefficient_seidel.pdf

265. A. Grosjean, *Tout un quartier chauffé grâce au CERN*, Tribune de Genève (2018), https://www.tdg.ch/geneve/actu-genevoise/Tout-un-quartier-chauffe-grce-au-CERN/story/28974479

266. K. Biesheuvel, R. de Boer, S. Smeding, Waste Heat recovery in industrial batch processes: analysis of combines heat storage and heat pump application, in *Proceedings of the 12th IEA Heat Pump Conference*, no. 12 in HPC (IEA, Rotterdam, The Netherlands, June, 2017), http://hpc2017.org/wp-content/uploads/2017/05/O.3.8.1-Waste-Heat-recovery-in-industrial-batch-processes-analysis-of-combined-heat-storage.pdf

267. F. Campana, M. Bianchi, L. Branchini, A. De Pascale, A. Peretto, M. Baresi, A. Fermi, N. Rossetti, R. Vescovo, Energ. Convers. Manage. **76**, 244 (2013)

268. P. Colonna, E. Casati, C. Trapp, T. Mathijssen, J. Larjola, T. Turunen-Saaresti, A. Uusitalo, J. Eng. Gas Turbines Power **137**, 100801 (2015)

269. *Accord entre le Gouvernement de la République française et l'Organisation européenne pour la Recherche nucléaire relatif au statut juridique de ladite Organisation en France* (CERN, Geneva, Switzerland, 1973), https://cds.cern.ch/record/436804

270. *Convention entre le Conseil fédéral de la Confédération suisse et le Gouvernement de la République française relative à l'extension en territoire français du domaine de l'Organisation européenne pour la recherche nucléaire*, Le Conseil fédéral (Chancellerie fédérale, Palais fédéral ouest, 3003 Berne, Switzerland, September 13, 1965), https://www.admin.ch/opc/fr/classified-compilation/19650161

271. A. Poiron, M. Zahnd, *FCC Layout Review in Switzerland* deliverable report contract ca 3797383, (Ecotec, December, 2017), *Preprint* EDMS 1838912, `https://edms.cern.ch/document/1838912`

272. Le Conseil fédéral suisse, *Ordonnance relative à l'étude de l'impact sur l'environnement 814.011 (UVPV)*, Recueil officiel du droit fédéral (RO) (2016), `https://www.admin.ch/opc/fr/classified-compilation/19880226/index.html`

273. Office fédéral de l'environnement OFEV, *Directive de la Confédération sur l'étude de l'impact sur l'environnement (Manuel EIE)*, Serie L'environnement pratique (2009), `https://www.bafu.admin.ch/bafu/fr/home/themes/eie/publications/manuel-eie.html`

274. Le Président de la République, *Code de l'environnement*, Journal officiel de la République française (2018), `https://www.legifrance.gouv.fr/affichCode.do?cidTexte=LEGITEXT000006074220&dateTexte=20180924`

275. UNECE, *Convention on environmental impact assessment in a transboundary context* Convention ECE/MP.EIA/21/Amend.1 (United Nations, Avenue de la Paix 8, 1202 Genève, Suisse, October, 2017), `http://www.unece.org/env/eia/about/eia_text.html`

276. Office Fédéral de la santé publique, *Radioactivité de l'environnement et doses de rayonnements en Suisse, Rapport 2017*, Project Website (2018), `http://www.bag.admin.ch/ura-jb`

277. R. Rata, M. Widorski, *Radiological studies for the FCC-hh arc sections*, EDMS 1905211 (2018)

278. R. Rata, M. Widorski, *Radiological studies for the FCC-hh collimation regions*, EDMS 1975526 (2018)

279. R. Rata, M. Widorski, *Radiological studies for the FCC-hh experimental caverns*, EDMS 1976620 (2018)

280. A. Bibet-Chevalier, D. Chanal, *Étude de sensibilité du scenario d'implantation du project FCC en France et de ses opportunités* Rapport d'étude du Cerema FCC-INF-RPT-040 and EDMS 1853668, CEREMA (April 26, 2018), `https://edms.cern.ch/document/1853668`

281. Le Conseil fédéral suisse, *Ordonnance sur l'aménagement du territoire (OAT) 700.1*, Recueil officiel du droit fédéral (RO) (2016), `https://www.admin.ch/opc/fr/classified-compilation/national.html`

282. *GeniLac*, Website, `http://www.citedelenergie.ch/fileadmin/user_upload/Energiestadt/de/Dateien/Instrumente/6_Kommunikation/6_5_2_GeniLa.pdf`

283. M. Magistris, H. Vincke, M. Widorski, *Radioactive Waste Estimates for the FCC project* EDMS 1992036 (CERN, Geneva, Switzerland, 2018), Preprint EDMS 1992036, `https://cds.cern.ch/record/1992036`

284. Départment du Rhône-Métropole de Lyon, *Plan de prévention et de gestion des déchets non dangereux du Rhône et de la Métropole de Lyon* version définitive, Départment du Rhône-Métropole de Lyon (June, 2015), `http://www.sindra.org/wp-content/uploads/2017/01/Plan-dC3A9chets-non-dangereux-RhC3B4ne-MC3A9tropole-de-Lyon.pdf`

285. Le Président de la République, *Loi n. 2015-992 du 17 août 2015 relative à la transition énergétique pour la croissance verte*, J. Officiel République Fr. **14263** (2018) `https://www.legifrance.gouv.fr/affichTexte.do?cidTexte=JORFTEXT000031044385`

286. République et Canton de Genève, *Genève – Plan directeur cantonal 2030* permière mise à jour, Direction de la planification directrice cantonale et régionale, service du plan directeur cantonal (February, 2017), `https://www.ge.ch/consulter-plans-amenagement-adoptes/plan-directeur-cantonal`

287. P. Joxe, J. Officiel République Fr. **33**, 2064 (2018)

288. Le Président de la République, J. Officiel République Fr. **75**, 5568 (2003)

289. UNECE, Treaty Ser. **2161**, 447 (1998)

290. CEREMA, *Rapport d'études sur les impacts pour l'État en matière de procédures et d'engagements financiers* report, Secrétariat Gégnéral pour les Affaires Régionales

d'Auvergne-Rhône-Alpes (April, 2018), This report is for government-internal purposes only

291. Le Président de la République, J. Officiel République Fr. **248** (2002), https://www.legifrance.gouv.fr/affichTexte.do?cidTexte=JORFTEXT 000000232649&categorieLien=id

292. Le Président de la République, J. Officiel République Fr. **0181** (2016) https://www.legifrance.gouv.fr/affichTexte.do?cidTexte=JORFTEXT 000032966723&categorieLien=id

293. Commission nationale du débat public, *Comment ça marche ?* site internet de l'institution, (Commission nationale du débat public, 244 boulevard Saint-Germain 75007 Paris France, October, 2002), https://www.debatpublic.fr/comment-ca-marche

294. Journal officiel de la République française (JORF), J. Officiel République Fr. 0261 (2014), https://www.legifrance.gouv.fr/affichTexte.do;jsessionid= 62A9EC171A12674F234586C187CE51F1.tplgfr24s_3?cidTexte=JORFTEXT 000029730657&dateTexte=20141111

295. Direction de l'ARE, *Surfaces d'assolement selon le plan sectoriel SA* Modèle de géodonnées minimal. Documentation sur le modèle. 68, Office fédéral du développement territorial ARE, Worblenstrasse 66, CH-3063 Ittingen, Schweiz (November, 2015), https://www.are.admin.ch/are/fr/home/ developpement-et-amenagement-du-territoire/strategie-et-planification/ conceptions-et-plans-sectoriels/plans-sectoriels-de-la-confederation/ sda.html

296. Conseil d'Etat de la République et canton de Genève, *Surfaces d'assolement selon le plan sectoriel SA* Législation K 1 70.13, État de Genève, 2, rue Henri-Fazy, case postale 3964, 1211 Genève 3, (January, 2008), https://www.ge.ch/legislation/rsg/ f/s/rsg_k1_70p13.html

297. G. Catalano et al., *Guide to Cost-Beneft Analysis of Investment Projects* (Regional and Urban Policy, European Union, December, 2014), pp. 321–333, ISBN 978-92-79-34796-2

298. *Questionnaire for submission of proposals for roadmap 2018*, Website (September, 2016), https://ec.europa.eu/research/infrastructures/pdf/esfri/esfri_ roadmap/esfri_rd2018_questionnaire.pdf

299. *RI impact pathways H2020 INFRASUPP project 777563, January 2018 to June 2020*, Website (September, 2018), https://cordis.europa.eu/project/rcn/212964_ en.html

300. M. Florio, E. Sirtori, Technol. Forecast. Soc. Change **112**, 65 (2016)

301. M. Florio, S. Forte, E. Sirtori, *Forecasting the Socio-Economic Impact of the Large Hadron Collider: a Cost-Benefit Analysis to 2025 and Beyond* report, Università di Milano, Milano, Italy, Dipartimento di Economia, Management e Metodi Quantitativi, Universitaà di Milano , via Conservatorio 7, I-20122 Milano, Italy (March, 2016), arXiv:1603.00886 [physics.soc-ph]

302. M. Florio et al., *Exploring Cost-Benefit Analysis of Research, Development and Innovation Infrastructures: An Evaluation Framework* working paper 01/2016, CSIL Centre for Industrial Studies, Corso Monforte, 15, 20122 Milano MI, Italy (March, 2016), arXiv:1603.03654 [physics.soc-ph]

303. *United Nations Statistical Commission, System of National Accounts 2008*, Website (2008), https://unstats.un.org/unsd/nationalaccount/sna2008.asp

304. P. Johansson, B. Kriström, *Cost-Benefit Analysis for Project Appraisal* (Cambridge University Press, October, 2015), ISBN 9781107548220

305. P. Herson, L. McNeil, Phys. Today **70**, 39 (2017)

306. T. Camporesi, G. Catalano, M. Florio, F. Giffoni, Eur. J. Phys. **38**, 025703 (2017)

307. G. Catalano, M. Florio, V. Morretta, T. Portaluri, *The Value of Human Capital Formation at CERN*, CERN-ACC-2018-0025 (CERN, Geneva, Switzerland, August 22, 2018), Preprint CERN-ACC-2018-0025, https://cds.cern.ch/record/2635864

308. Economisti Associati, *Marie Curie researchers and their long-term career development: A comparative study* final report (European Union, Publications Office of the European Union, March, 2014), http://ec.europa.eu/research/fp7/pdf/mca/marie_curie_researchers_and_their_long-term_career_development.pdf

309. A. Bibet-Chevalier and D. Chanal, *Étude des impacts pour l'État du projet de future collosionneur circulaire du CERN en matière de procédures et d'engagements financiers* Rapport d'étude du Cerema pour le SGAR Auvergne-Rhône-Alpes EDMS 1959547 V1.0, CEREMA (March, 2018), https://edms.cern.ch/document/1959547/1.0, Access to the report is subject to an NDA

310. *European Advances Superconductor Innovation and Training Network*, Website http://easitrain.web.cern.ch

311. CEBR, *The importance of physics to the economics of Europe* executive summary report of the centre for economics and business research, European Physical Society, 68200 Mulhouse, France (January, 2013), http://www.eps.org/?page=policy_economy

312. M. Bianchi-Streit et al., *Economic Utility Resulting From CERN Contracts (Second Study)*, CERN Yellow Reports: Monographs (CERN, Geneva, Switzerland, 1984), https://cds.cern.ch/record/156911

313. P. Castelnovo, M. Florio, S. Forte, L. Rossi, E. Sirtori, Res. Policy **47**, 1853 (2018)

314. M. Florio, F. Giffoni, A. Giunta, E. Sirtori, Ind. Corporate Change **27**, 915 (2018)

315. A. Bastianin, M. Florio, *Industrial Spillovers from the LHC/HL-LHC Programme at CERN*, CERN-ACC-2018-0026 (CERN, Geneva, Switzerland, August 23, 2018), Preprint CERN-ACC-2018-0026, https://cds.cern.ch/record/2635876

316. P. Seidel, Applied superconductivity: handbook on devices and applications, in *The Art of Computer Programming* (Wiley, February, 2015), p. 1238, ISBN 978-3-527-41209-9

317. P. Lebrun, Mater. Sci. Eng. **171**, 012001 (2017)

318. E. Autio, M. Bianchi-Streit, A.P. Hameri, *Technology Transfer and Technological Learning Through CERN's Procurement Activity*, CERN Yellow Reports: Monographs (CERN, Geneva, Switzerland, 2003), https://cds.cern.ch/record/680242

319. *Sept projets innovants pour les déblais du Grand Paris*, Website (2017), https://www.usinenouvelle.com/article/sept-projets-innovants-pour-les-deblais-du-grand-paris.N520469

320. T.B. Lee, M. Fischetti, *Weaving the Web: The Original Design and Ultimate Destiny of the World Wide Web by Its Inventor.* Harper Business, 1 ed., (November, 2000), ISBN 978-0062515872

321. L. Mascetti, H. Gonzalez Labrador, M. Lamanna, J.T. Moscicki, A.J. Peters, J. Phys.: Conf. Ser. **644**, 062037 (2015)

322. A. Alberini, A. Longo, J. Cult. Econ. **30**, 287 (2006)

323. R.C. Bishop, N.W. Bouwes, P.P. Caulkins, Am. J. Agric. Econ. **68**, 291 (1986)

324. J.P. Poor, J.M. Smith, J. Cult. Econ. **28**, 217 (2004)

325. M. Florio, S. Forte, E. Sirtori, Technol. Forecast. Soc. Change **112**, 38 (2016)

326. C. Risen, J. Am. Inst. Archit. (2018), https://www.architectmagazine.com/awards/studio-prize/studio-prize-the-new-grand-tour-a-new-visitors-center-for-cern_o

327. G. Catalano, I.C. Garido, *Cultural Effects at CERN*, CERN-ACC-2018-0048 (CERN, Geneva, Switzerland, November, 2018), https://cds.cern.ch/record/2649022

328. R.D. Cabana, J.E. Petro, *Kennedy Space Center. Future Development Concept*, KSC Center Master Plan 2012–2031 (NASA, John F. Kennedy Space Center, FL 32899, USA, 2012), https://www.nasa.gov/centers/kennedy/pdf/634026main_future-concept.pdf

329. A.J. Barr, A. Haas, C. Kalderon, *"That looks weird" = evaluating citizen scientists' ability to detect unusual features in ATLAS images of collisions at the Large Hadron Collider*, Report (University of Oxford, UK and New York University, USA and University of Lund, Sweden, 2017), arXiv:1610.02214 [physics.soc-ph], https://arxiv.org/pdf/1610.02214.pdf

330. *The Zooniverse project: publications*, Website https://www.zooniverse.org/about/publications

331. *EXTREME – alla ricerca delle particelle. Museo Nazionale Scienza e Tecnologia Leonardo Da Vinci, Milano, Italia*, Website (2016), http://www.museoscienza.org/extreme

332. *Anfang – Wie alles begann. Von Galaxien, Quarks und Kollisionen. Naturhistorisches Museum Wien, Austria*, Website (2016), http://www.nhm-wien.ac.at/anfang

333. F. Giffoni, F. Massimo, *Scientific research at CERN as a public good: a Survey to French citizens*, CERN-ACC-2018-0024 (CERN, Geneva, Switzerland, August, 2018), Preprint CERN-ACC-2018-0024, https://cds.cern.ch/record/2635861

334. M. Cabriol, *La France booste le budget du CNES en 2017*, La Tribune newspaper website, https://www.latribune.fr/entreprises-finance/industrie/aeronautique-defense/la-france-booste-le-budget-du-cnes-en-2017-629755.html

335. A. Augier, B. Gindre, *Préparation de l'accompagnement stratégie en concertation socio-territoriale dans le cadre de l'étude FCC*, Final project report EDMS 1745888 (IDDEST – Institut durable de développement économique, social & territorial, January, 2017), Access to the report is subject to a NDA

336. M. Sauvain, *Rapport d'étude relatif aux procédures administratives sur le territoire suisse* Rapport de la Structure de Concertation Permanente EDMS 20258995 V1.0, Latitude Durable (November, 2018), https://edms.cern.ch/document/2025895, Access to the report is subject to an NDA

337. European Strategy Forum on Research Infrastructures, *Strategy Report on Research Infrstructures, Roadmap 2018* Roadmap 2018 (ESFRI, August, 2018), http://roadmap2018.esfri.eu/media/1066/esfri-roadmap-2018.pdf

338. European Strategy Forum on Research Infrastructures, *Public Roadmap 2018 Guide* Guide 2018 (ESFRI, December, 2016), https://ec.europa.eu/research/infrastructures/pdf/esfri/esfri_roadmap/esfri_rd2018_guide_for_appplicants.pdf

339. A. Ballarino, L. Bottura, *Targets for R&D on Nb3Sn conductor for high-energy physics*, IEEE Trans. on Appl. Supercon. **15**, 1 (2015)

340. B. Bordini, The Nb_3Sn wire procured by CERN for the high luminosity upgrade of the large Hadron collider, in *Proceedings of the ASC'18*, IEEE Conference Proceedings (IEEE, Seattle, USA, October, 2018), forthcoming in 2018 on IEEE XPlore

341. CERN EP Department, *R&D on Experimental Technologies*, Project Website, https://ep-dep.web.cern.ch/rd-experimental-technologies

342. CERN EP Department, *First Workshop on R&D on Experimental Technologies*, Indico Website, https://indico.cern.ch/event/696066/

343. CERN EP Department, *Second Workshop on R&D on Experimental Technologies*, Indico Website, https://indico.cern.ch/event/743661/